

Isotope Science Facility at Michigan State University

Upgrade of the NSCL rare isotope
research capabilities

MSUCL-1345

November 2006

| | |
|--|------------|
| Preface | 5 |
| Acknowledgements | 5 |
| Executive Summary | 7 |
| 1. Introduction and overview | 9 |
| 1.1 Perspectives on rare isotope research | 11 |
| 1.2 Overview of the NSCL | 14 |
| 1.2.1 Research tradition | 14 |
| 1.2.2 NSCL's role as a national user facility | 17 |
| 1.2.3 Synergy of research, education, and outreach | 18 |
| 1.2.4 Cross-disciplinary research and technical outreach | 19 |
| 1.3 Planning considerations | 19 |
| 1.4 ISF layout, cost-reduction option, and upgrade options | 23 |
| 1.5 Scientific opportunities with the ISF | 29 |
| 1.5.1 The context of mesoscopic theory | 29 |
| 1.5.2 Properties of nuclei with unusual neutron-to-proton ratios | 31 |
| 1.5.3 The context of astrophysics | 35 |
| 1.5.4 Tests of fundamental symmetries | 38 |
| 1.5.5 Applications in other disciplines | 39 |
| 1.6 Document organization | 39 |
| 2. Physics of nuclei | 41 |
| 2.1 At the neutron dripline | 43 |
| 2.1.1 Existence | 44 |
| 2.1.2 Beyond the neutron dripline | 44 |
| 2.1.3 Search for two-neutron emitters | 46 |
| 2.1.4 Beta-delayed neutron emission | 48 |
| 2.1.5 Halos | 49 |
| 2.1.6 Neutron skins | 51 |
| 2.2 Along the path of the proton dripline | 54 |
| 2.2.1 Mapping the proton dripline | 55 |
| 2.2.2 Proton radioactivity | 57 |
| 2.2.3 Two-proton emitters | 58 |
| 2.2.4 Short-lived proton-unbound states | 59 |
| 2.3 Evolution of shell gaps | 60 |
| 2.3.1 Signatures of shell gaps from masses and nucleon separation energies | 62 |
| 2.3.2 Information on shell gaps from yrast excitations | 64 |
| 2.3.3 Single-particle structure near shell closures | 69 |
| 2.3.4 Search for new islands of inversion | 74 |
| 2.3.5 Magnetic moments and mirror symmetry | 76 |
| 2.3.6 Electric quadrupole moments and core polarization | 77 |
| 2.3.7 The shell structure of the heaviest elements | 79 |
| 2.4 Nature of the nuclear wave function and the correlated many-body system | 82 |
| 2.4.1 Spectroscopic factors and correlation effects | 82 |
| 2.4.2 Two-nucleon correlations | 85 |
| 2.4.3 Proton-neutron pairing | 88 |
| 2.5 Physics of deformed nuclei | 89 |
| 2.5.1 Nuclear sizes and shapes | 90 |
| 2.5.2 Deformation driven shell gaps | 95 |
| 2.5.3 Competing shapes | 104 |
| 2.5.4 Collectivity beyond the first 2^+ state | 107 |
| 2.6 Nuclei at high angular momentum | 115 |
| 2.6.1 Super- and hyperdeformation | 116 |

| | | |
|------------|--|------------|
| 2.6.2 | Broken symmetries at high spin | 117 |
| 2.6.3 | High-spin states at band termination and beyond | 119 |
| 2.6.4 | Quantum rotational structures built on exotic isomeric states | 119 |
| 2.7 | Spin-isospin response of nuclei | 121 |
| 2.7.1 | Charge-exchange experiments in inverse kinematics | 124 |
| 2.7.2 | Unstable probes for spin-isospin modes in stable nuclei | 125 |
| 2.8 | Nuclear reactions and the properties of asymmetric nuclear matter | 126 |
| 2.8.1 | The equation of state of asymmetric matter | 126 |
| 2.8.2 | Level densities and the mixed phase of nuclear matter | 133 |
| 2.8.3 | Low energy collision dynamics | 135 |
| 2.8.4 | Fission | 136 |
| 3. | Nuclear astrophysics | 139 |
| 3.1 | The origin of the heavy elements | 139 |
| 3.1.1 | The rapid neutron capture process | 139 |
| 3.1.2 | The p-process | 146 |
| 3.2 | How do stars explode? | 148 |
| 3.2.1 | X-ray bursts and superbursts | 148 |
| 3.2.2 | Supernovae | 152 |
| 3.2.3 | Classical novae | 158 |
| 3.3 | The nature of neutron stars | 160 |
| 3.3.1 | Crust processes in accreting neutron stars | 160 |
| 3.3.2 | The equation of state of dense asymmetric nuclear matter | 163 |
| 4. | Studies of fundamental interactions | 165 |
| 4.1 | Test of CVC and determination of V_{ud} | 165 |
| 4.2 | Atomic parity violation | 167 |
| 4.3 | Tests of parity and time reversal symmetries | 168 |
| 4.4 | Search for new interactions in the weak nucleon current | 169 |
| 4.5 | Search for induced currents in weak interactions | 171 |
| 5. | Isotope Science Facility (ISF) | 173 |
| 5.1 | Driver linac | 175 |
| 5.1.1 | Front end | 176 |
| 5.1.2 | Linac superconducting cavity design | 198 |
| 5.1.3 | Superconducting cavity cryogenic requirements | 201 |
| 5.1.4 | Beam loading, rf, and microphonics requirements | 204 |
| 5.1.5 | Cavity research and development | 206 |
| 5.1.6 | Cryomodule development | 208 |
| 5.1.7 | Accelerating segments | 215 |
| 5.1.8 | Linac stripping sections and beam switchyard | 219 |
| 5.1.9 | End-to-end beam simulations | 231 |
| 5.1.10 | Beam diagnostics | 240 |
| 5.2 | Reaccelerator linac | 242 |
| 5.3 | RF systems and cryogenics | 243 |
| 5.3.1 | Low-level rf | 243 |
| 5.3.2 | High-level rf | 245 |
| 5.3.3 | Cryogenics | 245 |
| 5.4 | Rare isotope beam production | 246 |
| 5.4.1 | Target building | 247 |
| 5.4.2 | In-flight isotope production | 251 |
| 5.5 | Low-energy beam generation via gas stopping of fragment beams | 272 |
| 5.5.1 | Limitations of classical gas stopper concepts | 273 |
| 5.5.2 | The cyclotron stopper | 276 |
| 5.5.3 | Development of the low-energy beam generation system | 285 |

| | | |
|------------|---|------------|
| 5.5.4 | Reacceleration of low-energy beams | 285 |
| 5.6 | Experimental areas | 296 |
| 5.6.1 | Low-energy beam experimental areas | 296 |
| 5.6.2 | Fast beam experimental area | 301 |
| 5.7 | Conventional facilities | 303 |
| 6. | Future upgrade options | 309 |
| 6.1 | Driver linac upgrade | 312 |
| 6.1.1 | SRF cavity design | 312 |
| 6.1.2 | SRF cryogenic requirements | 314 |
| 6.1.3 | SRF beam loading, rf, and microphonics requirements | 316 |
| 6.1.4 | Cryomodule development | 317 |
| 6.1.5 | RF systems and cryogenics | 319 |
| 6.1.6 | The 200 MeV/u beamline | 320 |
| 6.1.7 | Linac segment 4 | 322 |
| 6.1.8 | The 400 MeV/u beamline | 324 |
| 6.1.9 | The 400 MeV/u beam switchyard | 325 |
| 6.1.10 | Beamline to ISOL target 1 | 330 |
| 6.2 | ISOL beam production | 331 |
| 6.2.1 | Rare isotope beam production with the ISOL method | 332 |
| 6.2.2 | ISOL target station | 336 |
| 6.2.3 | High-resolution mass separation | 340 |
| 6.3 | Second target area | 340 |
| 6.3.1 | ISOL beam production | 342 |
| 6.3.2 | In-flight beam production | 342 |
| 6.4 | Experimental areas | 342 |
| 6.5 | Conventional facilities | 344 |
| 7. | NSCL site option | 347 |
| 7.1 | Driver linac | 347 |
| 7.1.1 | Driver linac with cyclotron injector | 349 |
| 7.1.2 | Driver linac with linac injector | 360 |
| 7.2 | Rare isotope beam production | 360 |
| 7.2.1 | Production target | 361 |
| 7.2.2 | Fragment separator | 361 |
| 7.2.3 | Low-energy beam generation and reacceleration | 365 |
| 7.3 | Experimental areas | 366 |
| 7.4 | Conventional facilities | 368 |
| 8. | Project cost estimate | 373 |
| 8.1 | Cost estimating plan | 373 |
| 8.1.1 | Work breakdown structure | 374 |
| 8.1.2 | Confidence indicator and basis of estimate | 374 |
| 8.1.3 | Contingency, risk analyses, and risk assessment methodology | 375 |
| 8.1.4 | Labor pricing | 376 |
| 8.1.5 | Escalation | 376 |
| 8.2 | ISF (south campus option) costs | 376 |
| 8.3 | Costs of future upgrade options | 380 |
| 8.4 | NSCL site option costs | 381 |
| 8.5 | Cost summary | 385 |
| | Epitome | 387 |
| | References | 389 |
| | Abbreviations | 409 |



Preface

This document describes plans for building a new nuclear science facility – the working name is Isotope Science Facility, or ISF – that would greatly strengthen U.S. research capabilities with beams of rare isotopes. The heart of the ISF is a high-power superconducting heavy-ion linear accelerator capable of delivering primary beams that range from protons to uranium with variable energies of at least 200 MeV/nucleon and beam power reaching up to 400 kW. The primary beams will be used to produce secondary rare isotope beams that can be studied at rest, as reaccelerated beams, and as fast beams at intensities higher by several orders of magnitude than those currently available in the United States. The new beam intensities will be competitive with, and often exceed, those at facilities that will be completed elsewhere during the next 10 to 15 years.

The ISF, to be built on the campus of Michigan State University (MSU), will replace NSCL's Coupled Cyclotron Facility (CCF) and greatly enhance its capabilities as a national user facility for rare isotope research and center for educating the next generation of nuclear scientists. ISF construction will take full advantage of NSCL expertise in rare isotope research. Major cost savings will be achieved by reuse of NSCL equipment.

Acknowledgments

The ISF design was developed at MSU with detailed input from the nuclear science community. The design process relied on many documents that have outlined the scientific case for rare isotope science and various facilities considered to carry out this science. Most of these documents are available at www.orau.org/ria/history.htm.

The material contained in this document came from many sources. The scientific justification for the ISF benefited from presentations and discussions with more than three hundred participants at 10 scientific meetings and workshops held within the last two years at the NSCL, many discussions with NSCL users, and input of the NSCL User Executive Committee. We wish to acknowledge the many scientists listed below who participated in focused workshops on ISF topics, discussions of key points, and recent research collaborations; all of them helped shape the science focus and the evolving plans for the ISF. In particular, we thank the colleagues who provided in-depth editorial review and comment on this document. We apologize in advance to anyone that we have inadvertently neglected to mention.

Any and all requests for additional information are welcome and should be addressed to Konrad Gelbke at the NSCL.

Larry Ahle, LLNL
Andrei Andreyev, TRIUMF
Naftali Auerbach, Tel-Aviv University
Pierre Bauer, FNAL
James R. Beene, ORNL
Jeff Blackmon, ORNL
Jason Boles, LLNL
Pierre Bricault, TRIUMF
Thomas W. Burgess, ORNL
Ed Cackett, University of Michigan

Friedhelm Ames, TRIUMF
Claire Antoine, FNAL/Saclay
Bruce Barrett, University of Arizona
Edward Beebe, BNL
John Behr, TRIUMF
Cristian Boffo, FNAL
Todd Bredeweg, LANL
James Brown, Wabash College
Peter Butler, University of Liverpool
Pierre Capel, TRIUMF

Robert Charity, Washington University
Yanglai Cho, ANL
Tim Chupp, University of Michigan
Charlie Cooper, FNAL
Barry Davids, TRIUMF
Daniel DeVries, University of Michigan
Massimo Di Toro, LNS/INFN
Hans Emling, GSI
Michael Famiano, Western Michigan Univ.
Zsolt Fulop, ATOMKI, Hungary
Alejandro Garcia, Univ. of Washington
Paul Garrett, University of Guelph
Joachim Goerres, University Notre Dame
Uwe Greife, Colorado School of Mines
Alex Gurevich, University of Wisconsin
Joseph Hamilton, Vanderbilt University
Alexander Heger, LANL
Frank Herfurth, GSI
Meredith Howard, Ohio State University
Sylvie Hudan, Indiana University
Robert Janssens, ANL
Oliver Kester, GSI
I-Yang Lee, LBNL
Bao-An Li, Texas A&M University
W. Gary Love, University of Georgia
David Lunney, Orsay
Lou Mansur, ORNL
Bradley Meyer, Clemson University
Robert B. Moore, McGill University
Witek Nazarewicz, ORNL
Meiring Nortier, LANL
Takaharu Otsuka, University of Tokyo
Jean Michel Poutissou, TRIUMF
Claude R. Reed, ANL
Susana Reyes, LLNL
Warren Rogers, Westmont College
Paul Schmor, TRIUMF
Nathal Severijns, Katholieke Univ. Leuven
Lee G. Sobotka, Washington University
Mark Stoyer, LLNL
Sam Tabor, Florida State University
Jan Toke, University of Rochester
Paul Vetter, LBNL
Michiharu Wada, RIKEN
Tom Wangler, LANL
Mark W. Wendel, ORNL
Ingo Wiedenhoever, Florida State Univ.
Andreas Woehr, Univ. of Notre Dame
Phil Woods, University of Edinburgh
Kevin Yoon, Northwestern University

Alan Chen, McMaster University
Phillipe Chomaz, GANIL
David L. Conner, ORNL
Manoel Couder, University Notre Dame
David Dean, ORNL
Paul DeYoung, Hope College
Jens Dilling, TRIUMF
Paul Fallon, LBNL
Joseph Finck, Central Michigan University
Tony A. Gabriel, ORNL
Umesh Garg, University of Notre Dame
Hans Geissel, GSI
Itacil C. Gomes, IC Gomes Consulting
Robert Grzywacz, University of Tennessee
Ikuko Hamamoto, Lund University
Muhsin N. Harakeh, KVI Groningen
Lawrence Heilbronn, LBNL
Rolf-Dietmar Herzberg, Univ. of Liverpool
Ruth Howes, Marquette University
Christian Iliadis, Univ. of North Carolina
Kate Jones, Rutgers University
Peter Lee, University of Wisconsin
Daniela Leitner, LBNL
Jose Lopez-Urrutia, MPI Heidelberg
Sergei Lukyanov, Flerov Institute
Augusto Macchiavelli, LBNL
Cliff Mark, TRIUMF
Yoichi Momozaki, ANL
Lutz Moritz, TRIUMF
Jerry Nolen, ANL
Erich Ormand, LLNL
Peter Parker, Yale University
David Radford, ORNL
Igor Remec, ORNL
Mark Riley, Florida State University
Hiro Sakurai, RIKEN
David Seidman, Northwestern University
Ed Smith, Ohio State University
Werner Stein, LLNL
Daniel W. Stracener, ORNL
Wan-Peng Tan, University of Notre Dame
Jeffrey A. Tostevin, University of Surrey
David Vieira, LANL
Phil Walker, University of Surrey
Frederik Wendander, CERN
Kipp Whittaker, LLNL
Michael Wiescher, Notre Dame
Hermann H. Wolter, University of Munich
Alan Wuosmaa, Univ. of Western Michigan
Dave Youngblood, Texas A&M University

Executive summary

This document describes the science motivation and technical plans for upgrading the rare isotope research capability at the National Superconducting Cyclotron Laboratory (NSCL) by replacing its Coupled Cyclotron Facility (CCF) with a more powerful facility – the Isotope Science Facility (ISF). The ISF will provide the nuclear science research community with significantly increased intensities and varieties of world-class beams of rare isotopes. It will take full advantage of the in-flight production technique's short beam development and fast isotope separation times and provide maximum flexibility to experimenters to choose the most appropriate approach to each problem.

ISF construction will build upon the strength and expertise of NSCL faculty and staff and utilize NSCL equipment (extant and under construction) to achieve major cost savings. The proposed site is a new location on the MSU south campus, which offers an unconstrained and fully optimized facility layout with ample space for future science-driven upgrades. Transition from CCF operation to ISF operation can be accomplished with about six months disruption of the ongoing experimental program. The construction cost in FY06 dollars is slightly less than \$500 million. A less favored alternative of building the ISF on the current NSCL site would reduce the cost by roughly 20%, but would require significant sacrifices.

The heart of the proposed ISF is a high-power superconducting heavy-ion linear accelerator capable of delivering beams of all stable elements with variable energies up to at least 200 MeV/nucleon and beam power up to 400 kW. This accelerator will make it possible to produce rare isotope beams with even the shortest half-lives at unprecedented intensities, using in-flight production and separation techniques.

The ISF reaccelerated beam facility will incorporate an advanced cyclotron stopper, an EBIT (Electron Beam Ion Trap) charge-breeder, and, for reacceleration, a superconducting linac that will be built at the NSCL over the next few years. The ISF reacceleration linac will be capable of reaccelerating thermalized beams of rare isotopes to energies of at least 12 MeV/nucleon over the entire mass range. Together with the fast beams from in-flight production, the ISF will provide a broad spectrum of rare isotope beams with energies between 0 and 200 MeV/nucleon. ISF beam intensities will be competitive with and often exceed those at the facilities worldwide that will be completed during the next 10 to 15 years. Such intensities are higher by several orders of magnitude than those currently possible at the CCF or anywhere else today.

The ISF relies on modular, expandable, and optimized concepts to fulfill the evolving needs of the rare isotope research community. The modular approach allows upgrades to proceed with minimal impact on the existing research program. For example, if needed, higher energy (primary or secondary) beams are possible by a straightforward addition of accelerator cryo-modules. The civil infrastructure for a high-power ISOL target for rare isotope production is part of the current baseline ISF plan. This will allow for full implementation of a high-power ISOL target and the associated isobar separator with a modest upgrade and minimal facility downtime. The future scientific needs of the community will dictate the priority for these or any other upgrades.

The ISF will build on the tradition within MSU, the NSCL, and the user community of excellent undergraduate, graduate, and post-doctoral education. Its location on the MSU campus will greatly facilitate educating the next generation of nuclear scientists by continuing the NSCL's hands-on approach to scientific education in experimental and theoretical nuclear physics, nuclear chemistry, accelerator physics and engineering, nuclear astrophysics, and related instrumentation and societal applications. The university setting also facilitates public awareness and understanding of nuclear science as well as the development of cross-disciplinary teams.

The ISF will allow major advances in nuclear science and nuclear astrophysics by providing intense beams of nuclei far from stability at energies from a few keV to up to 200 MeV/nucleon. The main experimental program will be exploring the limits of nuclear stability and determining nuclear properties in the uncharted regions of nuclei with very unusual proton-to-neutron ratios. ISF-produced data will guide the development of reliable theoretical models with predictive power for key nuclear properties. The broader impact of the ISF experimental program and the new predictive models will provide insight into the nature of many-body quantum systems and mesoscopic science. ISF research will explore the unique features of nuclei and facilitate intellectual links to studies of mesoscopic systems in chemistry, biology, and nanoscience.

Intense beams of neutron-rich isotopes will add to our knowledge of the very heavy elements by allowing the synthesis of transactinide nuclei that are more neutron rich than those possible with stable beams. These nuclei are predicted to be more strongly bound and longer-lived and thus could be accessible to chemical study.

Nuclear data generated by the ISF will help to develop reliable models of astrophysical environments that describe nucleosynthesis and stellar evolution in the cosmos, especially models of explosive events, such as X-ray bursts, core-collapse supernovae, thermonuclear (Type Ia) supernovae, and novae. Sound astrophysical models are needed to extract reliable information on astrophysical objects from the high-quality observational data produced by ground and space-based observatories.

Energetic nucleus-nucleus collision experiments at the ISF will allow exploration of the equation of state of neutron-rich nuclear matter near normal and subnormal nuclear densities. This knowledge plays an important role in determining the properties of neutron stars.

Rare isotopes produced by the ISF can be used in testing fundamental symmetries that describe the strong and weak forces in nature and searching for new physics beyond the Standard Model. The availability of a broad range of isotopes makes it possible to select the best, specific nuclear system that can isolate or amplify specific physics of interest.

The ISF also will produce many new isotopes in research quantities offering opportunities for cross-disciplinary work, such as research linked to national security, biomedicine, or nuclear energy. Often such work can proceed concurrently, provided that the required infrastructure is put in place by appropriate modular additions.

1. Introduction and overview

Nuclear science probes the origin, evolution, and structure of matter comprising the cosmos – stars, planets, and humankind. The coming two decades promise breathtaking progress in this quest and in the development and application of new nuclear techniques for material science, medicine, and bio- and nanotechnology. Countries in Europe and Asia are investing in advanced new rare isotope facilities to compete globally in this important field of science. While the current facilities at the National Superconducting Cyclotron Laboratory (NSCL) are on the cutting edge, additional investments are needed to ensure ongoing U.S. competitiveness.

Nuclear physics research began at Michigan State University (MSU) in 1958. Since then MSU has become known for its innovations in nuclear science and associated cross-disciplinary and societal applications, both in the United States and worldwide. Major contributions have been made in the fields of nuclear structure, nuclear astrophysics, heavy-ion reaction mechanisms, accelerator physics, beam dynamics, and experimental techniques. Over the years, the NSCL has evolved into the largest campus-based nuclear science facility, with approximately 300 employees, including 28 faculty and about 100 students, half of them doctoral students. MSU awards approximately 10% of the nation's nuclear science doctorates. The NSCL is one of three nuclear science user facilities explicitly mentioned in the highest priority recommendation of the most recent (2002) Long Range Plan for Nuclear Science [NSAC02] of the DOE/NSF Nuclear Science Advisory Committee (NSAC).

In 2001, the NSCL finished its most recent capability upgrade, completing the Coupled Cyclotron Facility (CCF) on time and on budget. Currently, the CCF operates with greater than 90% availability and produces world-class beams of rare isotopes using the in-flight separation technique. Beams delivered to experiments are shown in Figure 1.1. The CCF serves a user community of more than 700 registered scientists. Demand far exceeds the available beam time and constitutes a strong science-driven pressure for an upgrade to an enhanced, next-generation capability.

In his July 2006 Memorandum to the National Science Board [NSB06], NSF Director Arden Bement, Jr. describes NSCL's likely preeminent status for the next decade while addressing challenges that lay further in the future:

“The NSCL is the premier laboratory in North America for generating isotopes using the beam fragmentation method... As the nation's largest university-campus based nuclear-science facility, the NSCL plays a unique role in educating the next generation of nuclear scientists and accelerator physicists and engineers by providing outstanding hands-on learning opportunities to a large number of undergraduate and graduate students and postdocs... The management of NSCL by the MSU faculty has been exemplary; the operation of the facility and service to a broad community has been excellent; and the funding level has been reviewed by a series of review panels and found to be very cost effective... The lifetime of NSCL in its present reincarnation is on the order of ten years. The NSCL is now in a world-leadership position and will be a primary center of rare isotope studies until overtaken by the next generation rare isotope facility, sometime in the next decade... Thus, the NSCL-CCF serves as a focal point, both for the immediate generation of experiments, and for planning, design and possible construction of any

- The facility enhances the nation’s nuclear workforce by providing a center for education and research. The ISF leverages the many benefits inherent in a campus-based facility, such as the student population, academic environment, and myriad opportunities for cross-disciplinary research.
- The ISF builds upon existing expertise related to accelerator physics, rare isotope research, and experience in operating a major national user facility.
- The ISF will allow modular science-driven upgrades in the future that could be implemented cost-effectively and without major disruption of the ongoing research and education program.

This report is intended for those readers in the U.S. and international nuclear and accelerator science communities seeking more details than can be reasonably presented within the page constraints of a journal article or conference proceedings. Of course, we continue to welcome comments and suggestions for improvements of the ISF design.

1.1 Perspectives on rare isotope research

At the center of each atom is the atomic nucleus. Though ten thousand times smaller than the atom itself, the nucleus contains more than 99.9% of the atomic mass. Atomic nuclei are made of positively charged protons and of neutrons that do not carry a net electric charge. The number of protons in a given nucleus determines its element. Fewer than 100 elements occur naturally on Earth and each exhibits essentially distinct chemical behaviors.

For more than a century, scientists have known that atoms of a given element come in variants, or isotopes, distinguished by mass. Isotopes of a given element have different numbers of neutrons. An element’s various isotopes are chemically indistinguishable but can have vastly different nuclear properties.

Of all the combinations of protons and neutrons, fewer than 300 form stable nuclei, i.e., they do not decay on time scales comparable to the age of our solar system. All other nuclei spontaneously decay and thus are radioactive. Lifetimes for these unstable nuclei range from shorter than hundredths of a second to longer than billions of years.

When displayed as points on a graph of proton number versus neutron number, the stable isotopes lie along the line of stability. Some distance from this line, also referred to as the valley of stability, lies a scientific frontier beyond which the properties of nuclei are unknown (see Figure 1.2).

Today, scientists lack the tools necessary to explore this terra incognita of rare isotopes that all decayed in our solar system and hence do not normally exist on Earth. Yet thousands of these isotopes are continually created and play a fleeting though important role in the cosmos. The evolution of stars from birth to often cataclysmic death is intertwined with the nuclear reactions that occur inside stars and are responsible for the formation of many elements. The resulting elemental abundances influenced the processes that formed our solar system and ultimately led to life on Earth. Inadequate knowledge of important nuclear properties limits understanding of these important astrophysical processes, which today is rudimentary, at best.

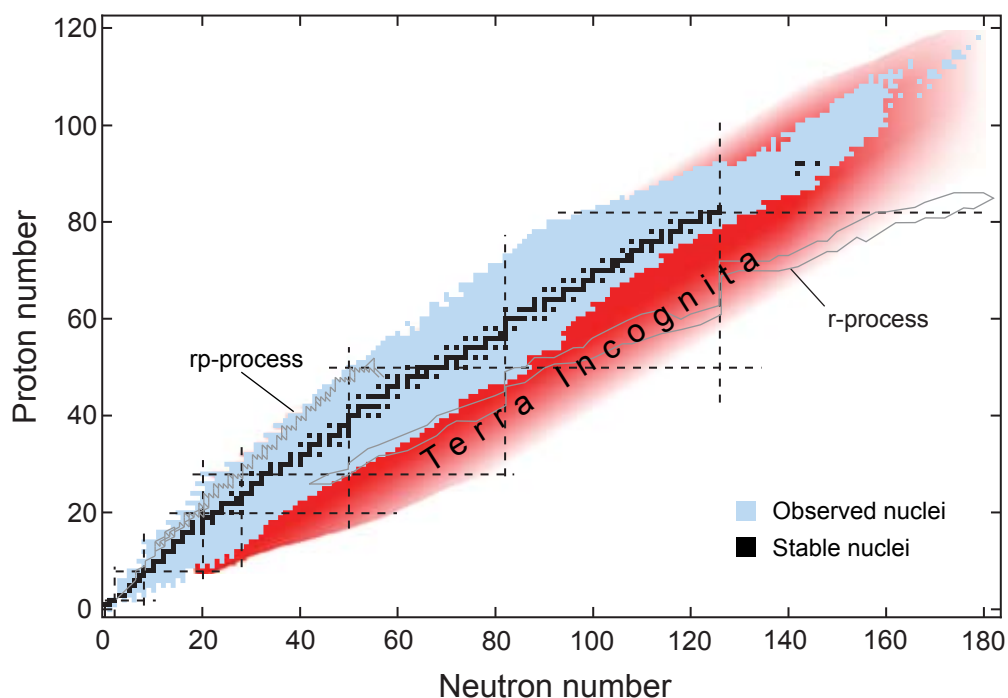


Figure 1.2: Chart of nuclei (element or proton number Z versus neutron number N): stable nuclei along the valley of stability are shown in black, isotopes that have been detected at least once on Earth are shown in blue, and the large terrain of unknown nuclei is shown in red. The estimated paths for the r- and rp-processes for explosive nucleosynthesis in the cosmos are indicated by solid lines.

Technical advances now make it possible to create and study many short-lived nuclei in the laboratory. Because they are far from the valley of stability, such nuclei challenge theories developed to explain properties of nuclei near the line of stability. Additionally, nuclei are an example of mesoscopic systems such as atomic clusters or quantum dots that are important in other fields of physics today. Among these systems, nuclei present a particular advantage to researchers. Namely, nuclei consist of two distinct types of fermions, neutrons and protons, whose relative number can be varied in a system of constant size.

Microscopic treatments combined with advanced computation techniques provide fairly accurate descriptions of the properties of very light (12 nucleons or fewer: $A = N + Z \leq 12$) nuclei. Computational limitations make such treatments unfeasible for heavier nuclei and additional approximations to the many-body quantum problem are necessary. Major advances should result from investigation of nuclei with very different proton-to-neutron admixtures and targeted experiments that isolate important ingredients of many-body theory. For example, if a nuclear property depends on the difference in neutron and proton numbers, $N - Z$, this property will be enhanced far from the valley of stability, where this difference might be 25 rather than 5 , and thus will require a much more accurate theoretical explanation. Such investigations require an advanced and versatile rare isotope research facility such as the ISF.

Beams of rare isotopes very far from stability are needed to determine the nature of nuclear processes that underlie the evolution of stars and the origin of the elements. Extremely neutron- and proton-rich isotopes strongly influence processes

that take place in various explosive stellar environments. A more thorough understanding of such isotopes will better enable us to interpret observations of novae, supernovae, or X-ray-bursts made with ground- or space-based instruments.

Rare isotopes from the ISF are also useful to make tests of fundamental symmetries and the Standard Model of particle physics. The ISF will provide access to sufficient quantities of specific isotopes for which the physics of interest is isolated or amplified.

The application of rare isotope research to astronomy and fundamental symmetries are examples of the broader impact of this field. Cross-disciplinary links to astrophysics, fundamental interaction studies, and the physics of mesoscopic systems will be further discussed in the main body of this document. Biomedical research and medicine, science-based stockpile stewardship, and transmutation of nuclear waste will benefit from research at ISF and from anticipated targeted upgrades of the facility. The ISF will result in a stream of well-trained nuclear science Ph.D.'s who understand atomic nuclei and rare isotopes and are intellectually equipped to advance various cross-disciplinary applications.

The importance of the core ISF science mission has been demonstrated by rare isotope research begun at the NSCL and at other facilities worldwide, including ATLAS (ANL), GANIL (France), GSI (Germany), ISAC (TRIUMF, Canada), HRIBF (ORNL), ISOLDE (CERN, Switzerland), and RIKEN (Japan). However, pushing the science forward requires a new generation of more powerful facilities, such as the ISF, which are wholly dedicated to the production and study of short-lived isotopes very far from the line of stability.

Two techniques of isotope production and separation are currently pursued worldwide: production at rest followed by Isotope-Separation-On-Line (ISOL-technique) and production and separation in flight using intermediate energy ($\sim 100\text{--}1000$ MeV/nucleon) heavy ions.

The traditional ISOL technique produces isotopes at rest in thick targets from which they must be extracted by diffusion and effusion before they can be ionized, separated, and accelerated. Typical diffusion and effusion times are on the order of seconds. For very short-lived isotopes with lifetimes in the millisecond range, losses due to decay in the target material can become large. Beam development typically involves both physical and chemical methods and requires a substantial amount of time and effort, often months. The ISOL technique has been the technique of choice for producing high-quality low-energy beams for studies at rest (e.g., in ion or atom traps) and for studies near the Coulomb barrier with transfer reactions, multistep Coulomb excitation, and sub-barrier fusion or capture reactions. For decades the ISOLDE facility at CERN (Switzerland) led the advances in the field. More recently, the ISAC facility at TRIUMF (Canada) has become the premier ISOL facility on the American continent with a driver accelerator capable of producing a 500 MeV proton beam of up to 150 kW beam power. Other important ISOL capabilities exist at ORNL and GANIL (France) and Louvain-la-Neuve (Belgium).

The in-flight technique entails accelerating heavy ions to intermediate energies ($\sim 100\text{--}1000$ MeV/nucleon) and producing fast moving secondary nuclei in a transmission target, often by projectile fragmentation or fission. The fast moving rare

isotopes are separated in flight. Among other advantages, the in-flight technique allows for sub-microsecond isotope separation by purely physical methods and with short beam development times (1–2 days). Losses from decays are negligible. In-flight production and separation is the technique of choice for experiments requiring energetic beams: knockout reactions, charge-exchange reactions, spin-flip excitations, and studies of giant resonances, etc. In most cases, the in-flight technique is preferred for studying very short-lived isotopes and rare isotopes of refractory elements that are difficult or impossible to access with the ISOL technique. In-flight separation also provides a greater reach toward the driplines, both because thick targets can be used and because ions in mixed beams (cocktail beams) can be identified one by one, thus allowing simultaneous experiments on many different isotopes. Rare isotopes produced with this technique have recently been stopped in and extracted from a helium gas cell and used in precision ion-trap experiments. There is great interest in developing efficient techniques for reaccelerating such beams. In-flight capabilities exist at the NSCL, GSI (Germany), GANIL (France), and RIKEN (Japan). With the exception of the NSCL, all these laboratories are implementing major capability upgrades.

While complementary, the ISOL and in-flight production techniques also allow a seamless overlap and provide beams of all elements over a wide range of half-lives and energies from rest to the level of GeV/nucleon. Several important questions can be addressed both with reaccelerated beams and with fast beams separated in flight, allowing case-by-case optimization as well as important crosschecks between complementary approaches, e.g., when the extracted physics requires a solid understanding of the reaction mechanism.

In comparison with other facilities under construction or approved for construction in the world, the ISF will be unique by using a high-power heavy-ion driver linac capable of producing nearly 10 times more beam power. The ISF is designed to take full advantage of the enormously versatile in-flight production technique and to provide opportunities for experiments over the full gamut of energies from rest to approximately 200 MeV/nucleon. Rare isotopes produced and separated in flight can be used directly for fast-beam experiments at 20–200 MeV/nucleon. The fragments can also be stopped in a gas cell from which they can be extracted and used for very-low energy experiments, or they can be reaccelerated up to 12 MeV/nucleon. The ISF will have cutting-edge capabilities for rare isotope research and, in addition, flexibility for implementing selected science-driven upgrade options without significant disruption of the ongoing research program.

1.2 Overview of the NSCL

1.2.1 Research tradition

The MSU nuclear physics program began in 1958 as an initiative of the Department of Physics. In 1961, the NSF funded construction of the K50 cyclotron, which became the world's first high-resolution isochronous cyclotron using new single-turn extraction techniques developed at MSU. During the next two decades, the MSU faculty established an international reputation for its high-quality nuclear science research and instrumentation development program. University researchers achieved unprecedented resolution for charged-particle spectroscopy experiments that combined the advantages of single turn extraction, dispersion matching,

and an Enge magnetic spectrograph. High-resolution neutron spectroscopy experiments were made possible over a wide range of angles by means of an innovative “swinger” magnet. This device allowed for variation of the incident beam-direction and measurement of angular distributions of neutrons with a fixed neutron-detector and a very long flight path.

In 1975, NSF approved construction of a prototype superconducting magnet that later became the main magnet for the NSCL’s K500 cyclotron, the world’s first operational superconducting cyclotron. Constructing the magnet laid the foundation for the laboratory’s leadership in applications of superconductivity to nuclear physics accelerators and beam transport and analysis systems.

In 1978, the NSF/DOE Nuclear Science Advisory Committee (NSAC) recommended construction of the NSCL as a national user facility, involving construction of a K1200 cyclotron, a larger version of the K500. In 1982, the first beam was extracted from the K500 cyclotron and the K500 nuclear science program was initiated with a modest array of equipment, largely carried over from the K50. In 1988, the first beam was extracted from the K1200 cyclotron, and an interim research program was initiated with a new 92” scattering chamber and a partially completed 4π charged-particle array installed in series on a temporary beamline. Concurrently, the remaining superconducting beam transport system was completed.

In October 1990, the full experimental program began after an eight-month shutdown to install the superconducting beam transport system and the superconducting A1200 fragment separator/beam-analysis system, the world’s first superconducting fragment separator. The K1200 cyclotron was injected by newly developed Electron Cyclotron Resonance (ECR) ion sources and was equipped with a variety of new devices for research in nuclear science. During the next nine years, the K1200 cyclotron operated in support of a national user program in experimental heavy-ion science that attracted scientists from around the world. In particular, the K1200 and its A1200 beam analysis system became a major source of beams with rare isotopes, mostly of modest intensities. Rare, short-lived isotopes were produced via projectile fragmentation of the primary cyclotron beam and then separated in flight with the A1200 fragment separator/beam-analysis system. The NSCL was the first laboratory in the world that allowed transport of these rare isotope beams to all its beamlines, setting the stage for its current leadership position in rare isotope research.

In 1993, the NSF approved construction of the S800, a high-resolution large-solid-angle superconducting magnetic spectrograph that was completed in 1996. The S800 remains a state-of-the art instrument with a maximum rigidity of 1.2 GeV/c, an energy resolution of 10^4 , an energy range of 10%, and a large angular acceptance: $\Delta\theta = 10^\circ$ and $\Delta\phi = 7^\circ$. The S800 was used in many pioneering experiments and plays a crucial role in the NSCL’s rare-isotope research program.

In 1994, the NSCL proposed a major capability upgrade by refurbishing and coupling its two superconducting cyclotrons (the K500 and the K1200) and building a high-acceptance superconducting fragment separator, still the world’s largest acceptance fragment separator. The technology developed for the A1900 was used in the fragment separator at the next generation rare isotope facility nearing completion at RIKEN. In 1995, NSAC recommended an immediate NSCL upgrade and the NSF approved the construction of the CCF in 1996. Research with the stand-alone

K1200 continued until the end of June 1999. Operation of the NSCL as a national user facility was suspended from July 1999 through May 2001 to allow the needed reconfiguration of the highbay. The CCF was completed in time and within budget. Operations began in July 2001.

In recent years, the NSCL has designed, built, and implemented a state-of-the-art array of experiment apparatus, much of it unique at the time of conception. Examples include various advanced charged-particle, γ -ray, and neutron detection arrays; high-speed tracking detectors; a highly granular β -detection system suitable for use with cocktail beams; a superconducting sweeper magnet to allow neutron coincidence experiments around zero degrees; and a helium-gas cell followed by a low energy beam transport and ion trap system (LEBIT) for precision mass measurements. In the future, LEBIT will be used for laser spectroscopy of short-lived isotopes produced by projectile fragmentation. A new Radio Frequency Fragment Separator (RFFS) for background suppression with very proton-rich beams and a digital data-acquisition system for improved γ -ray tracking are nearing completion. The current NSCL facility layout is shown in Figure 1.3.

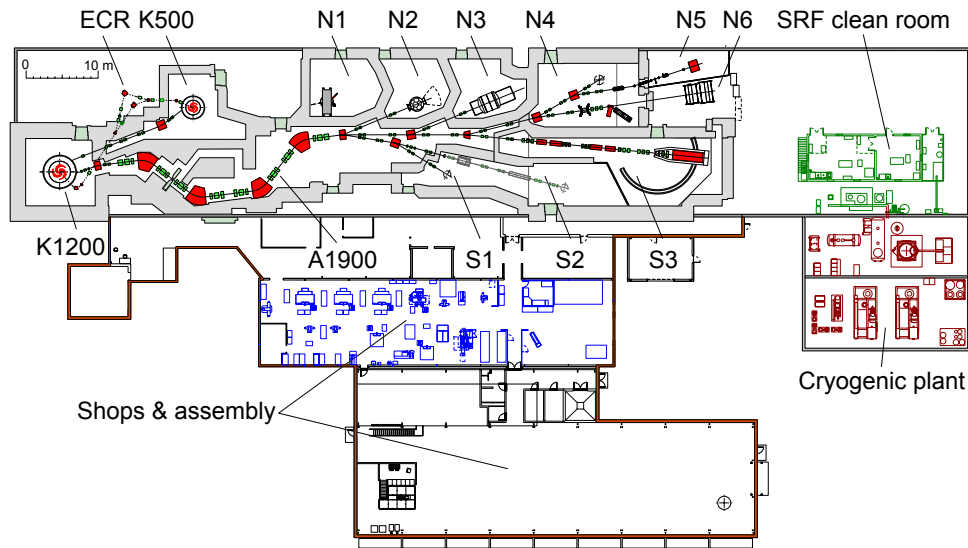


Figure 1.3: Layout of the NSCL's technical facilities as of September 2006.

By the end of 2007, the experimental area will have undergone a significant reconfiguration to remove equipment no longer used, allow more efficient use of existing or new equipment, and shorten the time needed to tune and deliver rare isotope beams.

In the coming years, the NSCL will design and build a novel high-performance cyclotron stopper followed by an Electron Beam Ion Trap (EBIT) charge breeder and a 3.2 MeV/nucleon superconducting linac. This comprises a full performance test of the gas-stopping and reacceleration concept that is at the heart of the proposed reacceleration capability. High-intensity beams with energies near 100 MeV/nucleon will be brought to rest in the stopper, extracted quickly with minimum energy losses, and reaccelerated in an efficient linear accelerator. Figure 1.4 illustrates the planned evolution of the NSCL facility over the next few years.

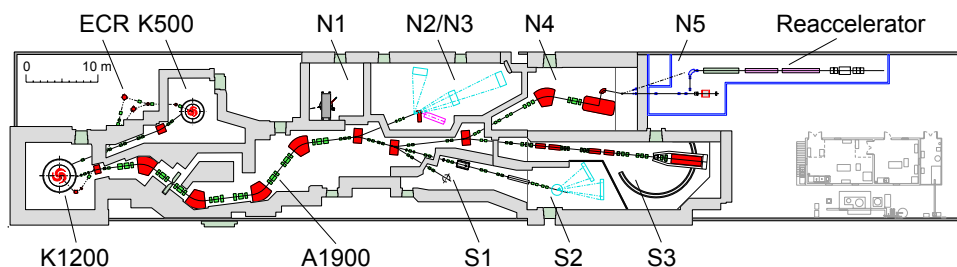


Figure 1.4: Current three-year plan for reconfiguring the NSCL highbay showing rearranged and new equipment in the north experimental vaults (N2–N5) and construction of a reaccelerator.

1.2.2 NSCL's role as a national user facility

The cooperative agreement (PHY-0110253) between NSF and MSU states, “The overall mission of the National Superconducting Cyclotron Laboratory (NSCL) is to provide forefront research opportunities for the national nuclear physics community.... Under this Agreement, MSU will continue to operate the NSCL for support of its users and for support of the research of the MSU staff and students in nuclear science and in accelerator and instrumentation physics.”

The NSCL's coupled cyclotrons are capable of accelerating beams of light to medium mass up to 200 MeV/nucleon (for $Q/A = 0.5$) with beam power up to 1–2 kW, depending on the ion species and ion source performance. The intensities and energy per nucleon decrease significantly for beams heavier than $A \sim 80$. For example, bismuth has been accelerated up to 80 MeV/nucleon with a beam power of 17 W; for uranium, the beam power is even lower. The updated list of driver beams is given at the NSCL website www.nsl.msue.edu/aud/exp/propexp/beamlist.php.

The NSCL serves a national and international user group of more than 700 registered members. Formal contact and interaction with the user group occurs primarily through monthly teleconferences with the elected User Executive Committee and at least one large annual user meeting. In addition, users receive regular updates via postings at the NSCL website and a bimonthly newsletter. Research at the NSCL is primarily devoted to basic nuclear physics, nuclear astrophysics, accelerator physics, and associated instrumentation research and development. About 5–10% of beam time is allocated to cross-disciplinary and applied research.

Beam time is approved by the NSCL director who is advised by the NSCL Program Advisory Committee (PAC), which consists of seven internationally accomplished experts. One PAC member is an NSCL faculty member and six are from other institutions. The PAC typically meets every seven or eight months to evaluate and rank written proposals for beam time according to scientific merit and feasibility. The proposal quality is generally very high, but many very good proposals cannot be approved since requests far exceed the available time.

In the most recent 12-month period (October 1, 2005 – September 30, 2006) the NSCL operated for a total of 6,007 hours with a facility availability of 92.73%. During this period, a total of 40 primary beam tunes and 57 rare isotope beam tunes were delivered to experimental users. By this measure, the NSCL's CCF is the most versatile and reliable rare isotope user facility in the North America. User satisfaction as determined by various survey mechanisms is very high.

Over the years, the demand for rare isotope beams has moved from light nuclei ($A \leq 20$) to mid-mass nuclei ($A \leq 100$), and the scientific need for a major capability upgrade to provide these heavier beams has often been expressed and documented in the U.S. nuclear science community. A preliminary version of the proposed capability upgrade was vetted and strongly endorsed at the annual user meeting held on the MSU campus May 31 – June 2, 2006.

1.2.3 Synergy of research, education, and outreach

The location of the NSCL on the campus of a major research university provides an effective research and teaching environment. Academic studies combine with hands-on training for students and young researchers. In addition, the NSCL has developed an integrated approach to reaching out to the general public, K-12 teachers and precollege students.

The NSCL plays a major role in training the next generation of nuclear scientists. The laboratory typically employs 100 students at any time, with approximately a 50–50 mix of undergraduate and graduate students. Undergraduates participate in the various day-to-day activities of the lab, e.g., in technical, service, or supervised research environments. Graduate students do their thesis research in experimental or theoretical nuclear physics, astro-nuclear physics, nuclear chemistry, or accelerator physics and engineering. During the last 10 years, more than 10% of the nation's nuclear science Ph.D.'s were trained at the NSCL. The laboratory's open academic environment allows flexible working groups and a broad educational experience that forms an excellent basis for diverse future careers. NSCL graduates are highly regarded for being very well trained. More than 20 postdoctoral research associates reside at the NSCL, supported by funds from the NSF, MSU, DOE, and other sources.

Former students and postdocs occupy important positions across many fields in universities, national laboratories, and the private sector. Recent NSCL graduates now work in nuclear medicine, airport security, environmental protection, weapons stewardship, national security, nuclear fusion, and areas related to the radiation safety of space travel. Others have chosen to apply their problem-solving and goal-oriented teamwork skills in diverse areas of the economy, including car manufacturing, electronics, computing, risk assessment, and finance.

The NSCL plays an important role in attracting undergraduate students to basic science research by providing a stimulating environment and exposing them to basic physics research and related technologies, including nuclear theory, applied superconductivity, and accelerators designed for cancer therapy. For more than a decade, the NSCL has made available summer internships to talented undergraduate students through an NSF- and MSU-funded Research Experience for Undergraduates (REU) program, especially targeting students from underrepresented groups. In recent years, the NSCL has been the largest contributor to the Conference Experience for Undergraduates (CEU) program at the APS Division of Nuclear Physics meetings.

The formation of the Modular Neutron Array (MoNA) collaboration proved an innovative way to involve undergraduates from other institutions in NSCL research. This collaboration involves faculty and students from the NSCL, Florida State University, and eight predominantly undergraduate institutions: Central

Michigan University, Concordia College, Hope College, Indiana University at South Bend, Marquette University, Wabash College, Western Michigan University, and Westmont College. The MoNA collaboration began with an NSF-funded MRI grant for constructing and commissioning a highly efficient, position-sensitive neutron detector (MoNA) and has since evolved into a research collaboration that involves many external undergraduate students in PAC-approved experiments at the NSCL.

In addition to open houses, guided tours of the facility to some 2000 visitors annually, community lectures, and other activities, the NSCL has targeted specific groups in its outreach activities, especially pre-college students at all levels and pre-college science teachers. The goal is to leverage the laboratory's educational impact. An example is the Physics of Atomic Nuclei (PAN) program, an ongoing summer research intern program for precollege science teachers and high school students supported by NSCL faculty and infrastructure.

1.2.4 Cross-disciplinary research and technical outreach

Over the years, the NSCL has pioneered medical applications of superconducting accelerator technology. The NSCL designed [Blo89] and constructed a gantry-mounted, superconducting K100 medical cyclotron, funded by Harper Hospital in Detroit, for neutron therapy. The NSCL's conceptual design [Blo93] of a superconducting cyclotron for the treatment of cancer patients using proton beams has been adopted and further refined by ACCEL Corporation with technical advice from NSCL faculty and staff. Two such cyclotrons already have been built in Germany and Switzerland, and additional ones are under construction.

The NSCL also serves as a technical resource for other research institutions in the United States and abroad. The laboratory continues to provide backup expertise for Harper Hospital's neutron therapy cyclotron. Commercial companies have licensed a number of special electronics modules that were developed at the NSCL. The laboratory also actively pursues technology transfer activities. The NSCL provided the design for superconducting cyclotrons at Texas A&M University (at the Cyclotron Institute) and Calcutta, India (at the Variable Energy Cyclotron Center). The main magnet coil for the Texas A&M cyclotron was fabricated at the NSCL. Laboratory personnel have contributed to the design of the ORNL-RIB cyclotron's central region and helped solve beam dynamics problems that occurred in the new proton therapy cyclotron at Massachusetts General Hospital.

The NSCL has considerable expertise in detector and data acquisition technology and makes this expertise available to universities and national laboratories by providing needed detectors and/or technical advice. The NSCL-developed data acquisition (NSCLDaq) and analysis (SpecTel) systems have been adopted by more than twenty institutions that perform experiments in areas ranging from atomic and nuclear physics to health care research.

1.3 Planning considerations

We strongly considered the scientific opportunities identified by NSAC in its 2002 Long-Range Plan [NSAC02], the National Research Council Decadal Survey [NRC99] and other recent community documents in our planning for how to best meet the emerging nuclear physics needs in the coming decade and beyond. Two

central principles guided our planning considerations: recognition of key physics opportunities and the need for an optimum cost-benefit ratio. Intensive discussions at a number of workshops and conferences, quantitative evaluations of many alternative options, and consultations with individual users have led to the concept, described here, for a transition to the new ISF.

Additional important considerations were risk-mitigation, performance and cost optimization, and flexibility to incorporate future science-driven upgrades without significant disruption of the ongoing research and education activities. This was accomplished by incorporating existing state-of-the-art NSCL equipment into the ISF whenever possible and sensible, building on the existing strengths and expertise of the NSCL staff and faculty, collaborating and consulting with leading laboratories and experts worldwide, emphasizing the use of fully developed high-performance technologies, and aggressively developing promising new technologies for efficiently stopping, manipulating, and reaccelerating intense beams of short-lived isotopes that are not available elsewhere in the world.

Figure 1.5 illustrates the building blocks of a rare isotope research facility based on a medium-energy heavy-ion driver. For isotope production and separation in flight, the options are to use the resulting fast beams directly for experiments, to bring them at rest in solids (often solid detectors), or to stop them in a gas cell and extract them for further use either at very low energies, as in traps, or at higher energies after reacceleration. The ISF will provide cutting-edge capabilities for all techniques, fast beam techniques and stopping and reacceleration, each of which will be needed to take full advantage of the capabilities offered by a high-power heavy ion driver.

Experiments with fast beams and reaccelerated beams often address different and complementary aspects of nuclear properties. Reaccelerated beams have higher

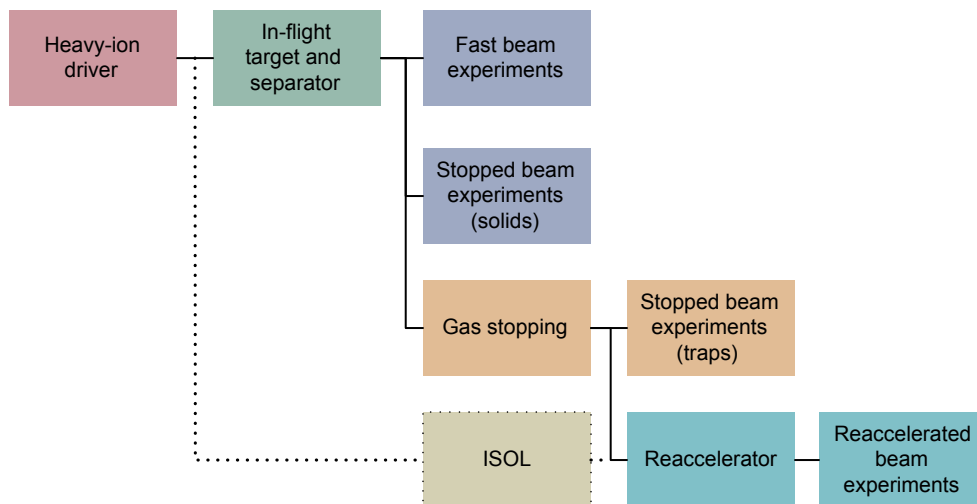


Figure 1.5: Schematic building blocks of a rare isotope research facility based upon a heavy ion driver. For isotope production and separation in flight, one can use the resulting fast beams directly, bring them to rest in solids, or stop them in a gas cell and extract them for use at very low energies or at higher energies after reacceleration. Light-ion beams can be used to produce isotopes at rest in a thick target from which they must be extracted by diffusion and effusion (ISOL technique) before they can be used for experiments at very low energies or, after acceleration, at higher energies.

beam quality than fast beams and allow the use of the many experimental techniques developed at low-energy stable-beam facilities around the world.

Fast beams have the advantage of allowing tracking and tagging of each beam particle, which is often critical for reduction of background. Fast beams also provide the option of using cocktail beams when working far from stability, where intensities are low. Many of the present fast beam techniques were developed during the last decade at a small handful of laboratories around the world. NSCL faculty, staff, and users helped to pioneer in this effort.

Reaccelerated beams of isotopes produced in flight have better beam quality but lower intensities than the corresponding fast beams. The relatively low energies of reaccelerated beams requires the use of thin targets, often 100–10,000 times thinner than can be used in fast beam experiments. As a consequence, experiments with reaccelerated beams typically have much smaller luminosities than experiments with fast beams. The scientific reach toward the driplines of reaccelerated beams is, therefore, significantly smaller than that for fast beams. This is illustrated in two representative examples given in Figures 1.6 and 1.7. In these figures it is assumed, for simplicity, that no losses occur during stopping and reacceleration.

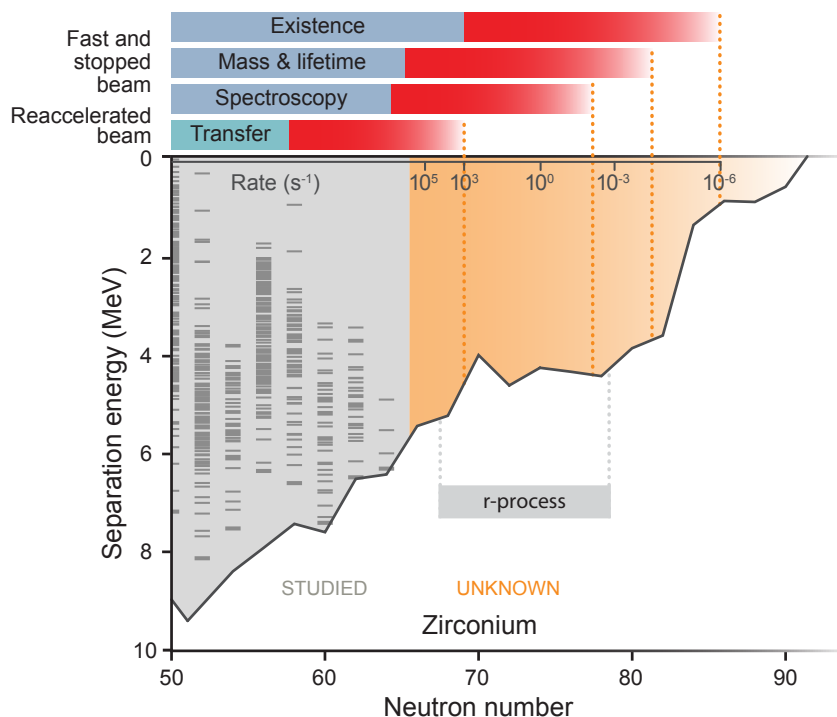
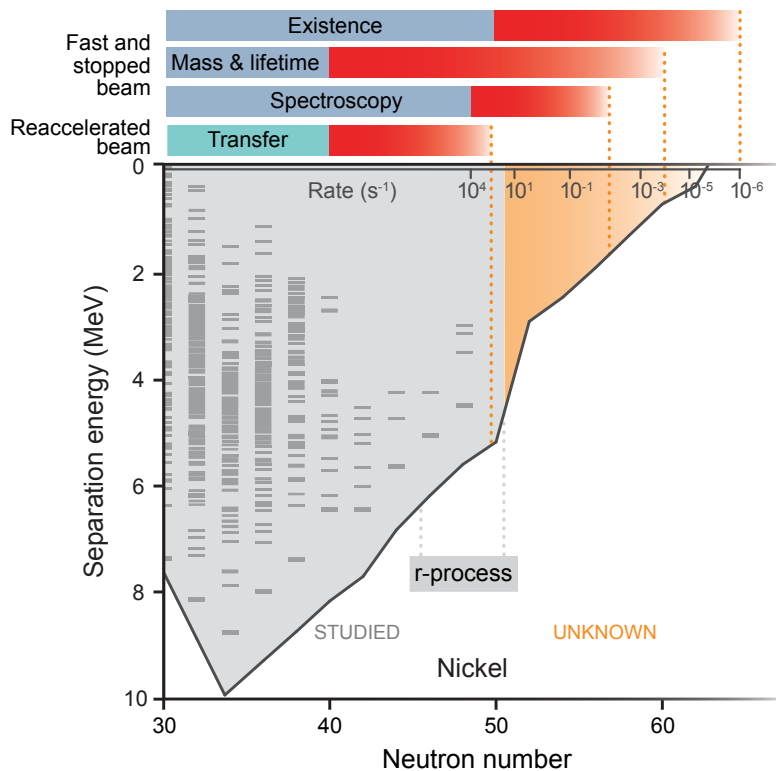
The intensity losses from stopping, extracting, and reaccelerating beams of rare isotopes produced by the in-flight technique are not yet known. Full performance tests of the concept are required. Since the NSCL is the only U.S. laboratory where a complete systems test can be performed, the development of a high-performance gas-stopper and reaccelerator, and a full performance test of the in-flight production, gas-stopping, and reacceleration sequence are of high priority for the NSCL.

In short, implementing both fast and reaccelerated beam capabilities, assures a versatile and cutting edge program that makes full use of existing NSCL equipment while building on the technical and scientific leadership of NSCL staff and users in research with fast and stopped beams of rare isotopes.

The ISF will allow acceleration of light ion beams that can be used for isotope production at rest in a thick target and extraction by diffusion and effusion (ISOL technique). For certain (nonrefractory) elements, the beams produced by the ISOL technique can have a much higher intensity than can be achieved by the in-flight technique.

The development of new beams with the ISOL technique is known to be difficult and very time consuming. Furthermore, ISOL targets typically last for only a relatively short time in the radiation environment created by the high-power driver beams. New ISOL beams, therefore, require long development times, typically months to a year, as compared to one or two days of development for new beams produced with the in-flight technique. ISOL beams also require a sizeable support team and technical infrastructure comparable to that at the existing ISOLDE or ISAC facilities.

Uniqueness, maximum possible scientific reach, and high-performance gains as compared to existing North American facilities were given high priority for choosing the initial baseline layout of the ISF. A world-class ISOL capability already exists at TRIUMF; the driver accelerator is capable of producing a 500 MeV proton beam with 150 kW beam power. However, the target technology for using such high power beams in routine operation is not yet at hand. From the North American perspective, full instrumentation of a high-power ISOL station appears less



Figures 1.6 and 1.7: Schematic illustration of the scientific reach with reaccelerated and with fast beams of neutron-rich nickel isotopes (top) and zirconium isotopes (bottom). Known nuclei and levels are indicated in gray. Unknown nuclei are indicated in orange. Also indicated are nuclei important for the r-process. Investigations very far from stability require fast beam techniques. The gains in sensitivity for fast beams are largely due to the luminosity gains that can be realized with thick targets and, to a lesser extent, due to forward-focused kinematics.

pressing than full and immediate exploitation of the extraordinary intensity gains, by many orders of magnitude, that will be possible for in-flight beams produced with the ISF's proposed 200 MeV, 400 kW heavy-ion driver. Hence, we propose to incorporate only difficult-to-add civil infrastructure for a 400 kW ISOL target station into the baseline of the ISF and defer full instrumentation and operation of a 400 kW ISOL target to an optional performance upgrade. This approach maximizes the initial science gains for all North American facilities without forfeiting the option of adding a higher-power (>150 kW) ISOL capability to the ISF, or to another U.S. high-power light-particle accelerator.

Justification, at least for the initial program at the ISF, can be seen from Figure 1.8. In this figure, the predicted yields of reaccelerated beams produced by the in-flight technique are compared to beams produced by the ISOL technique. Noting that 100–150 kW ISOL targets will likely exist at TRIUMF when the ISF comes online, it appears prudent to focus the initial program at the ISF on the in-flight production techniques where world-leading expertise exists and where the development of new beams can be rapidly accomplished.

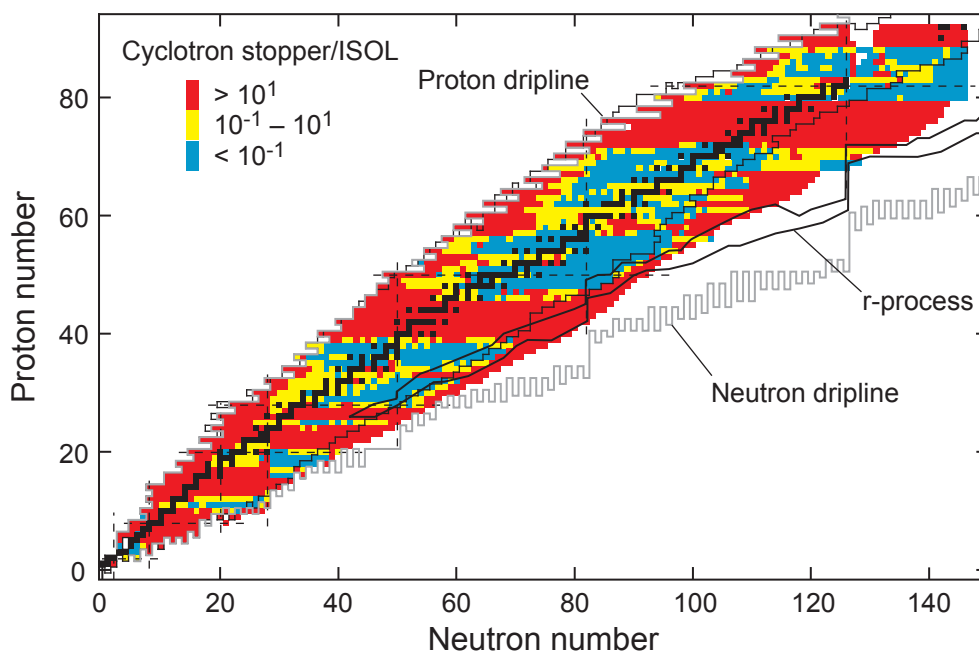


Figure 1.8: Predicted ratio of isotope yields produced in flight and extracted from a high-performance cyclotron stopper over the isotope yields expected for a 400 kW ISOL target.

1.4 ISF layout, cost-reduction option, and upgrade options

Based upon the considerations discussed in the previous section, the ISF should include the following equipment:

- a high-power superconducting heavy-ion linac capable of accelerating beams of all stable elements to at least 200 MeV/nucleon and up to a beam power of 400 kW (200 MeV/nucleon is the minimum estimated energy that allows clear separation of heavy r-process nuclei, such as ^{200}W)
- a fully equipped in-flight production target area plus fragment-separator

- the civil infrastructure for a high-power ISOL target plus fragment analyzer
- a fast beams research area instrumented with the full arsenal of experimental equipment from the NSCL
- an advanced gas-stopper for efficient stopping and rapid extraction of high-intensity beams of short-lived isotopes
- a low energy experimental area for physics with ions of less than 100 keV
- an efficient reaccelerator capable of accelerating short-lived isotopes extracted either from the gas-stopper or from an ISOL target to energies well above the Coulomb barrier (the initial choice is 12 MeV/nucleon with an upgrade option to higher energies)
- an experimental area for research with beams reaccelerated to near- or sub-Coulomb barrier energies
- an experimental area for research with beams reaccelerated to energies up to 12 MeV/nucleon
- an office building suitable for a continued synergy of research and education
- options for various science-driven upgrades, including increased driver energy, additional fragmentation and/or ISOL target stations, multi-user capability, and additional expansions of the various experimental areas

A facility satisfying all these criteria cannot be fit on the existing site of the current NSCL facility. Therefore, it is proposed to develop a new site with new civil infrastructure for the ISF, to build and precommission the driver linac, and then to make the transition from CCF operations to ISF operations by moving existing NSCL equipment to the ISF. This transition can be done with minimum disruption of the ongoing research and education program. If staged and planned properly, no more than half a year will be needed from termination of the CCF's experimental program to a first experiment at the ISF, provided the ISF is built at a new site on the MSU campus. The university's 5,000-acre campus offers several options for a site that satisfies all the criteria discussed above. MSU will make an appropriately selected site available at no cost to the federal government for the full life cycle of the facility, from construction to decommissioning.

Developing a new site with civil infrastructure is attractive because it offers the opportunity for a fully optimized layout with simple-to-implement modular upgrade options and avoids many of the initially hidden costs associated with adding to and later modernizing old infrastructure. The needed initial investment is slightly less than \$500 million (in FY06 dollars). We therefore considered and developed the option of upgrading on the present site. This option reduced the initial investment by roughly 20%. However, implementation of such a cost-reduction option will impose significant sacrifices, including longer disruption of the ongoing research and education program, rather serious limitations for facility improvements, such as additional floor-space for new experimental apparatus, and very limited options for future science-driven upgrades. The two site options are discussed in detail in Sections 5–7; a brief comparison is given in the Epitome.

Figure 1.9 shows our current plan for the ISF at a new site on the MSU campus. Suggestions for improving and altering the proposed ISF facility according to

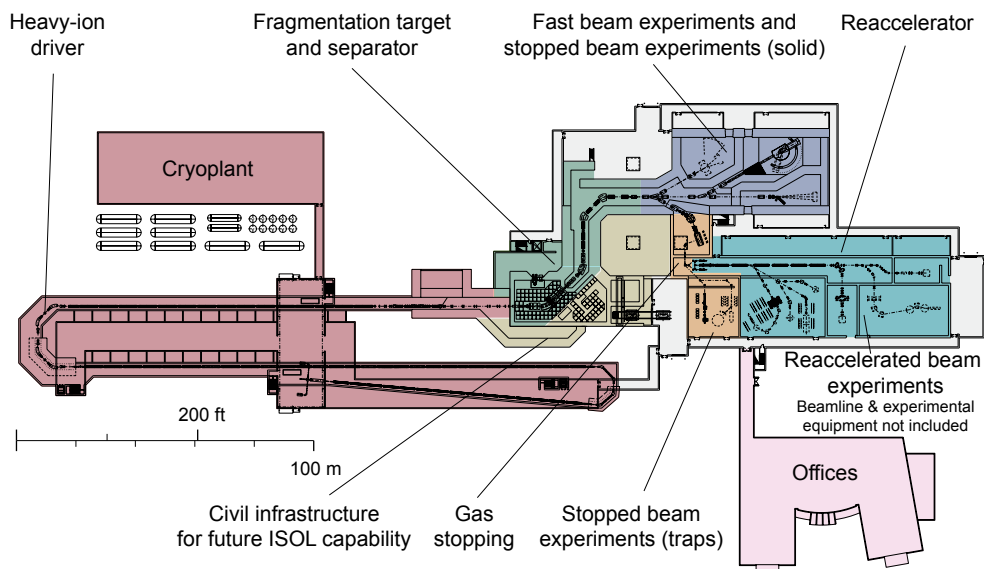


Figure 1.9: Layout of the ISF (south-campus option). This layout requires a new site on the south-campus of MSU and envisages new buildings. Existing equipment from the NSCL will be moved and incorporated into this site. The scientific reach of the ISF is illustrated in Figure 1.12.

additional needs of the science community can be accommodated provided that federal funding for such options is available. The detailed science motivation, technical description and cost summary will be given in the main body of this document.

The choice of a high-power 200 MeV/nucleon heavy ion driver accelerator for the ISF represents a compromise between cost and performance. It provides world-class capabilities for the foreseeable future. It also allows the ISF to make effective use of the entire array of state-of-the-art and often unique equipment and technical know-how that currently exists and continues to be developed at the NSCL. The ISF rare isotope intensities will compete favorably with the best rare isotope facilities worldwide, especially those that make use of state-of-the-art in-flight production techniques. Additionally, the facility will have gas stopping and reacceleration capabilities that have not yet been considered at the in-flight facilities abroad.

The ISF initially will have four major areas for experiments with rare isotopes produced via the in-flight technique: a fast beams area for experiments that do not require stopping ions in a gas cell and three experimental areas based on stopping intense beams of rare isotopes from over 100 MeV/nucleon with minimal losses and fast extraction times. The first area, for very low energy ion beams (< 100 keV), will be used for precision experiments, such as mass measurements in ion traps or laser spectroscopy experiments. The second area will be dedicated to experiments at sub-Coulomb barrier energies, such as “safe” Coulomb excitation and direct capture reactions of astrophysical interest. The third experimental area will be for experiments above the Coulomb barrier up to the current design energy of 12 MeV/nucleon for the ISF reaccelerator. Higher reacceleration energies could be made available via a future upgrade.

Noting that world-leading ISOL capabilities currently exist in North America, the ISF will have the civil infrastructure that allows development of a high-power ISOL target in the future, when the current ISOL target technologies have advanced to the state that construction of a high-power ISOL capability becomes compelling.

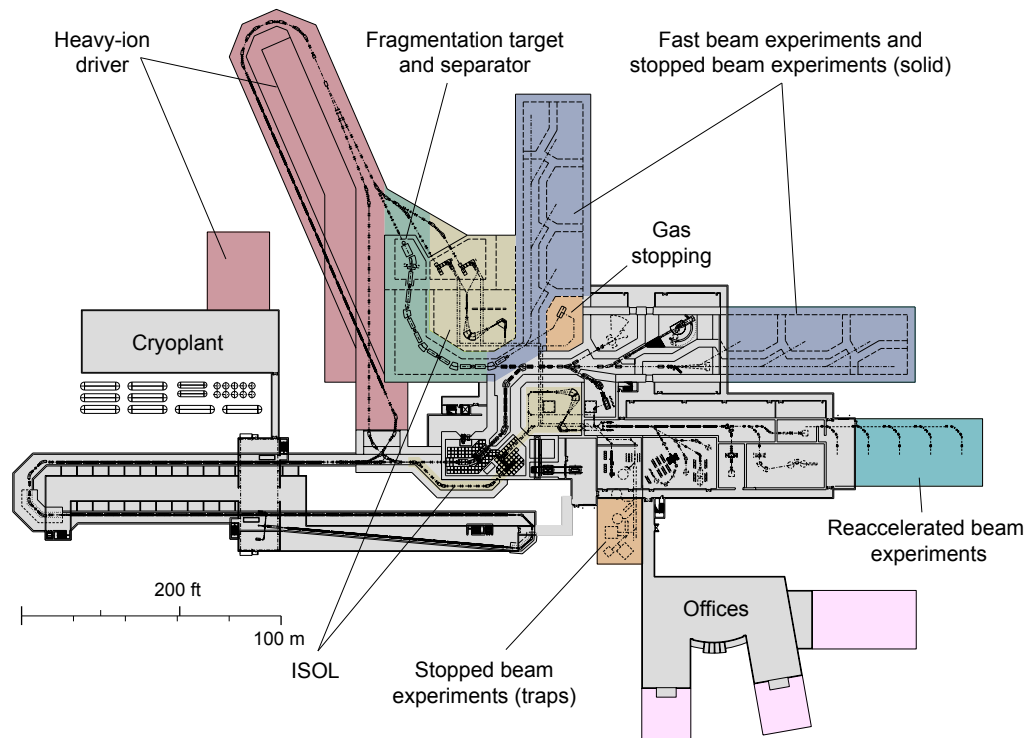


Figure 1.10: Illustration of various upgrade options for the ISF (south-campus option). The specific upgrades shown correspond to implementation of the full RIA capability. Unforeseen, science-driven alternatives can be readily developed and implemented with minimal disruption of the ongoing science and education program.

Figure 1.10 illustrates various science-driven upgrade options that can be implemented in a modular way if and when the science needs are compelling and when funding is available. Implementing all options shown in the example of Figure 1.10 would result in a facility with the full capability of the Rare Isotope Accelerator (RIA). Alternative upgrade paths can be developed easily and accommodated at the new site.

Figure 1.11 shows what can be achieved by adding a high-power driver linac to the existing NSCL site. This option is roughly 20% less expensive, but will lead to a significantly longer disruption of the existing research and education (~18 months compared to ~6 months for the new site). This option would require demolition and relocation of the current shop and assembly areas, and construction of an additional office annex. While this upgrade option offers the same isotope production capabilities as the new south-campus facility, the required construction is logistically more complex, will likely take more time, will require more expensive construction methods, and will be more disruptive to the operation of the NSCL as a national user facility. Moreover, future facility improvements or alterations will be difficult and expensive compared to future upgrades of the south campus facility. Future science-driven upgrades of the existing NSCL site will be strongly constrained by the site's relatively small size.

Figure 1.12 illustrates the broad scientific reach of the ISF. The figure shows the intensities after the fragment separator calculated with the latest version of MSU's LISE program [Tar04]. This program incorporates our current best knowledge of

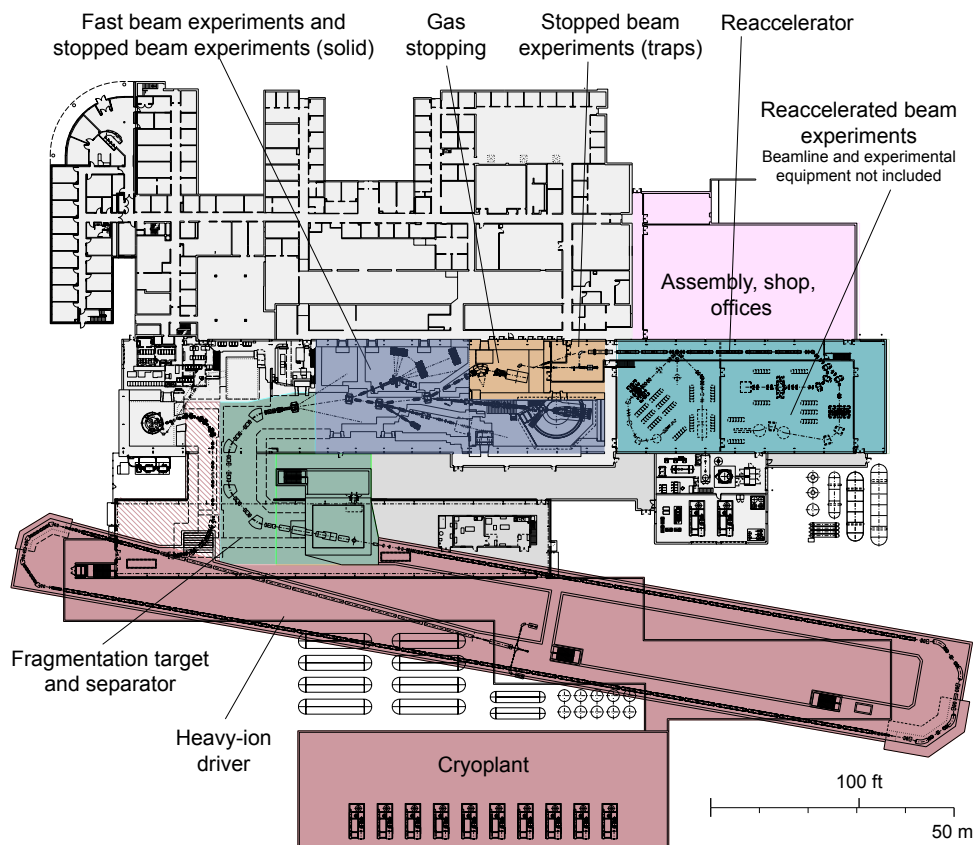


Figure 1.11: Layout of the ISF (NSCL site upgrade option). This option makes use of the existing NSCL infrastructure but requires demolition of the existing shop and assembly buildings and new construction to accommodate these important infrastructure functions before major construction of the ISF could begin. The scientific reach of this facility is similar to that illustrated in Figure 1.12 for the initial south-campus option, but additional improvements will be much more difficult to accommodate.

isotope yields from in-flight production and separation, based on the proposed fragment separator and assuming the availability of 200 MeV driver beams with 400 kW beam power for all stable elements. It should be noted that predictions for isotopes very far from stability represent extrapolations into the unknown and have, therefore, uncertainties that can be large. Therefore, efficient separation and transport to the various experimental areas will be important considerations. MSU has a team of experts with many years of experience in these techniques. This team will remain at the cutting-edge of the evolving science field of rare isotope research and will, at the same time, bring their growing know-how and expertise into the ISF planning process. The unsurpassed expertise of the MSU team in rare isotope production and research techniques is the best guarantor for an efficient and rapid transition from operating the CCF to operating the ISF as a national user facility.

Figure 1.13 shows the intensity gains for isotopes produced with the in-flight technique at the ISF compared to the CCF capabilities that are projected to be available by 2008, after the commissioning of an advanced superconducting ion source with two-frequency heating (SuSI) and an improved injection line to the K500 cyclotron. For most lighter nuclei, the intensity gains with the ISF will be between factors of 100–1,000; for all heavy nuclei, the gain factors are at least three orders

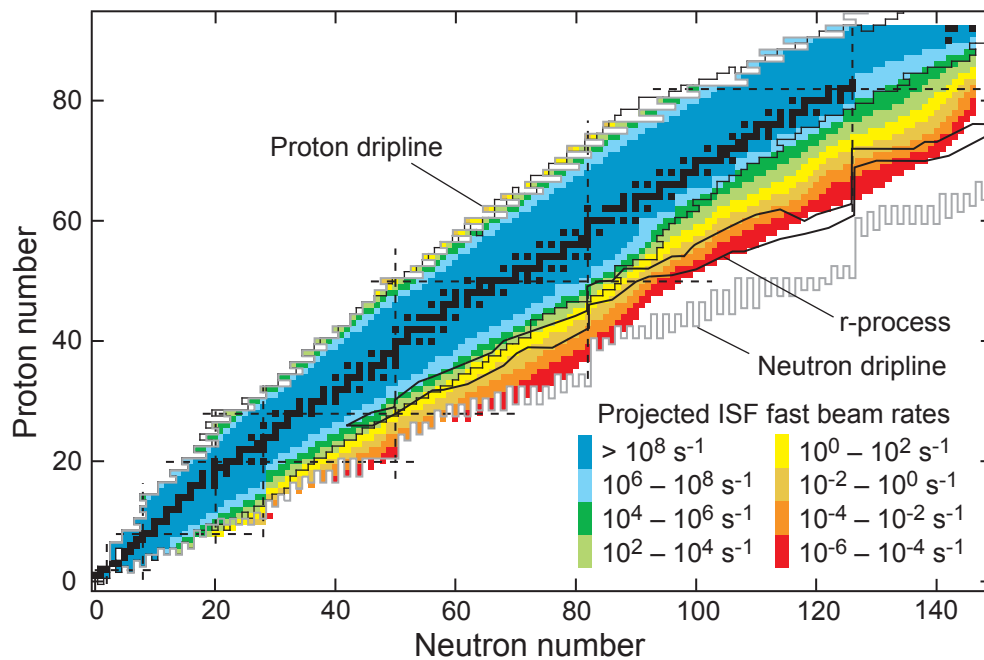


Figure 1.12: Scientific reach of the ISF. Shown are the intensities after the fragment separator calculated for in-flight production and separation, based on the proposed fragment separator and assuming the availability of 200 MeV driver beams with 400 kW beam power for all stable elements. It should be noted that predictions for isotopes very far from stability represent extrapolations into the unknown and have, therefore, uncertainties that can be as large as one or two orders of magnitude.

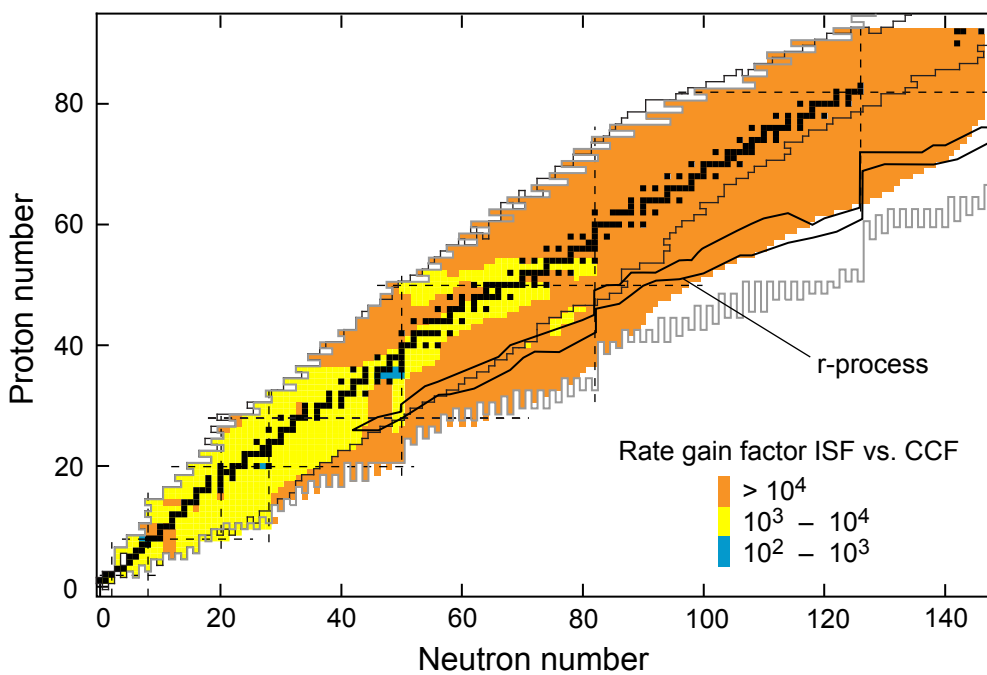


Figure 1.13: Rare isotope intensities achievable at the ISF with the in-flight technique as compared to the anticipated CCF capabilities projected to be available by 2008.

of magnitude and in many cases four or more orders of magnitude. The predicted rare isotope intensities at the ISF are competitive with and often exceed the intensities projected for the advanced fragmentation facilities currently under construction or approved for construction in other countries.

1.5 Scientific opportunities with the ISF

ISF construction will make possible a rich scientific program that explores the limits of nuclear stability and determines properties of nuclei with very unusual proton-to-neutron compositions. The data obtained at the ISF are needed to stimulate and guide development of reliable theoretical models with predictive power for key nuclear properties. The models will provide insight into the nature of many-body quantum systems and mesoscopic science, due to the unique features of nuclei in comparison to related systems in chemistry, biology and nanoscience. The nuclear data from the ISF will also provide critical input for models of astrophysical environments that describe nucleosynthesis and stellar evolution in the cosmos. Only reliable astrophysical models can extract reliable information on astrophysical properties from the high quality observational data produced by ground- and space-based observatories.

The ability to conduct experiments with intense beams of rare isotopes is the key to pushing this field of science forward. Experimenters need to select beams best suited to a given problem, which in turn requires a broad array of beams to be available. For this purpose, short development times will be advantageous. Experience from laboratories such as TRIUMF, ORNL, NSCL, GSI, and RIKEN shows that it will be important to have available as broad an arsenal of experimental techniques and beam energies as possible to ensure that users can select the optimum tools and beam energies.

The ISF offers the unsurpassed flexibility of the in-flight technique with its short beam development time and rapid, chemistry-independent beam preparation. It is unique by allowing measurements over the full gamut of beam energies, from rest to 200 MeV/nucleon. The data very far from stability will provide the greatest leverage and sensitivity to unknown parameters in nuclear theories. Very far from stability, the intensities are so low that rate considerations become a serious feasibility constraint. For studies of the most neutron-rich nuclei, the luminosity and intensity advantages of fast beams will be crucial. Except for experiments that require very high intensities, that can so far only be achieved for certain isotopes with the ISOL technique, the ISF provides the approach of choice.

Next we summarize, at a conceptual level, the important themes, key experimental tools, and theoretical developments needed to address the science. We also highlight some additional opportunities that can be realized at the ISF to make important contributions to other areas of science and technology or to society more broadly. Considerably more detail, including specific examples, is given in the main body of this document.

1.5.1 The context of mesoscopic theory

To a very good approximation, nuclei can be described as self-sustaining finite droplets of a two-component – neutron and proton – Fermi-liquid, whose detailed properties depend on the delicate interplay of the strong, electromagnetic, and

weak interactions. Advances in computation techniques have allowed rather accurate microscopic calculations of the properties of very light ($A \leq 16$) nuclei. For heavier nuclei, full microscopic treatments rapidly become unfeasible, and additional approximations must be introduced to solve the underlying many-body quantum problem.

ISF data will provide an essential stimulus and a firm experimental foundation for advances in nuclear theory. The first step is to determine the effective two- and three-nucleon (and perhaps even four-nucleon) forces that form the basis of *ab initio* theories. While much is understood, key isospin dependencies are unknown and remain to be determined from light dripline nuclei. To determine the appropriate approximations and effective interactions needed to model heavier nuclei, a broad range of nuclear species must be made available, including key nuclei near doubly magic numbers. The qualitatively different features of isotopes near the limits of stability will further test and provide constraints for models and elucidate the properties of clustering and pairing in weakly bound systems.

Within this theoretical framework, there is a strong intellectual overlap and cross-fertilization with the theoretical descriptions of other mesoscopic quantum systems. Important examples of high interest in condensed matter physics are nanotechnology and the quest for quantum computers. Another important example is quantum optics, where the interaction of a finite number of particles is described by effective forces. The basic quantum many-body problem raises fundamental issues in nanoscience with regard to design and engineering of artificial mesoscopic systems in which complexity emerges from elementary interactions of a relatively small number of constituents. Nuclear science addresses similar questions at the femtometer scale. Nuclei far from stability are mesoscopic systems of marginal stability, for which coupling to the continuum is important; they are “open” mesoscopic quantum systems. The description of the interplay of internal structure and external interactions involves theoretical concepts similar to those encountered in other branches of physics: information processing, quantum chaos, decoherence, and phase transformations.

Major advances in nuclear theory will come from confronting theoretical model predictions with new experimental information on neutron-rich nuclei of as yet unknown properties. One will, for example, be able to constrain the nuclear energy density functional approach by constraining poorly known terms in the energy functional and connecting it to *ab initio* calculations for light nuclei. Access to new nuclei with specific features, such as weak binding, closed shells, or special symmetries, can be used to validate the predictive power of these models. Another important objective, especially for astrophysics, is to improve the accuracy of theoretical mass predictions by at least a factor of five for an increased range of experimentally known nuclear masses. Such an improvement will enhance predictive power for regions that cannot be accessed experimentally. Reliable energy functional and matter densities also will improve our understanding of fission barriers and neutron capture rates on actinides.

ISF research will stimulate advances in the theory of both static and dynamic mesoscopic systems. Nuclear reactions are our tool for probing nuclear properties. Reactions with loosely bound nuclei far from stability present new theoretical challenges owing, for example, to the closeness of continuum states and the extended halo structure of very neutron-rich nuclei. A thorough understanding of

these issues is needed to connect the results of reaction measurements with nuclear properties. The discovery of halo nuclei has already stimulated the development of continuum shell models that promise to provide a major advance in unifying structure and reaction theory. We expect the much broader and comprehensive experimental program at the ISF to stimulate further advances in the theory of both static and dynamic mesoscopic systems.

Many ISF experiments will be devoted to the study of low-energy quantum properties of rare isotopes. Another important goal is to determine the nature of the equation of state of asymmetric, very neutron-rich nuclear matter, a quantity also relevant for understanding the properties of neutron stars. Investigations of near-central nucleus-nucleus collisions at high energies will bear strongly on this issue. Their goal is to determine the dependence of the nuclear energy, optical potentials, and strong-interaction cross-sections on nuclear density, neutron-proton asymmetry, and temperature. Changes in the clusterization at low densities with changing neutron-proton asymmetry are of special interest, particularly in the astrophysical context. The extraction of the needed information is closely tied to the development of a practical quantum transport theory and to detailed numerical simulations with high-performance computers. These theoretical developments are intellectually connected to quantum transport theories developed for understanding the properties of small electronic devices, early cosmology, and plasmas.

1.5.2 Properties of nuclei with unusual neutron-to-proton ratios

The ISF will explore unknown territory in the chart of nuclei. Many of the most interesting problems, involving halo nuclei, properties of extremely neutron-rich nuclei, and the isospin dependence of the equation of state, require beams of very neutron-rich, short-lived isotopes for which in-flight production and separation is the technique of choice.

The detailed nature of the rare isotope research program at the ISF can only be guessed at this time, but the number of novel projectile-target combinations is so large that many new and unforeseeable discoveries will be made.

Progress will come from quantitative measurements that address specific and often detailed questions with appropriately chosen experimental techniques. In this subsection, we will give a short synopsis of some of the important questions and the experimental approaches to these questions. Many of these techniques have been developed at rare isotope research centers in recent years and others are still under development.

Exploring the limits of nuclear existence

The limits of nuclear stability provide a key benchmark of nuclear models. These limits also highlight the emergence of new phenomena that lead to extra binding and an extension of the expected limits of stability, such as has been discovered for halo nuclei. The limits of binding for extremely neutron-deficient nuclei and the location of the proton dripline are fairly well defined. But very little is known about the limits of binding of very neutron-rich nuclei and the location of the neutron dripline; such limits are established experimentally only for the eight lightest elements. It will be impossible for the ISF or any other proposed facility to reach the neutron dripline for the heaviest elements, but the ISF will be able to reach

the neutron dripline into the manganese ($Z = 25$) and possibly into the zirconium ($Z = 40$) region. For heavier nuclei, detailed studies of nuclear properties far from the line of stability will allow stringent tests of current theories of nuclear structure in a new territory and will guide the development of nuclear models with greatly improved predictive power. Indeed, there is broad agreement in the science community that the critical path to improvements in nuclear modeling passes through nuclei far removed from the line of stability. Their properties must be known to determine effective degrees of freedom and constrain the effective interactions: the tensor force, the symmetry energy, and isospin dependent three-body forces. All such interactions, so far, are only poorly determined.

Experiments at the extremes of stability are best performed with rare isotopes produced in flight directly – without stopping and reacceleration – and by taking advantage of the growing arsenal of “fast-beam” experimental techniques developed at fragmentation facilities. These techniques played a critical role in elucidating many unexpected phenomena, including the discovery of neutron halos and the dramatic modifications of nuclear shell structure far from stability. Detailed studies of the structure of nuclei like ^{11}Li and unbound nuclei along the dripline like ^{10}Li provide significant tests for nuclear theory. The dramatic shift of energy levels in the region beyond ^{24}O , the lack of stability of ^{26}O and ^{28}O , along with the binding of the fluorine isotopes up to ^{31}F , could only be established experimentally when the needed beams became available in the past few years. Critical for these investigations is the fast separation and transport of very short-lived nuclei (with millisecond half-lives) to sophisticated experimental devices.

Intense reaccelerated beams of neutron-rich isotopes may also add to our knowledge of very heavy elements by allowing the synthesis of trans-actinides more neutron-rich than is possible with stable beams. Some of these more neutron-rich isotopes are likely to be more strongly bound; some are predicted to have half-lives of up to one year. This opens new, exciting opportunities for the study of the chemistry of these unusual elements. An improved understanding of their binding should also help reduce theoretical uncertainties in the shell-stabilization of super-heavy elements.

Exploring nuclei with unusual properties

Nuclei close to the line of stability exhibit similar binding for neutrons and protons. That is, the Fermi-surfaces for these protons and neutrons lie at comparable energies. This situation is different for very neutron-rich nuclei, for which the Fermi surface for protons lies far below the continuum but the Fermi surface for neutrons lies close to it. As a consequence, qualitative changes are expected.

Very neutron-rich nuclei are predicted to exhibit peripheries of nearly pure neutron matter, such as neutron skins and neutron halos. For example, it should be possible at the ISF to produce nuclei with surfaces of nearly pure neutron matter at nuclear density – nuclei with up to one-femtometer thick neutron-skins. So far, halo and skin phenomena have been positively identified for very light nuclei. The two-neutron halo of ^{11}Li is a prominent example. Very little is known about the existence and quantitative features of extended neutron distributions in heavier nuclei. Of particular interest are the properties of possible multi-neutron distributions that could exhibit unusual cluster or molecular structures which otherwise may only occur at the surfaces of neutron stars. Such nuclei will also offer a unique opportunity to study the nucleon-nucleon interaction in nearly pure neutron matter.

Exploring changes in shell structure

An important and time-honored concept for the description of nuclear properties is that of single-particle motion in an average mean field. In nuclei near stability we find bunchings of low-lying energy levels with related pronounced shell gaps. As a consequence, certain numbers of protons and neutrons (the “magic numbers”) lead to particularly stable nuclei. The detailed location and magnitude of shell gaps depend on specifics of the mean field and the residual (effective) interaction between the protons and neutrons.

These quantitative ingredients must be determined empirically and are fairly well established for nuclei close to the line of stability. Effective interactions far from stability – pairing, proton-neutron, spin-orbit, and tensor – are different and modify the resulting shell structure and magic numbers. Quantitative experimental information is needed to guide the refinement of theoretical treatments with improved predictive power for these neutron-rich isotopes.

Apart from quantitative measurements of binding energies and the location of low-lying quantum states, many other experimental observables are needed to characterize the nuclei of interest and allow sufficiently stringent tests of theoretical models. The determination of the single-particle components of nuclear wave functions by nucleon removal or nucleon addition reactions provides critical guidance to theoretical approaches that reduce the complex many-body problem to tractable and accurate approximations. The shell model, which describes nuclei in terms of an inert core surrounded by valence nucleons, is a particularly important example of such approaches.

Exploring nuclear shapes

A few nuclei near the magic numbers have spherical shapes. Nonspherical shapes are expected and observed in nuclei with proton and neutron numbers far removed from the magic numbers, and indeed, a rich variety of nuclear shapes has been found. Measurements of nuclear shapes provide sensitive tests and guidance for nuclear theory. For example, the experimental observation of nonspherical shapes in magic nuclei far from stability provides direct evidence of shell quenching in neutron-rich nuclei.

While axially symmetric spheroids are the most common nuclear deformations, more complex shapes, characterized by triaxial, octupole, hexadecapole, and tetrahedral deformation have been predicted for some rare isotopes. These isotopes cannot be studied with present facilities, however the ISF will permit such studies with both reaccelerated and fast beams.

At high angular momentum, calculations predict that some nuclei take on extremely oblong, hyperdeformed shapes. Hyperdeformed nuclei are expected to have a two-center distribution with significant mass asymmetry, resulting in two nearly uncorrelated single nucleon spectra. Under such conditions, one should expect an intriguing phenomenon – the coexistence of a deformed superfluid phase and normal spherical phase in a single finite system. Searches for hyper-deformation have so far been inconclusive. It appears that currently available beam and target combinations cannot produce nuclei with enough angular momentum to exhibit hyper-deformation. ISF’s reacceleration capability will be of critical importance for these investigations. One will be able to use fusion reactions induced by neutron-rich

beams to make high-spin nuclei near the line of stability. This differs from fusion reactions with stable beams that invariably make neutron-deficient nuclei.

The availability of beams of a large variety of rare isotopes also offers the opportunity to extend studies of various dynamical symmetries in nuclei and the transitions between the symmetry phases in new and to-date inaccessible regions of the nuclear landscape. For example, some “transitional” nuclei that bridge spherical and deformed shapes are expected to exhibit critical point symmetries that can be identified by unique experimental signatures in the level schemes and transition probabilities. Such critical point nuclei are expected to exist far from stability. So far such nuclei remain unexplored, but they will become accessible at the ISF.

Nuclei with very unusual proton-to-neutron admixtures are expected to show different shape-driving forces for protons and neutrons that lead to different proton and neutron deformations. For example, the first 2^+ state of ^{16}C has been interpreted as prolate deformation of the neutron distribution, with the protons residing in a spherical core. Such an egg-shaped nucleus is an example of an unexpected structure that has not been found near stability.

Protons and neutrons can oscillate independently inside the nucleus. Linear oscillations produce the giant dipole resonance. In a nucleus with a low-density neutron distribution, the vibration of the neutron skin against the core can produce a pygmy resonance characterized by a shift of part of the dipole response to very low energy. Angular oscillations of protons against neutrons produce a new class of “mixed” symmetry states in nuclei near closed shells. Phenomenological models predict these states to be present in both stable and exotic nuclei. However, such states have only been observed in stable nuclei.

In addition to measurements of the location of individual quantum states, other experimental techniques will be needed to address the physics outlined above. Such techniques include determining electromagnetic transition rates with low- and intermediate-energy Coulomb excitation, measuring magnetic moments with newly developed ultra-sensitive angular correlation techniques, and measuring excited states lifetimes with various Doppler-shift techniques.

Exploring spin-isospin modes of excitation

Charge-exchange reactions are a powerful tool for studying spin-isospin modes of excitation. One important goal is the measurement of the Gamow-Teller response, in particular for nuclei ($A \sim 40\text{--}120$). These nuclei undergo weak transitions during the late evolution of stars, just before and during the core collapse that results in a supernova explosion. In essence, the data from charge-exchange experiments are used to test and improve nuclear models, which in turn can be applied in network calculations taking into account the high temperatures and densities in the stellar environment.

More generally, charge-exchange reactions allow the study of the isovector response of nuclei and are thus sensitive to differences in the behavior of neutrons and protons. For light unstable nuclei, charge-exchange reactions can provide information complementary to that from other spectroscopic tools. In heavy systems, the properties of isovector giant resonances provide insight into macroscopic isovector properties of nuclei. The sum-rule strength of the spin-dipole resonance,

for example, is a measure of the neutron-skin thickness. Knowledge of these resonances will also help to reduce the large existing uncertainties in the isovector part of the effective nucleon-nucleon interaction. Experiments away from the valley of stability are important since the sensitivity to the most important parameters is strongly enhanced.

The needed experiments with unstable beams require high intensities and beam energies (>100 MeV/nucleon) and sophisticated detection equipment such as that currently under development at the NSCL. The ISF will allow charge-exchange studies on many of the *sd*-shell ($A \leq 40$) nuclei and on essentially all nuclei that are important for modeling weak rates in stellar evolution ($A \sim 40\text{--}120$). Isovector giant resonances can be studied far from stability and up to masses in the lead ($A \sim 208$) region.

1.5.3 The context of astrophysics

Astrophysics and nuclear physics are intimately connected fields. Nuclear processes, for example, shape much of the visible universe.

Unstable nuclei play a critical role in cosmic explosions and in neutron stars, but their study has been mostly out of the reach of terrestrial experiments. With the beams available at the ISF and progress in observational astronomy, a new understanding of these phenomena will become possible. To put together the pieces of the puzzle, interdisciplinary connections between astrophysics and nuclear physics must be fostered. The Joint Institute for Nuclear Astrophysics (JINA), a multi-institution NSF-funded Physics Frontier Center, has taken the first important steps in that direction.

Three important questions stand out:

(i) What is the origin of the heavy elements?

The question of the origin of the heavy elements in nature has been identified as one of the most important open questions at the intersection of astrophysics and particle physics for the twenty-first century. Approximately half of the elements from strontium to uranium have been created in an elusive rapid neutron-capture process (*r*-process). Current theoretical models cannot predict the needed nuclear properties with sufficient accuracy. Measured data are needed to allow meaningful calculations of the characteristic nuclear production patterns for proposed *r*-process models and to allow meaningful comparisons with astronomical abundance observations. The ISF will allow first-ever measurements of the properties of a large fraction of the very short-lived, very neutron-rich nuclei that participate in this process. This endeavor will guide the search for the *r*-process site and allow one to disentangle multiple types of *r*-processes that might occur in nature.

The *p*-process is responsible for the origin of the rare neutron-deficient isotopes of heavy elements. The majority of the reaction rates on unstable nuclei used to model the *p*-process in massive stars and supernovae are based on theoretical predictions. In terms of reactions involving α particles, very few experimental constraints exist in the entire mass region of the *p*-process. With the new facility, this situation will change dramatically, and most *p*-process reactions will be within reach.

(ii) How do stars explode?

This section describes four types of explosive events in the cosmos: X-ray bursts, core-collapse supernovae, thermonuclear (Type Ia) supernovae, and novae. It addresses the nature of the nuclear physics needed for their accurate description and the role that will be played by the ISF.

X-ray bursts from the surface of neutron stars are the most frequent thermonuclear explosions in the universe. Unfortunately, their modeling has been severely hampered by nuclear physics uncertainties. The proton and helium reaction rates with heavy unstable nuclei that power these events are poorly known. Beams from the ISF will make it possible to address this problem and provide most of the nuclear physics information needed in X-ray burst models. This will open the door for quantitative interpretation of observations provided by many space-based X-ray observatories, constrain the properties of the underlying neutron stars, and provide the basis for an understanding of the wide range of unexplained observed phenomena.

Observations of X-ray superbursts and the time-dependent cooling of neutron star crusts, when the mass transfer from the companion star is interrupted, could provide constraints on the existence and nature of exotic phases of matter in the neutron star core. Currently we lack an understanding of the physics of very neutron-deficient and very neutron-rich nuclei, which is necessary to reach meaningful conclusions.

Core-collapse supernova explosions are among the most energetic astrophysical events. They are major cosmic sources of the elements and drivers of the chemical evolution of our Galaxy. Unfortunately, most existing models of core-collapse supernovae do not produce explosions. In addition to a better understanding of the relevant hydrodynamics, including instabilities, convection and asymmetries, and of neutrino interactions with matter, we also need a better understanding of nuclear physics. The ISF's experimental program will address the nuclear physics issues by providing critically needed data that can test calculations of electron capture rates on heavy, unstable nuclei. Improved constraints on the equation of state of dense matter are also important in this context.

Thermonuclear supernovae are important cosmic sources of iron and nickel isotopes. They are also used as distance indicators in cosmology as their intrinsic brightness can be empirically calibrated. At large distances this provides constraints on the acceleration of the universe and the dark energy equation of state. A key problem is the current lack of understanding of the explosion mechanism, which makes it difficult to assess the systematic uncertainties in calibrating supernova brightness at high redshift. Measurements of electron capture rates made possible at the ISF will lead to the development of more accurate models for isotope production in thermonuclear supernovae. Comparison with observed isotopic abundances in the solar system will provide a unique empirical constraint for the wide variety of supernova models under discussion.

Novae are thermonuclear explosions on the surface of accreting white dwarfs. They are less frequent than X-ray bursts but have the great advantage that their nuclear reaction products are ejected into space and thus can be studied with modern observatories. The ISF will make it possible to measure the key reaction rates needed

to interpret the observed abundances using nova models. With such experimental constraints, key questions concerning the amount of ejected mass, the contribution of novae to the formation of the elements in the cosmos, and the mechanism for mixing of white dwarf matter into the burning layer can be addressed. Novae also offer an avenue for understanding accreting white dwarf systems in general, which for different system parameters are thought to be the progenitors of thermonuclear supernovae.

(iii) What is the nature of dense nuclear matter in neutron stars?

The crust of accreting neutron stars links observations of surface phenomena such as X-ray bursts or cooling behavior to the interior properties of the star. The nuclear processes occurring in the crust are influenced by reactions in the neutron star's surface and in its interior. Together the reactions influence the crust's thermal properties and composition. These processes also have been linked to crust deformation that might lead to gravitational wave emission from accreting neutron stars. Many of the relevant extremely neutron-rich nuclei will become accessible at the ISF. This will contribute to a new understanding of crust processes in accreting neutron stars and might hold the key for solving open questions such as the puzzling properties of superbursts and the existence of enhanced neutrino cooling in neutron star cores.

Understanding the interior of neutron stars requires knowledge of the equation of state of dense, neutron-rich nuclear matter. Considerable progress has been made in constraining the equation of state via nucleus-nucleus collision experiments with stable nuclei, but very little is known about the asymmetry energy term which describes the dependence of the equation of state on the proton-to-neutron ratio. Such knowledge is needed for extrapolating the equation of state to the neutron-rich matter in neutron stars and supernovae. Nucleus-nucleus collision experiments with beams of energetic rare isotopes from the ISF provide the means to explore the asymmetry energy term near normal and subnormal nuclear densities. Data on the size of neutron skins in neutron-rich nuclei can provide additional constraints on the low-density behavior of the asymmetry term. The determination of the pairing properties of neutron-rich nuclei will provide a key for understanding the occurrence of superfluidity in different parts of neutron stars.

Nuclear astrophysics experiments

The measurements needed to address these astrophysics questions often overlap in technique and motivation with those motivated by basic nuclear physics questions, but the selection of the particular nuclei to be studied will be driven by their impact on resolving uncertainties of astrophysics calculations. Of particular importance in the astrophysics context are:

- measurements of half-lives and binding energy for r-process nuclei
- indirect measurements using Coulomb breakup, transfer reactions, knockout reactions, or proton scattering to constrain (n,γ) , (γ,n) , (p,γ) , (γ,p) , (α,γ) , and (γ,α) rates on unstable nuclei in the r-, p- and rp-processes
- direct measurements of key reaction rates in the rp-process in novae and X-ray bursts and for the α -process at low astrophysical energies in inverse kinematics

-
- measurements of weak interaction rates on mass 50–100 nuclei, which play an important role in supernovae explosions
 - investigations of energetic nucleus-nucleus collisions at small impact parameters to constrain the asymmetry term of the equation of state of nuclear matter

The experimental program needed to address this science effectively requires the full gamut of beam energies available at the ISF for precision mass measurements at rest or time-of-flight mass measurements with fast beams of the rarest isotopes; sub- and near-Coulomb barrier reaction rate investigations with very intense beams of rare isotopes; and transfer reactions, inelastic scattering, and charge-exchange reactions with beam energies ranging from several times the Coulomb barrier to more than 100 MeV/nucleon.

1.5.4 Tests of fundamental symmetries

In the past, nuclear experiments have contributed much to our understanding of the weak interaction. For example, nuclear physics experiments first directly detected neutrinos and parity violation, established the vector – axial vector structure of the weak current, determined the neutrino helicity, and provided first evidence for neutrino mixing. Powerful nuclear many-body mechanisms are known to exist. Such mechanisms can significantly enhance and amplify observable effects from interaction terms that violate fundamental symmetries. Rare isotopes can make an important contribution to tests of fundamental symmetries that describe the strong and weak forces in nature and the search for new physics beyond the Standard Model. The availability of a broad range of isotopes makes it possible to select a specific nuclear system that can isolate or amplify specific physics of interest.

Much of this physics requires intense sources of isotopes at rest and may eventually require the implementation of an advanced ISOL capability. It seems likely the required high-precision, high-sensitivity experiments will be performed only after the first few years of ISF operation, when reliable operation at full intensity has become routine.

Key opportunities for testing fundamental symmetries include the following possibilities:

- Sensitive searches for a static Electric Dipole Moment (EDM), which is forbidden by time-reversal symmetry, are possible with the availability of intense sources of ^{223}Rn , $^{223,225}\text{Ra}$, or $^{221,225}\text{Fr}$. These nuclei have special symmetries that can be used to enhance the effects to be studied.
- Atomic parity violation experiments aim to measure the weak charge of a nucleus and to provide information on the running of the Weinberg angle with momentum transfer. Improved sensitivity becomes feasible with the availability of a broad range of francium isotopes. Performing measurements for a whole series of isotopes makes it possible to reduce theoretical uncertainties related to the calculation of the electron density distribution.
- Tests for new interactions, such as right-handed currents in β -decay, can be made in search for new physics on the TeV scale. These studies

are a complement to those performed at large accelerators, such as the Large Hadron Collider at CERN, and search for new physics on the same scale.

Other important aspects of fundamental interactions can be studied. For example, depending on the rate of progress over the next decade, abundant quantities of rare isotopes can contribute to ongoing searches for scalar, axial-vector and tensor weak-interactions; precision measurements of V_{ud} needed for testing the unitarity of the weak quark mixing matrix; and searches for the Majorana mass-term in nuclear double β -decay.

1.5.5 Applications in other disciplines

Radioisotopes play an important role in other scientific disciplines. For example, isotopes act as tracers in chemical and imaging studies. The ISF will produce many new isotopes in research quantities and could produce larger quantities of near-stable isotopes and large fluxes of neutrons and muons, which offer additional opportunities for advances in applied technologies, including national security, medical technology, and nuclear energy. Often such work can proceed “parasitically,” with minimal impact on the main scientific program, provided that the needed infrastructure is put in place by an appropriate upgrade and addition.

MSU is uniquely suited to exploit such potential cross-disciplinary or societal applications at the ISF. The university is home to two medical schools and a veterinary medicine program, including a large radiology center equipped with modern PET and NMR equipment and a cyclotron for medical isotope production. Additionally, MSU has strong programs in environmental science, material science, agriculture, food toxicology, biochemistry, and biology.

While the current baseline for the ISF does not include application-specific infrastructure, such additions could be implemented with additional funding. Possible areas for applied research are in national security and stockpile stewardship, biomedicine, materials research, toxicology, nuclear energy, and waste transmutation. More details, examples, and references can be found in [Gee06] and in Appendix B of [RIA06].

1.6 Document organization

The remainder of this document is organized in the following way. The science reach of the ISF is outlined in the next three sections: Physics of Nuclei (Section 2), Nuclear Astrophysics (Section 3), and Studies of Fundamental Interactions (Section 4). A technical description and the layout of the ISF is described in Section 5, with possible upgrade options discussed in Section 6. The cost-saving alternative of constructing the ISF on the present NSCL site is described in Section 7. The project cost estimate is given in Section 8. The document concludes with an Epitome that gives a brief comparison of the two ISF site options and a list of references and abbreviations.



2. Physics of nuclei

Atomic nuclei provide a rich laboratory for the study of quantum phenomena and mesoscopic science. The challenge is to develop a comprehensive understanding of the nuclear system and to understand how collective and single-particle phenomena result from the nuclear constituents and interactions.

The introduction to this document outlined a broad view of how progress in nuclear theory and astrophysical modeling requires the study of rare isotopes. In this section we discuss the more detailed experimental program and specific linkages to theory that addresses the broader issues outlined in the introduction. For example, as described below, the delineation of the limits of nuclear binding will provide a key benchmark for nuclear models and will help illuminate the approximations (specifically, the formulation of an improved density functional theory) needed to model the nuclear many-body problem. In total, these steps, although sometimes individually incremental, lead toward a significant advance in our understanding of nuclei and, therefore, to further advances in many other fields of science.

This section (and the following two) make the connection between the measurement of specific nuclear features and the impact of these studies on science in general and

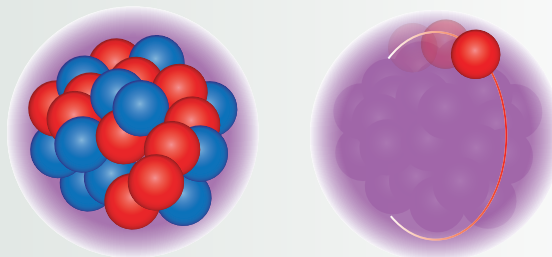
Confrontation and convergence – nuclear structure theory in the next decade

Nuclear structure theory in the twentieth century has seen the theoretical and computational development of many models and methods. These include *ab initio* methods, shell model configuration interaction methods, Energy Density Functional (EDF) methods, group theoretical methods, and nucleon cluster (alpha) methods. Each of these approaches has unique regions of applicability as well as limitations. They have been developed largely independently from one another by confrontation with the experimental data that are within their ranges of applicability.

In the next decade, nuclear theory will advance through the confrontation of models with one another as well as with experimental data. This will lead to a synthesis and convergence of our theoretical understanding of nuclear properties. The differences in the nuclear methods are largely determined by the types of degrees of freedom that are explicitly allocated. Starting with the degrees of freedom at the deepest level, quarks and mesons, the modern methods of effective field theory bridge the gap between quantum chromodynamics and nuclear many-body theory operating in terms of nucleons. The *ab initio* method with the full set of nucleonic degrees of freedom is the most fundamental in terms of the direct connection to the nucleon-nucleon and three-nucleon interactions, but it is limited in applicability to very light nuclei. We are now challenged to understand how the shell model degrees of freedom emerge from the *ab initio* wave functions. The group-theoretical methods deal with new collective degrees of freedom that arise from coherent many-body motion.

The interactions between nucleons and the treatments of these interactions in the different models provide the crucial connections to be explored. For example, we need to under-

stand the role of three-nucleon interactions for the single-particle energies in configuration-interaction and EDF methods, and how the energy density functionals can be constrained and improved with a connection to *ab initio* wave functions. These types of problems are addressed in a new SciDAC collaboration for building a Universal Nuclear Energy Density Functional (UNEDF). MSU is part of this multi-University and multi-National Laboratory collaboration lead by George Bertsch and supported by the DOE program for Scientific Discovery through Advanced Computing. The UNEDF will provide the theoretical and computational basis for predicting nuclear properties for all nuclei. Measured properties of the very proton-rich and neutron-rich isotopes available at the ISF will impose the most important constraints and test the predictive power of new theories that attempt extrapolations towards the driplines and neutron matter.



Schematic illustration of different theoretical approaches to describing the nucleus. The *ab initio* approach (left) takes into account the motion of all nucleons and their interactions. In the energy density functional approach (right) the motion of one nucleon is determined by an average interaction with all other nucleons.

mesoscopic science in particular. By adding or subtracting nucleons from a nucleus one by one and performing the experiments outlined below, we can study the emergence of complexity and self-organization and the development or quenching of stability and openness – typical characteristics of mesoscopic systems. The nuclei farthest from stability are especially important and provide the best vehicle for understanding the interplay of internal structure, reactions with other objects of a similar nature, and decays to the continuum.

The quest to realize these broader impacts and provide the underpinnings for improvements in nuclear theory will involve a number of experimental campaigns. These are described in the following subsections. They range from the global exploration of the nuclear landscape and the limits of stability to specific measurement of the shell structure of nuclei aimed at elucidating the most important degrees of freedom and determining relevant effective interactions over the whole nuclear territory. For these campaigns, highly sensitive tools have been developed; for example, intermediate energy Coulomb excitation, which allows the extraction of critical information from experiments with beam intensities of only a few ten-thousands of atoms per day. Key programs will be the measurement of the nuclear mass surface and studies of the half-lives and decay modes of exotic nuclei.

Beyond the single-particle nature of nuclei, their many-body aspects must also be explored. These include bulk motions of many nucleons that can be effectively described as collective excitations, e.g., rotations, vibrations, or giant resonance oscillations. The response of nuclei to the weak force is also of critical importance.

The atomic nucleus as a mesoscopic system

The atomic nucleus is the prototype of a mesoscopic system – a system where individual quantum states can be studied and have an influence on its properties, yet with a large enough number of constituents so that there are statistical regularities associated with macroscopic observables [Zel04]. Besides atomic nuclei, mesoscopic systems include atoms and molecules, atomic clusters, quantum dots and quantum wires, microwave cavities, atomic traps, and prototypes of quantum computers.

A common starting point for the understanding of such systems is usually a mean field description that determines the many-body symmetry of the system and provides a basis for the emerging elementary single-particle-like excitations, the quasiparticles. The next step has to account for the interaction between quasiparticles. The theory of nuclear structure combines those two aspects, and its predictive power is tested by a variety of experimental observations in atomic nuclei. Nuclear theory, in turn, has guided the theoretical development for other branches of mesoscopic science [Rei02]. In general, different subfields of theoretical physics develop in parallel, cross-fertilizing each other with ideas, approaches, and computational methods. For instance, the random phase approximation (RPA) was invented to apply to electron plasmas; it was taken over, reformulated, and converted into a standard theoretical tool for describing shape vibrations and giant resonances observed in inelastic excitations of nuclei; later, the same description was

utilized for highly excited collective vibrations in atomic clusters [Ber99].

There are many examples where theoretical models developed for nuclear mesoscopic systems have been successfully applied to other mesoscopic systems such as atomic clusters, quantum dots, and atoms in traps. In some cases, such as the applications of coupled-cluster theory in quantum chemistry, the models have been further refined and more highly developed in their application to other areas of science. They have become powerful tools for mesoscopic systems in general and for nuclear physics in particular. Modern ideas of many-body quantum chaos and the corresponding mathematics of random matrices originated from studies of complex nuclear spectra. This theory is currently indispensable for understanding multiphoton processes in quantum optics and for inventing the tools that avoid the danger of decoherence in future quantum computers.

In atomic nuclei and in quantum dots one can study significant changes that are brought about by adding and subtracting the constituents one by one – a characteristic typical of mesoscopic systems. Atomic nuclei are self-sustaining drops of a Fermi liquid with two components, protons and neutrons. The coexistence of these two components, their strong and weak interactions, and their mutual transformations make nuclei unique mesoscopic systems with their own specific features of high theoretical interest.

Finally, the bulk nature of nuclear matter and the equation of state of asymmetric matter are necessary to complete the picture of the quantum many-body nature of nuclear material.

The following subsections illustrate how recent or planned research is addressing specific nuclear science challenges and how the ISF will allow major advances in the field. Rather than attempting to provide a complete survey of all ongoing or planned rare isotope research activities worldwide, this document builds on the experience and work performed by the NSCL user community. We believe that the examples given provide a compelling scientific rationale for the ISF. An attempt to be complete would be futile, and a plethora of additional examples, techniques, and scientific opportunities exist beyond those explicitly mentioned. Such additional science opportunities further strengthen the case for the ISF and can be accommodated within the modular design approach of the ISF. Possible upgrade options are described in Section 6.

2.1 At the neutron dripline

The first crucial question posed in the section on atomic nuclei in the DOE/NSF Nuclear Science Advisory Committee's 2002 Long Range Plan [NSAC02] was, "What are the limits of nuclear existence?" One can recognize that the more colloquial phrasing of "How many neutrons and protons can be combined to form a nucleus?" is fundamental to the understanding of the nuclear forces and structure. The proton dripline lies relatively close to the valley of β -stability due to the large effect of the Coulomb energy for proton-rich nuclei. As a consequence of the vicinity to stable isotopes, many theoretical predictions for nuclei close to the proton dripline have been found to be generally accurate.

The predicted location of the neutron dripline, however, is highly uncertain, and theoretical predictions vary considerably since the neutron binding energy approaches zero more gradually. For example, only two proton-rich radioactive fluorine isotopes exist, while there are at least ten neutron-rich isotopes beyond the stable ^{19}F . Experimental determination of the neutron dripline thus provides a definitive test of a given nuclear model, e.g., whether a certain predicted neutron-rich nucleus is bound or not.

The divergence of present models in their predictions of the neutron dripline underscores the limitations of our current understanding of the effective interaction at large neutron excess. The neutron dripline is extremely difficult to reach, and the best tool to produce and study most short-lived nuclei has proven to be the "fast" technique of projectile fragmentation.

Interesting new features of nuclear structure have been uncovered in the most neutron-rich nuclei during recent years, such as neutron skins, neutron halos, and dramatic changes in level spacings and ordering that were not predicted by nuclear models. The present knowledge of the neutron dripline itself is limited to nuclei with proton numbers smaller than nine. The current goal is to extend this limit to 11 (sodium) with incremental improvements of the existing NSCL facility. Major advances in understanding the most exotic neutron-rich nuclei require the significantly higher primary beam intensities that will become available at the ISF. The broad range of new possibilities for the study of the most neutron-rich isotopes at the ISF will be described in the following subsections.

2.1.1 Existence

The NSCL has played a key role in establishing the location of the neutron dripline up to proton number eight (^{24}O) and in the characterization of the properties of low- Z neutron-rich nuclei (see the review, [Tho04]). The neutron dripline for the $N = 12$ isotones was established with the nonobservation of ^{16}Be [Bau03], and a few events of ^{31}F , which is the most neutron-rich fluorine isotope currently known [Sak99], were identified. The observation of a few events requires approximately two days of a primary beam of ^{48}Ca at an average intensity of ~ 10 pnA at the current CCF. The transport time from the production target to the image of the fragment separator, where each ion is identified on an event-by-event basis, is typically less than $1\ \mu\text{s}$ – small compared to the shortest β -decay half-lives (~ 1 ms) – and hence decay losses are negligible. Intensities of one particle per day are sufficient to establish the existence of an isotope. It is important to emphasize that the rapid shift of the neutron dripline from ^{24}O to at least ^{31}F was unexpected. Theoretical models ranging from the USD shell model to relativistic mean field calculations predicted that ^{26}O and ^{28}O would be bound.

Reaching the NSAC milestone of determining the neutron dripline up to sodium ($Z = 11$) will require significantly higher intensities because the dripline rapidly shifts to heavier isotopes for nuclei beyond fluorine. The observations of ^{34}Ne , ^{37}Na , and ^{38}Mg at RIKEN [Not02] and GANIL [Luk02] represent the heaviest isotopes in the fluorine-magnesium region. The next step to establish the location of the neutron dripline is the determination of whether ^{33}F , ^{36}Ne , ^{39}Na , and ^{40}Mg are neutron bound. With the high intensity (~ 100 pnA) ^{48}Ca beam just becoming available at the CCF, we will likely be able to produce these isotopes in sufficient quantities to advance the knowledge of the location of the dripline by four elements. ^{40}Mg would be the heaviest nucleus along the $Z = (A-4)/3$ line; isotopes beyond this line are out of reach at present facilities.

Significantly higher beam intensities of heavier neutron-rich beams such as ^{86}Kr will be available at the ISF to push this limit to higher atomic numbers. Figure 2.1 shows the present and future expected limit of known neutron-rich isotopes. The ISF is expected to push the limit at least up to the nickel isotopes ($Z = 28$) or mass numbers of about 60.

2.1.2 Beyond the neutron dripline

Along the neutron dripline where the neutron binding energy becomes zero, the relatively small enhancement of the total binding energy for paired neutrons has an important impact. The stability of nuclei with even numbers of neutrons compared to their neighbors with odd numbers creates a saw-tooth pattern in which the heaviest odd- N isotopes of a given element are neutron-unbound, while heavier isotopes with an even number of neutrons can be bound. Well-known examples are ^{10}Li (unbound) and ^{11}Li or ^{21}C (unbound) and ^{22}C . The properties of the inter-leaving neutron-unbound nuclei provide important insights into the neutron-nucleus interaction far from stability, the coupling to the continuum in neutron-rich systems, and the delicate structure of multi-neutron halos or skins. In addition, the wave functions of the even- N nuclei at the dripline are not well-known, and studies of the adjacent neutron-unbound (odd- N) nuclei can yield single-particle information crucial for the characterization of the heavier bound nuclei.

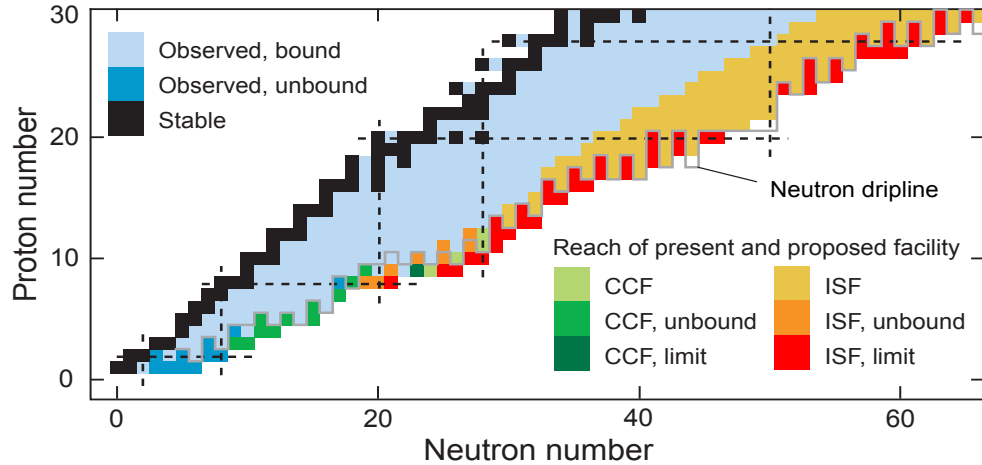


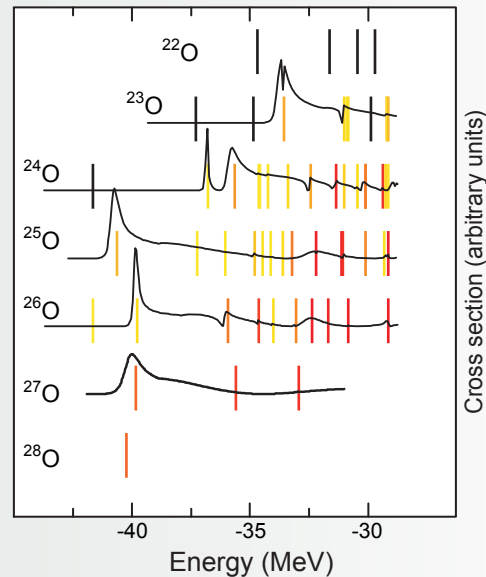
Figure 2.1: Section of the chart of nuclei for light neutron-rich nuclei. Known nuclei are shown in black or blue, nuclei in reach of the CCF and the ISF in green and red, respectively. The light shading indicates nuclei predicted to be bound and that are in reach of the CCF and the ISF. The intermediate shading shows unbound nuclei where spectroscopy has been performed or can be done. The dark shading represents isotopes beyond the dripline, which can be confirmed to be unbound with the CCF and the ISF.

Open and marginally stable systems

A special area of mesoscopic physics covers marginally stable systems. Nuclei provide one of the best laboratories for studying marginally stable systems. Nuclear physics experiments with rare isotopes can reach nuclei far from stability and even beyond the driplines. With their low separation energies, the weakly bound nuclei have only few (if any) particle-stable excited states. Even small excitations can bring such systems into the continuum. The presence of the continuum influences, through virtual couplings, the intrinsic structure of the bound system. This is particularly important for atomic nuclei near the driplines. In all nuclei the level density increases exponentially with excitation energy, and above the nucleon decay thresholds the states that are usually modeled as discrete states are, in reality, resonances. Patterns of overlapping resonances, in contrast to those of isolated resonances, can be very complicated [Eri63]. Conventional theoretical methods do not always account for the proximity of continuum.

What we learn about marginally stable systems in nuclear physics is important for non-nuclear mesoscopic systems as well. Quantum dots are in fact open quantum billiards. The states of atoms in traps are usually metastable. Quantum wires or Josephson junctions should have wire connections to become a part of a circuit. This connection to the open environment is a source of decoherence and one of the main problems in understanding and advancing the development of quantum computers. In all cases, the interaction with and through the continuum influences the internal structure. Weakly bound nuclei will give unique information on how such systems exist, react, and decay. Along with new data, we need a consistent theoretical approach to open systems. Such an approach must unify the description of discrete spectrum, continuum, coupling between them, and reactions on such systems. Recent progress in

theory [Mic04,Vol03a,Vol05] is strongly connected with more powerful computational capabilities available. The main physical problem here is related to our lack of knowledge of the effective nucleon interaction in the continuum, and theoretical advances here depend strongly on experimental success.



Bound excited states and continuum states in oxygen isotopes calculated in a unified model including those nuclei beyond the dripline. ^{24}O is the heaviest bound oxygen isotope. Excited states are indicated as vertical lines (the color indicates widths that, as a rule, increase with excitation energy). The solid black curves indicate the relative cross sections for neutron scattering to the unbound states. Adapted from [Vol06].

The intense fragment beams of the most exotic bound nuclei have been used at the NSCL and elsewhere to extend mass determinations from reaction Q -value measurements to neutron-rich nuclei beyond the dripline, where the ground state is an unbound resonance. In a typical experiment, the energies and angles of the neutron and the fragment must be detected with sufficient precision to allow reconstruction of the energies of the resonant states from the decay of the unbound nucleus. The observed decay energy determines the mass while the width of the resonance is related to the angular momentum of the state. Just as for traditional transfer reactions, different reaction channels provide complementary information, and both proton and neutron removal reactions are important and necessary.

The nuclear masses and the angular momenta of the ground-state wave functions of these unbound nuclei provide information on the shell structure at the neutron dripline that cannot be obtained by other means. For example, measurements of light unbound nuclei have been instrumental in the understanding of the disappearance of the $N = 8$ shell closure at the dripline [Kry93,Tho99,Che01]. The study of unbound nuclei will also be crucial in elucidating the emergence of $N = 14$ and $N = 16$ subshell closures and the disappearance of the $N = 20$ shell gap in the region of heavy oxygen nuclei.

The first measurement of the decay energy of unbound ^{25}O was completed recently at the NSCL [Hof06]. This nucleus forms the “corner” of the neutron dripline where the oxygen isotopes are cut short at $A = 24$ and the fluorine isotopes extend out to at least $A = 31$. The decay energy, which is directly related to the mass of the resonance, is critical for understanding the evolution of the $N = 20$ shell in this region. In the near term, the two-proton knockout reaction from ^{26}F will be used to populate ^{24}N and thereby extend the mass measurements along the chain of $N = 16$ isotones.

The $N = 14$ subshell can be tested similarly with mass measurements of the ^{21}C and ^{20}B ground-state resonances. These nuclei will be populated with one- and two-proton knockout reactions from ^{22}N , respectively. All these experiments are at the feasibility limit of the present CCF facility. Those nuclei are indicated as the medium-shaded green squares in Figure 2.1. The extension of this technique to heavier unbound nuclei will be straightforward with the more intense fast beams from the ISF. Beam intensities at the level of only 10^3 s^{-1} are sufficient for studies of these reactions that benefit from the combination of kinematic focusing and highly efficient detection systems. Nuclei up to magnesium (with $N \sim 26$) will be accessible with fast fragmentation beams, allowing extended studies of this neutron orbital up to the shell closure at $N = 28$.

2.1.3 Search for two-neutron emitters

Similar to the study of nuclei that simultaneously emit two protons, as discussed in Section 2.2.3, the study of nuclei that emit two neutrons can reveal details of the neutron-neutron pairing interaction and the two-valence neutron wave functions. The study of two-neutron emitters has so far been limited to the breakup of the two-neutron halo nucleus ^{11}Li . The breakup of this “Borromean” nucleus into three components (no two of which form a bound system) is sequential because the reaction proceeds via the population of the unbound intermediate nucleus ^{10}Li [Sim99].

A new opportunity to observe correlated two-neutron emission is the decay of ^{26}O . Recent shell model calculations predict that ^{26}O is *unbound* with respect to two-neutron emission by 550 keV but *bound* by 750 keV with respect to one-neutron emission [Sig05]. Thus ^{26}O (produced, for example, by one-proton knockout from ^{27}F) may decay via the emission of two correlated neutrons. Similar to the two-proton decay studies it is necessary to determine the decay energy of the intermediate resonance ^{25}O . This measurement was recently completed by the MoNA collaboration at the NSCL.

Heavier nuclei that might decay by two-neutron emission are presently out of reach and will only be accessible at the ISF. If the search for ^{33}F , ^{36}Ne , ^{39}Na , and ^{40}Mg , mentioned above, shows that some of these isotopes are unbound, they automatically become ideal candidates to explore the process of decay by the emission of two neutrons. The two-neutron decay of these nuclei could be hindered (leading to potentially long lifetimes) given the current expectation that the nuclear shapes of the ground states of the parent and daughter nuclei are different [Sto03].

In even heavier nuclei it might not be necessary to approach the neutron dripline so closely in order to observe two-neutron emitters. The possibility of two-neutron emission from isomeric states of neutron-rich nuclei was predicted in 1971

Invariant mass measurements of unbound nuclei

Studies of nuclei close to the neutron dripline and of nuclear systems even beyond the neutron dripline have greatly expanded in recent years. The binding energy of a single neutron vanishes at the neutron dripline, and heavier nuclei are unbound with respect to prompt neutron emission, falling apart on an extremely short time scale. A well-established technique to study neutron-unbound systems relies on population of the unbound nuclear state in a simple nuclear reaction (e.g., particle knock-out or Coulomb dissociation) followed by detection of all of the decay products, i.e., the neutron (or neutrons) and the charged fragment, in coincidence. Measurement of the two energies (E_n and E_f) and the two momentum vectors (\vec{p}_n and \vec{p}_f) of these particles enable the reconstruction of the invariant mass or the decay energy E_d . The decay energy is the invariant mass of the unbound system minus the sum of the separate particles' masses and is written as

$$E_d = \sqrt{m_f^2 + m_n^2 + 2(E_f E_n - \vec{p}_f \cdot \vec{p}_n)} - (m_f + m_n).$$

These measurements are performed with a large-gap dipole magnet or "sweeper magnet" that diverts the beam and other charged particles to the side so that the forward-going and undeflected neutrons can be detected cleanly in a high-efficiency neutron detector such as the MoNA device at the NSCL.

As an example, Figure A shows the present setup at the NSCL and Figure B shows the reconstructed decay energy spectrum of the neutron-unbound nucleus ^7He .

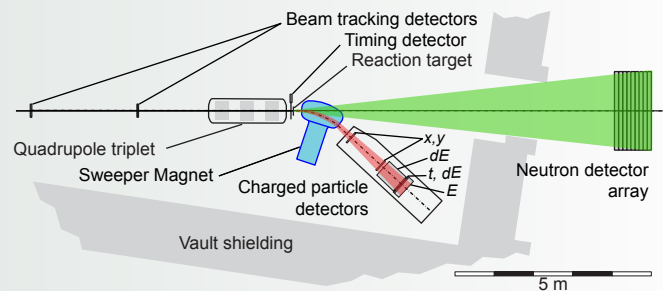


Figure A: Schematic setup of an invariant-mass measurement using a sweeper magnet in combination with a neutron detector array for coincident detection of charged particles and neutrons near zero degrees.

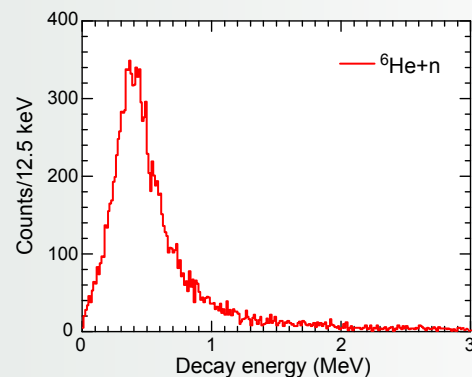


Figure B: The reconstructed decay energy spectrum for the neutron-unbound ground state in ^7He which is unbound by 450 keV and has a width of 160 keV. The data were taken during the commissioning of the Sweeper Magnet and the MoNA neutron detector at the NSCL.

[Pek71]. For example, the $21/2^+$ isomer in ^{63}Ti was predicted to decay by two-neutron emission with a lifetime of about 100 s. ^{63}Ti will be produced at the ISF at the rate of approximately 1 s^{-1} and the observation of this exotic decay (two-neutron radioactivity) will come into reach.

Another closely related and potentially very exotic case is the ^{28}O ground-state resonance that should also be accessible at the ISF. This nucleus had been assumed to be bound for many years due to its doubly magic nucleon numbers. However, it has since been shown to be well beyond the dripline for oxygen. ^{28}O could even decay by the emission of two pairs of di-neutrons.

2.1.4 Beta-delayed neutron emission

Another important consequence of the decline in the neutron binding energy as one approaches the neutron dripline is the increased importance of β -delayed neutron emission. It is well-known that the Q value for β decay can exceed the separation energy for protons and for neutrons at the limits of isospin within an isotopic chain. However, as indicated in Figure 2.2 for the magnesium isotopes, the sharp decrease in stability at the proton dripline limits the number of β -delayed proton emitters, whereas the lack of a Coulomb barrier leads to a gradual decline in stability and a large range of β -delayed neutron emitters within an isotopic chain.

Studies of neutrons that are emitted after β decay have provided detailed spectroscopic information on the exotic daughter nuclei and present important input data for astrophysical r-process calculations as discussed in Section 3.1.1. For example, simple neutron counting [Hos05] provides information on the branching ratios between mass chains while the combination of γ -ray and neutron time-of-flight spectroscopy [Sum06 and references therein] can provide a very detailed picture

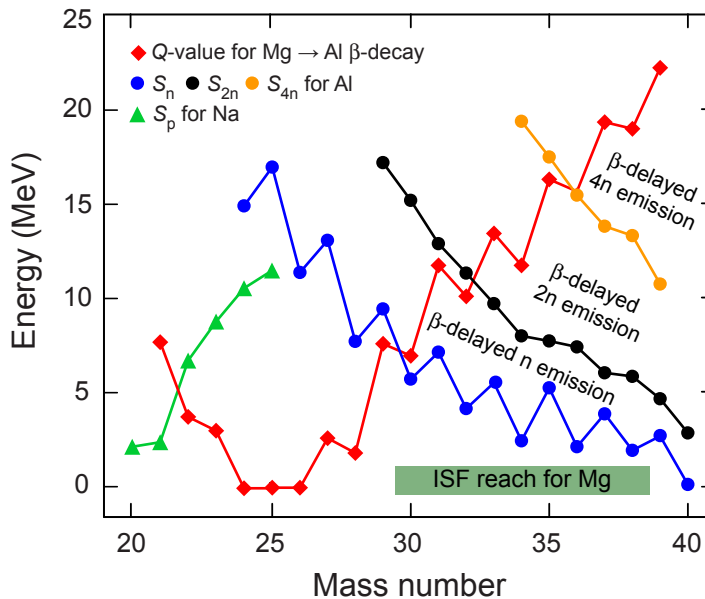


Figure 2.2: Q values for β decay of magnesium isotopes are shown as a function of neutron number (red diamonds). The Q value can be seen to exceed the proton separation energy (green triangles) in only a few cases, while it exceeds the neutron separation energy (blue circles) in many cases. In addition, emission of multiple neutrons (black and orange circles) will become an important decay mode of neutron-rich nuclei accessible at the ISF.

of the level structure of the β -decay daughter nucleus. Beta-delayed neutron spectroscopy has been applied to nuclei that range from ^8He to ^{23}O at the NSCL facility. The number of nuclei that will require neutron spectroscopy to unravel their level structure will dramatically increase as the isotopic chains are extended towards the neutron dripline above oxygen ($Z = 8$).

2.1.5 Halos

Weakly bound few-body systems have been found to exhibit properties very different from those of well-bound systems, for example, halo structures. The study of these neutron halos is important for a better understanding of nuclear structure close to the driplines and also helps to understand the universal features of weakly bound few-body systems. For example, halo structures are also found in atomic and molecular systems [Rii00,Jen04]. Close to the neutron dripline, a number of nuclei have been found to exhibit neutron halos [Han95], and many more are predicted to exist [Jen04].

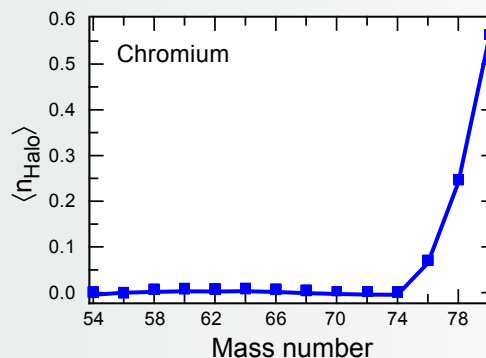
Whenever the last few neutrons are weakly bound in a nucleus, quantum mechanical tunneling allows the extension of the neutron wave function far beyond the nuclear core. The short-range attraction of the nuclear potential is weak in this extended region and, as a result, the nucleus develops a diffuse halo with one or a few neutrons distributed over a large volume. The radial wave function of such a halo nucleus depends critically on the neutron separation energy. Thus, precise measurements of nuclear masses and separation energies of these exotic

Limits of existence and halo phenomena

The nuclear energy density functional approach finds its microscopic roots in the Hohenberg-Kohn theorem [Hoh64], which states that the ground-state energy of a many-body interacting system can be written as a functional of its one-body density. As a result, the main purpose of energy density functional approaches is to deliver ground-state bulk properties of medium- to heavy-mass nuclei, such as binding energy, matter and charge densities, fission barriers, etc. The main difficulties reside in the actual construction of the energy functional. Among others, the properties of the energy functional at the nuclear surface are currently not well understood, especially for nuclei with large neutron excess.

To tackle the low-density part of the functional and the gradient corrections that play an important role at the nuclear surface, in-depth systematic studies of dripline and halo systems are of great interest. An interesting question is whether or not the halo phenomenon exists in medium-mass nuclei in the same form as it is usually observed in light nuclei where a cluster picture applies (a core plus one or two well-separated neutrons). As was shown recently [Rot06], halos actually display a more collective nature as nuclei become heavier, with several low- ℓ orbitals contributing to them. The figure shows the emergence of a neutron halo for dripline chromium isotopes as predicted by Hartree-Fock-Bogolubov calculations. The vertical axis shows the average number of neutrons contained in the nuclear halo [Rot06]. The halo develops in the chromium

chain beyond the closed-shell nucleus ^{74}Cr , when neutrons fill several loosely bound low- ℓ states up to the predicted dripline at ^{80}Cr . The halo factor (0.5) is comparable in absolute value to what is found in light nuclei, although more orbitals participate in the present case. In the end, studying the collectivity of the halo in the most exotic medium mass nuclei will help to test and constrain cutting edge microscopic energy functionals.



Average number of neutrons participating in the nuclear halo as predicted by HFB calculations for the chromium isotopes ($Z = 24$). It is comparable in absolute value to what is found in light nuclei although more orbitals participate in the present case. At the ISF, interaction cross sections should be experimentally accessible up to ^{78}Cr .

systems provide important information for theoretical descriptions as well as for the identification of new halo candidates.

Examples of halo nuclei studied in some detail include ${}^{11}\text{Li}$, ${}^{11}\text{Be}$, ${}^{14}\text{Be}$, and ${}^{19}\text{C}$ [Han95]. With the exception of ${}^{11}\text{Be}$, none of the neutron separation energies are known to better than 10%; however, even the accuracy of these measurements has recently been questioned. For example, the presently adopted two-neutron separation energy for ${}^{11}\text{Li}$ disagrees with the preliminary result from the recent direct mass measurements with the radio-frequency spectrometer MISTRAL at ISOLDE [Lun05]. Recall that the binding energy is approaching zero for these nuclei, and a small shift can have important implications on physical properties and theoretical descriptions.

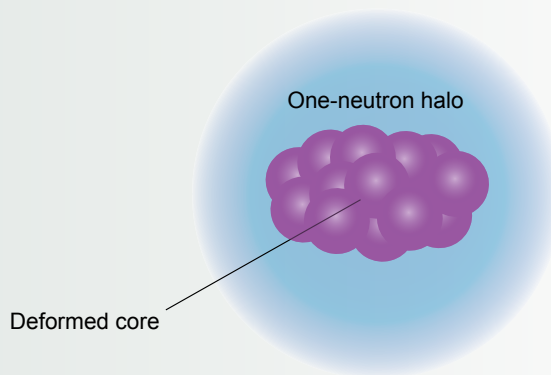
Projectile fragmentation facilities provide a unique opportunity to study the short-lived halo nuclei, and, indeed, most of the information on these systems has been obtained at these facilities. The production rates can be high, and precision Penning-trap mass spectrometry can be applied to determine their binding energies.

The LEBIT system at the NSCL has recently demonstrated that Penning-trap mass measurements of short-lived nuclei from projectile fragmentation are possible for nuclei with half-lives as short as 90 milliseconds. The even shorter half-lives of halo nuclei (a few to a few tens of milliseconds) make such measurements challenging. Nevertheless, LEBIT beam manipulations can be optimized for the study of the shortest-lived isotopes. The combination of the high production rates at the NSCL and the high magnet field of the Penning trap can make significant improvements of the mass values and separation energies. Taking the efficiency achieved with the combined NSCL gas stopping station and LEBIT as a conservative lower limit for future improvements, mass measurements with uncertainties between one and five keV are achievable. The masses of all halo

Do spherical neutron halos in deformed nuclei exist?

The strong interaction between neutrons and protons dominates the Coulomb interaction so that the density distributions of the neutron and proton fluids are usually similar in nuclei close to stability. For example, if one distribution is spherical, then the other will be spherical. Similarly, if one distribution has a prolate deformation, the other will have a prolate deformation.

Neutron halos are preferentially formed when a loosely bound neutron is in an $\ell = 0$ single-particle state. The density distribution of these $\ell = 0$ states is spherical. Since there is no angular momentum barrier, the size of the halo can become arbitrarily large. Due to the uncertainty principle, an extended density distribution corresponds to a small momentum distribution and a relatively small kinetic energy. Consequently, nuclei with loose binding have a preference for neutrons occupying low- ℓ single-particle states. Thus, we may find situations near the neutron dripline where the valence neutron has a spherical density distribution with a very large rms radius even when the core protons and neutrons are deformed.



Schematic illustration of a deformed core of protons and neutrons surrounded by the spherical distribution of a loosely bound neutron.

nuclei listed above and also heavier nuclei like ^{22}N or ^{23}O – which were recently shown to have increased matter radii [Oza01] – can be measured with these small uncertainties.

A number of heavier halo nuclei are expected to exist beyond fluorine [Jen04], but these predictions are largely based on estimates using unknown, extrapolated mass values. Precise mass measurements of these halo candidates may be possible at the ISF, which will determine if the neutron separation energies are small, the first requirement for halo structure. Even if the most exotic nuclei remain beyond the reach of the precise mass measurement, significant improvement of mass values of neighboring nuclei (see Section 2.5.2.1) will enhance the ability to predict the location and structure of the neutron dripline.

Mass measurements will reveal the presence of halos in nuclei; however, to study the nature, structure, and possible correlations of the halo nuclei, it is necessary to excite them in nuclear reactions. Neutron halo nuclei are unlikely to have any bound excited states due to their low binding energies, although ^{11}Be is a notable exception. Hence, any reactions to explore the structure of the halos will lead to states in the continuum that will decay into the fragment core and the halo neutron(s). The continuum can be a straightforward two-body continuum (as in ^{11}Be , which breaks up into $^{10}\text{Be}+n$) or a more complicated three-body (as in the case of the Borromean nucleus ^{11}Li , which breaks up in $^9\text{Li}+n+n$) or even a five-body continuum (as in the case of ^8He , which breaks up into $^4\text{He}+n+n+n+n$).

Breakup reactions, where the halo nucleus is excited via nuclear or Coulomb interaction, are versatile tools to study continuum properties. For example, measuring the coincidence of ^{10}Be with neutrons following the breakup of ^{11}Be , the resonant state energies were accurately determined, and spin assignments were made [Fuk04]. Triple coincidence experiments following the breakup of ^{11}Li ($^9\text{Li}+n+n$) found evidence for a strong spatial correlation between the two neutrons in the halo [Nak06].

Currently these measurements are limited to the lithium to beryllium region. With the beam intensities available at the ISF, these studies can be extended to the heavy carbon and oxygen isotopes, where the occupation of the $s_{1/2}$ orbit between the $N = 14$ and $N = 16$ subshells plays a crucial role for the halo formation. Inclusive breakup experiments could be possible into the nickel region.

2.1.6 Neutron skins

One of the major opportunities of the ISF will be to explore new forms of nuclear matter. The occurrence of unusual nuclear configurations often provide the most stringent tests for our understanding of nuclei or offer the possibility to highlight a certain aspect of the nuclear force that is otherwise difficult to isolate. Halos, discussed in the previous section, are one example where the interactions of neutrons in a low-density environment can be studied. A related feature is the skin of neutrons or protons on the surface of a nucleus that can occur when the neutron and proton Fermi levels are very different [Tan95]. For such nuclei, the nuclear surface can be a region of nearly pure neutron (or proton) material. This effect can be dramatic for the extremely neutron-rich nuclei produced at the ISF, where the skin may be more than one femtometer thick.

To illustrate this effect, Figure 2.3 shows the neutron skin, ($\langle r_n^2 \rangle - \langle r_p^2 \rangle$), as a function of mass number A for the nickel isotopes. The difference of rms neutron and proton radii was obtained in Skyrme Hartree-Fock calculations using the Skx Skyrme functional [Bro98] (shown as the green symbols under the assumption of either a soft or a stiff asymmetry term). The corresponding neutron and proton separation energies are shown and illustrate that the neutron Fermi level becomes much higher than the proton Fermi level as the neutron number increases. The intensities of the nickel isotopes available at the ISF are indicated at the top of the figure. Reaction studies of these nuclei will provide a model-dependent estimate for the neutron radius with beam rates as low as 10^{-3} s^{-1} , and hence nuclei with neutron skins as large as 0.7 fm can be studied.

Many authors have argued that the size of the neutron skin is related to the symmetry energy in nuclei, and thus provides a way to extract this key quantity, which determines, for example, the radii of neutron stars [Ste05a]. If the volume symmetry energy is low, then the excess neutrons in the neutron skin will tend to pull the core protons out into the skin. If the symmetry energy is high, the core protons will be disturbed less. Information on the symmetry energy is not the only information that can be extracted from the study of neutron skins. The size and systematics of

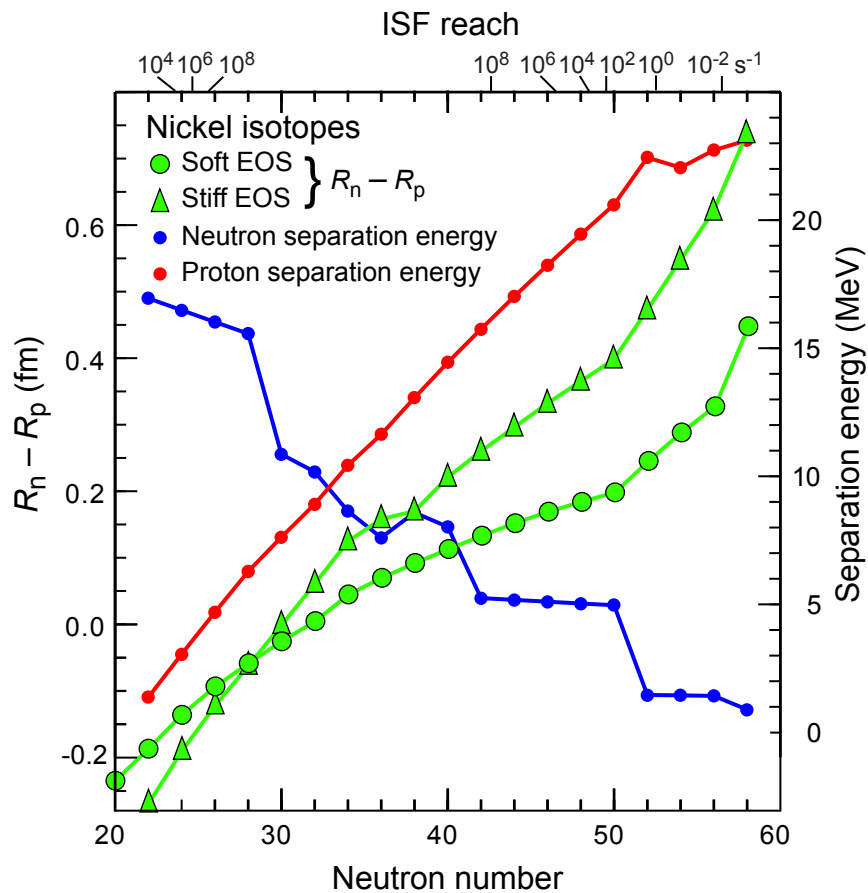


Figure 2.3: The difference of rms neutron and proton radii for nickel isotopes calculated in Skyrme Hartree-Fock using the Skx Skyrme functional with a soft and a stiff asymmetry term in the equation of state [Bro98]. The origin of the skin effect is the difference of proton and neutron Fermi energies, illustrated by the red and blue points and lines, respectively. The top of the figure provides the rates of the various isotopes in particles per second. Sufficient intensity is available for the study of neutron skins out to $N = 58$ and a skin size of up to 0.7 fm, as described in the text.

neutron skins and nuclear binding can also lead to key information, such as the ratio of the volume to surface symmetry energy [Dan03,Sat06]. In addition, the neutron-skin thickness in exotic nuclei will provide crucial information about the isovector properties of nuclear matter and the parameterization of the Skyrme interaction [Yos06].

At present, the symmetry energy (and the ratio of volume to surface contribution), its density dependence, and other related phenomena are not known. Depending on the value of the symmetry energy, stable nuclei are expected to have a small neutron skin of about 0.2 fm or less. The neutron skin of ^{208}Pb , for example, is predicted to be of the order of 0.08 to 0.2 fm, but this value has not yet been measured accurately. The accurate measurement of the neutron skin thickness in ^{208}Pb is the subject of an experiment from the HAPPEX collaboration at JLAB [Hor01].

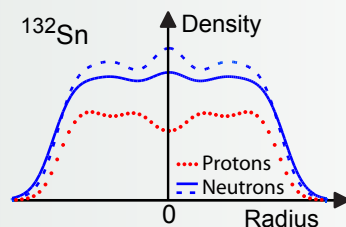
There is experimental evidence for more extreme cases of neutron skins – found at GSI – where skins of about 0.5 fm were deduced in a model-dependent way for the neutron-rich sodium isotopes [Suz95]. Interaction cross sections of sodium isotopes ($A = 20\text{--}23, 25\text{--}32$) with a carbon target were measured at 950 MeV/nucleon. The effective root-mean-square matter radii of these isotopes were deduced from a Glauber-type calculation. In comparison with charge radii inferred from isotope-shift measurements of the same isotopes, the neutron radii were deduced [Suz95]. Although more model dependent than the proposed JLAB HAPPEX experiment, these type of measurements can be made over a wide range of mass number, A , and for skins up to approximately 0.7 fm. The measurement of interaction cross sections requires only 0.01 particles per second; isotope shift measurements determined from laser spectroscopy require a similar intensity. However, to fully exploit the potential science of the study of extreme skins, improvements in reaction theory will be needed to reach the required precision and accuracy.

Constraining the equation of state for neutron-rich matter by nuclear structure investigations

The nuclear equation of state describes the relationships between the energy, pressure, temperature, density, and neutron-proton asymmetry of nuclear matter. The matter energy can be represented as a sum of two terms. The first term describes symmetric matter for which the neutron-proton asymmetry is zero (i.e., there are equal numbers of neutrons and protons). The second term, the symmetry energy, describes changes in the energy with changing neutron-proton asymmetry. Properties of neutron stars are very sensitive to the symmetry energy term. Currently this term is not well determined, and the uncertainties hamper predictions of neutron-star structure [Lat04].

The surface-volume competition in nuclei can lead to significantly different neutron-to-proton ratios in the interior and surface of a nucleus. Partitioning of the particle distributions depends on the relative magnitude of the surface and volume symmetry energies [Mye69,Ste05a]; in more detail, the neutron-to-proton ratio as a function of radius reflects the dependence of the symmetry energy on density. Constraints on the neutron-proton partitioning within the nucleus can be obtained from nuclear masses and other observables, such as the evolution of neutron-skin properties over a wide range of isotopes [Dan03]. Neutron skins can be accessed through measurements of in-

teraction cross sections and precise measurements of proton scattering. Measurements of giant isovector resonances over a broad range of isotopes provide complementary information that can help constrain the symmetry energy term. The ISF will provide experimental access to a wide range of new isotopes for such studies.



Schematic illustration of the nuclear density distributions for protons (red) and neutrons (blue) in ^{132}Sn . The density dependence of the symmetry energy will determine the neutron-to-proton density ratio as a function of radius. The figure shows the neutron density for two possible equations-of-state: one with an energy per neutron that increases relatively fast with density (solid blue line) and one that increases relatively slowly (dashed blue line).

Another promising tool for the extraction of charge and matter radii for exotic isotopes is proton scattering in inverse kinematics [Amo06]. Variants of the technique, in normal kinematics, have been applied to proton-scattering data on ^{208}Pb and indicate a skin thickness of about 0.17 fm [Kar02,Cla03a]. If confirmed by the JLAB experiments, this technique will likely be on a firm footing for the extraction of neutron rms radii in exotic isotopes. Proton scattering in inverse kinematics will require intensities of the order of one particle per second at 100 to 200 MeV/nucleon to obtain sufficient precision. The higher energy is needed to improve the validity of the reaction theory and to allow for thicker targets and hence increased sensitivity.

An important feature of nuclei with pronounced skins is that their continuum structure may be quite different than that of normal nuclei. In particular, there may be low-lying resonance modes of excitation (the soft modes). For example, investigations of the resonance structure of dripline nuclei found considerable isovector dipole strength at low excitation energies [Ham98,Sag02,Paa05]. In addition, the isoscalar strength is also moved to lower excitation. The hints of these effects have been seen in Coulomb excitation experiments on tin [Adr05] and oxygen isotopes [Lei01a,Try02]. As shown in Figure 2.3, similar experiments at the ISF will be possible over a wider range of isotopes and out to $N = 50$ and skin thicknesses greater than 0.4 fm.

Another interesting, potential effect of the neutron skin would be the enhancement of sub-barrier fusion cross sections [Tak91,Hus92], a topic that is the subject of current research and debate. If it could be shown that a neutron skin enhances the fusion cross section, the enhancement may provide a path to create neutron-rich superheavy elements with enhanced stability relative to the neutron deficient nuclei that can be produced with stable beams. However, it has been shown experimentally that weak binding in light projectile nuclei reduces the sub-barrier fusion cross section due to breakup effects (see for example [Ito06,Raa04]). Breakup effects should be smaller in more bound, heavier nuclei, such as the heavy nickel isotopes, and a large enhancement might be possible. A hint of such large enhancement has been seen recently in the fusion of ^{132}Sn [Lia06]. Energies of less than 5 MeV/nucleon and intensities of greater than 1000 s^{-1} are required for these sub-barrier fusion studies. Rates of greater than 10^9 s^{-1} are necessary for production of new superheavy isotopes. These intensities will be available over a reasonable range of reaccelerated isotopes after stopping in the new cyclotron stopper.

2.2 Along the path of the proton dripline

The study of symmetric nuclei with an equal number of protons and neutrons as well as their close neighbors is essential to the understanding of pairing effects and isospin symmetry, two fundamental concepts on which most models of nuclei and the nuclear force are built. Symmetric nuclei heavier than ^{56}Ni move closer to the proton dripline as the valley of stability deviates from $N = Z$ with increasing mass. The most important of these nuclei is the heaviest bound doubly magic $N = Z$ nucleus ^{100}Sn , of which very little is known at present. For example, the β decay of this nucleus has been predicted to proceed through a single, low-energy 1^+ level in ^{100}In due to the unusual location of the Gamow-Teller resonance well within the Q -value window (see Section 2.5.2.2).

The ISF will provide a large gain in sensitivity in the study of ^{100}Sn and similar nuclei in its region. Production cross section measurements to date range between

10 and 100 pb [Lew95,Cha96], corresponding to rates of about 1 to 10 per day with present facilities. The projected rate of 0.4 s^{-1} at the ISF will allow detailed studies of ^{100}Sn and its neighbors. Past experimental attempts to study ^{100}Sn have been hindered by the low purity of the most proton-rich beams produced by projectile fragmentation. The NSCL is currently constructing a Radio Frequency Fragment Separator (RFFS) that will greatly improve the purity of neutron-deficient projectile fragments.

Until now, the proton dripline has been established up to nickel for odd- Z nuclei and partially between $Z = 29$ and $Z = 82$ [Tho04]. However, more detailed knowledge of some key nuclei in the mid-mass range, such as ^{64}Ge or ^{68}Se , is important for understanding the rp-process (see Section 3.2). The decay of neutron-deficient nuclei beyond the proton dripline is hindered by the Coulomb barrier even though these nuclei are unbound. Hundreds of such nuclei with lifetimes longer than the typical flight time through fragment separators ($\sim 100 \text{ ns}$) are yet to be observed [Tho04] and can only be studied using fast rare isotope beams such as those that will be provided by the ISF. Knowledge of the proton-separation energies in the proximity of the proton dripline (and not just the location of the dripline) is critical for understanding nucleosynthesis processes in explosive stellar environments. Therefore, it is important to map out the properties of a broad range of nuclei in this region.

2.2.1 Mapping the proton dripline

The observation or nonobservation of a nucleus by itself provides important information for nuclear models. The proton emission lifetimes are directly correlated with nuclear binding energies so that the lower lifetime limits of extremely proton-rich nuclei can be used to constrain mass models where direct mass measurements are not yet possible. For example, the observation of ^{48}Ni [Bla00] contradicts the extrapolations of the atomic mass evaluation [Aud03], while it is consistent with the calculations by Brown, Ormand, and Cole [Bro91,Orm96,Cole96].

In the light mass region below zinc ($Z = 30$) only a few isotopes remain that have not yet been observed but could exist with half-lives longer than 100 ns. For example, no dedicated search has been performed for the even- Z nuclei ^{26}S , ^{30}Ar and ^{34}Ca . The sensitivity of previous experiments in this mass region was not sufficient to observe these isotopes nor to determine a limit on the production [Lan86]. The few remaining isotopes can be accessed and will likely be studied at existing facilities.

Figure 2.4 shows the proton-rich side of the nuclear chart for elements heavier than zinc. Stable isotopes are shown in black and currently known isotopes in blue. The grey line indicates the proton dripline. Although the proton dripline has been reached for almost all the elements shown in the figure, many isotopes exist beyond the dripline with half-lives larger than 100 ns as indicated by the purple line. The half-life limits for nuclei below yttrium ($Z = 39$) and above ruthenium ($Z = 45$) were taken from [Bro02a] and [Her97], respectively. The limits for nuclei between these elements are only estimates because no detailed calculations exist at present.

Experiments that search for new proton-rich isotopes rely on the detection of a well-resolved mass peak in the focal plane of a fragment separator. With the simultaneous measurement of several identification parameters at the focal plane,

Filtering nuclei on the proton-rich side: the radio frequency fragment separator

A crucial element of rare isotope beam production from projectile fragmentation is the fragment separator, for example, the A1900 at the NSCL. The rare isotopes of interest are filtered by the magnetic rigidity of the separator which is directly related to the momentum-to-charge ratio of the fragments. The purity of the beams obtained by this method is sufficient for most experiments, because contaminants can be identified event-by-event; however, for implantation and decay experiments, large impurity rates can become unacceptable because they destroy the time correlation between implantation and decay.

The momentum distributions of projectile fragmentation residues have long tails at the low momentum side. For fragments along the proton dripline, the tails of less exotic nuclei fall at the same magnetic rigidity as the fragments of interest (see Figure A). For example, the purity of ^{100}Sn at the A1900 is approximately 10^{-6} . An additional separation technique that takes advantage of the velocity difference of the fragments has been developed at RIKEN [Yam04]. Such a Radio Frequency Fragment Separator (RFFS) can reduce the impurities by several orders of magnitude.

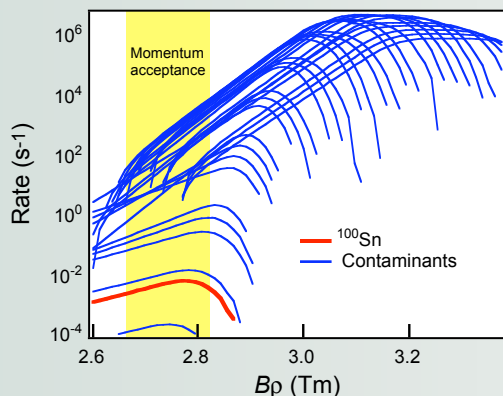


Figure A: Momentum distributions of the numerous contaminants contained in a ^{100}Sn projectile fragment beam at the exit of the A1900 fragment separator. Although the magnetic rigidity ($B\rho$) of the main contaminants is far away from the ^{100}Sn centroid, their exponential low-momentum tails leak into the momentum acceptance of the A1900.

The RFFS relies on the difference in the arrival times among the various isotopes selected by the fragment separator combined with the micro-structure of the beam itself. A uniform RF electric field is applied transverse to the beam direction in the RFFS such that the ions are deflected to a greater or lesser extent depending on the phase of the applied RF during the time that they traverse the device. The phase of the RF is tuned such that a set of slits placed downstream from the RFFS blocks the bulk of the contaminants.

Figure B shows the effect of the RF filtering when the phase of the RFFS is tuned to optimize transmission of ^{100}Sn . The purity is improved by about three orders of magnitude. Some low-Z contaminants are still present in the beam after the RFFS because their arrival time with respect to the ^{100}Sn ions matches a full 2π rotation of the phase.

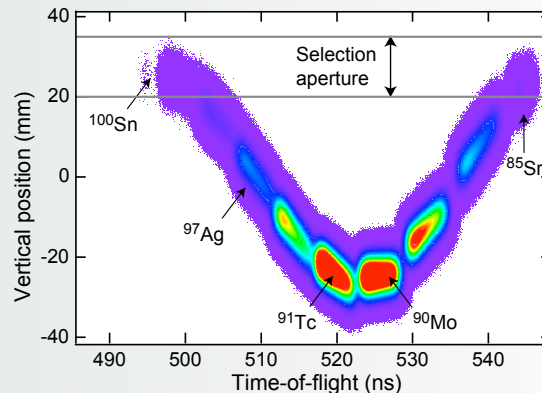


Figure B: Simulation of the purification technique applied to a ^{100}Sn projectile fragment beam by the RFFS. The vertical deflection at the aperture position is shown as a function of time-of-flight for a secondary beam produced in the A1900 fragment separator. The simulation shows the suppression of the most intense contaminants to a level that measurements can be performed on the most exotic isotopes.

A mechanical drawing of the RFFS currently under construction at the NSCL is shown in Figure C. It contains two resonator plates with a frequency that can be adjusted between 18 and 28 MHz. The figure also shows the locations of the two frequency tuners for each plate (top and bottom), the RF coupler from which the power is fed from the RF amplifier on the right-hand side, and the fine frequency tuner needed for regulation via a feedback loop.

At the ISF the RFFS will make it possible to discover new isotopes and measure their lifetimes along and beyond the proton dripline that are out of reach for present facilities.

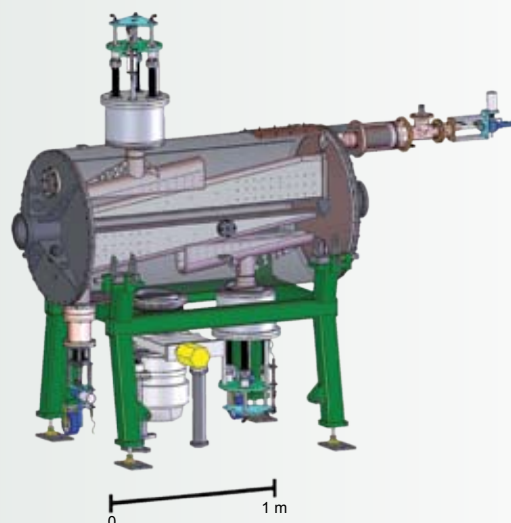


Figure C: Mechanical drawing of the RF cavity for the RFFS under construction at the NSCL. The ions experience a transverse RF electric field between the two plates held by the resonator wedges centered in the tank. The two coarse tuners, the fine tuner (bottom left), and the RF coupler (top right) are also shown.

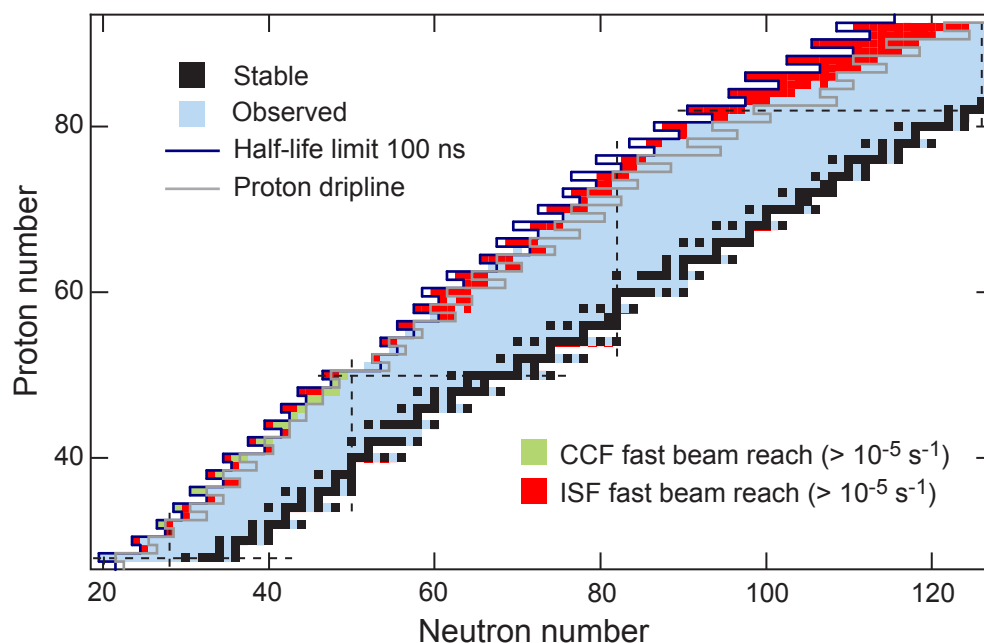


Figure 2.4: The proton-rich side of the nuclear chart. Known nuclei are colored in blue and those accessible by the CCF in green; those within reach of the ISF are shown in red. The grey line shows the calculated proton dripline and the purple line indicates the predicted limit of nuclei with lifetimes greater than about 100 ns.

extremely low background levels can be achieved. As few as three counts are sufficient for the identification of a new isotope. This was recently demonstrated by the first observation of ^{60}Ge and ^{64}Se with the A1900 fragment separator at the NSCL [Sto05a]. During the same measurement, missing events in the particle identification can determine an upper lifetime limit for isotopes (^{59}Ga and ^{63}As). The experiment was not limited by the intensity of the primary beam but by the large amounts of beam impurities at the A1900 focal plane. The RFFS will reduce these impurities by orders of magnitude, making similar measurements to search for even more proton-rich isotopes feasible. It should be possible to establish the (non)observation of all proton-rich nuclei up to krypton within the next few years. In addition, as many as twenty new isotopes between $Z = 32$ and $Z = 49$ are accessible as indicated by the green squares in Figure 2.4.

The availability of higher intensity beams at the ISF will allow us to discover all new proton-rich isotopes and establish the limit of observation up to tin. The mass region beyond tin is currently only reachable with fusion-evaporation reactions. However, the production rates of proton-rich nuclei from fragmentation beams at the ISF are competitive and will become a viable alternative to produce and study these nuclei. The reach of the ISF along the proton dripline is shown as red squares in Figure 2.4. The lifetimes in this mass region are long enough so that not only the existence but also the lifetime can be measured directly as described in the next section.

2.2.2 Proton radioactivity

When the Q -value for proton decay is positive, a nucleus can decay by emission of a proton. However, the proton has to penetrate a barrier formed by a sum of the Coulomb and centrifugal potentials. Therefore, the decay by proton emission

offers the opportunity to extract unique information about the structure and ordering of quantal states in the nucleus [Woo97]. In particular, spectroscopic factors can be directly deduced from the lifetime of such decays because they involve only one nucleon and no preformation factor, in contrast to α decay.

The lightest nucleus for which ground-state one-proton radioactivity has been observed is ^{105}Sb ($Z = 51$) [Tig94]. For lighter nuclei, there is only a small energy window between Coulomb-barrier heights where β -decay dominates and the barriers where the lifetimes for proton emission become too short (smaller than a few microseconds). This time is not sufficient to separate and implant the nuclei in a detector to observe their decay. Thus it is less likely that one-proton radioactivity occurs below $Z = 50$. Potential candidates that will be in reach of the ISF are the odd- Z nuclei ^{75}Y , ^{88}Rh , ^{93}Ag , and ^{97}In as well as isomer excited states in odd-odd $N = Z$ nuclei. First evidence for proton radioactivity of the 21^+ high-spin isomer in ^{94}Ag has been reported recently [Muk05a].

Above $Z = 50$ a large number of proton emitters have already been identified, some of them from highly deformed states. As mentioned in the previous subsection, this is currently the regime of fusion-evaporation reactions with intense stable beams. Recent observations of proton emitters include ^{135}Tb [Woo04] or ^{121}Pr [Rob05]. Although the ISF provides the opportunity to populate proton emitters even further away from stability using fusion-evaporation reactions with reaccelerated rare isotope beams, it is expected that this region can be better explored directly with fast fragmentation beams. For example, the most neutron-deficient europium isotope ^{130}Eu was first produced with a fusion-evaporation reaction $^{58}\text{Ni}(^{78}\text{Kr}, p5n)$ with a beam intensity of 3.5 pA at about 75 events per day [Dav04]. The ISF is predicted to produce 2,400 events per hour of ^{130}Eu using fast fragmentation. With these rates it will be possible to reach about three new nuclei in each isotopic chain.

2.2.3 Two-proton emitters

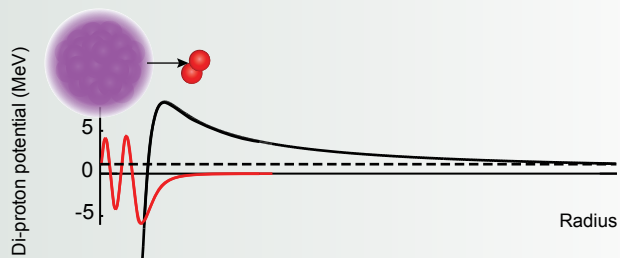
The pairing interaction in nuclei results in the odd-even staggering in the nuclear ground state binding energies. Near the proton dripline this leads to nuclei with even Z values that are bound to one-proton decay but unstable to two-proton decay [Gol60]. The relative rate for sequential one-proton decay and direct two-proton decay depends on the Q value and width of the intermediate states for the one-proton decay channel. The direct two-proton decay can proceed via the emission of two strongly correlated protons, a di-proton, due to the pairing interaction – a strong attractive interaction in the $\ell = 0$ relative proton-proton angular momentum channel. If the nuclear wave function contains low- ℓ single-particle components, the direct two-proton decay may also proceed by simultaneous emission of two uncorrelated protons. The directional correlation between the two emitted protons depends on the decay mode and could be a coherent superposition of all three modes – sequential, simultaneous and di-proton – which must be appropriately included in theoretical descriptions of the angular correlation of the emitted protons. To compare with theory, experiments must obtain accurate Q values, lifetimes, branching ratios (relative to β -decay) and angular correlations between the emitted protons.

In light nuclei the intermediate states for one-proton decay are usually broad (100 keV or more) leading to a competition between the sequential and direct two-proton decay paths. In heavier nuclei the higher Coulomb barrier leads to much

Di-proton decay

Most nuclei beyond the proton dripline decay by the emission of a single proton. But in rare circumstances the single-proton decay is energetically forbidden and two protons are emitted at the same time. This special condition is energetically governed by the attractive pairing interaction between two protons. The pairing interaction arises because the angular momenta of the two protons are paired in time-reversed orbitals. The decay rate for this exotic process is extremely sensitive to the dynamics of the pairing interaction in nuclear matter. This process is similar to Josephson tunneling in condensed matter physics, when electrons penetrate the barrier between two superconductors maintaining their correlations.

Some events corresponding to two-proton decay have recently been observed for ^{45}Fe , ^{48}Ni , and ^{54}Zn [Dos05,Bla05]. However, the correlation between the two protons, which is needed to establish the di-proton character of the process, has not yet been measured. The ISF will provide rare isotope beams with the intensity needed to study this correlation and to quantify the role of pairing correlations between protons at the nuclear surface.



The figure illustrates the correlated two-proton emission from ^{48}Ni . The di-proton starts inside the nucleus with a radial form factor shown by the red line. At the nuclear surface it tunnels through the Coulomb barrier (black line) until its decay energy (the dashed line) is above the Coulomb barrier at the extreme right around 60 fm from the nucleus.

narrower intermediate states (on the order of 1 keV or less) suppressing the sequential decay. The best possibility to observe the di-proton decay mode is in the mass region between chromium and tin ($Z = 24\text{--}50$).

Two proton decay has recently been observed for ^{45}Fe [Gio02,Pfu02,Dos05], ^{48}Ni [Dos05], and ^{54}Zn [Bla05]. However, only a few events were observed, insufficient to determine the directional correlation between the two protons needed to characterize the type of decay mode. Although further experiments are planned in the near future, they will most likely be limited by statistics.

A quantitative comparison of the decay pattern with theory will only be possible with the beam intensity available at the ISF. In addition to ^{45}Fe , ^{48}Ni , and ^{54}Zn , with expected rates of 10^1 s^{-1} , 10^{-1} s^{-1} , and 10^1 s^{-1} , respectively, heavier potential candidates for di-proton decay [Bro02a,Her97] will also be accessible. The expected rates at the ISF for ^{64}Se , ^{67}Kr , and ^{71}Sr of $5 \times 10^2 \text{ s}^{-1}$, 5 s^{-1} , and 10^{-1} s^{-1} , respectively, are sufficient to characterize their di-proton decay.

2.2.4 Short-lived proton-unbound states

The study of one- and two-proton emitters described in the previous sections has been limited to nuclei with lifetimes longer than a few microseconds [Kar03] because proton emission is typically observed after implantation of the decaying nucleus in a solid-state detector. The technique of particle-decay spectroscopy observes the decay in flight and can thus explore proton emitters even further beyond the dripline with much shorter lifetimes. In this method the mass (and excited states) of the unbound nucleus can be determined from the energy and angles of the decay products. This technique has been previously applied to study proton-unbound excited states in light nuclei [Nay02].

The masses of short-lived proton-unbound nuclei are currently only known for light proton-rich nuclei up to $Z = 11$ [Tho04]. Current facilities should be able to access the first unbound isotope of the odd- Z elements up to ^{69}Br . The masses of these isotopes are important for the modeling of the astrophysical rp process.

Especially important cases are ^{69}Br and ^{73}Rb , but heavier nuclei might play a role as well. While ^{69}Br might be reached at existing facilities, only the high-beam intensities available at the ISF will make it possible to measure the masses and excited states of all key rp-process nuclei (see Section 3.2.1).

Spectroscopic information of short-lived proton-unbound nuclei can also be obtained by elastic resonance scattering in inverse kinematics. For example, in order to study unbound states in ^{11}N , a ^{10}C beam is scattered off a hydrogen target, and the protons are detected at 0° . It has been demonstrated that decelerated beams produced in projectile fragmentation can be used to identify unbound states with this method [Mar00,Pet03]. However, for the extraction of high-resolution spectroscopic information, high-quality reaccelerated beams are necessary [Cas06]. These experiments can be performed with beam intensities of about 10^3 s^{-1} . Currently this method has been limited to the light mass region up to fluorine, but with the availability of high-quality reaccelerated beams from the ISF these studies can be extended to medium-mass nuclei relevant for the understanding of the rp-process.

2.3 Evolution of shell gaps

The evolution of properties of atomic nuclei with respect to changes in proton and neutron numbers is one of the crucial questions that must be answered to gain an understanding of the structure of atomic nuclei. Shell closures form the basis of local models and define effective degrees of freedom that must be taken into account to form a quantitative picture of the atomic nucleus. The nuclear potential and the resulting shell structure are well established for stable nuclei. Modifications of the potential for nuclear systems beyond the valley of β stability have already been found. These modifications lead to the development of new magic numbers and the breakdown of the shell gaps established closer to stability [Ots01] (see Figure 2.5). In a regime of asymmetric numbers of protons and neutrons, such changes in the single-particle structure are driven by the spin-isospin component of the nucleon-nucleon interaction, in particular by the tensor force [Ots05]. For example, particle-hole excitations across the $N = 20$ shell gap become energetically favored in the vicinity of ^{32}Mg leading to the island of inversion [Thi75,War96] (see Section 2.3.4).

It has long been predicted that weak binding and the proximity of the Fermi surface to the particle continuum for nuclei close to the neutron dripline result in a large diffuseness of the nuclear surface [Dob94,Dob96]. The resulting shallow single-particle potentials together with enhanced pairing correlations could yield a uniformly spaced, single-particle energy spectrum. The characteristic bunching of single-particle states that gives rise to the shell gaps and magic numbers would disappear. The properties of nuclei at the dripline would be different from stable nuclei. Furthermore, the empirically known spin-orbit force, which is responsible for the formation of magic numbers in heavier nuclei, becomes uncertain when extrapolated towards neutron matter [Pud96].

Experimental information on the emergence and disappearance of magic numbers in exotic nuclei is currently limited to light nuclei. The study of the evolution of shell gaps over a much broader range of exotic nuclear systems comprises an important program that will be carried out at the ISF. The evolution of the shell gaps also has a large impact on the modeling of nucleosynthesis in the rapid neutron-capture process, which is particularly sensitive to the structure of nuclei far from stability. For example, it is possible that shell quenching is the mechanism that can

Nuclear Shell Structure

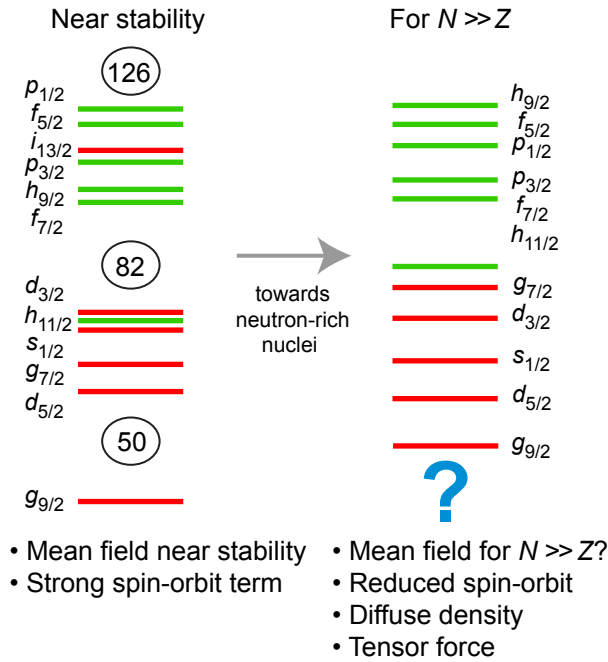


Figure 2.5: The nuclear shell structure near stability is well established. Large gaps in the single-particle energy spectrum lead to the characteristic bunching of energy levels. Towards neutron-rich nuclei, a reduced spin-orbit force, diffuse density and the increasing importance of the tensor force are expected to modify the shell structure significantly. In the scenario shown in this figure, the shell gaps have disappeared and the single-particle states are more evenly spaced. Adapted from [Dob96].

Tensor interaction and shell gaps

The spacing of the single-particle energies relative to the strength of the residual interaction determines the collective properties of nuclei. The relatively large energy gaps between single-particle states giving rise to magic numbers is the most important factor governing nuclear structure. Modern shell model approaches incorporate the tensor interaction in the residual two-body forces where it is found to have a strong influence on the relative single-particle orbital spacing and the related shell gaps [Ots05].

Recent work has focused on incorporating the tensor interaction into energy density functional models [Ots06]. To isolate the tensor contribution it is important to experimentally establish the proton-number and neutron-number dependent trends in single-particle energies in odd-even nuclei surrounding the most exotic nuclei that may be doubly magic which include ^{42}Si , ^{60}Ca , ^{70}Ca , ^{78}Ni , ^{100}Sn , and ^{122}Zr .



↑ Spin ● Wave function of relative motion

Intuitive illustration of the diagonal tensor interaction energy. The tensor force is nonzero only for the spin-triplet state ($S = 1$) and is attractive if the relative motion wave function (yellow) is aligned in the same direction as the spin (black). This is the situation shown on the left, where a nucleon with angular momentum $j_{<} = l - 1/2$ interacts with another nucleon in the state $j'_{>} = l' + 1/2$. On the right side, where the nucleon with angular momentum $j_{>} = l + 1/2$ interacts with another nucleon in the state with $j'_{<} = l' - 1/2$, the relative motion wave function is aligned along an axis orthogonal to the spin direction and the tensor interaction is repulsive. The right side also holds for the orbits $j_{<} = l - 1/2$ and $j'_{<} = l' - 1/2$. Adapted from [Ots05].

explain the minima in the calculated r-process abundances of the elements (see Section 3.1.1).

Elucidation of the shell structure of nuclei cannot be achieved with one experimental technique. The approach described in the following provides a means to obtain a comprehensive set of measurements to track the changes in nuclear structure in exotic regimes and to identify their driving forces. Only by the use of complementary experimental techniques with different sensitivities to nuclear properties will one be able to construct a complete picture.

2.3.1 Signatures of shell gaps from masses and nucleon separation energies

Proof of an isotope's existence is of particular importance in the proximity of a dripline where the nucleon separation energy becomes small. Here, subtle effects determine whether a nucleus is stable against direct nucleon emission. The mass or binding energy of an isotope is one of the most basic properties directly accessible to experimenters. The systematic investigation of masses as a function of isospin and mass number has already been key to the discovery of new nuclear structure effects. Examples are the first indications of loosely bound systems, later identified as halo nuclei, and the disappearance of the magic number $N = 20$ in the island of inversion [Thi75,War90]. The first experimental evidence for the development of a new magic number at $N = 16$ stemmed from discontinuities in the monotonic evolution of the neutron separation energy S_n [Oza00]. In addition, masses of very neutron-rich isotopes are key ingredients in the modeling of the nucleosynthesis via the rapid neutron-capture process (see Section 3.1.1).

At the NSCL, indications for the subshell closures at $N = 32$ and 34 , predicted by modern shell model calculations to be caused by a strong neutron-proton monopole interaction, have been studied in β decay [Lid04a,Lid04b] and Coulomb excitation experiments [Din05]. Limited or no information exists on separation energies in this region of the nuclear chart. Within the next few years, the masses and separation energies of the $N = 32$ and 34 isotones down to ^{52}Ca and ^{54}Ca are expected to be measured with a precision of better than 50 keV. The evolution of neutron separation energies will provide a clear signature for a subshell closure and complement the information obtained from spectroscopy. Masses along the closed neutron shell at $N = 28$ will be measured to address the outstanding questions concerning the robustness of this shell gap for the isotopes ^{44}S and ^{42}Si .

Nuclei far from stability in the vicinity of $N = Z = 50$; $N = Z = 82$, and $N = 126$ will be in reach with the ISF. The mass of the doubly magic nucleus ^{78}Ni will be accessible and the $N = 82$ shell gap can be probed out to ^{128}Pd . Tin isotopes up to mass number $A = 138$ and lead isotopes out to $A = 224$ will be available for Penning-trap mass measurements. The neutron shell gap at $N = 126$ can be probed out to ^{199}Ta . Figure 2.6 shows that a considerable improvement in masses will be achieved at these critical doubly magic isotopes far from stability.

Two experimental pathways for the determination of nuclear masses will be available at the ISF. Precision techniques, such as the Penning-trap experiments at the ISF, will allow us to perform precision mass measurements of neutron-rich nuclei that have half-lives > 10 ms and are provided with rates of a few particles per minute. Relative mass accuracies of better than 10^{-7} will be realized. However,

Precise masses from Penning-trap mass spectrometry

Penning-trap mass spectrometry is a technique that provides highly precise and accurate mass measurements of both stable and unstable nuclei. The key to high precision is the storage of ions for an extended period of time in a small volume. Penning-trap mass spectroscopy is applied to exotic isotopes with half-lives below 100 ms to obtain mass precision of 10^{-7} and better. Precision of $< 10^{-8}$ can be achieved for longer-lived, less-exotic isotopes.

The mass is determined from the cyclotron frequency, $\omega_c = q/m \cdot B$, of an ion with a charge-to-mass ratio q/m in a well-known magnetic field, B . Ion manipulation and storage is made possible by superimposing electric fields created by electrode configurations shown in the figures to the right on the magnetic field (Figures A and B). The cyclotron frequency, ω_c , of the stored ion is determined by finding the resonance between the ion motion in the trap and an applied radio-frequency field.

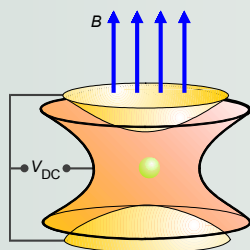


Figure A: Basic configuration of a Penning trap in which a strong magnetic field is combined with a static electric quadrupole field to trap ions.



Figure B: The electrodes from the 9.4 Tesla Penning-trap mass spectrometer at the LEBIT facility at the NSCL.

Penning-trap mass spectrometry of rare isotopes was pioneered at ISOLDE at CERN with very low energy rare isotope beams from an ISOL system. The fragmentation of fast beams

provides access to the largest range of chemical elements and the farthest reach from stability. The large challenge that had to be overcome to apply Penning-trap mass spectroscopy to fast-beam fragments was to reduce the kinetic energy of the ions by about nine orders of magnitude before they could be trapped.

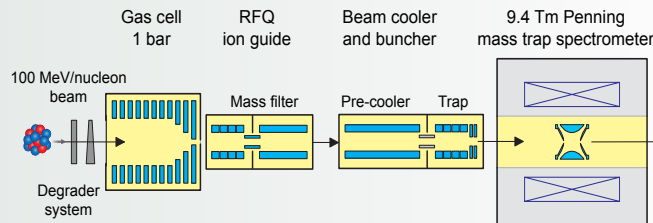


Figure C: Schematic layout of the Low-Energy Beam and Ion Trap facility (LEBIT) at the NSCL. Fast fragment beams are slowed down and stopped in a gas cell. The thermal ions are extracted and formed into a pulsed, low-energy ion beam by means of a radio-frequency ion guide (RFQ) and a beam cooler and buncher device. The ion pulses are captured in the 9.4-Tesla Penning-trap mass spectrometer where their cyclotron frequency is measured.

The LEBIT facility at the NSCL was the first to employ appropriate gas stopping and low-energy beam manipulation techniques on fast ions for Penning-trap mass measurements (Figure C). A number of rare isotopes important for fundamental interaction studies and nuclear structure studies as well as for nuclear astrophysics have been completed. Examples include ^{66}As , $T_{1/2} = 96$ ms, and ^{38}Ca , $T_{1/2} = 440$ ms, which was measured with a mass precision of 8×10^{-9} (Figure D).

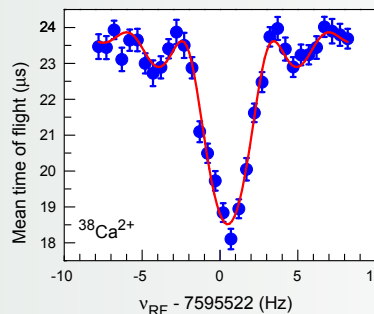


Figure D: The cyclotron resonance curve observed for $^{38}\text{Ca}^{2+}$ ions. Similar high quality measurements are required to achieve mass precisions $< 10^{-8}$. Adapted from [Bol06b].

Penning-trap measurements are difficult for the shortest-lived nuclei that are produced at low rates. In such cases, time-of-flight techniques using fast secondary cocktail beams produced by projectile fragmentation will provide an initial coarse mapping of masses.

At the present NSCL facility, a program to measure masses based on the time of flight between the A1900 fragment separator and the focal plane of the S800

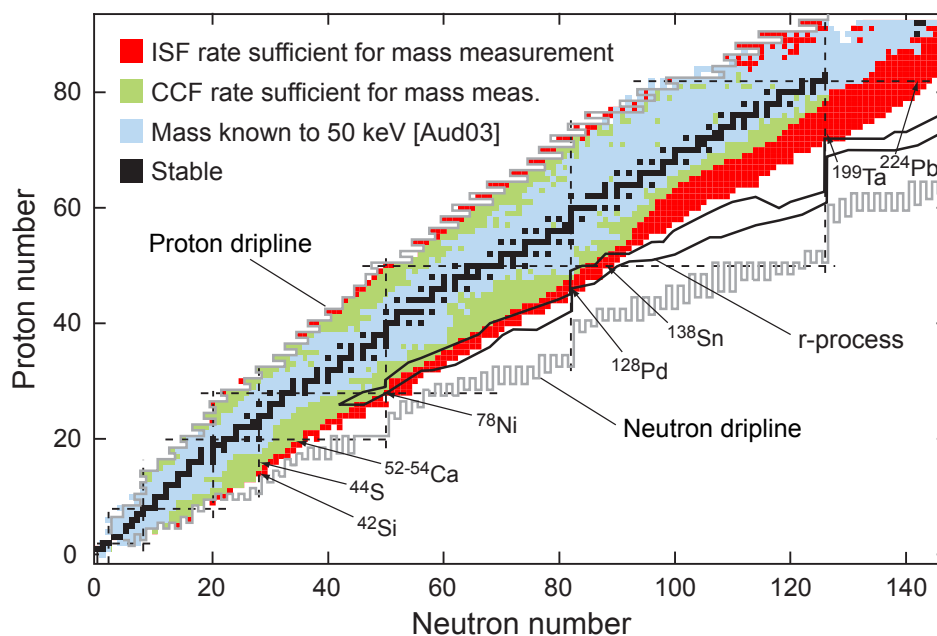


Figure 2.6: Exotic nuclei in reach for mass measurements to 50 keV precision with the Cyclotron stopper at the ISF compared to the reach at the CCF. The masses for nuclei shown in blue are known to 50 keV [Aud03]. Nuclei in green will be available for mass measurements at the CCF (e.g., ^{44}S and $^{52-54}\text{Ca}$); nuclei in red will be in reach with the ISF (e.g., ^{42}Si , ^{78}Ni , ^{128}Pd , $^{134-138}\text{Sn}$, ^{199}Ta , and ^{224}Pb).

spectrograph has been implemented. A mass resolution of the order of 10^{-4} and a final mass accuracy of the order of 10^{-6} is expected. At the ISF this method will be extended further towards the neutron dripline and the region of the r-process for $28 < Z < 50$.

2.3.2 Information on shell gaps from yrast excitations

Some even-even nuclei have relatively high-energy first 2^+ states and are thus distinct from their even-even neighbors. A high energy of the first excited 2^+ state and a corresponding low $B(E2;0^+ \rightarrow 2^+)$ electromagnetic transition strength, are characteristic signatures of shell closures. Figure 2.7 shows the evolution of first 2^+ energies across the nuclear chart. The magic numbers at 28, 50, 82, and 126 are clearly visible and illustrate the potential of this observable for the study of shell closures. The level spacing between higher-lying yrast states can also provide important information on the presence of shell gaps. Large jumps in transition energies at higher spin values are often assessed as an indicator of excitations that involve breaking of the core; states with higher angular momentum are generated from excitations across a shell gap.

For example, in the chain of titanium isotopes, the predicted subshell closures at neutron numbers $N = 32$ and 34 have been studied using complementary experimental approaches that access different signatures for a shell gap. β -decay experiments provided the identification of yrast states in ^{54}Ti [Jan02] and ^{56}Ti [Lid04a]. The location of the first 2^+ state already indicated the presence of a subshell closure in ^{54}Ti but provided no indication for a gap at neutron number $N = 34$. Subsequently, deep-inelastic reactions induced by a ^{48}Ca beam on ^{238}U and ^{208}Pb targets at the

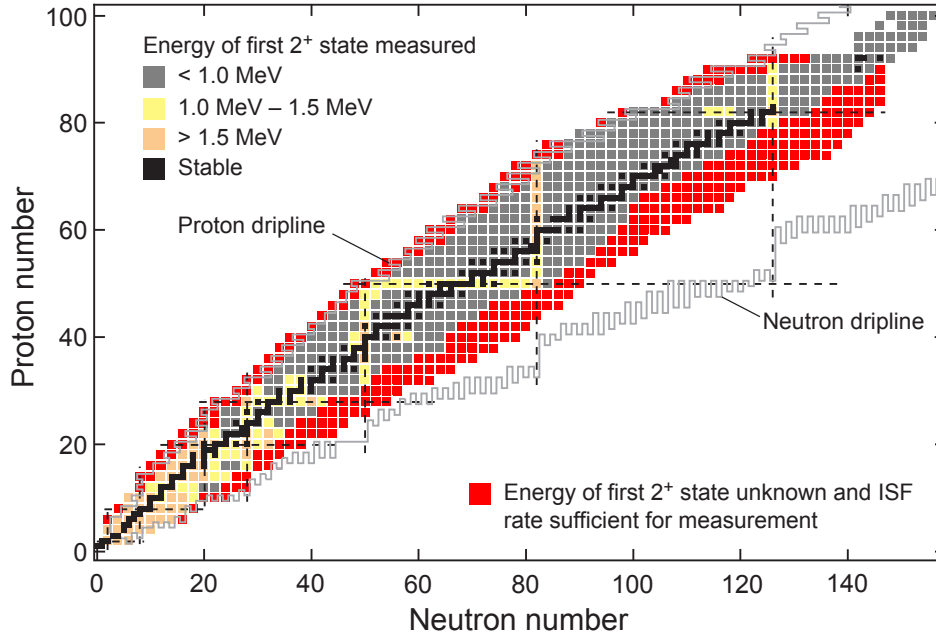


Figure 2.7: Map of the energy of the first excited 2^+ states in even-even nuclei. The 2^+ energy reveals the presence of shell closures. The shell gaps at nucleon numbers 28, 50, and 126 are clearly visible by their relatively high excitation energy. The first 2^+ states of even-even nuclei marked in red are currently unknown and will be accessible at the ISF using Coulomb excitation, nucleon knockout experiments, or β -decay studies.

ATLAS facility at ANL were used to extend the yrast level schemes of these nuclei up to higher spin values [Jan02,For04]. A large jump in the excitation energy between the 6^+ and the 8^+ states in the yrast band of ^{54}Ti further supported the conclusions from the β -decay studies. Finally, the results of the $B(E2)$ transition-rate measurements for the excitation of the first 2^+ states in the chain of titanium isotopes confirmed a shell closure at $N = 32$ and the absence of a similarly pronounced gap at $N = 34$ [Din05]. The following sections highlight how $B(E2)$ transition-rate measurements, β -delayed γ -ray spectroscopy, and deep-inelastic reactions will be used at the ISF to establish yrast structures to study the persistence of the familiar shell gaps far from the valley of stability.

2.3.2.1 Transition matrix elements and quadrupole collectivity

Collective quadrupole excitations in exotic even-even nuclei can be explored with intermediate-energy Coulomb excitation measurements. This well-established and widely used experimental technique has been employed at exotic-beam rates as low as a few particles per second. Chains of isotopes are usually accessible with the same setup, providing a consistent set of measurements and minimizing systematic uncertainties. The study of isotopic chains provides a benchmark for theory since the evolution of collectivity can be probed as a function of neutron number. For example, the persistence of the $N = 28$ shell has been studied in the nickel isotopes $^{54-56}\text{Ni}$ [Yur04a,Yur04b]. Shell model calculations employing the most modern effective interactions over-predict the degree of fragmentation of $E2$ strength for the neutron-deficient nucleus ^{54}Ni [Yur04b] and currently fail to describe the experimentally observed trend of quadrupole collectivity in the neutron-deficient nickel isotopes near the doubly magic $N = Z = 28$.

In the next few years, the appearance of new shell gaps at $N = 32$ and 34 will be probed in the chains of chromium and calcium isotopes to map the effect of the proton-neutron interaction on the development of new shell closures. With effective interactions becoming available for the fp shell including the $g_{9/2}$ orbit, experimental studies will be extended to examine the persistence and the breakdown of magic numbers to heavier nuclei up to $N = 50$. ^{80}Zn will be the most neutron-rich $N = 50$ isotone accessible to Coulomb excitation studies with the existing facilities.

Major advances will be possible at the ISF. The quadrupole collectivity of the important doubly magic nucleus ^{78}Ni can be determined with projected rates of several particles per second. Neutron-rich, even-even nuclei along both $N = 82$ and 126 will be in reach including $^{128}\text{Pd}_{82}$ (5 s^{-1}), $^{202}\text{Os}_{126}$ (several hundred particles per second), and $^{200}\text{W}_{126}$ (tens of particles per second). Knowledge of the shell structure of these key nuclei is vital for the modeling of the rp -process path (see Section 3.2.1).

Intermediate-energy Coulomb excitation

Coulomb excitation is a well-established and widely used experimental technique to explore collective excitations of a wide range of nuclei. This method was initially employed to excite stable target nuclei with the electromagnetic field of incident stable heavy-ion beams at bombarding energies below the Coulomb barrier. The availability of fast rare isotope beams at energies well above the Coulomb barrier produced in projectile fragmentation reactions prompted the development of the intermediate-energy Coulomb excitation technique [Mot95,Gla98].

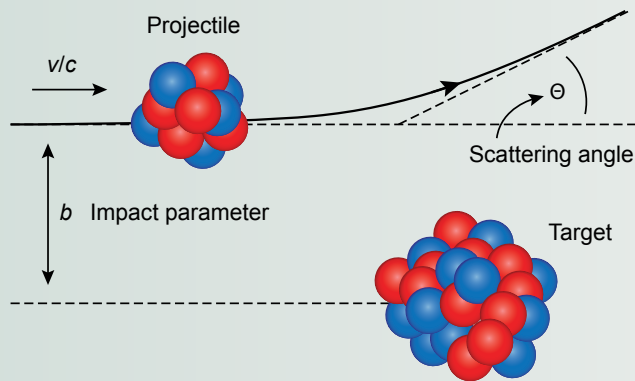


Figure A: Schematic illustration of a projectile nucleus scattering from a high- Z target nucleus. Collective states of the exotic projectile are excited as it passes through the Coulomb field of the stable target nucleus.

Intermediate-energy Coulomb excitation relies on scattering exotic nuclei from stable, high- Z targets (Figure A) at large impact parameters where nuclear interactions are negligible. The deexcitation γ -rays are then detected in coincidence with the scattered product (Figure B). Restrictions on the impact parameter can be placed by appropriate choice of the maximum scattering angle. The Coulomb excitation cross sections can be determined from the ratio of the number of observed deexcitation γ rays to the number of incoming projectiles.

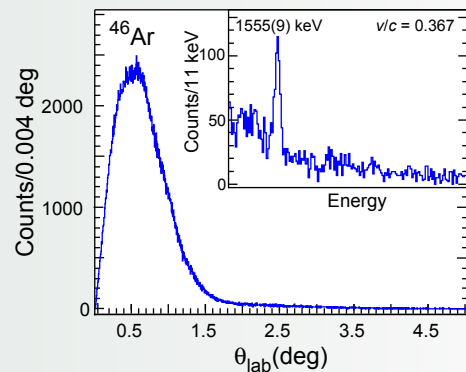


Figure B: Angular distribution of ^{46}Ar projectiles scattered from a gold target and coincident deexcitation γ -ray spectrum (inset). Adapted from [Gad03].

The measured cross sections provide a measure of the absolute $B(E\lambda; i_i \rightarrow i_f)$ transition strengths – a fundamental quantity related to the collective nature of a nucleus. Figure C demonstrates for the $^{46}\text{Ar} + ^{197}\text{Au}$ reaction [Gad03] that the deduced $B(E2; 0^+ \rightarrow 2^+)$ value is independent of the choice of the maximum scattering angle and thus the impact parameter over the measured range.

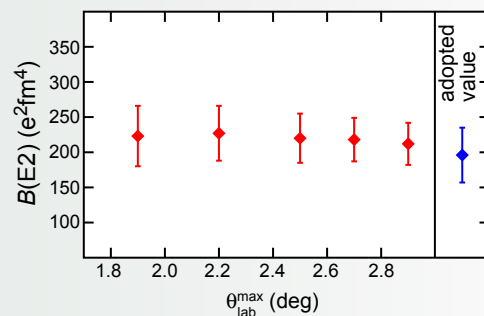


Figure C: Absolute $B(E2; 0^+ \rightarrow 2^+)$ strength for the excitation of ^{46}Ar scattered by a gold target. The consistency of the results for the various maximum scattering angles proves the robustness of the experimental approach. Adapted from [Gad03].

A complementary approach for extracting electromagnetic transition matrix elements can be realized by Doppler shift and time-of-flight measurements with a plunger device. This method, which is well established at stable-beam facilities [Fos74,Kru00], has been adopted for fast beams at the NSCL [Che06]. In contrast to Coulomb excitation, the plunger method does not rely on the measurement of absolute cross sections. This technique is especially suitable for the determination of electromagnetic transition rates in odd-mass and odd-odd nuclei that can be used to explore the valence proton-neutron residual interaction just outside a closed shell.

Recoil distance method lifetime measurements

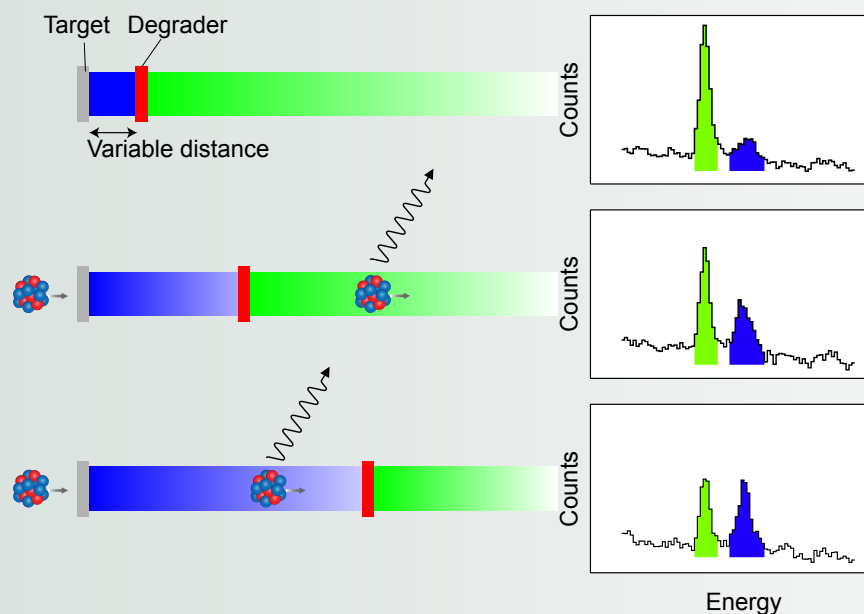
The measurements of excited-state lifetimes are a sensitive tool to extract electromagnetic transition matrix elements. Lifetimes in the picosecond range can be reliably measured with the Recoil Distance Method (RDM). The RDM, also called the plunger technique, has been used at stable beam facilities in fusion-evaporation reactions where the velocity of the evaporation residues is small. At the NSCL the plunger technique was used for the first time with fast fragmentation beams [Che06].

The rare isotopes of interest produced in a fragmentation reaction travel with a velocity $v/c \sim 0.3$ and are excited in a secondary target (see Figure A). The excited isotope decays in flight by γ -ray emission after traversing a distance that depends on both the velocity of the emitting isotope and the lifetime of the excited state. A stationary degrader is positioned downstream from the plunger target to reduce the velocity of the excited nuclei to $v/c \sim 0.2$. Depending on whether the γ -ray decay oc-

curred in flight before or after degrader, the γ -rays will exhibit different Doppler shifts. Consequently, the γ -ray spectra will contain two peaks for each transition, as shown in the right side of the figure. The lifetime of the state can be inferred from the relative intensities of the peaks as a function of the target-degrader distance.

The excited states of interest can be populated using different reaction mechanisms. For example, in recent experiments at the NSCL, the lifetime of the first excited state in ^{114}Pd and ^{64}Ge were measured using intermediate-energy Coulomb excitation and single-neutron knockout, respectively.

At the ISF, the scientific reach will not only be enhanced by the more intense rare isotope beams but also by the use of the high-resolution, high-efficient γ -ray tracking array GRETINA [Lee04]. Lifetimes below one picosecond are expected to be accessible in such experiments.



Left: Schematic arrangement of the excitation target (gray) and the degrader (red) in a plunger lifetime measurement with a short (top), intermediate (middle), and a long (bottom) flight path. The regions for decay upstream and downstream from the degrader are marked in blue and green and correspond to ion velocities of $v/c \sim 0.3$ and $v/c \sim 0.2$, respectively. Right: Experimental spectra obtained using the NSCL plunger system [Che06]; peaks marked with blue and green correspond to the reaction products decaying upstream and downstream of the degrader, respectively.

2.3.2.2 Reaching the extremes with β decay

Beta-decay studies are unique and highly sensitive probes of nuclear structure, owing to their inherent selectivity. They can provide data for nuclei farthest from stability where production rates are extremely low. In that respect, β -decay data are often the last normalization points before extending nuclear theories into the unknown. The persistence of shell gaps and changes in nuclear structure can be

Beta-decay correlation technique with fast ions

Multistrip silicon detectors are very powerful devices for correlating implanted ions and their subsequent charged-particle decays. They have proven invaluable in high-sensitivity experiments searching for superheavy elements and studying nuclear decays along the proton dripline.

The experimental setup of the technique is shown schematically in Figure A. When a rare isotope is implanted into a pixel of the segmented silicon detector, its identity (mass and nuclear charge) as well as the time and location, i.e., the detector pixel, of its implantation are recorded. When the implanted isotope decays at some later time, this second event is detected in the same detector pixel that can be unambiguously assigned to the implanted isotope – as long as no other particle has been implanted in that very same pixel in the interim. The energy of the emitted particle and the time of the decay are recorded and provide information about the decay energy and the half-life.

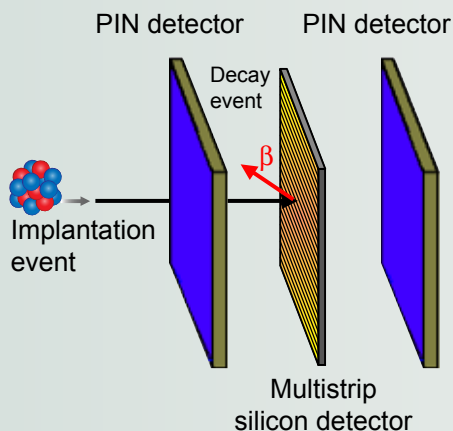


Figure A: Schematic of the use of a double-sided silicon microstrip detector (center) for the correlation of the implantation of fast exotic ions with their β decay.

A modern detector can have several thousand pixels, allowing experiments at correspondingly higher implantation rates than possible with a single detector. The fabrication of silicon wafers of thickness 1 mm and greater has permitted the extension of the charged-particle measurements to β -decay. The challenge here was the required large dynamic range; the implanted nucleus deposits several GeV of energy into the silicon detector, while the energy loss signal from β decay is only a few hundred keV. At the NSCL, dual gain, low noise preamplifiers were developed specifically for this application.

As an example of the sensitivity of this approach, the half-life of ^{78}Ni was determined for the first time in an experiment at the NSCL that produced only 11 ^{78}Ni nuclei. The half-life is extracted from such small data sets by finding the maximum of a likelihood function describing the decay pattern of the parent, daughter, and granddaughter nuclei for each individual event. As demonstrated in Figure B, the technique also allows experiments with “cocktail beams” containing admixtures of several rare isotopes.

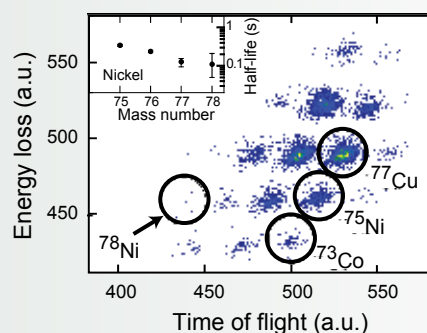


Figure B: Particle identification spectrum for ^{78}Ni attained at the NSCL based on energy-loss and time-of-flight. The inset shows the decay curve for ^{78}Ni . Adapted from [Hos05].

The multistrip detector can also be used as the trigger for other sophisticated detector systems, for example, a high-resolution germanium array or a neutron array, to obtain additional information on delayed γ ray and neutron emission, respectively, from the exotic ions. As an example, Figure C shows the β -delayed γ -ray spectrum of ^{56}Sc , produced at a rate of approximately three ions per minute.

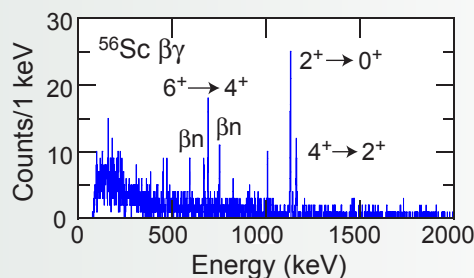


Figure C: The β -delayed γ -ray spectrum obtained for ^{56}Sc at the NSCL at an implantation rate of approximately three ^{56}Sc ions per minute. The β and γ detection efficiencies were 30% and ~5%, respectively. Adapted from [Lid04b].

probed in regions approaching the key nuclei ^{100}Sn , ^{48}Ni , and ^{128}Pd at existing facilities via β -delayed γ -ray spectroscopy. For example, first indications that the $N = 82$ shell gap is reduced far from stability come from β -decay experiments in the neutron-rich cadmium/palladium region, including measurements of the systematic changes in the energy of the first excited 2^+ state in cadmium isotopes towards $N = 82$ from β -delayed γ -ray spectroscopy [Dil03,Kau00]. β -delayed γ -ray spectroscopy studies are possible at rates of several nuclei per minute and the energies of the first 2^+ and 4^+ states in very exotic nuclei are accessible.

At the ISF, the intensities of neutron-rich heavy nuclei produced from uranium fission will permit an evaluation of the low-energy quantum states in the neutron-rich palladium isotopes out to $A = 128$ by β -delayed γ -ray spectroscopy (the parent ^{128}Rh will be available at a rate of several particles per minute). Along the $N = 126$ isotonic chain, excited states in ^{200}W and ^{198}Hf will be populated in β decay from the parent isotopes ^{200}Ta and ^{198}Lu , respectively. The production rates of 1 s^{-1} for ^{200}Ta and 10^{-1} s^{-1} for ^{198}Lu are sufficient to observe delayed γ rays using a high-efficiency, high-resolution germanium array. β - γ coincidence studies in the proton closed-shell nickel and tin nuclei will provide the first complete picture of the systematic variation of the 2^+ and 4^+ states across the $N = 28$ – 50 (for nickel) and $N = 50$ – 82 (for tin) neutron shells.

2.3.2.3 Spectroscopy of yrast states with deep-inelastic reactions

Deep-inelastic collisions between neutron-rich projectiles and heavy target-nuclei with an even larger N/Z ratio can produce reaction residues that are more neutron rich than the beam nuclei. This process is driven by the exchange of protons and neutrons between the target and projectile during the collision. Typically, excited states with higher angular momentum are populated in these reactions. Reactions induced by stable beams (e.g., ^{48}Ca) on heavy targets (e.g., uranium or lead) at beam energies just above the Coulomb barrier have been employed to study states with moderate spin values in nuclei more neutron rich than the projectile (e.g., ^{54}Ti , ^{56}Ti [Jan02,For04]). Identification of final reaction products is achieved by γ -ray cross-correlations in the case of lead targets. The correlation method, however, is not possible for the heaviest targets (uranium) due to the high fission probability. Therefore, the data analysis for deep-inelastic experiments with uranium targets relies on known transitions identified in other experiments (β decay or Coulomb-excitation studies).

In-beam γ -ray spectroscopy following deep-inelastic collisions will be extended to utilize the exotic, reaccelerated beams at the ISF. For example, ^{38}Si ($> 10^6\text{ s}^{-1}$) and ^{44}S , ^{70}Ni , ^{76}Zn ($> 10^7\text{ s}^{-1}$) and ^{46}Ar ($> 10^9\text{ s}^{-1}$) will be available at intensities sufficient to perform γ -ray spectroscopy following deep-inelastic collisions. This choice of projectiles will allow one to build the medium-spin excitation level schemes of nuclei at and around ^{42}Si ($N = 28$), ^{48}S ($N = 32$), and approaching ^{78}Ni ($Z = 28$, $N = 50$). High-resolution γ -ray spectroscopy in conjunction with particle identification in a magnetic spectrograph can be used to study the γ -ray decay properties of the produced neutron-rich, exotic nuclei.

2.3.3 Single-particle structure near shell closures

Direct nuclear reactions are a powerful tool for identifying the single-particle components of the nuclear wave function. Nucleon knockout and the more traditional

transfer reactions are complementary approaches. While knockout reactions solely probe *hole* strengths, nucleon transfer reactions like (d,p), (t,d) and (³He,d) populate *particle* levels. Orbital angular momentum quantum numbers, the relative location of single-particle states, and spectroscopic factors are accessible with experiments employing direct reactions. Sensitivity to the orbital angular momentum provides a means to identify single-particle/single-hole states; their relative location gives information on the size of shell gaps, and the spectroscopic factor relates to the nucleon's occupation of a single-particle level. The sections below detail the capabilities and experimental reach of nucleon knockout and particle transfer reactions. Both techniques will be employed at the ISF to investigate the origin and strength of the interactions that drive the modifications of shell gaps in exotic nuclear systems.

2.3.3.1 Nucleon knockout reactions

One-nucleon knockout is a direct reaction that is particularly well suited for high-sensitivity experiments with fast beams of rare isotopes produced in projectile fragmentation [Han01,Han03a]. In peripheral collision with a light target nucleus, a nucleon is removed from the projectile. The parallel momentum distribution of the knockout residues is sensitive to the orbital angular momentum of the removed nucleon and to possible deformation of the projectiles [Sak00,Bat05]. Gamma-ray spectroscopy serves to identify the final state populated in the heavy knockout residue.

Spectroscopic factors are deduced from the experimental cross sections for the knockout to individual final states, in comparison to reaction theory. Single-nucleon knockout is usually combined with γ -ray spectroscopy to extract exclusive momentum distributions and spectroscopic factors for excited states. For example, the one-neutron knockout reaction ${}^9\text{Be}({}^{12}\text{Be}, {}^{11}\text{Be}+\gamma)\text{X}$ provided direct evidence for the occupancy of the neutron $s_{1/2}$ orbit in the ground state of ${}^{12}\text{Be}$ and revealed the breakdown of the $N = 8$ shell closure in the proximity of the neutron dripline [Nav00,Pai06]. Particle rates as low as 0.1 s^{-1} are sufficient for the utilization of this method.

The sudden removal of two like nucleons proceeds as a direct reaction in binding-energy regimes where two-step processes are energetically suppressed. Two-proton knockout from neutron-deficient projectiles and two-neutron knockout from proton-rich nuclei belong to this class of direct reactions and provide nuclear structure information [Baz03,Tos04,Yon06]. The magnitude of the inclusive cross section and the feeding pattern of excited states in the two-nucleon knockout residues have been recently used as indicators of the presence of subshell closures [Fri05a,Gad06].

The combination of one- and two-proton knockout from ${}^{44}\text{S}$ was used to infer the proton magicity of the very exotic $N = 28$ nucleus ${}^{42}\text{Si}$. The one-proton knockout to ${}^{43}\text{P}$ showed the near-degeneracy of the proton $s_{1/2}$ and $d_{3/2}$ orbits while the small inclusive cross section for the two-proton removal from ${}^{44}\text{S}$ to ${}^{42}\text{Si}$ – indicative of the reduced availability of valence protons in a schematic picture – established the presence of a large $Z = 14$ proton gap at neutron number $N = 28$ [Fri05a,Fri06]. Both one and two-nucleon knockout reactions have been pioneered in experiments at the NSCL [Han03a].

It is anticipated that knockout studies will be used to explore the role of the $N = 40$ (harmonic oscillator) shell closure from ^{64}Cr to ^{80}Zr and the single-particle properties of neutron-rich nickel isotopes out to $A = 74$ at existing facilities. Only with beam intensities available at the ISF will the key doubly magic nuclei ^{78}Ni and ^{100}Sn (at rates of several particles per second) be accessible to knockout studies. Figure 2.8 shows the projected ISF reach for one-nucleon knockout reactions aimed at studying the evolution of the single-particle structure along the magic numbers $N = Z = 28, 50, 82$ and $N = 40$.

One-nucleon knockout reactions with fast ion beams

One-nucleon knockout reactions from fast-moving projectiles can be used to explore the single-particle structure of the exotic projectile. The sudden removal of a single nucleon from the projectile nucleus in a peripheral collision with a light target can be treated as a direct reaction (see Figure A). The knockout residue can be produced in a variety of nuclear states depending on its structure and the structure of the projectile.

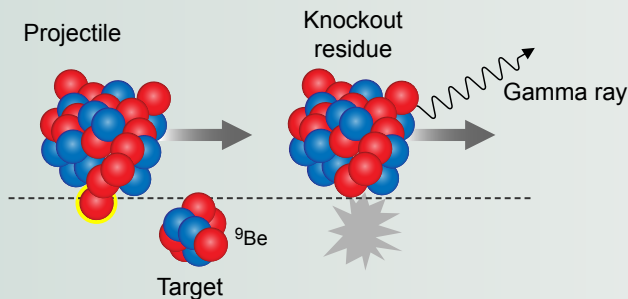


Figure A: A single nucleon can be removed from the fast-moving projectile in a peripheral collision with a light target nucleus. The process shown schematically in the figure corresponds to “stripping,” in which the nucleon removed from the projectile is absorbed by the target. Adapted from [War03].

Gamma-ray spectroscopy can be used to identify the final state. As an example, Figure B shows the γ -ray spectrum detected in coincidence with ^{33}Ar nuclei produced in the one-neutron knockout reaction from ^{34}Ar on a beryllium target. The three γ -ray transitions show that three excited states were populated in the neutron-removal reaction and provide information on the nuclear structure of the ground state of the projectile of ^{34}Ar .

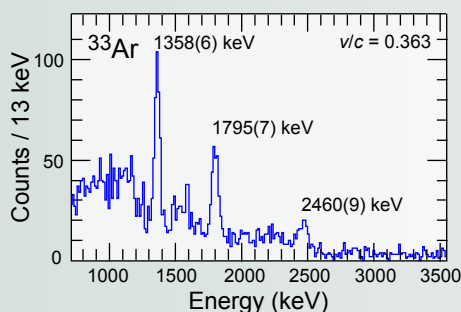


Figure B: The γ -ray spectrum detected in coincidence with ^{33}Ar nuclei produced in the reaction of a beam of ^{34}Ar ions with a beryllium target. Adapted from [Gad04a].

In addition to the relative population of the excited states determined from the γ -ray spectrum, it is possible to extract the orbital angular momenta of these states. The shape of the longitudinal momentum distribution of the knockout residue is sensitive to the orbital angular momentum ℓ of the knocked-out nucleon. For example, Figure C shows the measured parallel momentum distributions for ^{33}Ar residues left in either the ground or one of the excited states. Comparison to the calculations displayed in the figure clearly indicates that the orbital angular momenta were $\ell = 0$ and $\ell = 2$ for the ground and excited states, respectively. Thus the neutron was removed from either the s or d orbital in ^{34}Ar to produce the respective final states in ^{33}Ar .

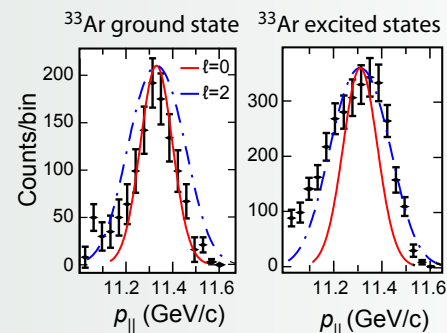


Figure C: The parallel momentum distribution of ^{33}Ar one-neutron knockout residues. The knockout reaction left the ^{33}Ar nuclei either in the ground state (left) or in an excited state (right). Adapted from [Gad04a].

The cross sections for the knockout to individual final states can be compared to detailed reaction theory (formulated in eikonal and sudden approximation at intermediate projectile energies) to provide spectroscopic factors for the final states observed in these very exotic nuclei. The spectroscopic factor relates to the occupation number of a single-particle orbit and thus provides information on the nuclear structure that is otherwise not available.

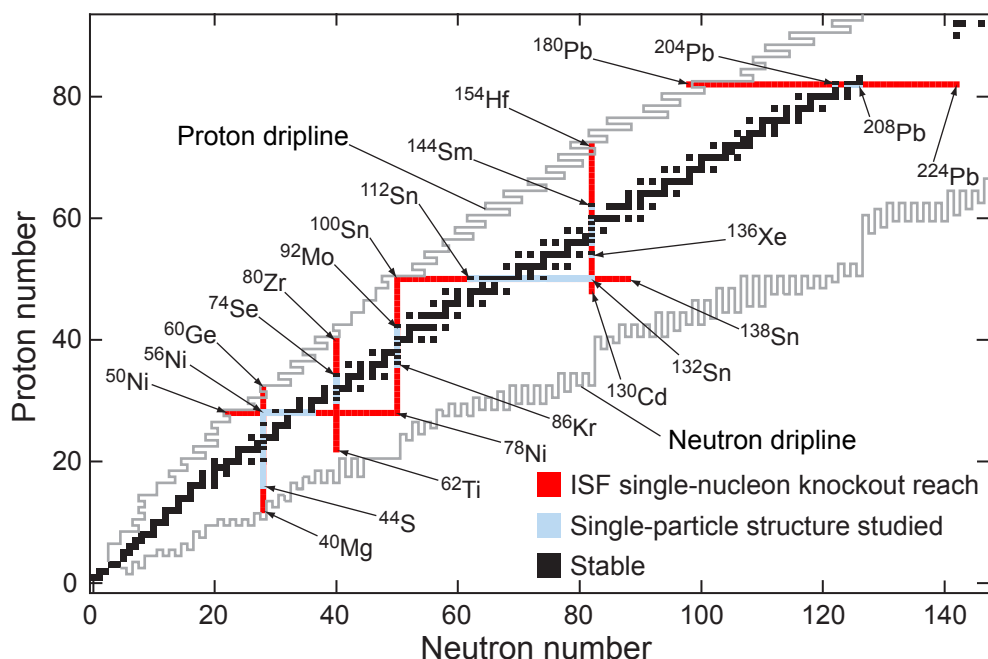


Figure 2.8: Projected ISF reach with single-nucleon knockout reactions for the study of changes in the single-particle structure of magic nuclei. Nuclei along $N = Z = 28, 50, 82$ and $N = 40$, for which the single-particle structure has been studied, are marked in blue; the projected ISF reach (rate requirement 0.1 s^{-1}) is shown in red.

2.3.3.2 Nucleon transfer reactions

Transfer reactions access many excited states simultaneously, and their strong kinematic matching allows optimization of the reaction for the population of states with orbital angular momenta of interest [Aus70,Gle04]. The particle-addition reactions such as (d,p) and $({}^3\text{He},d)$ or (α,t) are especially valuable probes of single-particle structure in the vicinity of closed shells.

Studies of single-neutron states along isotopic chains yield information about the contributions of different components of the interactions, such as the spin-orbit interaction and the tensor force. Figure 2.9 shows the binding energy difference obtained for the $g_{7/2}$ and $h_{11/2}$ states in the $Z = 51$ antimony isotopes studied with ${}^A\text{Sn}(\alpha,t){}^{A+1}\text{Sb}$ transfer reactions [Sch04a,War04]. The decreasing binding energy towards larger masses is interpreted as a change of the spin-orbit interaction toward the more neutron-rich isotopes [Sch04a]. Recent calculations suggest the change may be caused by the increased importance of the tensor interaction in conjunction with the decreased influence of the spin-orbit force [Ots05].

The data shown in Figure 2.9 are limited by the availability of stable tin isotopes that can serve as targets. First experiments using rare isotope beams on light targets for transfer reactions in inverse kinematics have only been performed recently. Beam energies at and above the Coulomb barrier have been employed [Reh98, Jon04,Tho05,Wuo05a,Wuo05b,Koz06a,Gau06,Mic06,Obe06]. Such experiments typically require beam rates of at least 10^4 s^{-1} .

Of particular interest is the $Z = 28$ nickel isotopic chain. Calculations aimed at studying the role of the tensor force in exotic nuclei predict a descent of the $f_{5/2}$ proton intruder states for nickel isotopes between ${}^{68}\text{Ni}$ and ${}^{78}\text{Ni}$ [Ots05]. In the next

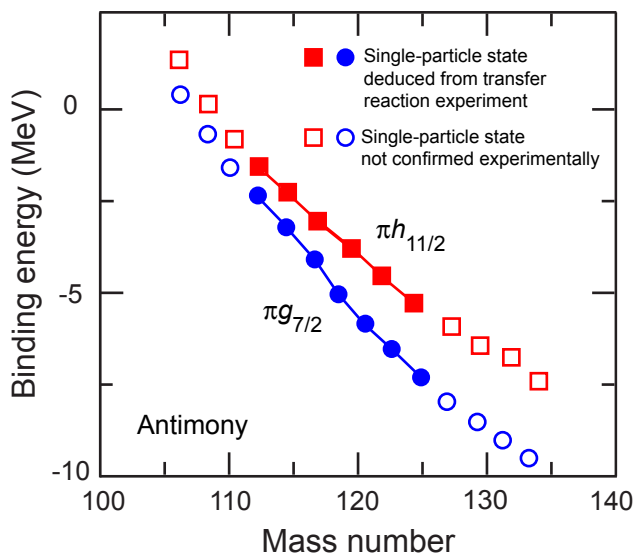


Figure 2.9: Evolution of the proton $h_{11/2}$ and $g_{7/2}$ strength in the $Z=51$ isotopes $^{113}\text{Sb} - ^{125}\text{Sb}$ as deduced from $^{112-124}\text{Sn}(\alpha, t)^{113-125}\text{Sb}$ transfer reactions. The smooth variation in energy separation between the two orbitals is interpreted to originate from a decreasing overall spin-orbit splitting that primarily affects the energy of the $h_{11/2}$ intruder state. The single-particle nature of the states in $^{113}\text{Sb} - ^{125}\text{Sb}$ (solid symbols) was deduced from transfer reactions. The open symbols indicate states where spins have been assigned but their single-particle nature has not been confirmed by transfer reactions. Adapted from [Sch04a].

few years, one would expect that the single-particle structure of the nickel isotopes can be studied with transfer reactions up to mass number 70. At the ISF, reaccelerated beams of $Z=28$ isotopes up to mass number 74 will be accessible at rates of more than 10^4 s^{-1} , sufficient for transfer reactions. This may allow us to observe the crossing of the proton $2p_{3/2}$ and $1f_{5/2}$ levels.

Similarly, the single-particle or single-hole structure in the vicinity of the doubly magic nuclei ^{22}O , $^{22,42}\text{Si}$, ^{44}S , and $^{36,52}\text{Ca}$ will be accessible to transfer reaction studies with reaccelerated beams or decelerated fast beams at the ISF.

Heavier beams, such as ^{82}Ge and ^{80}Zr , will have enough intensity in the near future to allow for experiments with nucleon-addition transfer reactions. It will also be possible to track the single-proton states along the $N=51$ isotone chain where single-particle states in ^{91}Zr , ^{93}Mo , and ^{95}Ru have been established experimentally [Gra02] and the increasing differences in the relative effective single-particle energy have been observed for the neutron $g_{7/2}$ and $h_{11/2}$ orbits. The ISF will allow us to extend this study to ^{97}Pd and ^{99}Cd nuclei by using ^{96}Pd , ^{98}Cd beams in inverse kinematics. These data will be very important for understanding the different isospin-dependent contributions to the effective interactions that are the crucial input to modern shell model calculations [Ots05].

Beyond the $N, Z=50$ shell closures, very little is known about the existence and evolution of subshell closures. The ISF will allow an exploration of the interesting region between the magic numbers 50 and 82. For example, one will be able to study the $Z=82$ isotopes using beams from ^{181}Pb to ^{217}Pb and the $N=82$ isotones with beams from cadmium to lutetium. The increased intensity of the heavy beams from the ISF is needed to make substantial impact in the understanding of the evolution of shell gaps in heavy nuclei.

Direct nucleon transfer reactions for nuclear structure and reaction studies

Direct nuclear reactions have been used for the past 40 years to provide detailed spectroscopic information on the ground and low-lying states of nuclei. Single nucleon transfer reactions have been a reliable source of information about the single particle properties of nuclear wave functions, such as orbital angular momentum, excitation energy, and single-particle occupation probabilities or spectroscopic factors. Measurements in normal kinematics can be performed with light-ion beams on stable targets. Figure A shows the proton angular distributions following the neutron transfer reaction $^{58}\text{Ni}(d,p)^{59}\text{Ni}$ [Cho73].

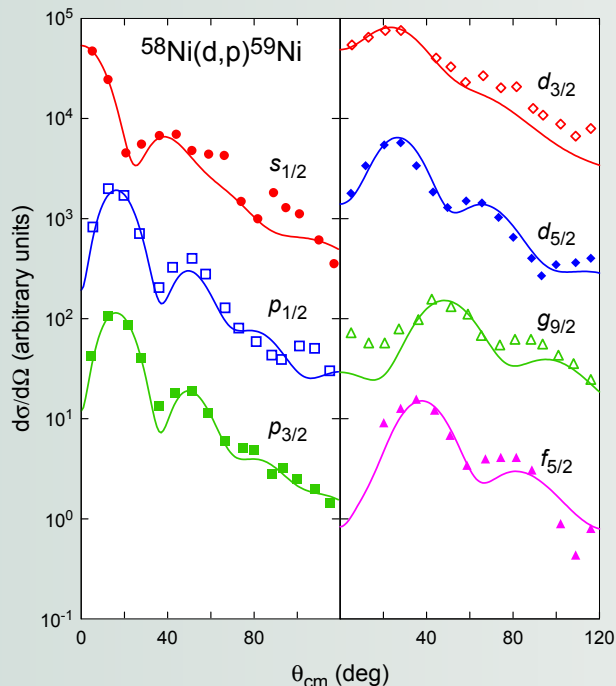


Figure A: Angular distributions of the protons from the neutron transfer reaction $^{58}\text{Ni}(d,p)^{59}\text{Ni}$ for selected states [Cho73]. The angular distributions are mostly sensitive to the orbital angular momentum of the states. The curves are predictions from DWBA calculations.

To explore single-particle properties in nuclei far from stability “reverse-kinematics” experiments are necessary. In these experiments, the rare isotopes impinge on an appropriate light-ion target, e.g., hydrogen (p and d) or helium (^3He , ^4He) gas targets. Figure B shows the schematics of an experimental setup for inverse kinematics transfer reactions on a proton target, for example in the form of a polyethylene (CH_2)_n foil. The projectile-like fragments emerging after the reaction are forward focused and can be detected with a large-acceptance spectrometer. The deuterons from the (p,d) transfer reaction are scattered into a compressed angular cone in the laboratory frame due to the large center-of-mass velocity. The most exotic – and most interesting – rare isotope beams require the use of highly efficient, large-solid-angle, highly granular charged-particle detector arrays of good energy and position resolution.

Since the optimum energy range for transfer reactions is between 10–40 MeV per nucleon, reaccelerated beams as well as decelerated beams from the ISF will greatly enhance the opportunities of using transfer reactions to investigate the structure of the exotic nuclei.

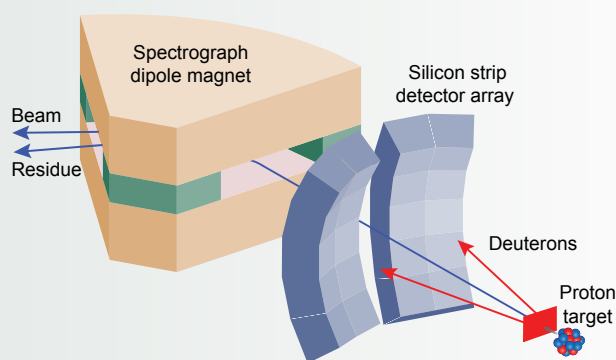


Figure B: Schematics of an experimental setup for transfer reactions using rare isotope beams on a hydrogen target in inverse kinematics. After collisions with the target, the beam-like particles are detected by a spectrometer while the deuterons are detected by a large-area detector array.

2.3.4 Search for new islands of inversion

Particle-hole excitations across a shell gap into the next higher oscillator shell can become energetically favored if stabilized by deformation and pairing correlations. This is one of the mechanisms leading to the erosion of traditional magic numbers and the generation of new shell gaps. The occurrence of the resulting intruder configurations is of particular importance for nuclei near closed shells since those configurations mark the boundary of the model space.

In the islands of inversion, the normal and intruder configurations are inverted with the strongly deformed intruder configuration becoming the ground state. In the islands of inversion, the interplay of single-particle structure and deformation leads to dramatic nuclear structure changes. Direct mass measurements of $^{31,32}\text{Na}$ revealed that the $N = 20$ isotones in the vicinity of ^{32}Mg are more tightly bound than expected, assuming an $N = 20$ neutron sd shell closure. This behavior and

an unexpected onset of collectivity observed for ^{32}Mg could subsequently be explained as filling of the neutron $f_{7/2}$ intruder orbit for $Z < 14$. An impressive arsenal of experimental techniques has been employed to delineate the island of inversion and to elucidate the physics behind its existence, including mass measurements, Coulomb excitation, nucleon knockout reactions, β decay, measurements of magnetic moments, and hadronic scattering. For example, the one-neutron knockout $^9\text{Be}(^{30}\text{Mg},^{29}\text{Mg}+\gamma)\text{X}$ allowed one to quantify the amount of intruder contribution to the ground states of ^{30}Mg for the first time by measuring spectroscopic factors for the knockout populating negative-parity intruder states (see Figure 2.10).

Experimental efforts over the next few years will provide a well-defined entrance into the island of inversion centered on ^{31}Na ; however, critical data on how the island develops towards the neutron dripline will require beam intensities that will be realized at the ISF. For example, ^{36}Mg , ^{32}Ne and ^{34}Ne , ^{38}Mg will be available at rates $> 10^4 \text{ s}^{-1}$ and $> 10^2 \text{ s}^{-1}$, respectively. The intruder content in the ground state wave functions of these nuclei will be quantified and the extent of the island will be traced on the neutron-rich side.

The region around ^{62}Ti is a site where energetically favored intruder configurations formed by particle-hole excitations across the $N = 40$ harmonic oscillator shell gap might lead to a new island of inversion [Bro01] (see Figure 2.11). At the ISF, ^{62}Ti and its neighbors will be available at a rate of several particles per second. Nuclear-structure studies will include β decay, Coulomb-excitation, and nucleon-knockout experiments. At the boundaries of those regions of deformation, where gradually or suddenly descending intruder states determine the nuclear structure, deep-inelastic reactions employing reaccelerated beams can be used to access excited states at medium spin values and track their evolution as the asymmetry between proton and neutron numbers increases.

The observation of new islands of inversion will provide important benchmarks to test shell model interactions far from stability. Further cases will help explore these phenomena and illuminate the underlying physics of such transitions between symmetry phases.

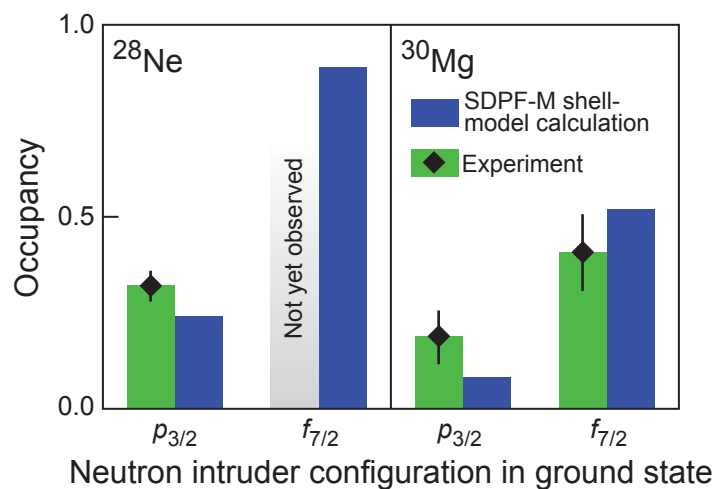


Figure 2.10: Summed $7/2^-$ and $3/2^-$ intruder fp spectroscopic strengths measured from $^9\text{Be}(^{28}\text{Ne},^{27}\text{Ne}+\gamma)\text{X}$ and $^9\text{Be}(^{30}\text{Mg},^{29}\text{Mg}+\gamma)\text{X}$ one-neutron knockout reactions compared to SDPF-M shell model calculations [Ter06]. The onset of intruder configurations illustrates the distinct change in nuclear structure when entering the island of inversion in the chains of neon and magnesium isotopes.

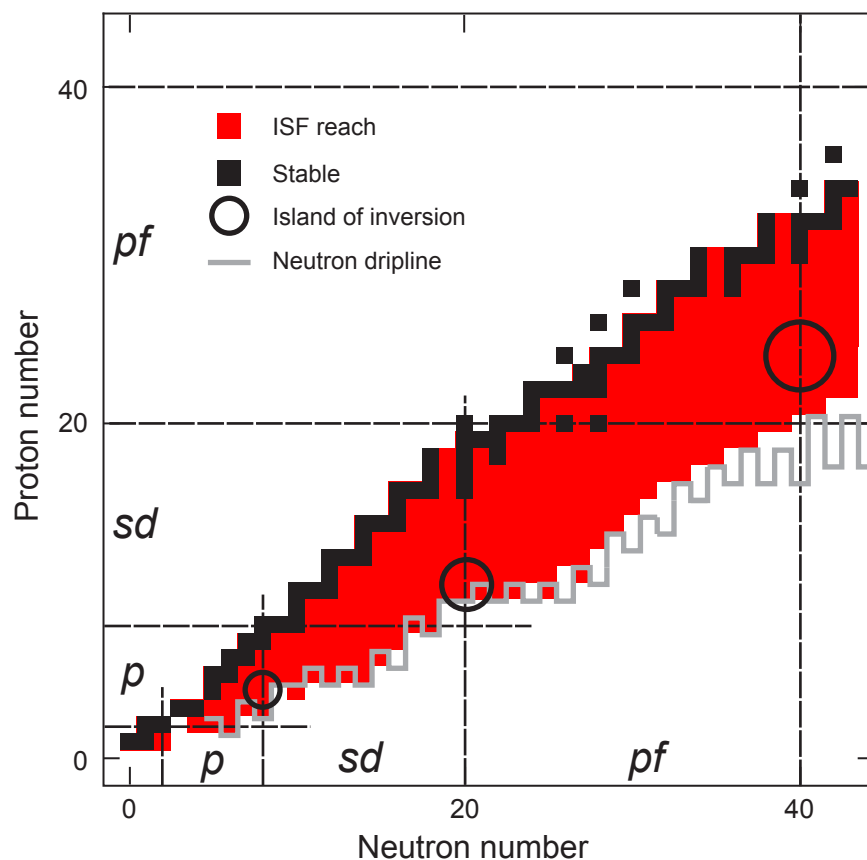


Figure 2.11: Measured and predicted islands of inversion across the neutron-rich side of the nuclear chart. The islands around ^{12}Be ($N = 8$) and ^{31}Na ($N = 20$) are studied at present facilities. At the ISF, a new possible island of inversion around ^{64}Cr ($N = 40$) will become accessible to spectroscopic studies with β decay, Coulomb excitation, and one-nucleon knockout. The rates required for these studies are 10^{-3} s^{-1} (β -decay parent), 1 s^{-1} , and 0.1 s^{-1} (knockout projectile), respectively.

2.3.5 Magnetic moments and mirror symmetry

The magnetic dipole moment is sensitive to the relative amplitudes of different orbital components of the nuclear wave function and thus provides an assessment of the nuclear shell model. This is especially true for mirror nuclei, which differ only in the exchange of proton and neutron numbers. For example, the expectation values of both spin and orbital angular momentum can be deduced from the known ground-state magnetic moments of both mirror partners [Sug69]. Discrepancies between expectation values that are deduced experimentally and calculated by theory are indicative of underlying problems with the theoretical approaches. For mirror nuclei close to the proton dripline, such theoretical shortcomings include continuum effects due to weak binding, the breakdown of isospin conservation as a result of extreme Z/N ratios, and the modification of shell gaps as the driplines are approached.

Two unexpected results of mirror moment measurements involved determination of the spin expectation value, $\langle \sigma \rangle$. Firstly, the deduced $\langle \sigma \rangle$ value for the $^9\text{Li} - ^9\text{C}$ mirror system [Mat96,Huh98] was found to be 50% larger than the extreme single-particle prediction; it remains a challenge to nuclear structure theory. The ^9C nucleus lies along the proton dripline ($S_p \sim 1.3 \text{ MeV}$) and has an extreme proton-to-neutron

ratio of 2:1. Neither the inclusion of isospin-non-conserving terms into the nuclear Hamiltonian [Huh98] nor the mixing of intruder configurations into the ${}^{\circ}\text{C}$ ground state [Uts04] could fully account for the deviant behavior of $\langle\sigma\rangle$ for the isospin $T = 3/2$, $A = 9$ mirror partners. Secondly, the measurement of the ground-state magnetic moment of the neutron-deficient isotope ${}^{57}\text{Cu}$ was recently performed at the NSCL, which completed the required moment measurements for the $T = 1/2$, $A = 57$ mirror partners. A large and negative value for $\langle\sigma\rangle$ at $A = 57$ was deduced, very different from extreme single-particle model expectations [Min06]. The new ${}^{57}\text{Cu}$ magnetic moment result suggests a breaking of the ${}^{56}\text{Ni}$ doubly magic core.

In the near future, the focus on ground-state magnetic moment measurements will remain in the region of light nuclei. Experimental efforts outside the U.S. at this time revolve around the island of inversion around ${}^{32}\text{Mg}$ [Ney05,Uen05]. The experimental magnetic moments in this region can be used to deduce the intruder contribution to the ground states of nuclei bordering the island of inversion. At the NSCL, we will continue our ground-state moment measurements in the vicinity of ${}^{56}\text{Ni}$ to understand the driving forces behind the shell breaking of this doubly magic core.

An impressive range of neutron-deficient nuclei will be made available at the ISF to measure ground-state magnetic dipole moments. For example, the highest mass for which the $T = 3/2$ mirror partners are currently known is $A = 35$ [Mer06]. The heaviest bound $T_z = -3/2$ nucleus, ${}^{55}\text{Cu}$, has an estimated production rate of $1 \times 10^5 \text{ s}^{-1}$ and could be studied by β -NMR directly following fragmentation or via laser polarization, where the pumping scheme for Cu atoms is well established. The ${}^{57}\text{Cu}$ nucleus discussed above represents the heaviest $T_z = -1/2$ nucleus whose ground-state magnetic moment has been experimentally determined, which represents the middle of the fp shell. The ISF would provide sufficient yields of $N = Z - 1$ nuclei to extend the study of mirror moments into the $1g_{9/2}$ shell model space. For example, the yield of ${}^{79}\text{Sr}$ is expected to be $1 \times 10^4 \text{ s}^{-1}$, well beyond the requirements for a successful β -NMR measurement. At such heavy masses, nuclear moment data for the $T_z = +1/2$ member of the isospin doublet are sparse and will require further study. Completion of the proposed measurements would provide a serious test of the nuclear models through the spin and orbital expectation values, as the extreme proton-to-neutron ratios in nuclei available at the ISF may modify the mirror symmetries observed in stable nuclei.

2.3.6 Electric quadrupole moments and core polarization

The electric quadrupole moment is another observable that tests effective interactions within the shell model. The quadrupole moment Q can be expressed as a sum of the matter quadrupole moments for protons and neutrons $Q = e_p Q_p + e_n Q_n$, where e_p (e_n) is the proton (neutron) effective charge. The effective charge provides a correction to the quadrupole operator to account for terms in the wave functions that are absent due to a truncation of the model space, in particular those related to the giant quadrupole resonance. When the binding energy of a nucleon becomes small, as is the case for valence neutrons in nuclei along the neutron dripline, the polarization effect on the nucleus attributed to the loosely-bound valence nucleon should diminish [Sag01], resulting in a decrease in the neutron effective charge. The measured quadrupole moments of the neutron-rich boron isotopes have been observed to remain essentially constant ($Q \sim 35 \text{ mb}$) when going from ${}^{13}\text{B}$ to ${}^{17}\text{B}$

[Izu96] (see Figure 2.12). For the odd-mass boron isotopes, $e_p = 1.3$, $e_n = 0.5$ reproduce the $^{11,13}\text{B}$ quadrupole moments well, while $e_p = 1.3$, $e_n = 0.1$ are required to fit $Q(^{15}\text{B})$. These data indicate that different polarization charges are necessary to describe the quadrupole moments of isotopes close to the neutron driplines [Ume03].

It is imperative to quantify the change of the polarization charge in nuclei beyond the $p(sd)$ shell, and the most neutron-rich odd- Z isotopes of fluorine, sodium, and aluminum are excellent candidates. The heaviest isotope with a measured Q is

Spin-polarization techniques for nuclear moment measurements

The ground-state moments of short-lived nuclei can be measured by applying nuclear resonance methods, for example β -NMR and β -NQR, to the exotic β -emitting nuclei. These measurements require spin polarization of the nuclear ensemble, and polarization techniques are available for both fast and slow secondary beams.

Spin polarization of the fast projectile-like residues from projectile fragmentation reactions was first observed at RIKEN [Asa90]. The fragments detected at a small angle with respect to the beam axis were shown to have a polarized spin in the low-intensity wings of the momentum distribution (see left side of Figure A). A qualitative description of the polarization mechanism can be found in a model that considers conservation of linear and angular momentum and assumes peripheral interactions between the fast projectile and target (right side of Figure A).

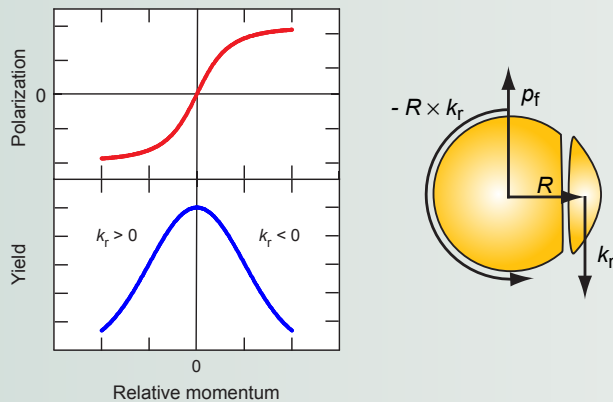


Figure A: Spin polarization (upper part) and the yield (lower part) first observed in projectile fragmentation reactions on a heavy target. The polarization is created when a momentum, k , acts at a radius, R , on the outgoing fragment to generate angular momentum.

A different method to induce spin polarization in fast projectiles has recently been pioneered at the NSCL. Figure B shows that single-nucleon pickup reactions at intermediate energies [Gro03] can generate spin polarization in nuclei. The nuclei become polarized because the transferred nucleon's Fermi momentum lies preferentially along the beam direction and the projectile-target interaction is peripheral in nature. In this case, large spin polarization is observed near the maximum

of the yield curve. This critical aspect of nucleon pick-up reactions provides increased sensitivity for resonance measurements of exotic nuclei.

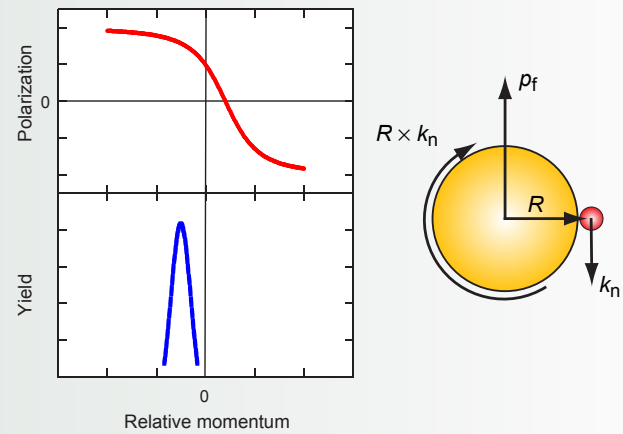


Figure B: Representation of the spin polarization (upper part) and the yield (lower part) from proton pickup reactions at intermediate energies. The Fermi momentum of the picked up nucleon generates polarized angular momentum in the projectile remnant.

Spin polarization in slow beams of exotic atoms can be created by optical pumping with lasers. The technique relies on the fact that the energy degeneracy of hyperfine magnetic substates is broken in a weak magnetic field. Circularly-polarized laser light is used to selectively populate the magnetic substates as indicated in Figure C, producing a net change in the overall population. The atomic spin polarization is transferred to nuclear spin polarization when the atoms pass into a strong magnetic field due to the decoupling of the electron and nuclear spins.

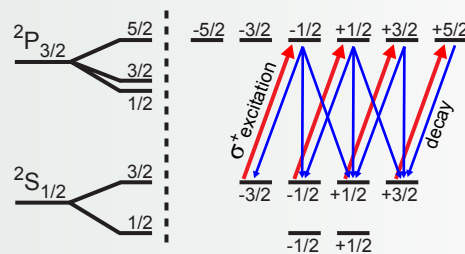


Figure C: Scheme of laser optical pumping to achieve atomic polarization. Adapted from [Col02].

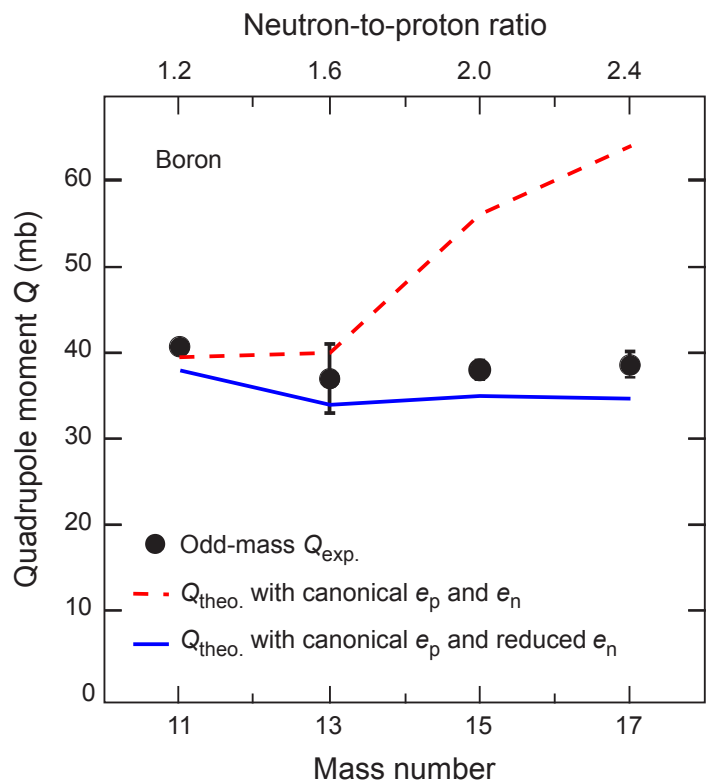


Figure 2.12: Ground-state quadrupole moments of the odd-A boron isotopes. The results of shell model calculations employing a canonical neutron effective charge cannot reproduce the quadrupole moments of the boron isotopes farthest removed from stability. Adapted from [Uen04].

^{21}F [Sat99], which is ten neutrons removed from the most neutron-rich isotope ^{31}F identified to date. Over the next few years, it will be possible to extend quadrupole moments measurements to ^{26}F at the NSCL; however, the ISF will be required to approach the dripline, where significant changes to the effective neutron charge are expected.

Several experimental techniques can be applied to measure electric quadrupole moments of nuclear ground states. For short-lived nuclei produced in low yields, the most appropriate technique is the Nuclear Quadrupole Resonance method applied to β -emitting nuclei (β -NQR). This method has been employed at both fast beam (RIKEN) and ISOL (TRIUMF/ISAC) facilities, and a high power (250 W) β -NQR system is under construction at the NSCL. At the ISF, β -NQR will be applicable for fast as well as reaccelerated rare isotope beams to measure the ground state quadrupole moments of the extremely neutron-rich isotopes ^{29}F (rate $6 \times 10^2 \text{ s}^{-1}$), ^{35}Na ($2 \times 10^2 \text{ s}^{-1}$), and ^{40}Al ($1.4 \times 10^3 \text{ s}^{-1}$) using β -NQR spectroscopy.

2.3.7 The shell structure of the heaviest elements

The study of the existence of superheavy elements has been a long-standing experimental and theoretical quest. For the heaviest elements, the interplay between the strong and weak nuclear forces and the repulsive Coulomb interaction determines the shell structure and the limit of the number of nucleons that can be bound into a nucleus. In transactinide nuclei ($Z \geq 103$), the liquid drop contribution to the binding energy decreases and only the stabilizing shell effects remain, which can be studied with unprecedented clarity.

Theoretical uncertainties are large when extrapolating to the unexplored regions of the nuclear chart. One early prediction of the shell model was the occurrence of a superheavy doubly magic spherical shell closure for $^{398}114_{184}$ [Mel67,Nil68,Nil69]. This proton shell closure was created by the large spin-orbit splitting between the $2f_{7/2}$ and $2f_{5/2}$ proton states and is still predicted by macroscopic-microscopic calculations [Pat89,Pat91,Mol92,Smo97,Cwi96,Cha97]. Most modern self-consistent approaches do not predict $Z = 114$ as a magic number but favor $Z = 120$ or $Z = 126$ together with neutron gaps at $N = 172$ and $N = 184$ [Ben99,Hee02,Ben03,Afa03,Cwi05]. The single-particle level density is high in these nuclei and thus small shifts in the relative location of single-particle orbits – e.g., mediated by the Coulomb, spin-orbit, or tensor interaction – can have a large effect on the level density. Consequently, an entire region of superheavy nuclei can benefit from the low level density near the Fermi surface and acquire substantial shell stabilization [Ben01,Rut97].

The nuclear structure information on heavy elements with $100 < Z < 106$ will constrain theoretical models to probe and ultimately improve their predictive power on the quest for the description of superheavy elements. Two main experimental approaches have been used to determine the nuclear structure of superheavy elements.

One approach uses spectroscopy following α decay in odd-mass nuclei, which connects levels with a similar single-particle structure. This allows a systematic identification and tracking of the single-particle structure [Lei04,Hes06]. However, the exploration is limited to only a few levels populated in α decays. The second approach employs in-beam spectroscopy of nuclei around ^{254}No [Rei99,Lei99]. Fusion-evaporation reactions induced by high-intensity ^{48}Ca beams on lead and mercury targets at about 220 MeV beam energy were employed. The ground-state rotational bands were measured up to spins of $22 \hbar$ [Rei99,Rei00]. In addition, collective properties such as the moment of inertia or low-lying multi quasiparticle levels were observed.

In ^{254}No itself, recent studies have revealed the presence of isomeric states with distinct configurations [Her06,Tan06] (see Figure 2.13). The presence of the rotational band indicates a large deformation of ^{254}No . The deformed Nilsson orbitals that originate from spherical single-particle states around $Z = 120$ come down in energy and lie close to the Fermi surface in ^{254}No . The sequence of levels at a deformation of $\beta \sim 0.3$ probes Nilsson orbits that originate from the spherical $1h_{9/2}$, $1i_{13/2}$, $2f_{5/2}$, and $2f_{7/2}$ single-particle states. Those states, especially the $2f_{5/2}$ and $2f_{7/2}$ spin-orbit partners, are important because the strength of the spin-orbit force governs the size of a possible shell gap at $Z = 114$. Also, Nilsson orbits stemming from the $1i_{11/2}$ and $1j_{15/2}$ orbitals located well above $Z = 126$ approach the Fermi surface in the proximity of nobelium [Her04]. This example illustrates how nuclear structure studies in the $A \sim 250$ mass region provide important information needed for the development of theories that can more reliably predict the shell structure of superheavy nuclei.

At present stable-beam facilities, the fusion of intense, stable beams of carbon, fluorine, and oxygen isotopes with heavy, radioactive plutonium, curium, and californium targets might allow one to study cross sections and the details of the reaction mechanisms leading, for example, to (trans)fermium nuclei up to seaborgium. With the reacceleration capability of the ISF, nuclear spectroscopy of even more neutron-rich heavy elements up to $Z = 106$ – induced by neutron-rich, reaccelerated beams

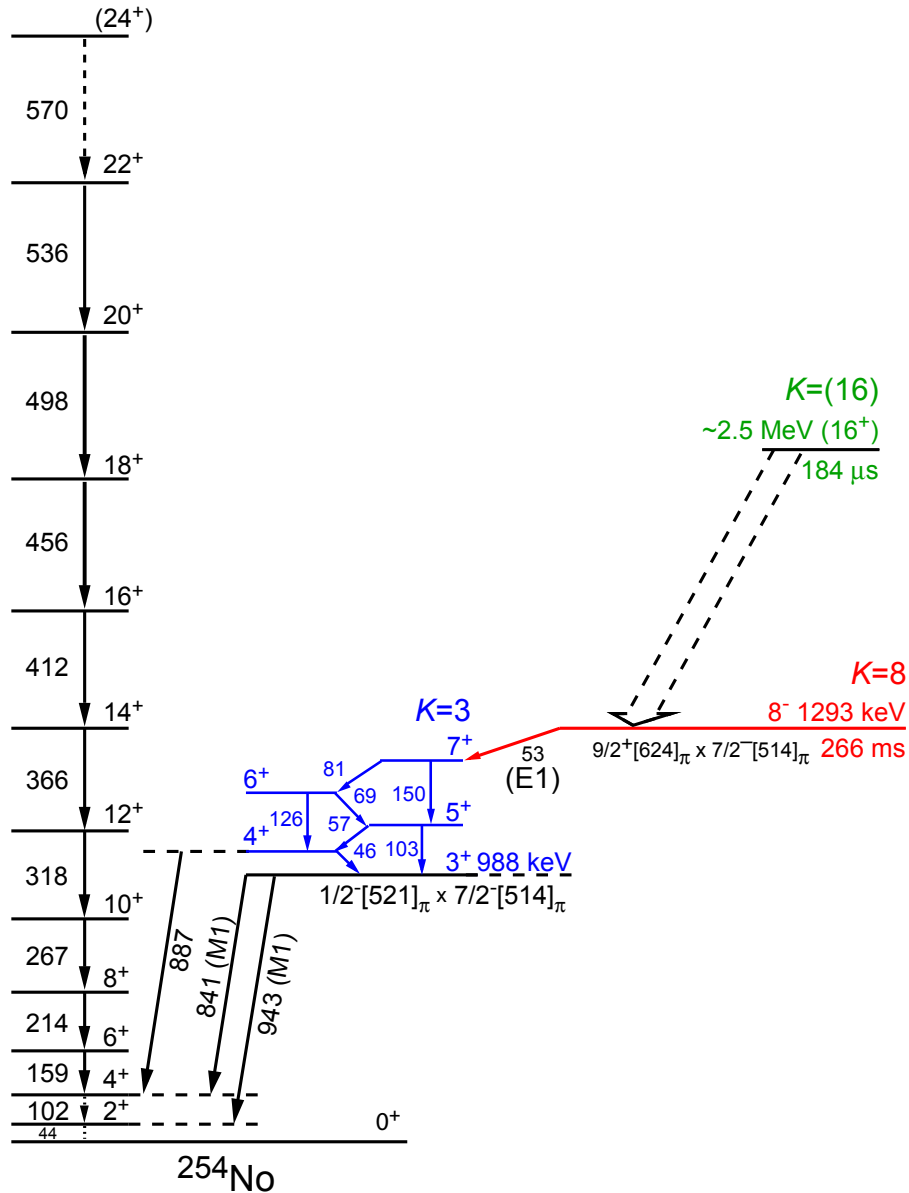


Figure 2.13: Proposed level scheme of ^{254}No . The levels are grouped according to the projection of the total angular momentum on the symmetry axis of the nucleus (K quantum number). Three excited structures – two of them isomeric – have been identified. Two of these structures are attributed to a two-proton excitation [Her06]. These states are of particular significance because their energy is sensitive to single-particle levels above the predicted $Z = 114$ shell gap. Adapted from [Her06].

of carbon, nitrogen, oxygen, and fluorine (^{16}C , ^{18}N , ^{20}O , and $^{20,21}\text{F}$ at rates of $> 10^9 \text{ s}^{-1}$) on plutonium, curium, and californium targets – is envisioned using α , electron, and γ -ray spectroscopy in conjunction with recoil tagging in a mass separator.

At the ISF, fusion reactions induced by heavier, neutron-rich, reaccelerated neon, sodium, and magnesium beams on californium targets, for example, will potentially lead to nuclei that form the anchor points of the α -decay chains of the newest, heaviest elements. They could thus provide a solid footing for experiments aimed at the synthesis of superheavy nuclei.

2.4 Nature of the nuclear wave function and the correlated many-body system

The nucleus is a many-body system that exhibits both single-particle and collective dynamics. The single-particle motion and its symmetry are determined by the properties of the mean field. The collectivity results from the mixing of independent particle configurations by coherent parts of the residual interaction beyond the mean field. The motion of many particles becomes correlated; this synchronization influences all aspects of nuclear structure, including energies of excited states, transition probabilities, occupation numbers, decay widths, and nuclear reaction cross sections.

Different components of the residual interactions induce specific correlations. Pairing of identical nucleons (isospin $T = 1$) mediated by the attraction of two protons or two neutrons on time-reversed orbits is the strongest effect due to the full overlap of the spatial wave functions. The pairing correlations not only determine the low-lying level schemes, they also contribute to binding energies (odd-even staggering) and, in loosely bound nuclei, might serve as a decisive factor making nuclei such as ^{11}Li particle stable. Along the $N = Z$ line we expect deuteron-like proton-neutron pairing correlations (isospin $T = 0$). Long-range correlations, due to multipole-multipole forces and core polarization, drive collective oscillations of the nucleus, including low-lying shape vibrations and giant resonances. Such correlations determine the nuclear response to the external field, for example, in photoabsorption and Coulomb excitation. Short-range correlations originate from the repulsive core of nuclear forces at small distances. They fragment the single-particle strength and strongly influence Gamow-Teller transitions and cross sections measured in particle removal reactions.

Modern shell model approaches are the most precise tools for quantitative descriptions of nuclei. Apart from the lightest nuclei, where computations with bare nucleon-nucleon forces are feasible, these calculations are based on effective interactions in a truncated single-particle space. Such interactions are suggested and tested by empirical data mainly known for nuclei near stability. The large variety of rare isotope beams available at the ISF will offer unique opportunities to explore nuclear correlations in regimes of extreme imbalance between proton and neutron numbers. The new data based on spectroscopy of rare isotopes, knockout reactions, and transfer reactions will immensely improve the foundations of theory and advance its predictive power.

2.4.1 Spectroscopic factors and correlation effects

In a shell model picture, deeply-bound states are fully occupied by protons and neutrons. At and above the Fermi surface, correlation effects and configuration mixing lead to occupation numbers gradually decreasing to zero. The occupancy is not a direct observable but is reflected in the spectroscopic factor C^2S . The experimental determination of spectroscopic factors thus probes the foundations of the nuclear shell model.

For stable nuclei, absolute spectroscopic factors are most accurately determined using the $(e,e'p)$ proton removal reaction. The results of electron-induced knockout experiments suggest that single-proton states in selected stable nuclei have their occupancy reduced by factors of order $C^2S_{\text{exp}}/C^2S_{\text{th}} = 0.6\text{--}0.7$ relative to

independent-particle models [Kra01]. Most (e,e'p) studies focus on closed-shell and doubly magic nuclei and are currently limited to stable nuclei.

The “classic” tools to study single-particle states with hadronic probes have been light-ion induced transfer reactions at incident beam energies below 50 MeV/nucleon. Single-nucleon transfer reactions, such as (d,p) and (p,d), probe neutron states, while reactions such as (d,³He), (³He,d), and (⁴He,t) probe proton states. The extracted neutron spectroscopic factors from (d,p) and (p,d) reactions on targets with $Z \leq 24$ are consistent with the reductions reported from the (e,e'p) studies, when the transferred-neutron bound state and nucleon-target optical potential geometries are constrained using Hartree-Fock calculations [Lee06a].

Single-nucleon knockout reactions combined with γ -ray spectroscopy were pioneered at the NSCL. They have developed into another versatile tool for the quantitative characterization of the single-particle structure [Han01,Han03a]. For nuclei close to stability, similar reduction factors of about 0.6 were extracted [Bro02b,Gad04a] while significant differences were observed for nuclei close to the driplines. A strong dependence on the asymmetry at the Fermi surface was observed. The knockout of the weakly-bound neutron ($S_n = 1.21$ MeV) of ¹⁵C to the ground state of ¹⁴C yielded a reduction of only 0.90(4)(5) [Ter04]. At the proton dripline, the one-neutron knockout from ³²Ar to ³¹Ar ($S_n = 21.99$ MeV) revealed a strong reduction (0.24(3)(4)) of the occupation of the $0d_{5/2}$ neutron state [Gad04b].

Figure 2.14 summarizes the results of the different techniques. The ratios of the experimental spectroscopic factors C^2S_{exp} to those of the p , sd , and pf shell model calculations $C^2S_{\text{shell model}}$ are plotted as a function of the difference between the

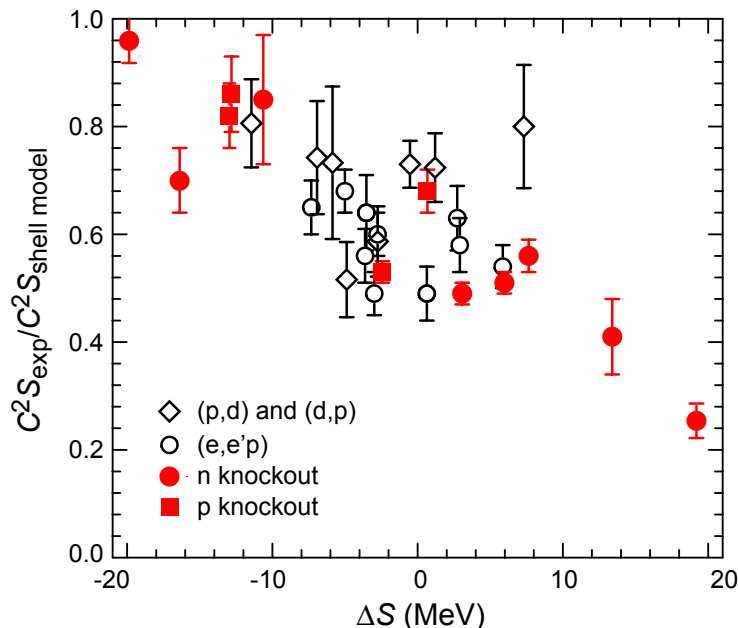


Figure 2.14: Ratios of experimentally deduced spectroscopic factors C^2S_{exp} to those of the large-basis shell model calculations $C^2S_{\text{shell model}}$ for nuclei with $A = 12-49$ as a function of the difference of neutron and proton separation energies, ΔS . ΔS is $S_n - S_p$ for neutron spectroscopic factors and equals $S_p - S_n$ for proton spectroscopic factors, where S_n and S_p are the neutron- and proton separation energies. Open diamonds are results from transfer reactions, open circles from (e,e'p) measurements, and solid circles and squares represent neutron and proton knockout experiments, respectively. Adapted from [Lee06a].

neutron and proton separation energies ΔS . ΔS is equal to $S_n - S_p$ and $S_p - S_n$ for neutron and proton spectroscopic factors, respectively. It reflects the asymmetry dependent relative shifts of the neutron and proton Fermi surfaces. Data obtained from (p,d) and (d,p) transfer reactions on stable calcium isotopes [Lee06a] are displayed by open diamonds. The filled squares and the filled circles are the results from proton-knockout and neutron-knockout reactions, respectively. Spectroscopic factors studied with the (e,e'p) reactions [Kra01] are plotted as open circles. The strong dependence of the reduction on the separation energy difference is clearly seen.

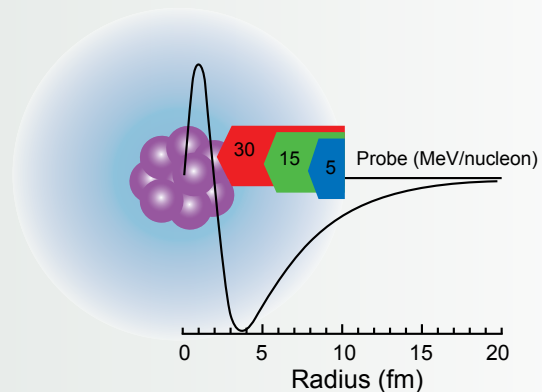
The observed reduction in the (e,e'p) reactions has been attributed to correlation effects – short-range correlations and the coupling to surface phonons and giant resonances – that are not included in the *p*, *sd*, or *pf* model space wave functions [Dic04]. The (e,e'p) reactions are limited to probing proton spectroscopic factors in stable nuclei. Only transfer and knockout reactions will be able to explore the origin of these reductions and their dependence on isospin.

As mentioned in Section 2.3.3, transfer and knockout reactions are complementary techniques. Knockout reactions are confined to the study of hole states at high incident projectile energy. In addition to the *hole* states, transfer reactions such as (d,p) and (³He,d) also study *particle* states. However, kinematics and transfer momentum matching often limit transfer reactions to low incident energy provided by reaccelerated beams and decelerated fast beams. Typically, transfer reactions require beam intensities upwards of 10^4 s^{-1} , while for knockout reactions particle rates as low as 0.1 s^{-1} have been sufficient. Hence, knockout reactions have a much larger scientific reach.

One-nucleon transfer reactions as a probe of nuclear properties

One-nucleon transfer reactions are a sensitive tool to extract nuclear overlap functions. For example, the cross section and angular distribution of the reaction $^{18}\text{C}(d,p)^{19}\text{C}$ gives information on the structure of ^{19}C . Specifically, its overlap with one neutron coupled to the ground state of ^{18}C . The overlap function extracted from experiment can be compared to those obtained with modern nuclear structure models. In the shell model, the overlap function is related to the orbital occupancies as well as their radial wave functions.

As shown in the figure, low-energy reactions only probe the radially asymptotic part of the overlap function due to the Coulomb barrier in the reaction. For many nuclear astrophysics applications, this “asymptotic normalization” [Muk05b] is the most important quantity. However, to understand the full many-body structure (and hence be able to predict asymptotic normalizations for unmeasured reactions) we need to probe the overlap function to smaller radii. In the example shown, the influence of the node in the overlap function at 2 fm can only be observed when the deuteron energy is near 30 MeV/nucleon. The difficulty of these experiments at higher beam energies is that the cross sections decrease with energy. The cross sections for the reaction $^{18}\text{C}(d,p)^{19}\text{C}$ decrease from about 100 mb/sr at 5 MeV/nucleon to 1 mb/sr for 30 MeV/nucleon.



The overlap function for $^{19}\text{C} \rightarrow n+^{18}\text{C}$ in arbitrary units. The radial sensitivity of the $^{18}\text{C}(d,p)^{19}\text{C}$ cross section is represented by the colored bars for different beam energies.

In the example above, ^{18}C is a short-lived radioactive isotope, so the experiment has to be performed in inverse kinematics on a deuteron target: $d(^{18}\text{C},^{19}\text{C})p$. The required beam energy of $\sim 30 \text{ MeV/nucleon}$ of ^{18}C is just at the boundary for using reaccelerated or decelerated beams. Both options will be available with sufficient intensities for a quantitative study of overlap functions at the ISF.

In the near future, spectroscopic factors from (p,d) or (d,p) transfer reactions on ^{46}Ar ($\Delta S = -10.6$ MeV) and ^{34}Ar ($\Delta S = 12.4$ MeV) will be deduced. Knockout studies will also be pursued in the *sd* shell in the proximity of the proton dripline where, for example, the one-proton knockout (one-neutron knockout) from ^{24}Si probes weakly-bound proton-hole states (deeply-bound neutron-hole states). So far, the study of deeply bound proton states in neutron-rich *sd*-shell nuclei has not been possible because the necessary rare isotope beams near the dripline are unavailable.

At the ISF, spectroscopic factors can be investigated in very neutron-rich systems, extending the range of accessible values of ΔS by a factor of two. For example, from ^{20}Mg to ^{35}Mg ΔS ranges from 20.9 MeV to -23.2 MeV, one of the largest range of the ΔS values within one isotope chain. Particle and hole states can be studied with (p,d) and (d,p) transfer reactions out to ^{35}Mg , while one-nucleon knockout reactions even reach out to $^{39,40}\text{Mg}$. Calcium isotopes will be accessible with transfer reactions up to $A = 52$ and with knockout reactions out to ^{58}Ca . Only with the rates expected at the ISF will very exotic nuclei in the *fp* shell come into reach for studies with direct reactions. For example, ^{50}Ni and ^{78}Ni will be available at rates of tens of particles per second for knockout studies and from ^{52}Ni to ^{74}Ni for complementary exploration with nucleon-adding transfer reactions.

The examples discussed above nicely illustrate how important new insight is gained from measurements very far from stability.

2.4.2 Two-nucleon correlations

Two-particle correlations play an important role in nuclei. A particularly important example is the pairing correlation of identical nucleons in time-conjugate orbits. They govern, for example, the even-odd mass differences and the reduction of the level density in the low-energy spectra of even-even nuclei. In stable nuclei, the pairing correlations determine the low-lying level structure, γ -transition probabilities, β -decay lifetimes, collective vibrational modes, and rotational moments of inertia. For nuclei near the dripline, the particle separation energy is small and the pairing energy becomes important for the very existence of a particle-bound nucleus. Another new aspect is that the pairing correlations couple to the continuum. The understanding of this physics would help in modeling the crust of neutron stars where the nuclei are embedded in a neutron gas. New theoretical descriptions have to be developed that go beyond the mean field (BCS or HBF) approximations.

The spatial correlation of two like nucleons can be studied with direct two-proton or two-neutron knockout reactions. When intermediate-energy, neutron-rich (neutron-deficient) projectiles react with a light target, for example, ^9Be , the knockout of two protons (two neutrons) proceeds as a direct reaction [Baz03,Yon06]. The detection of coincident γ rays provides partial cross sections for the knockout to specific final states. Unlike the (p,t) pair transfer reaction, which probes the correlation associated with the $S = 0$ and (relative) $\ell = 0$ nucleon pairs, the sudden two-nucleon knockout has no specific S or ℓ selection but is still sensitive to the wave functions.

This sensitivity is demonstrated in Figure 2.15 for the example of two-neutron knockout from proton-rich nuclei. The neutron-neutron pairing correlation leads to an enhanced cross section for the population of the 0^+ ground state of the knockout

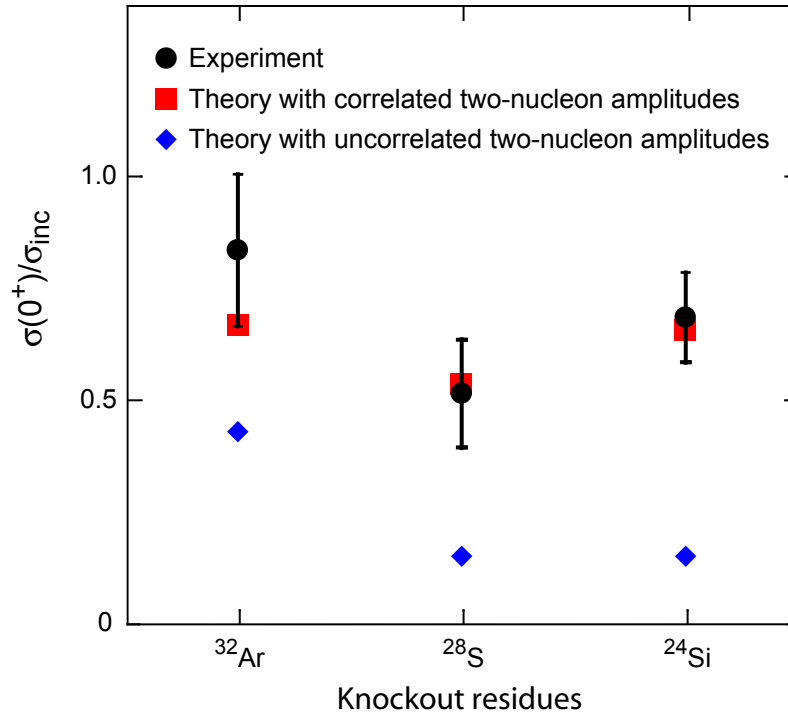


Figure 2.15: Relative population of the ground state of ^{32}Ar , ^{28}S , and ^{24}Si in two-neutron knockout reactions in comparison to reaction theory. The fraction of the cross section to the ground state is compared to calculations that assume the removal of two uncorrelated neutrons (diamonds) and to calculations that include two-neutron amplitudes from a many-body shell model as input (squares) [Yon06,Tos06]. The sensitivity to pairing is visible in the enhanced population of the ground state and the need for correlated many-body wave functions for a description of this observation. Adapted from [Yon06].

residues. Typical cross sections are between 0.12 mb and 1.2 mb and show a pronounced structure dependence. There is thus a strong interplay between nuclear structure and the reaction process. The sensitivity of this reaction mechanism to nucleon pairing and the details of correlated many-body shell model wave functions will make it possible to deduce nuclear structure information from the magnitude and distribution of experimental cross sections in comparison to theory. The reaction model combines eikonal reaction theory with many-body wave functions from modern shell model calculations [Tos04]. Such investigations will serve as benchmark tests for theoretical models with respect to microscopic two-nucleon transition densities.

In the near future, nucleon-nucleon correlations can be studied with knockout reactions on the neutron-rich nickel isotopes out to ^{70}Ni . However, to get closer to the driplines, the investigation of the most exotic nickel isotopes will only be possible at the ISF: ^{52}Ni ($> 10^7 \text{ s}^{-1}$) to ^{76}Ni ($> 10^3 \text{ s}^{-1}$). The other long chain of isotopes of tin from $A = 102$ ($> 10^3 \text{ s}^{-1}$) to $A = 134$ ($> 10^4 \text{ s}^{-1}$) will be in reach for the study with two-nucleon knockout reactions. The investigation of chains reaching from the very neutron-rich to the very neutron-deficient isotopes provides the unprecedented opportunity to probe nucleon-nucleon correlations as a function of isospin.

In spherical nuclei, pairing correlations can be described by the pairwise coupling of nucleons in $J^\pi = 0^+$ states. Reactions in which two particles are transferred to a

nucleus in an $L = 0$, $S = 0$, and $T = 1$ state provide a specific probe of pair correlations. Experimentally, this has been realized with (t,p) and (p,t) reactions [Bro73]. In general, the momentum matching of transferring two nucleons requires low energy beams. These experiments are best done with the reaccelerated beams of the ISF. The (p,t) transfer reaction in inverse kinematics, in which a correlated pair of neutrons is added from the projectile, can be extended to ^{50}Ca ($> 10^6 \text{ s}^{-1}$) and ^{46}Ar ($> 10^9 \text{ s}^{-1}$). A significant reduction of the $L = 0$ (t,p) strength in $^{38,40,42}\text{Ar}$ relative to $^{42,44,46,48}\text{Ca}$ [Bje67,Bay68,Cas73] has been observed. This reduction may result from a dramatic change in the nuclear structure of the excited 0^+ states [Cas73]. The ISF will make it possible to track the pairing interaction along the chain of neutron-rich nickel isotopes out to ^{70}Ni projectiles ($> 10^5 \text{ s}^{-1}$) and in the tin isotopes from ^{104}Sn to ^{132}Sn .

Another region of interest is the pairing strength near the doubly magic nucleus ^{132}Sn . In $^{132-136}\text{Te}$, the decreasing excitation energy of the first 2^+ state is accompanied by a drop in the electromagnetic $B(E2;0^+ \rightarrow 2^+)$ excitation strength [Rad02]. QRPA calculations tied the experimental observation to a reduction in neutron pairing strength above neutron number $N = 82$ [Ter02]. With the ISF, the pairing strength of these Te isotopes can be measured directly via (p,t) reactions.

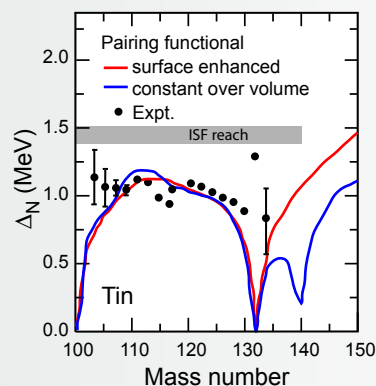
Pairing correlations in energy density functional approaches

The structure of atomic nuclei depends significantly on its superfluid nature. Properties affected include masses, separation energies, densities, deformations, individual excitation spectra, and collective excitation modes such as rotation or vibration and as shown by systematics of the first 2^+ energies. The role of pairing correlations in nuclei is particularly emphasized when going toward the neutron dripline because of the proximity of the Fermi surface to the single-particle continuum. There the scattering of virtual pairs of quasiparticles into the continuum gives rise to a variety of new phenomena in ground states and excited states of nuclei. Also, nuclear superfluidity strongly influences properties of neutron stars. For example, the odd-even mass staggering in atomic nuclei due to pairing may influence the nonequilibrium processes in the crust of accreting neutron stars.

Despite its major role, our current knowledge of the pairing force and of the nature of pairing correlations in nuclei is rather poor. The main challenges are to understand the density dependence of the pairing part of the energy density functional, in particular its volume-to-surface ratio, its isospin dependence, and its low-density behavior. Nuclear matter calculations and experimental data (e.g., isotope shifts, moment of inertia, and odd-even mass staggering) suggest that the pairing strength is enhanced at surface densities compared to the nuclear saturation density.

To illustrate the problem, in the figure we compare calculated neutron pairing gaps along the tin isotopic chain with the gaps deduced from experimental masses. The gaps are calculated with two state-of-the-art phenomenological pairing functionals: one having a constant strength over the nuclear volume, the other displaying an enhanced strength at the nuclear surface, with the strengths being adjusted for ^{120}Sn . The surface

and volume results are similar for nuclei near stability and agree reasonably with experiment. On the other hand, their predictions differ significantly beyond ^{132}Sn . The discrepancies between theory and experiment at $A = 132$ are dominated by effects other than pairing near shell closures. Thus, it is clear that masses of more neutron-rich medium mass nuclei (but also moments of inertia and single-particle excitations of medium-shell systems), in connection with undergoing efforts to derive functionals from first principles, will play a crucial role in pinning down the unknown properties of the pairing functional. New masses measured at the ISF with accuracy on the order of 50 keV will help us to discriminate between these models.



Average neutron gaps Δ_N predicted by Hartree-Fock-Bogoliubov calculations for the tin isotopes using state-of-the-art pairing functionals. Full circles are experimental five-point odd-even mass differences taken from [Aud03]. The calculations use pairing functionals that are constant over the volume (blue line) and nuclear-surface enhanced (red line).

Comparison of single-particle removal or pickup reactions to the corresponding two-particle reactions should also yield information about like-nucleon pairing interactions. To bypass complications arising from the use of a ^3H gas target for (t,p) reactions, it is desirable to use heavy-ion induced pair-transfer reactions. Pair transfer induced by light targets, for example $(^9\text{Be},^7\text{Be})$ or $(^{14}\text{C},^{12}\text{C})$, in inverse kinematics can be explored for pair-adding reactions with the current CCF facility at NSCL. The perfected method can then be used for a full-fledged program at the ISF.

2.4.3 Proton-neutron pairing

In nuclei with a large proton-neutron imbalance, proton-proton or neutron-neutron pairs are favored. Along the $N = Z$ line, proton-neutron pairs can be formed. The large spatial overlap of single-particle orbitals occupied by protons and neutrons in $N = Z$ nuclei provides a unique opportunity for studying the proton-neutron interaction, in particular, the proton-neutron pairing correlations. For a proton and a neutron in the same j -shell, the exclusion principle dictates that a pair can be either of a familiar isospin-triplet spin-singlet ($T = 1, S = 0$), or in a more exotic, deuteron-like isospin-singlet spin-triplet ($T = 0, S = 1$) state. The mutual strength, interplay, and impact of the corresponding isovector ($T = 1$) and isoscalar ($T = 0$) pairing interactions is a subject of one of the most exciting and challenging debates in the nuclear structure community [Goo79,Mar99a,Sat01,Vol03b,She05].

The collective superfluid phase and pairing vibrations resulting from the isovector pairing interactions are well identified and documented near the line of stability. However, further investigation with heavier $N = Z$ rare isotopes will help clarify the question of how isoscalar pairing gives rise to new collective modes. The answer to this question is being sought by examining binding energy differences, properties of ground states of odd-odd self-conjugate nuclei, and rotational properties such as moments of inertia and high-spin pair alignments as well as two-particle cross sections along the $N = Z$ line [Isa95,Mar99a,Mac00,Sat01,Dob03,Cak05].

In particular, the $(^3\text{He},p)$ and/or $(p,^3\text{He})$ reactions may provide valuable new information from proton-neutron pair transfer cross sections. For an even-even $N = Z$ target ($T = 0, S = 0$), the proton-neutron pair transfer populates both isovector and isoscalar states in the corresponding self-conjugate odd-odd nucleus.

Superfluidity and superconductivity

Nuclei provide beautiful examples of small superfluid systems. The superfluidity, or superconductivity, of the nuclear Fermi liquid is explained, as it is in metals, by pairing correlations of nucleons with the coherence length of the pair exceeding the size of the nucleus. In macroscopic systems, the standard Bardeen-Cooper-Schrieffer (BCS) theory gives practically an exact solution.

However, in finite systems the deviations from the BCS theory are significant and its application requires a more precise theoretical consideration [Vol01,Vol03b,Zel03]. All phase transformations in atomic nuclei are smoothed [Zel96a,Zel96b] in analogy to small superconducting samples [Lea81].

Beyond BCS theory, the superconducting correlation energy is still important outside the region of the non-zero BCS solution. In loosely bound nuclei, pairing might be the main agent

ensuring the stability of the system and it will lead to exotic decay modes, such as two-nucleon radioactivity. Nuclei with two-particle halos can be considered unique examples of systems with a single Cooper pair. The experimental search for multi-particle halos is of paramount interest because such isotopes provide nature's purest chance to study the Cooper pairing phenomenon.

Another exciting question that needs to be addressed experimentally is the search for unusual types of pairing, such as isoscalar (proton-neutron) and spin-triplet pairing. Such new pairing modes can be important for nuclear matter in various stages of stellar evolution [Bla01,Yak01,Yak04], and a reliable understanding of these effects in exotic nuclei will influence our understanding of astrophysical reactions, nucleosynthesis, and the physics of neutron stars.

From measurements of absolute $\sigma(T = 1)$, $\sigma(T = 0)$, or relative $\sigma(T = 1)/\sigma(T = 0)$ cross sections to these isovector/isoscalar states, information on the character and strength of $T = 1$ and $T = 0$ pair correlations can be inferred.

The experimental challenge in these studies comes from the fact that the pair transfer needs to be studied in inverse kinematics with protons emerging at a backward angle with $\sigma \sim 1$ mb/sr cross sections. For ~ 100 $\mu\text{g}/\text{cm}^2$ gas-cell targets, a beam of even-even $N = Z$ nuclei at 10^5 s^{-1} is required. These intensities are not available at present for medium- and heavy-mass nuclei where a superfluid phase associated with the isoscalar pairing could possibly develop. However, the ISF will provide the required beam intensities up to ^{80}Zr . Moreover, it is estimated that exclusive cross section measurements in a knockout of a correlated proton-neutron pair can be employed to explore the role of isoscalar pairing at beam rates of $\sim 10^3$ s^{-1} . With the ISF, studies of the $T = 0$ pairing interaction can be extended up to ^{92}Pd in the immediate vicinity of the doubly magic self-conjugate nucleus ^{100}Sn .

2.5 Physics of deformed nuclei

The mesoscopic nature of nuclei is clearly manifested in the diversity of nuclear shapes and deformations. By adding a relatively small number of particles to a spherical, doubly magic core, one can induce the self-consistent core polarization and shift the equilibrium shape to a potential minimum corresponding to a non-spherical shape. Such collective effects might be even more pronounced far from stability, with a large number of available valence particles and strong imbalance between population of protons and neutrons.

The study of deformed nuclei, in many ways, is a complementary endeavor to the exploration of spherical shell structure. New shell structures may appear reinforcing different degrees of freedom, similar to the well-known 2:1 axes ratio in superdeformed nuclei. New symmetries, with mutual phase transformations and coexistence as a function of isospin, angular momentum, and excitation energy make the expected picture exceedingly rich.

Among the exotic collective phenomena that may occur in nuclei at low excitation energies (below 3 MeV), we expect static octupole and higher-order deformations, coexistence of various deformed and spherical shapes, and proton-neutron oscillations that may produce states of mixed proton-neutron symmetry. These phenomena, analogs of which may also exist close to stability, can be strongly influenced by the proximity of the continuum.

At much higher energies, giant resonances of a variety of multipolarities can be excited and characterized to test, in a very general way, the treatment of collective modes by mean field theories, including the nuclear matter parameters employed by both relativistic and nonrelativistic approaches. The strength distribution and damping characteristics may be very different from what is known in stable nuclei.

In the following four subsections, this broad field will be first discussed in terms of the basic shapes, followed by a description of how these shapes evolve due to gaps between deformed single-particle states. A discussion of the interplay between collective and single particle properties and, finally, the collective behavior at higher excitation energies round out this section. Each subsection contains descriptions of experimental techniques that will be available at the ISF to explore these nuclear features towards the extremes of neutron-to-proton asymmetries.

2.5.1 Nuclear sizes and shapes

Nuclear shape is a basic bulk property of the nucleus. The characterization of quadrupole, octupole, and higher-order deformations is crucial to the understanding of mesoscopic flexibility of the self-consistent nuclear field and to the fundamental development of global models attempting to reproduce macroscopic nuclear properties over the wide range of nuclei.

The simplest approaches to the characterization of nuclear properties assume the nucleus takes on a spherical shape. However, it is well-documented that many nuclei exhibit prolate deformation and, in rare instances, oblate-deformed shapes occur. More exotic shapes, beyond axially symmetric quadrupole deformations, are expected across the nuclear chart.

At the neutron dripline, single- and multi-neutron halo structures appear. In these nuclei, the neutron wave function(s) extend well outside the nuclear core in the classically forbidden region. Halo nuclei provide a laboratory to systematically study the tails of the nuclear potential, as discussed in more detail in Section 2.1.5. Neutron-rich nuclei also show evidence for anomalous deformation modes; for example, experimental studies [Ima04,Ong06] of the collectivity of the first excited 2^+ state in ^{16}C suggest pure neutron prolate deformation near the ground state.

The subsections below highlight the opportunities at the ISF to measure the size of exotic nuclei and to explore the quadrupole and octupole deformation occurring in these short-lived systems.

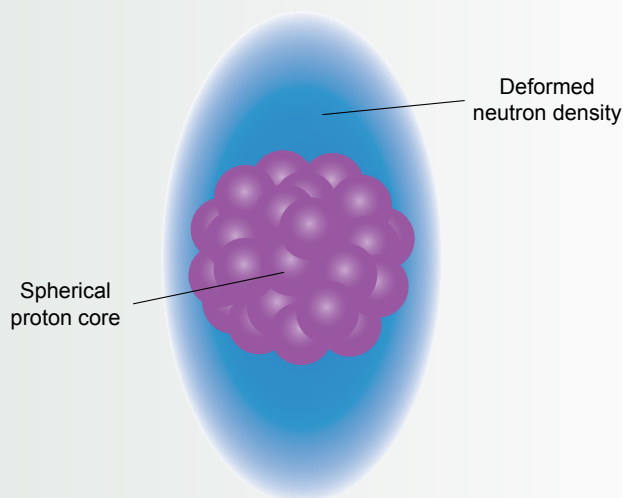
2.5.1.1 Charge radii and laser spectroscopy

Nuclear charge radii are very sensitive to the valence orbits and to nuclear deformation. The charge radius can be extracted from laser spectroscopic studies via isotopic shift measurements. Most of the laser spectroscopic data to date have been obtained at ISOL facilities and are mainly limited to alkali and alkali Earth metals, noble gases, and rare earth elements where rare isotope production rates

What type of nuclei are egg-shaped?

Very asymmetric proton- versus neutron-density distributions may arise when the shell gaps for protons and neutrons are very different. Near the valley of stability the proton and neutron density distributions usually have similar shapes even when the shell gaps are different. This is due to the near equality of the proton and neutron rms radii together with the strong interaction between protons and neutrons that maximizes the binding energy when the shapes are similar.

What happens when there is a large neutron skin? One possibility is provided by the example of ^{16}C where it has recently been found [Ong06] that the proton matrix element for the 0^+ to 2^+ transition is anomalously small compared to the neutron matrix element. This leads to an egg-shape with the proton distribution forming a spherical yolk and the neutron distribution in a prolate outer skin. A similar situation could occur for heavier neutron-rich nuclei with a proton shell closure, such as silicon and nickel isotopes. The ISF will allow experimental investigation of the proton and neutron shapes in neutron-rich silicon and nickel isotopes.



Schematic illustration of the unusual egg-shaped neutron distribution, surrounding a spherical core of protons.

exceed 10^4 s^{-1} [Klu03]. In the short term, it is expected that improvements to primary beam intensities at current ISOL facilities will extend charge radius measurements in previously studied elements towards the driplines.

The recent measurement of the charge radius of ^{11}Li [San06] completed at ISAC/TRIUMF serves as an excellent example. The implementation of gas cells for ion generation, combined with cooling and bunching techniques, has also extended the suitability of laser spectroscopy studies to refractory elements [Nie02].

There still exists a dearth of information on the charge radii of light and medium mass nuclei, attributed to difficulties in the production of metallic and refractory rare isotope beams. Light and medium mass nuclei have low single-particle level densities and noticeable cluster components, and changes in single-particle level ordering can result in rapid changes in nuclear shape.

The planned laser spectroscopy facility at LEBIT, which will be available at the current CCF in 2010, will be used to measure charge radii of refractory elements. Charge radii in the neutron *pf*-shell region, which includes the transition metal elements titanium through nickel, are needed to answer unresolved questions regarding the shell stability at $N = 34$ [Hon04] and the role of the deformation-driving neutron $g_{9/2}$ orbital in defining nuclear shapes beyond $N = 40$.

While the CCF will make it possible to perform measurements on refractory elements, only the increased production rate at the ISF will allow laser spectroscopy for long isotopic chains to the largest neutron excesses. Systematic studies of the charge radii of metallic beams of manganese, iron, and cobalt will be feasible out to ^{67}Mn , ^{70}Fe , and ^{73}Co , respectively. Figure 2.16 shows a comparison of present laser spectroscopy data (blue squares) and the reach for laser spectroscopy at the ISF (red squares). It is clear that the present data are fairly limited and the beams available at the ISF will cover long isotopic chains for all elements.

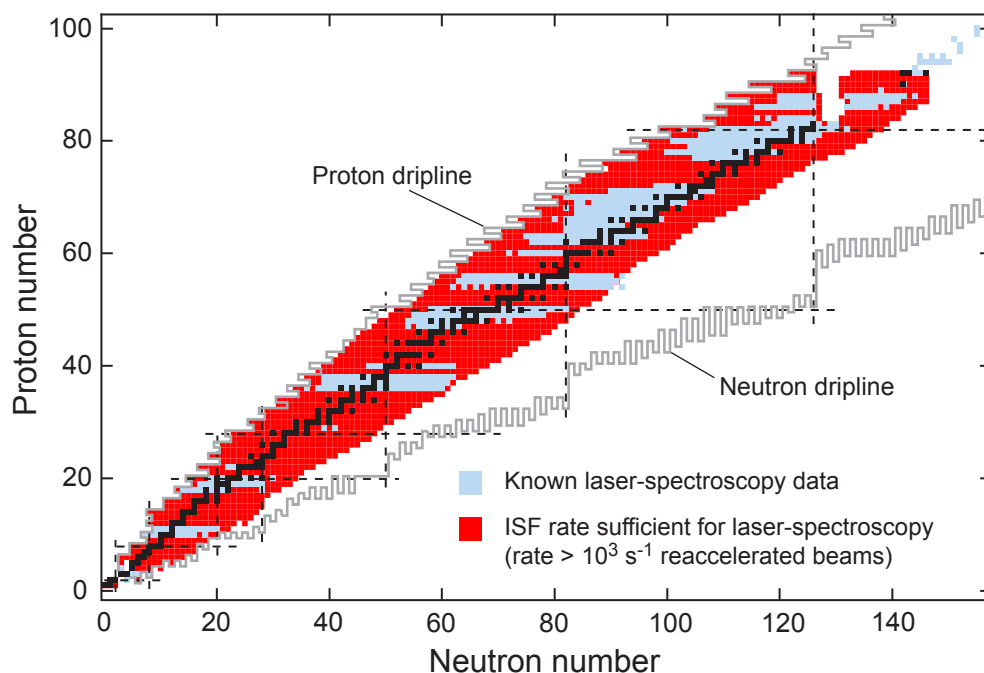


Figure 2.16: Chart of the nuclei depicting nuclei studied via laser spectroscopy [Klu03]. Known data are indicated in blue, while the reach of the ISF is shown in red.

2.5.1.2 Static quadrupole deformation

The deviation of the nuclear shape from spherical symmetry is directly measured via the electric quadrupole moment. Nonzero quadrupole moments of nuclei far from stability serve as indicators of new regions of deformation. Most of the available data on nuclear quadrupole moments was obtained via collinear laser spectroscopy experiments, where the hyperfine structures provide direct information on the signs as well as the magnitudes of nuclear magnetic dipole and quadrupole moments. However, a majority of these data have been collected for heavier nuclei, and the nuclear landscape below $Z = 50$ remains largely unexplored.

For light stable nuclei, the quadrupole moments are known for $T = 1/2$ nuclei and are described well by shell model calculations in the sd model space as shown in Figure 2.17. Very limited data are available for ground state quadrupole moments of light radioactive nuclei apart from systematic studies of a few isotopic chains. Such measurements have been vital in characterizing the large deformations observed along $N = 20$ for the neutron-rich magnesium and sodium isotopes. Sodium, as an alkali metal, has a well-characterized atomic structure and is readily accessible at online isotope separator facilities [Hub78,Kei00].

In the region of light nuclei, the goal over the next few years is to extend the measurements of quadrupole moments to nuclei with extreme neutron-to-proton ratios. For neutron-rich nuclei, ground state quadrupole moment measurements of magnesium and aluminum isotopes [Uen04] are currently planned to define the limits of the island of inversion around ^{32}Mg . On the neutron-deficient side of the valley of stability, one of the strongest pieces of evidence for halo structures in proton dripline nuclei is the quadrupole moment of ^8B [Min92]. A measurement of the ground state quadrupole moment of ^{35}K , which has a small proton separation energy ($S_p = 78$ keV), will aim to find similar evidence for a proton halo structure.

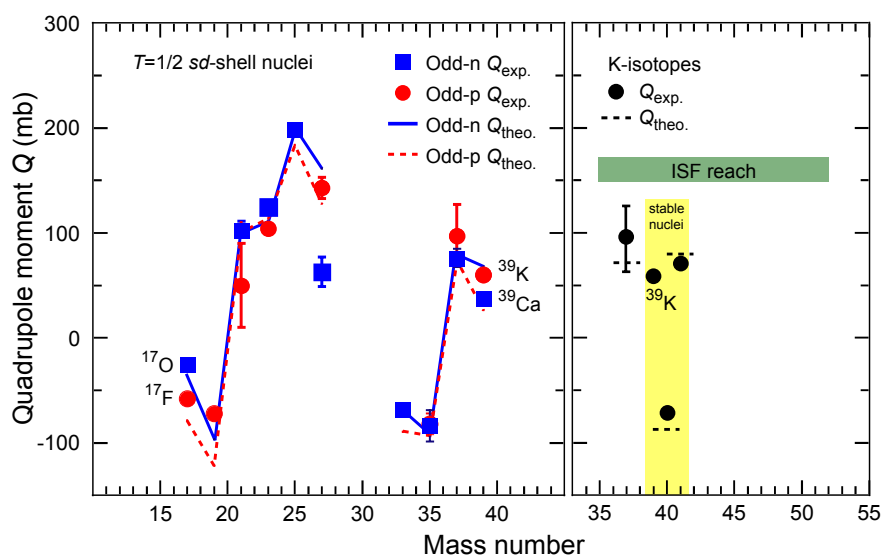


Figure 2.17: Experimental ground-state quadrupole moments of $T = 1/2$ nuclei in the sd shell are shown to the left. Shell model calculations in the sd model space reproduce the experimental values well. On the right side, the experimental quadrupole moments for the potassium isotopes are shown. In most cases below $Z = 50$, quadrupole moment data are limited to nuclei nearest stability. The ISF will open opportunities to measure ground-state quadrupole moments of very neutron-rich nuclei.

With the ISF, it will be possible to significantly extend the current knowledge of quadrupole moments in nuclei below $Z = 50$ to address several issues at the frontier of nuclear physics, including finding direct evidence for oblate ground states ($Q < 0$) for $N = Z$ nuclei around ^{72}Kr , exploring collective phenomena in nuclei near ^{56}Ni , and investigating the sharp transitions to ground state deformed structures near $N = 40$ and $N = 60$ attributed to neutron $g_{9/2}$ and $h_{11/2}$ intruder orbitals, respectively.

Two techniques will be employed to realize such measurements: collinear laser spectroscopy and β -detected Nuclear Quadrupole Resonance (β -NQR) measurements. The laser spectroscopy measurements require low-energy (~ 60 keV) beams, which will be available after the gas stopping system. Atomic hyperfine structures will be accessible for nuclei produced at rates above 10^4 s $^{-1}$. Beam cooling and bunching, as planned for the low-energy beamline, will improve the sensitivity of the method [Nie02]. The β -NQR technique will be applied using either the direct fragmentation process [Asa90,Gro03] or optical pumping of low-energy beams (~ 60 keV) from the gas stopping station (see Section 2.3.5). Secondary beam rates of 10^2 s $^{-1}$ are sufficient for a β -NQR measurement if the nuclear spin polarization is at or above 1%.

Systematic studies of long chains of isotopes, which are crucial for identifying the sudden onset of new regions of nuclear deformation, will become possible. For example, quadrupole moment data currently available for krypton isotopes ranging from $A = 75$ to 91 remain short of ^{72}Kr , where oblate deformation is expected in the ground state [Gad05]. The rate estimates for the ISF will allow us to extend the known ground state quadrupole moments in the krypton isotopes to very neutron-deficient ^{69}Kr (rate 6×10^2 s $^{-1}$) and neutron-rich ^{97}Kr (rate 8×10^3 s $^{-1}$). The latter measurement crosses $N = 60$, which shows a dramatic onset of deformation for higher- Z nuclei [Cam02].

It will also be possible to explore shape transitions in nuclei near $N = 40$. Quadrupole moments for the titanium isotopes are only available for the stable $^{47,49}\text{Ti}$ and long-lived ^{45}Ti ($T_{1/2} = 3.1$ h). The ISF will extend the reach of quadrupole moments in the titanium isotopes over the range from ^{39}Ti (5×10^3 s $^{-1}$) at the proton dripline to ^{61}Ti (1×10^2 s $^{-1}$), which neighbors $N = 40$ and will permit resolution of the open question on the existence of a deformed or spherical shell gap at $N = 40$ for very neutron-rich nuclei.

2.5.1.3 Static octupole deformation

While quadrupole deformation is typically observed in mid-shell nuclei throughout the nuclear chart, higher-order static multipole deformations (octupole, hexadecapole, etc.) occur much less often. Octupole deformations are expected in nuclei where the proton and neutron Fermi surfaces lie near degenerate single-particle orbitals that differ by $\Delta\ell = 3$, $\Delta j = 3$. Such shapes were predicted by Strutinsky-type potential-energy calculations just above closed shells, at nucleon numbers 34, 56, 90, and 134 [Naz84].

The experimental fingerprint of octupole-deformed, pear-like nuclear shapes, is the coexistence of even-spin, positive-parity and odd-spin, negative parity collective bands that are observed to be nearly interleaved. Such patterns are especially interesting because they are known to enhance the signatures of nuclear forces violating parity and time reversal invariance [Fla95a,Spe97]. Failure to identify

such experimental signatures in exotic nuclei may provide important evidence for changes to the single-particle level ordering predicted by some theories as the limits of the nuclear chart are approached.

Progress in the study of octupole deformations in medium mass nuclei will be realized in the next few years. The most promising nuclei are those near and along the $N = Z$ line, including ^{68}Se [Fis03] and ^{114}Ba [Hee94]. The yrast structure of ^{68}Se , for example, is now known up to spin $26\hbar$, but information on negative parity states and electromagnetic transition strengths in this nucleus is still virtually nonexistent.

In slightly heavier nuclei, octupole deformation near the ground state has been suggested to occur in the ^{146}Ba region [Phi86]. However, the best evidence for static ground state octupole deformation is in the $A \sim 230$ mass region, in $_{86}\text{Rn}$, $_{88}\text{Ra}$, and $_{90}\text{Th}$ [Coc97]. Static octupole deformations in transactinide nuclei are also evident in the behavior of the yrast band structure. A delay in the onset of alignment for the plutonium isotopes, in particular $^{238-240}\text{Pu}$ [Wie99a,Zhu05], has been observed as shown in Figure 2.18. The heavier plutonium isotopes all show alignment of the (assumed) $i_{13/2}$ protons at $\sim 250 \hbar\omega$. The dramatic change in the systematic trends of structure alignments in the band may be attributed to octupole correlations and possibly evidence for the onset of static octupole deformation in these nuclei.

Two methods are best suited to search for the regular band structures that serve as the fingerprint for static octupole deformation. With multiple Coulomb excitation at energies near and below the Coulomb barrier, the nucleus can be excited to states of relatively high spins. For example, collective bands up to spin $31\hbar$ were reported in [War96] from Coulomb excitation of a ^{209}Bi beam on ^{238}U targets. At the ISF, multistep Coulomb excitation will be possible in neutron-rich selenium isotopes in the vicinity of ^{90}Se (reaccelerated rate $6 \times 10^4 \text{ s}^{-1}$). The presence or absence of octupole deformation can then be inferred from properties of the excited levels, including spin-parity assignments and electromagnetic transition rates.

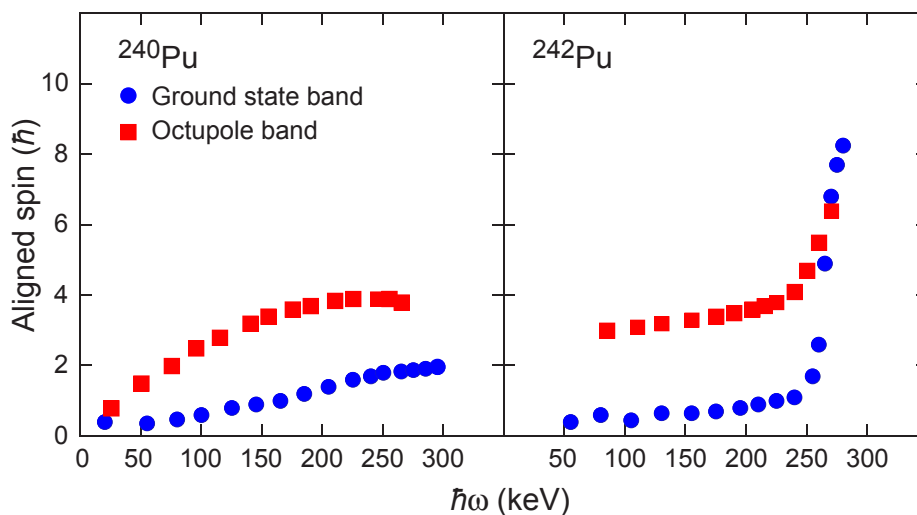


Figure 2.18: Alignment spins for the ground state and octupole bands in the even- A plutonium isotopes as a function of rotational frequency. Delayed alignment is observed in ^{240}Pu , a possible signature of static octupole deformation in this nucleus. Adapted from [Wie99a].

Next-generation γ -ray detection

The detection of γ -rays has a vital and ubiquitous role in nuclear science. Discrete γ -rays emitted from excited states provide the fingerprints of the structure of the isotope under investigation. Advances in nuclear spectroscopy are tightly coupled to the capability of the γ -ray detector to resolve individual γ -rays in the presence of many others. GREYINA is a new γ -ray spectrometer under construction at the Lawrence Berkeley National Laboratory in which the novel concept of γ -ray tracking is used to achieve a higher resolving power compared to any existing γ -ray spectrometer [Lee04]. The individual germanium crystals in GREYINA are electrically segmented so that the scattering of an incident photon can be tracked in each crystal and into neighboring crystals. Knowing the path that each photon takes until it deposits all of its energy after multiple interactions allows precise reconstruction of the first interaction point and the energy of the emitted photon. GREYINA will be a national user facility and can be used at the ISF, e.g., surrounding the target area of the S800 spectrograph (see Figure A), for precision measurements with the most exotic nuclei.

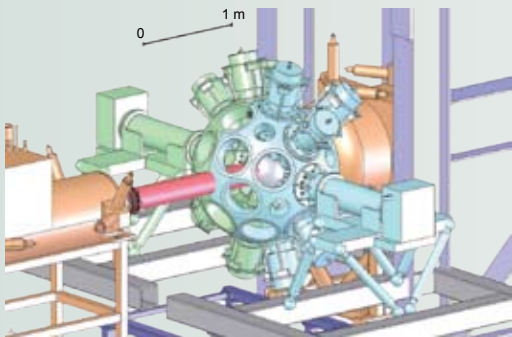


Figure A: Model of GREYINA positioned in front of the S800 spectrograph. The mounting structure can accommodate additional detectors supplementing GREYINA.

GREYINA is scheduled to be completed in 2009 and will add major discovery potential to experiments with both reaccelerated and fast exotic beams. The large gain in resolving power for a typical in-beam experiment with fast exotic beams expected with GREYINA is illustrated in Figure B. GREYINA is the first step towards GREYTA, an array with about four times the number of germanium crystals. GREYTA's resolving power for typical fusion-evaporation reactions will exceed that of current state-of-the-art detectors by a factor of up to 1,000.

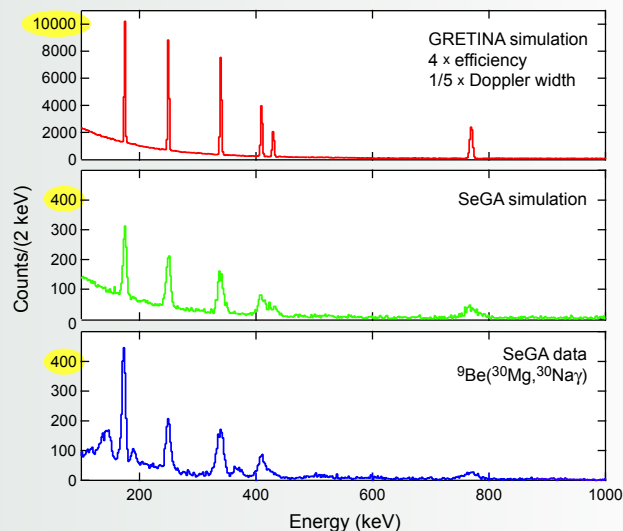


Figure B: Experimental data taken recently with the SeGA array (bottom panel) and simulations of that data (middle panel). The same simulation was then used to predict the performance of GREYINA in an otherwise identical experiment (top panel), exhibiting the superior resolving power. Note the different scales highlighted in yellow. Adapted from [Lee06b].

The second method is fusion-evaporation reactions with reaccelerated beams. The fusion of ^{16}C and ^{20}O projectiles on targets of thorium and uranium will populate potential negative parity band structures in the higher- Z transactinide nuclei. For example, with reaccelerated ^{16}C beam rates from the ISF of $4 \times 10^9 \text{ s}^{-1}$, the reaction $^{16}\text{C} + ^{238}\text{U}$ produces ^{254}Cf compound nuclei with sufficient intensity to allow one to identify and assign band structures, examine deformed single-particle states, and search for evidence of octupole excitations. Currently, the spectroscopy of californium isotopes is known only up to ^{251}Cf , which was populated by α -decay from ^{255}Fm [Ahm05].

For both the fusion evaporation and sub-barrier Coulomb excitation measurements, high resolution and high-fold γ -ray spectroscopy will be required at high efficiency, and an array similar to Gammasphere or GREYINA detector array is essential. In addition, for the transuranic nuclei, conversion electron spectrometers are needed to observe the transitions at lower energies.

2.5.2 Deformation driven shell gaps

The large energy gaps between adjacent single-particle states in the nuclear shell model provide a basis for understanding the magic numbers and their associated

added stability that is evidenced experimentally in atomic masses, level densities, and the low-energy quantum structure of nuclei. In a similar manner, energy gaps are apparent between adjacent deformed single-particle states, where the Nilsson diagram can be used to pinpoint regions of expected “stable,” axially deformed shapes.

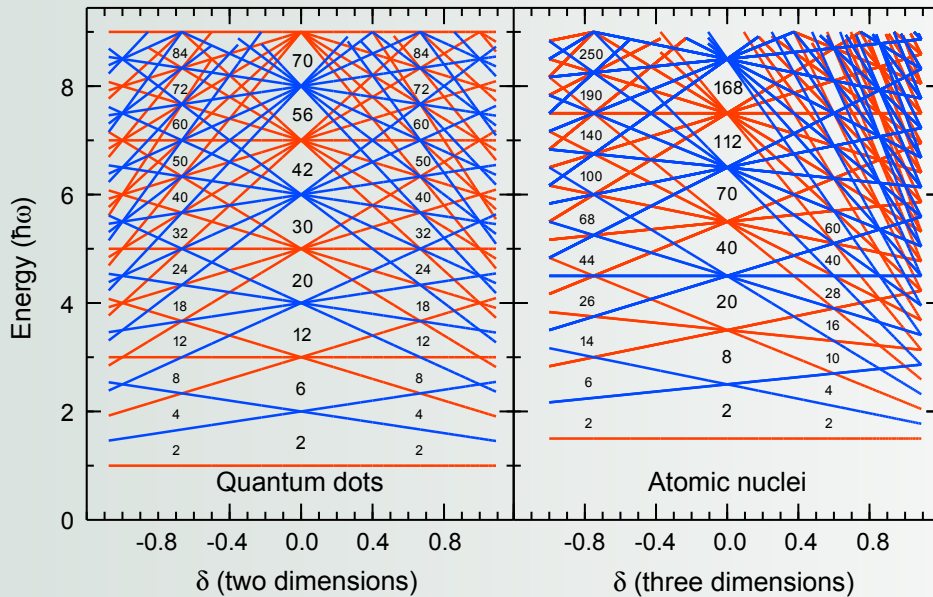
The appearance of superdeformation, where the nucleus exhibits deformation values $\beta \sim 0.6$ at higher spin in specific regions of the nuclear chart, provides an excellent example of the reinforcement of highly-deformed structures due to deformed single-particle shell gaps (see Section 2.6.1). The evolution of single-particle states

Single-particle motion and shell structure

All mesoscopic systems reveal shell structure associated with single-particle motion. This is a general quantum-mechanical consequence of the interference between different degrees of freedom in a finite system. A starting point for a general theoretical approach is based on a mean field determined by the (a priori unknown) energy density functional. In large atomic clusters and in atomic traps, even supershells are found that can be traced back to classical periodic orbits [Bra93].

The details of the shell structure are determined by the symmetry of the mean field; they can drastically change, and shape phase transitions can occur. A new set of magic numbers ordering arises, for example, for the axially symmetric superdeformation with an axis ratio close to 2:1. The same picture applies to quantum dots where the shape can be artificially defined by external voltage gates.

The structure of shells and magic numbers might change significantly as we move away from the valley of stability. The relative role of different components of the nucleon-nucleon forces (spin-orbital, spin-spin, tensor, exchange, three-body, etc.) changes with proton-to-neutron ratio as well as in areas of different nuclear density. This leads to new phenomena. The orbits with low orbital momentum and small binding energy can form halos that are unique to nuclear physics. Most other mesoscopic systems are governed by the Coulomb interaction. For example, in Rydberg atomic states the external electron is moving in a classically allowed region while the wave functions of halo nucleons are stretched into the classically forbidden region. More unusual types of single-particle motion are possible in very exotic nuclei, such as molecular configurations, peripheral clusters, and many-body halos. They can be accompanied by exotic collective modes of both vibrational and rotational type. A crucial theoretical question in such exotic situations is whether the concept of the mean field remains valid.



Calculated single-particle energies in the harmonic oscillator. The two-dimensional case for quantum dots is shown on the left-hand side where δ is the difference between the deformations in each of the two dimensions. The prototype of the shell properties in atomic nuclei is the axially symmetric three-dimensional oscillator shown on the right-hand side. Here, δ is a measure of the axial deformation from oblate (negative δ) to prolate (positive δ). In both plots, the numbers indicate the total number of particles filled up to the gap. The red lines are positive parity levels and the blue lines are negative parity levels. Adapted from [Rei02] and [Boh75].

far from stability, best demonstrated to date in light nuclei where certain magic numbers disappear ($N = 20$) and others emerge ($N = 14, 16, 32$), will alter the nucleon numbers of the deformed shell gaps. This alteration will result in the unexpected appearance of new regions of nuclear deformation.

The following subsections describe the methods that will be available at the ISF to identify low-energy deformed structures in nuclei far removed from stability. The appearance and disappearance of deformed shell gaps is closely related to the appearance and disappearance of spherical shell gaps (see Section 2.3). Thus, these methods are also very similar to the experiments described in Section 2.3.

2.5.2.1 Mass measurements

Mass measurements serve as first indicators of the unexpected appearance of ground state nuclear deformation because they can be completed with very small sample sizes. As an example, the masses of the neutron-rich sodium isotopes first called into question the validity of the $N = 20$ shell closure for neutron-rich nuclei [Thi75].

More recently, the masses of neutron-rich sulfur isotopes out to ^{44}S have been measured at the NSCL with high-precision mass spectrometry using Penning traps following the gas stopping of fast fragmentation beams. This systematic study will significantly impact our understanding of nuclear deformation along $N = 28$ for neutron-rich nuclei.

The problem of theoretical uncertainties concerning the onset of deformation will require access to medium and heavy neutron-rich nuclei. For example, global mass calculations using the transformed harmonic oscillator basis [Sto03] predict moderate deformation in the ground state of the heavy tin isotopes ($A > 140$). Figure 2.19 shows the predicted deformations across the whole nuclear chart, including the deformation for the neutron-rich tin isotopes. Most other theoretical approaches found only small deformations for the very neutron-rich tin isotopes due to their semimagic nature [Mol95].

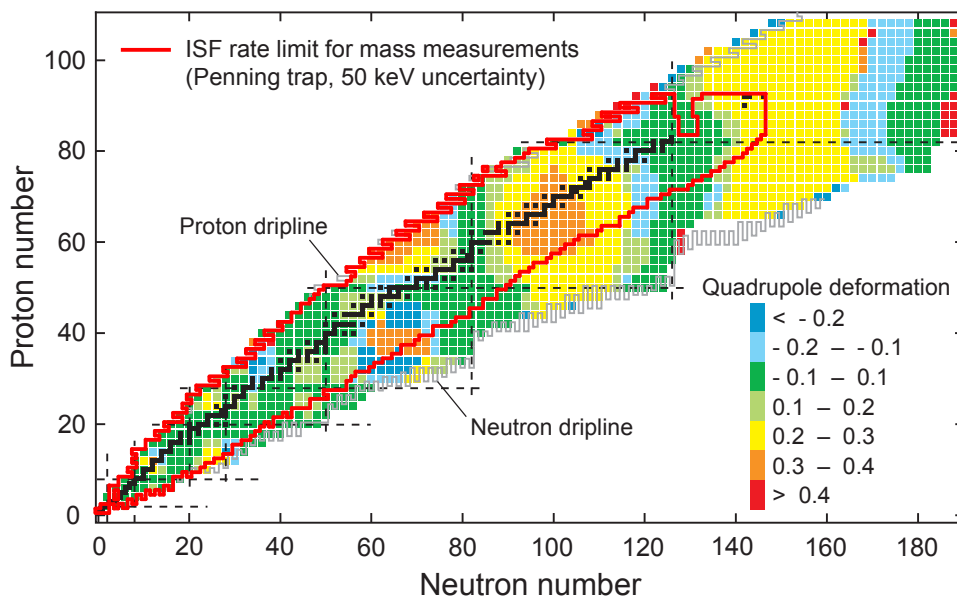


Figure 2.19: Ground state deformations resulting from global mass calculations. One unusual result from this approach is the moderately prolate deformation predicted for the most neutron-rich tin isotopes. Adapted from [Sto03].

Large-scale predictions of nuclear masses

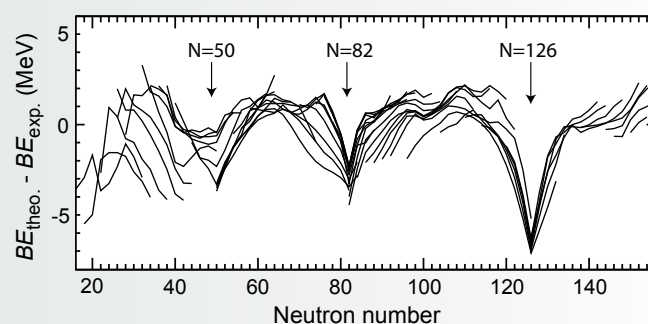
An important goal of nuclear theory is to reproduce known nuclear masses and to make reliable predictions of yet unknown ones. Nuclear masses determine neutron separation energies and β -decay Q -values – quantities of crucial importance to the understanding of the r -process which contributes to the nucleosynthesis of many elements heavier than iron. Nuclear masses may also be crucial to the description of non-equilibrium processes in the crust of accreting neutron stars. The nuclear energy density functional approach, a method rooted in the fundamentals of the quantum many-body problem, is the most promising approach to predict masses over the entire table of nuclei.

At present, Skyrme or Gogny energy functionals achieve a root mean squared (rms) accuracy of about 1.5 MeV for masses [Ber05] (0.7 MeV if further phenomenological corrections are added [Gor06]), of about 0.5 MeV for neutron separation energies, and of about 0.7 MeV for β -decay Q -values [Gor06]. The ultimate “nuclear accuracy” needed for r -process applications is on the order of 0.1 MeV for neutron separation energies which usually corresponds to 0.3 MeV for nuclear masses. Such an accuracy requirement represents a formidable theoretical challenge: the “chemical accuracy” needed for ionization energies of molecules in chemistry is on the order of 1% (a few kcal/mol out of a few hundred kcal/mol) where only the well-known Coulomb force must be treated. In comparison, the required “nuclear accuracy” corresponds to about 0.05% of the total binding energy for ^{208}Pb and, in addition, the strong interaction must be treated.

The challenge for the nuclear energy density functional method is to gain a factor of five in the accuracy with which known masses are reproduced. The main deficiency of current Skyrme or Gogny functional approaches is an overbinding of (doubly) magic nuclei compared to open-shell nuclei as shown in the figure for $N = 50, 82, 126$. It has recently been shown that one can correct for this defect, to a large extent, by including explicit correlations beyond the mean field associated with surface vibrations and the restoration of symmetries [Ben06] as well as pairing vibrations [Bar04]. Such an explicit treatment of correlations is very challenging for large-scale calculations, and it is

not yet clear how it can be incorporated into the construction of new functionals.

Beyond the reproduction of known masses, the key is whether or not the extrapolations to unknown masses for r -process nuclei are similarly accurate. In particular, inaccurate systematic trends as one goes away from the valley of stability must be avoided. Macroscopic-microscopic models [Mol95] work well for known masses, however, fully microscopic methods may have higher predictive power far away from stability. In the next decade, the goal is to meet the computational challenge required for the microscopic approach as well as to improve the energy density functionals by confrontation with results of ab initio approaches for light nuclei and configuration-interaction results for medium-heavy nuclei. Guidance and constraints from additional mass measurements far from stability will be critical for this endeavor.



Difference between theoretical and experimental binding energies as a function of neutron number. The theoretical results have been obtained from three-dimensional Skyrme energy density functional calculations, including pairing correlations. The lines connect nuclei in isotopic chains. The minima near $N = 50, 82,$ and 126 are regions where the theoretical results have too much binding compared to experiment, given the convention that stronger binding corresponds to more negative energy. Adapted from [Ber05].

The ISF will provide rates of neutron-rich tin isotopes that will allow a systematic measurement of masses up to ^{140}Sn ($\sim 5 \times 10^{-1} \text{ s}^{-1}$) at the edge of this newly predicted region of nuclear deformation. One difficulty in measuring these masses is the decreasing lifetimes of isotopes with increasing neutron number. Lifetime estimates extend to ^{138}Sn with a predicted β -decay partial half-life of 87 ms [Tac90].

At the NSCL, high-precision ($\delta m/m < 10^{-8}$) measurements have already been performed using a linear gas stopper and the LEBIT Penning trap for isotopes with nuclear half-lives well below 1 s [Bol06b]. This Penning-trap mass spectrometer will be available at the ISF and further improvements to gas stopping will shorten the time to thermalize secondary beams and enhance the reach of Penning-trap mass measurement coupled with fast beam production methods.

2.5.2.2 Gamow-Teller β decay and nuclear deformation

Along the $N = Z$ line, both proton and neutron deformed single-particle spectra show significant gaps in the adjacent Nilsson states at particle number 38. The sensitivity of the half-lives of the nuclei in the vicinity of ^{76}Sr to the ground state deformation of parent and daughter has been demonstrated [Fri95]. The Gamow-Teller (GT) strength accessible within the β -decay Q -value window strongly depends on the sign and magnitude of the nuclear quadrupole deformation.

For example, the self-conjugate nucleus ^{76}Sr is expected to have a large prolate deformation in the ground state, as deduced from $B(GT)$ measurements of its β -decay [Nac04] and the energy spacing of the lowest yrast states. A precise half-life measurement and details regarding direct population of excited 1^+ states in the odd-odd ^{76}Rb daughter also reached similar conclusions [Des04].

While rapidly changing ground-state nuclear deformations are expected at $N \sim Z \sim 40$, as clearly demonstrated by the Nilsson level diagram (see also Figure 2.21), a gradual return to a spherical shape is expected as ^{100}Sn is approached. However, beyond initial half-life measurements in the even-even [Fae02] and odd- A [Lon98] self-conjugate nuclei above ^{76}Sr , little spectroscopic data are available to evaluate ground state deformations either toward ^{100}Sn or other nuclei with $N \leq Z$ near the proton dripline.

Beta-decay studies planned at the NSCL and other fast beam facilities promise to make progress on higher-precision half-life measurements in $N = Z$ nuclei up to ^{100}Sn in the next few years. Initial studies of the main β -decay branching will also be made via delayed γ -ray spectroscopy. This holds especially true for the case of ^{100}Sn , where the preponderance of $B(GT)$ strength is expected to be distributed over only a few β -decay branches [Bro94]. Figure 2.20 shows the measured Gamow-Teller strength for silver, indium, and tin isotopes [Kar05]. The expected $B(GT)$ of ^{100}Sn has been extrapolated from the trend of the heavier mass tin isotopes. The actual measurement of this $B(GT)$ strength will require the significantly increased production rates that will become available at the ISF.

The main technique that will be used to explore the β -decay properties of neutron-deficient $N \leq Z$ nuclei at the ISF will be β -delayed γ -ray correlation measurements (see Section 2.3.2.2). Along $N = Z$, the half-lives may be as long as several seconds, and therefore total implantation rates must be kept below 100 s^{-1} in order to unambiguously correlate the implantation with the decay.

In order to achieve the necessary purity, a second stage separation following the fragment separator is required. At the NSCL, a radio frequency fragment separator (see Section 2.2.1) is currently being installed. It will be available at the ISF and will allow initial studies of $0^+ \rightarrow 1^+$ GT decays near the dripline in the even-even isotopes ^{82}Mo (50 s^{-1}), ^{86}Ru (10 s^{-1}), ^{90}Pd (1 s^{-1}), ^{94}Cd (0.1 s^{-1}), and ^{98}Sn ($2 \times 10^{-2} \text{ s}^{-1}$).

More extensive $B(GT)$ studies will require the application of total absorption spectroscopy (TAS). Such measurements on $N \sim Z$ nuclei have been successfully carried out at CERN-ISOLDE [Nac04] and GSI [Kar06]. The TAS technique is applicable to beams with intensities as low as 0.5 s^{-1} ; therefore, a majority of the $Z = N - 2$ nuclei towards ^{100}Sn will be accessible.

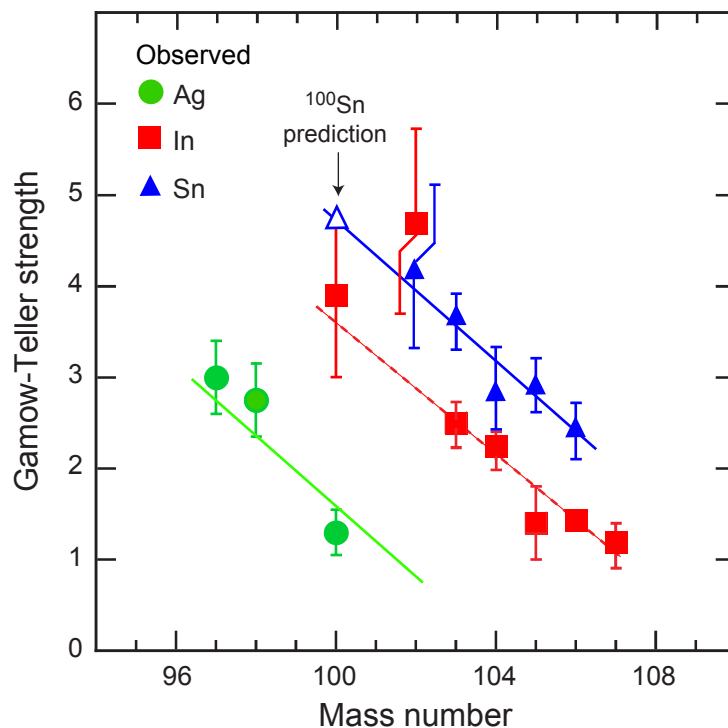


Figure 2.20: Experimental $B(GT)$ values for neutron-deficient silver, indium, and tin isotopes. Extrapolation of the tin experimental points provides an estimated $B(GT) = 4.7$ for ^{100}Sn decay. Adapted from [Kar05].

2.5.2.3 Quadrupole collectivity and transition moments

The fp shell with $28 < N = Z < 50$ is already large enough to exhibit all aspects of collective behavior and a remarkable diversity of shapes and deformations. This is due to the occurrence of well-deformed shell gaps amplified by the simultaneous occupation of identical deformation-driving orbitals by protons and neutrons.

Intermediate-energy Coulomb excitation has been used to track the evolution of quadrupole collectivity along the $N = Z$ line. At the NSCL, the isotopes ^{52}Fe , ^{56}Ni , and ^{72}Kr have already been studied. The nucleus ^{72}Kr is currently the heaviest selfconjugate nucleus for which the $B(E2)$ excitation strength could be measured [Gad05]. A variety of models suggest that ^{72}Kr is one of the rare nuclei with oblate deformation in the ground state. Figure 2.21 demonstrates the various shell gaps opening at different deformations. In the near future, the study of $N = Z$ nuclei will be extended beyond $N = Z = 40$ (^{80}Zr , ^{84}Mo , etc.), including the odd-odd selfconjugate nuclei to track the sensitive interplay between protons and neutrons.

The ISF will produce sufficient rates of $N < Z$ nuclei in the region near ^{72}Kr to track the development of collectivity out to the predicted two-proton dripline limit. The isotopes ^{60}Ge , ^{64}Se , and ^{70}Kr are all expected to have oblate deformation in the ground state, while ^{72}Sr should remain prolate [Sto03]. $B(E2)$ measurements for the $0^+ \rightarrow 2^+$ transitions in these dripline nuclei will evaluate the magnitude of collectivity and verify or refute the theoretical expectations for these weakly-bound systems. While studies of proton decay in odd- Z nuclei above $Z = 50$ have firmly established the deformed character of the ^{131}Eu and ^{141}Ho [Dav98] nuclei expected from global model predictions, no such studies are possible in lighter nuclei with $Z < 50$ with current facilities.

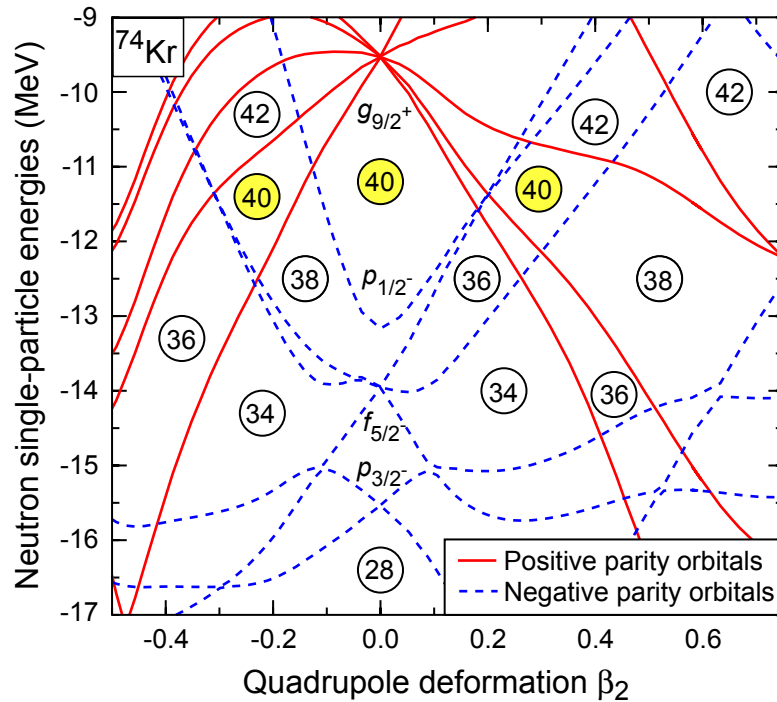


Figure 2.21: Deformed single-particle level energies for ^{74}Kr . A rich variety of structures are expected in this region and revealed in the Nilsson scheme by the energy gaps observed at particle number 40 for various shapes (oblate, spherical, and prolate). Adapted from [Ben06].

Intermediate-energy Coulomb excitation will be one of the methods used at the ISF to deduce the magnitude of the $B(E2)$ values in the even-even nuclei near the two-proton dripline. Expected rates of the nuclei of interest at the ISF are ^{60}Ge (250 s^{-1}), ^{64}Se (100 s^{-1}), ^{68}Kr (25 s^{-1}), and ^{72}Sr (2 s^{-1}). All are within the sensitivity limits of the SeGA-S800 experimental setup currently employed at the NSCL for fast beam Coulomb excitation. The S800 will also be available at the ISF and, coupled with GRETINA, the sensitivity should be even higher.

Lifetime measurements with a Plunger will serve as an alternative method for deducing transition probabilities as described in Section 2.3.2.1.

2.5.2.4 Magnetic moments of isomeric states

Experimental studies of isomeric states and their γ -ray de-excitation pathways help determine the evolution of spherical and deformed single-particle states. The magnetic moment is also sensitive to the single-particle structure of the wave function. The well-known form of the magnetic moment operator means that theoretical comparisons can then distinguish between spherical or deformed single-particle contributions to the wave function.

The nuclei in the vicinity of ^{68}Ni have microsecond isomeric states [Grz98], believed to be associated with neutrons occupying the $g_{9/2}$ single-particle orbital. Magnetic moments of isomers can be measured using the Time Dependent Perturbed Angular Distribution (TDPAD) method following the production of spin-aligned isomers in projectile fragmentation reactions [Mat04]. At the NSCL, the magnetic moments of isomers in $^{67,69,70}\text{Ni}$ were recently measured by this technique. The

magnetic moment value for the 8^+ isomer in ^{70}Ni agrees well with shell model expectations for a neutron $(g_{9/2})^2$ configuration [Geo06].

The even-even iron ($Z = 26$) and chromium ($Z = 24$) isotopes just below ^{68}Ni show evidence for moderate deformation in the ground state [Han99a,Sor03]. The appearance of deformation in this region is believed to result from the presence of deformed shell gaps, which arise from the downsloping $9/2^+[404]$ Nilsson level. Indeed, a low-energy $9/2^+$ isomeric state has been identified in ^{59}Cr at an energy of 503 keV [Fre04] and interpreted as evidence for moderate oblate deformation in this nucleus.

Another area where isomeric states are prolific but questions still remain regarding their underlying structure is in nuclei just below ^{132}Sn . Microsecond isomers have been identified in both even- and odd- A cadmium and silver isotopes [Tom06,Hel03]. The yrast structure of the even-even cadmium isotopes show anomalous behavior as $N = 82$ is approached (see Figure 2.22). The first excited 2^+ states were observed to remain constant, as opposed to the rapid increase typically seen when coming upon a shell closure.

The unexpected behavior of the cadmium 2^+ states has been interpreted as evidence for shell quenching at $N = 82$ [Kau00]. The magnetic moments of the isomeric states will provide important new information to determine what changes in underlying shell structure are responsible for the anomalous 2^+ energies below ^{132}Sn .

Isomer magnetic moment measurements will be possible at the ISF for a wide range of proton- and neutron-rich nuclei, including the isomeric states in the cadmium and silver isotopes below ^{132}Sn . The measurements require an initial nuclear spin alignment that is generated in the fast fragmentation process as first shown for the case of the $19/2^-$ isomer in ^{45}Sc [Sch94]. The TDPAD method requires a small dipole magnet ($H_0 \sim 5\text{kG}$) and photon detectors with good timing resolution.

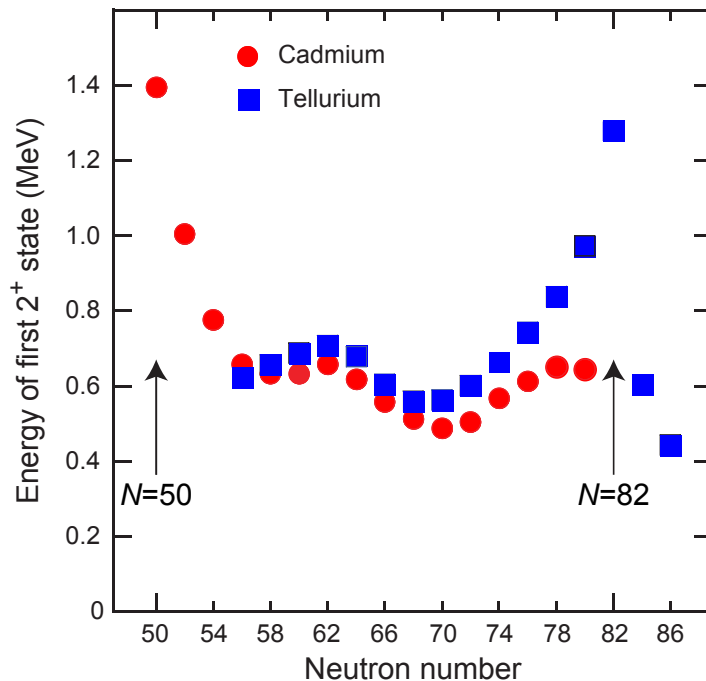


Figure 2.22: Systematic variation of the first excited 2^+ state in the even-even cadmium and tellurium nuclei. The expected increase in $E(2^+)$ values toward $N = 82$ for the cadmium isotopes is not evident in the data, and it has been suggested as evidence for quenching of the $N = 82$ shell gap.

At the NSCL, four detectors from the Segmented Germanium Array were successfully used to observe the perturbed angular distributions of γ rays depopulating the microsecond isomers in $^{67,69,70}\text{Ni}$. The low multiplicity of the isomeric decays will also permit the use of lower resolution BaF_2 detectors. The benefits of BaF_2 are the higher γ -ray efficiencies and the improved timing performance. At the ISF, BaF_2 detectors will probably be replaced with newly developed scintillation detectors, for example $\text{LaBr}_3:\text{Ce}$ [Van02] or $\text{LaCl}_3:\text{Ce}$ [Amb06], which have excellent timing as well as high energy resolution. The expected fast beam production rates of the even-even $^{126,128,130}\text{Cd}$ at the ISF are 2×10^6 , 4×10^5 , and 7×10^3 , respectively. Assuming an isomer fraction of 1% and lifetime of order $1 \mu\text{s}$, the rates are comparable to those realized in the successful NSCL measurements on the neutron-rich nickel isotopes.

2.5.2.5 Tetrahedral shapes

In addition to axially deformed quadrupole and octupole deformation, shell gaps for other more exotic deformations can develop. Recent theoretical predictions [Dud02] indicate that shell-gaps comparable or even larger than those at spherical shapes may exist in nuclei characterized by the double-tetrahedral symmetry group when the corresponding deformation is that of $\alpha_{32}(Y_{3,2} + Y_{3,-2})$, where $Y_{\lambda,\mu}$ are the spherical harmonics and α is the amplitude. Predictions for the electric dipole moment in the body-fixed frame for the tetrahedral symmetry are very different from those for the well-known axially symmetric $\alpha_{30}Y_{30}$ (pear-like) octupole deformation; the electric dipole moment is enhanced for the latter while it is zero for the former.

The predicted tetrahedral “magic numbers” include $Z = 40$ and $N = 40, 56, 70$. Figure 2.23 shows the emergence of the $Z = 40$ gap for tetrahedral deformation. The competition between the tetrahedral shape and more common axially-deformed quadrupole and octupole deformations will lead to shape coexistence in the

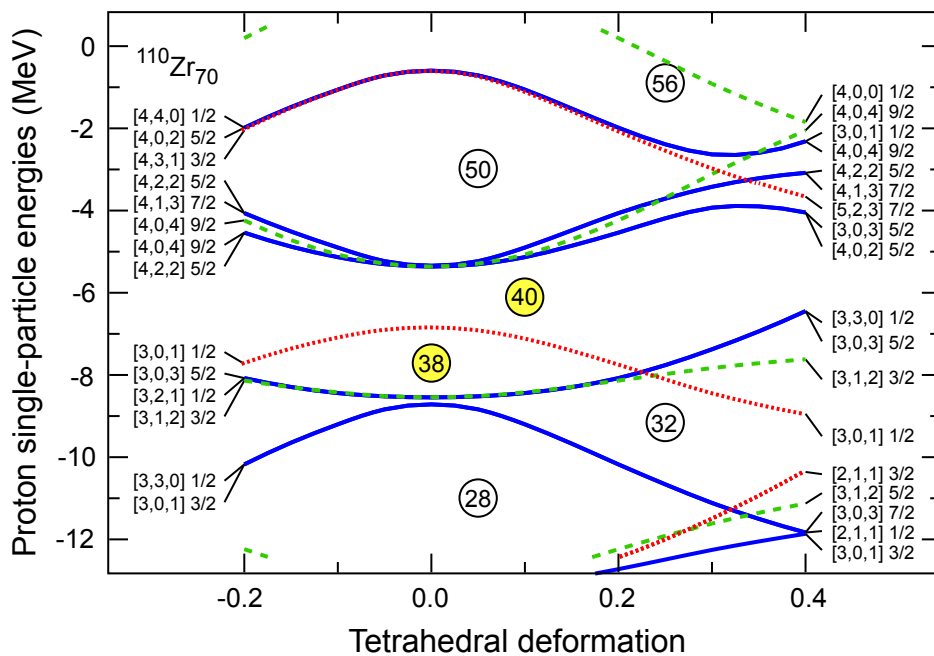


Figure 2.23: Calculated single-particle proton spectrum for tetrahedral deformation α_{32} . A significant gap between adjacent single-particle levels is expected at particle numbers 32 and 40. Adapted from [Sch04b].

neutron-deficient and neutron-rich zirconium isotopes. Pairing interactions will play an important role in defining the shape [Zbe06]. Empirical evidence for the tetrahedral symmetry group in nuclei is critical for testing the application of mean field approaches to nuclei far removed from the stability line.

There are several possible experimental signatures for the tetrahedral symmetry. A pair of rotational bands, one with even spin/positive parity and the other with odd spin/negative parity, is expected. The transition strengths between the negative and positive parity bands are predicted to differ from the patterns seen for pear-like octupole bands [Dud06]. The existence of 0^+ and 0^- states is also predicted, where the decay of the 0^- state will be hindered, leading to long-lived isomerism, suitable for delayed γ -ray spectroscopy. Numerous cross-gap transitions should form multiplets of energies corresponding to the shell gap. Such multiplets, which result from the high degeneracy of single particle levels in the tetrahedral mean-field, might be observed with the sensitivity of planned γ -ray tracking arrays.

A tetrahedral ground state is predicted for the $^{110-112}\text{Zr}$ isotopes [Sch04b]. These nuclei are 14–16 neutrons removed from the last stable zirconium isotope (^{96}Zr), and the search for their tetrahedral shapes will only be possible at the next generation of rare isotope beam facilities. At the ISF, the fast beam rate of ^{110}Nb is predicted to be $2 \times 10^4 \text{ s}^{-1}$, and initial studies of excited states in ^{110}Zr via β -delayed γ -ray spectroscopy will be feasible.

Such studies will be carried out on the low-energy beamline following the cyclotron stopper and will require a moving tape system along with a modest array of high-resolution germanium detectors. The use of high-resolution silicon detectors for electron spectroscopy will also permit multipolarity assignments to γ rays to distinguish $E1$ and $E2$ photon types. Evidence for isomeric states will also be obtained from delayed spectroscopy measurements.

2.5.3 Competing shapes

One of the interesting features of nuclei as mesoscopic systems is that they can exhibit both single-particle and collective degrees of freedom at nearly degenerate energies. The most extreme example of such phenomenon is exhibited in ^{186}Pb (see Figure 2.24), where the first two excited states were found to have $J^\pi = 0^+$ and were assigned as bandheads of nearly degenerate competing oblate and prolate shapes [And00]. At the ISF, it will be possible to extend measurements of nuclear deformation into a regime where the difference between the Fermi energies of the neutrons and protons is large. Electromagnetic and hadronic probes will be utilized to explore the role of protons and neutrons in defining nuclear deformation under these systems.

2.5.3.1 Collective and single particle contributions to magnetic moments

The gyromagnetic ratio of the first excited 2^+ state, $g(2^+)$, in even-even nuclei depends sensitively on the collective and single-particle contributions to the wave function. At the collective limit, the value of $g(2^+)$ is equal to Z/A . For nuclei near closed shells, the individual proton or neutron contributions can be inferred from the closeness of $g(2^+)$ to the single-particle g factors of the valence nucleon(s).

The transition between single-particle and collective degrees of freedom can readily be tracked through a systematic study of $g(2^+)$ along an isotopic or isotonic

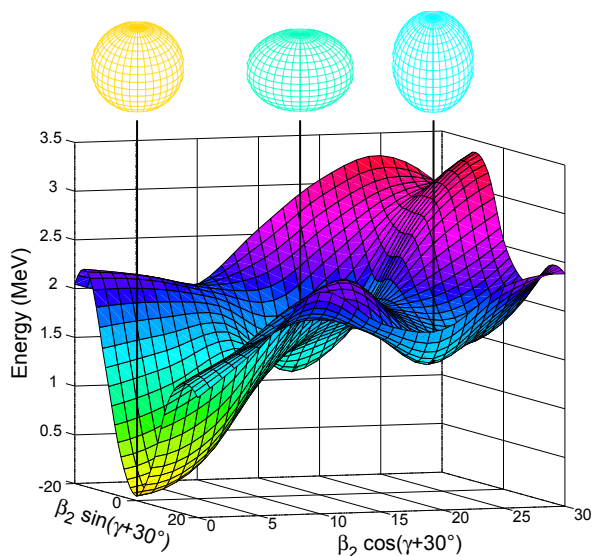


Figure 2.24: Potential energy surface calculated for ^{186}Pd . Coexisting oblate, prolate, and spherical shapes are expected near the ground state. The identification of two excited 0^+ states below the first excited 2^+ state provided experimental evidence for low-energy shape coexistence in this nucleus. Adapted from [And00].

chain. Current information on $g(2^+)$ values obtained mainly through the use of the transient field technique [Ben80] is essentially limited to stable nuclei.

Extension of this technique to radioactive nuclei has only been realized recently; the $g(2^+)$ of ^{76}Kr was measured at LBNL using a secondary beam of ^{76}Kr with an energy below the Coulomb barrier (~ 3 MeV/nucleon), while the $g(2^+)$ values for $^{38,40}\text{S}$ were determined at the NSCL with the secondary beams produced by projectile fragmentation.

The $g(2^+)$ values of $^{38,40}\text{S}$ [Dav06] were found to fall midway between the predictions of the extreme single-particle model (spherical shape) and the hydrodynamical limit of Z/A (prolate deformed shape), and it was concluded that both protons and neutrons played integral roles in defining the onset of deformation in the sulfur isotopes beyond $N = 20$.

In the next few years, we plan to extend our successful high velocity transient field program to nuclei at the NSCL with higher Z to study nuclei around semi-magic, neutron-rich ^{68}Ni . Although, information on the $N = 40$ harmonic oscillator shell gap in neutron-rich nuclei is accumulating, a consistent picture has yet to emerge. A comparison of $g(2^+)$ values in the nickel isotopes out to $^{70}\text{Ni}_{42}$ and in the iron isotopes to $^{64}\text{Fe}_{38}$ will provide crucial data to evaluate the contribution of proton excitations to the first excited 2^+ states, which drop precipitously in iron despite the $N = 40$ subshell closure [Han99a]. However, neutron-rich fp shell nuclei beyond $N = 40$ will require the higher production rates available at the ISF.

To measure excited state g factors in short-lived nuclei at the ISF, both fast and re-accelerated beam transient field techniques will be applied. Both methods require a modest array of high-purity germanium detectors to measure γ -ray angular distributions. Beam intensities as low as 10^4 s^{-1} are sufficient for this technique.

The use of the transient field technique with reaccelerated beams offers a unique opportunity to tune the beam energy to maximize the integral hyperfine field strength, increasing the sensitivity of the method. The fast-beam method, on the other hand, can use the secondary beams produced directly in the fragmentation process and does not suffer from losses from gas stopping and reacceleration. These experiments require the use of highly segmented detectors to correct for the Doppler shift of the γ -rays emitted in flight.

At the ISF, the known $g(2^+)$ values will be extended beyond $N = 40$ with measurements of ^{64}Cr ($1 \times 10^4 \text{ s}^{-1}$), ^{70}Fe ($1 \times 10^4 \text{ s}^{-1}$), and ^{74}Ni ($2 \times 10^5 \text{ s}^{-1}$). In addition, the study of the role of proton versus neutron excitations in nuclei beyond ^{132}Sn will become possible. Initial measurements of $g(2^+)$ values in the neutron-rich tellurium isotopes have been completed at ORNL using the recoil-in-vacuum technique [Sto05b].

The $B(E2; 0^+ \rightarrow 2^+)$ measurements in the neutron-rich tellurium isotopes near $N = 82$ suggest that the neutron-neutron pairing strength is diminished [Ter02]. Systematic determinations of $g(2^+)$ for the tin, tellurium, xenon, and barium isotopes at and beyond $N = 82$ will define the roles that both neutrons and protons play in the low-energy structure of these nuclei. The region above ^{132}Sn can be explored out to $^{138}\text{Te}_{86}$ ($8 \times 10^4 \text{ s}^{-1}$), $^{144}\text{Xe}_{90}$ ($1 \times 10^4 \text{ s}^{-1}$), and $^{148}\text{Ba}_{92}$ ($0.8 \times 10^4 \text{ s}^{-1}$) at the ISF, utilizing either transient field or recoil-in-vacuum methods.

Open questions also remain in the light mass region. In the vicinity of the island of inversion, the roles of both protons and neutrons in defining the sudden onset of deformation along $N = 20$ for magnesium and sodium isotopes are not clear. The ^{34}Mg rate at the ISF is expected to be greater than 10^5 s^{-1} , adequate to deduce $g(2^+)$ with the high velocity transient field method.

2.5.3.2 Contributions of protons and neutrons to quadrupole deformation

The neutron and proton degrees of freedom can be examined separately with a combination of electromagnetic and hadronic probes. For an electromagnetic probe, such as Coulomb excitation, only the proton contribution is obtained. Proton scattering at intermediate beam energies, on the other hand, probes the hadronic response of a nucleus. The combination of the two yields information on proton and neutron transition matrix elements M_p and M_n . The ratio M_n/M_p , in comparison to N/Z (hydrodynamic limit), provides a sensitive test of the model predictions and the persistence of shell closures far from stability.

Earlier implementations of inverse-kinematics proton inelastic scattering experiments typically involved detection of the protons in coincidence with the projectiles, where thin targets had to be employed to reduce the angular straggling of the scattered protons. Such a restriction posed a lower limit on the beam intensity of the order of several thousand per second.

In the thick-target technique, γ rays are detected in coincidence with the recoiling nucleus to tag the inelastic process. Experiments employing both thin and thick targets have been performed with fast fragmentation beams at the NSCL for sd -shell nuclei [Kel97,Mar99b,Mar99c,Jew99,Ril99] and for nuclei in the lower fp shell [Ril05].

Further improvements to the technique have recently been made with the use of liquid hydrogen targets in which the characterization of the first 2^+ state in ^{30}Ne [Yan03] was obtained with a rare isotope beam rate on target of only 0.2 s^{-1} .

The ratio $M_n/M_p = 1.19(N/Z)$ derived for ^{46}Ar shows that neutron excitations contribute to the structure of the first excited 2^+ state, even though ^{46}Ar has a closed neutron shell with $N = 28$ (see Figure 2.25). The $N = 28$ isotones above ^{48}Ca all have $M_n/M_p < (N/Z)$, and a first 2^+ state that is dominated more by proton excitations than expected. With the increased intensities that will be available at the ISF, more precise measurements can be performed. The more neutron-rich ^{44}S and ^{42}Si isotones will become available, and one will be able to address the persistence of the $N = 28$ shell closure in these neutron-rich nuclei where large differences of the proton and neutron contributions to the deformation have been predicted [La199].

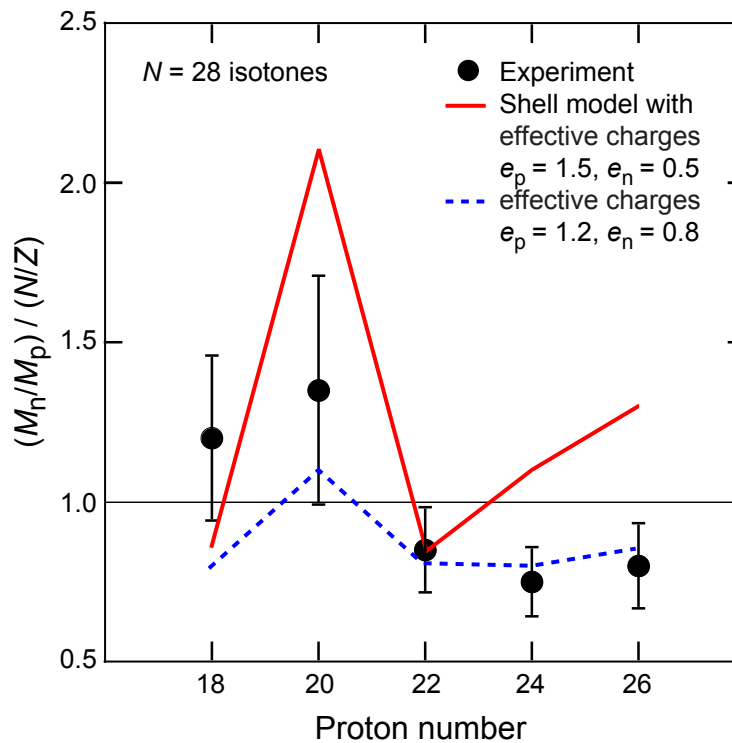


Figure 2.25: The ratio M_n/M_p for the $N = 28$ isotones. The most neutron-rich isotopes show experimental values that exceed unity, suggesting that neutron excitations across the $N = 28$ shell gap are needed to describe the wave function of the first excited 2^+ state in ^{46}Ar . Adapted from [Ril05].

The yields available at the ISF will permit the extension of proton scattering and Coulomb excitation measurements for $N = 28$ isotones down to ^{40}Mg with an expected production rate of 3 s^{-1} if ^{40}Mg is neutron bound. The extraction of M_n/M_p will give important data for proton and neutron contributions that lead to a possible reduction of the $N = 28$ shell gap.

Other shell gaps on the neutron-rich side of the nuclear chart will also be explored, including those at $N = 32$ (fast beam rates of ^{52}Ca , ^{50}Ar , and ^{48}S are expected to be $1 \times 10^5 \text{ s}^{-1}$, $3 \times 10^2 \text{ s}^{-1}$, and 0.2 s^{-1} , respectively) and $N = 40$ (^{64}Cr and ^{62}Ti have expected fast beam rates of $1 \times 10^4 \text{ s}^{-1}$ and 22 s^{-1} , respectively).

2.5.4 Collectivity beyond the first 2^+ state

Information on the excitation energy and transition probability of the first-excited 2^+ state in even-even nuclei provides some information on nuclear collectivity but

cannot distinguish between static deformation of the mean field and soft collective vibrations. Static quadrupole deformation is best characterized through the observation of complete rotational band structures that may extend to very high spins and energies. In addition, many collective features of nuclei do not manifest themselves until significant nuclear excitation has occurred.

For example, the collective motion of protons and neutrons can be in the form of a linear or angular displacement (see Figure 2.26). The angular displacement known as the scissors mode has been observed first in the rare earth nuclei at energies near 3 MeV [Boh84]. Such proton-neutron oscillations in even- A nuclei produce proton-neutron mixed-symmetry states that show enhanced M1 transition matrix elements [Ari77].

At even greater excitation energies, linear proton-neutron displacement in the form of the giant dipole resonance occurs. Investigations of the Giant Dipole Resonance (GDR) can give insight on the accuracy of mean field calculations. These calculations are particularly sensitive to the shape of the GDR for nuclei with extreme neutron-to-proton ratios. The splitting of the giant dipole resonance into transverse and longitudinal modes with respect to the deformation axis gives direct evidence of quadrupole deformation. Experimental information on the evolution of giant resonances far from the valley of stability is essentially nonexistent.

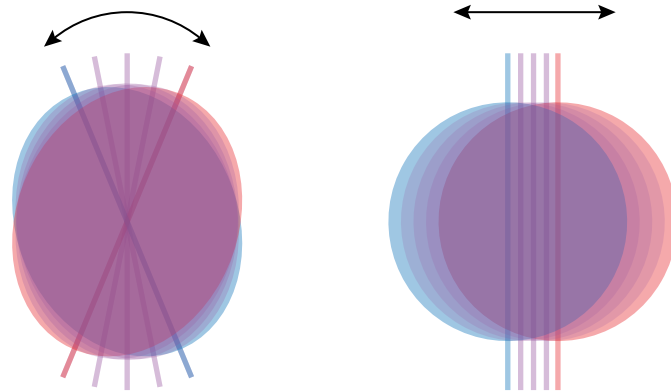


Figure 2.26: Proton-neutron displacements. The left image depicts an angular displacement representative of the scissors mode. The right image shows a linear displacement representative of the giant dipole resonance mode.

2.5.4.1 Critical-point symmetries and nuclear phase transitions

Similar to quantum chemistry, a diversity of spatial symmetries is possible in the two-component nuclear fluid. Their stability, coexistence, and experimental signatures can significantly change as we move away from the valley of stability. A theoretical description is provided by group theory combining spatial and isospin symmetries.

Algebraic models have provided a useful paradigm to track the progression of nuclear shapes. Collective nuclei described as harmonic vibrators, deformed symmetric rotors, and γ -unstable nuclei have well defined symmetries that, in the context of the phenomenological interacting boson model (IBM) are characterized by the $U(5)$, $SU(3)$, and $O(6)$ limits and transitions between them [Iac06]. The low-energy states of nuclei reveal such symmetries in well-defined regions of the nuclear

chart. For example, static quadrupole-deformed nuclei show regular rotational band structures expected in the $SU(3)$ limit in the rare earth region, where the valence numbers of both protons and neutrons fall midway between two major shells.

Multi-phonon structures associated with the $U(5)$ symmetry limit have been observed in nuclei whose proton and neutron numbers are close to those of closed shell nuclei. Such limiting symmetries have very recognizable signatures that are readily obtained for nuclei near stability. As an example, the ratio of the energies of the yrast 4^+ and 2^+ levels, $R_{4/2^+}$, differs significantly for the $SU(3)$ and $U(5)$ limits, with values of 3.33 and 2.0, respectively. Good examples of $O(6)$ symmetry corresponding to the quadrupole vibrator with strong quartic anharmonicity were found in palladium and ruthenium nuclei near $A = 100$ [Vor83,Vor85].

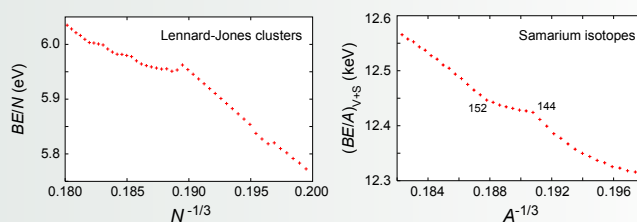
Recently, Iachello has proposed dynamical symmetries that define the critical points for transitions between the $U(5)$, $O(6)$, and $SU(3)$ limits. One example is the $E(5)$ symmetry [Iac00], based on the crossing of spherical and deformed potential minima; the analytical solutions for the low-energy quantum levels and transition matrix elements depend only on an overall energy scaling factor. An example of such an $E(5)$ symmetry in finite nuclear systems was first suggested in ^{134}Ba [Cas01], and other examples in near-stable nuclei have also been proposed [Fra01,Zha02,Zam02].

Another critical point symmetry, the $X(5)$ symmetry [Iac00], represents the phase transition from the harmonic vibrator to the deformed symmetric rotor. Potential $X(5)$ candidate nuclei were compiled by Clark et al. [Cla03b], and initial studies of nuclei in the $A = 100$ [Biz02], $A = 150$ [Cas01,Kru02], and $A = 180$ [Dew05] regions have been carried out.

Nuclear shapes and symmetries

The discreteness of the particle number in nuclei gives rise to new, specifically, nuclear symmetries that can go unnoticed in large macroscopic systems. Such symmetries are usually associated with special transformation groups that leave the system invariant. In many cases these symmetries are similar to what is known in elementary particle physics, including the elusive supersymmetry between bosons and fermions. In nuclear physics, we can regulate the proton and neutron numbers in experiments with rare isotopes and thus enhance conditions for the manifestation of new symmetries. At higher excitation energies in nuclei, different symmetries in different quantum states can coexist and phase transformations between them can be studied.

Similar phenomena are known in large molecules. Silicon clusters reveal a clear shape evolution; as the number of atoms increases, such clusters evolve from quasi-molecular structures, through prolate deformation, to the compact shape of a small solid. While short-range nuclear forces are very different from covalent bonds in silicon clusters, the emerging complexity is quite analogous, and this is at the center of studying meso-atomic physics.



Binding energy per atom as a function of $N^{-1/3}$ for neutral silicon clusters of N atoms is juxtaposed to the binding energy per nucleon for samarium isotopes as a function of $A^{-1/3}$. The atomic clusters are described with the Lennard-Jones potential in agreement with the data [Bac00]. In the nuclear case the experimental data are shown, where the liquid drop contributions for Coulomb energy, symmetry energy, and pairing correlations are subtracted, leaving only volume and surface contributions. The similarity of the two patterns indicates a common shape instability and possible shape coexistence at a number of constituents close to 148. The samarium isotopes in this region are known for symmetry changes and coexistence of deformed and spherical states. Adapted from [Hor05].

More recently, Iachello proposed the $Y(5)$ symmetry [Iac03]. This symmetry corresponds to a phase transition from an axially to a triaxially deformed shape. Until now, no example for the manifestation of the $Y(5)$ symmetry in nuclei has been found.

Experimental data needed to identify nuclei with these critical-point symmetries include measurements of the energies and lifetimes of a small set of well-defined states with low angular momentum (less than $10\hbar$) as well as inter-band and intra-band transition matrix elements. Over the next several years, there will be continued progress on the measurement of such experimental properties for nuclei that lie on and near the stability line. This includes rare earth nuclei near $N = 90$ for $X(5)$ symmetry and lighter nuclei near ^{134}Ba and ^{102}Pd for $E(5)$ symmetry.

Extension of the study of dynamic phase transitions to nuclei far removed from stability will require secondary beams with intensities of order 10^4 and higher, where β -decay studies, Coulomb excitation below the barrier, and lifetime measurements can be used to extract the required experimental fingerprints.

The neutron-rich barium and cerium isotopes in the $A \sim 150$ region as well as the neutron-rich krypton isotopes beyond $N = 62$ are candidates for $X(5)$ critical point symmetry [McC05]. These nuclei will be available at the ISF at reaccelerated beam rates adequate for detailed Coulomb excitation, lifetime, and β -decay studies. The expected reaccelerated beam intensity of ^{148}Ba and ^{152}Ce are $1 \times 10^4 \text{ s}^{-1}$ and $4 \times 10^3 \text{ s}^{-1}$, respectively, and the krypton isotopes could be systematically studied out to ^{96}Kr ($2 \times 10^4 \text{ s}^{-1}$).

The ISF will also produce neutron-rich isotopes of ruthenium and palladium isotopes that are potential $E(5)$ symmetry candidates [McC05]. The reaccelerated beam rates of $^{120,122}\text{Pd}$ are predicted at $2 \times 10^6 \text{ s}^{-1}$ and $1 \times 10^5 \text{ s}^{-1}$, respectively, sufficient to perform the needed experiments. Figure 2.27 shows the regions of the nuclear chart where $X(5)$ (top) and $E(5)$ (bottom) critical point symmetries are predicted. The reach of the ISF to populate and identify these symmetries is indicated.

Coulomb excitation experiments with reaccelerated beams will require a high-resolution germanium detector array. Proposed lifetime measurements will be completed using a plunger device to observe attenuated Doppler shifts. The high-rate β -decay experiments will be best completed using the beams immediately out of the cyclotron stopper, without reacceleration. A fast moving tape system will be needed to remove daughter activities, since the half-lives of the nuclei of interest are very short (less than one second in most cases).

2.5.4.2 Proton-neutron mixed symmetry states

An important question concerning nuclear systems with strong proton-neutron imbalance is, "What collective motions are possible?" This is analogous to current studies of multicomponent systems in atomic traps where, however, only long-range Coulomb or Van der Waals forces are acting.

The interacting boson model (IBM) is a phenomenological approach for characterizing nuclear collective motion by treating valence proton and neutron pairs as bosons having either s-wave ($\ell = 0$) or d-wave ($\ell = 2$) angular momentum. The degree of nuclear collectivity can then be quantified by the available valence bosons.

The IBM-2 model [Ari77,Ots78] treats proton and neutron bosons separately and introduces the concept of F -spin as a boson counterpart of the nucleon isospin. F -spin $+1/2$ represents the proton-boson F -spin projection, while neutron bosons have F -spin $-1/2$. In the IBM-2, the lowest-energy nuclear states have the maximum F -spin of $F = N/2$, where N is the total number of bosons. They are symmetric with respect to the pairwise exchange of proton and neutron bosons.

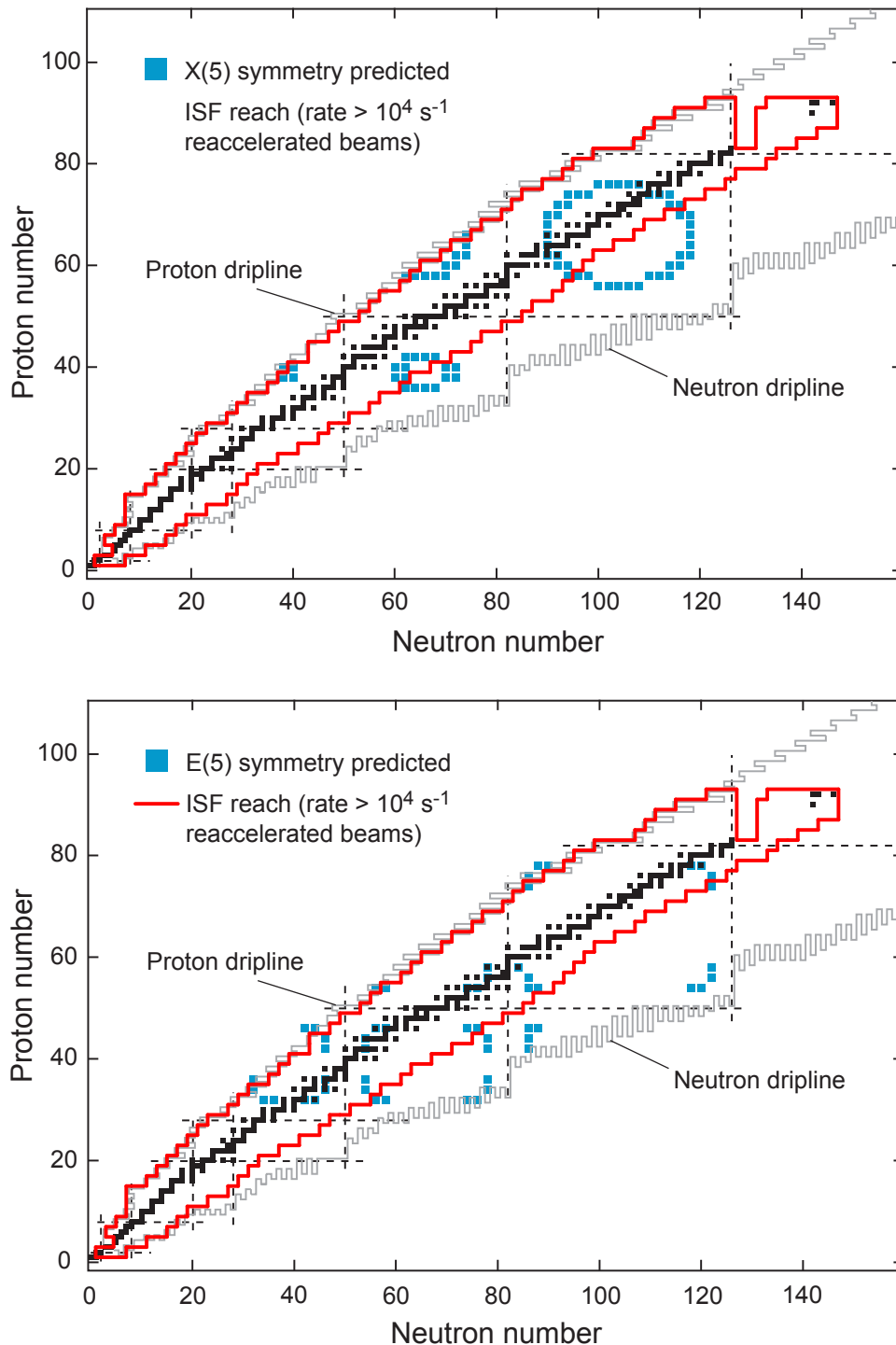


Figure 2.27: Chart of the nuclei where regions of X(5) (top) and E(5) (bottom) critical-point symmetries are expected [McC05]. The red line encloses nuclei for which the reaccelerated beam intensities will be sufficient to search for these symmetries.

There are states that contain at least one pair of bosons that is antisymmetric under the exchange of boson isospin labels. Such states have $F < N/2$ and are mixed-symmetry states. These states represent proton and neutron “out-of-phase” displacements and represent a collective mode that has an identifiable signature – the existence of strong $M1$ transitions to the symmetric states. Even-even nuclei with one proton or neutron boson residing outside (sub) shell closures are expected to exhibit exceptionally pure mixed-symmetry states with $J^\pi = 2^+, 3^+$ at energies around 3 MeV [Rai06].

The first example of a mixed-symmetry multiphonon structure, comprising a one-phonon state and a two-phonon multiplet, has been observed in the nucleus ^{94}Mo [Fra03]. The low-spin level scheme of the near-spherical nucleus ^{94}Mo has been investigated by γ -ray spectroscopy using a variety of population mechanisms. For most of the low-spin levels up to 4 MeV, transition matrix elements enabled the identification of mixed-symmetry multiphonon structures from absolute $M1$ and $E2$ transition strengths.

Coulomb excitation studies at energies below the Coulomb barrier provide a means to measure transition matrix elements of nuclei expected to exhibit proton-neutron oscillations of the mixed-symmetry type. The interesting isotopes around $N \sim 50$ and $N \sim 82$ close to stability, ($^{88}\text{Sr}_{52}$, $^{92}\text{Zr}_{52}$, $^{96}\text{Mo}_{52}$) and ($^{142}\text{Sm}_{80}$ and $^{150}\text{Dy}_{84}$), respectively, will likely be studied at current facilities in the near future.

However, potential candidates for low-energy mixed symmetry states in neutron-rich nuclei that are awaiting verification include $^{88}\text{Kr}_{52}$ and $^{90}\text{Kr}_{54}$ (near $N \sim 50$) and the neutron-rich tellurium isotopes with $N \sim 82$. Production rates at the ISF of greater than 10^6 s^{-1} should be sufficient to reach the mixed-symmetry states, which are populated with a low probability compared to normal-symmetry states. Coulomb excitation at energies below the barrier will require reaccelerated beams of these species as well as a high-resolution germanium detector array for γ -ray detection.

The estimated reaccelerated beam rates for ^{88}Kr and ^{90}Kr are $4 \times 10^7 \text{ s}^{-1}$ and $1 \times 10^7 \text{ s}^{-1}$, respectively. The rates in the neutron-rich tellurium isotopes are above 10^6 s^{-1} out to ^{136}Te , which is just beyond the $N = 82$ shell closure. These rates are above the minimum requirements needed to successfully observe strong $M1$ decay transitions following the multistep Coulomb excitation of weakly collective $E2$ transitions that connect (1) the symmetric ground state to the 2^+ mixed-symmetry state(s) and (2) the mixed-symmetry states to the scissors mode.

2.5.4.3 Giant dipole resonance and pygmy resonances

The giant dipole resonance (GDR) is a sensitive tool for studying nonuniform charge distributions in nuclei. For example, the halo structure in neutron-rich light nuclei could result in a completely different electromagnetic response compared to stable nuclei [Han99b]. A vibration of the neutron halo or skin with respect to the core would shift part of the dipole strength from the normal giant resonance region (~ 22 MeV) to much lower energies of about 1 MeV.

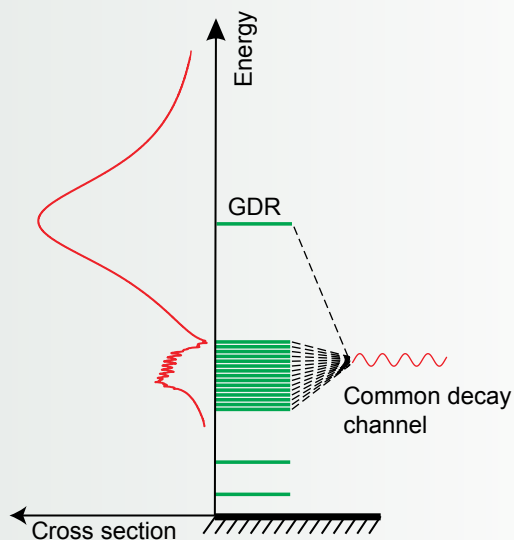
A shift of GDR strength towards lower energies is also predicted to occur for heavier nuclei as the neutron dripline [Suz90, Isa92] is approached. The GDR strength will be strongly fragmented (Landau damping). This redistribution of collectivity is due to the modification of the mean field as a function of the N/Z ratio. Another

Many-body quantum chaos

As excitation energy and level density increase in atomic nuclei, many-body states become exceedingly complicated superpositions of simple independent-particle configurations. It is now established [Bro81,Zel96b,Guh98,Zel04] that local characteristics of spectra in this domain practically coincide with those predicted by the theory of quantum chaos and modeled by random matrices.

The complexity of wave functions in the chaotic domain leads to the strong enhancement of weak perturbations, such as parity nonconservation [Fla95b]. This complexity also provides a means of extracting information about the fine structure states from experiments with poor resolution [Kil87]. Coupling of low-lying states to the chaotic domain leads to new computational approaches, for example, the exponential extrapolation method [Hor99].

A new aspect of quantum chaos emerges for marginally stable systems. The proximity to the continuum changes the manifestations of chaos, in some cases paradoxically introducing the element of self-organization [Sok89,Rot91,Sok92] through strong coupling with the continuum. In atomic nuclei, this can be seen, for example, in the formation of soft collective modes, low-lying branches of giant resonances [Sok90,Zel06b]. Such excitations near the threshold are typical for open mesoscopic systems. For very neutron-rich nuclei, the neutron excess may oscillate against the stable core, spectacularly illustrating the interplay between intrinsic degrees of collectivity and open decay channels. The ideas of internal chaotic mixing and external self-organization through the continuum are analogous to superradiance in quantum optics.



Schematic illustration of the GDR in a loosely bound nucleus. The green lines are the unperturbed particle-hole energies. The upper part of the red curve is the usual GDR as observed in stable nuclei. The lower part of the red curve shows the enhancement of the strength at low energy due to coupling with the continuum. As one approaches the neutron dripline the pygmy branch of the GDR is formed. The many states in the pygmy part overlap and decay coherently into the common decay channel. Adapted from [Zel06a].

important aspect is the proximity of the continuum for all virtual particle-hole excitations [Zel06a].

Measuring the response of extreme neutron-rich systems will help us understand the collective motion of these neutron-rich nuclei and extrapolate to the collective motion of neutron matter. The saturation of the total dipole sum rule is of special interest since it reflects the role of exchange forces in the condition of extreme isospin asymmetry.

The existence and strength of the soft component of the GDR in neutron-rich nuclei can potentially have a large influence on the path of the r-process. During much of the r-process, photodisintegration and radiative capture are in equilibrium; however, as the temperature and neutron density decrease at the end of the neutron-producing event, the nucleosynthesis depends on the absolute rates of the (n,γ) and (γ,n) processes.

These in turn depend on the GDR strength function. Thus, the shape of the GDR strength function has a significant impact on the relative abundances produced in the r-process. Recent work by Adrich et al. [Adr05] shows evidence for collective excitation at ~ 10 MeV in $^{130,132}\text{Sn}$. Such a shift of the GDR strength was expected from calculations, and its experimental verification has significant importance to both nuclear structure and nuclear astrophysics near the neutron-rich waiting point nuclei.

The study of the GDR in exotic nuclei relies on its large excitation cross-section and a clean separation and/or identification from other giant resonances. Two important factors are necessary to excite the GDR strongly in the projectiles: high beam energies and high-Z targets. At high beam energies, GDR formation is dominated by Coulomb excitation, which is proportional to Z^2 of the target. Coulomb excitation can be viewed as an exchange of virtual photons, and the virtual photon spectrum is a strong function of the beam energy. Cross sections increase dramatically up to 200 MeV/nucleon and match well with the planned energies of the ISF.

The main peak of the GDR is located above the particle evaporation threshold, and thus the excited projectiles will break up in flight. Two experimental techniques can be applied to reconstruct the excitation function of the projectile. In the method of virtual photon scattering, the γ -ray decay to the ground state is detected [Var98]. In virtual photon absorption, the excitation energy is reconstructed from the breakup fragment and the neutron(s) [Aum99a,Aum99b]. Both experiments demonstrated the feasibility of the methods and the great opportunities for future applications with fast fragmentation beams.

A beam intensity of at least 10^6 s^{-1} is needed to make these studies feasible. For heavier beams, somewhat smaller intensities should be sufficient, since the excitation cross section scales with NZ/A , yielding a factor of about 10 between ^{11}Li ($5 \times 10^7 \text{ s}^{-1}$) and ^{86}Rb ($1 \times 10^{10} \text{ s}^{-1}$).

The recent results on the tin isotopes [Adr05] discussed above continue to make the region around the closed shell nucleus ^{132}Sn of high interest. Several important waiting points in the r-process path are only 1–2 mass units away from ^{132}Sn , towards more neutron-rich nuclei. The yield of ^{130}Cd is expected to be $7 \times 10^3 \text{ s}^{-1}$, of the same order as the recent ^{132}Sn measurements [Adr05].

Theoretical work by Vretenar et al. [Vre01] suggests that in ^{68}Ni a low-energy resonance below 10 MeV may occur, and the expected ^{68}Ni rate of $9 \times 10^8 \text{ s}^{-1}$ is sufficient to pursue such a study.

2.5.4.4 Isoscalar giant monopole resonance and nuclear compressibility

The compressibility of a nucleus is determined by the effective interaction between the nucleons in their many-body environment. The isovector properties of this interaction determine the dependence of the compressibility on neutron excess. Consequently, the measurements of the giant monopole resonance in neutron-rich nuclei will shed light on fundamental properties of the effective force, and on the nuclear compressibility.

The experimental and theoretical exploration of the properties of neutron star matter and the determination of the Equation of State (EOS) associated with such high-density matter are of key importance for understanding the physics of neutron stars and supernova explosions. The properties of a neutron star depend on the nuclear equation of state, which includes both the nuclear matter compressibility and symmetry energy. Therefore, it is important to determine these quantities.

For small-amplitude density oscillations, the compressibility of nuclear matter of normal density can be obtained from the frequencies and strengths of nuclear vibrations that involve the compression of nuclear material, the isoscalar monopole, and isoscalar dipole resonances [Bla80]. To extract the compressibility of infinite

nuclear matter from the measured Giant Monopole Resonance (GMR) energy, it is necessary to understand the correction factors due to surface effects in finite nuclei.

The dependence on isospin is currently not well understood because the current data are limited to stable nuclei [You97,You99]. The most recent value of the nuclear compressibility extracted from the GMR in a microscopic framework is 240 ± 20 MeV [Col04]. For a further reduction of the error bar, the density dependence of the symmetry energy has to be better understood.

Although a systematic study of the properties of the GMR has been performed for stable isotopes [Gar06], a much better sensitivity for the relevant parameters can be obtained if information would become available on the GMR in unstable nuclei. Indeed, calculations predict significant differences of the GMR strength distribution in very neutron-rich nuclei compared to stable nuclei. For example, the GMR centroid for the neutron-rich calcium isotopes is expected to shift to lower energies as compared to the stable calcium isotopes [Sag98].

The GMR in exotic nuclei can be excited by inelastic deuteron, α , or ${}^6\text{Li}$ -scattering in inverse kinematics. For medium mass nuclei and a beam energy of 10 MeV/nucleon, the α -particle scattering angle for the excitation energy range of interest (10–20 MeV) is 1–3 degrees in the center-of-mass system (50–80 degrees in the laboratory frame). The cross section for the excitation of the monopole is about 100 mb/sr and peaks at 0° . It can be distinguished from the giant quadrupole resonance only at angles less than 2° . The GMR is located above the particle threshold and the projectile will break up in flight. Thus it will be necessary to detect the scattered deuterons or α particles, which will be extremely difficult because of their low energies (less than 1 MeV).

Beam intensities larger than 10^7 s^{-1} are necessary for these experiments. This will, for example, allow the measurement of the GMR with fast beams in nickel over a range ${}^{54}\text{Ni}$ ($2 \times 10^7 \text{ s}^{-1}$) to ${}^{71}\text{Ni}$ ($2 \times 10^7 \text{ s}^{-1}$). Up to now, the GMR is known in only two nickel isotopes, ${}^{58}\text{Ni}$ [You96] and ${}^{60}\text{Ni}$ [Bue84], which have isospin $T_z = 1$ and 2, respectively. Recently, the nucleus ${}^{56}\text{Ni}$ ($T_z = 0$) was studied at GANIL via deuteron scattering at 50 MeV/nucleon using the MAYA detector system at a beam intensity of $5 \times 10^4 \text{ s}^{-1}$ [Mon06a]. Other interesting cases include ${}^{132}\text{Sn}$ ($3 \times 10^6 \text{ s}^{-1}$), where a measurement of the GMR would help considerably in determining the value of the compressibility of infinite neutron matter [Pea92], and ${}^{104}\text{Zr}$ ($2 \times 10^6 \text{ s}^{-1}$).

2.6 Nuclei at high angular momentum

Fast nuclear rotation is known to stabilize exotic nuclear configurations. This is well documented for very elongated superdeformed and triaxially-deformed shapes associated with quadrupole deformation as well as reflection-asymmetric shapes related to octupole degrees of freedom in the nucleus [Nol88,Jan91]. The shape stabilization at high angular momentum is attributed to valence nucleons, which occupy deformed single-particle states with high total spin quantum numbers. Properties of rotational bands reflect the symmetries of the underlying intrinsic states, providing a convenient tool for nuclear structure studies and a critical testing ground for nuclear shell theory. Also, it is at the highest spins when the dramatic interplay between collective and single-particle degrees of freedom in nuclei are manifested at band termination. Nuclear behavior at these highest spin values may also reveal information on a possible phase transition from superfluidity

based on spin-singlet to spin-triplet pairs [Sha90,Sha00]. The following examples illustrate the current state-of-the art of the field and project into exciting research opportunities, which are offered by the ISF.

2.6.1 Super- and hyperdeformation

Very elongated ellipsoidal superdeformed nuclear shapes with an axis ratio of $\sim 2:1$ have been the subject of experimental and theoretical studies in the past two decades. These exotic shapes are favored by the single-particle spectrum for axially symmetric deformed nuclear potentials. Large energy gaps between adjacent single-particle states in a deformed potential are revealed at both the 2:1 and 3:1 axis ratios for prolate and oblate nuclear deformations (see Section 2.5.2.1) [Dud88,Cha01].

The advent of large multi-detector arrays of Compton-suppressed germanium detectors [Nol94] has led to the discovery of superdeformation in ^{152}Dy [Twi86] (see Figure 2.28) and subsequently to the identification of several regions of rotational structures built on superdeformed shapes. The experimental confirmation of static nuclear superdeformation constitutes the best representation of single-nucleonic motion in a deformed nuclear potential.

Measurements of transition quadrupole moments, absolute excitation energies, spins, and parities of the bands have been completed [Sin02]. The results have validated the existence of large quadrupole moments that directly reflect the superdeformed axially symmetric structure. Convincing empirical evidence for the existence of nuclear hyperdeformed structures is still lacking, and current searches for hyperdeformed rotational bands challenge the sensitivity limits of available large multidetector germanium arrays. In addition, new theoretical ideas are emerging [Dud04] that may guide the experimental search for hyperdeformation.

Current information on nuclear structure at high angular momentum is limited to proton-rich nuclei. Little is known about neutron-rich nuclei, which cannot be easily reached with stable targets and projectiles in fusion-evaporation reactions.

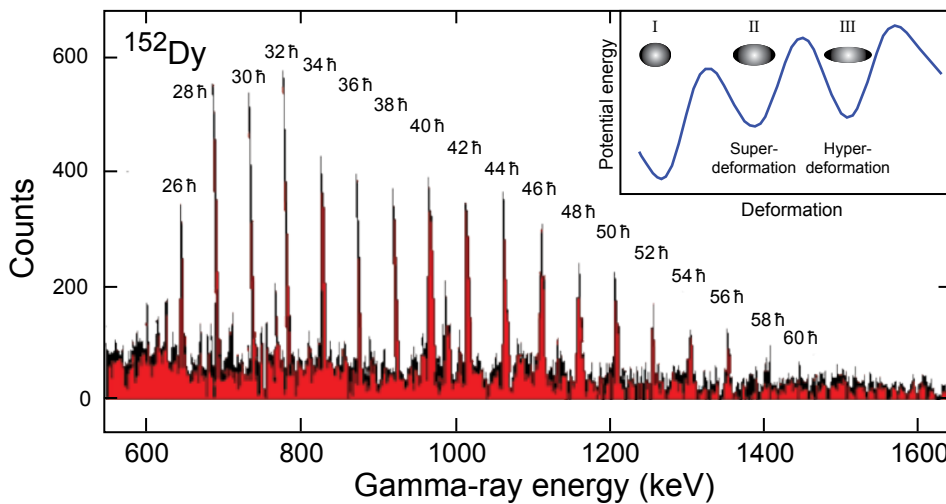


Figure 2.28: Spectrum of the lowest energy band arising from a superdeformed ($\beta \sim 0.6$) prolate shape in ^{152}Dy . Nineteen γ -ray transitions from 602 keV to 1449 keV with an almost constant energy separation of 47 keV were observed in the $^{108}\text{Pd}(^{48}\text{Ca},n)$ reaction at 205 MeV. The insert illustrates the minima in the potential energy surface, corresponding to normal deformation (I), superdeformation (II), and hyperdeformation (III). Adapted from [Nol88].

Fission and deep-inelastic reactions have been used to investigate low- and intermediate-spin states in neutron-rich nuclei, but the study of high-spin states and the identification of superdeformed bands remains a challenge there. Experimental factors that play a role in the lack of information on neutron-rich nuclei at high spin include the limitations on the maximum angular momentum achieved in the reactions that produce neutron-rich nuclei (mainly fragmentation, fission, and deep inelastic collisions) and the sensitivity losses from the large number of open reaction channels.

Some of the best cases for super- and hyperdeformed nuclei are predicted to exist in neutron-rich isotopes. One example of superdeformed shapes is in the mercury region. The barrier between superdeformed and normal deformed shapes increases with mass number for $^{190-198}\text{Hg}$ [Bon90]. However, the most neutron-rich mercury isotope with an identified superdeformed band is ^{195}Hg [Sin02]. The heavier mercury isotopes are not accessible with the beam and target combinations available at present-day facilities. Hyperdeformation was originally predicted near ^{166}Er , ^{168}Yb , and ^{170}Hf [Dud88]. Again, high spin states in these nuclei are beyond reach with stable target and beam combinations. More recently, very highly deformed shapes were calculated to exist near $Z = 50$ [Cha01,Afa05]. Studies of high angular momentum states in ^{108}Cd have revealed a rotational band based on the $\pi i_{13/2}$ intruder orbital. The resulting dynamic moments of inertia and deduced quadrupole moments suggest an axis ratio larger than 1.8:1 [Cla01,Goe02]. The target and projectile combination in the ^{108}Cd experiment involved the most neutron-rich stable isotopes ($^{64}\text{Ni} + ^{48}\text{Ca}$) currently available for fusion evaporation studies in this mass region. Therefore, access to high-spin states in more neutron-rich cadmium isotopes towards the region of expected hyperdeformed shapes in ^{128}Cd will require rare isotope beams with energies above the Coulomb barrier.

Reaccelerated neutron-rich beams will not be available at sufficient rates at existing facilities, and programs to define the boundaries of predicted superdeformed and hyperdeformed shapes will await the next generation of exotic beam facilities. The ISF will have sufficient rates of near-stable neutron-rich reaccelerated beams to investigate high-spin states in nuclei with moderate neutron access via fusion-evaporation reactions. For example, a reaccelerated ^{90}Kr beam incident on a ^{26}Mg target will populate high-spin states in ^{112}Cd in the $4n$ evaporation channel with maximum angular momentum $\sim 70\hbar$. Beyond neutron number $N = 64$, the neutron $j_{15/2}$ orbital will be occupied. In combination with the occupied proton and neutron $i_{13/2}$ states, this will drive nuclear shapes to extremely large deformations. The expected reaccelerated beam rate of ^{90}Kr at the ISF is $1 \times 10^7 \text{ s}^{-1}$. Experiments at these low intensities will become feasible with the expected three orders of magnitude increase in resolving power achievable with the planned next-generation γ -ray detector GRETA. The data attained on high-spin states at the ISF with neutron-rich reaccelerated beams and GRETA will yield results that are statistically comparable to those obtained with today's state-of-the-art detectors for superdeformed bands in neutron-deficient nuclei.

2.6.2 Broken symmetries at high spin

Symmetries play a key role in the understanding of nuclear physics phenomena. Among several symmetries [Boh75,Fra01] significant to nuclear structure studies, three have a direct impact on rotational structures observed in nuclei at high spin.

The first two symmetries, rotational and spatial inversion invariances, are a consequence of the isotropy of space. The third, time reversal symmetry, results from the reversibility of motion in time. Rotational bands in deformed nuclei and parity doublets in nuclei with octupole deformation result from rotational and spatial inversion invariances. Correspondingly, time reversal symmetry brings about the formation of left- and right-handed chiral structures and the appearance of strongly-coupled doublet bands of the same spin and parity.

Reflection-asymmetric or octupole shapes are predicted to exist in regions with the proton and neutron Fermi surfaces of single-particle orbitals with $\Delta\ell = \Delta j = 3$. The cases identified so far in the $A \sim 150$ and $A \sim 220 - 230$ regions resemble pear-like statically deformed nuclear shapes, characterized by parity doublet band structures, enhanced $E1$ transitions, and anomalous decoupling parameters [But96]. Reaccelerated beams from the ISF will provide access to other regions of nuclei with octupole deformation. For example, strong correlations are expected in nuclei near ^{112}Ba , with $N \sim Z \sim 56$. Here, the proton and neutron $d_{5/2}$ and $h_{11/2}$ orbitals reside near the Fermi surface and satisfy the $\Delta\ell = \Delta j = 3$ rule for expected static octupole shapes. The most neutron-deficient barium isotope with excited states identified is ^{118}Ba [Smi98], populated in the $^{58}\text{Ni}(^{64}\text{Zn}, 2p2n)$ fusion evaporation reaction. At the ISF, possible octupole rotational bands can be excited in ^{114}Ba with the $^{58}\text{Ni}(^{60}\text{Zn}, 2p2n)$ reaction. The expected intensity of a ^{60}Zn reaccelerated beam is $9 \times 10^7 \text{ s}^{-1}$ and will be sufficient for in-beam γ -ray spectroscopy with the high-resolution germanium detector array GRETA.

Doublet bands related to spontaneous chiral symmetry breaking are expected in odd-odd nuclei with triaxial shapes [Fra01]. Nuclear chirality results when the angular momenta of the valence proton, the valence neutron, and the core rotation are mutually perpendicular. These three mutually perpendicular angular momenta can be arranged to form a left- and a right-handed system, which are related by the chiral operator, a combination of time reversal and rotation by 180° . When chiral symmetry is broken in the body-fixed frame, the restoration of the symmetry in the laboratory frame is manifested as degenerate doublet $\Delta I = 1$ bands. While the signatures of nuclear chirality are understood from recent theoretical efforts [Koi04], candidate nuclei demonstrating all the required signatures without ambiguity are needed to rigorously test these predictions. Odd-odd nuclei in the $A \sim 130$ [Sta01] and $A \sim 100$ [Vam04] regions have been studied extensively, and chiral symmetry breaking has been inferred from doublet band structures and intraband transition strengths. While exploration of chiral symmetry in nuclei on the neutron-deficient side of stability will continue, access to stable and neutron-rich nuclei showing spontaneous chiral symmetry breaking will be very limited by available stable beam and target combinations. In many cases, the beam and target combinations generate only limited angular momentum in the compound nucleus, insufficient to investigate the chiral band structures.

The odd-odd iridium isotopes with $A \sim 190$ are good candidates to access the proton-particle $i_{13/2}$ and neutron-hole $i_{13/2}$ configurations in the intermediate spin range [Dim00]. In the lighter iridium isotopes, band structures are established up to $A = 176$ and spin $\sim 30 \hbar$ with the $^{149}\text{Sm}(^{31}\text{P}, 4n)$ fusion evaporation reaction. The heaviest odd-odd iridium isotope studied to date with heavy-ion fusion-evaporation reactions is ^{188}Ir . This nucleus was produced with the $^{187}\text{Re}(\alpha, 3n)$ reaction, populating states up to spin $10 \hbar$. This reaction did not populate potential chiral doublet bands, since the band head is expected to have spin $9 \hbar$.

At the ISF, beams of $^{36-38}\text{P}$ (with intensities of $\sim 6 \times 10^9 \text{ s}^{-1}$) will be available to study $\pi i_{13/2} \nu i_{13/2}$ structures in iridium isotopes up to $A \sim 184$, while the reactions with lighter neutron-rich projectiles may be used to study the chain up to $A \sim 194$.

2.6.3 High-spin states at band termination and beyond

Generation of angular momentum in atomic nuclei can result either from single-particle excitations or from collective rotation. The energy required for these excitation modes depends on the proton and neutron number as well as on the range of nuclear spins to be populated. A collective rotational band, built on unique-parity intruder configurations near closed shells, shows unique experimental signatures with increasing angular momentum. As the rotational frequency increases, valence particles align their angular momenta, resulting in a decrease in the dynamic moments of inertia and a decrease in transition quadrupole moments. When the momenta of the available valence particles of the intruder configuration have aligned, the band sequence terminates at a spin value that exhausts the sum of the aligned single-particle spins. Atomic nuclei represent the only finite multi-fermion system in which this feature has been identified [Afa99]. Smooth band termination is characterized by a gradual transition from prolate to non-collective oblate shape. Abrupt band terminations in normal-parity configurations and away from closed shells have also been observed [Eva04].

Band termination should be a general feature exhibited by nuclei near major shell closures. However, only a few regions of the nuclear chart have been investigated due to the limited number of projectile and target combinations that can populate band structures to sufficiently high spin. Smooth band termination is established in nuclei near the $A = 110$ region. The nucleus ^{110}Sb was studied via the $^{54}\text{Fe}(^{59}\text{Co}, 2\text{pn})$ fusion evaporation reaction [Lan97], and termination at spin $45 \hbar$ was observed as shown in Figure 2.29. Terminating states below spin $40 \hbar$ are expected in ^{107}Sb and in lighter $Z = 51$ isotopes. While the study of ^{107}Sb is possible with stable beams in the $^{58}\text{Ni}(^{58}\text{Ni}, \text{p}2\alpha)$ reaction [Laf00], it is hindered by the relatively small cross section for the $\text{p}2\alpha$ evaporation channel. The corresponding structures in semi-magic tin isotopes are identified only up to ^{106}Sn [Wad94] due to similar experimental limitations in the low-probability exit channels. The ISF will have sufficient reaccelerated beam intensities of neutron-deficient ^{50}Fe and ^{54}Ni projectiles to study band termination in ^{102}Sn and ^{104}Sn , only a few nucleons away from the doubly magic nucleus ^{100}Sn . Such studies will require a high resolution germanium array with capability for high γ -ray multiplicity measurements. Data on quadrupole transition matrix elements and quadrupole transition moments will be crucial for establishing decreasing collective strength near the band termination point.

2.6.4 Quantum rotational structures built on exotic isomeric states

High-spin isomeric beams will add a new and important dimension to nuclear structure studies at the ISF. Isomeric states themselves provide a mechanism for probing effective interactions in the corresponding valence-particle configurations at high spin. Indeed, data on effective interaction strengths in $N \sim Z$ towards ^{100}Sn are largely based on experimentally determined spins and excitation energies of isomeric states in fpg shell nuclei. The absence of isomerism of the 8^+ neutron $g_{9/2}$ seniority-2 state in the even-even nickel isotopes also served to refine the shell model effective interactions that will impact the structure of doubly magic ^{78}Ni [Lis04].

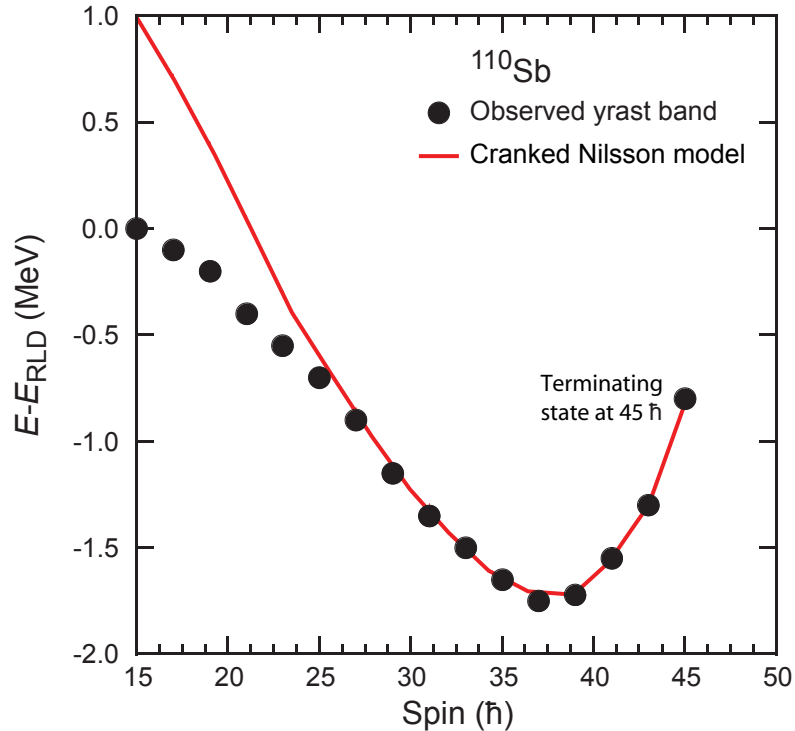


Figure 2.29: Smooth band termination observed in ^{110}Sb . The energies plotted for each value of angular momentum are the excitation energies from which the Rotating Liquid Drop (RLD) model reference energy has been subtracted. Band termination is observed at $J = 45 \hbar$. Adapted from [Lan97].

The identification of microsecond isomeric states reached a boom in recent years, driven by the implementation of high-resolution germanium detectors at fast beam facilities [Grz98]. Further searches for isomeric states in neutron-rich nuclei will continue in the near future, mostly at NSCL and other fragmentation facilities. The focus of these studies will be predominantly the regions near the doubly magic nuclei ^{132}Sn and ^{208}Pb . The continued development of high intensity uranium beams for production of neutron-rich fast beams both by fragmentation and fission reactions will make available a wide variety of previously unexplored nuclei that may show evidence for isomerism.

The frontier in isomer beam research in the longer term, however, is the application of these beams in reactions studies. Firstly, the isomeric states themselves can be investigated in detail by a number of established methods, including elastic and inelastic scattering, transfer and pick-up reactions, and Coulomb excitation below barrier energies. Such studies will reveal precise information on the wave function of the isomeric state and excited-state band structure(s) that directly feed into the isomer. Secondly, fusion reactions with isomeric high-spin beams can be employed as a tool for populating high-spin, low excitation-energy entry states in compound nuclei.

Isomeric beams at the ISF will be produced directly in the intermediate-energy fragmentation or fission reactions and slowed to thermal energies in the cyclotron stopper. The beams will then be reaccelerated to energies up to 12 MeV/nucleon for nuclear structure studies. The combined times for stopping, charge breeding,

and reacceleration beams at the ISF will not exceed more than a few milliseconds; therefore, a wide variety of nuclei with relatively high spins will be available. The use of isomer beams in reaction studies will require high-purity of the isomeric state. In some cases, the large difference in ground- and isomeric-state half-lives will make beam purification simple. For example, ^{212}Po has a ground-state half-life of 0.3 microseconds, while the isomeric state has a half-life of 45 seconds. The expected reaccelerated beam intensity of ^{212}Po at the ISF is $4 \times 10^6 \text{ s}^{-1}$. Even if the isomer were populated at only 1% of the total ^{212}Po production rate, there would still be sufficient reaccelerated beam intensity of this nucleus to pursue multistep Coulomb excitation, transfer, and inelastic scattering experiments.

2.7 Spin-isospin response of nuclei

Charge-exchange reactions induced by stable beams impinging on stable targets have been widely used to study the spin-isospin response of nuclei [Ost92,Har01]. Most experiments have focused on extraction of allowed (Gamow-Teller) strength distributions. In contrast to studies of β -decay (see Sections 2.3.2.2 and 2.5.2.2) in which only nuclear states in a narrow energy window are accessible, charge-exchange reactions probe the entire response function, including the giant-resonance region. However, little information is available for unstable nuclei, besides what is known from β -decay. We will show here that there are compelling reasons for obtaining this information.

Measurements of the allowed spin-isospin response of light asymmetric nuclei are needed for assessing the validity of, and suggesting improvements to, nuclear structure models up to high excitation energy and, more generally, improving our understanding of properties of such nuclei. Both $\Delta T_z = -1$ (i.e., (p,n)-type) and $\Delta T_z = +1$ (i.e., (n,p)-type) reactions are important. The allowed response is sensitive to the presence of intruder orbits and nuclear deformations. Therefore, charge-exchange experiments in the island of inversion ($N = 20$, $Z < 14$) could provide important complementary information to existing data obtained with other techniques (see Section 2.3). Measurements of the allowed response in very light systems will allow testing the accuracy of no-core shell models. Such measurements will become more critical when the region where such models can be applied is extended to heavier masses. As an example, recent charge-exchange experiments on $A = 14$ nuclei have revealed significant difficulties for such models, even if a $6\hbar\omega$ model-space is used [Neg06]. This points to additional degrees of freedoms, such as mixing between the shell model and cluster configurations.

Weak-transition rates, for $L = 0$ (Gamow-Teller or allowed transitions) and $L = 1$ (first-forbidden transitions) on both stable and unstable nuclei, are important for understanding stellar evolution. Weak transitions play crucial roles in type-II (core collapse) and type-Ia (thermonuclear) supernovae [Lan03]; these astrophysical applications are an important motivation for studying spin-isospin excitations. Further details are given in Section 3.2.2. The relevant mass region is $40 < A < 120$. Strength distributions in pf and sdg-shell nuclei associated with electron-capture ($\Delta T_z = +1$ charge-exchange reactions) are most important, but transitions associated with β -decay from pf-shell nuclei ($\Delta T_z = -1$ charge-exchange reactions) are also relevant [Lan03].

A large number of transitions, mostly involving unstable nuclei, play a role in late stellar evolution. Moreover, since reactions in the stellar environment take place at

relatively high temperatures and densities, transitions can occur between excited states. Such transitions cannot be studied directly in the laboratory. Rather, experiments must focus on testing the theory on a representative set of nuclei in the relevant regions of the nuclear chart. Rate predictions from the validated models can then be used with greater confidence in stellar evolution codes.

A third major motivation for charge-exchange experiments with unstable nuclei is the study of isovector giant resonances. In hydrodynamical models, these resonances are associated with out-of-phase density oscillations of the proton and neutron fluids in nuclei [Har01]. Their study provides access to macroscopic nuclear matter properties associated with the difference between the two fluid components. Another degree of freedom arises from spin oscillations of the nucleons. An important goal is to obtain a systematic pattern of the energy and collectivity of the various giant resonances, starting with the isovector giant spin-flip resonances, along several chains of isotopes in different mass regions. This should reduce the uncertainties in the isovector part of the nucleon-nucleon effective interaction [Fra05] and the symmetry potential of the equation of state [Dan03] (see also Section 2.8.1). Such studies are needed to improve the reliability of shell model or mean-field calculations (such as the quasi-particle random-phase approximation (QRPA)), which have many applications, including the description of astrophysical phenomena [Lan03] (see Section 3) and neutrino-less double β -decay [Ell02,Eji05], where in addition to $L = 0,1$, higher multipoles contribute significantly. For these purposes, measurements in both the $\Delta T_z = +1$ and $\Delta T_z = -1$ direction are important.

A measurement of the centroids of the excitation energies of the isovector giant resonances can provide important information about nuclear structure. The energy splitting of the isobaric analog state and the centroid of the Gamow-Teller resonance provides a measure of the neutron-skin thickness [Vre03]. In addition, measurements on a single nucleus in both directions allow one to extract model-independent sum-rules that are directly related to the neutron-skin thickness [Kra99]. The neutron-skin thickness is closely related to the equation of state in asymmetric nuclear matter [Bro00a,Yos04a,Yos06]. The advantage of studying isovector giant resonances far from the line of stability is that signatures of reduced collectivity, modified strength distributions, and changing macroscopic properties such as neutron-skin thicknesses, are expected to be significantly enhanced [Vit98] compared to results for stable targets. Consequently, constraints on theoretical models will become much more stringent.

As mentioned, charge-exchange experiments have, so far, been mainly restricted to experiments on stable nuclei. The main reasons for this are that charge-exchange experiments with unstable nuclei must be performed in inverse kinematics and at small center-of-mass scattering angles so as to reliably separate various multipole contributions ($L = 0$ and $L = 1$, for example). As a result, the outgoing light recoil nucleus (or neutron in case of the (p,n) reaction) typically has very low energy. To have well-defined two-body kinematics, it is necessary to tag the events with these low-energy recoils; otherwise the decay of the heavy ejectile nucleus in flight may lead to misidentification of events. In addition, the excitation energy in the excited unstable nucleus must be determined with good precision. These requirements greatly influence and complicate the design of experiments as we discuss below.

Only recently have systematic attempts to overcome the various hurdles been pursued, partially motivated by the prospects of increased capabilities at the next generation of unstable beam facilities. At NSCL, such efforts include the development of the (p,n) and ($^7\text{Li},^7\text{Be}$) reactions in inverse kinematics, as detailed below. In addition to the complexity of the experiments, charge-exchange cross sections are relatively small and the required beam intensities are, therefore, high. Beam intensities of $\sim 10^6 \text{ s}^{-1}$ must be available. As a consequence, although the experimental techniques can be developed at the CCF and first charge-exchange experiments on unstable nuclei a few isotopes away from stability and up to mass ~ 120 can be performed, the research will strongly benefit from the next generation of rare isotope beam facilities.

In Figure 2.30 the capabilities of the ISF are compared with those of the CCF. With the CCF one could typically extend measurements up to three or four isotopes away from the line of stability; at the ISF that number is roughly doubled and extends up to much heavier masses. For the measurements of weak rates of importance for stellar evolution, the extended reach at the ISF results in more or less complete coverage of the relevant regions (*pf* and *sdg* shell nuclei) of the nuclear chart. For the study of isovector giant resonances, the improved capabilities at the ISF are even greater. As an example, consider the chain of tin isotopes. Charge-exchange measurements in the $\Delta T_z = -1$ direction on the stable tin nuclei (ranging from $A = 112$ to 124) already exist [Pha95,Kra99]. At the CCF, they can be extended only on the proton-rich side, to $A = 109$. At the ISF, tin isotopes from $A = 104$ to $A = 132$ could be studied, more than doubling the span in isospin of the target nucleus. With a limited range in isotopes, various theoretical models predicting neutron-skin thicknesses can be only marginally tested [Sag05]. This situation would be very much improved with the expanded reach of the ISF.

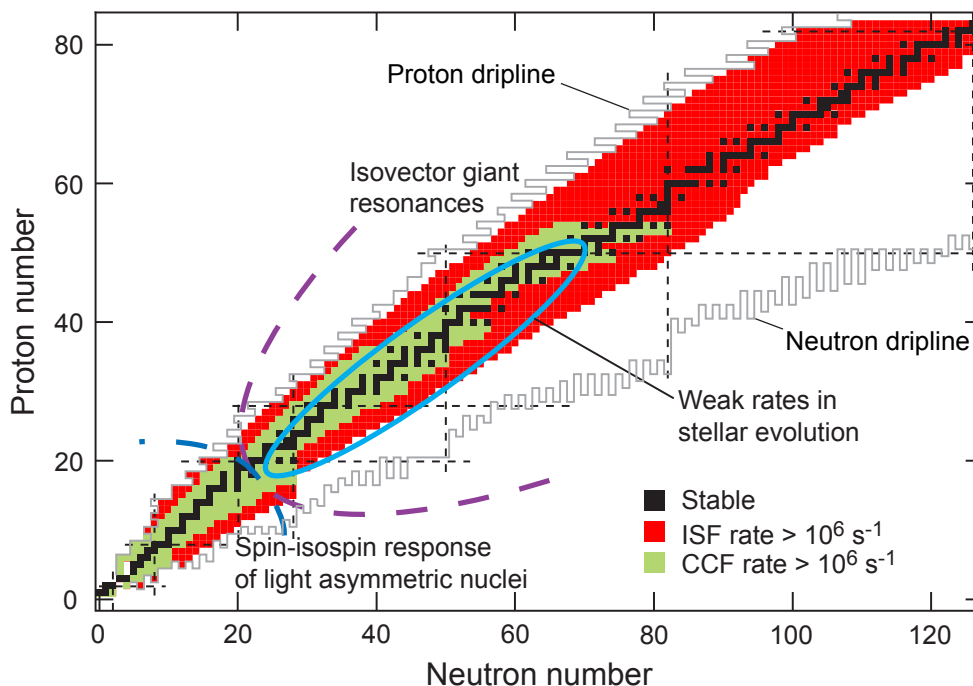


Figure 2.30: Overview of the physics program with charge-exchange reactions in inverse kinematics. To perform such experiments, beam intensities in excess of 10^6 s^{-1} are required. The regions in the chart of nuclei where such rates will be achieved at the CCF are indicated in green. The increased reach at the ISF is indicated in red.

An important boundary condition for charge-exchange experiments that aim to extract reliable multipole isovector strengths is that beam energies must exceed ~ 100 MeV/nucleon, where the dominant scalar-isoscalar part of the central interaction has a broad minimum ranging up to about 400 MeV/nucleon. Moreover, in this bombarding-energy domain, the spin-isospin part of the interaction dominates over the pure isospin part, thus favoring strongly spin-isospin transitions over pure isospin transitions [Lov81,Fra83]. Fast fragmentation with primary beam energies of about 200 MeV/nucleon, which will become available at the ISF, is ideally suited for this purpose. The resulting energies of the secondary beams will fall in the window where most stable-beam experiments have been performed and reliable information about reaction mechanisms is available.

2.7.1 Charge-exchange experiments in inverse kinematics

In the $\Delta T_z = -1$ direction, the (p,n) and ($^3\text{He},t$) reactions have been the preferred probes for experiments performed in forward kinematics. The (p, n) reaction has the best understood reaction mechanism, but the ($^3\text{He},t$) reaction yields better resolution and the charged particle exit channel makes measurements and data analysis relatively easy. Experiments with heavier ions, e.g., ($^{12}\text{C},^{12}\text{B}$), have larger uncertainties due to the structure of the probes and the achievable resolution is poorer.

In inverse kinematics experiments with rare isotope beams, the use of the (p,n) reaction is preferable. Experiments with probes other than (p,n), i.e., with low-energy charged recoil particles, would require the use of very thin targets or, possibly, time-projection chambers, greatly limiting the event rates and or complicating the experiments. Relative to reactions with a charged particle in the exit channel, the (p,n) reaction allows the use of much thicker targets (CH_2 or liquid/frozen hydrogen) which yields much higher event rates. The fast heavy residual nucleus can easily be detected in a spectrometer. The main complication is that low-energy neutrons (100 keV–5 MeV) have to be detected with reasonable efficiency, time-of-flight resolution (necessary for reconstructing the excitation energy), and angular resolution. Studies for such a neutron detector are already underway and will be implemented at the CCF. An alternative method is to perform the experiments in a storage ring to increase the luminosity [Exl01].

In the $\Delta T_z = +1$ direction, the (n,p), ($d,^2\text{He}$), and ($t,^3\text{He}$) reactions are the preferred probes in forward kinematics experiments, although heavier probes such as the ($^7\text{Li},^7\text{Be}$) and ($^{12}\text{C},^{12}\text{N}$) reactions have been used as well. In absence of a neutron target, there is no obviously superior technique for inverse kinematics experiments; in all cases the slow recoil particle is charged and can only be detected when thin solid or (active) gas targets are used. One way around this is the use of the ($^7\text{Li},^7\text{Be}+\gamma$) reaction in inverse kinematics. The transition to the first excited $1/2^-$ state in ^7Be defines the reaction as spin-transfer, and the reaction can be tagged by measuring the 0.43-MeV decay photon in a high-resolution photon detector such as SeGA or GRETINA. This method is currently being tested at the CCF. It would greatly benefit from increased beam intensity, since thin targets (<3 mg/cm 2) have to be used to obtain excitation energy resolutions better than 1 MeV. With the higher rates available at the ISF, the ($d,^2\text{He}$) reaction could become a viable probe as well. Use of this probe requires a measurement of the two protons originating from the unbound ^2He particle with sufficient energy and angular resolution to reconstruct

the internal energy and scattering angle of the ${}^2\text{He}$ particle. Target thicknesses of less than 1 mg/cm^2 must be used to achieve sufficient precision. Therefore, a reasonable event rate can only be achieved if high beam intensities are available. Detailed simulations indicate that good spin-transfer selectivity and resolutions near 1 MeV could be achieved.

2.7.2 Unstable probes for spin-isospin modes in stable nuclei

The increased beam intensities for rare isotope beams available at the ISF would also provide new opportunities for experiments on stable targets. A good example is the improved capability for $(t,{}^3\text{He})$ experiments with a secondary triton beam. At the NSCL, the $(t,{}^3\text{He})$ reaction around 120 MeV/nucleon has been developed [She99,Zeg05,Zeg06,Hit06] as a new tool for studying weak-interaction strengths in the electron-capture direction. This capability provides an attractive alternative to the existing (n,p) [Jac88] and $(d,{}^2\text{He})$ [Rak02] probes for weak strength that is important in core-collapse supernovae. We have demonstrated that the excitation energy spectrum in the $\Delta T_z = +1$ direction can be measured with a resolution of about 200 keV , compared to about 1 MeV for the (n,p) reaction, using dispersion-matching techniques at the S800 spectrometer. Compared to the $(d,{}^2\text{He})$ reaction, the reaction mechanism is relatively simple and is studied in detail using the mirror $({}^3\text{He},t)$ reaction for which many data exist.

The $(t,{}^3\text{He})$ experiments at the NSCL are currently beam-intensity limited ($\sim 10^7$ tritons per second). At the ISF, a gain of at least a factor of 100 can be achieved bringing the intensity close to that of stable beam experiments. Such increased capability is important especially since the body of experimental data available to validate the model input for stellar evolution scenario is still limited even for stable nuclei, especially beyond the pf -shell.

At high excitation energies, above the Gamow-Teller and dipole resonances, exotic collective modes are expected. A good example is the Isovector Spin Giant Monopole Resonance (IVSGMR). This resonance is a $2\hbar\omega$ excitation associated with zero angular momentum transfer but with spin transfer and can be regarded as an overtone of the Gamow-Teller resonance [Aue84,Ham00]. The measurement of its properties would provide crucial tests for microscopic-model calculations with effective nucleon-nucleon interactions at high excitation energies. Although its existence is proven [Zeg03], no systematic experimental information is available. Because of the high excitation energy of this resonance ($\sim 20\text{--}50\text{ MeV}$), the reaction takes place at high momentum transfer, strongly reducing the cross section for the IVSGMR transition. The momentum transfer can be strongly reduced if probes are chosen with large positive Q -values, such as $({}^{12}\text{B},{}^{12}\text{C})$ or $({}^{12}\text{N},{}^{12}\text{C})$ reactions. For the excitation of the IVSGMR, the use of these reactions carries the additional advantage that ${}^{12}\text{B}$ is strongly absorbed at the surface of the target nucleus and the cross section is enhanced compared to that for the weakly absorbed (n,p) probe. This is due to the nature of the radial transition density; it has a node close to the nuclear surface and interior, and exterior contributions cancel for a weakly absorbed probe [Aue89]. With the availability of high-intensity rare isotope beams of ${}^{12}\text{B}$ and ${}^{12}\text{N}$ ($\sim 10^{10}\text{ s}^{-1}$) one could perform detailed studies of this and other isovector collective excitations using a high-resolution spectrometer [Sak06].

2.8 Nuclear reactions and the properties of asymmetric nuclear matter

The ISF will make it possible to significantly constrain the Equation of State (EOS) of neutron-rich matter that governs many properties of neutron-rich nuclei and neutron stars. It will also allow the determination of thermal properties, such as the level densities and fission barriers of neutron-rich nuclei and facilitate extrapolations to neutron and fission decays that occur far from the valley of stability, as in the astrophysical r-process. In addition, the ISF will enable one to investigate the transport of neutrons and protons during collisions between nuclei with very different neutron and proton densities. Such investigations provide insight into the influence of isovector modes on collision dynamics and provide opportunities to explore the dynamical electric dipole γ -ray emission associated with these modes.

2.8.1 The equation of state of asymmetric matter

The nuclear equation of state is a fundamental property of nuclear matter. It describes the relationships between the energy, pressure, temperature, density, and isospin asymmetry $\delta = (\rho_n - \rho_p) / \rho$ for a nuclear system. The energy relationship can be divided into a contribution independent of the isospin asymmetry and a term that is proportional to the square of the asymmetry. This latter symmetry energy term is associated with the volume symmetry energy term in semi-empirical liquid drop mass formulae.

Ground state properties of nuclei and their isoscalar collective vibrations have constrained the nuclear EOS for isospin symmetric matter (equal neutron and proton densities) near saturation density. Measurements of collective flow and kaon production in energetic nucleus-nucleus collisions have extended the constraints on the EOS for symmetric matter to densities approaching five times saturation density [Dan02,Fuc01]. In contrast, the extrapolation of the EOS to neutron-rich matter, which is governed by the density dependence of the symmetry energy, has comparatively few experimental constraints [Dan02,Lat01].

Investigations that provide a better understanding of the density dependence of the symmetry energy term will also provide an improved understanding of masses [Mye98,Dan03], fission barriers [Kel06], energies of isovector collective vibrations [Lip82,Dan03], differences between the neutron and proton rms radii in neutron-rich nuclei [Hor01], and the role of isovector modes in fusion and strongly damped collisions.

The EOS of asymmetric matter governs many properties of neutron stars and of type II supernovae, as discussed in Sections 3.3 and 3.4. In such environments, macroscopic quantities of asymmetric nuclear matter exist at a wide range of densities. Experimental information about the EOS can help provide improved predictions for neutron star observables, such as stellar radii and moments of inertia, maximum masses [Lat01], crustal vibration frequencies [Wat06], and neutron star cooling rates [Yak04], which are currently investigated with ground-based and satellite observatories. Theoretical calculations of these observables depend very strongly on the density dependence of the symmetry-energy term in the EOS. Experimental data currently provide few constraints on the range of possible density dependencies.

In the following sections, we discuss observables that are sensitive to the density dependence of the symmetry energy, to the neutron and proton effective masses, and to the in-medium cross sections. Although more observables are available [Li04a,Bar05], the discussion is restricted to isospin diffusion [Shi03,Tsa04], neutron vs. proton emission and flow [Li00,Li02], and pion production [Li04b,Yon06]. By investigating these observables, one is able to probe a range of densities that can be controlled by selecting the incident energy and impact parameter of the collision. The ISF will allow probing of these quantities using nuclei far from stability with very large neutron-to-proton asymmetries that provide the greatest sensitivity to the symmetry energy.

2.8.1.1 Isospin diffusion

If two nuclei with different isospin asymmetries come into contact, neutrons and protons diffuse across the neck that joins them. This isospin diffusion will continue until the two nuclei separate or until the chemical potentials for neutrons and protons in both nuclei become equal. The rate of diffusion is influenced by the initial densities of neutrons and protons in the nuclei, the neutron and proton mean free paths, and the nucleon mean field potentials, to which the symmetry energy contributes. In the dynamical environment of a semicentral collision, nuclei with different isospin asymmetries can be brought into contact for a short time. The

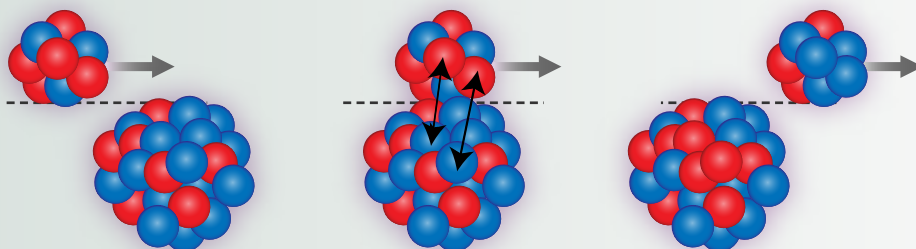
Equation of state for neutron-rich matter from nuclear reactions

The pressure that sustains neutron stars [Lat04] is strongly affected by the symmetry term in the nuclear equation of state. As pressure is proportional to the derivative of energy with respect to density, it depends both on the magnitude of the symmetry energy and on the variation of the symmetry energy with density, both of which can be explored in central nucleus-nucleus collision experiments. The effects of the symmetry energy can be isolated in such experiments by comparing results from collisions of nuclei with different proton-to-neutron asymmetries [Tsa01,Ghe04]. The wider an experimental proton-to-neutron asymmetry is accessible for similar nuclear masses, the greater is the potential significance of the results.

The symmetry energy gives rise to a different propagation of protons and neutrons through the nuclear medium. During nuclear collisions, the symmetry energy influences the rate

with which nucleons diffuse between the projectile and target in the reaction region, the relative magnitudes of neutron and proton yields, differences in the neutron and proton collective flows, and relative isotope abundance of emitted fragments [Li04a,Bar05]. Some of these observables have been investigated in intermediate energy reactions that create low-density nuclear matter during the expansion phase after the collisions. At the ISF, we will investigate the symmetry energy at densities above normal nuclear matter density and over a wider range of isotopes than is possible at existing facilities.

From the theoretical side, the reaction observables are modeled with semiclassical Boltzmann-type transport models and with statistical models. Observables used in confronting theory and experiment are explicitly constructed to minimize model uncertainties [Tsa04].



Schematic illustration of the collision between two nuclei with different numbers of protons and neutrons. The symmetry energy affects the rate at which protons flow relative to neutrons (the black lines) between the target and projectile regions during the collision [Shi03,Tsa04].

diffusion of the isospin asymmetry between these nuclei is sensitive to the symmetry energy in the neck, which can be at sub-saturation densities, $\rho/\rho_0 \sim 0.5-1$ [Shi03,Tsa04]. To isolate this diffusion, isospin diffusion investigations compare “mixed” collisions involving a neutron-rich nucleus and a neutron-deficient nucleus to “symmetric” collisions involving two neutron-deficient nuclei or two neutron-rich nuclei [Tsa04]. In the absence of diffusion, the isospin asymmetry of the projectile-like fragment after the collision should be independent of the original asymmetry of the target. In the limit of rapid diffusion, the isospin asymmetries of both target and projectile residues come to isospin equilibrium.

To isolate isospin diffusion effects, the isospin asymmetry δ of a projectile-like residue can be linearly rescaled to obtain an isospin transport ratio R_i [Tsa04] that has the limiting values of $R_i = 1$ for a neutron-rich projectile on a neutron-deficient target in the absence of isospin diffusion and $R_i \sim 0$ in the limit of isospin equilibrium. The cross-hatched region in Figure 2.31 shows experimental values for R_i measured for semiperipheral collisions of neutron-rich ^{124}Sn projectiles on a neutron-deficient ^{112}Sn target at incident energy of $E/A = 50$ MeV. The circles show corresponding values for R_i [Li06] calculated with the Boltzmann-Ühling-Uhlenbeck (BUU) equation at an impact parameter of $b \sim 6$ fm for symmetry energy terms

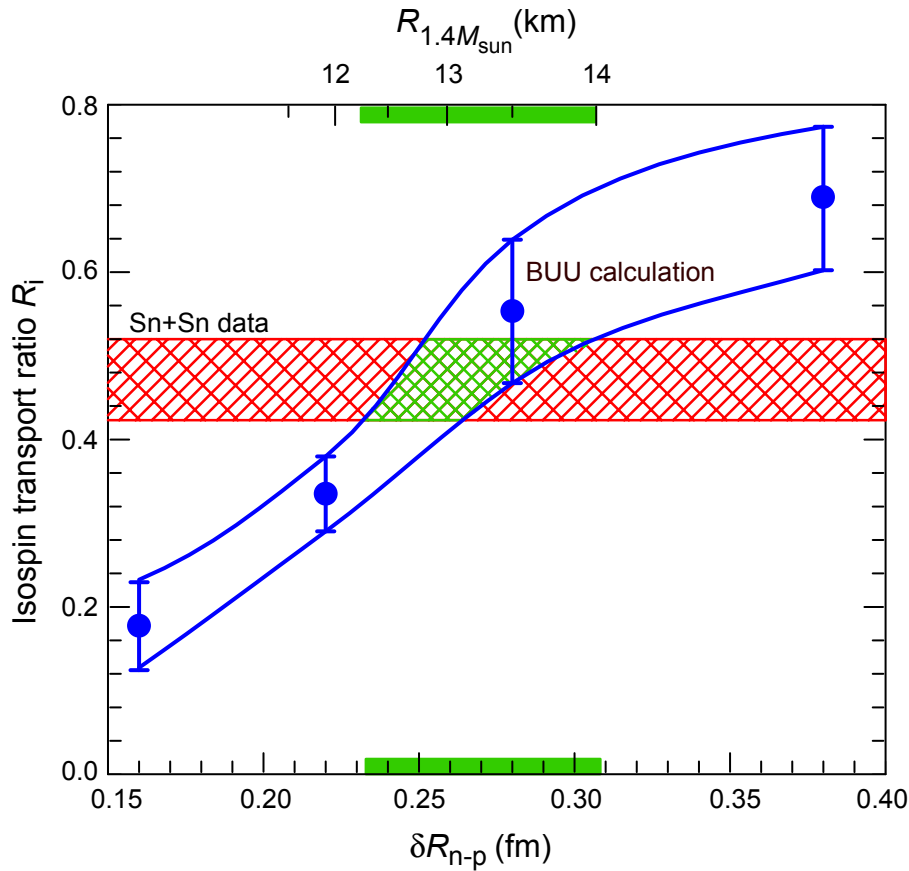


Figure 2.31: Comparison of measured [Tsa04] (red cross-hatched region) and calculated [Li06] (solid points) values for the isospin transport ratio R_i . The theoretical error bars represent the statistical uncertainties of the theoretical simulations. The top and bottom scale summarize model calculations [Li06] for radii of 1.4 solar mass neutron stars (top scale) and for the difference between neutron and proton radii of ^{208}Pb (bottom scale) for those symmetry energy functions that were used in calculating the isospin transport ratio.

with different density dependencies. These calculated results are arranged from left to right in the order of increasing stiffness of the density dependence. The intersection of theoretical and experimental values provides some indication of the range of density dependencies for which the data and calculations are consistent. The figure also summarizes model calculations [Li06], with the same symmetry energies, of the radius of 1.4 solar mass neutron stars (top scale) and of the difference between neutron and proton radii for ^{208}Pb (bottom scale). The solid green bars indicate the range of model expectations consistent with the results of the isospin diffusion measurements. If there were no model uncertainties in the calculations for any of these quantities, the diffusion measurements would provide constraints on the symmetry energy, neutron star radii, and neutron and proton radii for ^{208}Pb as indicated in the figure and in reference [Li06].

Known factors that limit the accuracy of these constraints include the accuracy of the measured transport ratio R_i and uncertainties concerning the isospin dependencies of the nucleon effective masses and medium modified nucleon-nucleon cross sections used in the calculations of the diffusion observable. The experimental accuracy can be improved by maximizing the asymmetry difference between projectile and target, which increases the number of transferred neutrons. Experiments with ^{132}Sn and ^{104}Sn beams will be feasible at the ISF, thereby increasing the available asymmetry gradient between the projectile and target nuclei by more than 50% compared to current capabilities and thus decreasing the systematic errors significantly.

Experiments with lighter rare isotope projectiles are needed to assess whether theoretical predictions for the diffusion rate through the surfaces of the nuclei scale properly with system size. Rare isotope nickel beams from the CCF range from ^{56}Ni and ^{68}Ni , corresponding to an increase of the available asymmetry gradient between the projectile and target nuclei by 35–55% over that available with stable nickel beams. The ISF will be able to extend this reach from ^{53}Ni to ^{74}Ni , an increase of more than 100% over that available with stable nickel beams.

2.8.1.2 Neutron and proton effective masses

Calculations for the isospin diffusion observable also display sensitivities to the assumed values for the neutron (m_n^*) and proton (m_p^*) effective masses, which reflect the nonlocality of the isovector mean field potential [Li06,Che05], and to the isospin dependent in-medium nucleon-nucleon cross sections [Li06] (see Section 2.8.1.3). Neutron and proton effective masses are identical in symmetric matter but may differ in neutron-rich systems; some calculations predict larger effective masses for neutrons than protons while others predict the opposite [Bar05]. In dense astrophysical systems, this mass difference influences the heat capacity of matter, the neutron and proton chemical potentials, and the phase space for scattering and decay processes in the nuclear medium.

Stringent constraints on the density dependence of the symmetry energy will therefore require measurements of other transport observables that can constrain the effective masses of protons and neutrons. To illustrate possible measurements, Figure 2.32 shows predictions for the ratio of the neutron and proton transverse momentum spectra for nucleons emitted with center-of-mass rapidities y_{cm} of $|y_{\text{cm}}/y_{\text{beam,cm}}| < 0.3$ in central $^{132}\text{Sn}+^{124}\text{Sn}$ collisions at 100 MeV/nucleon [Riz05]. (In the nonrelativistic limit, the rapidity of a particle is proportional to the component

Quantum transport theory for central nucleus-nucleus collisions

Semi-central nuclear reactions are violent processes. Along with the complexity of multiparticle dynamics in such reactions, quantum effects play a significant role in the dynamics. At low energies, this is due to the fact that the nucleon de-Broglie wavelength is comparable to nuclear dimensions. While the de-Broglie wavelength shortens as energy increases, the nucleon mean-free path decreases because of the diminishing role of the Pauli principle. When these two lengths become comparable, binary collisions become correlated, which seriously affects the reaction dynamics [Dan84b].

The quantal time-dependent Hartree-Fock method has been employed, with some success, to describe low-energy collective excitations. Application of that method to central nuclear reactions has been limited, though, because the method does not account for elementary nucleon-nucleon collisions. Those collisions have been included in the more advanced Kadanoff-Baym quantal approach [Kad62] but only in highly simplified reaction scenarios [Dan84a,Toh87] due to computational

difficulties. Therefore, at practically all energies to date, more tractable phenomenological semiclassical approaches [Ber88] have been the dominant theoretical tool to describe the dynamics of central nucleus-nucleus collisions.

The practical strategies first developed for the Kadanoff-Baym approach in the context of nuclear reactions have been adapted and expanded upon, though, in other areas of science, in particular in the areas of electron transport in semiconducting devices and in plasma physics [Pec04,Kne03]. With the dramatic increase in computational capabilities, it now becomes feasible to perform realistic three-dimensional quantum transport calculations with elementary collisions of the Kadanoff-Baym type for nuclear reactions. Such calculations will have more predictive power and provide stronger connections to theories for nuclear structure and for nuclear collective excitations. Investigations of reactions with large neutron-to-proton asymmetries at the ISF will greatly benefit from such improved theories.

of its velocity parallel to the beam.) Calculations for $m_p^* > m_n^*$ are compared to those for $m_p^* < m_n^*$ in each panel; the left and right panels show calculations assuming weak and strong density dependencies of the symmetry energy, respectively [Riz05]. Similar information may be obtained by comparing ratios of ^3H and ^3He spectra [Che04]. Spectral ratios like this can be accurately measured with the ISF and used to investigate the effective neutron and proton masses. The availability of ISF beams will also permit measurements of other observables such as transverse and elliptical flow (not shown) that also display promising sensitivities to the neutron and proton effective masses as well as to the symmetry energy [Riz05,Bar05,Li04a,Che04]. Currently these experiments are only feasible with stable beams, which limits their sensitivities.

Complementary information about the neutron and proton effective masses can be obtained from the proton optical potentials determined by the elastic scattering of rare isotope beam nuclei from a hydrogen target. Just as the momentum dependencies of the isoscalar terms provide a constraint on the effective mass of nucleons in symmetric matter, the momentum dependencies of the isovector terms provide constraints on the difference between proton and neutron effective masses [Bar05]. For such studies, elastic scattering measurements at energies of 30 – 180 MeV/nucleon and beam intensities of 10^{5}s^{-1} are necessary. With the ISF, comparisons of elastic scattering with ^{35}Ca and ^{52}Ca or ^{53}Ni and ^{74}Ni will become feasible, providing a high degree of sensitivity to the energy dependence of the isovector part of the optical potential and, consequently, to the difference between neutron and proton effective masses near saturation density.

2.8.1.3 In-medium nucleon-nucleon cross sections

Both the nuclear mean field and the cross sections for scattering in the nuclear medium by the residual interaction are fundamentally related to the nucleon-nucleon interaction. Just as extrapolations of the mean field to neutron-rich matter have significant uncertainties, so do extrapolations of the in-medium cross sections. Indeed, a unified theoretical understanding of in-medium cross sections, effective masses, and the symmetry energy constitutes an important scientific

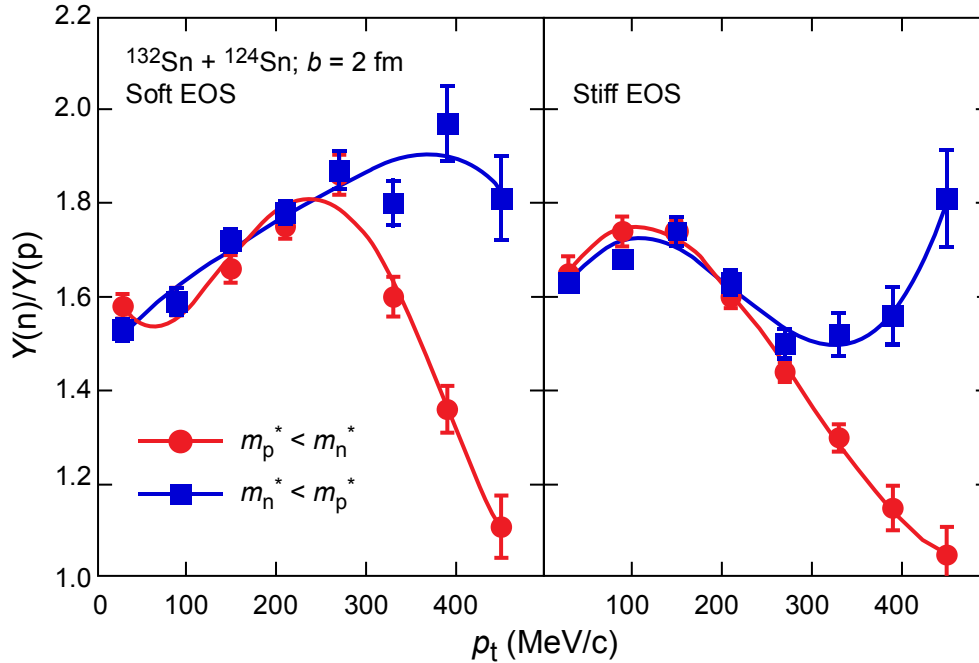


Figure 2.32: Ratio of neutron and proton spectra calculated for central $^{132}\text{Sn}+^{124}\text{Sn}$ collisions utilizing soft (left panel) and stiff symmetry energies (right panel). The red and blue points indicate calculations assuming $m_p^* < m_n^*$ and $m_p^* > m_n^*$, respectively. The lines are drawn to guide the eye. Adapted from [Riz05].

objective [Bro90,Fri05b] that could be greatly furthered by obtaining experimental constraints on all three quantities using beams of the ISF.

The isospin dependence of in-medium nucleon-nucleon cross sections in asymmetric matter has so far received little attention. In free space, σ_{np}/σ_{pp} decreases from about 2.5 to 1.5 as the energy of the incident nucleon is increased from 50 MeV to 200 MeV. Similar to the situation with the effective masses, some calculations predict σ_{np}/σ_{pp} inside the nuclear medium to decrease with density [Sam06], while others predict opposite trends [Qin00]. Theoretical studies have recently revealed a strong sensitivity of the rapidity dependence of the asymmetry of light particles to the isospin dependence of the in-medium cross sections [Li05]. Figure 2.33 shows the predictions calculated for a ^{100}Zn beam incident on a ^{40}Ca target. A factor of three difference in the asymmetry of free nucleons $(Y(n)-Y(p))/(Y(n)+Y(p))$ is predicted at target rapidity $(y/y_{\text{beam}})_{\text{cm}} = -1$ for the ^{100}Zn beam, depending on assumptions about the in-medium cross sections. In addition to this sensitivity to cross sections, there is sensitivity to the symmetry energy, shown in Figure 2.33, but that occurs primarily at beam rapidity $(y/y_{\text{beam}})_{\text{cm}} = 1$ in these reactions, well away from the domain where the cross section sensitivity exists.

A ^{100}Zn beam is not feasible at any rare isotope facility, but precise measures of the isospin dependent in-medium cross sections can be obtained at the ISF by comparing systems in which the projectile mass remains constant, e.g., $^{100}\text{Zr}+^{40}\text{Ca}$ and $^{100}\text{Ag}+^{40}\text{Ca}$, as well as by comparing systems in which the number of protons remains constant, e.g., $^{107}\text{Sn}+^{40}\text{Ca}$ and $^{127}\text{Sn}+^{40}\text{Ca}$. On the basis of scaling arguments, one expects somewhat more than a factor of 1.5 difference in the asymmetry of free nucleons at target rapidity for such beams, depending on assumptions about

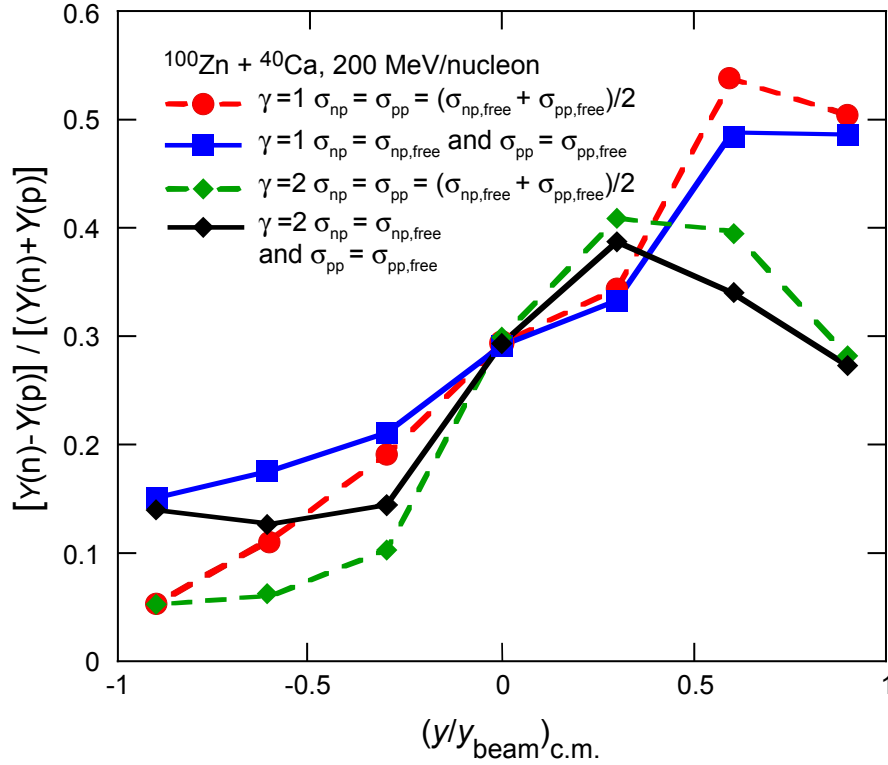


Figure 2.33: Asymmetry of nucleons $(Y(n)-Y(p))/(Y(n)+Y(p))$ in central $^{100}\text{Zn}+^{40}\text{Ca}$ collisions as a function of rapidity for different assumptions about the symmetry energy (soft: $\gamma = 1$ and stiff: $\gamma = 2$) and in-medium cross sections. The red and green points correspond to $\sigma_{np} = \sigma_{pp}$. The blue and black points assume cross sections equal their values in free space. Adapted from [Li05].

the in-medium cross sections. Thus, the mean free path for transmission of target neutrons and protons through the projectile can be measured as a function of the numbers of projectile and target nucleons, and the isospin dependence of the in-medium cross sections can be determined. At the present time, these measurements are feasible only for stable beam and stable target combinations that offer only limited sensitivity.

2.8.1.4 Pion production

Present constraints on the density dependence of the symmetry energy are least stringent at high densities $\rho > \rho_0$. Investigations in that region, which cannot be probed by structure studies, may provide important insights into the role of various two-body [Die03] and three-body [Zuo02] contributions to the symmetry energy. Investigations of pion production in nucleus-nucleus collisions provide unique opportunities to establish meaningful constraints on the symmetry energy at these densities. Calculations predict that the relative densities of neutrons and protons in the dense interior of a central nucleus-nucleus collision reflect the pressure of the symmetry energy, which is greater for a stiffer symmetry energy term with stronger density dependence [Li04b]. The left side of Figure 2.34 shows the ratio of the neutron/proton central densities at $r_{\text{cm}} = 0$ for $^{132}\text{Sn}+^{124}\text{Sn}$ collisions at 200 MeV/nucleon. The ratio decreases with time for a stiff symmetry energy, while remaining roughly constant for a soft symmetry energy. The larger ρ_n/ρ_p for the soft EOS results in a larger $Y(\pi^-)/Y(\pi^+)$ yield ratio [Li04b] as shown in the right

panel. Measurement of pions produced in $^{132}\text{Sn}+^{124}\text{Sn}$ and $^{105}\text{Sn}+^{112}\text{Sn}$ collisions at 182 MeV/nucleon can be performed with the ISF. In particular, the double ratio, $Y(\pi^-; ^{132}\text{Sn}+^{124}\text{Sn}) \cdot Y(\pi^+; ^{112}\text{Sn}+^{112}\text{Sn}) / \{Y(\pi^+; ^{132}\text{Sn}+^{124}\text{Sn}) \cdot Y(\pi^-; ^{112}\text{Sn}+^{112}\text{Sn})\}$, [Yon06] can be measured. Calculations suggest that this double ratio can distinguish between Coulomb effects and the density dependence of the symmetry energy [Yon06], while reducing uncertainties associated with the relative detection efficiencies for positive and negative pions.

The most suitable device for measuring the pion yields would be a large solid angle magnetic device such as a Time Projection Chamber (TPC). The highest sensitivity of pion production to the symmetry energy appears to occur at energies smaller than 500 MeV/nucleon below the free nucleon-nucleon production threshold [Qin05].

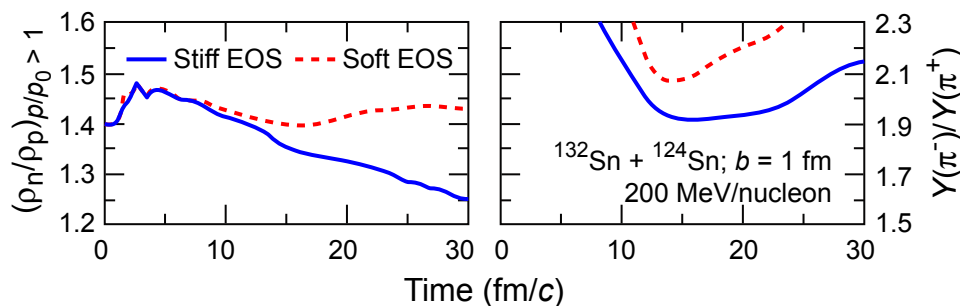


Figure 2.34: The left panel indicates the calculated ratio of neutron and proton central densities; the right panel indicates the calculated ratio of negative and positive pion yields as function of time during a central $^{132}\text{Sn}+^{124}\text{Sn}$ collision. The solid and dashed lines indicate the calculations using stiff and soft symmetry energy terms, respectively. Adapted from [Li04b].

2.8.2 Level densities and the mixed phase of nuclear matter

At subsaturation densities, finite temperatures, and a wide range of isospin asymmetries, nuclear matter exhibits characteristics of a mixed phase in astrophysical environments and in nuclear reactions. At densities of $\rho < \rho_s/3$, the mixed phase consists of separated nuclei, with the gaseous phase dominated by nucleons and the liquid phase by medium to heavy nuclei. The interplay between Coulomb and symmetry free energies limits the sizes of nuclei in this mixed phase. This limitation and the two-component (neutron and proton) nature of the nuclear fluid make the nuclear liquid-gas phase transition fundamentally different from that of neutral macroscopic fluids.

The isotopic distribution and heat capacities of nuclei in this mixed phase govern important properties of the matter in the vicinity of the shock front in a type II supernova, matter found in the inner crust of a neutron star and decompressed neutron star matter released during neutron star mergers (see also Section 3.3.2). While matter in the inner crust of a neutron star and that initially produced in neutron star mergers is more asymmetric than can be explored in laboratory experiments, matter in the vicinity of the shock front of a type II supernova is similar in many respects to that produced in multi-fragmentation reactions.

In such stellar processes, theoretical descriptions of a neutron-rich mixed phase at equilibrium and at densities of $\rho < \rho_s/3$ are very sensitive to uncertainties in the binding energies and level densities of very neutron-rich nuclei. In this section, we

A time projection chamber for studying the nuclear equation of state

Rare isotope beams provide an exciting opportunity to place experimental constraints on the density dependence of the asymmetry of the nuclear equation of state. Calculations predict that measurements of the isospin dependence of π^+ and π^- production in central heavy ion collisions and comparisons of neutron and proton flow observables will be particularly important. These observables display sensitivity to the density dependence of the asymmetry term at above-normal densities.

A time projection chamber (TPC) is the logical device for measuring of the pionic observables because a magnetic field allows the straightforward observation and differentiation of π^+ and π^- production. A TPC can also readily measure directed flow and elliptic flow for protons and light nuclei; neutron flow can be measured using external neutron detectors. In addition, the capability to isotopically identify light particles up to lithium will aid in the determination of the excitation energy and angular momenta in fissioning systems.

A TPC can also be run as an active target with hydrogen or isobutane as a counter gas. In such applications, the range of the beam particle in the gas can be directly measured in the TPC, allowing corrections for the energy loss of the incident ions on an event-by-event basis.

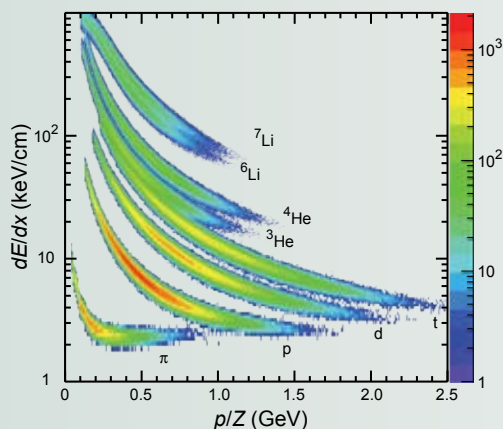


Figure A: A simulated particle identification spectrum showing the clear separation of charged particles from pions to ${}^7\text{Li}$ possible in a TPC.

Particle identification in a TPC is accomplished by measuring the specific energy loss combined with the momentum of each track. A simulated particle identification spectrum for pions, hydrogen isotopes, helium isotopes, and lithium isotopes is shown in Figure A, based on the resolution and acceptance of the STAR TPC in operation at RHIC. The various particles are clearly separated.

As indicated schematically in Figure B, the TPC magnet could have an open dipole design allowing multiple external detectors. For example, the TPC could be augmented with a forward multiple sampling ion chamber (MUSIC), time-of-flight walls (TOF), and neutron detectors (n). The MUSIC detector allows the study of forward-going heavy products from reactions in inverse-kinematics. The TOF detectors increase the range of particles that can be detected. The neutron detectors would allow the measurement of neutron flow and proton/neutron differential flow in an experiment that uses the TPC to determine the reaction plane and event centrality.

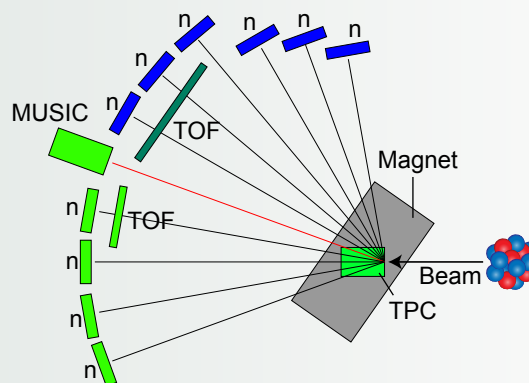


Figure B: The schematic layout of a TPC system, including the positions of discrete neutron detectors, the MUSIC detector for detecting projectile-like fragments, and the time-of-flight detectors for detecting light charged particles. In this drawing, details such as the exact positioning of detectors, vacuum chambers connecting the TPC and the MUSIC chambers or helium bags reducing the energy loss in flight, are not shown.

discuss level density measurements. (Nuclear binding energy measurements are discussed in Section 2.5.2.1.) We also discuss multi-fragmentation measurements that could test whether current theoretical models accurately describe neutron-rich low-density matter produced in the laboratory and whether such studies can be extrapolated to stellar environments.

Level density investigations have other motivations as well. Uncertainties in level densities strongly influence calculations of the production of unstable nuclei, their abundances in equilibrium environments, and their decays. These uncertainties influence both processes that occur in the laboratory and those that occur in stellar environments. Such uncertainties could be reduced significantly by experiments at the ISF.

For multifragmentation, supernovae, and neutron star mergers, the dependence of the level densities on the isospin asymmetry is needed for a range of temperatures up to the charge and asymmetry dependent “limiting temperature,” $T \sim 5\text{--}10$ MeV, beyond which nuclei play a negligible role [Lev85]. The asymmetry dependence of level densities is also needed for r-process nucleosynthesis. For this application, one mainly needs level densities at low excitation energies corresponding to temperatures of $T < 1$ MeV.

The extrapolation of the isospin dependence of the level density towards large neutron excess can be achieved by measuring the neutron spectra of a selected set of nuclei, such as ^{31}Na , ^{44}S , ^{72}Ni , ^{82}Ge , and ^{132}Sn , excited to moderate temperatures. Neutron spectra from the fusion of rare isotope beams with intensities of 10^5 s^{-1} or more on light nuclei (such as p, d, and ^{12}C) can provide level densities at $T < 1$ MeV. These measurements can be performed in inverse kinematics with reaccelerated rare isotope beams using a recoil spectrometer and an efficient array of neutron detectors. At higher temperatures, the charged particle decay branches can be nonnegligible. Fast beams and efficient charged particle detection capabilities will be necessary to perform these experiments.

Above a limiting temperature of 5–8 MeV, nuclei have no metastable levels but decay by multifragmentation. Calculations predict this limiting temperature to depend on the charge and asymmetry of the nucleus [Lev85], but the asymmetry dependence has not been confirmed. Measurements of the multi-fragmentation of ^{184}Pb and ^{211}Pb and ^{104}Sn and ^{132}Sn projectiles, at incident energies of about 180 MeV/nucleon, would allow an exploration of this issue. It would provide the data needed to determine whether current theories describe low-density neutron-rich matter formed in the laboratory. It would clarify whether extrapolations [Bot05] from such systems can be accurately made to the fragment abundances and EOS of matter in the vicinity of the shock front of a type II supernova.

2.8.3 Low energy collision dynamics

Multiparticle transfer processes in strongly damped binary collisions have been shown to be an important mechanism for producing neutron-rich rare isotopes [Cor02]. Such mechanisms would not be used for producing the secondary beams at the ISF but might be effective for producing excited rare isotopes in the experimental vaults for spectroscopy studies. To effectively use such mechanisms to produce specific isotopes, it is important to understand how their cross sections depend on the isospin asymmetry and the mass and structure of the rare isotope projectile. Theoretical models describe the widths of the charge and mass distributions as a function of the dissipated energy rather well for reactions induced by stable beams. In such models, the principle mechanism for dissipating the initial relative motion of projectile and target is the exchange of nucleons between the two nuclei; however, the mean values of the charge distributions follow the potential energy surface of the combined system more closely than such models predict [Pla88].

For reactions with stable beams, e.g., $^{58}\text{Ni}+^{238}\text{U}$ or $^{64}\text{Ni}+^{238}\text{U}$, where such effects have been observed [Pla88], the initial projectile and target charges of the combined system are close to the minimum in the potential surface; thus the shift in charge due to the potential energy should be small. With rare isotope beams, one can choose systems where the initial charges place the system far from the potential energy

minimum. For such systems, much larger shifts in charge will be expected, allowing this issue to be investigated quantitatively. For this purpose, it would be very instructive to compare $^{36}\text{Ca}+^{238}\text{U}$ to $^{51}\text{Ca}+^{238}\text{U}$ collisions or $^{54}\text{Ni}+^{238}\text{U}$ to $^{72}\text{Ni}+^{238}\text{U}$ collisions at energies of about 9 MeV/nucleon. These experiments would provide information concerning the evolution of the mean values and the widths of the charge, mass, and isotopic distributions as functions of the dissipated energy. Subsequent experiments with beams such as $^{21-23}\text{O}$, $^{26-28}\text{Ne}$, $^{26-31}\text{Na}$, $^{28-32}\text{Mg}$, $^{34-36}\text{Si}$, and $^{44-46}\text{Ar}$, could probe the extent to which the yields of the most neutron-rich isotopes produced depend on whether the neutron or proton shells in these nuclei are closed.

Fusion with rare isotopes provides a unique opportunity to probe the damping of the initial relative motion of projectile and target into thermal excitation. When the isospin asymmetries of the projectile and of the target are very different, calculations predict the excitation of dynamical dipole oscillations of the nucleons along the beam axis [Bar01]. The dynamical contribution to the electric dipole strength can be isolated by comparing the γ -ray emission following fusion of projectiles and targets with different isospin asymmetry to that involving projectiles and targets with similar asymmetry. Measurements of such collisions can illuminate how the giant dipole resonance influences isospin transport during the fusion process. Varying the incident energy may also allow investigations of the damping of dynamical dipole oscillations as a function of the temperature.

Recent investigations have reported that dynamical dipole emission may contribute up to 10–15% of the electric dipole strength in collisions of moderately asymmetric systems [Pie03]. Calculations predict the dipole strength to increase with energy from the barrier to the Fermi energy. Comparisons of $^9\text{Be}+^{100}\text{Ru}$ collisions to $^9\text{C}+^{100}\text{Mo}$ collisions at incident energies of $E/A = 6-30$ MeV would provide an excellent test of these ideas. For the $^9\text{C}+^{100}\text{Mo}$ system, for example, with $\delta_{\text{pro}} \sim -0.33$ and $\delta_{\text{targ}} \sim 0.16$, the dipole moment is large and the dynamical dipole emission should be strong. For the $^9\text{Be}+^{100}\text{Ru}$ system with $\delta_{\text{pro}} \sim \delta_{\text{targ}} \sim 0.11$, the dynamical dipole moment is small and dynamical dipole emission should be weak. The lower part of this incident energy domain would be performed with reaccelerated beams and the upper part with fast fragmentation beams.

2.8.4 Fission

Fission barriers and their consequent fission probabilities reflect a balance between the long-range Coulomb force and the surface tension. The fission probabilities for rare isotopes differ from those near the valley of β stability; these differences depend on the evolution of ground state and fission saddle point binding energies with both charge and mass. Because the relative contributions from surface and bulk energy terms differ for ground state and fission barrier masses, fission barriers test nuclear effective interactions differently than do the ground state masses and provide constraints on nuclear effective interactions that are independent of those provided by ground state masses.

The ability to predict fission barriers for rare isotopes is a research objective that is also important for r-process nucleosynthesis predictions. Simple liquid drop model considerations lead one to expect fission to be an increasingly dominant decay mode for rare isotopes with $Z^2 > 35A$; thus, fission should prevent possible astrophysical r-process pathways from going beyond $Z \sim 125$. The final r-process

abundance pattern may be strongly affected by fission cycling, in which high-fissile heavy nuclei provide fresh seed nuclei that initiate a new r-process cycle. Beta-delayed and neutrino-induced fission may play a role in limiting the r-process yields of thorium and uranium isotopes that are interesting cosmological chronometers. Furthermore, neutrino-induced fission during freeze-out has been proposed to partially correct the abundance trough observed around $A = 110\text{--}120$. To determine the role of these different fission aspects in the r-process, measurements of fission barriers and fission fragment distributions over a wide range of neutron-rich nuclei are crucial. However, most of these fissionable nuclei lie outside the domain of direct measurement and require an accurate extrapolation of measurements closer to the valley of stability.

Measurements of fission barriers with rare isotope beams at the ISF can provide an empirical basis for improved extrapolations of ground state and fission saddle point binding energies away from the valley of stability. Predicted intensities of neutron-deficient uranium isotopes are sufficient for measurements of fission barriers out to the proton dripline. If the barriers were merely measured down to ^{217}U (the lightest known isotope), this would more than double the isotopic range used to determine the asymmetry dependence of the fission barrier height and would constrain extrapolations towards the r-process much more stringently [Kel06].

To extract the fission barrier, measurements of fission decay are needed for a range of excitation energies from below to above the fission barrier. Rare isotopes can be induced to fission mainly by the Coulomb force using heavy targets or by the strong force using light targets. In every experiment, a range of excitation energies will be deposited in these projectiles reflecting a folding of the impact parameter range with the excitation energy distribution at each impact parameter.

The fast rare isotope beams at the ISF offer the advantage of inverse kinematics, which enables clean mass and charge identification with very high geometric efficiency. In addition, because thicker targets are feasible with fast beams, the required intensities of 10^4 s^{-1} are lower than those (10^6 s^{-1}) required for reaccelerated beams. The resulting accurate fission fragment mass and charge distributions enable one to assess distortions in the fragment mass distributions due to pairing and shell effects [Ben02].

Additional detectors capable of measuring charged particles emitted at larger angles, for example, a Time Projection Chamber (TPC) or a large solid angle silicon array, can make the detection efficiency for charged particles close to 100%. These large angle detectors will primarily be used for the detection of relatively low Z ($Z < 7$) fragments. The addition of large fast neutron detectors similar to MoNA can provide complementary information about the excitation energy of the fissioning system with efficiencies approaching 70%.

Such an efficient detection apparatus would provide more precise information about the excitation energies and angular momenta of fissioning systems than have been obtained to date. Even higher precision can be achieved if one uses a solid hydrogen target and measures the quasi-elastically scattered protons that recoil at forward angles after the collision, and thereby determines the excitation energy. Only small angular momenta can be expected for the fissionable systems that are produced, reducing the sensitivities of theoretical calculations for the fission decays to uncertainties in the angular momenta of these systems. In effect, one can control the excitation energy so as to measure the fission barrier.

Precise fission measurements can also be conducted by fusing fast beams or reaccelerated rare isotope beams on atoms within an active gas target. In this situation, one does not measure the charge of the fission fragments, but the excitation energy can be extracted by tracking the vertex for the nuclear interaction and correcting for the energy lost within the target.

The large range of nuclei where the fission barriers are unknown and that can be experimentally studied at the ISF are shown in Figure 2.35. Measurements near uranium have the strongest impact on the cosmo-chronometers [Kra04,Pha06], while the lighter nuclei provide unique information about deformation, pairing, and shell effects.

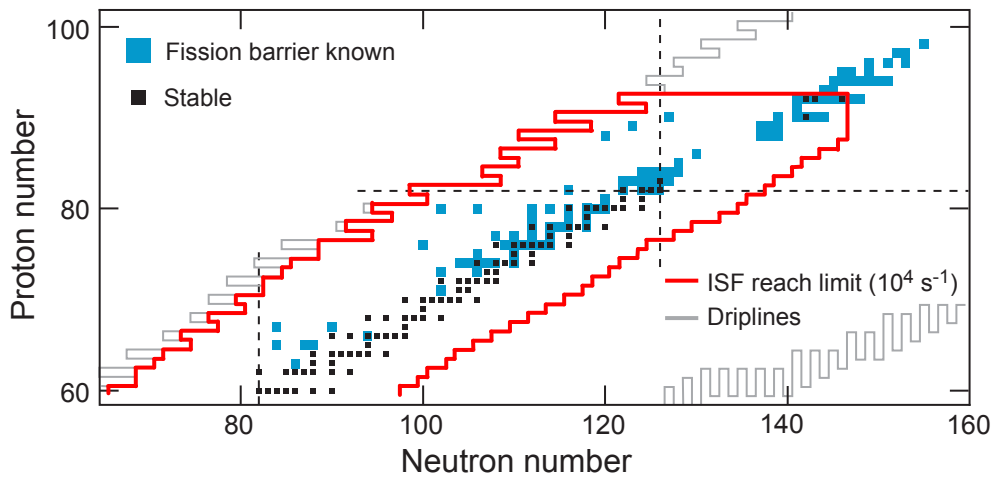


Figure 2.35: The red line bounds the region of nuclei for which fission barriers could be measured using rare isotope beams from the ISF. Stable nuclei are indicated in black. Nuclei with known fission barriers [Dah82,Pha06] are indicated in blue.

3. Nuclear astrophysics

Nuclear reactions in stars and stellar explosions generate energy and are responsible for the ongoing synthesis of the elements. They are, therefore, at the heart of many astrophysical phenomena, such as stars, novae, supernovae, and X-ray bursts. Nuclear physics determines the signatures of isotopic and elemental abundances found in the spectra of these objects, in characteristic γ radiation from nuclear decay, or in the composition of meteorites and presolar grains. The field of nuclear astrophysics ties together nuclear and particle physics on the microscopic scale with the physics of stars, galaxies, and the cosmos in a broad interdisciplinary approach. While some of the major open questions of the field have been asked for decades, many others are new, mostly posed by advances in astronomical observations. An example is the discovery of r-process abundance patterns in stars through high-resolution spectroscopic observations with ground-based observatories (for example Keck and VLT) as well as the Hubble Space Telescope. More of these stars are being discovered through extensive surveys, such as the Hamburg/ESO R-process Enhanced Star Survey (HERES) or the ongoing Sloan Extension for Galactic Understanding and Exploration (SEGUE). Superbursts, absorption lines, and ms-oscillations are new phenomena discovered in X-ray bursts by the Chandra X-ray observatory, XMM-Newton, the Rossi X-ray Timing Explorer (RXTE), and Beppo-SAX. Many, if not most of the current open questions of the field require understanding of the physics of unstable nuclei. Though pioneering advances have been made, progress has been hampered by limited beam intensities at current rare isotope beam facilities. The ISF will address this problem and contribute a critical piece of science that together with progress in observations and theory will lead to a major advance in our understanding of the cosmos.

The open questions of the field that most urgently require a better understanding of the physics of unstable nuclei can be broadly organized under three major themes: the origin of the heavy elements, stellar explosions, and neutron stars.

3.1 The origin of the heavy elements

3.1.1 The rapid neutron capture process

The rapid neutron capture process (r-process) is one of the major nucleosynthesis processes in nature [Cow91,Qia03]. It produces roughly half of the nuclei found in nature beyond the iron region. While many elements have contributions from multiple processes, there are some that are chiefly produced by the r-process, such as xenon, gold, platinum, and uranium. The fact that the site of the r-process and, therefore, its conditions and reaction sequences are still not known with certainty is one of the major open questions in science. The question of the origin of the heavy elements has been identified in the National Academies report “Connecting Quarks with the Cosmos” as one of the 11 science questions for the twenty-first century at the interface of particle- and astrophysics [BPA03].

3.1.1.1 r-process models

A number of theoretical models have been proposed as sites for the r-process. These include the neutrino-driven wind off a forming neutron star in core-collapse supernovae [Woo92,Tak94], jets in core-collapse supernovae [Cam01], neutron star mergers [Lat77,Fre99], and outflows from rapidly accreting disks in collapsars

powering γ -ray bursts [Sur05]. All these models have been shown to exhibit a rapid neutron capture process within the respective parameter space. However, they all fall short of producing sufficient amounts of r-process elements in the proportions that would explain abundance observations. Clearly more theoretical work is needed to overcome these issues. In the end, however, experimental constraints are needed to guide theory. This requires astronomical observations and a thorough understanding of the nuclear physics underlying the r-process [Kra93].

Overview of astrophysical processes to be investigated at the ISF

A variety of nuclear processes are responsible for the origin of the elements and for powering stars and stellar explosions. While some important processes such as the fusion reactions in stars or the slow neutron capture process (s-process) proceed with mostly stable nuclei, there are many processes that involve predominantly unstable nuclei. These processes will be the main focus of nuclear astrophysical research at the ISF.

The figure provides a schematic overview of the range of nuclei participating in each process and also indicates the extensive reach of the facility for rare isotope experiments. Clearly, most of the nuclei participating in all of the astrophysical processes can be studied at the proposed facility. Critical processes for the origin of the elements include the rapid neutron capture process (r-process) that produced about half of the nuclei beyond the iron region and was the sole source of uranium and thorium. The p-process was responsible for producing about thirty-five neutron deficient stable isotopes that cannot be produced by neutron capture reactions.

The rapid proton capture process (rp-process) plays an important part in stellar explosions and can, in principle, occur in a number of scenarios. A mild form of the rp-process that reaches nuclei up to $A \sim 40$ is thought to occur in nova explosions where its products can be observed in the ejecta. A full rp-process, the path displayed in the figure below, is the main energy

source of X-ray bursts. Recently it has been found that an rp-process can also occur in core-collapse supernovae, where it is accelerated by neutron-induced reactions. In this scenario neutrons are generated by neutrino interactions with protons. This vp-process might even proceed beyond the indicated mass range, and might contribute to galactic nucleosynthesis in a significant way.

X-ray bursts that are powered by the rp-process are thought to occur on the surface of neutron stars. Most of the ashes are not ejected by the explosion but are incorporated into the neutron star crust. The ashes then undergo a series of nuclear reactions, mostly electron captures and density-induced fusion reactions. These neutron star crust processes drive the composition, step by step, to the neutron dripline and are an important source of crustal heating.

Electron capture reactions also play an important role in supernova explosions. The figure indicates the region of nuclei that are important in core-collapse supernovae, where electron capture rates affect the dynamics of the collapse. Electron capture reactions on a small subset of stable and unstable nuclei near iron and nickel are also important for Type Ia supernovae, where the electron capture rates affect nucleosynthesis and, possibly, the explosive burning.

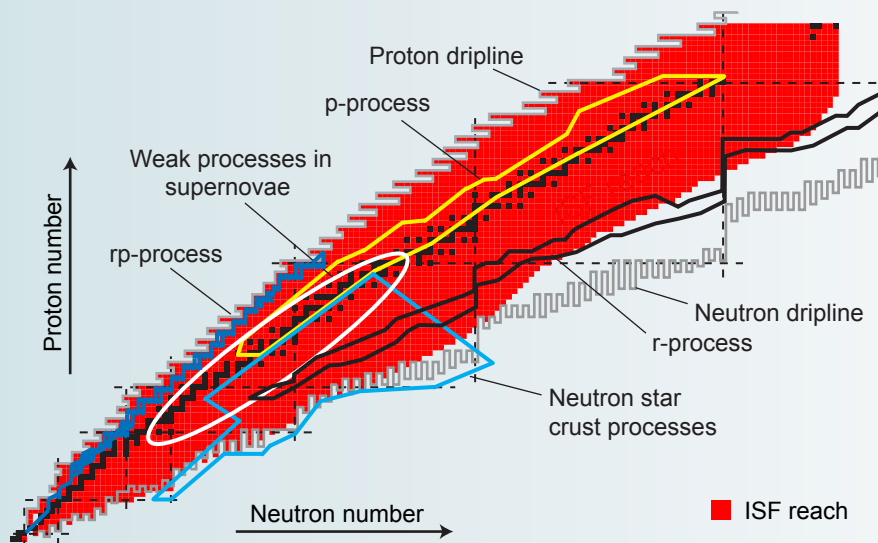


Chart of nuclei with a schematic overview of the major nuclear processes operating in the universe that involve predominantly unstable nuclei. Not shown, for example, are the stellar burning paths or the s-process, which are equally important but involve predominantly stable nuclei. The red area indicates the range of isotopes that will be available at the ISF.

3.1.1.2 Precision observations of r-process abundances

There has been tremendous progress on the observational side. Advances in our understanding of the s-process (mainly from measurements of neutron capture cross sections [Kae99] and s-process modeling) make it possible to extract the r-process contribution from the observed solar system abundances with increasing precision. At the same time, the discovery of detailed r-process abundance patterns in some rare, extremely metal-poor halo stars has tremendously broadened the available observational information on the r-process (see [Sne03] as an example and [Tru02] for a review). The material that these stars illuminate in their photosphere has been polluted by a single, or at most very few, r-process events. Provided the nuclear physics is at hand, this opens the door for comparing r-process model predictions with individual r-process events. In addition, the observations open a window to study the history of the operation of the r-process in our Galaxy. First results indicate that there might be two r-processes contributing to the solar system abundances [Pfe01, Tra04]. This is in line with evidence from meteoritic data on the decay products of radioactive r-process isotopes [Qia98]. In the coming years, ongoing surveys such as SEGUE will lead to the discovery of many more such r-process enhanced metal poor stars, which will allow one to study the behavior of the astrophysical events that created the r-process nuclei in detail.

3.1.1.3 Nuclear physics of the r-process

Similar progress is needed in our understanding of the nuclear physics of the r-process. Figure 3.1 demonstrates the sensitivity of r-process model calculations

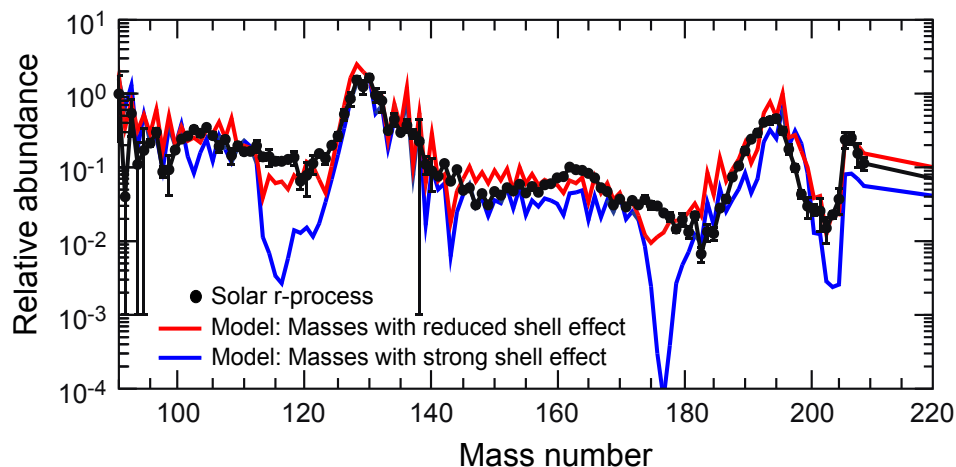
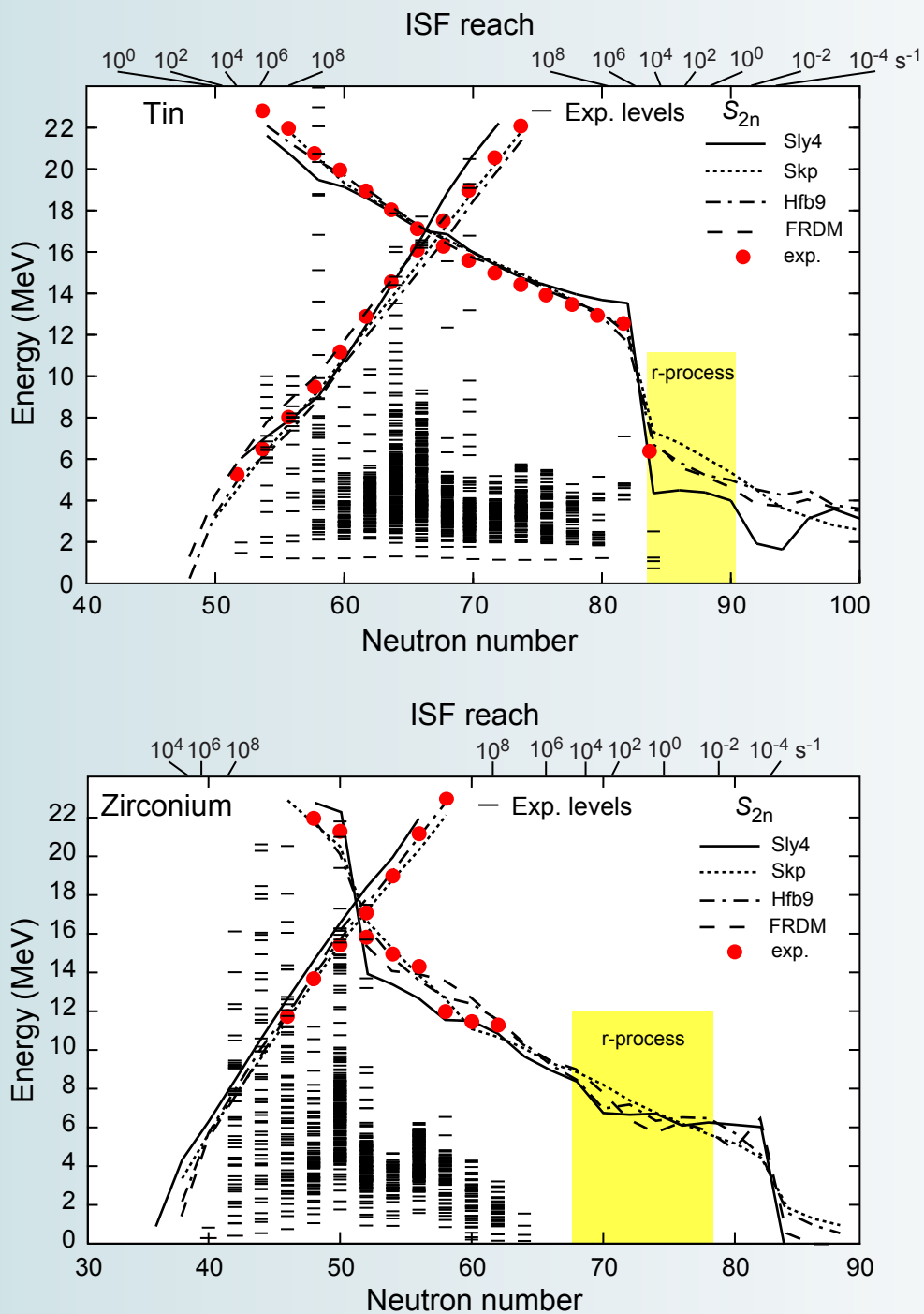


Figure 3.1: Influence of shell structure on r-process calculations. The black dots represent the contribution of the r-process to the observed isotopic abundances of the chemical elements in the solar system as a function of the mass number (“solar r-process”). This distribution is obtained by subtracting calculated contributions from the s-process and other, less important, processes from the observed solar abundance distribution. The abundances are given in usual units relative to one million silicon nuclei. In addition, we show the calculated abundances produced in two r-process models that only differ in the theoretical model used to predict the nuclear masses. One mass model shows pronounced shell closures, while the other has a reduced shell closure effect that might occur for very neutron-rich nuclei. All the relevant masses for the model discrepancies below $A \sim 130$ are either within reach at the ISF or can be extrapolated reliably. This will remove the nuclear physics uncertainty in r-process models so that the remaining differences to observations can be interpreted in terms of the nature of the r-process and its astrophysical site. Adapted from [Che95, Kra06].

Theoretical reach toward the dripline



The figures illustrate our present knowledge of even- N tin (top) and zirconium (bottom) isotopes together with the region of interest for the r -process. Observed energy levels for even-even nuclei are shown with the first excited states being 2^+ . The relatively high 2^+ energies at $N = 50$ and $N = 56$ for zirconium and $N = 82$ for tin are indications of the shell gaps at these magic numbers. Measured two-nucleon separation energies are indicated as red circles with two-proton separation energies extending up from the proton dripline on the left and the two-neutron separation energies going down to the neutron dripline on the right. The two-nucleon separation energies predicted by three different Skyrme interaction models [Dob04,Gor06] and the Finite-Range Droplet Model (FRDM) [Mol95] are shown by the lines. The source of the deviation for Sly4 from experiment near the magic numbers is partly understood and might be corrected by including ground-state correlations. For the regions of interest in the r -process, the predictions show divergences related to uncertainties in shape transitions and pairing energies that can be confronted by comparison to new experimental data from the ISF.

on the underlying nuclear physics assumptions. The critical nuclear physics are masses and decay properties (half-lives and branchings for β -delayed neutron emission), which determine path, timescale, and the abundance pattern produced by the r-process. Neutron capture rates play a role during freezeout. Depending on the scenario, fission rates and fragment distributions as well as neutrino interaction cross sections might be relevant as well. Knowledge of nuclear physics is specifically needed to answer the following questions:

- What are the abundances produced in the r-process for a given astrophysical model?
- What are the constraints on the conditions during the r-process as inferred from the observed abundances in the solar system and in stars?
- What are the individual contributions of the multiple r-processes that together with the s-process might produce the elements below barium?

As Figure 3.2 shows, only very few of the critical β -decay half-lives in the r-process are known today, severely limiting the ability of r-process models to predict abundance signatures. In recent years it has become possible to reach the r-process path with experiments for a wider range of elements between the $N = 50$ and $N = 82$ shell closures, mainly by making use of fragmentation beams at the NSCL [Hos05,Mon06b]. At the same time, ISOL facilities have continued to provide important data on critical isotopes in regions particularly suitable for that technique, for example, for the neutron-rich cadmium or tin isotopes [Dil03,She02,Kra00]. These few experiments have already put first experimental constraints on r-process models related to the processing time to form the $A \sim 80$ and $A \sim 130$ abundance peaks. Mass measurements require higher beam intensities than half-life measurements, reducing the experimental reach to isotopes with three to five fewer neutrons. Consequently mass measurements have reached the path of the r-process only in a few cases near shell closures [Sik05a,Dil03].

Within the next few years we can expect that existing facilities, such as the NSCL CCF, will continue to extend the border of known half-lives about halfway into the r-process path in the $N = 50$ – 82 range. While this will be an important step forward, many of the most neutron-rich nuclei in the critical region just below the $A = 130$ abundance peak (see Figure 3.1) as well as the entire r process beyond $N \sim 90$ will remain out of reach (see Figure 3.2). In addition, in any mass region of the r-process, most of the nuclear masses will remain inaccessible.

As shown in Figure 3.2, the picture would dramatically change with the fast beam capabilities of the ISF. At the ISF, all r-process nuclei up to $A \sim 140$ would be within reach for half-life measurements and most of them for mass measurements. For example, at the ISF all the masses of nuclei with $N \leq 82$ could be measured down to technetium (see also Section 2.3.1), providing data for neutron separation energies directly in the exotic $N \leq 82$, $Z \leq 44$ region, where differences in the trends of mass predictions due to nuclear structure effects lead to the notorious discrepancies in r-process model predictions for abundances below the $A = 130$ peak (see Figure 3.1). This would unambiguously settle the issue of the possible quenching of the $N = 82$ shell gap far from stability and its influence on the r-process (see also Section 2.3).

With the fast beam capability of the ISF it will be possible to measure many new half-lives in a single experiment using a mixed fragment beam. The different

Observations of r-process elements in stars

Observations of elemental abundances in very metal-poor stars are revolutionizing the field of nuclear astrophysics. Metal-poor stars are found among lower-mass stars in the halo of our Galaxy, where they formed within a few hundred million years after the Big Bang. At that time, the enrichment of iron in the Galaxy through supernova activity had not progressed very far. Thus, these stars have preserved information on the chemical composition at that specific location in the Galaxy at the time of their formation. The metal-poor halo stars, therefore, offer a way to look back in time and observe the products of nucleosynthesis in the first epochs of the chemical evolution of our Galaxy.

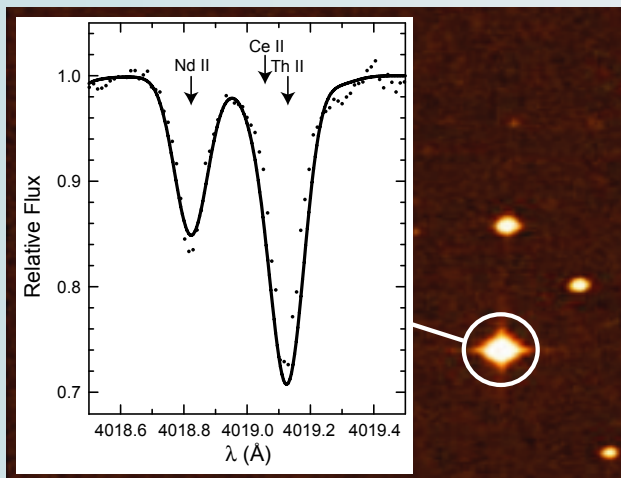


Figure A: A small portion of a high-resolution spectroscopic observation of the very metal-poor halo star CS 31082-001, obtained with the European 8 m VLT telescope, showing one of the eleven detectable absorption lines of the r-process element thorium (Th II) in this star. Comparisons of r-process model predictions based on experimental nuclear data with the observed element abundances constrain the r-process model conditions and, in the case where both thorium and uranium are detected, the age of these elements. Because these stars are extremely old, the latter also provides a lower limit for the age of the universe. Insert adapted from [Cay01,Bee06]. Image of star: This data is copyrighted by the Space Telescope Science Institute (STScI Digitized Sky Survey, © 1993, 1994, AURA, Inc. all rights reserved).

These very metal-poor stars that exhibit factors of 10–100 times more r-process elements than found in the Sun are especially interesting. They provide a glimpse of the elemental composition that may have been produced by a single r-process event in the early Galaxy. Figure A shows an example of the clear spectral signature of thorium, an element that can only be produced in the r-process, from one of these stars. Another prime example is the star labeled CS 22892-052, from which 57 elemental abundances have been determined to date. Figure B compares the observed abundance levels with the r-process contribution to elements in the Sun, which is thought to be a superposition of many r-process events. Although there are discrepancies for lighter elements, the abundances match for very heavy elements beyond barium. This provides important clues about the nature of the r-process.

The discrepancies among the distributions of lighter r-process elements have been interpreted as a hint that a second r-process might produce the missing abundances. However, matching the observations with r-process model calculations and attempts to use such calculations to disentangle the contributions of different r-processes have been hampered by the lack of nuclear data for the very neutron-rich nuclei.

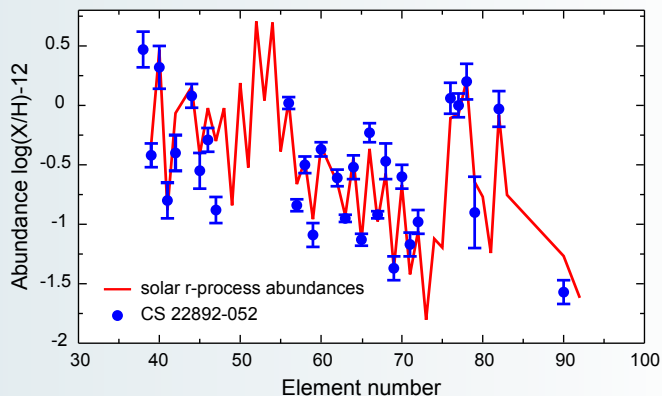


Figure B: The observed elemental abundances in the very-metal poor r-process enriched halo star CS 22892-052 (blue data points). For comparison, the contribution of the r-process to the solar system elemental abundance distribution is also shown (red curve). Clearly the surface composition of the star for heavy elements with $Z > 37$ is entirely determined by the r-process. Adapted from [Sne03,Cow06].

The few observations of thorium and uranium in metal-poor r-process-element enriched stars offer the possibility to determine the age of the r-process event that contributed to that star. Such an age determination requires a reliable r-process model that can predict the initial r-process abundance of thorium and uranium. Comparison of the predictions with the observed abundance then allows one to use the known nuclear decay rates to determine the age. Because these stars are so old, this method can provide an independent constraint on the age of the Galaxy and the universe. However, the reliable prediction of uranium and thorium production in the r-process is severely limited by a lack of nuclear data, especially for the r-process waiting point nuclei around $N = 126$, the last point of normalization of the r-process before entering the actinide region. This problem will be addressed by experiments at the ISF.

To date, only a handful of r-process element-enhanced, very metal-poor stars have been found. A larger sample is needed to explain the enrichment of the Galaxy with r-process elements over time and to explain variations and similarities among r-process events. Unfortunately, only about one in about 1.2 million halo stars is both r-process enriched and very metal-poor. Nevertheless, with ongoing powerful surveys such as SEGUE, there is the hopeful intention to identify and analyze hundreds of such stars in the near future. Large-scale surveys based on low- and medium-resolution spectroscopy locate the most promising candidates. Then, 8–10 m class telescopes are used to determine accurate element abundances from high-resolution spectra. The ISF will provide the nuclear data needed to fully interpret these observational data and to compare them with r-process models.

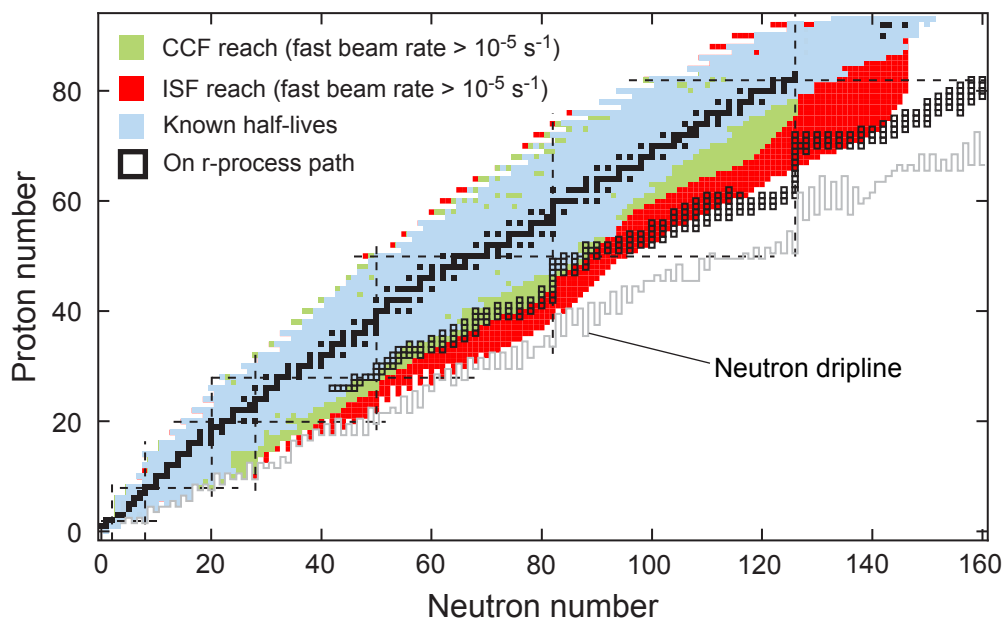


Figure 3.2: Reach of the ISF into the r-process path. Shown are nuclei with known β -decay half-lives (blue) and nuclei that are within reach for half-life measurements, either at existing facilities (NSCL, green), or at the ISF (red), assuming fast beams are used. Important nuclei in a typical r-process [Sch02] are indicated by thick open squares.

species can be easily disentangled using event-by-event particle identification, a well-developed technique that has been frequently used in the past [Fae02,Hos05, Mon06b,Sor93]. It will therefore be possible to measure all the half-lives marked in Figure 3.2 in a series of experiments over the lifetime of the ISF. This is important for r-process studies, because the reliable calculation of a wide range of abundances forming the characteristic abundance pattern is needed to extract all the information contained in observations.

In particular, the half-life and mass data from the ISF, together with mass extrapolations by a few isotopes, would allow one to reliably calculate the entire r-process up to $A \sim 140$. This is a critical mass range, where signatures from freeze-out timescales [Fre99], neutrino post-processing [Qia97], and possibly fission of nuclei at the endpoint of the r-process would be particularly prominent. Comparison with precision observations will then allow one to detect these signatures and to test r-process models. In addition, multiple r-processes might contribute to the observed abundances in this mass range. With the data from the ISF, contributions from individual processes could finally be disentangled reliably in a way similar to that in which the nuclear physics in the s-process is used today to disentangle s- and r-process contributions to the solar abundances.

As Figure 3.2 also shows, with the ISF, a range of r-process nuclei at the $N = 126$ shell closure also come into reach. This region is associated with the $A = 196$ abundance peak and represents the last bottle-neck for the r-process before proceeding into the lead and actinide region. It is therefore a critical normalization point for r-process models, especially for the prediction of the endpoint of the r-process and the production of uranium and thorium, which have been used as cosmic chronometers in the past [Cow91,Kra04]. All of the $N = 126$ r-process waiting points have been out of reach at existing facilities to date. While the ISF cannot reach all

$N = 126$ waiting points for half-life measurements, the ones that are within reach are closer to stability and are, therefore, expected to be the major contributors to the overall timescale for the r-process to pass through that region. In addition, the greatly improved understanding of nuclear structure, not only in the $N = 126$ region but also for lighter nuclei will allow much more reliable calculations of the β -decay properties and masses that will remain out of reach experimentally.

Neutron capture rates can play a role in some r-process models during freeze-out when the equilibrium between neutron capture and (γ, n) photodisintegration breaks down. During this phase, late-time neutron captures can modify the final abundance distribution somewhat [Fre99]. While neutron capture rates on short-lived unstable nuclei cannot be measured directly, experiments can provide critical information to estimate the reaction rates. Inverse kinematics (d, p) reactions at energies from 4–10 MeV/nucleon have been used in the past to obtain information on spectroscopic factors and to determine neutron capture rates for astrophysical purposes [Gau06, Ciz05]. Intensities of reaccelerated fragmentation beams at the ISF will be sufficient ($> 10^4 \text{ s}^{-1}$) to perform such measurements on a wide range of neutron-rich nuclei that over much of the $Z = 28$ –52 range comes within one to two isotopes of the main r-process path and, in a few cases, reaches it.

With fast beams at the ISF, one can probe dipole strength distributions via Coulomb excitation techniques over a similar range (see Section 2.3.2.1). In particular, the possible shift of $E1$ strength towards lower excitation energies for neutron-rich nuclei can influence the prediction of neutron capture rates for r-process calculations and needs to be understood [Gor98] (see Section 2.5.4.3). Together, these experiments will allow one to systematically test model predictions of neutron capture rates along isotopic chains up to the path of the r-process.

3.1.2 The p-process

Thirty-five neutron-deficient stable isotopes found in nature, ranging from ^{74}Se to ^{196}Hg , cannot be produced via neutron-capture processes. These relatively rare isotopes originate in the p-process, thought of as a process of (γ, n) , (γ, p) , and (γ, α) reactions acting on a seed of s-process nuclei, most likely in explosive O-Ne burning in core-collapse supernovae [Arn03]. Current p-process models can reproduce most of the observed abundances to within a factor of four only. A particular long-standing problem in nuclear astrophysics is the underproduction of the proton-rich isotopes of molybdenum and ruthenium by about an order of magnitude.

The critical nuclear physics in the p-process are the rates of (γ, p) , (γ, n) , (γ, α) , and (n, p) reactions. Reaction rates involving α particles are especially difficult to predict reliably, due to uncertainties in the α potentials used in statistical model calculations. Many of the important reaction rates, in particularly the (γ, α) chains that drive matter from heavy nuclei towards lighter nuclei, involve unstable nuclei [Rap06]. Nuclear data for the p-process are needed to:

- analyze observed p-process abundances in terms of other model deficiencies, such as the assumption of the seed abundance distribution or the temperature and density evolution in a particular model;
- test various alternative p-process models, such as the pre-explosive p-process in massive stars, accretion disks around black holes, type Ia

supernovae, or the collapse of a white dwarf induced by accretion of helium from a companion star by comparing abundance predictions with observations.

At existing facilities, the limited beam intensities leave Coulomb Dissociation [Bau96] as the only choice for the measurement of p-process reaction rates on unstable targets and with unstable final nuclei. Such measurements can in principle be performed with beam intensities of the order of 10^4 s^{-1} . It remains to be demonstrated that this method is suitable for heavy unstable nuclei near stability, where reaction rates are typically dominated by many resonances. Experiments are currently underway to investigate this issue [Son06]. If successful, existing facilities could apply this technique over the coming years to a number of p-process reaction rates. Fast beam intensities at the ISF are sufficient to easily measure all critical p-process reaction rates via Coulomb breakup. However, the Coulomb breakup technique relies on theoretical assumptions about the relevant multipolarities and γ -ray cascades when applied to resonant rates with well-bound nuclei and high level-densities.

At the ISF, intense (10^{8-9} s^{-1}) reaccelerated beams at astrophysical energies also become available for most of the p-process path. This will open the possibility for direct measurements of (p,γ) and (α,γ) reaction rates in inverse kinematics on proton or helium targets, respectively. The measured rates can then be related to the inverse (γ,p) and (γ,α) reaction rates via the detailed balance principle. In this case, a theoretical correction is required that accounts for the stellar enhancement factor due to the thermal population of the target nucleus in a stellar environment. The direct measurement of the particle capture rates is complementary to the measurement of the photodisintegration rates via Coulomb Breakup. Combining both methods will provide the necessary cross-checks to address model dependencies and theoretical uncertainties. At the ISF, all the reaction rates identified in recent p-process studies as important [Rap06], for example $^{126}\text{Ba}(\gamma,p)$, $^{110}\text{Sn}(\gamma,p)$, $^{104}\text{Cd}(\gamma,p)$, $^{100}\text{Pd}(\gamma,p)$, and $^{122}\text{Xe}(\gamma,\alpha)$ would be accessible for this approach.

Because of the problems of using “standard” p-process scenarios to predict all the observed abundances of nuclei in the solar system that originate in the p-process, a range of alternative sites has been explored in the past. This includes the rp-process in X-ray bursts that had been proposed as an alternative site for the nucleosynthesis of lighter p-process nuclei in the molybdenum-ruthenium region (see Section 3.2.1). More recently, it has been shown [Pru05,Fro05] that during the early stages, the neutrino-driven wind off a forming neutron star in a core-collapse supernova represents a proton-rich environment. In these proton-rich outflows, nucleosynthesis through an rp-process can occur. This is similar to the r-process thought to occur in the same scenario at later stages when the outflow becomes neutron rich. So the neutrino-driven wind can eject, at early times, rp-process ashes and, at late times, r-process ashes. Such an rp-process can possibly contribute to the nucleosynthesis of some proton-rich isotopes such as ^{45}Sc , ^{49}Ti , and ^{64}Zn . In addition it was shown [Fro05] that neutrino interactions generating neutrons and the associated neutron-induced reactions can bridge the major waiting points, for example ^{64}Ge , and result in reaction flows that might reach the lighter p-nuclei, including neutron-deficient molybdenum and ruthenium isotopes. This vp-process might even explain the strontium, yttrium, and zirconium abundances observed in very metal-poor stars that have been shown to not originate from the traditional s- or r-processes [Tra04].

Accurate nuclear physics is needed to calculate the abundance signatures of this scenario and to determine whether this indeed provides the solution to the long-standing puzzles of the origin of neutron-deficient molybdenum and ruthenium isotopes in the solar system and the observations of strontium, yttrium, and zirconium in stars [Tra04]. We are just beginning to delineate the nuclear physics needed to predict nucleosynthesis in this new scenario. Current models indicate a reaction flow resembling an rp-process, at least up to the tin region. In this case, the capabilities outlined in connection with the rp-process in X-ray bursts (see section 3.2.1) will also address an important part of the nuclear physics needed in proton-rich neutrino-driven winds.

3.2 How do stars explode?

3.2.1 X-ray bursts and superbursts

X-ray bursts are among the most interesting explosive astrophysical phenomena in our Galaxy [Str03,Sch06a]. With dozens of sources bursting regularly or irregularly, with recurrence times of hours to days, they are the most frequent thermonuclear explosions known. The brightness, frequency, and the fact that the same source can be repeatedly observed with different telescopes makes them a unique testing ground for explosive nuclear burning at extreme temperatures and densities. X-ray bursts occur on the surface of neutron stars accreting matter from a close companion star [Str03] (see Figure 3.3). X-ray bursts and the associated phenomena provide, therefore, a unique window into the physics of neutron stars. Not only do they probe neutron stars in different ways, but unlike isolated neutron stars that are constrained in properties by the formation mechanism, the mass accretion process changes the spin, mass, and thermal structure of the neutron star, considerably broadening the parameter space for neutron star studies.

X-ray bursts occur in a layer of often hydrogen- and helium-rich material that is accreted onto the surface of the neutron star. After a few hours of accretion, the material ignites and hydrogen and helium burn into heavier elements in a thermonuclear explosion that typically lasts for 10–100 s. The released nuclear energy powers an observable X-ray burst with an energy of 10^{39} – 10^{40} ergs (about the energy that the Sun emits in a month).

There are many open questions concerning the variety of burst timescales, light curve shapes or recurrence time behavior. The role of multidimensional effects such as ignition points, the spreading of the burning front across the star, or rotation is also not understood. In addition, a range of discoveries and new observational data by X-ray observatories, such as Beppo-SAX, RXTE, Chandra, and XMM-Newton, have revolutionized this field and dramatically broadened the range of known nuclear physics-driven phenomena. Examples include the discovery of millisecond oscillations during X-ray bursts [Str04], the detection of absorption lines that provide information on the surface composition and the gravitational redshift [Cot02], and the discovery of superbursts – extremely rare but about a factor of 1000 times more powerful X-ray bursts [Int04].

To interpret these phenomena and to address the many open questions, the astrophysics and the underlying nuclear physics need to be understood. Data from observations and from experimental nuclear physics are therefore needed. This is illustrated in Figure 3.4. The high quality observation of an X-ray burst light curve

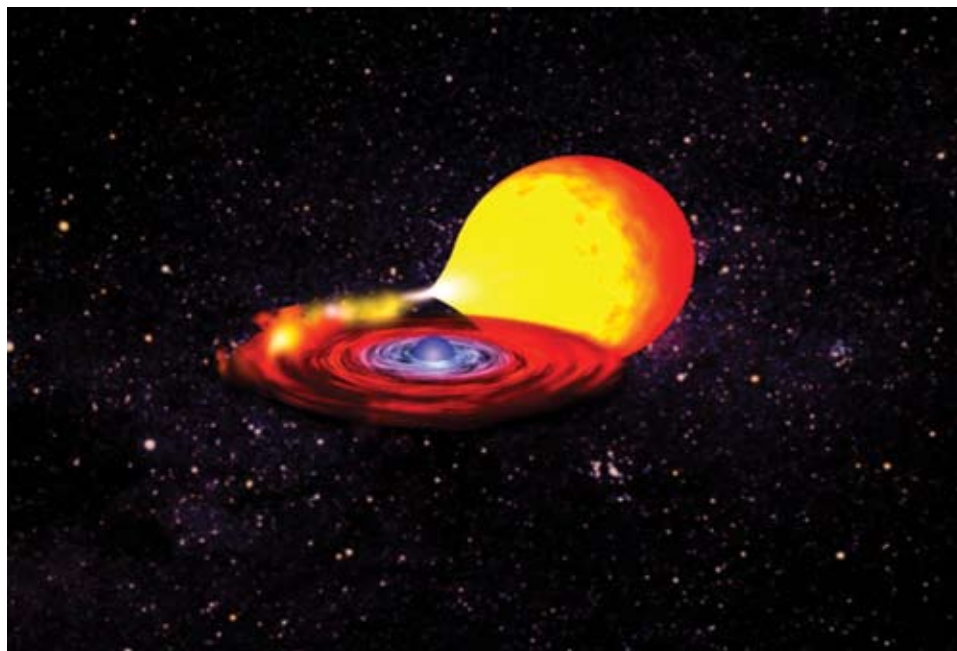


Figure 3.3: Artists view of an accreting neutron star in an X-ray binary system. The companion star (orange) has expanded and matter overflows through an accretion disc onto the surface of the neutron star (purple). Image used by permission of NASA.

and its changes over the years due to changes in the accretion rate provide the possibility of precision tests of X-ray burst models [Gal04]. However, the nuclear physics is still far from being accurate enough to perform such precise tests, as shown in the right panel of Figure 3.4 [Bro02a,Woo04].

Recent progress in theory has led to predictions of additional signatures of nuclear burning during X-ray bursts. It has been shown that ejection of some burned material during winds in particularly luminous radius expansion bursts could lead to observable signatures in the X-ray spectra [Wei06]. In addition, it has been found that the detailed composition of the burst ashes can greatly influence heating in the crust, affecting several observables, for example superbursts (see Section 3.3.1). Experimental data on the nuclear physics of X-ray bursts are therefore needed to:

- Understand the wide variety of observed X-ray burst light curves and interpret them to test X-ray burst models and to constrain system properties, such as the accreted composition. For example, the amount of hydrogen in the accreted matter is critical for determining distances [Gal06b] and to constrain the neutron star compactness and the equation of state for dense nuclear matter [Oze06]. The shape of the burst light curve can provide unique diagnostics of the amount of accreted hydrogen, provided one has a reliable burst model. However, it is also sensitive to the nuclear physics of the rp-process (see Figure 3.4) [Sch01], which needs to be well understood.
- Reliably calculate the composition of the burst ashes, which is a prerequisite for understanding all processes that occur deeper in the crust, such as superbursts or crustal heating (see Section 3.3.1).

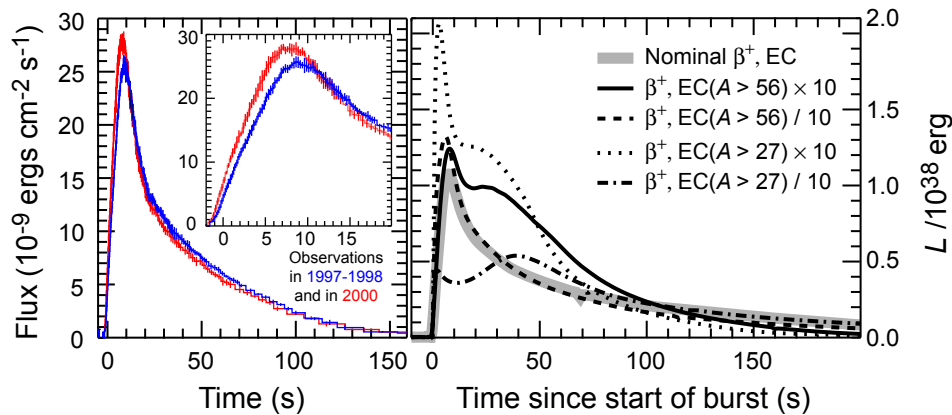


Figure 3.4: The left panel shows precision observations of X-ray burst light curves from GS 1826-24 by the RXTE observatory. The observations reveal systematic light curve changes from observations in the years 1997-1998 (blue) to observations in 2000 (red) that are likely related to changes in the accretion rate. Such measurements provide an excellent testing ground for X-ray burst models. The panel on the right shows predictions of X-ray burst light curves from state-of-the-art one-dimensional model calculations. The various curves are obtained for different assumptions on the nuclear physics of the rp-process. To approximate nuclear physics uncertainties that influence the effective lifetimes of the nuclei in the rp-process, β^+ and electron capture rates of two groups of nuclei (with $A > 56$ and with $A > 27$) have been increased and decreased by a factor of ten. Current precision in nuclear physics is not adequate to fully interpret the observations. Adapted from [Gal04,Gal06a] (left) and [Woo04] (right).

The nuclear processes driving X-ray bursts are the αp - and rp-processes [Wal81] proceeding along the proton dripline, in some bursts up to tellurium [Sch01,Woo04]. Masses, half-lives, and reaction rates for (p,α) and (α,p) reactions on unstable nuclei are important. See [Cha92,Sch98,Wie98,Sch06a] for more general reviews, [Sch06b] for the importance of masses, [Wie99b] on breakout reactions from the CNO cycles, and as an example [Fis06,Coo06] for the importance of a single reaction rate – in this case $^{15}\text{O}(\alpha,\gamma)$. The vast majority of half-lives have already been measured, and most of the masses are coming within reach at existing facilities. This has already led to important progress in the understanding of X-ray bursts. For example, mass and lifetime measurements around the key waiting point nuclei ^{64}Ge , ^{68}Se , and ^{72}Kr have already established that together these nuclei are likely to impose considerable delays in the rp-process (see [Sch06b] for a review). This has led to the interpretation of frequently observed, rather long X-ray bursts (~ 100 s) as signatures for an extended rp-process and, therefore, the presence of significant amounts of hydrogen at ignition (for example [Sch01]). This constrains the burning regime and the nature of the companion star (hydrogen-rich), and can improve distance estimates as the maximum possible burst luminosity is determined by the composition of the accreted material.

However, charged particle induced reaction rates have been difficult to measure because of the limited intensities of rare isotope beams (see review in [Sch06a] and discussion in Section 3.2.3). Most rates in the rp-process are still based exclusively on theory, and in most of the remaining cases experimental information needs to be complemented with theory. Theoretical predictions of rp-process reaction rates are extremely unreliable. Shell model calculations, which can be used up to $A \sim 60$, can predict excitation energies of resonant states. However, reaction rates are so

sensitive to resonance energies that the rather small uncertainties in the shell model predictions of around 100 keV still can translate into reaction rate uncertainties of many orders of magnitude. In addition, α strengths and the weak proton strength of some important resonances are difficult to calculate accurately. Beyond $A \sim 60$, statistical models are used to predict reaction rates, even though level densities near the proton dripline are too small for such an approach to be applicable. It is therefore essential to determine reaction rates experimentally.

Figure 3.5 shows the path of the reaction flow during an X-ray burst [Sch01] together with the intensities for reaccelerated beams at the ISF. A few of the reaction rates might be within reach at existing facilities (see discussion in Section 3.2.3). At the ISF, intensities of low energy reaccelerated beams will be sufficient to perform direct measurements of the vast majority of the relevant reaction rates up to $A \sim 40$, and on some rates up to $A \sim 56$ (see also Section 3.2.3).

In addition, the vast majority of the remaining reaction rates can be investigated by indirect techniques. Examples are Coulomb dissociation or neutron removal reactions with fast beams, which have been well established at existing facilities [Del93,Sch06c,Dav01,Mot04,Cle04]. Transfer reactions performed with lower energy reaccelerated beams, such as (d,n) , (d,p) , or $({}^3\text{He},d)$ can be used to extract

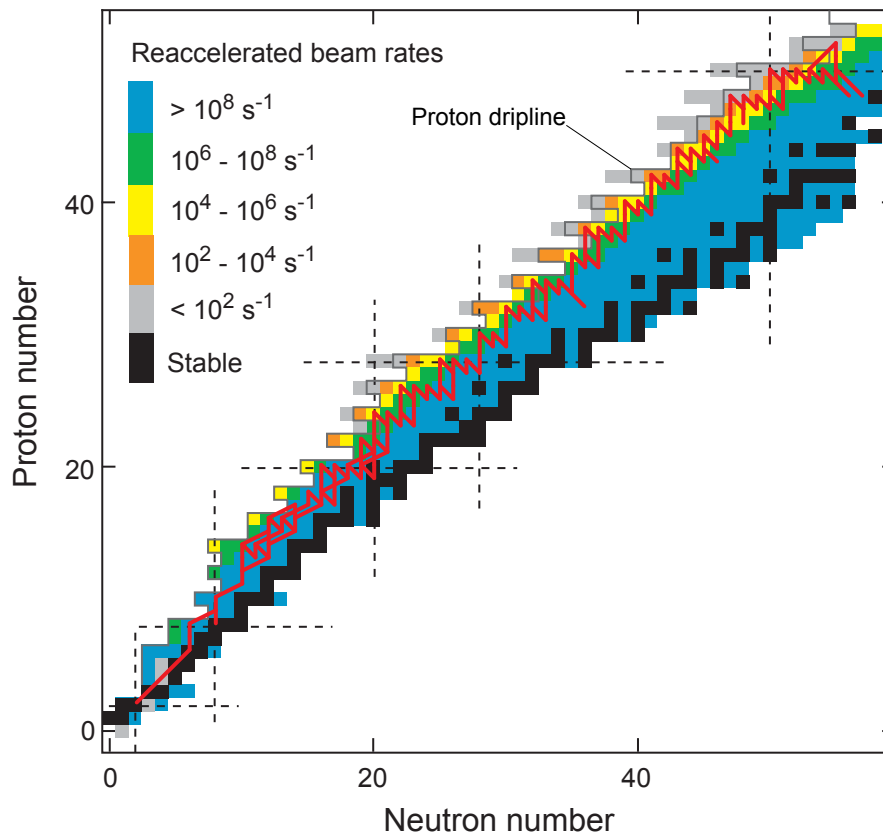


Figure 3.5: The time integrated reaction flow (solid red line) during an X-ray burst with particularly large amounts of hydrogen available at ignition [Sch01]. This calculation delineates the maximum extent of the rp-process that ends in a Sn-Sb-Te cycle. The colors indicate the intensities of low energy reaccelerated beams at the ISF. Direct measurements of reaction rates in inverse kinematics require at least 10^7 – 10^8 s⁻¹, often much more. Indirect techniques can already be applied with beam intensities in excess of 10^4 s⁻¹. The dashed lines indicate the classical shell closures.

proton spectroscopic factors, ANCs, or neutron spectroscopic factors in mirror nuclei (for example [Reh98,Muk06]). These techniques typically require beam intensities of at least 10^{4-5} s^{-1} . A particularly important region that will become accessible to extensive experimental investigations is that around the critical waiting points ^{64}Ge , ^{68}Se , and ^{72}Kr . These waiting points shape X-ray burst light curves and determine the amount of heavier nuclei produced. They can be strongly affected by proton capture rates [Sch06b] that are largely out of reach at existing facilities. Coulomb breakup measurements with fast beams would be especially important to determine proton capture rates on proton unstable targets with lifetimes below a few hundred nanoseconds, such as ^{69}Br or ^{73}Rb .

In addition, all the nuclear masses in the rp-process will be within reach for precision Penning-Trap based measurements at the ISF (see Section 2.3.1). This includes the heaviest relevant neutron-deficient nuclei around and just below ^{100}Sn , which are also relevant for the vp-process (see Section 3.1.2) and might still be out of reach at existing facilities. By combining, in a coordinated approach, the mass measurements, direct measurements of reaction rates on lighter targets, and a complementary range of indirect techniques applied to heavier targets taking advantage of both fast beams and reaccelerated beams, the vast majority of the nuclear data needed to model X-ray bursts reliably would become available.

3.2.2 Supernovae

Supernovae play a critical role in our understanding of the universe. They are the major sources of nucleosynthesis and, possibly, cosmic rays. They create neutron stars and black holes, and their shockwaves are among the main drivers of galactic chemical evolution and mixing. Supernovae are extremely bright and energetic, and are characterized by some of the most extreme conditions encountered anywhere in the universe. There are two major classes of supernovae. Core-collapse supernovae are the result of the collapse of the iron core of a massive star at the end of its evolution. Thermonuclear supernovae are powered by explosive carbon and oxygen burning of a white dwarf that through accretion of matter reaches a mass beyond the limit where electron pressure can balance gravity, the Chandrasekhar mass limit. Thermonuclear supernovae (observationally classified as type Ia) can be used as cosmological standard candles using measurements of their light-curve behavior. They serve therefore as cosmological distance indicators. Together with other observations, this has led to the discovery that the universe is undergoing an accelerating expansion and is dominated by dark energy [Lei01b].

For both types of supernovae, the driving mechanism is not well understood, and in both cases, nuclear physics, such as the equation of state and weak interactions, play an important role.

3.2.2.1 Core-collapse supernovae

We know that the majority of nuclei in the universe, including possibly the heavy elements made in the r-process, originate from core-collapse supernovae. But we do not yet understand the mechanism that transforms the gravitationally powered collapse into an explosion that ejects the outer layers of the star. Weak interactions surely play an important role in this scenario. As regulators of electron density, they help set the dynamics of the collapse and the amount of material the outgoing shock must traverse. The importance of accurate weak interaction rates has been

demonstrated by detailed simulations indicating that important core-collapse characteristics change when new shell model electron capture rates are used in place of earlier values [Heg01,Hix03]. Reliable estimates for electron capture rates are therefore among the important physics ingredients needed to judge the failure or success of a given supernova model.

Late in the precollapse evolution of a massive star, nuclei in the iron-mass range play the major role in capturing electrons. As the collapse proceeds toward nuclear density, nuclear statistical equilibrium shifts to heavy neutron-rich nuclei beyond $A \sim 60$, and a broad range of stable and neutron-rich nuclei becomes important. For the later phases of the collapse this became clear recently, when more realistic theoretical electron capture rates were incorporated in supernova models. Before, it had been the prevailing wisdom that weak interactions involving free protons and neutrons determined the electron abundance, but the new calculations demonstrate that Gamow-Teller electron captures and β -decays involving nuclei are more important [Hix03].

It is therefore important to experimentally constrain theoretical predictions for Gamow-Teller strength over the entire relevant mass range. This is especially true beyond the *pf*-shell, where accurate shell model calculations become difficult and the model-assumptions become questionable. Theoretical methods, for example employing mean-field techniques, are being used [Hix03] that have hardly been tested against experiment. It is crucial that such tests are performed; charge-exchange reactions can provide these necessary data, as is detailed in Section 2.7. Tests of strength distributions in unstable nuclei are especially important, since almost no experimental information is available beyond the small fraction that is accessible by β -decay.

Following the core-collapse process, the neutron star cools by emitting neutrinos, a high flux of neutrinos passes through the overlying shells of heavy elements, and nuclear transmutations via neutrino interactions are induced. Neutral current reactions, induced by energetic μ and τ neutrinos and their antiparticles are especially important, but charged-current reactions play a role as well. The excitation of the Gamow-Teller resonance state is possible, but due to the high energy of the neutrinos, the excitation of the giant dipole resonances through first-forbidden weak transitions becomes important. This neutrino-process is thought to be largely responsible for the production of a number of rare isotopes, including many of the odd- Z nuclei from boron to copper and nuclei such as ${}^7\text{Li}$, ${}^{11}\text{B}$, ${}^{19}\text{F}$, ${}^{138}\text{La}$, and ${}^{180}\text{Ta}$ [Woo90]. The uncertainties in the calculations, which employed rather simple models for the strength distributions, can be reduced by measurements of the relevant forbidden weak strengths via charge-exchange reactions. In the case of unstable nuclei, these resonances can be probed at the ISF using the (p,n) reaction in inverse kinematics as described in Section 2.7

In addition to weak interactions, a range of other nucleosynthesis processes involving unstable nuclei takes place in core-collapse supernovae. This might possibly include the r- and p-processes, which are discussed separately in Sections 3.2.1 and 3.2.2 respectively. A particularly important process in core-collapse supernovae is the α -process, which produces the γ -ray emitter ${}^{44}\text{Ti}$. ${}^{44}\text{Ti}$ decay γ -rays have been observed directly from the CasA supernova remnant by γ -ray observatories and ${}^{44}\text{Ti}$ has also been found incorporated in certain meteorites, where it can be identified through its decay product. The decay of ${}^{44}\text{Ti}$ also powers the late-time

light-curve of core-collapse supernovae. The amount of ^{44}Ti produced in a supernova can therefore be inferred from light curve observations, as has been done for supernova 1987a, for example. Such observations pose strong constraints on supernova models, provided the reaction rates relevant for ^{44}Ti production are accurately known. While some of the important reactions occurring on stable targets or the long-lived ^{44}Ti itself have been investigated experimentally [Nas06,Son00],

Core-collapse supernovae

Core-collapse supernovae are the result of the collapse of massive stars (at least eight times the mass of the Sun) that have exhausted the fuel to drive the fusion process and end up with a core that has been converted into iron. The outward thermal pressure from the nuclear reactions no longer balances the massive gravitational force and the star collapses. The density of the material in the star rapidly increases during the implosion and when the density exceeds nuclear matter density, the core rebounds, generating an outgoing shockwave. The shock-wave induces an explosion with an energy release of no less than 10^{53} ergs and nuclear material is disseminated into the interstellar medium leaving behind a variety of remnants that can be observed (Figure A).

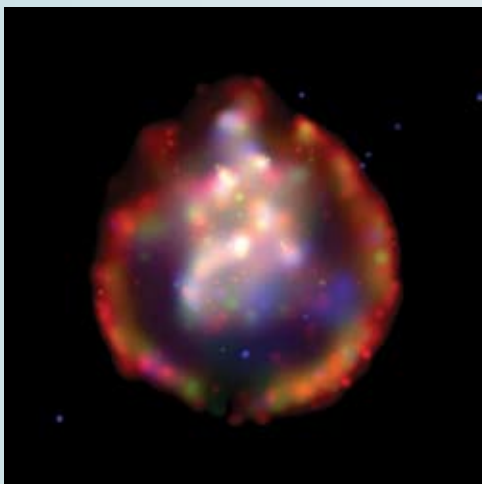


Figure A: Image of the supernova remnant SNR 0103-72.6 in the Small Magellanic Cloud taken by the Chandra X-ray Observatory. The remnant is about 10,000 years old (as seen today) and the ejected material has expanded to a radius of about 75 light years. The colors indicate different X-ray wavelength ranges. Spectral analysis provides information on the chemical composition across the remnant [Par03]. With images such as this, one can directly study supernova nucleosynthesis and the distribution of the elements in the ejecta. Image credit: NASA/CXC/SAO.

A large fraction of nuclei in the universe is thought to stem from core-collapse supernovae and since the supernovae are possible sites for the r-process, a substantial effort is currently going into unraveling the mechanism of the explosion. One of the major puzzles is that present simulations of the collapse are not able to convincingly produce an explosion; the outgoing shock wave stalls before reaching the surface

of the star. Therefore, theoretical efforts are focused on finding new mechanisms that can reenergize the shock wave [Woo05]. Improvements and additions to the current models are necessary, including the description of hydrodynamical properties like convection, asymmetries in the shock-wave process (Figure B), and the transport of radiation (in particular neutrinos) through the star [Fry04,Bur95,Kif06,Mez98,Lie05,Wal05,Bur06].

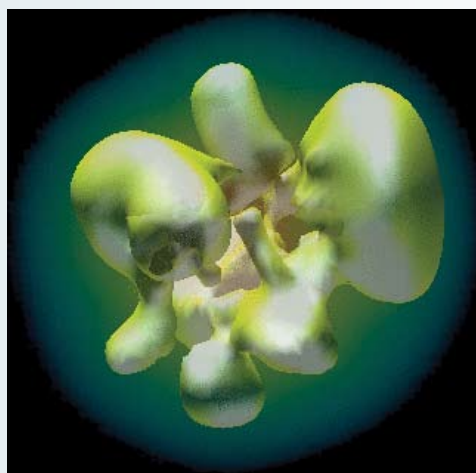


Figure B: Results of a three-dimensional simulation of the supernova explosion of a 15 solar-mass star [Fry04]. The simulation (here shown 40 ms after the bounce at nuclear density) was designed to study asymmetries in the explosion that may explain observations such as variations in γ -ray spectra, nucleosynthesis yields, and the shape of remnants. Image credit: C.L. Fryer and M.S. Warren.

Another crucial element in the description of supernovae is the accurate treatment of the nuclear reactions, in particular weak transitions among medium-heavy nuclei [Lan03]. The temperatures and densities inside the star are high, so that unstable nuclei that do not normally exist constitute a significant fraction of the matter inside the star. However, the accuracy of the theoretical calculations of weak reaction rates of unstable nuclei is not known, resulting in large uncertainties in the simulations. The calculations of the weak reaction rates must, therefore, be tested and further developed based on experimental data. Such data can be collected by studying charge-exchange reactions in inverse kinematics on unstable nuclei. The ISF will produce suitable beams of unstable nuclei at sufficient intensities to study the whole region of nuclei important for supernovae explosions.

proton capture on the unstable ^{45}V has also been identified as critical [The98]. With a reaccelerated rare isotope ^{45}V beam at the ISF, a direct measurement of this reaction rate would be possible (see Section 3.2.3. for a more in-depth discussion of this technique). With such a measurement, the ^{44}Ti yield of supernova models could be calculated much more reliably.

3.2.2.2 Thermonuclear supernovae (type Ia)

Thermonuclear supernovae (type Ia) make half of the iron-group elements in the universe and are crucial standard candles for determining the equation of state of dark energy. Despite their importance, open questions abound. The canonical Type Ia supernova model is a carbon-oxygen white dwarf, accreting matter from a companion star and growing in mass to near the Chandrasekhar limit, where an explosive process ensues. The nature of the binary systems involved is unclear. The extent to which the composition and age of the host stellar population affects the explosion is also uncertain. Multidimensional studies [Gam04,Ple04,Rop06] of the explosion have been performed, but the exact nature of the explosion, whether there is a transition from deflagration to detonation, for example, is still a matter of debate [Thi04].

Weak interactions can again play an important role in the explosion and the accompanying nucleosynthesis. During the explosion, the thermonuclear flame leaves an equilibrium distribution of iron-peak nuclei in its wake. Electron captures on these nuclei lower the pressure of the fluid, which retards the expansion of the star. Electron capture also reduces the amount of radioactive ^{56}Ni produced and thereby reduces the brightness of the explosion. The amount of ^{56}Ni produced is also affected by trace neutron-rich isotopes, such as ^{22}Ne . These are inherited from the progenitor white dwarf [Tim03]. Understanding these effects is necessary for a reliable description of systematic trends in Type Ia supernova brightness [Pod06].

Because these supernovae produce about half of the iron-group nuclei, they must not overproduce these isotopes by more than a factor of two, compared to abundances in the solar system. This constrains the explosion models, the central density of the progenitor white dwarf, and the flame speed [Iwa99]. However, one-dimensional simulations are also sensitive to the weak reaction rates used [Bra00]. If one is confident that the employed rates are reliable, one can use the nucleosynthesis patterns in the iron group to limit the central density and flame speed and, hence, validate evolution models. To have confidence in this procedure, the weak rates used in such models must be tested against experiments. Neutron-rich nuclei in the *pf*-shell are key; the lack of data for unstable nuclei in this region is an important limitation on an accurate description of Type Ia supernovae [Bra00].

3.2.2.3 Weak rates for supernovae simulations

In both core-collapse and thermonuclear supernovae (Type Ia), temperatures and densities are so high that energetic electrons can overcome negative electron capture thresholds, and electron captures on unstable neutron-rich nuclei become important. This is also the case for electron captures in neutron star crusts as discussed in Section 3.3.1. The relevant strengths cannot be studied with β -decay experiments under terrestrial conditions. However, charge-exchange reactions can be used to provide the experimental Gamow-Teller strengths necessary [Ost92] to validate theoretical nuclear structure models.

How this is done is shown in Figure 3.6 for the case of electron-capture on the ground state of ^{58}Ni populating states in ^{58}Co . Forward angle cross sections for the $^{58}\text{Ni}(t,^3\text{He})$ reaction [Col06] are proportional to the Gamow-Teller strength for transitions to the same states. In the top left panel of the figure, the measured strength distribution is compared with large-scale shell model calculations [Hag04] using the GXFP1 interaction [Hon04]. The calculation misses the strongest state, near an excitation energy of 2 MeV, but does well at higher energies. In contrast, the calculation using the KB3G interaction [Pov01] describes the data well at low energies

Thermonuclear supernovae

Thermonuclear (Type Ia) supernovae are thought to be the incineration of a carbon-oxygen white dwarf that accretes mass from a companion star (see Figure A). As the mass of the white dwarf approaches the Chandrasekhar limit (1.4 solar masses), the white dwarf contracts, the temperature in its center increases, and eventually the fusion of carbon nuclei in the interior heats the star faster than it can cool, leading to a runaway thermonuclear reaction that disrupts the white dwarf.



Figure A: Artist's impression of a white dwarf accreting material from a companion red giant in a binary stellar system. As the accreted material pushes the mass of the white dwarf near the Chandrasekhar limit, a runaway thermonuclear reaction launches a flame that incinerates the white dwarf and induces the supernova explosion. Image credit and copyright: David A. Hardy & PPARC.

The subsequent radioactive decay of the fusion products releases approximately 10^{51} ergs of energy and the supernova becomes as bright as its entire host galaxy (see Figure B). Type Ia supernovae are thought to produce about one-half of the iron-group nuclei in the cosmos and have the important added use as standard candles for measuring galactic distances and hence the geometry of the universe. The peak brightness of the explosion is correlated with the rate at which the explosion dims, enabling astronomers to calibrate the distance to faraway supernovae. The deduction that the universe is expanding was made by combining this information with a measurement of the redshift of the emitted light [Rie98,Per99].



Figure B: Image of the type Ia supernova 1994D observed with the Hubble Space Telescope in the Galaxy NGC 4526 at a distance of 108 million light years. The supernova is located in the lower-left corner and outshines the entire galaxy. Image credit: NASA, ESA, The Hubble Key Project Team, and The High-Z Supernova Search Team.

Despite their cosmological importance, many aspects of Type Ia supernovae are uncertain, including the nature of the progenitor system—is it really an accreting white dwarf? Recent studies suggest that there may be more than one type of progenitor [Man06] and there is the possibility that the calibration of the distance scale of the universe may be affected by changes in the composition of the white dwarf [Pod06]. Since Type Ia supernovae make about 50% of the iron-group nuclei in the universe, the isotopic abundances produced by different explosion scenarios can be tested against the solar abundance pattern. The ISF will play a critical role in allowing studies to constrain the weak reaction rates that are important in Type Ia explosions.

but fails to reproduce the high-energy tail (top right). As a consequence, at low stellar temperatures, the low-energy region of the Gamow-Teller strength distribution is most important for driving electron-captures, and the theoretical calculation employing the KB3G interaction (bottom panel) will be more accurate. This applies, for example, to the precollapse stage of a massive star. At higher temperatures, where weak transitions to high-lying states become increasingly important, the GXPF1 interaction provides more accurate rates. This applies to later stages of the core collapse.

Studies such as these should be performed for a wide range of nuclei and used to improve the shell model interactions and other input for the theoretical calculations. Ideally, this would lead to a consistent and realistic description of weak-transitions rates under a large variety of stellar conditions (e.g., density and temperature) and during the various stages of stellar evolution where different regions on the nuclear chart play a role.

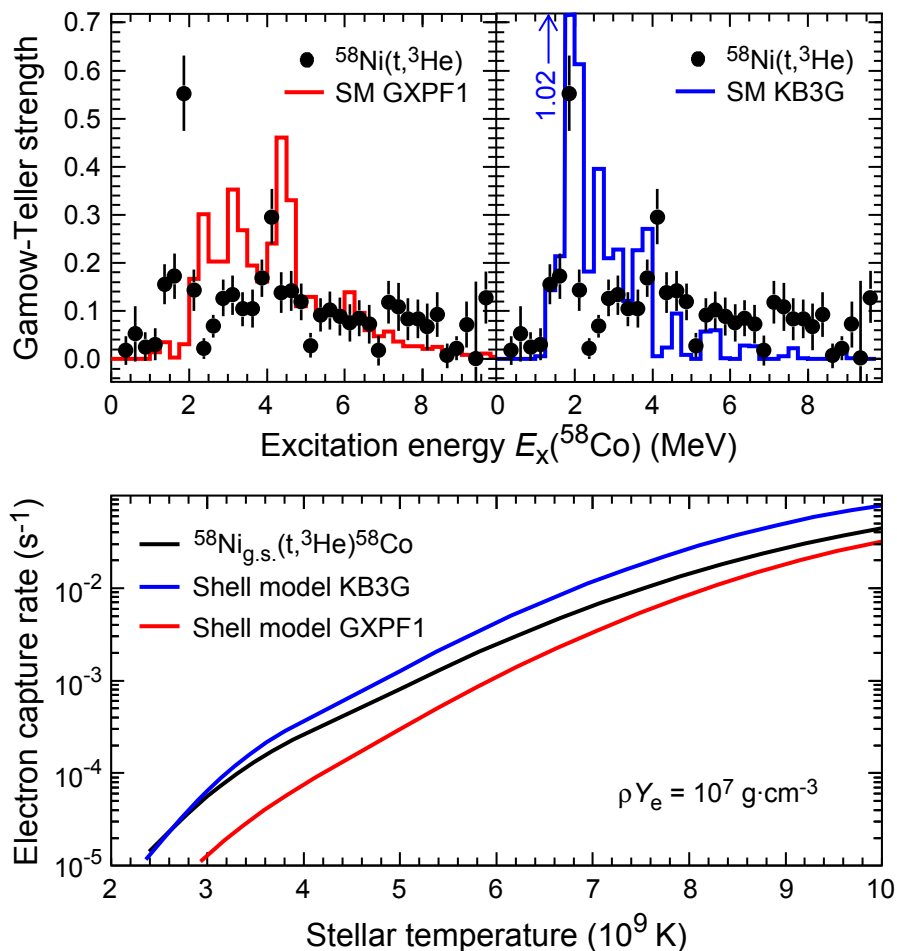


Figure 3.6: Comparison of the Gamow-Teller strength distribution in ^{58}Co extracted from $^{58}\text{Ni}(t,^3\text{He})$ data at 115 MeV/nucleon [Col06] and large-scale shell model calculations [Hag04], with the GXPF1 interaction [Hon04] (top left) and the KB3G interaction [Pov01] (top right). The bottom panel shows electron-capture rates based on the experimental and theoretical Gamow-Teller strength distributions and for conditions during the precollapse stage of a massive star (density (ρ) times electron fraction (Y_e) of 10^7 g cm^{-3}). Adapted from [Col06].

Experimental data on weak-interaction strengths of relevance for supernovae is restricted, with very few exceptions, to stable nuclei (see Section 2.7). In addition, the bulk of those experiments deal with nuclei in the *pf*-shell, whereas information for heavier nuclei (up to mass ~ 120) is equally important. Although some information on electron-capture rates on a few unstable nuclei can be deduced from stable-target experiments by assuming isospin symmetry [Fuj05], it is imperative to extend measurements to the full relevant mass range and to unstable nuclei

As explained in detail in Section 2.7 tools to perform charge-exchange experiments with unstable nuclei in inverse kinematics are currently being developed at the NSCL. Beam intensities required for such experiments must exceed 10^6 s^{-1} . As shown in Figure 2.30, the first steps into the unstable neutron-rich region in the relevant mass range (*pf* and *sdg*-shell nuclei) can be made at the CCF, but the ISF will enable one to cover the entire region of interest for type Ia and core-collapse supernovae. Data for a representative set of nuclei, including even-even, odd-odd, and odd-even species and a sampling of the mass range will be necessary and require advanced facilities such as the ISF. This would be sufficient to validate the structure models employed. These models can then be used to produce weak strengths for use in stellar evolution codes that take into account the effects of high stellar temperatures and densities.

Our knowledge of weak-transition rates in stable nuclei could also be rapidly expanded by experiments at the ISF; secondary triton beam intensities would be enhanced by at least two orders of magnitude compared to the capabilities at the CCF, thereby greatly increasing the number of cases that can be studied with the ($t, {}^3\text{He}$) charge-exchange reaction. Such experiments, performed with high resolution and high precision, would enable one to fine-tune the theoretical calculations, further increasing the reliability of the predicted reaction rates.

3.2.3 Classical novae

Classical novae are thermonuclear explosions on the surface of a white dwarf, accreting matter from a companion star in a close binary system [Jos05, Geh98, Sta72]. The ashes of the thermonuclear burning are ejected into space and its composition can be observed through spectral analysis. Dozens of novae are observed each year in our Galaxy. After the explosion occurs, the white dwarf continues to accrete matter until the next explosion, with recurrence times being estimated to be typically hundreds of thousands of years. Today several major problems remain unsolved and might indicate severe deficiencies in our understanding of novae. One of the central problems is how and at which stage white dwarf material, either carbon and oxygen, or oxygen and neon is mixed into the accreted surface layer (see [Ale04] for an example of recent work and references therein). These elements can be clearly identified in nova ejecta. This issue might directly determine the ignition condition and is therefore related to the missing mass problem [Sta99] that refers to the fact that many nova models underpredict the total mass of the ejecta compared to observations. Another open question is the contribution of novae to galactic nucleosynthesis. It seems likely that novae are the source of at least a significant fraction of ${}^{13}\text{C}$, ${}^{15}\text{N}$, and ${}^{17}\text{O}$ found in the solar system [Jos05]. They are also possible contributors to the galactic inventory of ${}^{26}\text{Al}$, a long-lived γ -ray emitter that has been detected by γ -ray observatories.

Novae are also likely producers of copious amounts of short-lived γ -ray emitters, such as ^{18}F or ^{22}Na . So far, existing γ -ray observatories have not succeeded in detecting the corresponding γ rays. An important problem is, therefore, the prediction of production efficiencies for γ -ray emitters in novae in order to judge the necessary sensitivities needed for detection and to interpret any future observations with advanced γ -ray telescopes. This depends directly on nuclear reaction rates. An understanding of the nuclear physics processes during nova explosions is also critical for using observed abundance patterns to constrain nova models and system parameters, such as the white dwarf mass. For example, recent theoretical work, where white dwarf core temperatures and ignition conditions for novae have been calculated self-consistently from the parameters of the binary system, could lead to a solution to the missing mass problem [Tow04]. However, changes in the ignition condition could have dramatic impact on the astrophysical conditions during the explosion and, therefore, on the nucleosynthesis paths. With reliable nuclear reaction rates, one could explore these effects and determine whether the produced abundances of the new models are in agreement with observations. This will either lead to the solution of the problem or reveal further fundamental deficiencies in our understanding of novae.

In summary, the nucleosynthesis in novae depends sensitively on nuclear reaction rates [Cha92,Wie98,Ili02]. Nuclear physics is therefore needed for nova simulations to:

- predict astronomical detection limits for γ rays from radioactive nuclei in matter ejected by novae
- determine the nucleosynthesis contribution of novae, and to novae
- test nova models using the observed composition of the ejecta and to determine the parameters of a particular system

Figure 3.7 indicates the possible reaction flow during a nova explosion. While proton capture rates on stable nuclei are also important, a mild rp-process can develop and proton captures on unstable nuclei can become important. The reactions that have been identified in the past as critical are also marked in Figure 3.7. Because of the sensitivity of the final abundances to these reaction rates, direct measurements with low energy rare isotope beams are needed. Pioneering experiments at existing facilities, such as Louvain-la-Neuve, ORNL, ANL, and ISAC have developed the necessary techniques. Reaction rates with outgoing charged particles have been measured in the past using rare isotope beams (for example [Bar02]), but only very few such reactions play a role in novae. A direct measurement of the proton capture rates requires significantly more beam intensities and have only been possible for very few cases to date [Rui06,Bis03,Dec91]. Some additional rates, especially when stronger resonances are involved, are coming into reach at existing facilities, such as ISAC or the planned development of low-energy beams at the NSCL. These include, for example, $^{23}\text{Mg}(p,\gamma)$, $^{25}\text{Al}(p,\gamma)$, and $^{30}\text{P}(p,\gamma)$ or a few relevant higher lying resonances in $^{29}\text{P}(p,\gamma)$ and $^{35}\text{Ar}(p,\gamma)$. In addition, indirect techniques with rare isotope beams, such as proton scattering (for example [Bar99]), that can be applied with much lower beam intensities have been used. Transfer reaction measurements with stable beams also contributed important information. Though less precise and more model-dependent in their interpretation than the direct measurements, such experiments will continue to improve reaction rate estimates using existing facilities for some cases.

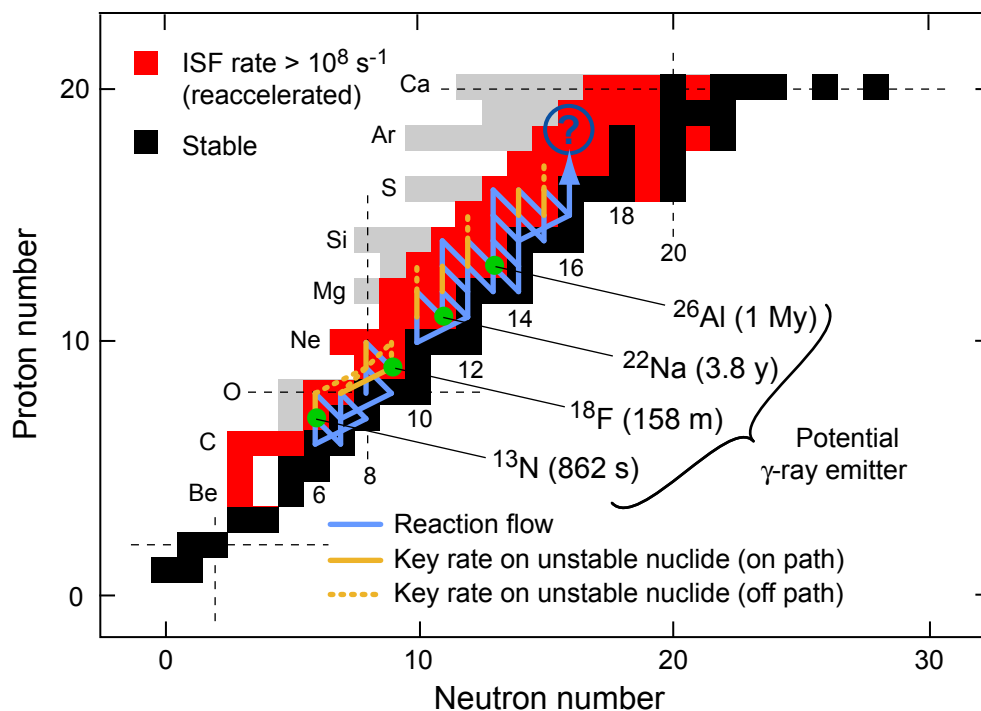


Figure 3.7: The reaction flow during a nova explosion on a rather massive O-Ne white dwarf. Dashed lines indicate the classical shell closures. Also shown is the reach of the ISF for reaccelerated low energy rare isotope beam intensities in excess of 10^8 s^{-1} . At such beam intensities, many direct reaction rate measurements become possible. Reactions on unstable nuclei that have been identified as important for nova nucleosynthesis in sensitivity studies or other work are marked in orange. Also marked are the nuclei that might serve as potentially observable γ -ray emitters (lifetimes in brackets). An accurate prediction of the abundances of these isotopes is particularly important to guide the search for γ -ray signatures in nova ejecta with γ -ray observatories. Adapted from [Ili99].

The intensities of reaccelerated beams at the ISF will be sufficient for direct measurements of the vast majority of the resonances in all reaction rates relevant for nova nucleosynthesis. Examples include the $^{27}\text{Si}(p,\gamma)$, $^{29}\text{P}(p,\gamma)$, $^{31}\text{S}(p,\gamma)$, $^{33,34}\text{Cl}(p,\gamma)$, $^{35}\text{Ar}(p,\gamma)$, and $^{37,38}\text{K}(p,\gamma)$ reaction rates. With the experimental nuclear astrophysics program at the ISF completed, and with continuing progress at stable beam facilities, the entire nuclear physics of nova explosions will be on a solid basis.

3.3 The nature of neutron stars

3.3.1 Crust processes in accreting neutron stars

Matter accreted onto the surface of a neutron star in an X-ray binary system experiences thermonuclear burning via α -capture reactions, the αp -process, or the rp-process either in a steady state or explosively in X-ray bursts within hours to days of arriving on the surface (see Section 3.2.1). Even in the most violent X-ray bursts, at most a few percent of the burned matter can be ejected as the gravitational binding energy exceeds the nuclear energy release by at least a factor of 40 [Wei06]. Most of the ashes therefore remain on the surface of the neutron star and are incorporated into the crust by the ongoing accretion. As a fluid element of ashes is continuously compressed, the rising electron Fermi-energy enables a series of

electron capture reactions that drive the composition towards the neutron dripline on timescales of the order of 10–100 years [Han03b]. Once the neutron dripline is reached, the further fate of the matter is not known with certainty and is subject to an ongoing debate. One possibility is that neutron emission and further electron captures produce lighter nuclei that eventually undergo density-induced fusion reactions [Han03b, Gas05, Yak06] (pynuclear fusion reactions are distinct from thermonuclear fusion, which is induced by temperature). Alternatively, neutron captures and β -decays could produce heavier nuclei, driving the crust composition back to its equilibrium composition [Jon05].

Understanding of the nuclear processes in the crust of accreting neutron stars is important because these processes represent the heat sources that set the thermal structure of the crust. They therefore directly affect a number of observables. Prominent examples are superbursts, which are most likely driven by thermonuclear explosions of carbon in a deep liquid ocean located between the solid crust and the gaseous atmosphere where the X-ray bursts occur. The thermal structure of the neutron star crust directly sets the ignition depth and therefore the recurrence time of superbursts [Bro04]. Both can be extracted from observations [Cum06]. It turns out that with our current, very limited understanding of the nuclear physics in neutron star crusts, heating is insufficient to explain the observed superburst properties. This has led some to speculate that superbursts occur on compact stars made of strange matter [Pag05].

Observations of the thermal luminosity emitted by the neutron stars in transient systems during quiescence are another observable of crustal heating. These systems are normal X-ray bursters until accretion shuts off for months or years. Recently it has become possible with X-ray observatories to observe the cooling behavior of the neutron star crust heated by the nuclear processes during the accretion phase [Wij04, Cac06, Sch06a]. Such data could constrain cooling processes and the existence of exotic phases in the neutron star core. A better understanding of the nuclear physics in neutron star crusts is clearly needed to:

- reliably identify the types of nuclear reaction sequences that occur in the crust of an accreting neutron star in model calculations
- determine whether nuclear reactions can heat the crust sufficiently so that deep ignition of carbon is a viable model for superbursts or whether more exotic scenarios are required to explain superbursts
- to interpret superburst and crust cooling observations in terms of neutron star crust and core properties
- to possibly predict additional observational signatures

The critical nuclear physics input are: masses, electron capture rates, and transition schemes for $A = 20$ – 104 nuclei ranging from stability to the neutron dripline. These quantities determine the depth at which a particular transition occurs and how much energy is released. Of particular relevance is the location of the low lying electron capture strength in the daughter nuclei to determine the fraction of energy emitted as neutrinos for each transition that is therefore not available to heat the crust. In addition, the strength distribution determines, together with neutron separation energies, to which degree neutron emission can occur before the neutron dripline is reached.

At the ISF, charge-exchange reactions on neutron-rich, unstable nuclei with fast beams can provide information on electron capture strength (see Section 2.7). Further away from stability, measurements of the low lying level structure of neutron-rich nuclei, for example with β -decay spectroscopy, would further constrain electron capture transition schemes predicted by theory. Shell and subshell closures and the associated shape changes are particularly important because they lead to rapid changes in strength distributions over a few isotopes or isotones. This can make crust processes dependent on the initial composition, which determines

X-ray bursts and neutron star crust processes

Neutron stars accreting matter from a companion star in a close stellar binary system can be observed as bright Galactic X-ray sources. Quasipersistent soft X-ray transients are a subset of these systems [Wij04,Cac06,Sch06a]. They exhibit extended periods of quiescence that can last years, decades, or even longer. Periods of outbursts follow, during which the accretion of matter from the companion star onto the neutron star turns on for years to decades (hence, quasipersistent). During these outbursts, the source brightens by a factor of 100–1000 and, in addition, shows regular X-ray bursts and superbursts.

Nuclear processes thought to occur during the outburst phase include the qp - and rp -process in X-ray bursts, explosive carbon burning in superbursts, and the processing of the ashes in the crust by electron captures and pycnonuclear fusion reactions. Pycnonuclear fusion reactions are induced by high density, unlike thermonuclear fusion reactions that are induced by high temperature. These nuclear processes heat the crust and change the temperature profile of the neutron star. Once accretion turns off again, the heating stops and the crust cools down. The current generation of advanced X-ray telescopes such as XMM-Newton and Chandra have observed this cooling behavior.

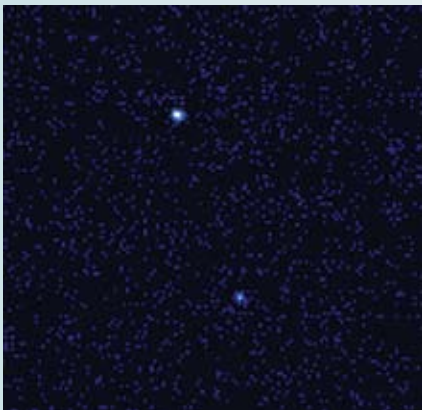


Figure A: Image of the X-ray binary KS 1731-260, observed with the Chandra X-ray observatory about a year after accretion turned off in 2001. Before this time, the object was a bright X-ray source showing normal X-ray bursts and even a superburst. Now the much fainter source is most likely powered by the cooling of the crust that had been heated by nuclear reactions during the accretion phase. Image credit: NASA/CXC/SAO.

An example of this behavior is the object labeled KS 1731-260 (see Figure A) that “turned off” in early 2001 after an active outburst period starting before October 1988. Repeated observations over many years since that time exhibit an exponential cooling behavior (see Figure B) [Cac06]. Both the cooling timescale and the asymptotic behavior can be used to constrain the properties of the crust and the core temperature. This, in turn, provides information about core cooling processes and the possible existence of exotic phases in the center of a neutron star that would alter the cooling processes. Comparison with similar data for another source, MXB 1659-29, revealed differences in the cooling timescale that point to differences in crust properties, possibly due to different composition of the material produced during X-ray bursts. The interpretation of these unprecedented data requires a detailed understanding of the underlying nuclear physics. The relevant nuclear physics includes the properties of the neutron deficient nuclei participating in the rp -process that occurs during the X-ray bursts observed in the outburst phase. This determines the X-ray burst ashes, which sets the initial composition of the material available for crust heating processes. In addition, the properties of the extremely neutron-rich nuclei participating in the crust heating processes themselves need to be known. Both issues will be addressed by the ISF.

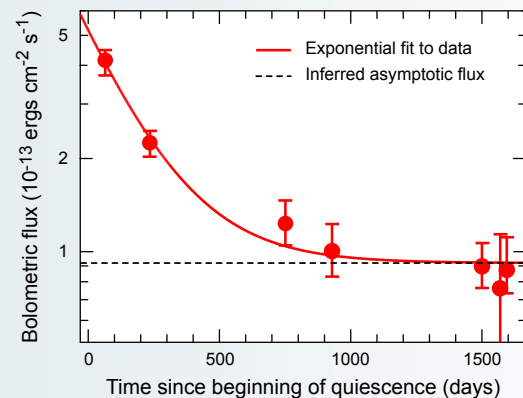


Figure B: X-ray flux from KS 1731-260 after accretion ended, as measured by repeated Chandra and XMM-Newton observations over many years. The drop in flux reflects the cooling of the neutron star crust. This is the first time that the leveling out of the flux to that presumably from the neutron star core has been observed. Adapted from [Cac06].

through which mass regions the electron capture chains ultimately pass until they reach the neutron dripline. Penning-Trap and TOF mass measurements at the ISF would dramatically extend the region of known masses for extremely neutron-rich nuclei (see Section 2.3.1). Finally, experiments with fast beams will also delineate the location of the neutron dripline up to $A \sim 60$ (see Section 2.1.1) into the relevant mass range for neutron star crust processes. This would be a major step towards a better understanding of neutron star crust processes.

3.3.2 The equation of state of dense asymmetric nuclear matter

Macroscopic, strongly interacting dense matter forms the interior of a neutron star and provides the pressure that supports it against gravitational collapse into a black hole. The nuclear symmetry energy provides all of the baryonic contributions to the pressure at saturation density and up to 70% of the pressure at twice saturation density. The symmetric matter EOS provides the remaining hadronic contributions to the pressure. It contributes significantly at densities larger than twice the saturation density but vanishes at saturation density. The EOS in the deep interior governs the maximum mass of neutron stars.

Reflecting its dominant contribution to the pressure, the symmetry energy governs the relationships between the neutron star mass, radius, and moment of inertia. Accurate values for the neutron star masses have been obtained for neutron stars in binary stellar systems, but the radii have not been determined for neutron stars with well-measured masses. Data from NASA's Chandra and the European Space Agency's XMM satellites on omega Cen, M13, 47 Tuc X7, and M28 have provided some information about the radii of neutron stars with unknown masses. Data from EXOSAT, the Rossi X-ray Timing Explorer (RXTE), and XMM have been combined to estimate the radius and mass for the EXO 0748-676 neutron star [Oze06], which is part of a low mass X-ray binary system. Within neutron star models, the radius of 13.4 ± 1.8 km and the high deduced mass $M = 2.1 \pm 0.3 M_{\odot}$ appear to preclude a soft EOS [Oze06]. These values rely, however, on many possibly incorrect assumptions going into the interpretation of the X-ray spectra. Conclusions would be more quantitative if comparable constraints on the symmetry energy could be provided by laboratory experiments discussed in Section 2.8.1 and by laboratory measurements at even higher incident energies.

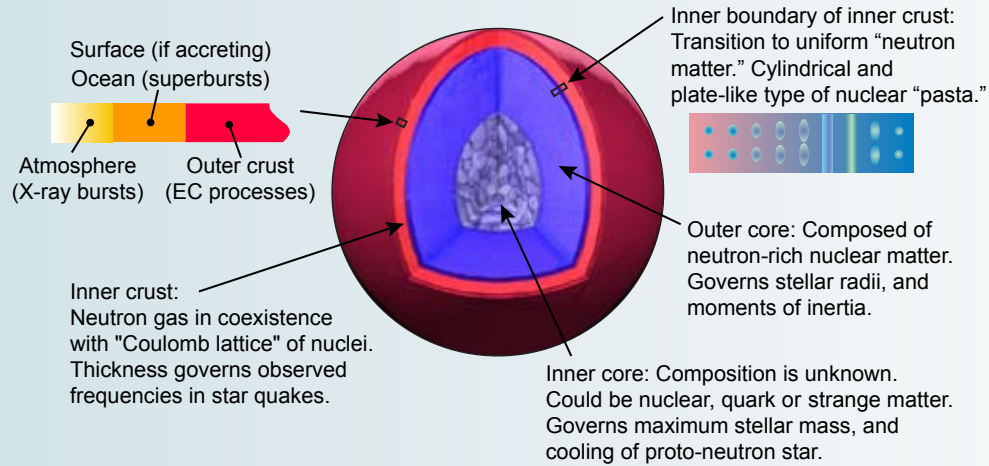
At a given depth in the dense interior, the matter will be in the phase or mixture of phases that has the lowest free energy. The inner crust of the neutron star is expected to be a mixed phase consisting of a Coulomb lattice of denser liquid nuclear droplets embedded in a neutron gas. The thickness of the inner crust, which is sensitive to the density dependence of the symmetry energy at saturation density and below, has recently been constrained by vibration frequencies observed in quakes on the neutron star SGR 1806-20. Experimental constraints on the symmetry energy at this density can be provided by the experiments discussed in Section 2.8.1. Deeper in the core, one may have nuclear matter or strange or quark matter phases depending on whether the symmetry energy of nuclear matter at the relevant density lowers the free energy of nuclear matter below or elevates it above that for the other phases.

The EOS and phase transition in nuclear matter also play a role in the dynamics of core-collapse supernovae. The EOS governs the binding energy of a neutron star formed in the collapse and therefore governs the energy release by neutrinos.

The EOS and the neutrino flux supply the pressure needed for a successful explosion. Neutrino trapping by the in-falling matter depends on the electron capture rates on the nuclei that coexist in a mixed phase along with a gas of nucleons, α particles, and other light nuclei. The capture rates depend on nuclear masses and isospin asymmetries, which, in turn, depend on the nuclear symmetry energy at subsaturation density and on the relevant nuclear level densities at a range of temperatures. Measurements that could be performed to determine these latter quantities are discussed in Section 2.8.1.

After its birth in a supernova, the neutron star will cool primarily by neutrino emission. The neutrino flux and the cooling rate will be significantly enhanced if the fraction of nucleons that are protons in the stellar core exceeds $1/9$, allowing neutrinos to be emitted via the direct nucleonic Urca processes $n \rightarrow p + e + \nu_e$, $p + e \rightarrow n + \nu_e$ that do not require an additional nucleon collision to conserve momentum. Sufficiently large proton fractions can occur in the inner core if the symmetry energy is strongly density dependent. Measurements that could be performed to constrain the symmetry energy at some of the relevant densities are discussed in Section 2.8.1.

The structure of a neutron star



The figure shows the complicated layered structure predicted for neutron stars due to the increase in pressure with depth. If a neutron star is part of a binary system, its outer surface may have a thin hydrogen atmosphere and a thin ocean mainly consisting of heavier nuclei produced by thermonuclear burning on the surface. Beneath the ocean of nuclei, the density is such that the neutron star will have a solid outer crust consisting of nuclei embedded in a degenerate electron gas. A transition from the outer crust to an inner crust will occur at the level that electron capture reactions raise the neutron chemical potential to the extent that nuclei can be embedded in a neutron gas. The density of the neutron gas in the inner crust increases with depth and the nuclei, arranged in a Coulomb lattice in this layer, become larger and more neutron-rich with depth. The transition to the outer core of uniform nuclear (mainly neutron) matter may proceed through a variety of geometrical "pasta" phases that start as high as the lower boundary of the inner crust. The nature of the stable phase of the inner core of the neutron star is not known; it could be nuclear matter, quark matter, or consist of pion or kaon condensates. Various astrophysical observables that provide information about these stellar regions are indicated in the figure.

4. Studies of fundamental interactions

Despite its large phenomenological success, the Standard Model is not generally considered a “fundamental” theory because it uses a large number of parameters that rely on experimentally determined quantities and a number of seemingly arbitrary assumptions. As a consequence, many possible extensions to the present Standard Model have been proposed that predict new exchange particles or extended symmetries.

Tests of the predictions of the Standard Model have to be performed in different energy regimes. High-energy collider and electron-electron scattering experiments are required as are precision decay studies and atomic spectroscopy. These results complement each other and are needed for indicating how the Standard Model may have to be modified. At low energies, precision measurements in nuclear β -decay [Sev06] are a powerful approach to search for violations of the fundamental symmetries and to search for new interactions. Furthermore, precise studies of atomic transitions give access to the study of parity nonconserving lepton-quark interaction. Low-energy rare isotope beams are an important tool for such studies. Progress will come from advances in rare isotope production, e.g., higher yields and better beam quality; the development of new experimental techniques, e.g., atom and ion trapping of rare isotopes; and the possibility of achieving high nuclear polarizations in beams and samples of rare isotopes. Another advance towards expanding the experimental opportunities for fundamental interaction and symmetry studies is the recently demonstrated conversion of beams of fast projectile fragments into high-quality low-energy beams that can be used for precision experiments. An advanced gas-stopping technique being implemented at the NSCL will be used at the ISF, providing intense low-energy rare isotope beams that are difficult or impossible to produce via the ISOL method.

4.1 Test of CVC and determination of V_{ud}

The study of superallowed β decays of nuclei near $N = Z$ has long been used as a powerful tool for probing basic concepts of the Standard Model of Electroweak Interactions [Har05a,Har05b]. One of its key features is the conserved vector current (CVC) hypothesis, which postulates that the vector-current part of the weak interaction is not influenced by the strong interaction. A consequence of CVC is that the strength of superallowed $0^+ \rightarrow 0^+$ β decays, given by the nuclear decay matrix element, should be the same for all nuclei undergoing superallowed β decay, except for a number of small theoretical corrections. The strength of superallowed Fermi-type β decays has been measured with very high precision for isotopes ranging from ^{10}C to ^{74}Rb . The resulting FT-values (Figure 4.1), which include small nuclear and radiative corrections at the percent level, confirm the CVC hypothesis remarkably well at a level of a few 10^{-4} .

From the average FT value, the weak vector coupling constant G_V can be determined. Combining this value of G_V with purely leptonic muon decay data gives us the most precise value of the up-down quark matrix element V_{ud} of the Cabibbo-Kobayashi-Maskawa (CKM) matrix, which relates the weak quark eigenstates to the mass quark eigenstates. Using the value for V_{ud} together with V_{us} from kaon decay and V_{ub} from B meson decay allows for a test of the unitarity of the CKM matrix. A nonunitarity of the CKM matrix could have important implications, such

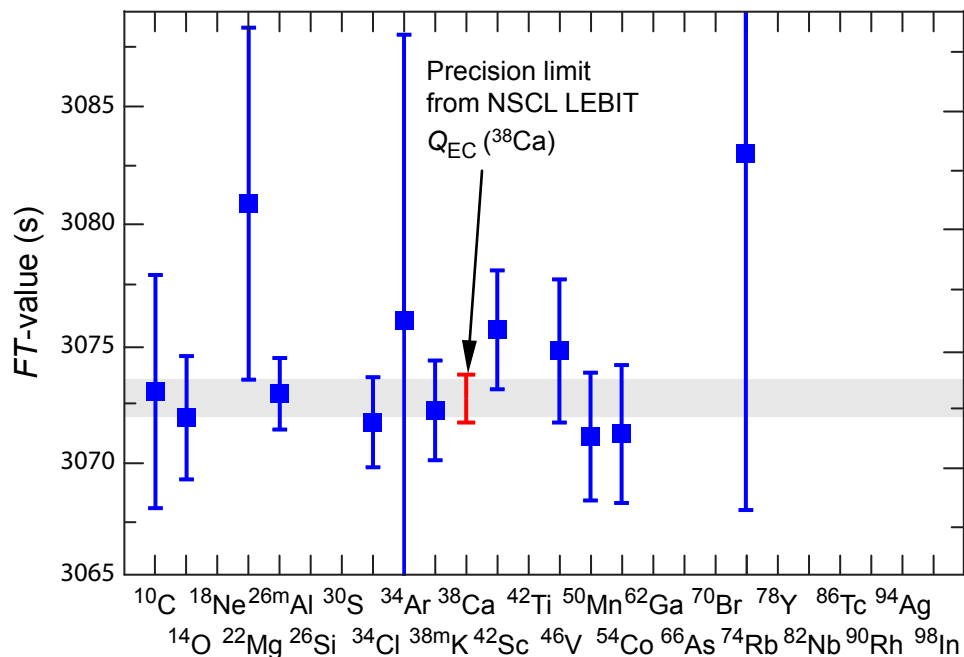


Figure 4.1: FT-values for superallowed β emitters. The horizontal band gives the uncertainty of the average value of 3073.5(12) s. Adapted from [Har05b]. In the case of ^{38}Ca , not all information exists to determine the FT-value. The error bar indicates the precision limit due to the Q_{EC} value alone, which has recently been improved by more than an order of magnitude in a Penning-trap mass measurement with the LEBIT facility at the NSCL [Bol06b].

as the existence of a fourth generation of quarks, exotic fermions, or the need to include right-handed currents in the weak interaction.

For more than 10 years, the unitarity test of the CKM matrix has resulted in a deviation from unitarity by more than two standard deviations. Results from newer kaon decay studies indicate a larger average value for V_{us} than previously assumed that would restore the unitarity of the CKM matrix within the present uncertainties [Yao06]. However, there are still open questions with respect to the calculation of the necessary kaon-to-pion form factor [Ram06]. Furthermore, recent precision mass measurements [Sav05] propose a significant change of the electron capture Q_{EC} value for ^{46}V . It appears prudent to revisit the well-known cases and to improve the precision and accuracy of the experimental data as new and improved techniques become available. It remains important to obtain new experimental data for the determination of precise FT-values of superallowed β emitters. Such data are necessary to extend the set of nuclei for testing CVC beyond the few well-known cases, to benchmark the calculation of the necessary theoretical corrections, and for eventually testing CVC and determining V_{ud} with higher precision.

The required measurements are precise mass differences between mother and daughter nuclei (giving the decay Q -value), decay half-lives, and $0^+ \rightarrow 0^+$ branching ratios. Of particular interest are those decays for which theoretical isospin-symmetry-breaking corrections are large. Assuming CVC, precise data on these candidates provide a sensitive test of the theoretical corrections and will help to improve their calculation. Examples of such candidates are ^{30}S , ^{38}Ca , ^{62}Ga , ^{66}As , and ^{70}Br . Work on these candidates is already going on. A recent example is ^{38}Ca

[Bol06b] in which a mass accuracy of 280 eV has been achieved via a Penning-trap mass measurement with the LEBIT facility at the NSCL. In order to test CVC under more extreme conditions, it is desirable to extend the study of superallowed decays to nuclei heavier than ^{74}Rb . These measurements are challenging because of decreasing production rates, short half-lives, and more complicated decay schemes. High beam rates are required together with high-efficiency detectors for γ rays, β rays, and conversion electrons. A high-performance Penning-trap mass spectrometer is needed for the mass measurements. Furthermore, improvements in the calculation of the theoretical corrections (see for example [Mar06]) will be decisive for utilizing the full impact of the new and improved experimental results.

At the present NSCL facility, it will be possible to determine masses and partial half-lives of most superallowed β emitters up to $A = 70$ with a precision useful for the test of CVC. For the mass measurements, an overall stopping, beam manipulation, and detection efficiency of 10% is assumed, which should be even exceeded once the cyclotron stopper is in place. With the beam rates available at the ISF, it will be possible to extend high precision studies of superallowed β emitters beyond $A = 74$ up to $A = 90$. With beam rates in most cases far above 1000 s^{-1} , the determination of the partial half-lives will be possible with a precision similar to that for the present well-known cases. Relative mass accuracies of better than 10^{-8} will be achievable for all isotopes along the $N = Z$ line with a high-performance Penning-trap mass spectrometer like the one in the LEBIT facility. New ft -values for heavier, superallowed β emitters will provide an excellent testing ground for shell model calculations that predict the required isospin-breaking corrections. Better Hamiltonians for the pf shell are becoming available [Hon02], and the computational ability to include $g_{9/2'}$ required for the heavier candidates, is becoming more feasible.

4.2 Atomic parity violation

The study of atomic parity violation has been pursued over about three decades, but accuracies below the 1% level have only been achieved in recent years. The atomic parity violation [Bou97] is predominantly caused by the direct Z_0 exchange between electrons and a nucleus. This neutral current leads to a mixing of S and P states in the atom, which can be observed in forbidden electric dipole transitions between states of the same parity. Since this mixing scales with Z^3 , the search for atomic parity violation is best performed in heavy atoms. Atomic parity violation studies provide important tests of the Standard Model and a precise determination of its parameters, such as the weak mixing angle θ_w . A small nuclear-spin dependent part of the atomic parity violation arises from the interaction of electrons with the nuclear Schiff moment and the anapole moment. Its observation provides a unique probe of parity violation in purely hadronic nuclear interactions [Hax01]. The anapole moment has been observed in an experiment with stable cesium atoms [Woo97].

A particularly interesting case in which to study atomic parity violation is francium [Gom06]. The size of the weak effects in francium is more than ten times larger than in cesium. Its atomic structure is simple enough to permit necessary atomic structure information to be calculated with the required precision. Furthermore, the choice of different isotopes allows nuclear corrections to be minimized. Eventually, the difference of the weak interactions with protons or with neutrons could be studied.

Pioneering work on francium has been performed at Stony Brook and experiments are planned at ISAC at TRIUMF. The low-energy beam rate required is about 10^6 s^{-1} [Gom06]. At the ISF, fast-beam fragmentation of uranium will provide beam rates for the long-lived isotopes ($T_{1/2} > 100 \text{ s}$) that are high enough for such studies.

4.3 Tests of parity and time reversal symmetries

The CPT theorem requires invariance under the combined application of three independent operations, namely charge conjugation (C), parity inversion (P), and time-reversal (T). Direct evidence for CP violation in the decay of the neutral kaon [Chr64], which is now implemented in the framework of the Standard Model, led immediately to searches for possible T violation. CP violation is thought to have played a crucial role in producing the excess of matter over antimatter early in the history of the universe [Din04]. The Standard Model does not violate the CP symmetry strongly enough to account for this excess. To understand baryogenesis, the physical process of generation of nucleons in the early universe, we must first discover the additional CP violation, if it indeed exists. As a complementary symmetry to the CP symmetry, a test of T invariance is essential to address such an important question.

One such effort is the determination of electric dipole moments (EDM), which violate parity as well as time-reversal invariance. Experiments to detect a nucleon EDM have been performed with ultra-cold neutrons and set a constraint as $|d_n| < 6.3 \times 10^{-26} \text{ ecm}$ (90% CL) [Har99]. On the other hand, the EDM of an atom (or molecule) may result from the EDMs of nucleons, electrons, and/or the P- and T- violating interactions among them. The most stringent constraint was set by the measurement of a diamagnetic ^{199}Hg state as $|d| < 2.1 \times 10^{-28} \text{ ecm}$ (95% CL) [Rom01]. An experiment on a paramagnetic ^{205}Tl state gave an electron EDM limit of $|d_e| < 4 \times 10^{-27} \text{ ecm}$ [Com94]. As shown in Figure 4.2, this is already close to the electron EDM prediction by the super symmetric model, the left-right symmetric model, and the Higgs model.

The sensitivity in observing EDMs can be enhanced by studying heavy rare isotopes. Due to relativistic effects, the measurable electron EDM in atomic systems is proportional to Z^3 [San65]. Therefore measurements on the heavier Z atoms are more sensitive to the EDM. Francium is a very good candidate because of its simple atomic structure. Hadronic EDMs observed in diamagnetic atoms can experience large enhancement factors (100–1000) if the nucleus is octupole-deformed [Fla95a,Spe97]. Such deformations exist in rare isotopes of radon, radium, and francium.

New experiments with higher precision are required in a variety of atomic systems. They will help us to learn to what extent EDMs exist and may contribute to the understanding of the matter-antimatter asymmetry in our universe. Examples of rare isotopes considered for EDM studies are ^{211}Rn , $^{223,225}\text{Ra}$, and ^{221}Fr . Rates for the low-energy beams higher than 10^7 s^{-1} are required for these studies and will be available at the ISF from fast beam fragmentation and gas stopping.

Complementary searches for CP violation can be performed in low energy β -decay experiments. Time-reversal violation tests via correlation experiments in β -decay require an odd number of spin and/or momentum vectors, which is odd in time-reversal operations. The results of the nuclear β -decay experiments on the neutron

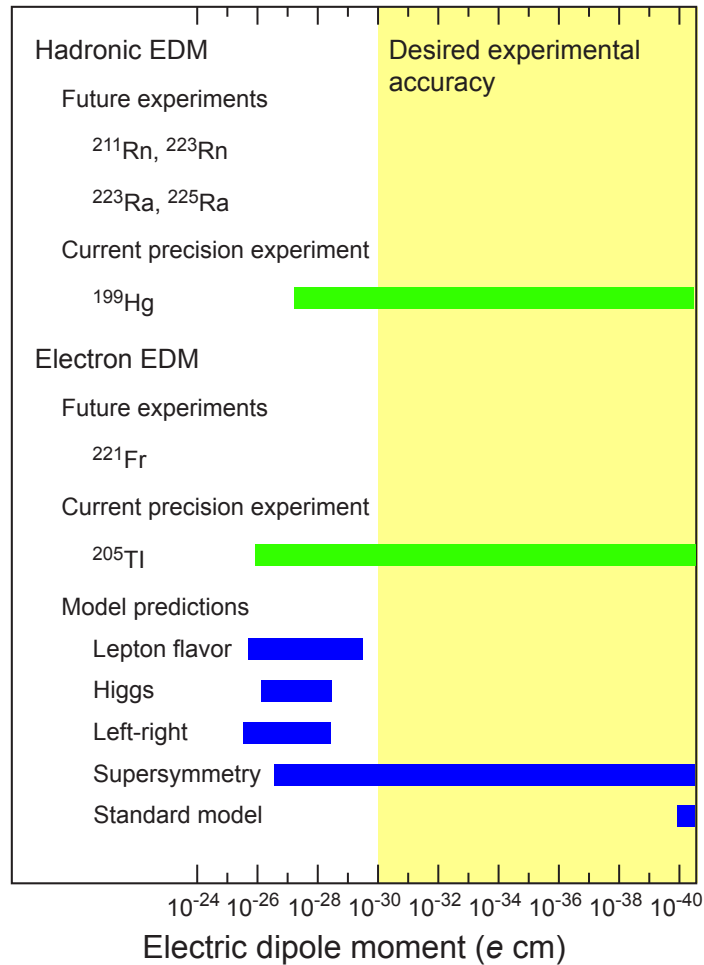


Figure 4.2: Experimental limits for electric dipole moments (EDM) observed in atoms together with rare isotopes that are candidates for future studies. In the case of the electron EDM, theoretical predictions are shown.

[Lis00,Sol04], ^8Li [Hub03], ^{19}Ne [Cal74,Bal77,Hal84], and ^{56}Co [Cal77] are all consistent with T invariance and the Standard Model. A potentially more precise time-reversal violation test can be obtained in a β - γ -ray angular correlation experiment from spin-aligned nuclei [Mor57,Hol72]. This type of experiment has been performed in the case of ^{56}Co ; however, it provides the poorest constraint on T-violating coefficients. The superallowed β emitter ^{36}K has been suggested as a very good candidate [You95]. Nuclear alignment can be achieved by laser polarization of a low-energy beam. The required beam intensity to achieve a result that provides a constraint on T-violation better than that from previously studied D and R coefficients is $> 10^7 \text{ s}^{-1}$. Another promising candidate is ^{52}Co . Since optical pumping is difficult, a beam intensity of about 10^8 s^{-1} is required to compensate for the smaller nuclear alignment obtained in the beam production reaction. Both experiments will be possible at the ISF.

4.4 Search for new interactions in the weak nucleon current

The Standard Model describes the β -decay process in terms of an exchange of charged vector bosons between the hadronic and leptonic currents. Only vector

and axial-vector type interactions are allowed in the Standard Model. However, scalar and tensor type interactions could exist and, at present, are only ruled out at a level of about 10%. Finding such new interactions would provide a signature of new physics beyond the Standard Model, possibly requiring the exchange of leptoquarks or new charged bosons.

The FT -value confirmation of CVC, discussed above, over wide ranges of Q -values, tests at least one explicit particle physics model of scalar interactions. The Q -dependence of the ft values sets direct stringent limits on scalars that couple to Standard Model neutrinos by constraining the “Fierz” scalar-vector interference term. In certain R -parity violating SUSY models, this observable could be large. The sensitivity for observation is inversely proportional to Q , so the higher Q -values available in heavier $N = Z$ nuclei constrain the baseline value. Greater sensitivity to this observable could test a particular assumption about the SUSY models that is difficult to constrain with collider studies [Ram06].

A promising approach to search for new interactions in the weak nucleon current are β -decay studies, in which the correlation between the directions of emission of the β -particle and the neutrino is studied. This correlation depends on the coupling constants for the various interactions and hence provides the key for the search for exotic currents. Scalar currents can be searched for in pure Fermi decays and tensor currents in pure Gamow-Teller decays.

Since the neutrino cannot be detected directly, the electron-neutrino angular correlation coefficient is determined by studying the correlation between the β particle and the recoiling ion. The direction of the recoiling ion can be either measured directly or can be deduced from the measurements of the Doppler shift of the γ radiation emitted or the kinematic shift observed in the delayed proton or α decay of the recoil nucleus.

These experiments are difficult because small effects have to be observed and sources of systematic errors have to be understood. Therefore, only a few high precision experiments have been performed to date. The most stringent limit on scalar currents comes from a delayed proton-emission experiment on ^{32}Ar at ISOLDE [Ade99] and an atom trap experiment with $^{38\text{m}}\text{K}$ at ISAC [Gor05]. The most precise experiment searching for tensor currents was carried out with ^6He at Oak Ridge more than four decades ago [Joh63]. All these experiments are still in agreement with Standard Model predictions. A recent atom trap experiment [Sci04] with ^{21}Na performed at Berkeley shows a large discrepancy with the Standard Model prediction, though further work confirms systematic trap effects – photo-assisted production of molecular dimers – that are in the process of being controlled.

New electron-neutrino correlation experiments are in preparation and it is interesting to note that they all use either ion or atom traps. The possibility of suspending ion or atom ensembles that are nearly free in space is the key to achieving the highest accuracy. Examples of new developments are WITCH [Koz06b] at ISOLDE, a large magnetic recoil spectrometer connected to a Penning trap, a Paul trap experiment [Rod05] at LPC-Caen for the search for tensor currents in ^6He decay, as well as the TRI μ P facility [Jun03] at KVI-Groningen, where atom traps will be employed for correlation studies similar to those performed at Berkeley and ISAC.

In addition to the nuclei already in use, other interesting candidates for electron-neutrino correlation studies in ion traps are ^{14}O , $^{26\text{m}}\text{Al}$, ^{33}Cl , ^{35}Ar , ^{42}Sc , ^{46}V , ^{50}Mn , and

^{54}Co . The minimum required beam rate depends on the specific experiment. A rate of 10^8 s^{-1} is assumed to be a reasonable lower limit for decay correlation studies using ion traps. With the likely exception of ^{35}Ar , it appears to be difficult or impossible to achieve such beam rates with the ISOL technique, even at a high beam power of 100 kW. At the NSCL, low-energy beam rates close to 10^8 s^{-1} will be available for $^{26\text{m}}\text{Al}$, ^{33}Cl , and ^{35}Ar . At the ISF, the rates exceed 10^8 s^{-1} for all candidates, making this facility a prime place for such studies.

4.5 Search for induced currents in weak interactions

The Standard Model predicts that β decays can be described by the vector – axial vector (VA) form of the weak nucleon current. Even if scalar (S) and tensor (T) interactions in the fundamental weak quark-lepton interactions do not exist, currents can be induced by the strong interaction due to pion exchange in the nucleus (for a review see [Gre85]).

In the vector current, two of the induced terms are the weak magnetism f_W and the induced scalar term f_S . In the framework of the CVC theorem, where the weak currents and the isovector part of electromagnetic current form an isospin triplet, f_W and f_S are exactly given. The scalar term f_S should be zero and, experimentally, has been determined to be small ($f_S < 0.0013$ [Har05b]). Theory predicts a nonzero value for the weak magnetism f_W , which is yet to be determined experimentally with good precision. In the case of the axial vector current, two terms may be induced, a pseudo-scalar term, f_P and a tensor term, f_T . The f_P term can be determined in muon capture reactions. The f_T term is known as a Second Class Current (SCC) [Wei58,Wil00]. According to the Standard Model, it should be zero. However, the small mass difference between proton and neutron (and hence up and down quarks) may result in a small but finite number, $f_T \sim 10^{-5}/\text{MeV}$ [Shi96]. The most stringent constraint $f_T < 2 \times 10^{-4}/\text{MeV}$, obtained from β -decay angular distribution from aligned ^{12}B and ^{12}N [Min02], does not reach that level.

One possibility for searching for weak magnetism f_W in the vector current interaction is a systematic and very precise measurement of the spectral shape of β -decay energy spectra observed in pure $1 \leftrightarrow 0$ Gamow-Teller transitions, where a simple interpretation of the shape factor is possible. Because the effect of f_W on the spectral shape appears in the form of $\sim f_W E_{\beta^+}$, high-energy β decays are preferred. At the NSCL, a remeasurement of a shape factor of ^{12}B and ^{12}N with higher precision would be possible. At the ISF, the $^{24\text{m}}\text{Na}$ and $^{24\text{m}}\text{Al}$ isospin $T = 1$ pair would be available with required beam rates $> 10^8 \text{ s}^{-1}$, allowing the currently very small set of test cases to be extended. For the determination of the shape of the β -decay energy spectrum with high precision and efficiency, an ion trap based spectrometer similar to the WITCH facility [Koz06b] at ISOLDE, already mentioned above, would be a good choice.

For a precise determination of the induced tensor term f_T in the axial vector current interaction, a measurement of the β decay angular distributions from spin-aligned mirror nuclei can be employed. Taking advantage of the mirror symmetry, the results for both nuclei allow systematic effects to be minimized, which is essential to extract the very small effect of the induced tensor term f_T . Polarized beams are required. Candidates for which polarization can be achieved via laser excitation are preferred because of the much larger degree of polarization achievable compared

to using reactions. A very promising example is ^{13}O . The high β -decay energy and a pure GT transition make ^{13}O very sensitive to f_T . The polarized ^{13}O beam can be obtained by optical pumping, starting from a metastable atomic state [Tin90]. For competitive measurements, low-energy ions with a beam rate of $> 10^7 \text{ s}^{-1}$ are typically required. The necessary measurement of the mirror partner ^{13}B is also possible at the NSCL. It could be performed if a ^{13}B experiment in progress at Osaka University would not succeed. It will be important to study more candidates to put a reliable limit on the induced tensor term. In addition to the $A = 13$ mirror system, the isospin $T = 3/2$ ^9Li - ^9C mirror pair can be studied at the NSCL. At the ISF, the studies could be extended to the $T = 1$ isospin pair $^{24\text{m}}\text{Na}$ - $^{24\text{m}}\text{Al}$, and the $T = 3/2$ pairs ^{21}F - ^{21}Mg and ^{25}Na - ^{25}Si .

5. Isotope Science Facility (ISF)

The ISF will be built on the southern part of the campus of MSU and will be fully integrated into other educational and research activities on campus. The site allows full design optimization without regard to space constraints and a full range of possible additions to maintain a world-leading program. A modestly less expensive option was evaluated that would utilize the present NSCL site as described in Section 7; however, the approximately 11-acre site poses design constraints even for the initial facility and virtually precludes further upgrades. The options are compared in the Epitome.

The initial facility layout is shown in Figure 5.1. Stable isotopes will be accelerated to ≥ 200 MeV/nucleon with a superconducting linac. The target area will have an initial implementation of an in-flight production target along with the conventional construction necessary to allow a later addition of an ISOL production target. Both a high energy physics program and a program with reaccelerated beams will be instituted using rare isotopes separated in flight. The low-energy, reaccelerated beam physics program will use rare isotope beams brought to rest in a novel gas stopping system and reaccelerated using an Electron Beam Ion Trap (EBIT) and a superconducting linac. Considerable cost savings will be realized by reuse of NSCL equipment, such as the A1900 fragment separator, fast beam experimental equipment, and beamline components. Based upon a preliminary evaluation, it is anticipated that the nuclear science program will be interrupted for about six months while the A1900 fragment separator is removed from the NSCL and reinstalled at the new facility.

As shown in Figure 5.1, the accelerator complex for the ISF consists of two superconducting linacs. The primary accelerator is the driver linac, which generates high intensity stable heavy ions for the production of rare isotopes. A smaller linac reaccelerates rare isotopes from rest to energies above the Coulomb barrier for nuclear physics studies.

The driver linac requirements are:

- acceleration of any stable isotope to energies ≥ 200 MeV/u
- delivery of at least 100 kW (up to 400 kW if ion-source performance permits) of stable isotope beam power to the rare isotope beam production targets
- low beam loss to minimize induced radioactivity and minimize any additional cryogenic load

Minimal beam losses, high reliability, and low cost are the main driving considerations in the design that we describe below. To meet the beam power requirement, the driver linac is designed to allow the acceleration of two-charge-state beams from the ion source for ions heavier than xenon. In addition, two charge-stripping sections will increase the charge state for the heaviest ions. Only one charge-stripping station will be used for light ions. The locations of these stripping stations have been chosen to minimize the required accelerating voltage. Table 5.1 gives the beam parameters of representative ions in the driver linac beam list.

The reaccelerator requirements are:

- capture and acceleration of the largest possible fraction of the rare isotopes produced;
- acceleration of rare isotopes to energies of ~ 12 MeV/u. Intermediate energies are available in different experimental areas, as shown in Figure 5.1.

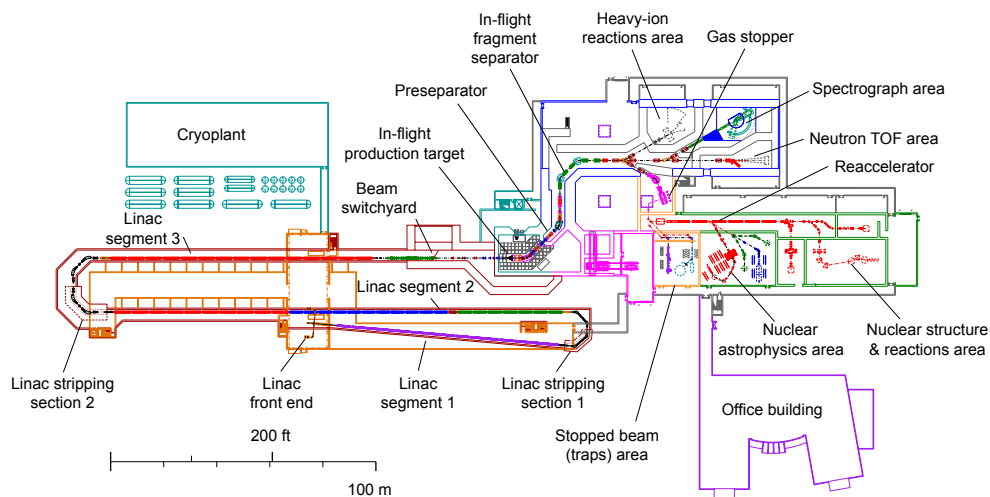


Figure 5.1: Layout of the accelerator complex and experimental areas. The driver linac consists of a room temperature front end and three superconducting linac segments, separated by two beam-stripping sections. The driver linac is designed to deliver up to 400 kW uranium beam power on a production target. Also shown is the reaccelerator linac, designed to deliver rare isotopes with energies in the range of 0.5 to 12 MeV/u.

Table 5.1: Driver linac parameters for representative primary ion beams. For each segment, e.g., segment 1 or stripping section 1, the charge state(s) Q , output energy E_{out} , and transmission efficiency (Trans. efficiency) are given. The current, in particle microamperes, is the electrical current divided by the charge state Q . The driver linac will provide protons at 525 MeV/u and ^3He at 376 MeV/u.

| Beam | | Ion | O | Ar | Kr | Xe | U |
|-------------------|---------------------|--------------------|-------|-------|-------|-------|-------|
| | | Z | 8 | 18 | 36 | 54 | 92 |
| | | A | 18 | 40 | 86 | 136 | 238 |
| Driver linac | Front end | I_{source} (pμA) | 104.3 | 46.7 | 28.2 | 20.8 | 13.2 |
| | | Q | 6 | 8 | 14 | 18 | 28–29 |
| | | E_{out} (MeV/u) | 0.3 | 0.3 | 0.3 | 0.3 | 0.3 |
| | | Trans. efficiency | 80% | 80% | 80% | 80% | 80% |
| | Segment 1 | Q | 6 | 8 | 14 | 18 | 28–29 |
| | | E_{out} (MeV/u) | 15.1 | 12.8 | 12.1 | 11.6 | 12.0 |
| | | Trans. efficiency | 100% | 100% | 100% | 100% | 100% |
| | Stripping section 1 | Q | 8 | 17–18 | 32–34 | 46–49 | 71–75 |
| | | E_{out} (MeV/u) | 14.9 | 12.6 | 11.9 | 11.4 | 11.8 |
| | | Trans. efficiency | 100% | 100% | 89% | 80% | 80% |
| | Segment 2 | Q | 8 | 17–18 | 32–34 | 46–49 | 71–75 |
| | | E_{out} (MeV/u) | 160.6 | 160.6 | 139.5 | 129.1 | 112.1 |
| | | Trans. efficiency | 100% | 100% | 100% | 100% | 100% |
| | Stripping section 2 | Q | 8 | 17–18 | 32–34 | 53–54 | 88–90 |
| | | E_{out} (MeV/u) | 160.6 | 160.6 | 139.5 | 123.9 | 109.5 |
| | | Trans. efficiency | 100% | 100% | 100% | 100% | 99% |
| | Segment 3 | Q | 8 | 17–18 | 32–34 | 53–54 | 88–90 |
| | | E_{out} (MeV/u) | 266.4 | 267.7 | 233.1 | 222.0 | 202.5 |
| Trans. efficiency | | 100% | 100% | 100% | 100% | 100% | |
| Output | | I (pμA) | 83.4 | 37.4 | 20.0 | 13.3 | 8.3 |
| | | Energy (MeV/u) | 266 | 268 | 233 | 222 | 203 |
| | | Power (kW) | 400 | 400 | 400 | 400 | 400 |

5.1 Driver linac

Figure 5.2 shows a conceptual schematic for uranium acceleration in the driver linac. The driver linac design utilizes a room temperature front end consisting of three systems. The first elements are the Electron Cyclotron Resonance (ECR) ion sources with concomitant high-voltage platforms and charge-state selection systems. Following the charge-state selection is the Low Energy Beam Transport (LEBT) system that bunches the beam and provides the match of the six-dimensional phase space to that required at the entrance of the Radio Frequency Quadrupole (RFQ). The RFQ is used to accelerate the beam from 12 keV/u to 300 keV/u, providing the appropriate velocity for injection into the superconducting driver linac. The Medium Energy Beam Transport (MEBT) matches the RFQ beam into the driver linac.

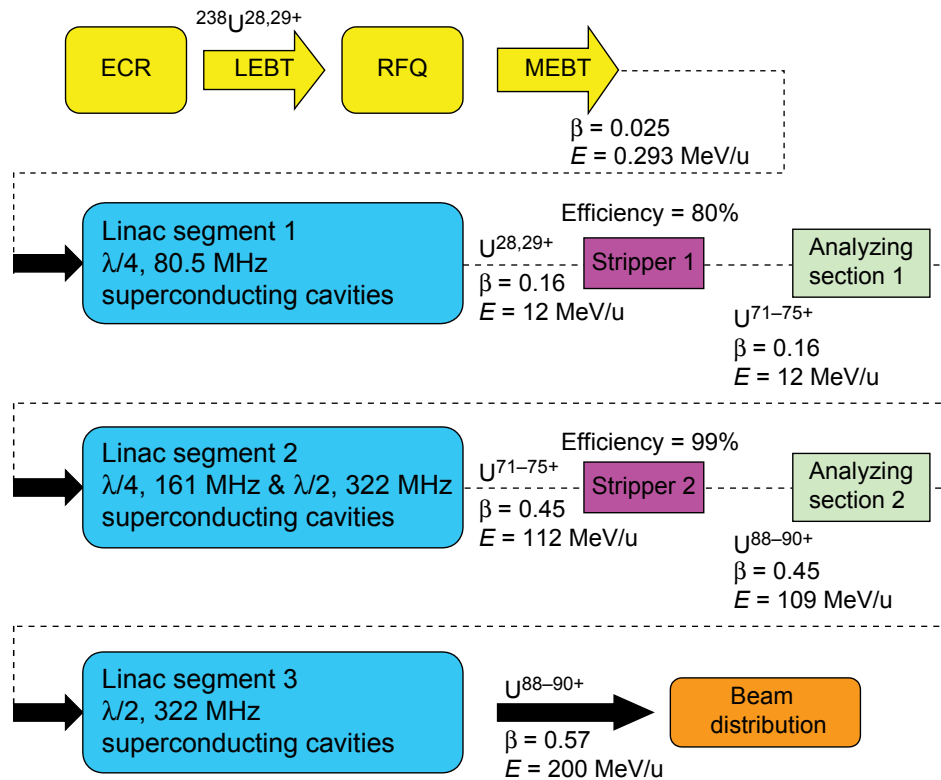


Figure 5.2: Conceptual schematic for uranium acceleration. The room temperature front end (yellow) prepares beam extracted from electron cyclotron resonance (ECR) ion sources for injection into the superconducting linac. The superconducting linac consists of three segments separated by two beam stripping sections.

The RFQ requirements are met with a room temperature structure, obviating the need for superconducting technology for the initial acceleration stage. However, beyond the RFQ, superconducting technology has been adopted, since it most efficiently achieves the cw operation needed to reach the required beam power.

The proposed driver and reaccelerator linacs are built upon the linac design for the Rare Isotope Accelerator (RIA) [Wu04] and largely use the same low energy superconducting accelerating structures (e.g., quarter-wave and half-wave resonators). A tenth harmonic system was chosen, making the lowest linac frequency 80.5 MHz. The design requires only five cavity types for the superconducting linacs, which simplifies the overall project in terms of research, design, fabrication, implementation, and operation.

5.1.1 Front end

The driver linac front end is comprised of ECR ion sources, the Low Energy Beam Transport line, the Radio Frequency Quadrupole, and the Medium Energy Beam Transport system, as illustrated in Figure 5.3. The dc ion beam from the ECR ion source is first analyzed by an achromatic charge-to-mass selection system. The selected charge-to-mass ratio is prebunched in the LEBT by a multiharmonic buncher and matched into the RFQ. The 80.5 MHz RFQ accelerates the beam from 12 keV/u to 300 keV/u. The MEBT then matches the beam into the superconducting linac for further acceleration.

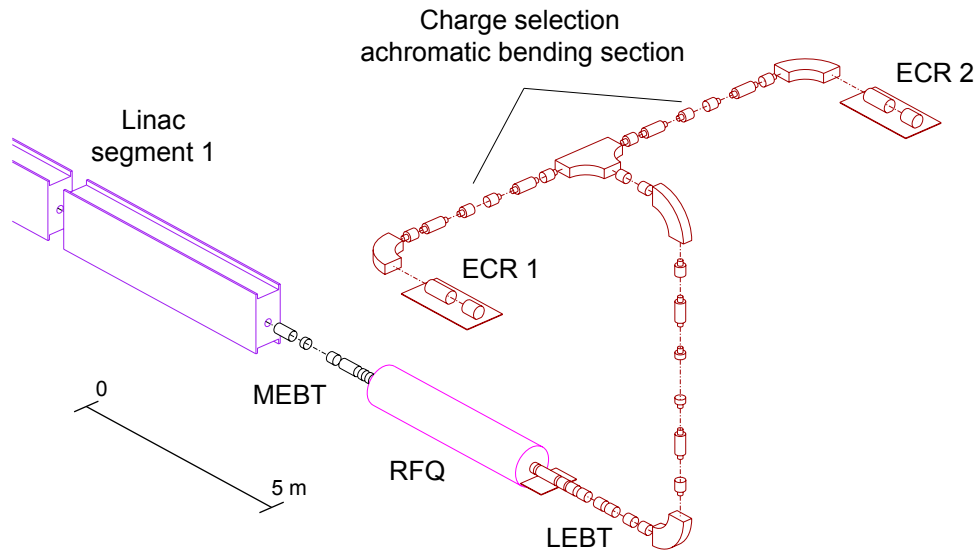


Figure 5.3: Schematic layout of the driver linac front end. The ECR source is followed by a beam selection system to select the correct ion and charge state(s). Either of the two ECR sources can provide beam to the low energy beam transport system, which matches the beam to the radio frequency quadrupole. The medium energy beam transport system matches the beam into the superconducting linac.

To increase the final beam power for the heaviest ions, a two-charge-state beam will be selected and accelerated in the front end. Since the heaviest ion beams are the most challenging, the front-end design effort focused on a two-charge-state uranium beam. A number of standard computer codes were used during the design process. The DIMAD [Ser85] and TRACE3D [Cra97] codes were used for the optics design. In addition, the PARMELA [You05] code was used to simultaneously track the multi-species beam, including three-dimensional space-charge forces, from the ECR to the entrance of the RFQ and from the exit of the RFQ through the MEBT. The beam dynamics analyses in the RFQ were performed with the PARMTEQM [Cra05] code and the results were crosschecked with the TOUTATIS [Dup00] code. The operational rf fields of the RFQ were calculated with MAFIA [MAF00].

5.1.1.1 ECR ion source

An ECR ion source can be used to ionize a wide range of elements to high levels of ionization [Don89,Gel96]. Development and refinement of ECR ion sources over the past 30 years have dramatically improved their performance. However, for most ions heavier than xenon, current ECR ion sources are unable to deliver enough current in a single charge state to achieve a final beam power of 400 kW from the driver linac. To circumvent the ion source beam current limitations for heavier ions, a two-charge-state injection mode is proposed similar to that proposed for RIA [Dei95,Ost00].

Research and development to improve ECR performance for heavier ions is currently being conducted by Lawrence Berkeley National Laboratory (LBNL) with the VENUS (Versatile ECR ion source for Nuclear Science) test facility [Lei03a,Lei03b]. Preliminary measurements for the production of several ions at VENUS have shown very promising results. For example, 16 pμA $^{136}\text{Xe}^{20+}$ and 9.7 pμA $^{209}\text{Bi}^{27+}$ have been extracted [Lei05]. A similar ion source, Superconducting

Source for Ions, (SuSI) [Zav05] is under development at NSCL, as shown in Figure 5.4. It is anticipated that the goal of 400 kW uranium beams can be achieved with these ECR sources.

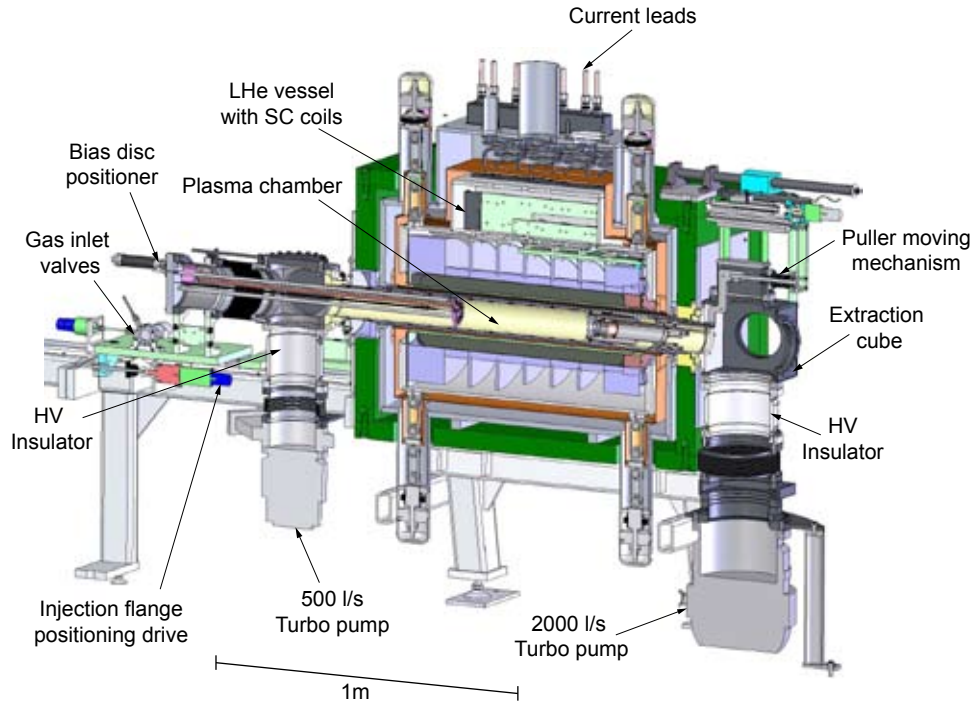


Figure 5.4: Layout of the Superconducting Source for Ions (SuSI) at NSCL.

The ECR extraction and acceleration voltages should be high to mitigate space-charge effects. Based on the initial results from VENUS, the nominal extraction voltage will be 30 kV and the ECR system will be placed on a 70 kV high-voltage platform. This preacceleration can be adjusted to ensure that all ions have the same velocity going into the RFQ. Due to space-charge effects, a high-current beam will diverge quickly after extraction from the ECR, and proper focusing near the ECR exit is needed to control the beam envelope and limit the emittance growth. In the proposed design, this focusing element will also be located on the 70 kV platform to match the beam from the source to the achromatic charge-selection system. Solenoids have been commonly used for the initial beam focusing. However, for a high intensity multi charge beam, solenoid focusing can create a hollow beam and thus emittance growth for the ion of interest. The focusing strength depends on the charge-to-mass ratio. Other, unwanted ions are focused at different positions to create a high space charge on the beam axis [Gre00,Zha04]. Therefore, electrostatic focusing elements (e.g., quadrupole or Einzel lenses), which have the same focusing strength for all charge states, should be a better alternative. Experience at the NSCL has shown that an electrostatic quadrupole lens has better performance than a solenoid [Ste05b]. Further studies are being conducted to compare the beam properties obtained with a solenoidal magnet with those obtained with electrostatic quadrupole and Einzel lenses.

Two ECR ion sources will be used to ensure reliability through redundancy and to allow offline beam development. Some of the ECR ion sources will need to be optimized for specific beams (e.g., metallic or gaseous feed material). The production of light ions at the appropriate intensity is not difficult and a single low-frequency

ECR source similar to the Advanced Room TEMperature Ion Source (ARTEMIS) currently in routine operation at the NSCL meets the requirements. Such sources are more flexible and cost-effective and are currently being used in several accelerator facilities.

To minimize problems associated with space charge forces at low energies when accelerating protons, singly charged tri-atomic hydrogen ions (H_3^+) will be used instead. The first stripper foil will convert the H_3^+ beam into a proton beam. Mono-atomic ion beams will be used for all other cases, including helium.

5.1.1.2 Beam selection system

After extraction from the ECR ion source, the beam must be filtered to select the desired ion and charge state(s). Although the intrinsic beam momentum spread from the ECR is typically $< 0.1\%$, a two-charge-state beam has a larger effective momentum spread. For example, a beam with charge states $^{238}\text{U}^{28+}$ and $^{238}\text{U}^{29+}$ is equivalent to a beam of charge state 28.5 with a momentum spread of 0.88%. Therefore, the charge-to-mass selection system must be achromatic to minimize emittance growth. A symmetric achromatic system requires only that $M_{26} = 0$ (the first order beam transport matrix element) at the mid plane to achieve a first-order achromatic condition [Bro82]. The symmetric configuration will also cancel most of the higher-order geometric aberrations [Wol87]. The design has two 90° dipoles, six quadrupoles, eight sextupoles, and a charge-state selection aperture, as shown in Figure 5.5. All of the beamline components will be room temperature magnetic elements.

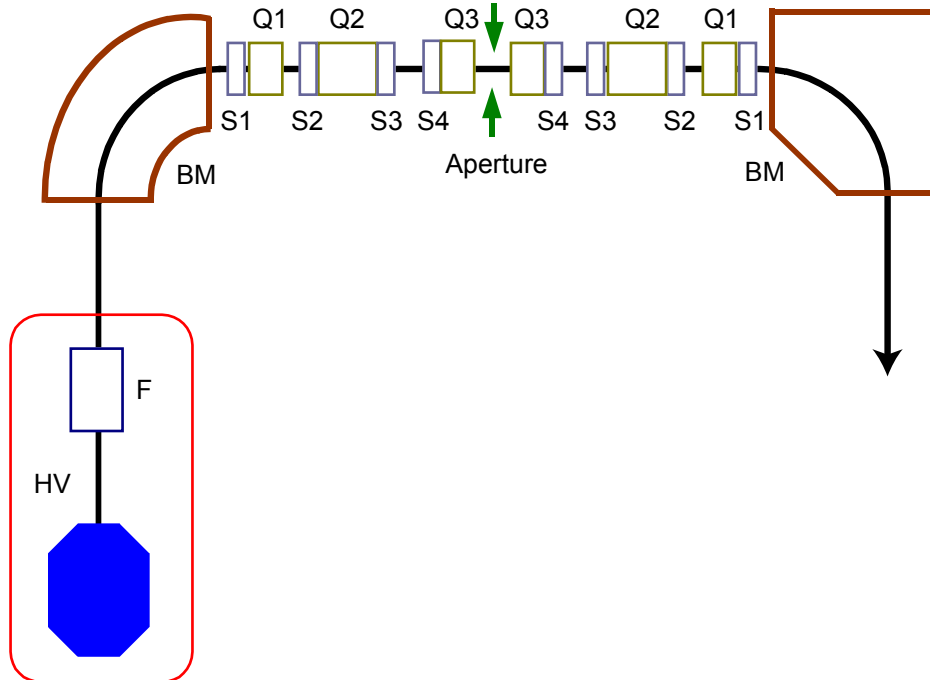


Figure 5.5: Schematic layout of the beam selection system. The ECR (blue octagon) and its focusing system (F) is mounted on a high voltage (HV) platform. Charge-state selection is performed in an achromatic section with two bending magnets (BM) separated by six quadrupoles (Q) and eight sextupoles (S), with an aperture at the midplane.

The 90° bending magnet will have a 63.7 cm radius of curvature with a resolving power of approximately 150 for a beam with a 100% normalized emittance of 0.6π mm mrad. To achieve the achromatic transport and maintain the beam envelopes within a reasonable range, a total of six quadrupoles are needed between the dipoles. Four pairs of sextupoles are used to correct second-order chromatic aberrations in both the horizontal and vertical planes, producing the required charge-to-mass resolution.

The horizontal aperture in the middle of the achromatic system, where the charge states of a given ion are completely separated by the dispersion, is used to select the desired charge state(s).

5.1.1.3 Low-energy beam transport

The objective of the Low-Energy Beam Transport (LEBT) is to bunch and match either the one or two-charge-state beams into the RFQ, as shown in Figure 5.6. The LEBT consists of a transverse matching section of four electrostatic quadrupoles, a Multi-Harmonic Buncher (MHB) to efficiently convert the dc beam from the ECR to a bunched beam with minimum longitudinal emittance, a high voltage platform with a solenoid, and a velocity equalizer for matching two-charge-state ion beams into the RFQ.

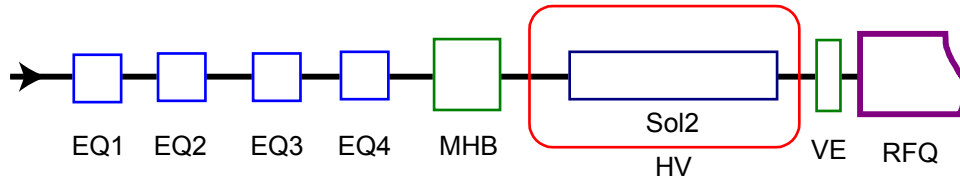


Figure 5.6: Schematic layout of the LEBT showing the Electrostatic Quadrupoles (EQ), Multi-Harmonic Buncher (MHB), High Voltage platform (HV), Solenoid (Sol2), and Velocity Equalizer (VE) for matching into the Radio Frequency Quadrupole (RFQ). The beam will travel from left to right in the figure.

LEBT system

The electrostatic quadrupole elements provide transverse focusing and phase space matching, converting the asymmetric beam from the charge state selection section into an axially symmetric beam at the multi-harmonic buncher. The quadrupoles will be able to accommodate a large range of Twiss parameters [Twi49]. Electrostatic quadrupoles will be used because they provide the same focusing strength for different charge states as the charge states were initially accelerated by the same high voltage.

The dc beam from the ECR source must be bunched before injection into the linac for acceleration. To achieve a short bunch length with high bunching efficiency, a multiple-harmonic buncher is necessary. Table 5.2 lists the harmonic coefficients for a three- and four-harmonic buncher system. Since the resulting beam quality was found to be similar and the bunching efficiency equivalent to within a few percent for the two systems, a single gap three-harmonic buncher was chosen. The buncher will operate at a fundamental frequency of 40.25 MHz for beams with two charge states and 80.5 MHz for beams with one charge state. Although the voltage coefficient is smaller for higher harmonics, the transit time factor is also lower. Therefore, the required rf power for each frequency is similar.

Table 5.2: Voltage Fourier coefficients for a three-harmonic and four-harmonic buncher.

| Number of harmonics | U_1 | U_2 | U_3 | U_4 |
|---------------------|-------|-------|-------|-------|
| 4 | 1 | 0.380 | 0.153 | 0.048 |
| 3 | 1 | 0.351 | 0.115 | 0 |

After the multi-harmonic buncher, the two-charge-state beams will be bunched as well as longitudinally separated from each other, as illustrated in Figure 5.7. At the entrance of the RFQ, the phase separation between bunches is 360° at an RFQ frequency of 80.5 MHz, so that the different charge states will be made to occupy alternate rf buckets in the RFQ. To accomplish this goal, the drift distance L must satisfy the relation

$$L = \frac{1}{f} \left(\frac{1}{v_2} - \frac{1}{v_1} \right)^{-1} \tag{5-1}$$

where f is the frequency of the RFQ, and v_1 and v_2 are the speeds of the higher and lower charge-state ions, respectively. The required drift distance L is different for different ions. Since the physical drift distance is fixed, a bipolar high-voltage platform is used. By applying a high voltage U_d to the platform, the velocities of the ions are changed before the drift within the platform. This velocity adjustment can be used to ensure that equation (5-1) is satisfied for all ions. To accommodate two-charge-state beam operation from xenon to uranium, the drift distance L was set to 0.9 m and the platform voltage will be adjusted by ± 50 kV to accommodate all ions.

A second buncher operating at 40.25 MHz in front of the RFQ is required for two-charge-state beam injection to act as a velocity equalizer (VE), so that both charge states will have the same energy at the RFQ entrance. Table 5.3 shows some of the parameters for two-charge-state operation of the bunchers. To simplify the system design and operation, neither the MHB nor the Voltage Equalizer (VE) are located on the high-voltage platform.

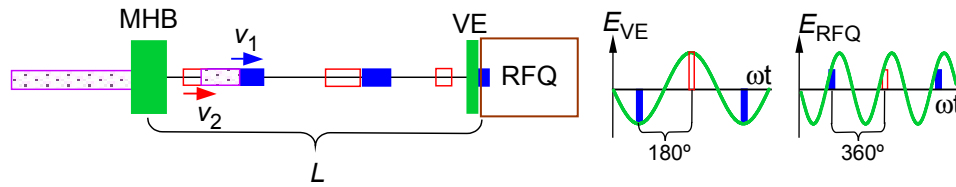


Figure 5.7: Schematic showing how the two-charge-state beam (blue and red) is bunched and separated between the MHB and the RFQ. Initially, the charge states overlap (pink dotted rectangles). The higher charge-state ions (solid blue rectangles) move faster than the lower charge-state ions (hollow red rectangles) and separate in phase. When they are 360° apart (at the RFQ frequency of 80.5 MHz), their velocities are equalized in the VE (operating at 40.25 MHz) before entering the RFQ.

Table 5.3: Sampled two-charge-state beam operation parameters for the bunchers.

| Ion | A | Q | U_d (kV) | Buncher voltage (kV) | |
|-----|-----|-------|------------|--------------------------------|-------|
| | | | | MHB (1 st harmonic) | VE |
| Xe | 136 | 19,20 | -37.8 | 2.728 | 2.260 |
| Au | 197 | 23,24 | 0 | 2.134 | 2.253 |
| U | 238 | 28,29 | +32.0 | 1.242 | 1.795 |

LEBT beam dynamics

To perform beam simulations for the LEBT, data from the VENUS ion source for bismuth were scaled such that both $^{238}\text{U}^{28+}$ and $^{238}\text{U}^{29+}$ reached ~ 0.14 mA, producing a total uranium current of 1.32 mA as shown in Figure 5.8. In addition, a total oxygen ion current of 1.5 mA from the support gas was assumed.

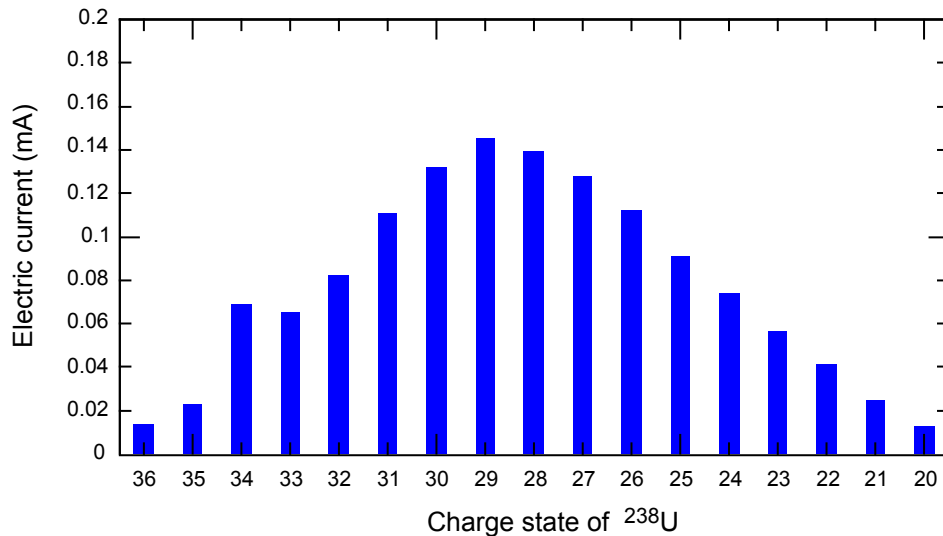


Figure 5.8: Charge-state distribution of uranium from the ECR scaled from the VENUS experimental data for bismuth. A current of 1.5 mA from oxygen ions (not shown) was also included in the beam simulations.

The PARMELA code [You05] was used for six-dimensional beam simulations, including space-charge forces in the LEBT. All ion species were assumed to have the same Twiss parameters [Twi49] at the exit of the ECR with a beam waist radius of 5 mm, which is a typical radius for a plasma extraction aperture [Lei01c]. The normalized uranium beam emittance was assumed to be similar to that of the measured bismuth beam, and an intrinsic energy spread of 0.1% was included. A total of ~ 1.4 million macroparticles were tracked from the ECR in the PARMELA simulations. These particles were initially distributed in a 4D water-bag transverse hyperspace with a uniform distribution in phase and energy spread, as indicated in Figure 5.9.

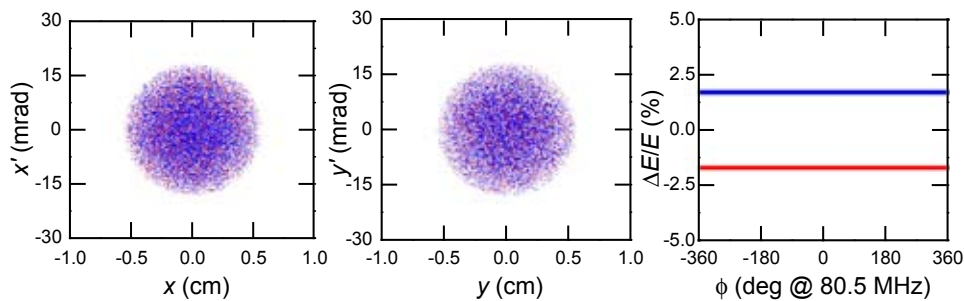


Figure 5.9: Initial transverse and longitudinal particle distributions of two-charge-state uranium (U^{28+} in red, U^{29+} in blue) at the exit of the ECR.

Figure 5.10 shows the transverse phase space of the $^{238}\text{U}^{28+}$ and $^{238}\text{U}^{29+}$ beams at the entrance, mid-plane, and exit of the achromatic charge selection system. At the mid plane of the beam selection system, the horizontal aperture will select the charge state(s) of interest. The transverse phase space of the two-charge-state uranium beam at the RFQ entrance is shown in Figure 5.11. The “S” shape of phase space is due to space-charge forces before beam selection. Transverse emittance growth in the achromatic transport section is small. The normalized 99.5% transverse emittance (an ellipse area in phase space including 99.5% of all of the particles) at the entrance to the RFQ is $\sim 1 \pi \text{ mm mrad}$ for the two-charge-state beam. The normalized rms emittance is about 10 times smaller than the 99.5% emittance. The cores of the two-charge-state beams overlap well, but the tail particles are slightly shifted with respect to each other, which increases the overall emittance.

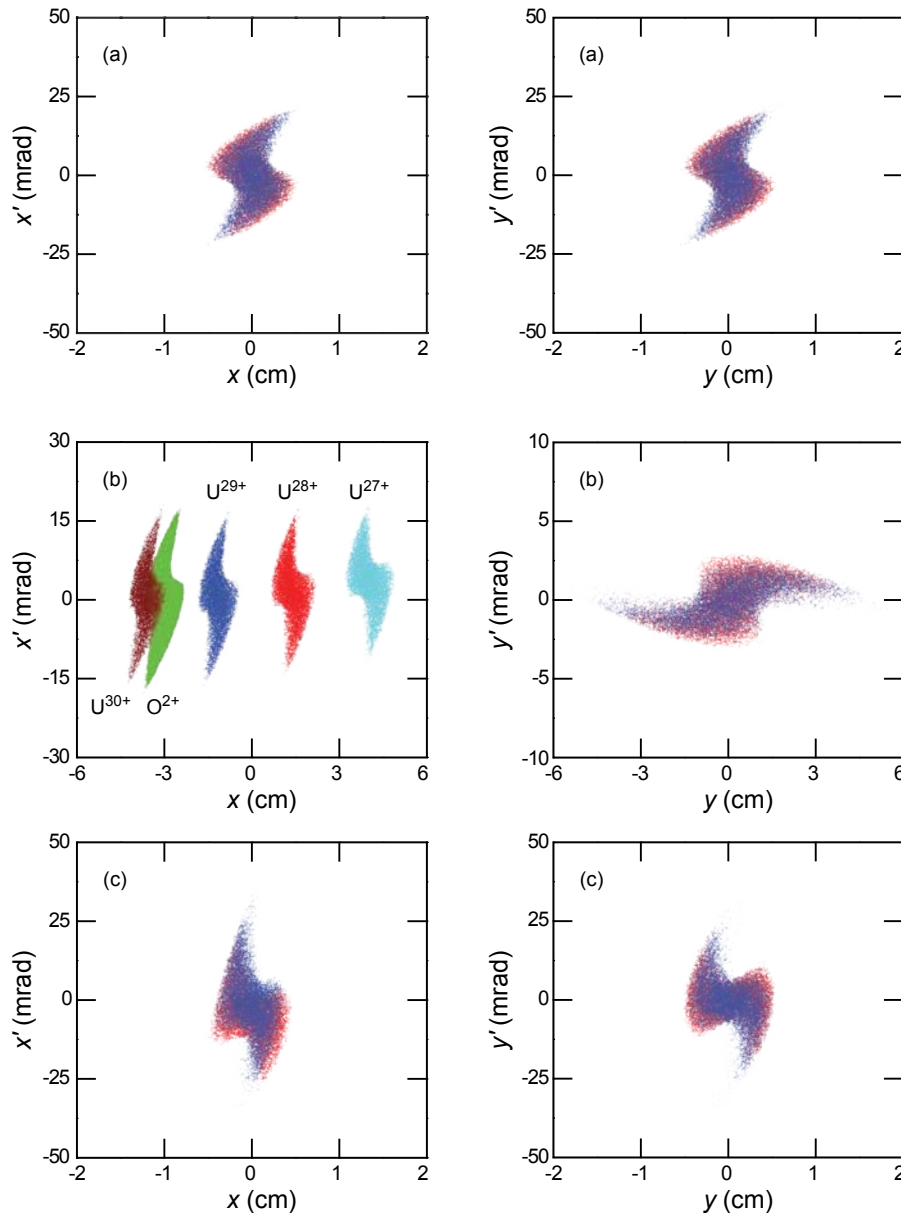


Figure 5.10: Transverse phase space of the two-charge-state uranium beam (U^{28+} in red, U^{29+} in blue) at three different positions in the achromatic beam selection system: (a) entrance, (b) mid-plane, and (c) exit. In panel (b) the other charge states that are removed by the slits are also shown. Note change in scales for panel (b).

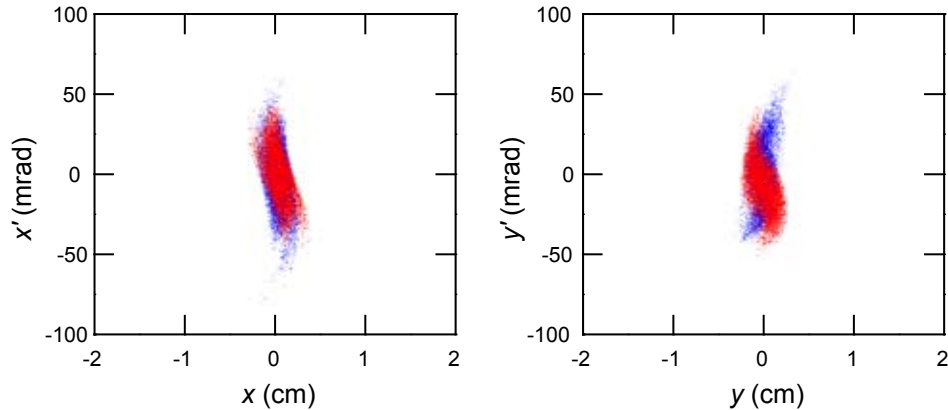


Figure 5.11: Transverse phase space of two-charge-state uranium beam (U^{28+} in red, U^{29+} in blue) at the entrance of the RFQ.

Figure 5.12 shows the longitudinal phase space of the two charge states of the ^{238}U beam at selected locations in the LEBT section obtained from PARMELA simulations. At the exit of the LEBT, more than 80% of the particles are bunched within 60° rf phase (at 80.5 MHz) by the MHB.

For xenon and lighter ions, the desired beam power can be obtained with single-charge-state injection with the multi-harmonic buncher operating at the RFQ frequency of 80.5 MHz. In this operation mode, neither the velocity equalizer nor the high voltage platform is required. At the entrance to the RFQ, the energy spread for a one-charge-state beam is about $\pm 1.3\%$ and occupies $\sim 50^\circ$ of rf phase. The PARMELA simulation results for a $^{136}\text{Xe}^{18+}$ beam phase space at the end of LEBT section are shown in Figure 5.13. Starting with a $15\ \mu\text{A}$ xenon beam with a normalized transverse full (100% of particles) emittance of $0.6\ \pi\cdot\text{mm}\cdot\text{mrad}$ and an energy spread of 0.1% after the charge selection system, the transverse emittance (99.5% particles) increases by less than 8% in the LEBT.

PARMELA simulations show no significant space charge effects for ions from helium up to uranium after charge selection. A 0.2 mA, 36 keV H_3^+ beam was tracked from the charge selection system up to the RFQ entrance. Figure 5.14 shows the results from simulations of the phase space for H_3^+ at the end of the LEBT section. The simulations indicate that the front-end system will provide beams appropriate for the acceleration of protons through uranium.

5.1.1.4 Radio frequency quadrupole

Radio Frequency Quadrupoles (RFQ) are widely used to bunch and accelerate beams from the ion source before the main linac, especially in high current accelerators [Wan98]. For high intensity beams, adiabatic bunching generally occurs over about 2/3 of the RFQ length. However, given the relatively low driver linac beam current requirements in the proposed facility, the quasi-linear bunching field from the multi-harmonic buncher upstream of the RFQ produces a smaller longitudinal output emittance than that required for adiabatic bunching in the RFQ [Sta94, Kos94]. An external buncher also allows the RFQ to be shorter and thus enhances its acceleration efficiency.

The ions must be accelerated synchronously with the rf field in the RFQ so that all ions have the same velocity profile along the RFQ. Since the electrodes' shape

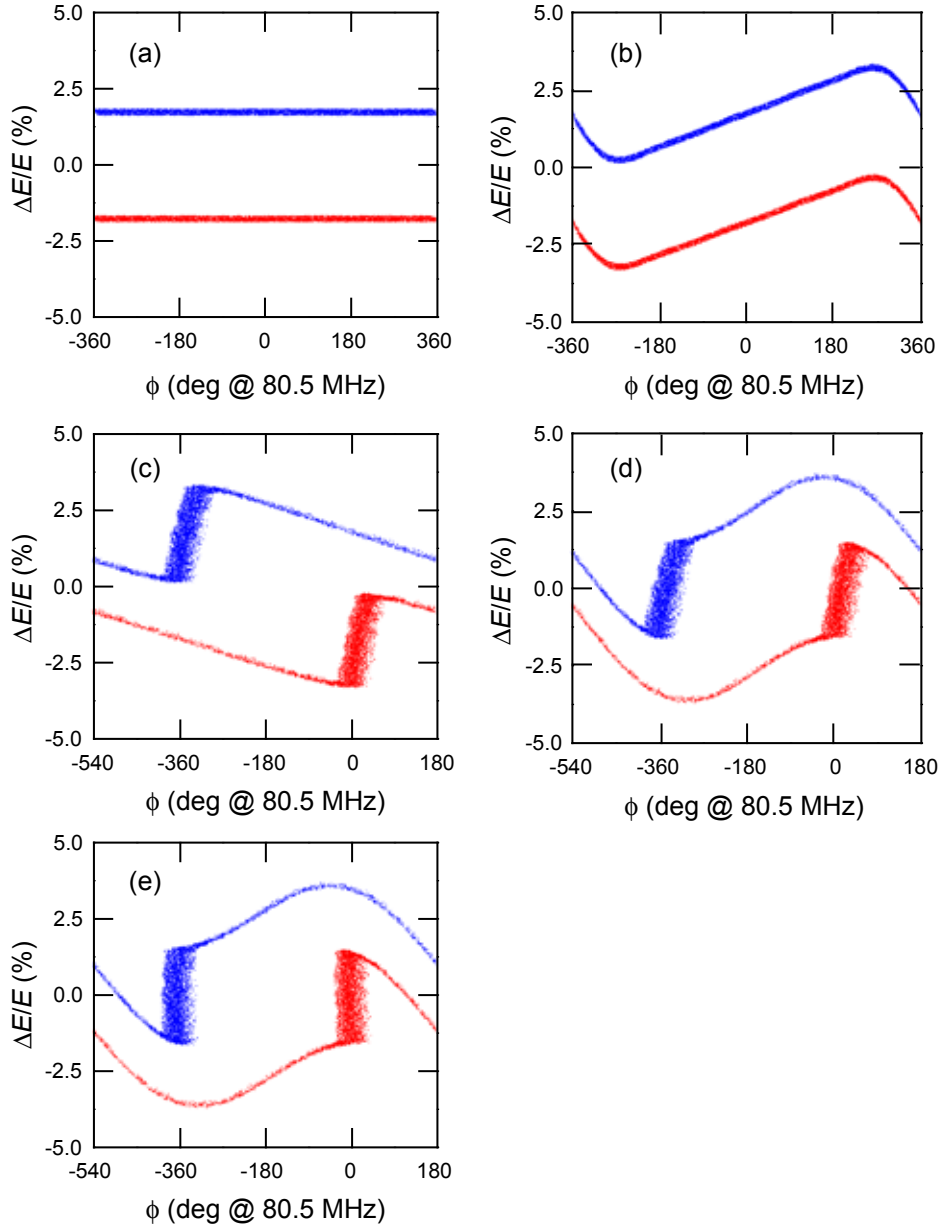


Figure 5.12: Longitudinal phase space of the two charge states of the uranium beam (U^{28+} in red, U^{29+} in blue): (a) before the multi-harmonic buncher (MHB), (b) after the MHB, (c) before the velocity equalizer, (d) after the velocity equalizer, and (e) at the entrance to the RFQ.

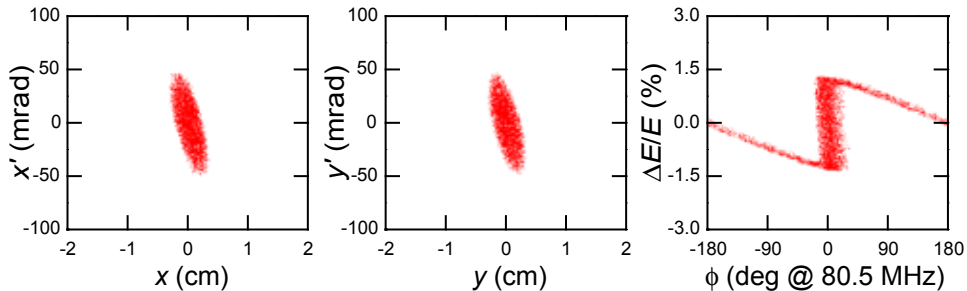


Figure 5.13: Simulated transverse and longitudinal phase space of a $15 \mu A$ $^{136}\text{Xe}^{18+}$ beam at the entrance of the RFQ.

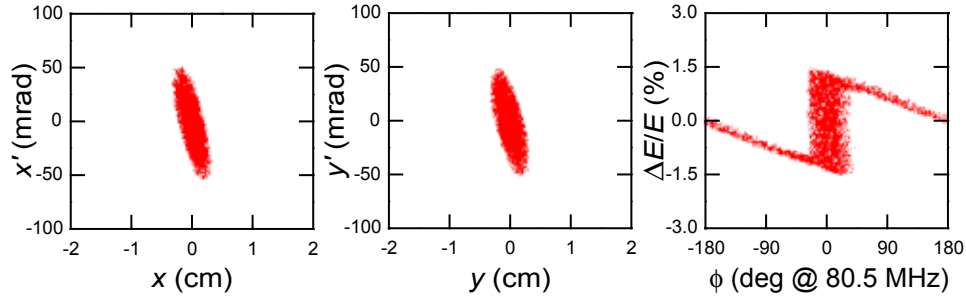


Figure 5.14: Simulated transverse and longitudinal phase space of a 0.2 mA H_3^+ beam at the entrance of the RFQ.

and rf frequency are fixed, only the input power (vane voltage) can be adjusted to accommodate the various ion species.

An improved RFQ structure with coupling windows will be employed to provide a large mode separation, high shunt impedance, and a compact structure. The 100% duty factor (cw) RFQ will operate at a resonant frequency of 80.5 MHz. This frequency was chosen to be the same as that in the lowest-frequency linac superconducting structures. The input energy of 12 keV/u is determined by the high voltage platform at the ECR, while the output energy of 300 keV/u was chosen to obtain a transit time factor of 0.5 for the first superconducting (SC) cavity in the driver linac. This choice comes from a tradeoff between the acceptance of the superconducting linac and the length of the RFQ.

RFQ design

The design goals were to minimize the longitudinal and transverse emittances, the rf power, and the size of the RFQ. An optimization program was used to find the RFQ parameters for minimum output longitudinal emittance and maximum transmission [Pod02]. The RFQ structure was then created using PARMTEQM [Cra05] in an iterative cell-by-cell procedure. Since the beam is already bunched by the multi-harmonic buncher before the RFQ, an initial synchronous phase of -30° and a modulation factor of 1.03 were chosen so that the longitudinal acceptance would be initially reduced. These values are a compromise between the need to remove the particles from the tails of the bunch and the desire to provide a linear field for the bunched particles. Figure 5.15 shows the results for simulation of the initial longitudinal distribution of the two-charge-state uranium beam from the LEBT together with static separatrices of different initial synchronous phases and modulation factors. The synchronous phase increases smoothly so that only the bunched beam is accepted for further acceleration. At the exit of the RFQ, there is a transition cell [Cra94] to bring the vanes to quadrupole symmetry so that the output beam has the same Twiss parameters in both the horizontal and vertical planes. The transition cell minimizes the effective emittance growth when the two-charge-state beam travels through the solenoidal magnet in the MEBT.

A nominal vane-to-vane voltage of 70 kV was adopted in the design, resulting in a moderate peak surface field of only $1.6 E_{\text{kilpatrick}}$ where $E_{\text{kilpatrick}}$ is the Kilpatrick field [Kil57]. The focusing strength was held constant ($B \sim 4.1$) along the structure leading to a constant average aperture diameter of 11 mm, so that the capacitance is independent of longitudinal position for easier cavity tuning. In this scheme,

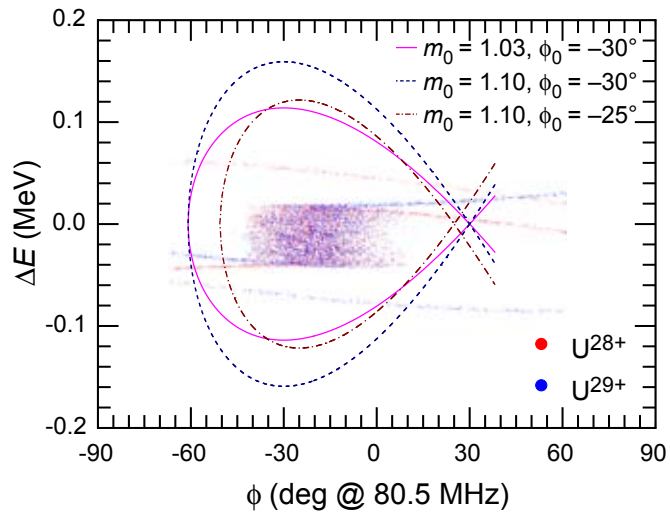


Figure 5.15: Longitudinal distribution of the two-charge-state uranium beam (U^{28+} in red, U^{29+} in blue) at injection into the RFQ. The static separatrices (outer boundary of stable region) for different initial synchronous phases ϕ_0 and modulation factors m_0 are also shown.

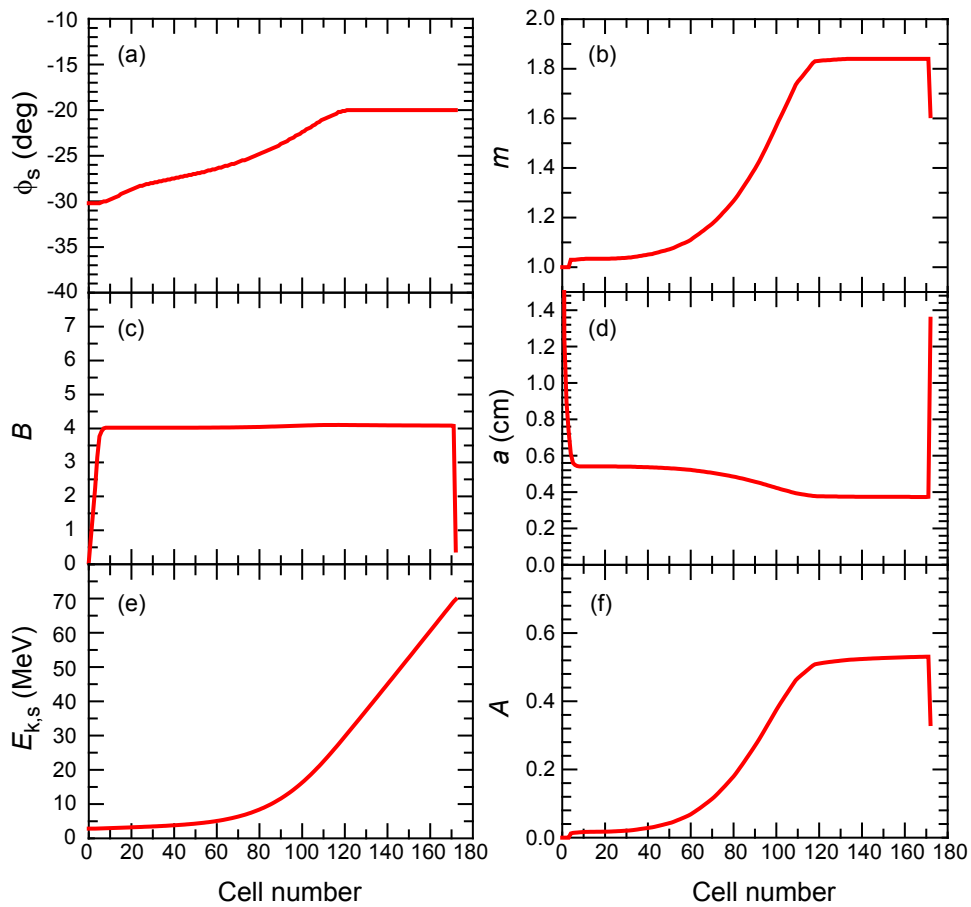


Figure 5.16: Evolution of (a) the synchronous phase, (b) the modulation factor, (c) the transverse focusing strength, (d) the minimum radius, (e) the synchronous beam energy, and (f) the acceleration efficiency along the RFQ.

the minimum vane radius decreases as the modulation increases along the RFQ, producing a normalized transverse acceptance of approximately 1.4π mm mrad. The transverse geometry of the vane-tip is circular with the same transverse radius of curvature throughout the RFQ, which makes the fabrication easier. The ratio between the vane tip radius and the vane average radius was chosen to be 0.82 as a compromise between the peak electric field and the effect of multipoles. Figure 5.16 shows the main parameters as a function of the cell number while the main parameters of the RFQ are listed in Table 5.4.

Table 5.4: Front-end RFQ parameters.

| Parameter (unit) | Value |
|--|-------------|
| Nominal inter-vane voltage (kV) | 70 |
| Vane length (m) | 3.96 |
| Average radius (mm) | 5.5 |
| Tip radius (mm) | 4.5 |
| Modulation factor | 1.03 → 1.84 |
| Number of cells | 174 |
| Synchronous phase (deg) | -30 → -20 |
| Focusing strength | 4.1 |
| Transverse acceptance (π mm mrad) | 1.4 |
| Input energy (keV/u) | 12 |
| Output energy (keV/u) | 293 |
| Effective transmission (%) | 82 |
| Peak field ($E_{\text{kilpatrick}}$) | 1.6 |

RFQ beam dynamics

The PARMTEQM code was also used for the beam dynamics simulations of the ^{238}U beam in the RFQ. The simulated beam from the LEBT was used as the input to PARMTEQM, as shown in Figure 5.17. The resulting particle distributions at the exit of the RFQ are shown in Figure 5.18. Figure 5.19 shows the evolution of the rms emittance, transmission, and phase advance along the RFQ. The transverse phase advance per focusing period is about 25° and is almost constant along the RFQ, while the longitudinal phase advance per period is around 15° . About 82% of the beam is captured and accelerated by the RFQ. There is no rms transverse emittance growth in the RFQ. However, the growth in the transverse emittance enclosing 99.5% of the particles for both charge states is about 8%, and the longitudinal emittance (99.5%) at the exit of the RFQ is 1.1π keV/u ns. The longitudinal emittance of a two-charge-state beam is somewhat larger than that of single-charge-state beam ($\sim 1 \pi$ keV/u ns), primarily due to the phase shift between the two-charge-state distributions.

The beam dynamics through the RFQ are similar for other ion beams, provided the inter-vane voltage is scaled to account for the different charge-to-mass ratios. The results from simulations with PARMTEQM for a single-charge-state xenon beam and a H_3^+ beam are shown in Figure 5.20. The output phase space distributions are similar to those for the two-charge-state uranium beam.

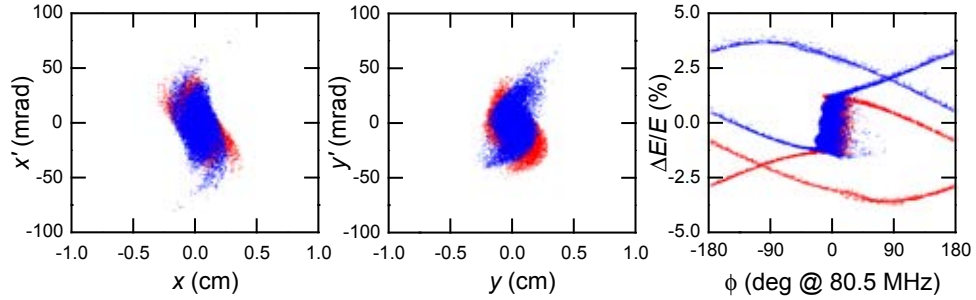


Figure 5.17: RFQ input distributions used in PARMTEQM for two uranium charge states (U^{28+} in red, U^{29+} in blue): horizontal (left), vertical (middle), and longitudinal (right) phase space.

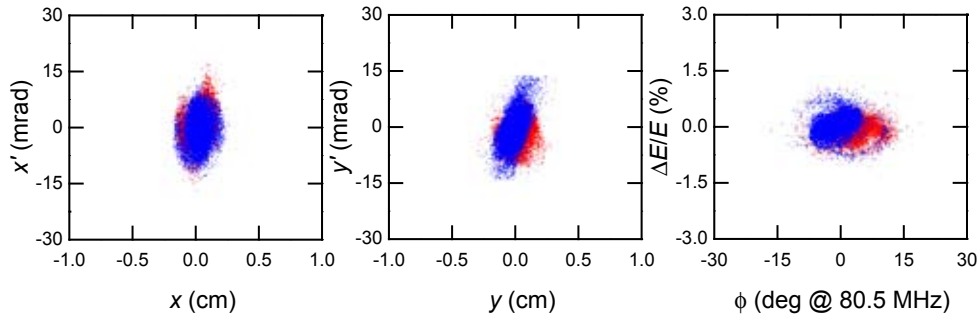


Figure 5.18: RFQ output distributions from PARMTEQM for two uranium charge states (U^{28+} in red, U^{29+} in blue): horizontal (left), vertical (middle), and longitudinal (right) phase space.

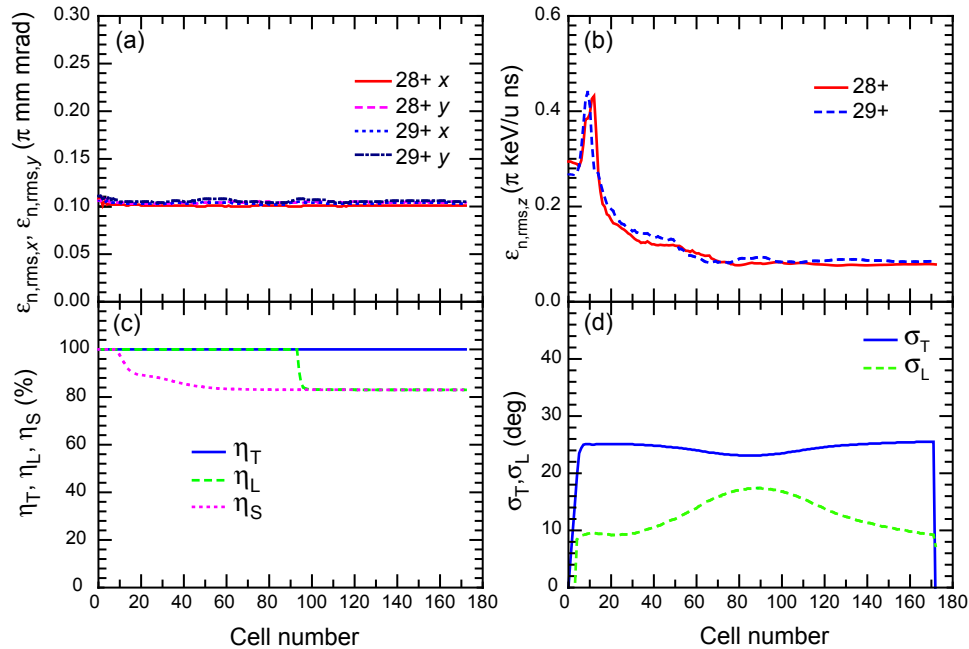


Figure 5.19: Evolution of (a) the normalized rms transverse emittance, (b) the longitudinal emittance, (c) the transverse and longitudinal transmission (η_T , η_L), and (d) transverse and longitudinal phase advance (σ_T , σ_L) along the RFQ for a two-charge-state uranium beam. In (c), η_S shows the percentage of particles within the stable region.

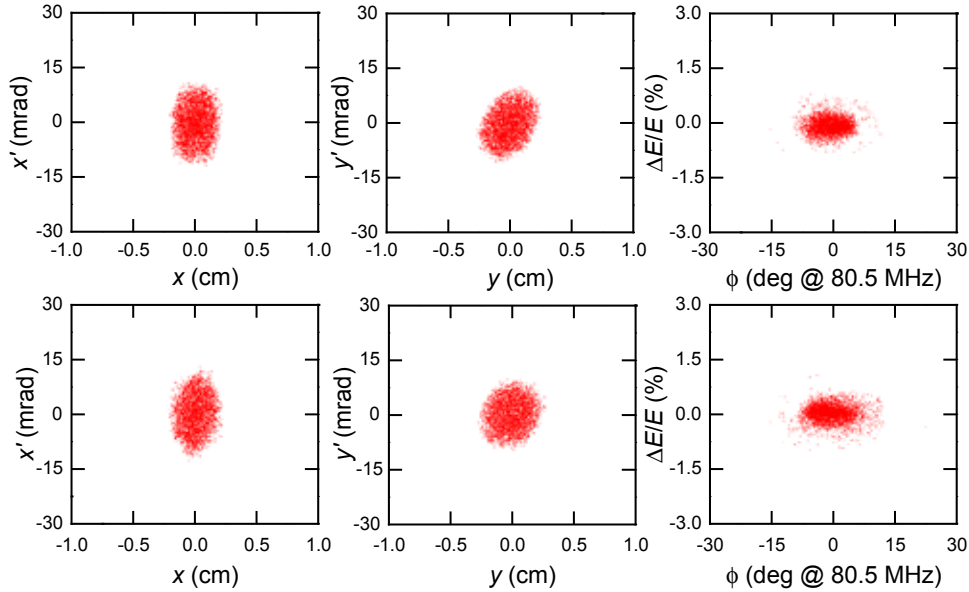


Figure 5.20: Simulation results for the RFQ output distributions from PARMTEQM for single-charge-state xenon (top) and H₃⁺ (bottom) beams: horizontal (left), vertical (middle), and longitudinal (right) phase space.

The TOUTATIS code [Dup00] was also used to cross check the simulations of the RFQ beam dynamics. The RFQ configuration designed with PARMTEQM was imported into TOUTATIS, along with the initial particle distributions from the LEBT. The results from TOUTATIS simulations were found to be very consistent with those from PARMTEQM in both transverse planes. The longitudinal results from the two codes also agreed reasonably well.

RFQ error evaluation

Error sensitivity studies for the RFQ were performed using the TOUTATIS and TraceWin codes [Dup05]. Three error sources were included: (1) manufacturing errors (e.g., vane profiles), (2) alignment errors (vane displacement, tilt, and rotation), and (3) rf field errors. Figure 5.21 shows the effect of rf field amplitude, manufacturing, and misalignment errors on the beam centroid. Tolerances of 0.1 mm in vane manufacturing, 0.2 mm in vane alignment, and 2% in field amplitude fluctuation are easily achievable. These tolerances provide acceptable beam centroid deviation.

Monte Carlo studies of the effects of these tolerances showed an increased beam loss of 0.8% and emittance growths of 4.6% and 3.6% in the transverse and longitudinal planes, respectively. Also, the beam power deposited on the vanes is very small. For example, Figure 5.22 shows the power deposited as a function of cell number for an RFQ with field errors of 5% and manufacturing errors of 0.2 mm. Thus, the specified tolerances will be adequate for good performance.

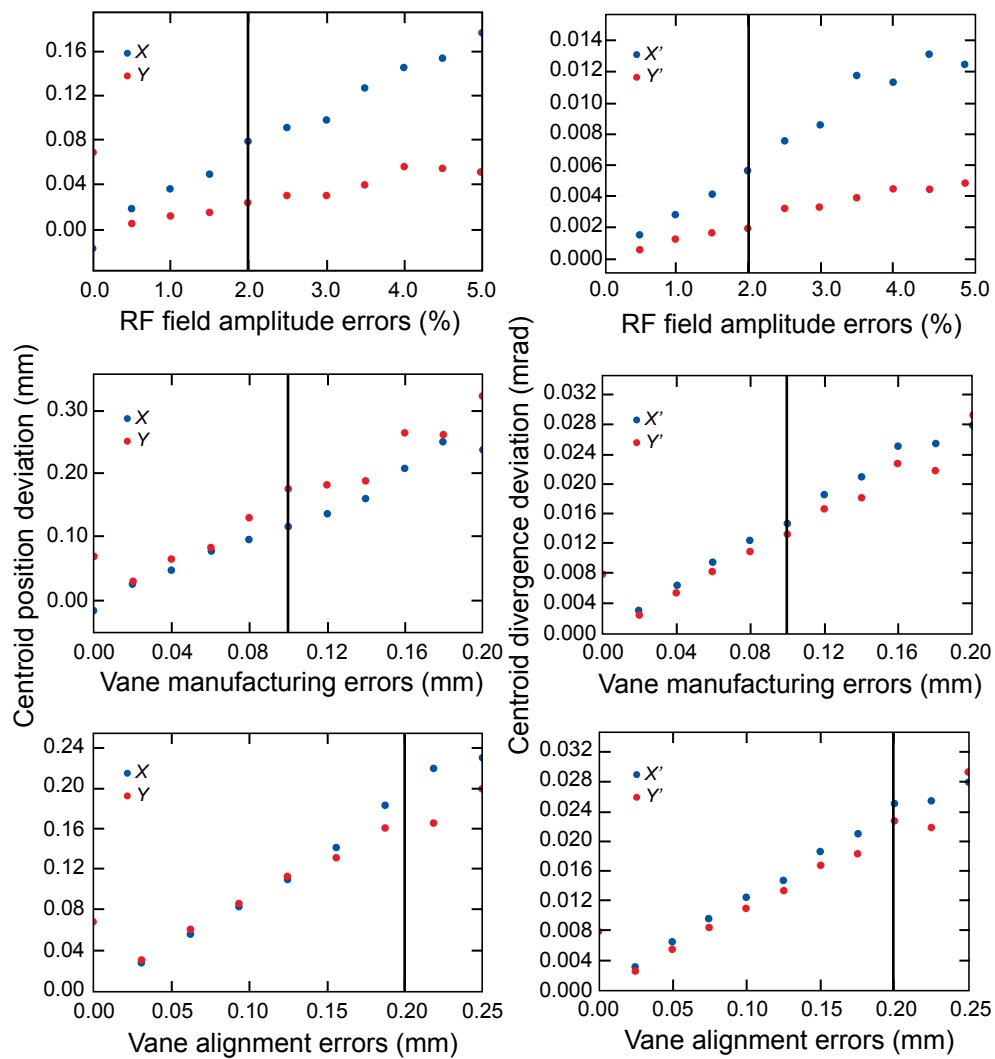


Figure 5.21: Beam centroid deviation in position (left) and angular divergence (right) as a function of the error in rf field amplitude (top), manufacturing (middle), and misalignment (bottom). Tolerances for the rf errors, vane manufacturing errors, and vane alignment errors are indicated by black vertical lines in all plots.

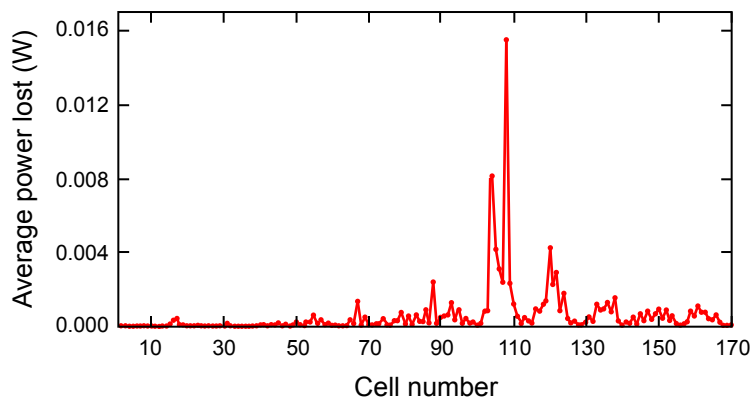


Figure 5.22: Average deposited power distribution as a function of RFQ cell number for the combination of $\pm 5\%$ error in rf field amplitude and ± 0.2 mm error in machining and alignment.

RFQ resonant structure

The design of the RFQ was based on an improved four-vane structure with magnetic coupling windows [And93]. In four-vane RFQs, the coupling among the quadrants of the resonator is weak, resulting in undesirable parasitic modes near the operating mode. The windows cut on the vanes and their offset between adjacent vanes improves the magnetic coupling of the resonator quadrants. These windows not only improve the azimuthal and longitudinal stability of the operating mode but also reduce the transverse dimension of the RFQ resonator in comparison to a typical four-vane structure. These features are especially useful for low-frequency RFQs [And94]. To optimize the rf efficiency, electrodynamic simulations using unmodulated vanes were performed with the MAFIA code. The structure simulated in MAFIA is shown in Figure 5.23. The MAFIA simulations covered the full length of the resonator in order to include all relevant higher-order parasitic modes. Table 5.5 lists the main parameters of the resonator.

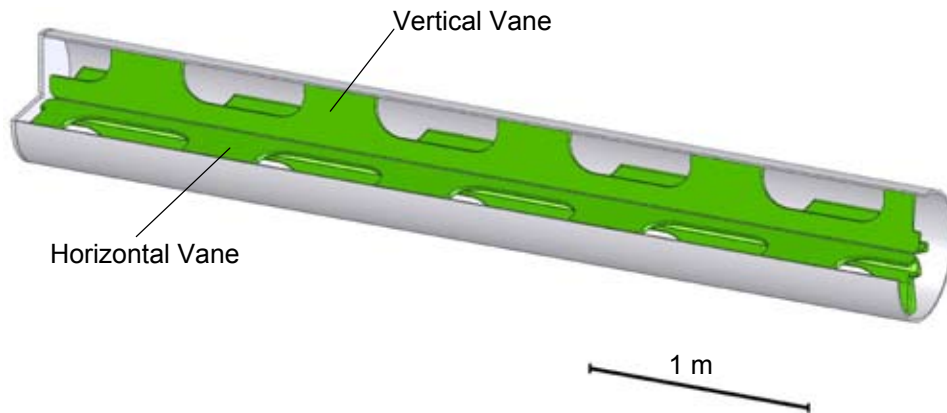


Figure 5.23: Schematic layout of the RFQ resonator operated at 80.5 MHz.

Increasing the segment length and the coupling window area improves the mode separation but reduces the shunt impedance. Dipole modes in the RFQ can cause emittance growth. A frequency difference of 10–15 MHz between the operating mode and the nearest dipole mode is sufficient to avoid problems with alignment and tuning [Bis98]. For instance, experience with the superconducting RFQ at INFN-Legnaro showed that an electrode alignment tolerance of ± 0.1 mm kept the imbalance between the four quadrants along the structure within ± 1 – 2 % [Bis00]. Additional cylindrical fine tuners will be used to compensate possible misalignment.

A resonator with a short segment length also has a smaller intervane voltage variation (ripple) along the axis. The intervane ripple is an inherent feature of all longitudinally nonuniform RFQs (see for example, Figure 5.24).

To minimize the intervane voltage ripple, the end segments are tuned with a 3 cm undercut of the vanes at either end of the structure. Figure 5.25 shows a close-up view of the input end of the RFQ with undercut vertical vanes; the on-axis longitudinal electric field of the gap is also shown. The shape of the coupling windows is also optimized for proper mode separation and low magnetic field and rf losses. Figure 5.26 shows the electric and magnetic field in the xy and yz planes, respectively.

Table 5.5: Main rf design parameters for the 80.5 MHz RFQ resonator; E_p = peak surface electric field; B_p = peak surface magnetic field.

| Parameter (unit) | Value |
|---|------------|
| Resonator length (m) | 4.02 |
| Tank inner diameter (m) | 0.54 |
| Segment length (m) | 0.44 |
| Number of segments | 9 |
| Window width (m) | 0.56 |
| Window height (m) | 0.17 |
| Average radius of aperture (cm) | 0.55 |
| Vane tip radius (cm) | 0.45 |
| Frequency of operating mode (MHz) | 80.5 |
| Frequency of nearest parasitic mode (MHz) | 88.6 |
| Frequency of 2 nd nearest parasitic mode (MHz) | 93.8 |
| Specific shunt impedance (k Ω ·m) | 389 |
| Quality factor | 13000 |
| E_p (MV/m) | 14 |
| B_p (mT) | 10 |
| Ripple of intervane voltage (%) | ± 0.35 |
| Power dissipation (at 70 kV) (kW) | 51 |
| Specific power losses (kW/m) | 13 |
| Capacitance per unit length (pF/m) | 135 |

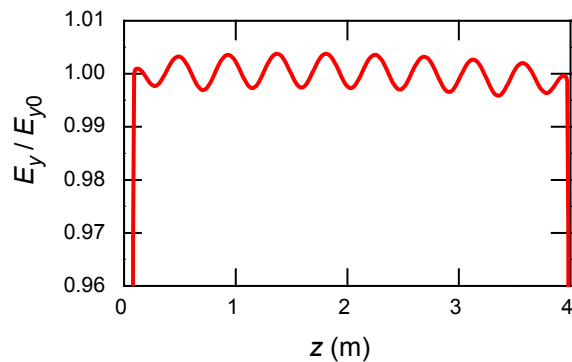


Figure 5.24: Normalized transverse electric field between adjacent vanes along the RFQ with undercuts at the ends (see the text and far left hand of Figure 5.25). Unmodulated vanes would show an electric field variation of $< \pm 0.35\%$.

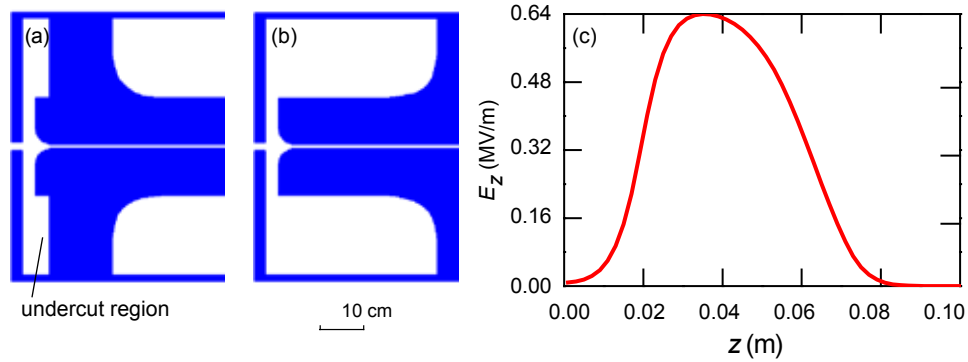


Figure 5.25: Detail of the upstream end of the RFQ showing (a) undercut vertical vanes, (b) horizontal vanes, and (c) the on-axis longitudinal electric field in the gap.

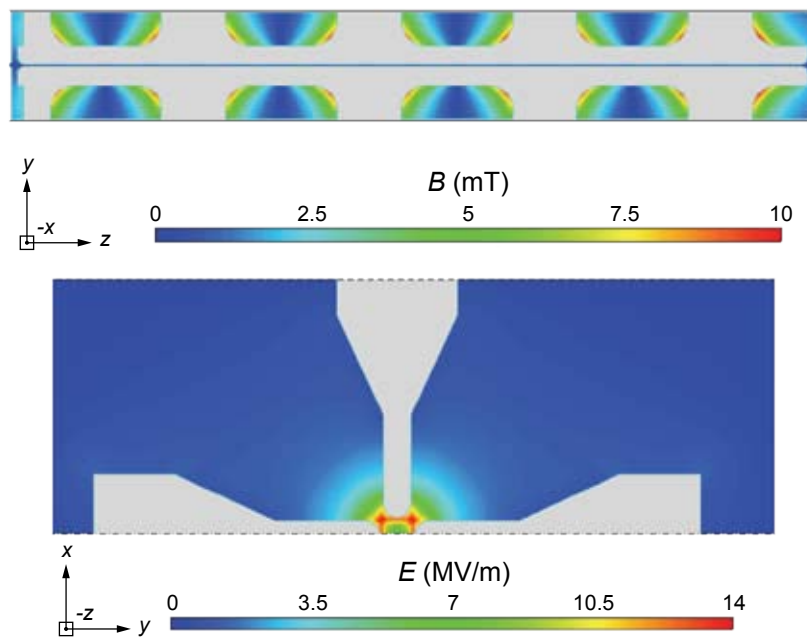


Figure 5.26: Top: magnetic field ($B_{\max} = 10$ mT) in the yz cross-section (vertical vanes). Bottom: electric field ($E_{\max} = 14$ MV/m) in the xy cross-section for the top half of the RFQ.

The resonator will consist of three sections with three segments per section, as shown schematically in Figure 5.27. The sections can be aligned independently and then assembled together. In the ideal case (unmodulated electrodes), no longitudinal current will flow through the joints between sections. In reality, there will be a small current due to the accelerating component of the electric field produced by the vane-tip modulation and misalignments. Hence a proper rf joint between the sections will be needed.

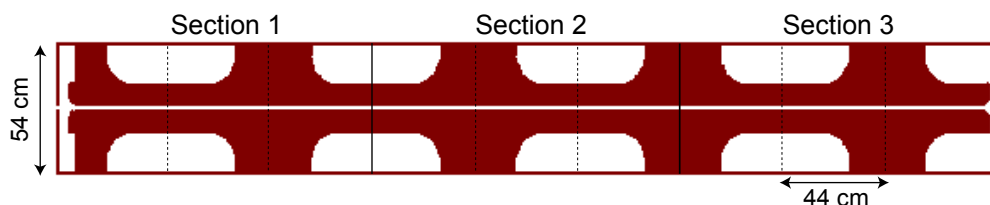


Figure 5.27: Sectional view of the RFQ in the yz plane.

5.1.1.5 Medium-energy beam transport

After the RFQ, the ion beam is transported and matched into the superconducting accelerator. A schematic layout of the Medium-Energy Beam Transport (MEBT) is shown in Figure 5.28. To minimize the transverse emittance growth of two-charge-state beams, only superconducting solenoidal magnets are used to provide transverse focusing. The quasi-symmetric beam from the RFQ is focused to a small beam waist at the rebuncher by the first solenoid. The second solenoid also provides transverse focusing and phase space matching to the entrance of the cryomodule. The rebuncher is an 80.5 MHz $\beta_{\text{opt}} = 0.0251 \lambda/4$ room temperature resonator located approximately in the middle of the MEBT and provides the longitudinal phase space match to the linac. Two collimating apertures in front of the solenoids are used to remove particles in the tails of the phase space distributions ($\sim 2\%$ of the total beam is stopped on the collimating elements).

Table 5.6 lists the beam parameters required at injection into the superconducting linac. The beam envelope in the MEBT section is shown in Figure 5.29.

Table 5.6: Required beam parameters at the entrance to the first cryomodule.

| E (MeV/u) | $\alpha_{x,y}$ | $\beta_{x,y}$ (m) | α_z | β_z (deg/%) at 80.5 MHz |
|-----------|----------------|-------------------|------------|----------------------------------|
| 0.293 | -1.05 | 0.376 | -0.68 | 12.9 |

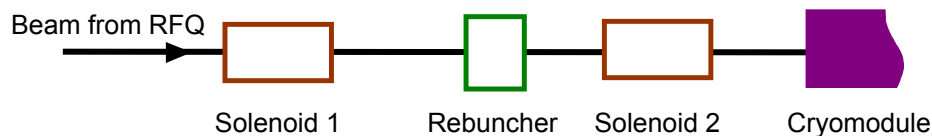


Figure 5.28: Schematic layout of the MEBT.

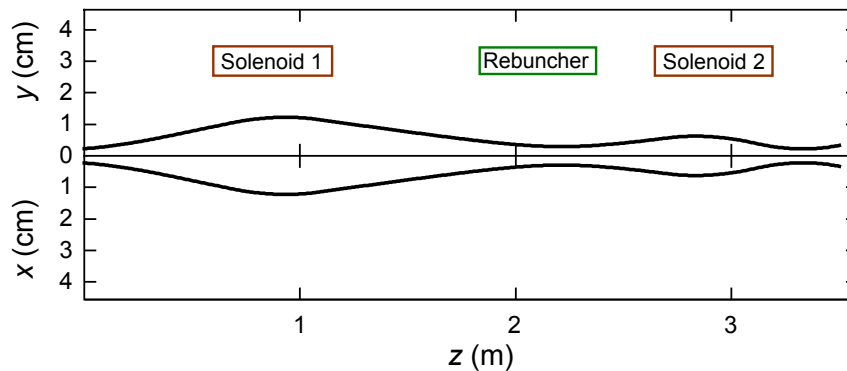


Figure 5.29: Beam envelope in the MEBT section.

MEBT rebuncher design

A two-gap normal conducting 80.5 MHz $\lambda/4$ resonator is used to provide longitudinal matching of the beam from the RFQ into the SC linac. The distance between the gap centers consistent with the beam velocity ($\beta = 0.0251$) is 4.6 cm. MAFIA was used for the cavity design and field calculations. Figure 5.30 shows sectional views of the proposed structure while Figure 5.31 shows the longitudinal field along the beam axis. The cavity parameters are listed in Table 5.7.

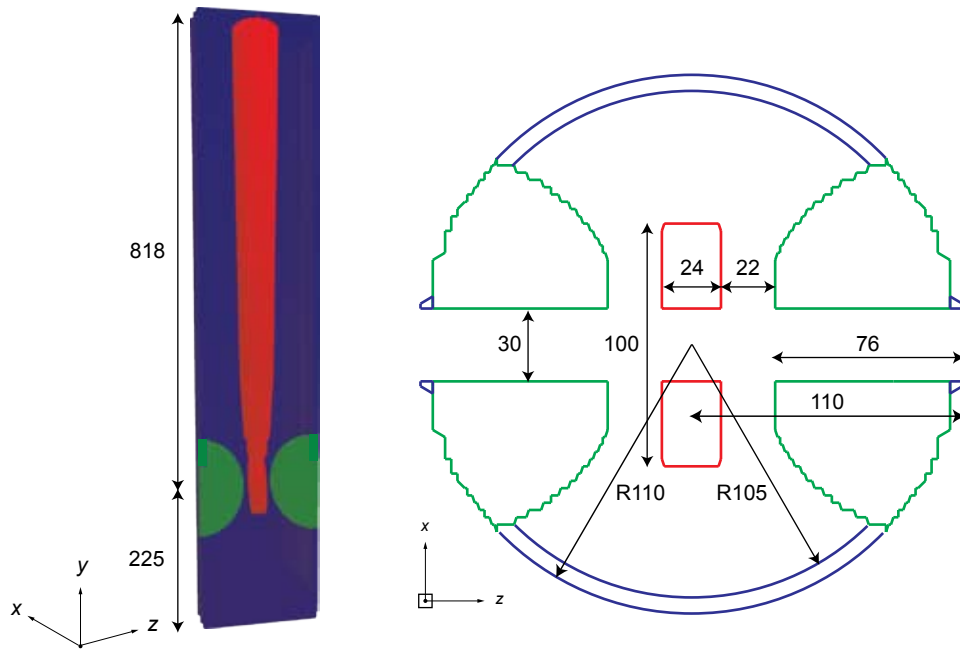


Figure 5.30: Sectional views of the rebuncher (dimensions in mm): vertical section (left) and horizontal section (right).

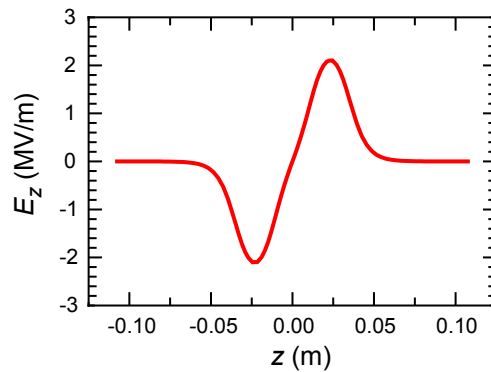


Figure 5.31: Accelerating field along the beam axis for the MEBT rebuncher.

Table 5.7: Main parameters of the MEBT rebuncher.

| Name | Value |
|----------------------------|--------|
| Frequency (MHz) | 80.5 |
| Optimum velocity (c) | 0.0251 |
| Aperture diameter (cm) | 3.0 |
| Cavity length (cm) | 22.0 |
| Effective voltage (kV) | 60.0 |
| Transit time factor | 0.765 |
| Quality factor | 9258 |
| Power dissipation (kW) | 1.12 |
| Peak electric field (MV/m) | 2.93 |
| Peak magnetic field (mT) | 3.75 |

MEBT beam dynamics

The transverse MEBT beam optics were evaluated using TRACE3D, while detailed beam simulations were performed with PARMELA. The simulation results indicate that the proposed MEBT design will provide adequate beam matching in both the transverse and longitudinal directions. In the transverse plane, the effective emittance (99.5% level) grows by about 20% for two-charge-state beams. The solenoid focusing strength depends on the charge state. Therefore, the beam ellipses for different charge states do not overlap completely. This causes the growth in the effective emittance. There is no emittance increase for single-charge-state beams.

The behavior of both a uranium beam, with charge states of 28^+ and 29^+ , and a single-charge-state xenon beam have been studied. Figure 5.32 and Figure 5.33 show the PARMELA simulation results for uranium and xenon beams at the exit of the RFQ (MEBT entrance) and at the entrance of the SC linac (MEBT exit), respectively. The impact of space charge, though included in the calculations, was found to be negligible.

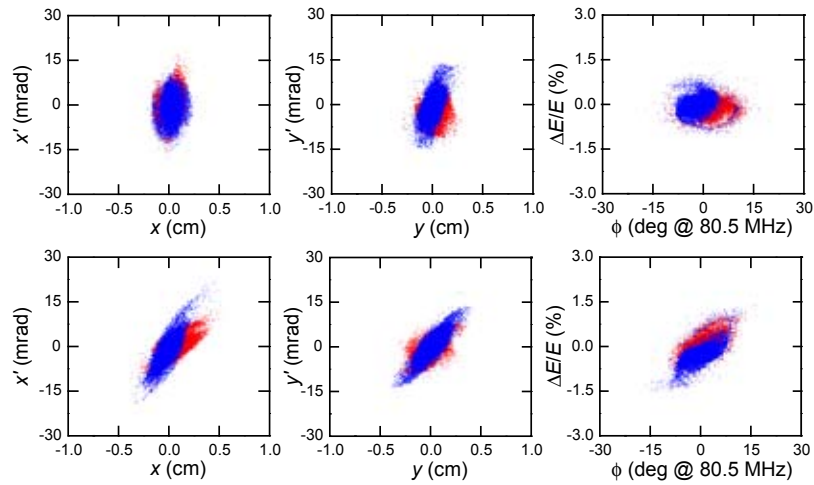


Figure 5.32: Results from the PARMELA simulations of the two-charge-state uranium beam (U^{28+} in red, U^{29+} in blue) with total beam current of $8 \mu\text{A}$ at the exit of the RFQ (top) and at the entrance to the linac (bottom): horizontal (left), vertical (middle), and longitudinal (right) phase space.

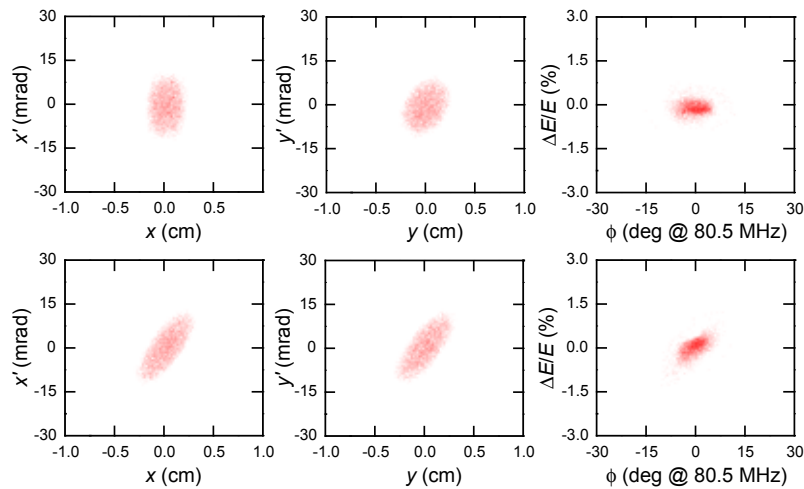


Figure 5.33: Results of the PARMELA simulation of a $12 \mu\text{A}$ xenon beam at the exit of the RFQ (top) and at the entrance to the linac (bottom): horizontal (left), vertical (middle), and longitudinal (right) phase space.

5.1.1.6 Summary of front-end system

Beam dynamics simulations for the most challenging two-charge-state uranium beam through the front end were performed. The beam travels from the ECR through the beam selection elements and pre-buncher in the LEBT, through the RFQ, and finally through the matching elements in the MEBT to the SC linac entrance. The normalized 99.5% transverse and longitudinal emittances of the two-charge-state uranium beam at the entrance to the superconducting linac are about 0.8π mm mrad and 1.1π keV/u ns, respectively. The corresponding rms emittances are about 10 times smaller. The emittance increase in the transverse plane in the front end was found to be mainly due to the space charge effects before charge selection and to the slightly different orientations of the charge-state distributions in phase space. In summary, the beam from the front end will be appropriate to obtain low losses through the linac and to meet performance requirements at the rare isotope production targets.

5.1.2 Linac superconducting cavity design

The driver linac will use superconducting drift tube cavities to accelerate beams from $\beta \sim 0.025$ (0.3 MeV/u) to $\beta \sim 0.57$ (200 MeV/u). Various alternative designs and optimization strategies have been considered and it was finally determined that a 10th harmonic linac based on 80.5 MHz is the most attractive solution. To minimize R&D and technical risk, the driver linac has a minimum number of cavity types and uses passive control of microphonics through the use of a mechanical damper in the center conductor of the $\lambda/4$ resonators. Five cavity types can efficiently cover the velocity range. Each cavity type is a two-gap structure characterized in terms of its optimum β (β_{opt}) the fractional particle velocity (v/c) for which it provides the maximum acceleration. The cavities are shown schematically in Figure 5.34 and the design parameters are given in Table 5.8.

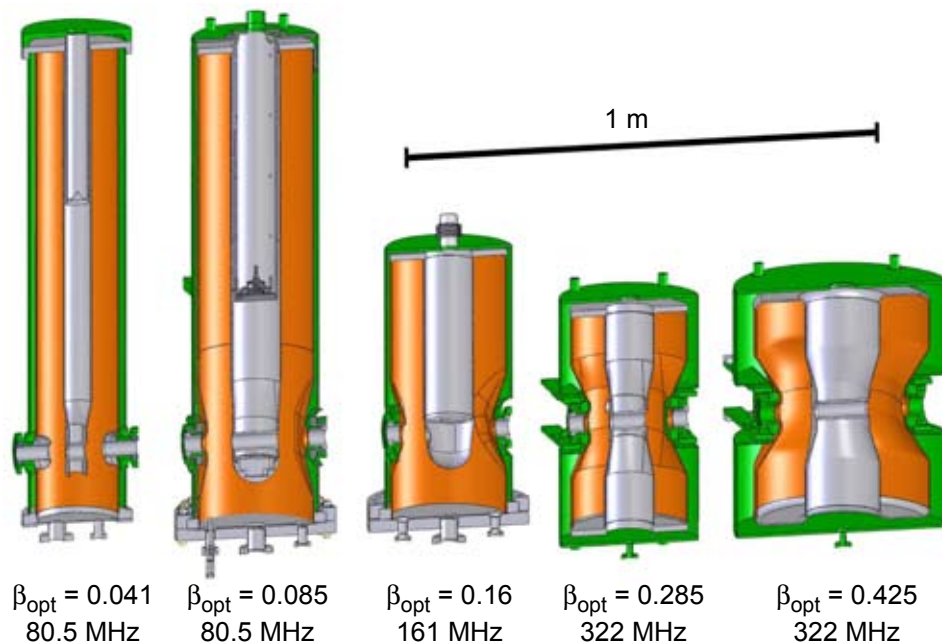


Figure 5.34: Cross sections of the superconducting rf cavities proposed for the linac. The inner and outer conductors are shown in gray and orange respectively. The titanium helium vessels are shown in green.

Table 5.8: Cavity parameters for the linac: β_{opt} is the optimum β , f is the resonant frequency, V_a is the accelerating voltage per cavity (at $\beta = \beta_{\text{opt}}$, including transit time effects), T is the operating temperature, and E_p and B_p are the peak surface electric and magnetic fields, respectively.

| Type | $\lambda/4$ | $\lambda/4$ | $\lambda/4$ | $\lambda/2$ | $\lambda/2$ |
|------------------------------|-------------|-------------|-------------|-------------|-------------|
| β_{opt} | 0.041 | 0.085 | 0.160 | 0.285 | 0.425 |
| f (MHz) | 80.5 | 80.5 | 161 | 322 | 322 |
| E_p (MV/m) | 16.5 | 20 | 20 | 25 | 30 |
| V_a (MV) | 0.46 | 1.18 | 1.04 | 1.58 | 2.51 |
| L (m) | 0.095 | 0.21 | 0.20 | 0.17 | 0.25 |
| E_{acc} (MV/m) | 4.84 | 5.62 | 5.20 | 9.29 | 9.98 |
| E_p/E_{acc} | 3.4 | 3.6 | 3.8 | 2.7 | 3.0 |
| B_p (mT) | 28.2 | 46.5 | 45.8 | 68.6 | 82.8 |
| Aperture (m) | 0.03 | 0.03 | 0.03 | 0.03 | 0.03 |
| Max transverse dimension (m) | 1.0 | 1.0 | 0.59 | 0.52 | 0.53 |
| Mass (kg) | 62 | 65 | 36 | 33 | 75 |
| T (K) | 4.5 | 4.5 | 4.5 | 2 | 2 |
| $\langle\phi_s\rangle$ | -30° | -30° | -35° | -35° | -30° |

The cavity for the lowest velocity particles has the smallest accelerating gaps, and thus has the most severe issues with control of microphonics. Therefore, an 80.5 MHz $\beta_{\text{opt}} = 0.041 \lambda/4$ resonator very similar to that already developed for INFN-Legnaro's heavy ion linac was selected [Fac99]. The second and third cavity types will be an 80.5 MHz $\beta_{\text{opt}} = 0.085 \lambda/4$ resonator and a 161 MHz $\beta_{\text{opt}} = 0.16 \lambda/4$ resonator [Har03], both of which have fewer difficulties with microphonics due to their longer accelerating gaps and larger diameters. The last two cavity types will be 322 MHz $\lambda/2$ resonators with $\beta_{\text{opt}} = 0.285$ [Gri03a] and $\beta_{\text{opt}} = 0.425$.

The effects of microphonics will be brought within appropriate limits through the utilization of passive mechanical dampers and the rf drive, thus avoiding the need for voltage-controlled reactance (VCX) tuners. VCX tuners have several disadvantages for operation in a large linac [Par00].

To ensure reliable linac performance, the design fields must be based on a thorough set of experimental data and should have reasonable safety factors. As can be seen in Table 5.8, conservative lower surface fields were chosen for the $\lambda/4$ resonators compared to those in the $\lambda/2$ resonators for the following reasons:

- The large gas load from the nearby RFQ
- The $\lambda/4$ resonators will have a large removable end flange with the potential for anomalous power losses at the rf joint.
- The $\lambda/4$ resonators' operating temperature is 4.5 K instead of 2 K; at higher temperatures, the Q tends to decrease more rapidly as the field increases due to the less effective heat transfer from the inner surface of the cavity. Operation at a lower field thus allows for a smaller cryogenic load.

The geometrical β value, β_{geo} , is defined as the velocity at which a particle crosses one cell (iris to iris) in one-half of an rf period. For multi-cell elliptical cavities with $\beta_{\text{geo}}=1$, the difference between β_{opt} and β_{geo} is negligible, but for lower β cavities the difference becomes significant. The effective lengths listed in Table 5.8 are the “active lengths,” including the accelerating gaps and the drift distance inside the center conductor but not including the beam tubes or the additional space between adjacent cavities.

The cavities generate their maximum accelerating voltage, V_a , at the optimum velocity of β_{opt} . Because the structures are multi gap, they are effective over a limited range of velocities. Figure 5.35 shows the transit time factor and energy gain as a function of β for a uranium beam along the driver linac (discussed below).

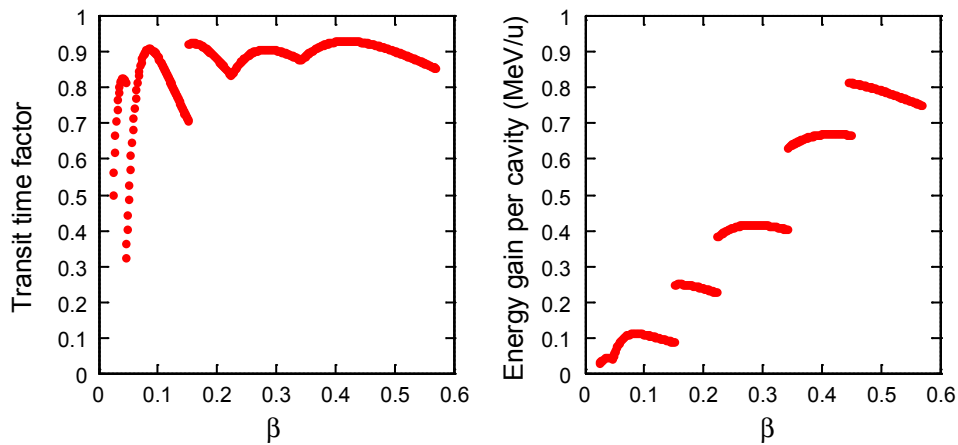


Figure 5.35: Cavity transit time factor and energy gain per cavity for uranium ions along the driver linac for charge states 29^+ in segment 1, 73^+ in segment 2, and 89^+ in segment 3.

Using the cavity parameters listed in Table 5.8, the number of driver-linac cavities, superconducting solenoids, and cryomodules needed to accelerate uranium to 200 MeV/u are given in Table 5.9. The magnets are NbTi solenoids with a 40 mm aperture. The required number and type of focusing elements and the number of cavities per cryomodule are based on beam dynamics issues discussed in Section 5.1.7. Using the same cavity layout, proton, ^3He , and ^{18}O beams can be accelerated to energies up to 525, 376, and 266 MeV/u, respectively (see Table 5.1).

The total number of cavities needed for the driver linac is 481, to be placed in 63 cryomodules. The reaccelerator linac discussed in Section 5.2 for the rare isotope beams will use the same $\beta_{\text{opt}} = 0.041$ and $0.085 \lambda/4$ resonators and will require a total of six additional cryomodules (see Section 5.2 for details).

Table 5.9: Driver linac cavity and cryomodule count for acceleration of uranium to 200 MeV/u using the design gradients in Table 5.8.

| Type | $\lambda/4$ | $\lambda/4$ | $\lambda/4$ | $\lambda/2$ | $\lambda/2$ |
|------------------------------------|-------------|-------------|-------------|-------------|------------------------|
| β_{opt} | 0.041 | 0.085 | 0.160 | 0.285 | 0.425 |
| Number of cavities | 20 | 106 | 58 | 92 | 205 |
| Magnet length (cm) | 10 | 20 | 50 | 50 | 50 |
| Number of magnets | 12 | 65 | 23 | 35 | 79 |
| Number of accelerating cryomodules | 2 | 13 | 7 | 11 | 25 |
| Number of matching cryomodules | 0 | 1 | 1 | 1 | 2 |
| Total number of cryomodules | 2 | 14 | 8 | 12 | 27 |
| Accelerating cryomodule length (m) | 4.97 | 5.80 | 5.56 | 5.41 | 6.69 |
| Matching cryomodule length (m) | — | 1.059 | 2.605 | 3.145 | #1: 2.247 #2: 4.086 |

5.1.3 Superconducting cavity cryogenic requirements

Superconducting cavities have losses that are strongly dependent on rf frequency and operating temperature. The cavities' operating temperatures are generally either above 4 K or below 2.2 K. The cryogenic analysis of the accelerator system must consider the Carnot efficiency of the cryogenic plant and the rf frequency of the cavities.

At atmospheric pressure, helium boils at 4.2 K. Boiling helium at higher pressure increases the temperature of the system and simplifies the compressors and reduces the problems associated with leaks (losses of helium instead of contamination of the helium gas with air). Heat is transferred to the helium via pool boiling with concomitant vibration.

Although rf losses are lower at 4.2 K, large-scale cryogenic plants generally operate at a temperature higher than 4.2 K [Rod99]. The operating temperature of choice for most low-frequency superconducting accelerators is 4.5 K; this includes ALPI [Por96], CESR-III [Bel00], the JAERI Tandem Booster [Tak98], KEK-B [Bel03], LEP [Bro00b], and ATLAS [Par00]. Thus, for operation above 4 K, 4.5 K is the operating temperature assumed in the following discussion.

At temperatures below 2.2 K, liquid helium is a superfluid with better thermal conductivity than normal state liquid helium. Heat is transferred via conduction without any pool boiling and the resultant vibration. However, the cryogenic plant is more complicated, and since most 2 K cryogenic plants are operated with saturated liquid below atmospheric pressure, leaks will cause contamination of the system with air.

The cryogenic load of the superconducting cavities was calculated to determine the required cryogenic plant capacity and cost. The dynamic heat load calculation

was done by calculating the cavity's rf power dissipation, P_0 , from fundamental cavity parameters. Using the definition of shunt impedance and geometry factor, P_0 can be written as

$$P_0 = \frac{V_a^2}{R} = \frac{V_a^2}{(R/Q)Q} = \frac{V_a^2}{(R/Q)G} R_s = \frac{V_a^2}{(R/Q)G} (R_{\text{BCS}} + R_{\text{res}}) \quad (5-2)$$

where R is the linac definition of the shunt impedance, Q is the cavity quality factor, V_a is the accelerating voltage, G is the geometry factor, R_s is the total rf surface resistance, R_{BCS} is the BCS surface resistance, and R_{res} is the residual surface resistance. An approximate expression for the BCS surface resistance is (see p. 88–89 in reference [Pad98])

$$R_{\text{BCS}} = 2 \times 10^{-4} \frac{C_{\text{RRR}}}{T_K} \left(\frac{f_{\text{GHz}}}{1.5} \right)^2 \exp\left(-\frac{17.67}{T_K}\right) \quad (5-3)$$

with R_{BCS} in $\text{n}\Omega$; f_{GHz} is the cavity frequency in GHz and T_K is the cavity temperature in K. The correction factor, C_{RRR} , ranges from 1 for reactor grade (RRR~25) niobium to 1.5 for high purity (RRR~250) niobium. (RRR is the Residual Resistivity Ratio which is correlated with the purity of niobium. The larger the value, the higher the purity.) The power dissipation is inversely proportional to $(R/Q)G$. The values of the parameters used to calculate the losses in each cavity type are given in Table 5.10.

Table 5.10: Electromagnetic and cryogenic parameters.

| Type | $\lambda/4$ | $\lambda/4$ | $\lambda/4$ | $\lambda/2$ | $\lambda/2$ |
|---|-------------------|-------------------|-------------------|----------------------|----------------------|
| β_{opt} | 0.041 | 0.085 | 0.160 | 0.285 | 0.425 |
| f (MHz) | 80.5 | 80.5 | 161 | 322 | 322 |
| T (K) | 4.5 | 4.5 | 4.5 | 2 | 2 |
| R/Q (Ω) | 424 | 416 | 381 | 199 | 210 |
| G (Ω) | 15.7 | 19.0 | 35.0 | 61.0 | 86 |
| $G \cdot R/Q$ ($\text{k}\Omega^2$) | 6.66 | 7.90 | 13.3 | 12.1 | 18.1 |
| E_p (MV/m) | 16.5 | 20 | 20 | 25 | 30 |
| V_a (MV) | 0.46 | 1.18 | 1.04 | 1.58 | 2.51 |
| U (J) | 0.99 | 6.69 | 2.81 | 6.19 | 14.93 |
| $R_{\text{BCS,min}}$ ($\text{n}\Omega$) | 2.5 | 2.5 | 10.1 | 0.7 | 0.7 |
| $R_{\text{res,min}}$ ($\text{n}\Omega$) | 5 | 5 | 5 | 5 | 5 |
| Q_{max} | 2.1×10^9 | 2.5×10^9 | 2.3×10^9 | 1.1×10^{10} | 1.5×10^{10} |
| $Q_{\text{design}} = Q_0$ | 5×10^8 | 5×10^8 | 5×10^8 | 5×10^9 | 7×10^9 |
| $P_{\text{design}} (\text{W/cav}) = P_0$ | 1.0 | 6.7 | 5.7 | 2.5 | 4.3 |

Since the accelerating voltage has already been specified, the only parameter left is the total surface resistance, which, as indicated above, consists of a BCS and a residual component. The variation of the BCS component of the surface resistance is shown as a function of temperature in Figure 5.36 for reactor grade

(RRR~25) and high purity (RRR~250) niobium at frequencies of 80.5, 161, and 322 MHz. We assume a low surface resistance RRR (RRR~25) for the calculation of R_{BCS} (this may be a bit optimistic, hence a safety factor is included below). The $\lambda/4$ resonators will operate at 4.5 K, and the $\lambda/2$ resonators will operate at 2 K, giving BCS surface resistances of 2.5, 10, and less than 1 n Ω for the 80.5, 161, and 322 MHz resonators, respectively.

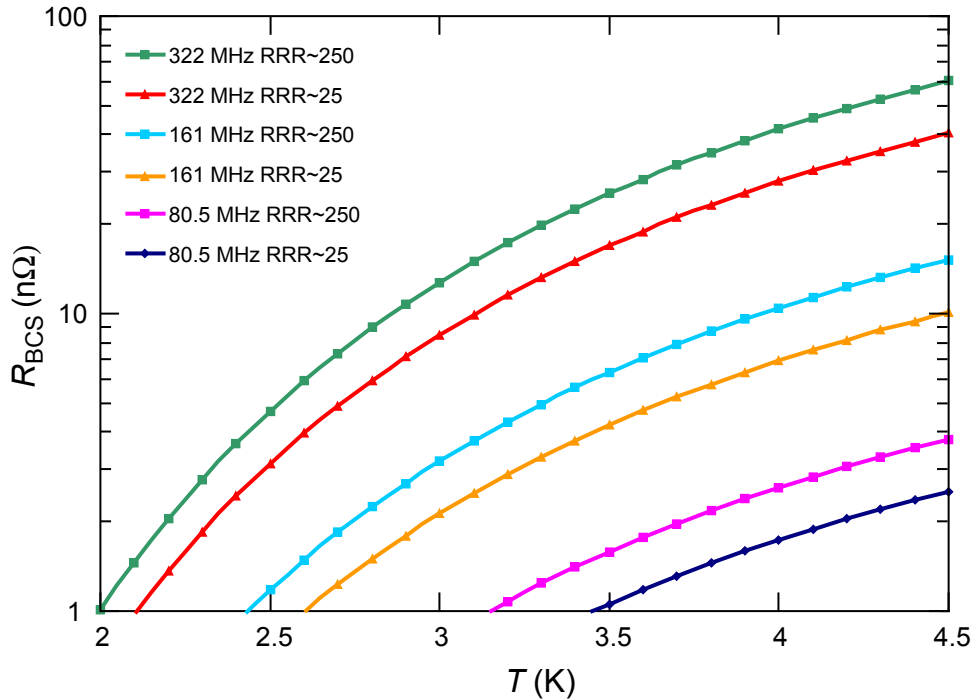


Figure 5.36: Range of R_{BCS} values for Nb resulting from varying RRR values as a function of temperature (T). The operating temperatures will be 2 K for the $\lambda/2$ resonators and 4.5 K for the $\lambda/4$ resonators.

The final parameter left to determine is the residual resistance. Well-processed elliptical cavities can yield residual resistances in the range of 2 to 10 n Ω [Pad98]. As a design criterion, we assume a residual resistance of 5 n Ω for all cavity types. Using these resistances, maximum values of Q (Q_{max}) have been estimated and are given in Table 5.10. Because it is difficult to predict the values of the BCS and residual resistance precisely, a safety factor is included. For the $\lambda/2$ cavities, a safety factor of two is used to obtain a Q_{design} that is half of Q_{max} . Since the $\lambda/4$ cavities will operate at 4.5 K, the Q can be expected to decrease more significantly as the field increases, so a safety factor of four is assumed.

The rf tests on the prototype cavities (see Section 5.1.5) provide a way to check the consistency of the design goals. The rf test results indicate that the Q_{design} values obtained by the methodology described above have a reasonable safety factor and are thus acceptable for determining the cryogenic load. The last row of Table 5.10 shows the power dissipated per cavity. To compare power levels at different cryogenic temperatures, the Carnot efficiency and mechanical efficiencies of 18% at 2 K and 30% at 4.5 K [Sch03a] must be included. This is done in Section 5.3.3.

Cryomodule heat loads shown in Table 5.11 were calculated from the number of cavities with their design dynamic load, adding 2 W for each magnet's leads and

a 25 W static load per cryomodule. The rf power dissipation represents a dynamic load that is only present during cavity operation, so the cryoplant has excess capacity when the rf load is not present. This excess capacity can be used for cooling down the cryomodules with the cavities turned off. The thermal shield of each cryomodule will use 50 K helium gas, giving less than a 100 W load per cryomodule.

Table 5.11: The calculated total/static cryogenic loads of the cryomodules.

| Cavity | | Accelerating modules | | Matching modules | |
|-----------|---------------|----------------------|------------|--------------------|------------|
| Frequency | β_{opt} | 2 K load | 4.5 K load | 2 K load | 4.5 K load |
| 80.5 MHz | 0.041 | — | 47/37 W | — | — |
| 80.5 MHz | 0.085 | — | 89/35 W | — | 28/15 W |
| 161 MHz | 0.160 | — | 77/31 W | — | 30/19 W |
| 322 MHz | 0.285 | 51/31 W | — | 34/24 W | — |
| 322 MHz | 0.425 | 65/31 W | — | 32/15 W 27/23 W | — |

5.1.4 Beam loading, rf, and microphonics requirements

Superconducting cavities require very little rf power to generate the accelerating gradient, having quality factors $Q_0 > 10^8$ for the $\lambda/4$ cavities and $Q_0 > 10^9$ for the $\lambda/2$ cavities. Some rf power is required for beam acceleration and control of microphonics. Ideally, beam loading is large enough so that the available rf power provides a system bandwidth much larger than any detuning. Under these circumstances, the rf generator power (P_g) equals the beam power (P_{beam}). However, if the cavity resonant frequency shifts away from the generator frequency, additional rf power is required to maintain the amplitude and phase of the acceleration field. The required P_g for a given beam loading, coupler strength ($Q_{ext} \cong Q_L$, where Q_L denotes cavity loaded Q , e.g., see page 147 of reference [Pad98]) and maximum detuning ($\pm\delta f$) is given by

$$\frac{P_g}{P_{beam}} = \frac{Q_{beam}}{4 Q_L} \left[\left(1 + \frac{Q_L}{Q_{beam}}\right)^2 + \left(\frac{\delta f}{\Delta_{beam}} \frac{Q_L}{Q_{beam}}\right)^2 \right] \quad (5-4)$$

where

$$Q_{beam} = \frac{\omega U}{I_{beam} V_a \cos \phi_s} = Q_0 \frac{P_0}{P_{beam}} \quad (5-5)$$

and the half-beam bandwidth

$$\Delta_{beam} = \frac{f}{2 Q_{beam}} \quad (5-6)$$

Figure 5.37 shows the normalized rf generator requirements as a function of beam loading and detuning. Assuming a generator power that is twice the beam power, we can solve for the value of Q_L/Q_{beam} which then gives the maximum value of $\delta f/\Delta_{beam}$, the last term in equation (5-4). The result is $Q_L/Q_{beam} = 0.33$, corresponding to a maximum allowable $\delta f = 2.8\Delta_{beam}$ to maintain amplitude and phase. Under these conditions, microphonics can detune the cavity over a bandwidth of

$$\Delta_{allowed} = 2\delta f = 5.6\Delta_{beam} \quad (5-7)$$

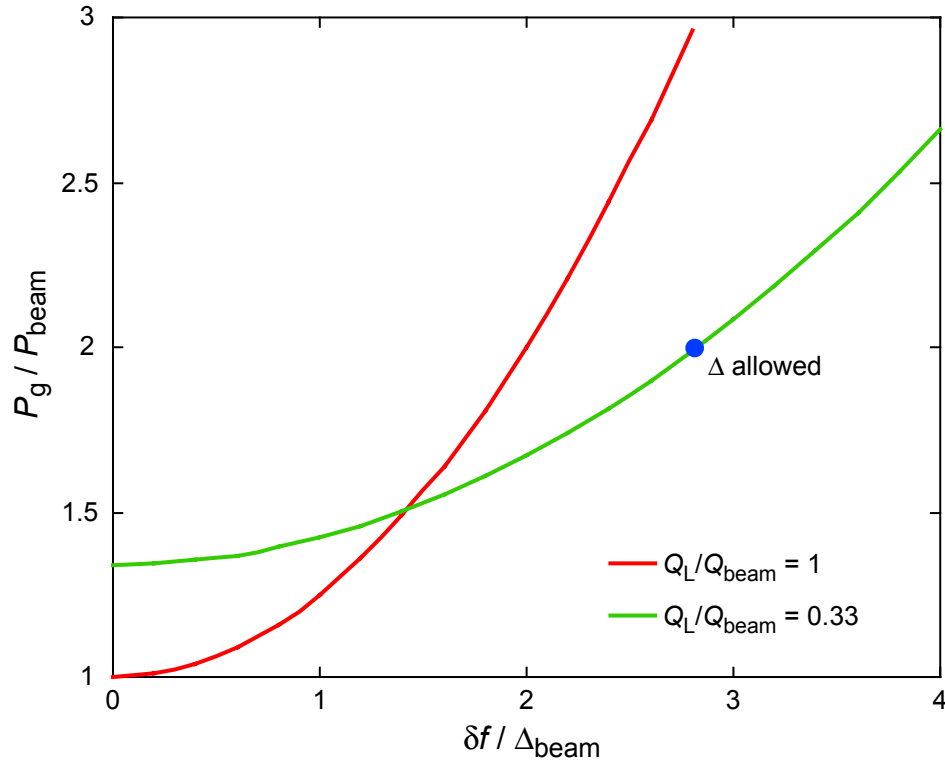


Figure 5.37: Normalized rf generator requirements as a function of beam loading and detuning.

while still being able to maintain operational control. The control bandwidth is slightly smaller than the Q_L bandwidth due to the decreased generator requirements.

The beam loading parameters for the design beam of uranium with a final beam power of 400 kW and a final energy of 200 MeV/u are shown in Table 5.12. The allowable detuning for this beam is also shown in Table 5.12. The beam power values shown in the table assume acceleration of a beam at a velocity that matches the design beam velocity of the cavity (i.e., $\beta = \beta_{\text{opt}}$). Since the beam velocity varies along the linac, in most of the cavities, the velocity will not match the design value exactly. In these cases, less power will be delivered to the beam and more power will be available for amplitude and phase control, resulting in a larger control bandwidth.

Measured microphonic excitation levels indicate that the bandwidth and loaded Q values are adequate, although some passive and active damping may be required. The parameters are similar to other existing and planned accelerators. For example, superconducting cavities with Q_L in the mid- 10^7 range are operated at the S-DALINAC in Darmstadt [Gra92], and cavities with Q_L in the low 10^7 range are planned for the Continuous Electron Beam Accelerator Facility (CEBAF) upgrade. Also, energy recovery linacs are planned to operate with Q_L in the 10^8 range.

Finally, Lorentz detuning, which is a shift in the cavity frequency due to the radiation pressure of the electromagnetic fields, must be compensated during ramp up. Unlike a pulsed rf accelerator, compensation of a cw linac can be done slowly using the tuner and, as a consequence, will not be a critical issue.

Table 5.12: Beam loading requirements by cavity type for uranium at 400 kW and 200 MeV/u. (I_{beam} denotes beam current, $\langle q \rangle$ denotes average charge state, $\langle \phi_s \rangle$ denotes average synchronous phase.)

| Type | $\lambda/4$ | $\lambda/4$ | $\lambda/4$ | $\lambda/2$ | $\lambda/2$ |
|---|-------------------|-------------------|-------------------|-------------------|-------------------|
| β_{opt} | 0.041 | 0.085 | 0.160 | 0.285 | 0.425 |
| V_a (MV) | 0.46 | 1.18 | 1.04 | 1.58 | 2.51 |
| I_{beam} (pμA) | 10.6 | 10.6 | 8.3 | 8.3 | 8.3 |
| $\langle Q \rangle$ | 28 | 28 | 73 | 73 | 89 |
| P_{beam} (W) | 118 | 350 | 510 | 784 | 1610 |
| Q_{beam} | 4.2×10^6 | 9.6×10^6 | 5.6×10^6 | 1.6×10^7 | 1.9×10^7 |
| P_g (W) | 236 | 700 | 1020 | 1570 | 3210 |
| Q_L | 1.4×10^6 | 3.2×10^6 | 1.9×10^6 | 5.3×10^6 | 6.2×10^6 |
| Control bandwidth Δ_{allowed} (Hz) | 54 | 23 | 81 | 56 | 47 |
| $\langle \phi_s \rangle$ (deg) | -30 | -30 | -35 | -35 | -30 |

5.1.5 Cavity research and development

A Research and Development (R&D) program has been undertaken to create prototypes and test the required superconducting cavity types. The number of cavity types was kept to a minimum to reduce development and production costs. For example, the reaccelerator linac will use some of the same $\lambda/4$ cryomodules as the driver linac. This will decrease the number of spares necessary for reliable operation. In addition, existing cavity designs and expertise from other laboratories have been employed as much as possible. For example, the proposed $\beta_{\text{opt}} = 0.041$ $\lambda/4$ resonator is very similar to a $\lambda/4$ resonator already produced in significant quantities and operated in a heavy-ion linac at INFN-Legnano [Fac99].

The $\beta_{\text{opt}} = 0.085$, $\beta_{\text{opt}} = 0.16$, and $\beta_{\text{opt}} = 0.285$ $\lambda/4$ and $\lambda/2$ resonators have been successfully prototyped and tested at MSU [Har03,Gri03a]. The only cavity remaining to be developed is a $\lambda/2$ resonator with $\beta_{\text{opt}} = 0.43$, which will be prototyped in 2007. All of the cavities have a 3 cm beam aperture and isolation of the beam vacuum from the cryostat vacuum, as is standard for elliptical cavities.

The $\beta_{\text{opt}} = 0.041$ $\lambda/4$ resonator operating at 80.5 MHz will use a passive mechanical damper to control microphonics instead of a VCX tuner. A VCX tuner (required for $\lambda/4$ resonators with frequencies below 80 MHz) maintains resonance by switching a reactance in and out of the cavity circuit, and therefore induces an inherent phase jitter of $\pm 1^\circ$ [Par00,Ost02a]. This phase jitter significantly blows up the longitudinal emittance of the beam such that the acceptance may be marginal [Ost04]. Since the 80.5 MHz $\lambda/4$ resonator will use passive damping instead of the VCX tuner, phase regulation of $\pm 0.5^\circ$ will be possible, which reduces the emittance growth of the beam to acceptable levels [And04].

The $\beta_{\text{opt}} = 0.085$ $\lambda/4$ resonator has larger gaps than the $\beta_{\text{opt}} = 0.041$ resonator, and is therefore less susceptible to microphonics. A prototype of this cavity was fabricated and tested in the summer of 2003 and significantly exceeded the required

quality factor and accelerating field [Har03]. A prototype $\beta_{\text{opt}} = 0.16 \lambda/4$ resonator was fabricated and also tested in the summer and fall of 2003. Initially, the performance of this cavity was not as good as expected due to heating of the tuning plate [Har03]; after modifications to improve the cooling of the tuning plate, the design goals were met. A prototype $\beta_{\text{opt}} = 0.285 \lambda/2$ resonator was successfully tested in 2002 and significantly exceeded the required quality factor and accelerating field [Gri03a].

Figure 5.38 shows photographs of the $\beta_{\text{opt}} = 0.085 \lambda/4$, $\beta_{\text{opt}} = 0.16 \lambda/4$, and $\beta_{\text{opt}} = 0.285 \lambda/2$ resonators prior to cool-down and rf testing. Some of the rf test results are shown in Figure 5.39. The design parameters are $E_p = 20 \text{ MV/m}$ and $Q_0 = 5 \times 10^8$ for the $\beta_{\text{opt}} = 0.085$ and $\beta_{\text{opt}} = 0.16 \lambda/4$ resonators and $E_p = 25 \text{ MV/m}$ and $Q_0 = 5 \times 10^9$ for the $\beta_{\text{opt}} = 0.285 \lambda/2$ resonator. As indicated above, the design goals are exceeded in all three prototype cavities. Note that the $\lambda/4$ resonators were tested at 4.2 K instead of the planned operation temperature of 4.5 K; as per equation (5-3), the quality factor can be expected to be slightly lower at the slightly higher operating temperature. The $\beta_{\text{opt}} = 0.085$ and $\beta_{\text{opt}} = 0.285$ resonators were fitted with helium vessels and were retested under conditions that better approximate a cryomodule environment. The titanium helium vessel was Tungsten-Inert-Gas (TIG) welded to NbTi adapter flanges that were themselves electron-beam welded to the cavity beam tubes. NbTi flanges with copper or indium gaskets were used to form the vacuum seals.

The final cavity type, a $\beta_{\text{opt}} = 0.425 \lambda/2$ resonator, is very similar to the $\beta_{\text{opt}} = 0.285 \lambda/2$ resonator of the same frequency because the radial dimensions basically scale with β_{opt} . A prototype is planned to be constructed and tested in 2007. We anticipate that the cavity performance will be comparable to that of the $\beta_{\text{opt}} = 0.285 \lambda/2$ resonator.

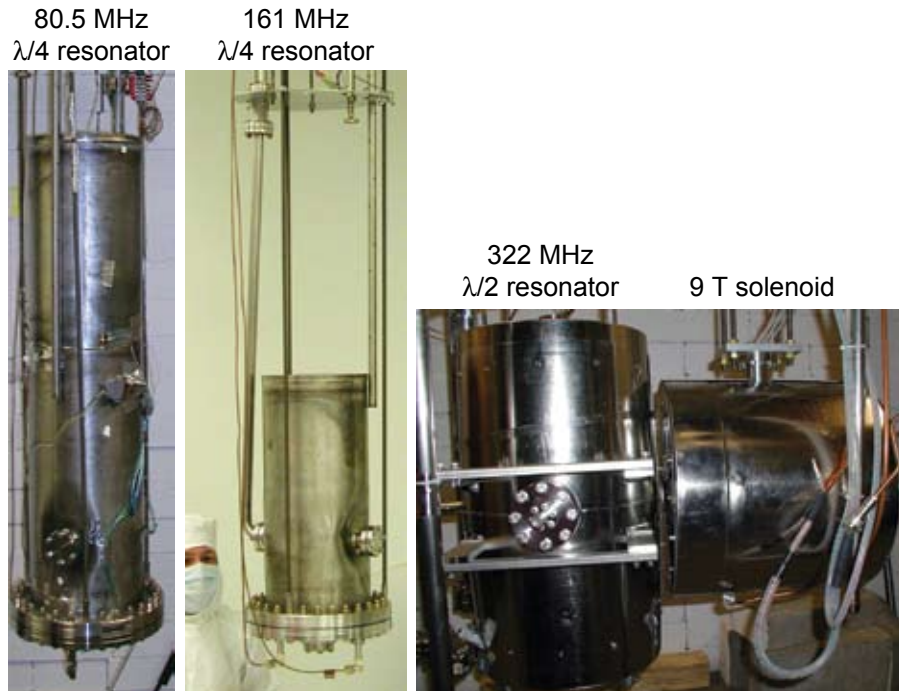


Figure 5.38: Prototype $\lambda/4$ and $\lambda/2$ resonators on the rf test stand. Left: 80.5 MHz $\beta_{\text{opt}} = 0.085 \lambda/4$ resonator. Middle: 161 MHz $\beta_{\text{opt}} = 0.16 \lambda/4$ resonator. Right: 322 MHz $\beta_{\text{opt}} = 0.285 \lambda/2$ resonator with helium vessel next to a shielded 9 T superconducting solenoid.

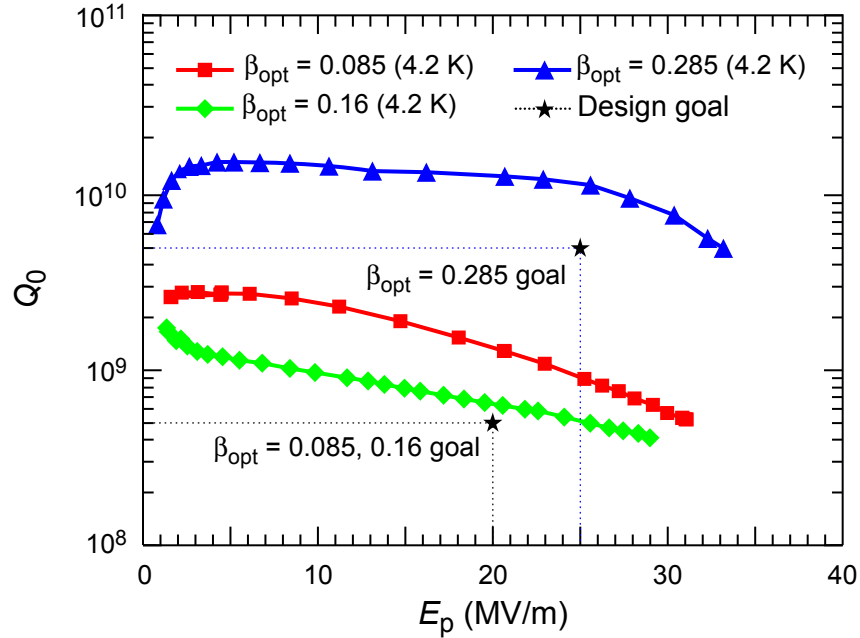


Figure 5.39: RF test results for prototype $\lambda/4$ and $\lambda/2$ resonators with design goals shown.

5.1.6 Cryomodule development

Five types of accelerating cryomodules will be required to house the resonators for the driver linac. The design of all of the cryomodules relies on a cold titanium alignment rail that supports the cavities and focusing elements [Gri03b]. An important aspect of this design is that the beamline vacuum will be isolated from the insulating vacuum. The rail will be hung from a plate that is the top element of a rectangular box. The rectangular box will be constructed from low carbon steel and assembled around the cold mass and finally welded together. Table 5.13 shows the number of cryomodules needed for the linacs.

Table 5.13: Number of cryomodules for the driver and reaccelerator linacs.

| | Driver (# accelerating modules) | Driver (# matching modules) | Reaccelerator (# accelerating modules) |
|--|---------------------------------------|-----------------------------------|--|
| $\lambda/4 \beta_{\text{opt}} = 0.041$ | 2 | 0 | 1 |
| $\lambda/4 \beta_{\text{opt}} = 0.085$ | 13 | 1 | 5 |
| $\lambda/2 \beta_{\text{opt}} = 0.160$ | 7 | 1 | — |
| $\lambda/2 \beta_{\text{opt}} = 0.285$ | 11 | 1 | — |
| $\lambda/2 \beta_{\text{opt}} = 0.43$ | 25 | 2 | — |
| Total | 58 | 5 | 6 |

5.1.6.1 Cryomodule design

The cryomodule designs are shown in Figure 5.40 through Figure 5.44. The $\lambda/4$ and $\lambda/2$ cryomodules require 9 T superconducting solenoids between the accelerating structures. Critical issues for the cryomodules are the cavity design gradient, the cryogenic load, microphonics, stray magnetic field from focusing elements, cost, and reliability.

The matching cryomodules necessary to manipulate the longitudinal phase space of the beam are shown in Figure 5.45 through Figure 5.49. A value-engineering analysis will be undertaken at a later point to explore the tradeoffs of employing larger, more expensive standard cryomodules in lieu of cheaper but specialized matching cryomodules.

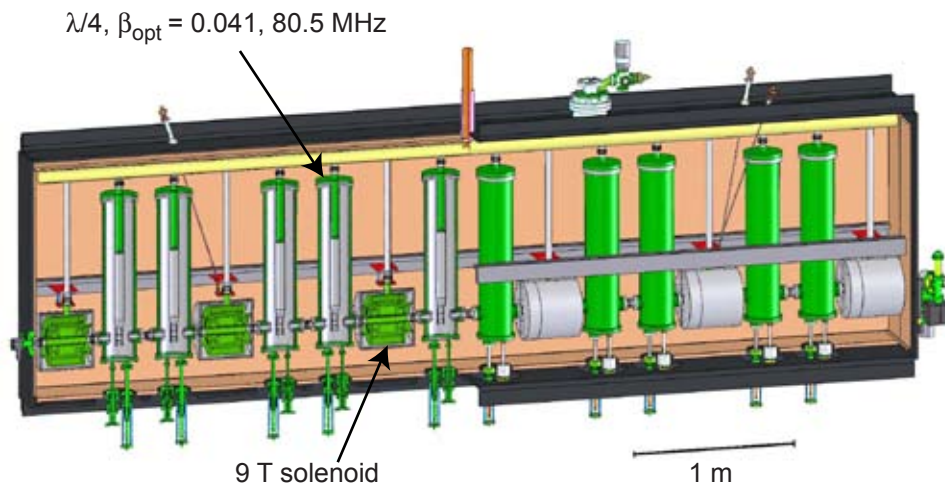


Figure 5.40: Cryomodule layout for $\lambda/4, \beta_{\text{opt}} = 0.041, 80.5 \text{ MHz}$ superconducting cavities. The left side of the figure shows a sectioned view.

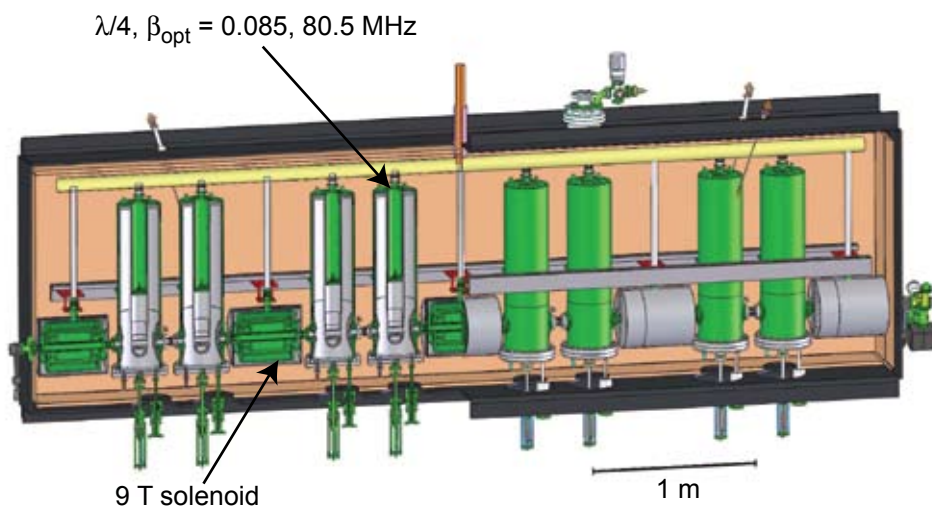


Figure 5.41: Cryomodule layout for $\lambda/4, \beta_{\text{opt}} = 0.085, 80.5 \text{ MHz}$ superconducting cavities. The left side of the figure shows a sectioned view.

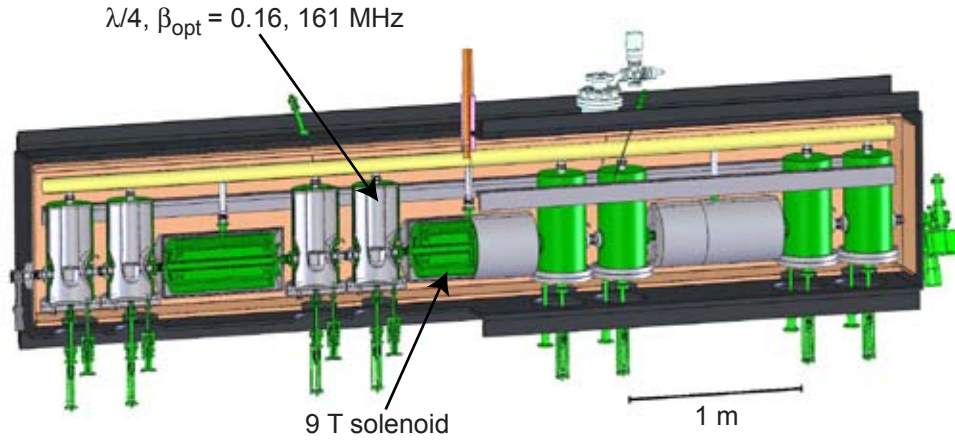


Figure 5.42: Cryomodule layout for $\lambda/4, \beta_{\text{opt}} = 0.16, 161 \text{ MHz}$ superconducting cavities. The left side of the figure shows a sectioned view.

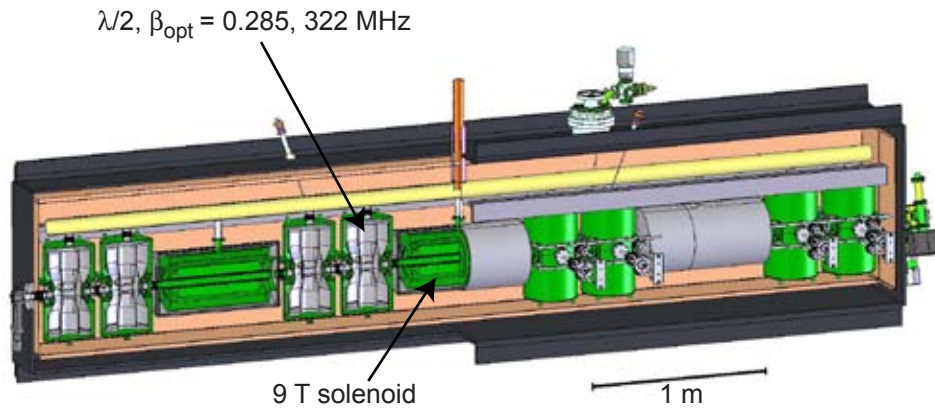


Figure 5.43: Cryomodule layout for $\lambda/2, \beta_{\text{opt}} = 0.285, 322 \text{ MHz}$ superconducting cavities. The left side of the figure shows a sectioned view.

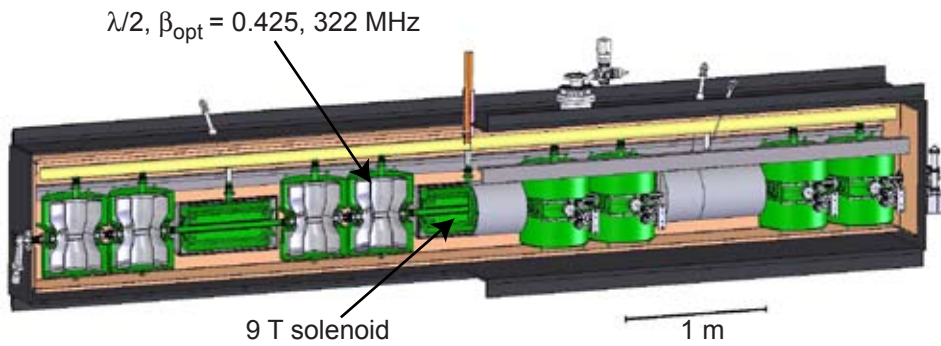


Figure 5.44: Cryomodule layout for $\lambda/2, \beta_{\text{opt}} = 0.425, 322 \text{ MHz}$ superconducting cavities. The left side of the figure shows a sectioned view.

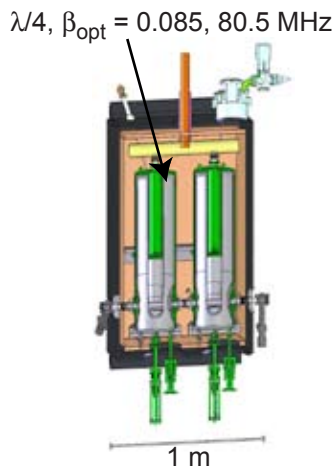


Figure 5.45: Special $\lambda/4$ $\beta_{opt} = 0.085$, 80.5 MHz cryomodule in stripping section 1 for longitudinal bunch-length control.

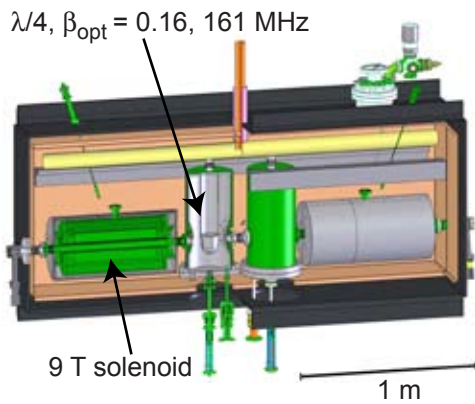


Figure 5.46: Special $\lambda/4$ $\beta_{opt} = 0.16$, 161 MHz cryomodule in stripping section 1 for longitudinal matching to 161 MHz cavities of linac segment 2. The left side of the figure shows a sectioned view.

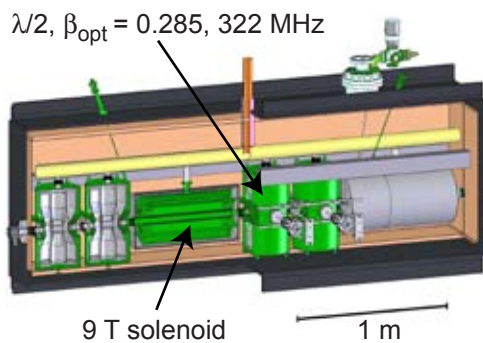


Figure 5.47: Special $\lambda/2$ $\beta_{opt} = 0.285$ cryomodule for longitudinal matching from 161 to 322 MHz. The left side of the figure shows a sectioned view.

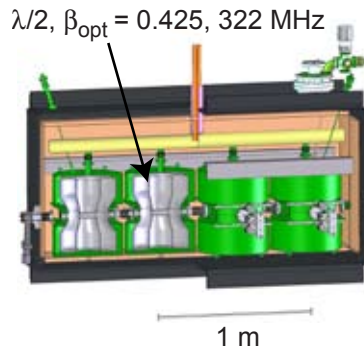


Figure 5.48: Special $\lambda/2$ $\beta_{\text{opt}} = 0.425$, 322 MHz cryomodule for longitudinal bunch-length control in stripping segment 2. The left side of the figure shows a sectioned view.

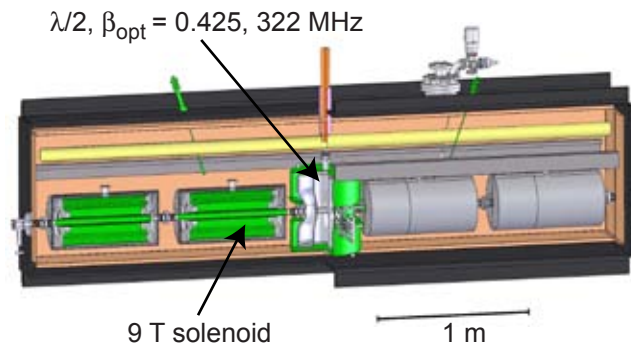


Figure 5.49: Special $\lambda/2$ $\beta_{\text{opt}} = 0.425$, 322 MHz cryomodule longitudinal matching into linac segment 3. The left side of the figure shows a sectioned view.

5.1.6.2 Cryomodule prototype

A prototype cryomodule containing the critical components of the production cryomodules is currently being fabricated and will be tested in 2007. The purpose of the prototype cryomodule is to quickly and inexpensively test the cryomodule design under realistic conditions and either demonstrate the desired performance or identify and correct problems with the design. Once testing of this prototype is complete, the cryomodule designs will be finalized, drawing packages will be completed, and production plans will be developed.

A drawing of the prototype cryomodule with a $\lambda/4$ and a $\lambda/2$ superconducting cavity, along with two superconducting magnets, is shown in Figure 5.50. Figure 5.51 shows photographs of some of the components being assembled. The cavities, power couplers, tuners, microphonic response, and shielding of the cavities from the stray magnetic field from the focusing elements will be tested. The prototype also includes a superferric quadrupole magnet that could replace the 9 T solenoidal magnets to provide the transverse focusing for the linac [Zel02].

The 9 T superconducting solenoidal magnet, shown in Figure 5.50, has an active length of 0.1 m. The coil package includes a steering dipole with a strength of 0.01 Tm. Solenoidal magnets of different lengths will be used for each cavity type, but the stray field issues will be the same since all of the solenoids have the same aperture and peak field.

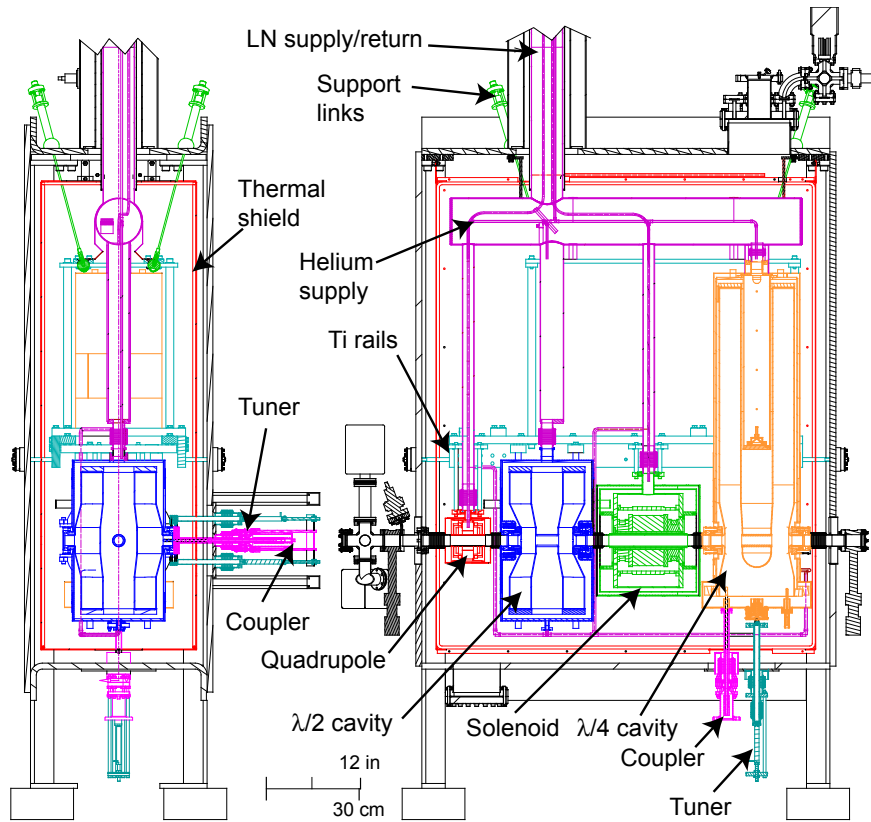


Figure 5.50: End view (left) and side view (right) of the prototype cryomodule for testing the low- β cavities and two types of superconducting magnets.



Figure 5.51: Photographs of components for the prototype cryomodule. Top left: cold mass in the clean room. Bottom left: module in assembly area. Right: test fit of the nitrogen shield to top plate.

A critical issue with the high-field solenoids is to assure that the residual magnetostatic field at the superconducting cavities is sufficiently small while the cryomodule is being cooled down. Magnetic flux may be trapped by the cavities when they become superconducting; trapped flux will degrade the rf performance of the cavities. The magnetic field at the cavity during transition must be below 10 μT for the $\lambda/4$ cavities and below 2.5 μT for the $\lambda/2$ cavities to reduce the stray contribution to the residual resistance to less than 10 n Ω for the $\lambda/4$ cavities and less than 5 n Ω for the $\lambda/2$ cavities. Contributions to the residual resistance below these levels will not significantly reduce the cavity quality factor.

A number of sources can contribute to the flux trapping problem. They include the residual field from the magnet components themselves, the field of other components in the cryomodule magnetized by the stray field of the magnet, and the Earth's magnetic field.

Several techniques will be used to minimize the magnetic field at the cavities. The solenoids will have an active shield, which will consist of a reverse-wound solenoid outside the main solenoid; this will trap the majority of the return flux inside the NbTi windings. The field will be further trapped inside the solenoid by passive shielding from a niobium Meissner shield and a layer of mu-metal. A type of mu-metal designed for magnetic shielding at cryogenic temperatures ("cryoperm") will be used for this purpose. A layer of mu-metal will also be placed around each cavity for additional shielding of the magnet fields and the Earth's field.

As an alternative to the high-field solenoidal magnets, a 31 T/m superferric quadrupole magnet is also being considered. The quadrupole magnet is easier to shield since the peak field is smaller (0.6 T) and is trapped by the pole tips and return yoke, but the focusing is less effective since a quadrupole does not provide simultaneous focusing in both transverse planes.

Since either quadrupole or solenoidal focusing elements were considered, the effect of the stray field from the solenoid or quadrupole on a superconducting cavity was tested in a vertical test stand. The $\lambda/2$ cavity was used in this test because it is more sensitive to a stray field than the $\lambda/4$ cavities. The right side of Figure 5.38 shows a photograph of the $\lambda/2$ cavity next to the solenoid magnet on the vertical Dewar insert in the same configuration as that needed for the prototype cryomodule. The magnet has cryoperm and niobium shields around it, and the vertical Dewar is also shielded from the Earth's field. The cavity was tested without the solenoid present to establish its baseline performance. The magnet was then installed next to the cavity and additional tests were done to check the effect of the magnetic field on the cavity performance. The magnet was operated at full field without degradation in the low-field Q_0 of the cavity. The residual field from the magnet did not degrade the performance of the cavity, either, even after the cavity was cycled above its transition temperature and back. Thus, the proximity of a solenoid magnet operating at full current does not produce any measurable degradation in cavity performance. Similar tests were performed with the superconducting quadrupole magnet that confirmed the magnet did not degrade the performance of the $\lambda/2$ cavity when proper magnetic shielding was present.

5.1.7 Accelerating segments

The driver linac will consist of three acceleration segments of superconducting cavities separated by two stripping sections (see Figure 5.2). Segment 1 will use 80.5 MHz $\lambda/4$ cavities, segment 2 will use 161 MHz $\lambda/4$ cavities and 322 MHz $\lambda/2$ cavities, and segment 3 will only use 322 MHz $\lambda/2$ cavities. All of the segments will contain superconducting solenoids for transverse focusing. There will be two charge-stripping sections between the accelerating segments to increase the average charge state of the primary beams; however, as indicated above, xenon and lighter ion beams will only be stripped once in the first stripping section.

All three linac segments will be able to accelerate multiple charge states of the primary beam to achieve the required primary beam power on the production target. Uranium will present the most challenges, since the beam will consist of two charge states in segment 1, five charge states in segment 2, and three charge states in segment 3. The basic parameters for the uranium beam in the three consecutive accelerating segments are presented in Sections 5.1.7.1 - 5.1.7.3, below. Detailed results for end-to-end simulations of beam transport without and with errors in rf phase and amplitude and hardware alignment are given in Section 5.1.9.3.

5.1.7.1 Accelerating segment 1

Segment 1 will be approximately 83 m long and will accelerate the uranium beam from 0.3 to 12 MeV/u. Two cryomodules, each containing ten $\beta_{\text{opt}} = 0.041 \lambda/4$ cavities operating at 80.5 MHz and six superconducting solenoidal magnets will accelerate the beam from 0.3 to ~ 1 MeV/u. Thirteen subsequent cryomodules, each containing eight $\beta_{\text{opt}} = 0.085 \lambda/4$ cavities operating at 80.5 MHz and five superconducting solenoidal magnets, will bring the beam to 12 MeV/u.

A beam dynamics simulation code was developed at MSU to efficiently determine the linac tuning [Dol05]. The code includes six-dimensional matching and multiple-charge-state acceleration. Figure 5.52 shows the longitudinal acceptance of segment 1 and the transverse and longitudinal phase advances for the uranium beam. No parametric resonance [Dup03,Ost02b] was expected, and none was observed in the simulations. As discussed above, the 99.5% longitudinal

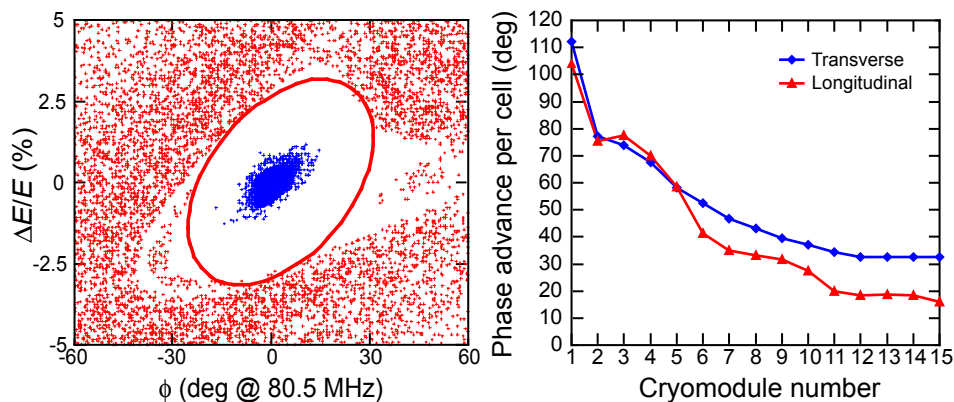


Figure 5.52: Left: longitudinal acceptance (area within red ellipse) of segment 1 together with the input uranium beam (blue). The full phase space displayed was populated with particles, and those particles that were lost are displayed as red dots. The acceptance to 99.5% emittance ratio is 7.3. Right: transverse and longitudinal phase advance for uranium beam along segment 1.

emittance of the uranium beam at the entrance of segment 1 will be approximately 1.1π keV/u ns. The longitudinal acceptance for this segment was found to be 8π keV/u ns, giving an acceptance to emittance ratio of 7.3. The transverse and longitudinal betatron functions for the uranium beam in segment 1 are shown in Figure 5.53. The beam parameters on entering and exiting the segment are summarized in Table 5.14. The simulation results substantiate that the design will meet the performance requirements.

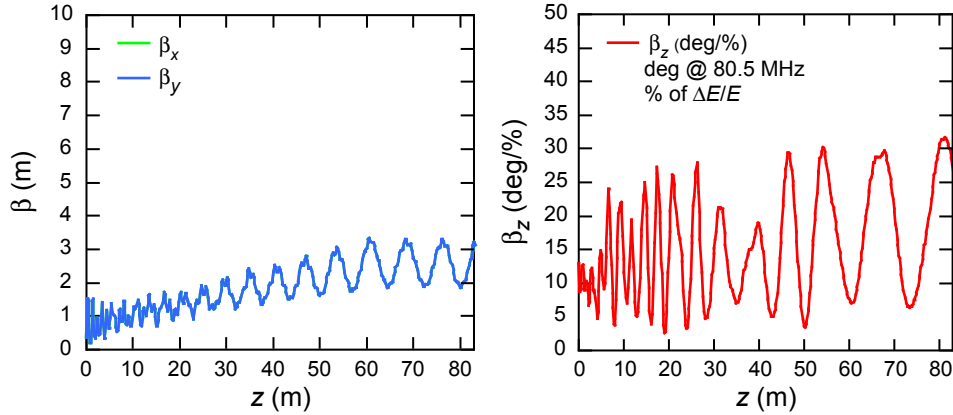


Figure 5.53: Transverse (left) and longitudinal (right) betatron functions in segment 1 for the uranium beam (29^+). The horizontal function (β_x – green) is not visible because it exactly follows the vertical function (β_y – blue).

Table 5.14: Uranium beam parameters for 29^+ charge state in segment 1. The other charge state (28^+) has similar values.

| | Input | Output |
|-------------------|-------|--------|
| Energy (MeV/u) | 0.29 | 11.40 |
| β_z (deg/%) | 12.9 | 26.48 |
| α_z | -0.68 | -0.65 |
| β_x (m) | 0.38 | 3.14 |
| α_x | -1.05 | 0.52 |
| β_y (m) | 0.38 | 3.14 |
| α_y | -1.05 | 0.52 |
| Q | 28–29 | 28–29 |
| A | 238 | 238 |

5.1.7.2 Accelerating segment 2

Segment 2 will be approximately 170 m long and will accelerate the uranium beam from 12 MeV/u to 110 MeV/u. The first seven cryomodules, each containing eight $\beta_{\text{opt}} = 0.16 \lambda/4$ cavities operating at 161 MHz, will be used to accelerate five charge states (71^+ to 75^+) of the uranium beam from 12 MeV/u to 25 MeV/u. The subsequent eleven cryomodules, each containing eight $\beta_{\text{opt}} = 0.285 \lambda/2$ cavities operating at 322 MHz, will be used to accelerate the beam from 25 MeV/u to 60 MeV/u.

A matching cryomodule with four $\beta_{\text{opt}} = 0.285 \lambda/2$ cavities at 322 MHz and two superconducting solenoidal magnets will provide six-dimensional matching at the transition point between the two frequencies. Finally, ten cryomodules, containing eight $\beta_{\text{opt}} = 0.425 \lambda/2$ cavities operating at 322 MHz, will be used to accelerate the beam from 60 MeV/u to 110 MeV/u. There are three superconducting solenoidal magnets in each cryomodule of segment 2 for transverse focusing.

Assuming no rf or alignment errors, the longitudinal emittance containing 99.5% of the particles of the uranium beam at the entrance of segment 2 is expected to be approximately $2.1 \pi \text{ keV/u ns}$. The longitudinal acceptance for this segment is $\sim 160 \pi \text{ keV/u ns}$, giving a comfortable acceptance to emittance ratio of ~ 75 . Figure 5.54 shows the longitudinal acceptance and the longitudinal and transverse phase advances as a function of distance along segment 2. No parametric resonances were expected or observed in the simulations. The transverse and longitudinal betatron functions for the uranium beam in segment 2 are shown in Figure 5.55, and the beam parameters on entering and exiting segment 2 are summarized in Table 5.15. The simulation results substantiate that the design will meet performance requirements.

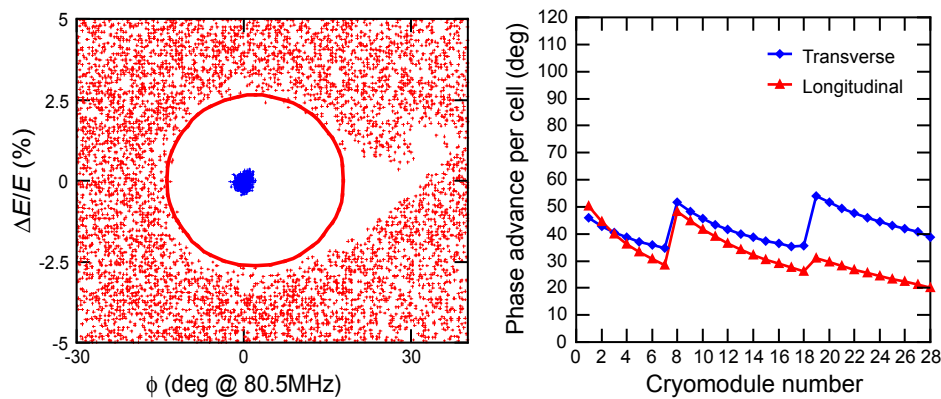


Figure 5.54: Left: longitudinal acceptance (area within red ellipse) of segment 2 together with the input uranium beam (blue). The full phase space displayed was populated with particles, and those particles that were lost are displayed as red dots. The acceptance to 99.5% emittance ratio is 75. Right: transverse and longitudinal phase advance for uranium beam along segment 2.

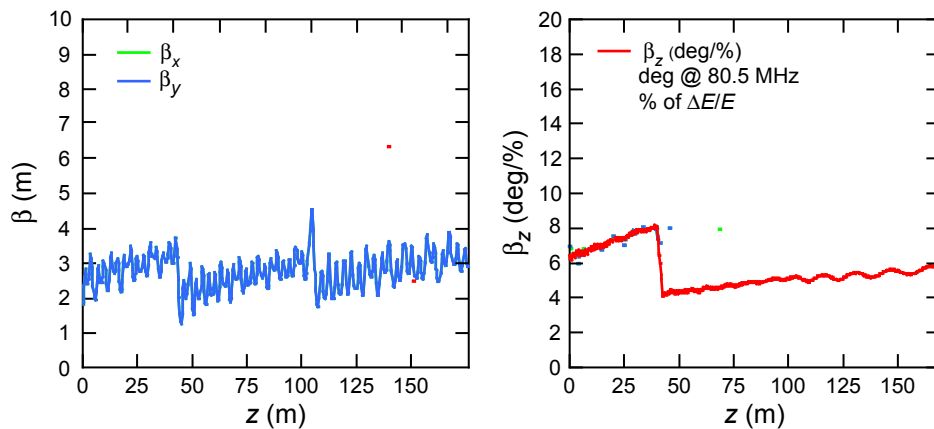


Figure 5.55: Transverse (left) and longitudinal (right) betatron functions in segment 2 for the uranium beam (73^+). The horizontal function (β_x – green) is not visible because it exactly follows the vertical function (β_y – blue) due to solenoidal focusing.

Table 5.15: Uranium beam parameters for 73^+ charge state in segment 2. The other charge states (71^+ , 72^+ , 74^+ , and 75^+) have similar values.

| | Input | Output |
|-------------------|-------|--------|
| Energy (MeV/u) | 11.18 | 111.92 |
| β_z (deg/%) | 6.07 | 5.69 |
| α_z | 0.05 | -0.08 |
| β_x (m) | 1.52 | 2.92 |
| α_x | -0.02 | 0.02 |
| β_y (m) | 1.52 | 2.92 |
| α_y | -0.02 | 0.02 |
| Q | 71–75 | 71–75 |
| A | 238 | 238 |

5.1.7.3 Accelerating segment 3

Segment 3 will be approximately 100 m long and will accelerate three charge states (88^+ to 90^+) of the uranium beam from 110 MeV/u to 200 MeV/u, using fifteen cryomodules each containing eight $\beta_{\text{opt}} = 0.425 \lambda/2$ cavities operating at 322 MHz. Each cryomodule of segment 3 contains three superconducting solenoidal magnets for transverse focusing. Assuming no rf or alignment errors, the longitudinal emittance containing 99.5% of the particles of the uranium beam at the entrance of segment 3 is expected to be approximately $10.2 \pi \text{ keV/u ns}$. The longitudinal acceptance for this segment is $\sim 520 \pi \text{ keV/u ns}$, giving a good acceptance-to-emittance ratio of ~ 50 . Figure 5.56 shows the overall longitudinal acceptance of segment 3 along with the uranium beam emittance, and the longitudinal and transverse phase advances along segment 3. As in segments 1 and 2, no parametric resonances were expected or observed in the simulations. The transverse and longitudinal betatron functions for the uranium beam in segment 3 are shown in Figure 5.57 and the beam parameters on entering and exiting segment 3 are summarized in Table 5.16. The simulation results substantiate that the design will meet performance requirements.

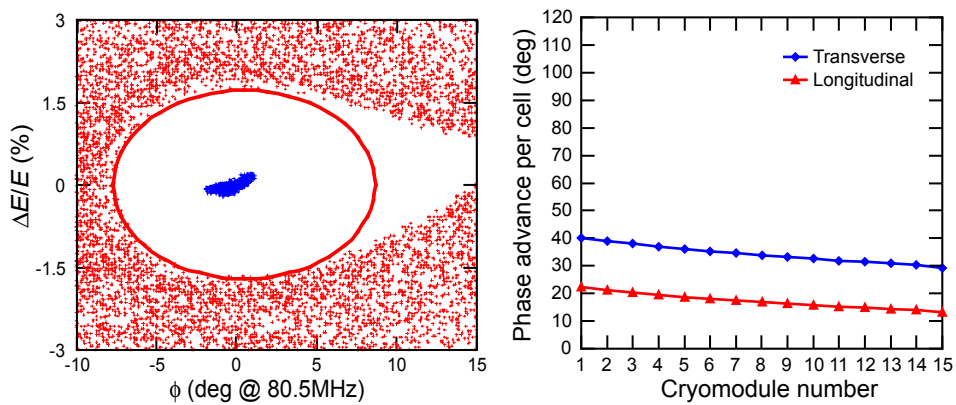


Figure 5.56: Left: longitudinal acceptance (area within red ellipse) of segment 3 together with the input uranium beam (blue). The full phase space displayed was populated with particles and those particles that were lost are displayed as red dots. The acceptance to 99.5% emittance ratio is 50. Right: transverse and longitudinal phase advance for uranium beam along segment 3.

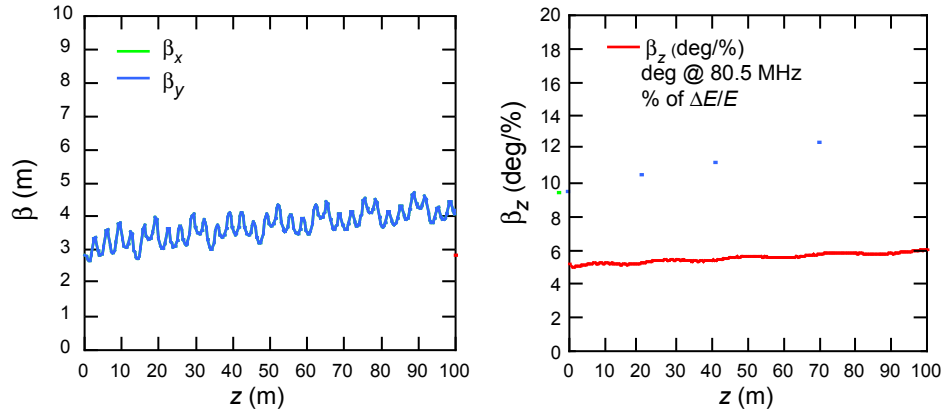


Figure 5.57: Transverse (left) and longitudinal (right) betatron functions in linac segment 3 for the uranium beam (89^+). The horizontal function (β_x – green) is not visible because it exactly follows the vertical function (β_y – blue) due to the solenoidal focusing.

Table 5.16: Uranium beam parameters for 89^+ charge state in linac segment 3. The other charge states (88^+ and 90^+) have similar values.

| | Input | Output |
|-------------------|--------|--------|
| Energy (MeV/u) | 108.83 | 200.00 |
| β_z (deg/%) | 5.02 | 5.98 |
| α_z | 0.01 | -0.03 |
| β_x (m) | 2.67 | 4.07 |
| α_x | 0.00 | -0.02 |
| β_y (m) | 2.67 | 4.07 |
| α_y | 0.00 | -0.02 |
| Q | 88–90 | 88–90 |
| A | 238 | 238 |

5.1.8 Linac stripping sections and beam switchyard

Two stripping sections will be used to increase the charge states of the stable isotope beams to provide more cost-efficient acceleration. A beam switchyard will be used to transport the beam from the exit of segment 3 to the production target. All of these sections are designed to transport heavy ion beams in several neighboring charge states simultaneously with minimal degradation of the emittance. The following sections present the basic parameters for the uranium beam for stripping section 1, stripping section 2, and the beam switchyard. The charge-stripping model used in the beam simulations is discussed in Section 5.1.8.4.

5.1.8.1 Stripping section 1

Stripping section 1 will transport and match the beam from the driver linac segment 1 into segment 2. In addition, this section will have a system to strip electrons from the beam to increase the charge state and to select the appropriate charge states for injection into segment 2. Figure 5.58 shows the layout of stripping section 1. The lattice has three distinct functional areas. First, the beam is transported

from the exit of the linac segment 1 to the stripper system. Second, the charge states to be accelerated are selected after the stripper system. Third, the beam is matched transversely and longitudinally into segment 2 of the driver linac.

The first segment of stripping section 1 will consist of a dog-leg (a bend angle configuration of $-\alpha, 2\alpha, -\alpha$) achromatic magnetic chicane that shifts the beam axis by 5 cm. This eliminates a line of sight path from the stripping foil back to the superconducting cavities of segment 1 and reduces the possibility of physical contamination of the cavities by stripper foil effluents. Four quadrupole magnets will be used to match the transverse phase space of the beam onto the stripping foil. The transverse phase space at the stripping target was chosen to mitigate the growth of the transverse emittance caused by multiple scattering, energy straggling, and foil thickness variation. The model described in Section 5.1.8.4 for modification of the beam phase space by the stripping foil is used in the beam dynamics simulations. A small transverse beam size and a short longitudinal bunch length are necessary to limit the emittance growth in the stripper foil. However, a small transverse beam size also leads to high beam power density on the stripper foil. The present design provides for a ~ 3 mm beam diameter and a $\sim 5^\circ$ total rf phase width on the stripper, leading to acceptable transverse and longitudinal emittance growth.

The second segment of stripping section 1 will be an achromat with a 185° bend angle. This will provide horizontal separation between the different charge states

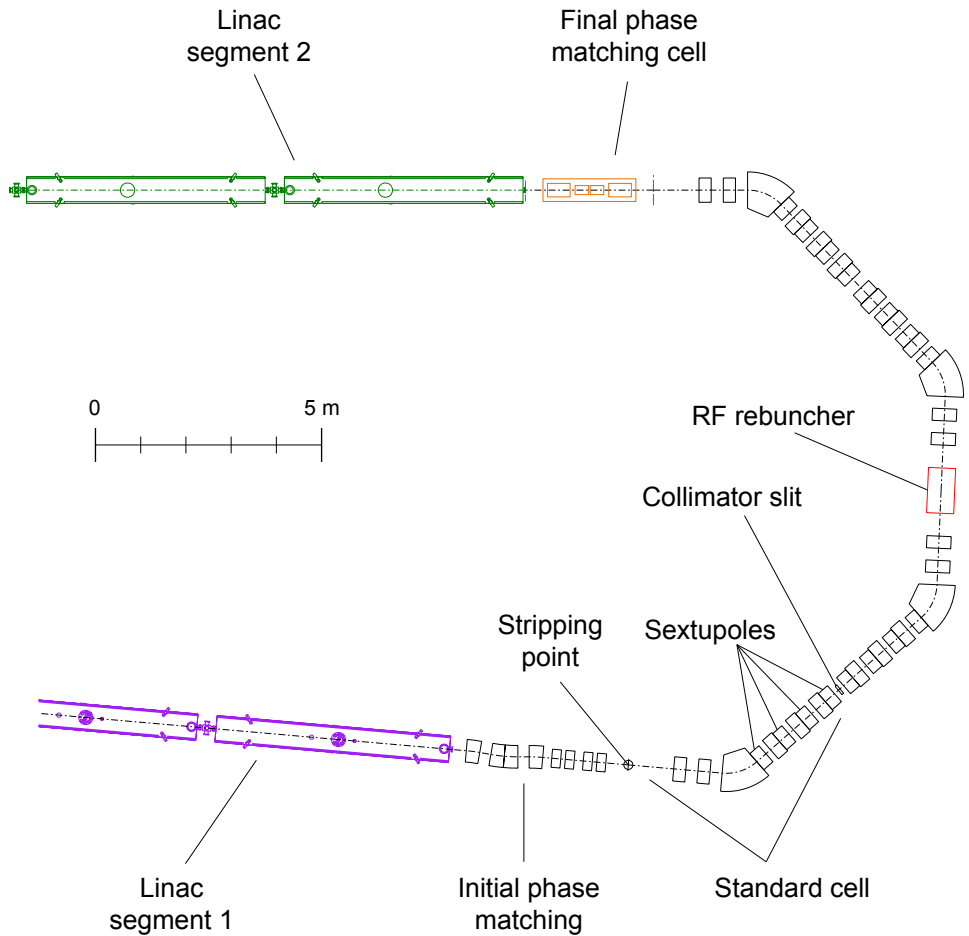


Figure 5.58: Schematic layout of stripping section 1.

emerging from the stripper foil, allowing charge-state selection and beam collimation at a given location while maintaining a reasonable longitudinal bunch length and limited transverse and longitudinal emittance growth. For uranium, the beam energy after the first charge-stripping foil will be 11.2 MeV/u, with a magnetic rigidity of 1.6 Tm; five charge states, 71^+ to 75^+ , will be retained and transported to segment 2 of the driver linac for further acceleration.

The 185° achromat will be composed of four identical standard cells (see Figure 5.58) mirror-reflected at each position in sequence, providing four-fold symmetry. Each cell will use a dipole magnet with a bending angle of 46.25° and five quadrupole magnets to achieve the first-order optical conditions for a second-order achromat. One cryomodule with two $\beta_{\text{opt}} = 0.085 \lambda/4$ cavities operating at 80.5 MHz will be used for rebunching in the middle of the achromat.

Due to the symmetry of the system, second-order geometric aberrations are completely cancelled. To preserve the transverse emittances, second-order chromatic aberrations will be cancelled by four sextupole magnets in each of the four cells of the bending achromat. Perturbations of the beam from third- and higher-order aberrations were found to be very small in the simulations and had no significant impact on the beam dynamics.

Charge-state selection occurs at the point with the maximum dispersion in the first cell of the achromat. The different charge states of the beam will be dispersed horizontally and selected by an aperture. For example, it will be possible to select five charge states for the uranium beam. As shown in Figure 5.59, the

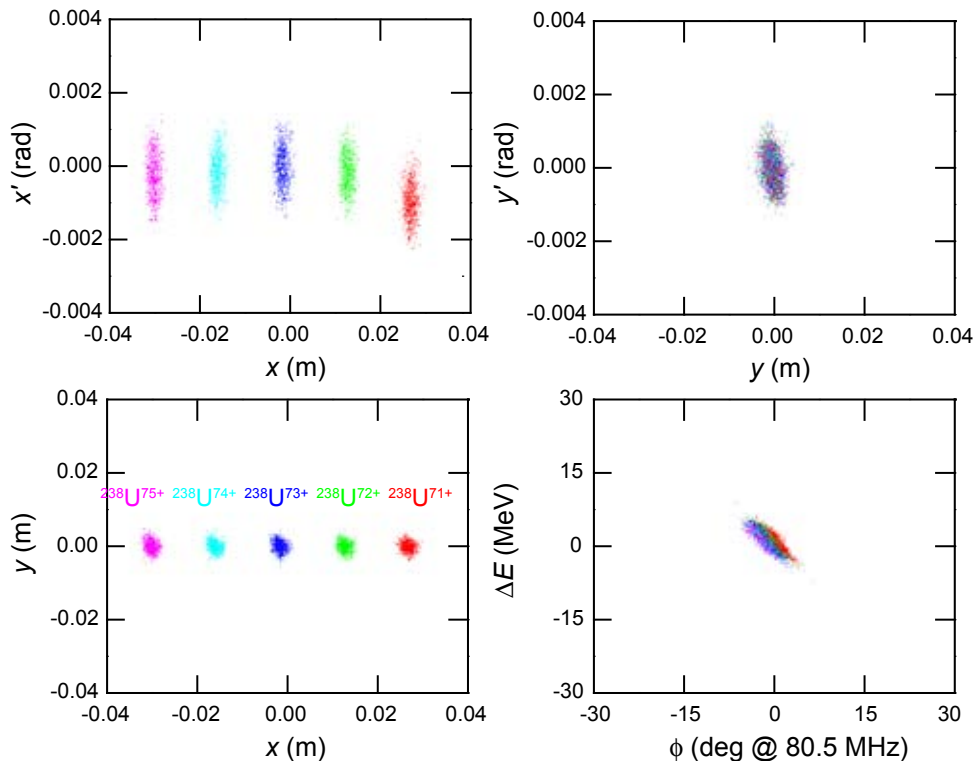


Figure 5.59: Beam phase space for five adjacent charge states (different colors) of a uranium beam at the charge-state selection location in stripping section 1. The plots show the horizontal (top left), vertical (top right), and longitudinal (bottom right) phase space distributions as well as the xy plane (bottom left).

average separation between charge states (15 mm) will be adequate for proper beam collimation.

The 185° section is not designed to be an isopath system. Therefore, the longitudinal phase space rotation will be different for different charge states. In addition, longitudinal focusing from the rebuncher is also slightly different for each charge state. Both effects will result in a small longitudinal emittance growth for multi-charge-state beams. Six-dimensional particle tracking studies with high statistics were performed with the IMPACT code [Qia04], which showed that both the transverse and longitudinal emittance growth were acceptably small. Details on the emittance growth are given in Section 5.1.9.3.

The third and final segment of stripping section 1 will be used to match the beam phase space into segment 2 of the driver linac. The matching cell uses a single cryomodule with two solenoidal magnets and two $\beta_{\text{opt}} = 0.16 \lambda/4$ cavities operated at 161 MHz. The transverse and longitudinal betatron functions for stripping section 1 are shown in Figure 5.60, and the input and output parameters for a uranium beam are listed in Table 5.17.

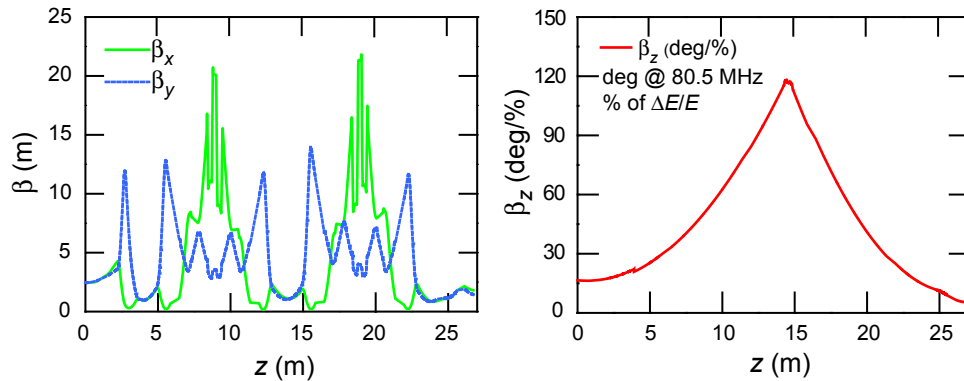


Figure 5.60: Transverse (left) and longitudinal (right) betatron functions of the uranium beam (73^+) in stripping section 1.

Table 5.17: Uranium beam parameters in stripping section 1. The input charge states are 28^+ to 29^+ . The output charge states are 71^+ to 75^+ . The beam parameters for an input beam of 29^+ and an output beam of 73^+ are given.

| | Input | Output |
|-------------------|-------|--------|
| Energy (MeV/u) | 11.40 | 11.18 |
| β_z (deg/%) | 15.31 | 6.72 |
| α_z | -0.05 | 0.07 |
| β_x (m) | 2.60 | 1.52 |
| α_x | 0.04 | -0.02 |
| β_y (m) | 2.60 | 1.52 |
| α_y | 0.04 | -0.02 |
| Q | 29 | 73 |
| A | 238 | 238 |

5.1.8.2 Stripping section 2

Stripping section 2 is very similar to stripping section 1. It will transport and match the beam from the driver linac segment 2 into segment 3. It will also provide electron stripping to further increase the charge state of the heaviest ion beams and select the appropriate charge states for injection into linac segment 3. Figure 5.61 shows the layout of stripping section 2. As in stripping section 1, the three distinct functions are performed in three segments. The first segment will transport the beam from the end of linac segment 2 to the second stripper system. The second segment will select the charge states and provide longitudinal phase space control. The last segment will match the beam into the driver linac segment 3.

For the uranium beam, three charge states (88^+ to 90^+) are retained and transported into segment 3 of the driver linac for further acceleration. The achromat has four standard cells with a total of 20 quadrupoles for a 180° bend. The maximum magnetic rigidity will be 4.2 Tm corresponding to a ~ 110 MeV/u 89^+ uranium beam. Stripping section 2 will have a reverse -10° dipole paired with each $+55^\circ$ dipole to achieve isochronous conditions for all charge states and thus will

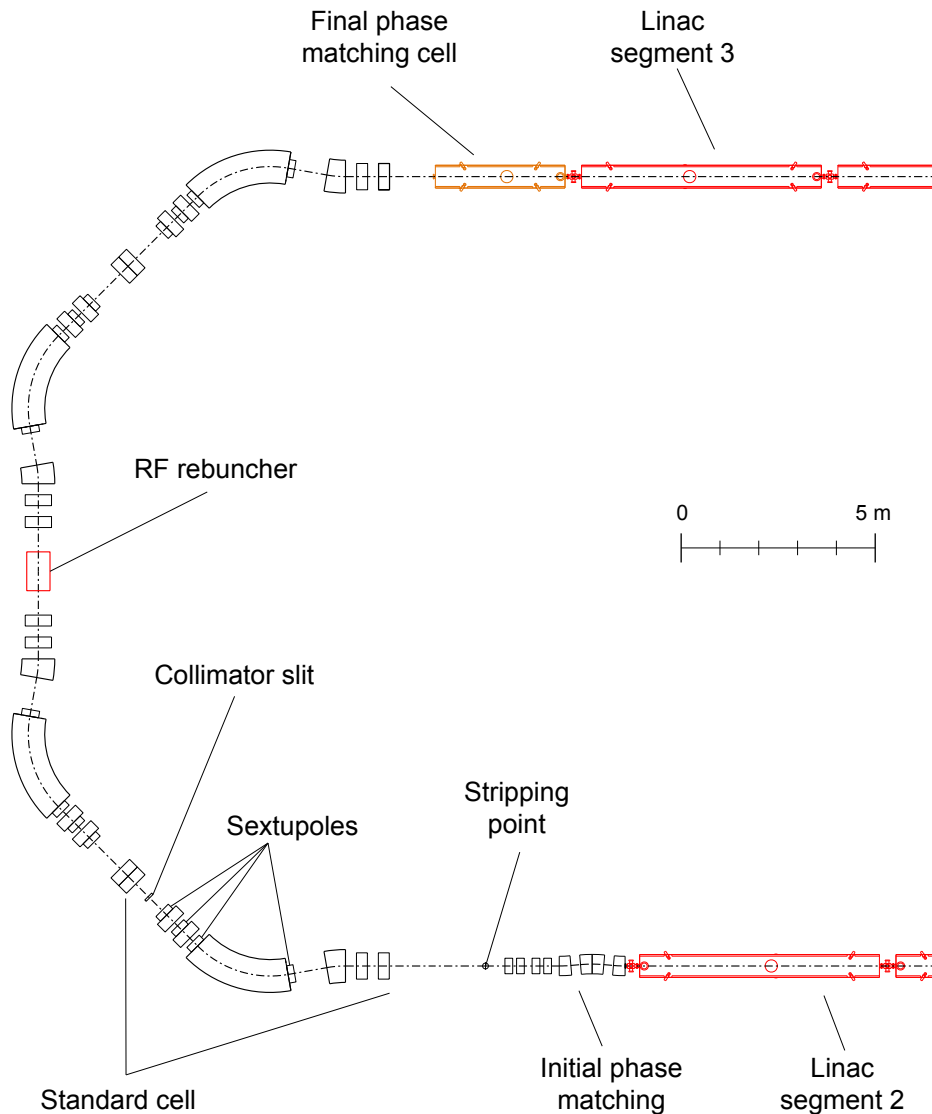


Figure 5.61: Schematic layout of stripping section 2.

avoid significant longitudinal emittance growth. Also, a cryomodule with four $\beta_{\text{opt}} = 0.425, \lambda/2$ cavities operated at 322 MHz will be used for rebunching in the middle of the achromat.

The last section of stripping section 2 is a matching cell. It will use a single cryomodule with four superconducting solenoidal magnets and one $\beta_{\text{opt}} = 0.425, \lambda/2$ cavity operating at 322 MHz. The transverse and longitudinal lattice functions of stripping section 2 are shown in Figure 5.62. The input and output parameters for a uranium beam are listed in Table 5.18.

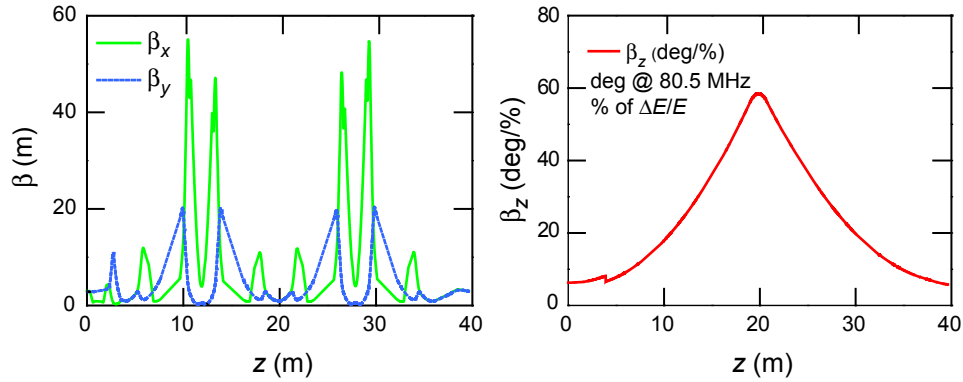


Figure 5.62: Transverse (left) and longitudinal (right) betatron functions of the uranium beam (89^+) in stripping section 2.

Table 5.18: Uranium beam parameters in stripping section 2. The input charge states are 71^+ to 75^+ . The output charge states are 88^+ to 90^+ . The beam parameters for an input beam of 73^+ and an output beam of 89^+ are given.

| | Input | Output |
|-------------------|--------|--------|
| Energy (MeV/u) | 111.92 | 108.83 |
| β_z (deg/%) | 5.69 | 5.02 |
| α_z | -0.08 | 0.01 |
| β_x (m) | 2.92 | 2.67 |
| α_x | 0.02 | 0.00 |
| β_y (m) | 2.92 | 2.67 |
| α_y | 0.02 | 0.00 |
| Q | 73 | 89 |
| A | 238 | 238 |

5.1.8.3 Beam switchyard

The initial facility will have one fragment separation target station with the option to add an ISOL target station in the future. Beam transport to the optional ISOL target is included in the discussion of optional upgrades (see Section 6).

The efficient delivery of multiple charge states of heavy ion beams to the fragment target is required along with a small beam size of ~ 1 mm diameter on target. To accommodate the multiple charge states and to achieve the required beam conditions

on target, the bending sections must satisfy second-order achromatic conditions, and sextupole magnets will be needed to limit the second-order chromatic aberrations. The beam switchyard design starts with output beam parameters from the superconducting linac for uranium listed in Table 5.19 and the beam phase space distributions shown in Figure 5.63.

Table 5.19: Output parameters for the uranium beam from the driver linac.

| Parameter | Value |
|--|---|
| Beam energy (MeV/u) | 200 |
| Charge states | 88 ⁺ , 89 ⁺ , 90 ⁺ |
| Magnetic rigidity (Tm) | 5.73 |
| Bunch frequency (MHz) | 80.5 |
| (99.5%) Transverse emittance (π mm mrad) | 1.5 |
| (99.5%) Longitudinal emittance (π keV/u ns) | 17.7 |

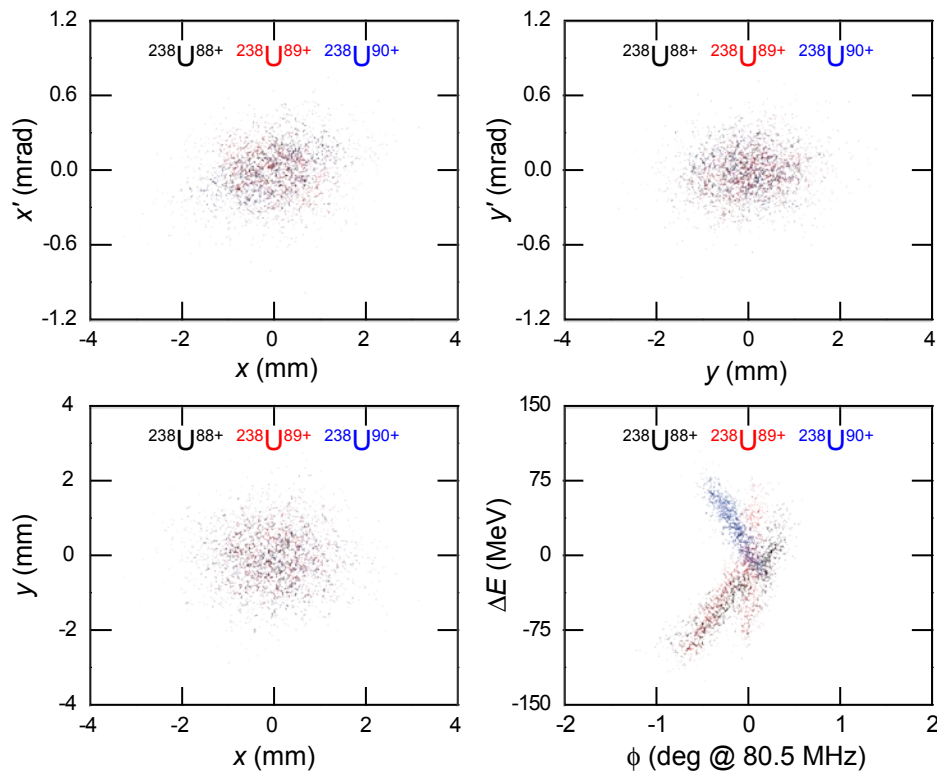


Figure 5.63: Beam phase space for three charge states (red, blue, and black) of the uranium beam at the exit of the driver linac. The horizontal (top left), vertical (top right), and longitudinal (bottom right) phase space are shown as well as the xy plane (bottom left).

Figure 5.64 shows the schematic layout of the beam switchyard. To reach the in-flight production target, the beam from the driver linac must go through an initial transverse focusing and phase matching section consisting of four quadrupole magnets. A vertical second-order achromat will then bend and shift the beamline about ~ 7 m up from driver linac tunnel level to ground level while limiting the

transverse emittance growth. After passing through two focusing cells each with a π phase advance, the beam will be focused on the in-flight production target by the final focusing section, which will consist of four quadrupole magnets and a solenoidal magnet. A separation of ~ 4 m will be needed between the last focusing element and the target for radiation shielding, as indicated in Figure 5.64.

The beam's transverse betatron functions and the corresponding beam envelope are shown in Figure 5.65.

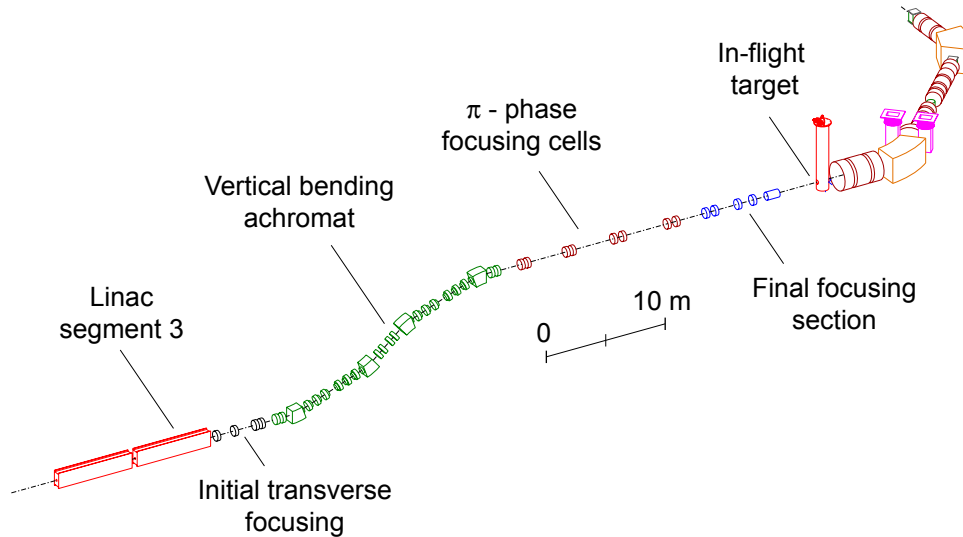


Figure 5.64: Schematic layout of the beam switchyard.

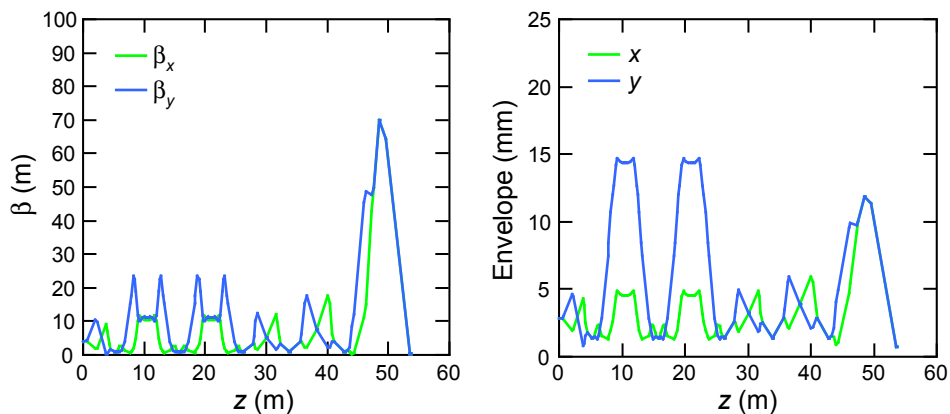


Figure 5.65: Betatron functions (left) and beam envelope (right) for uranium beam (89^+) in the beam switchyard.

The beam transport was evaluated by particle tracking using the IMPACT code with input beam distributions from driver linac simulations (Figure 5.63). The results indicate that the proposed beam switchyard meets all of the design requirements. The standard deviation of the beam transverse distributions on target are $\sigma \sim 0.25$ mm, which will be adequate to maintain a high acceptance in the downstream fragment separator. The transverse and longitudinal phase spaces on target are shown in Figure 5.66, and the corresponding beam distributions on target are shown in Figure 5.67.

The magnetic rigidity of the high energy beam will be approximately 5.73 Tm. Superconducting bending magnets will be required with a maximum magnetic pole tip field of ~1.9 T.

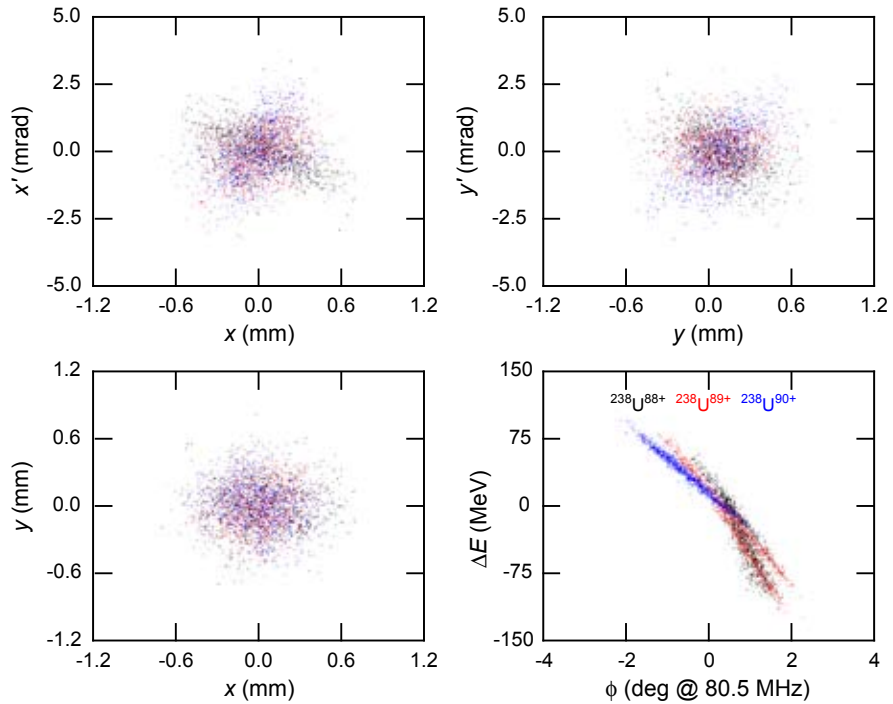


Figure 5.66: Phase space diagram of three charge states (blue, red, and black) of the uranium beam at the fragmentation target. The horizontal (top left), vertical (top right), and longitudinal (bottom right) phase space as well as the xy plane (bottom left) are shown.

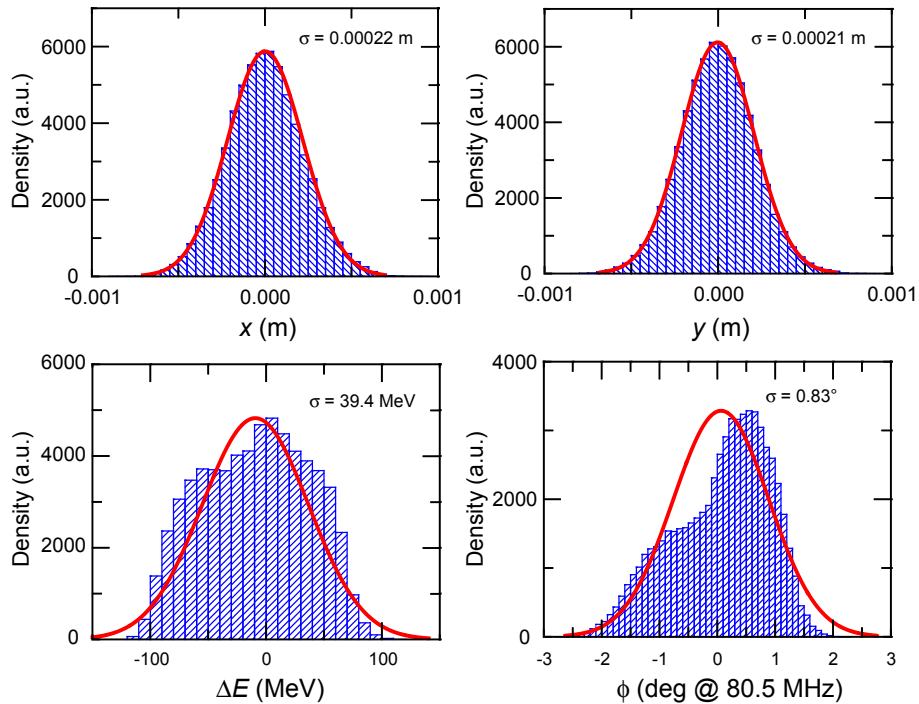


Figure 5.67: Horizontal (top left), vertical (top right), energy (bottom left), and phase (bottom right) distribution for uranium beam (with three charge states) at the fragmentation target. The σ values correspond to the Gaussian fit shown in red. The ordinate density is given in arbitrary units (a.u.).

5.1.8.4 Model for the charge stripping foils

The passage through thin foils is commonly used in heavy-ion linacs to increase the average beam charge state of the ions and minimize the required accelerating voltage. The low and intermediate energy ions are generally spread among several charge states after they travel through the stripping foil. Hence, the acceleration of multiple, adjacent charge states after the stripping foil is necessary to avoid a significant reduction in beam power. For this reason, each accelerating segment and stripping section of the driver linac was designed to have transverse and longitudinal acceptances that are large enough to accelerate multiple charge states while keeping uncontrolled beam power losses below 1 W/m.

To estimate the emittance growth by a heavy-ion beam in a stripper foil, a model was developed based on simulation results from the Monte Carlo energy-loss code SRIM [Zie04]. The SRIM code includes elastic and inelastic scattering as well as energy loss from ionization. The model was implemented in the beam tracking codes LANA [Gor96] and IMPACT [Qia04], so that each particle's charge state and phase space coordinates could be accurately transformed when the beam passes through a stripping foil.

The charge-state transformation is based on Baron's formula [Bar79]. For example, when a uranium beam at 9–12 MeV/u strikes a carbon foil of equilibrium thickness (as in Beam stripping section 1), 78% of the emerging particles will be in charge states between 71⁺ and 75⁺. In the beam dynamics codes, only these main charge states are tracked downstream of the stripping foil. The selected and tracked charge states for some of the typical stable ion beams are listed in Table 5.20.

Table 5.20: Charge-state selection for some stable ion beams in the driver linac (E_{in} denotes input energy, E_{out} denotes output energy, Q_{out} denotes output charge states used, Transmission eff denotes transmission efficiency). The second stripper is not used for light ions (see Table 5.1).

| Beam | Ion | O | Ar | Kr | Xe | U |
|--------------------------|-------------------|------|------|-------|-------|-------|
| | Z | 8 | 18 | 36 | 54 | 92 |
| | A | 18 | 40 | 86 | 136 | 238 |
| | Q | 6 | 8 | 14 | 18 | 28-29 |
| 1 st stripper | E_{in} (MeV/u) | 15.1 | 12.8 | 12.1 | 11.6 | 11.3 |
| | E_{out} (MeV/u) | 14.9 | 12.6 | 11.9 | 11.4 | 11.2 |
| | Q_{out} | 8 | 18 | 32-34 | 46-49 | 71-75 |
| | Transmission eff. | 100% | 100% | 89% | 80% | 78% |
| 2 nd stripper | E_{in} (MeV/u) | — | — | — | 129.1 | 113.5 |
| | E_{out} (MeV/u) | — | — | — | 123.9 | 108.9 |
| | Q_{out} | — | — | — | 53-54 | 88-90 |
| | Transmission eff. | — | — | — | 100% | 99% |

Since the foils are extremely thin, only the particles' momenta change while their spatial coordinates remain unchanged. Achieving small transverse and longitudinal beam sizes at the foils can mitigate transverse and longitudinal beam emittance growth due to the strippers.

The phase space coordinate transformation was performed using an analytical probability density function at each stripper foil. The analytical form of this function was determined empirically and its parameters were obtained by fitting the SRIM numerical results. For a single particle penetrating a stripping foil, we assumed a form given by the expression

$$f(\theta, E) = (\theta/\theta_N) \exp[-(\theta/\theta_1)^u] \exp\left[-\frac{1}{2}\left\{\frac{(E-E_0(\theta))}{E_1}\right\}^2\right] \quad (5-8)$$

and the angular dependence of the energy straggling was modeled as

$$E_0(\theta) = \varepsilon_0 + \varepsilon_1 \left(1 - \exp[-(\theta/\theta_2)^2]\right) \quad (5-9)$$

where θ is the multiple scattering angle; E is the particle's energy after the stripper; θ_N is a normalization constant; and u , θ_1 , θ_2 , E_1 , ε_0 and ε_1 are empirical parameters. All these parameters were numerically fit to the results of SRIM simulations for each beam. The SRIM code was run for a few discrete values of incoming beam energies and foil thicknesses, and the parameters were linearly interpolated when necessary. The same set of parameters was used for all charge states of a beam. Although the details of the stripper system design appropriate for high power have not been defined, we have assumed carbon stripper foils in this simulation. Table 5.21 lists the parameters used in the SRIM simulations for the two carbon stripping foils in the driver linac.

Table 5.21: Main parameters used in the SRIM simulations for the stripping foils.

| Parameter | Stripper | |
|---|-----------------|-----------------|
| | 1 st | 2 nd |
| Reference carbon foil thickness (μm) | 1.78 | 64.35 |
| Maximum foil thickness variation (%) | ± 5 | ± 5 |
| Reference beam energy (MeV/u) | 12 | 90 |

The empirical parameters were estimated using a bilinear interpolation formula. For a given parameter p , the interpolation is of the form

$$p = p_0 + p_1 \Delta E + p_2 \Delta t \quad (5-10)$$

where p_0 is the value of the parameter p at the reference energy and foil thickness in the SRIM simulations, p_1 and p_2 are the coefficients of the bilinear function with respect to the variation in energy ΔE and variation in foil thickness Δt obtained by fitting to SRIM data. Table 5.22 and Table 5.23 list the values of p_0 , p_1 , and p_2 for each of the parameters for the case of the uranium beam on the first and second stripper, respectively.

Figure 5.68 and Figure 5.69 show the probability density distributions for a single particle going through the first and second stripping foil, respectively. The distribution of particles emerging from the foil as a function of the output angle and output energy is shown for three cases: the nominal foil thicknesses (1.78 μm or 64.35 μm) and for +5% and -5% thickness variation.

Table 5.22: Parameters for the empirical model of the first stripper for a uranium beam.

| | | Coefficients of bilinear functions | | |
|------------|-----------------|------------------------------------|-------------------------------|--------------------------------------|
| | | p_0 | p_1 | p_2 |
| Parameters | θ_1 | 0.42 mrad | -0.040 mrad/(MeV/u) | 0.17 mrad/ μm |
| | θ_2 | 59 mrad | 0.0 mrad/(MeV/u) | 0.0 mrad/ μm |
| | u | 1.5 | -0.0088 (MeV/u) ⁻¹ | 0.10 (μm) ⁻¹ |
| | E_1 | 2.3 keV/u | 1.2×10^{-5} | 0.7 (keV/u)/ μm |
| | ε_0 | 12 MeV/u | 1.0 | -0.12 (MeV/u)/ μm |
| | ε_1 | 0.79 MeV/u | 0.0 | 0.0 (MeV/u)/ μm |

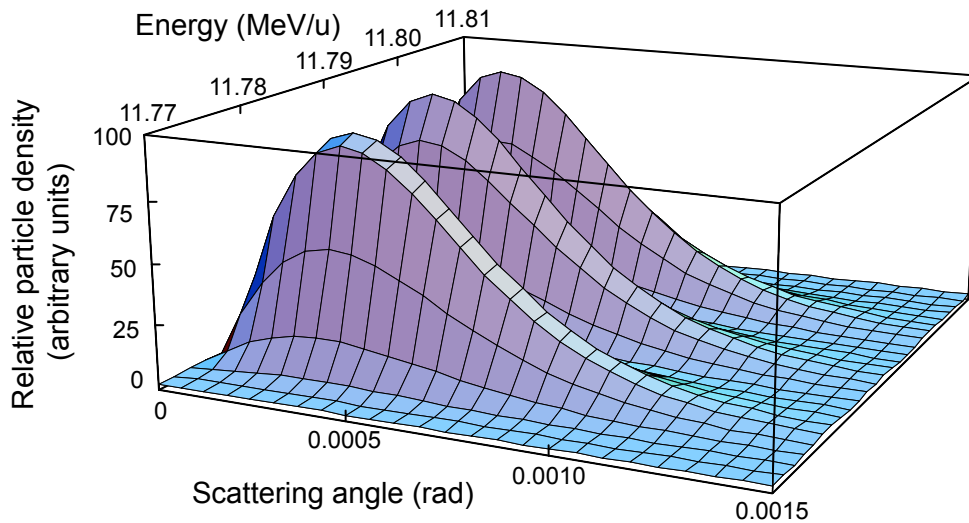


Figure 5.68: The probability density functions for a uranium beam on the first stripper foil are shown as a function of scattering angle θ and output beam energy. The middle distribution is for the nominal foil thickness; the two others are for foils with a +5% and -5% thickness variation from nominal.

Table 5.23: Parameters for the empirical model of the second stripper for a uranium beam.

| | | Coefficients of bilinear functions | | |
|------------|--------------|------------------------------------|-------------------------------|--|
| | | P_0 | P_1 | P_2 |
| Parameters | θ_1 | 0.48 mrad | -0.0071 mrad/(MeV/u) | 0.0042 mrad/ μm |
| | θ_2 | 45 mrad | 0.0 mrad/(MeV/u) | 0.0 mrad/ μm |
| | u | 1.7 | -0.0010 (MeV/u) ⁻¹ | 0.0011 (μm) ⁻¹ |
| | E_1 | 17 keV/u | 4.0×10^{-5} | 0.18 (keV/u)/ μm |
| | ϵ_0 | 87 MeV/u | 1.0 | -0.048 (MeV/u)/ μm |
| | ϵ_1 | 3.1 MeV/u | 0.0 | 0.0 (MeV/u)/ μm |

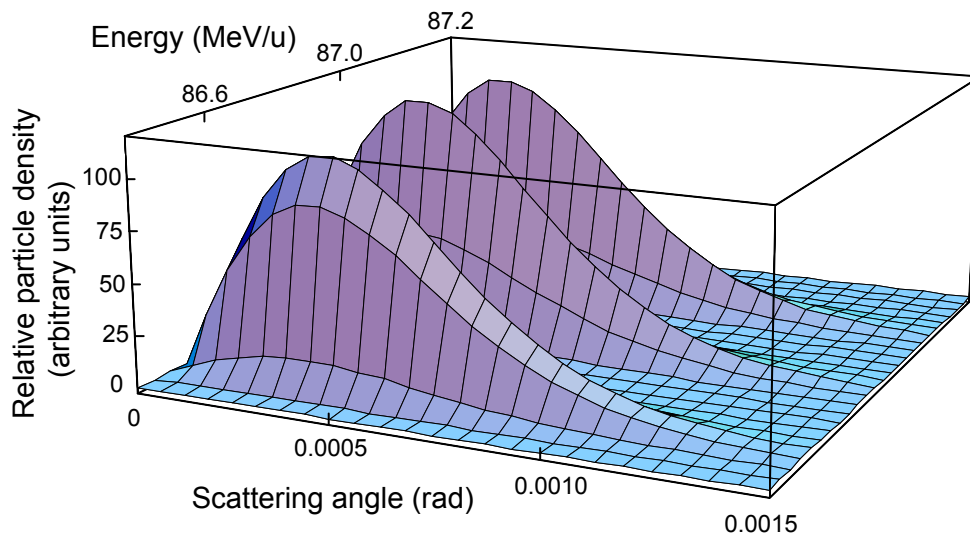


Figure 5.69: The probability density functions for a uranium beam on the second stripper foil is shown as a function of scattering angle θ and output beam energy. The middle distribution is for the nominal foil thickness; the two others are for foils with a +5% and -5% thickness variation from nominal.

5.1.9 End-to-end beam simulations

5.1.9.1 RF errors

The effects of dynamic rf errors (fluctuations of the cavity field amplitude and phase) on the beam transport were evaluated. An example source of rf error is microphonic excitation which perturbs the resonant frequency of the superconducting cavities [Gri04]. The rf errors have a significant impact on the beam dynamics but can be mitigated by the low level rf control system [Cha03] or by other compensation schemes [Mav03,Kan04]. When dynamic rf errors are present, the phase space area occupied by the ensemble of consecutive bunches increases, resulting in an effective emittance growth. The simulations indicate that the rf errors will have a negligible direct impact on the transverse emittance. No beam correction scheme is readily available to actively correct for dynamic rf errors, so the only way to limit the longitudinal emittance growth is to limit the amplitude of the rf errors.

As mentioned above, the low β cavities have the most severe problems with microphonics, due to their small accelerating gaps and large transverse dimensions. The design of the $\beta_{\text{opt}} = 0.041 \lambda/4$ cavity operated at 80.5 MHz used in linac segment 1 is based on an 80 MHz cavity operating in the superconducting heavy ion linac at INFN-Legnaro [Fac98]. This linac demonstrated that the maximum measured rf error can be as low as 0.2° for cw operation [Fac04]. Operational experience at the Spallation Neutron Source (SNS) [Ma06] showed that, even for superconducting cavities operated in a pulsed mode with strong Lorentz force detuning [Dol03], the rf errors could be controlled to be below $\pm 0.5^\circ$ in phase and $\pm 0.5\%$ in amplitude. Using these results, the rf tolerances for the superconducting cavities were set to $\pm 0.5^\circ$ in phase and $\pm 0.5\%$ in amplitude, as listed in Table 5.24. In the simulations, these errors were assumed to be uncorrelated and have a flat distribution.

Table 5.24: Tolerances for the rf errors in superconducting cavities of the driver linac.

| RF error tolerances | |
|----------------------------------|-----------------|
| Maximum rf phase fluctuation | $\pm 0.5^\circ$ |
| Maximum rf amplitude fluctuation | $\pm 0.5\%$ |

Longitudinal emittance growth produced by the rf errors listed in Table 5.24 was found to be acceptable in simulations of all three segments of the driver linac. The largest relative increase in longitudinal emittance will occur in segment 1, where the acceptance to emittance ratio is the smallest. But even for the most challenging case of a multiple charge states of a uranium beam, the results of simulations in segment 1 show that the emittance will remain well within the longitudinal acceptance of segment 2.

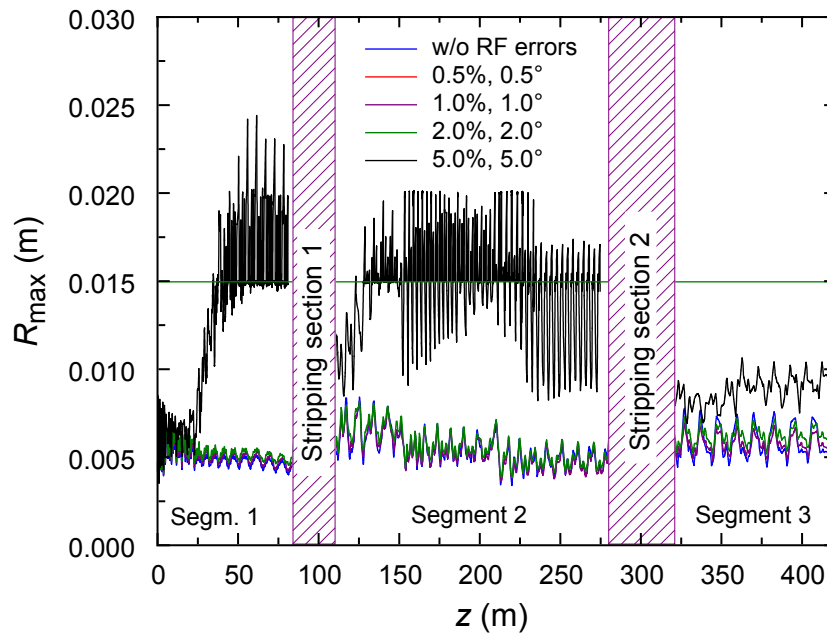


Figure 5.70: Maximum transverse beam envelope of the multiple charge states of uranium for different rf amplitude and phase errors in the driver linac. The maximum transverse aperture (0.015 m) is shown as a green line. Transverse beam losses are not observed until the rf error values reach $\pm 5\%$ in amplitude and $\pm 5^\circ$ in phase. The reduction in beam envelope after both stripping sections is due to collimation within the sections.

As a test of the sensitivity of the system, simulations were performed with larger rf errors in all segments. As illustrated in Figure 5.70, the results from these simulations indicate that transverse beam loss will only occur when rf errors reach $\pm 5^\circ$ in phase and $\pm 5\%$ in amplitude, an order of magnitude higher than the baseline tolerances listed in Table 5.24. These results demonstrate that the longitudinal acceptance of the driver linac will be more than adequate.

5.1.9.2 Alignment errors and correction scheme

The impacts of misalignment of the focusing elements and superconducting cavities as well as a correction scheme for the central orbit were investigated for all three accelerating segments of the driver linac. The steering effects from the misalignment of the superconducting solenoids are much larger than those due to misalignment of the superconducting cavities because of the strong transverse focusing provided by the solenoidal magnets compared to the weak transverse defocusing caused by the cavities. Nevertheless, misalignments of the cavities are also detrimental, since these elements have the smallest apertures. The required values for misalignment tolerances were investigated for each segment. The goal of these studies was to ensure that the beam envelope remained below $\sim 2/3$ of the available aperture after the central orbit correction was applied.

As indicated above, the first two cryomodules of segment 1 will each contain ten $\beta_{\text{opt}} = 0.041 \lambda/4$ cavities and six superconducting solenoidal magnets while the last thirteen cryomodules will each contain eight $\beta_{\text{opt}} = 0.085 \lambda/4$ cavities and five superconducting solenoidal magnets, as shown in Figure 5.71. The cavities in segment 1 will have an aperture diameter of 30 mm. Thus, the beam envelope should be no larger than 10 mm with errors in segment 1. The maximum beam size without errors in segment 1 will be about 5 mm. Therefore, a maximum central orbit distortion of ± 5 mm after alignment correction was set as the limit in segment 1. Similar reasoning was applied for segments 2 and 3.

Each superconducting solenoidal magnet has dipole windings to provide horizontal and vertical deflection of the central orbit. The beam position will be measured by Beam Position Monitors (BPMs) located in warm regions between the cryomodules to avoid the complexity and additional cold mass associated with placing BPMs inside cryomodules.

All of the cavities and focusing elements were misaligned as part of the error analysis simulations. The random alignment errors were assumed for each element with a Gaussian distribution truncated at $\pm 2\sigma$. For each set of alignment errors, the DIMAD code [Ser85] was used to minimize the central orbit deviations at the specified BPM locations using the available correcting elements and a least-squares minimization method. The alignment correction procedure starts with only the first pair of solenoidal magnets and correction coils turned on. The DIMAD code is used to find the settings of the correction coils that minimize the sum of the squares of the beam displacements in the two downstream BPMs. All of the superconducting cavities and focusing solenoidal magnets downstream from these two corrector magnets are turned off to allow the beam to drift within the cryomodules to the BPMs. Once the first pair of correction coils inside the first pair of solenoidal magnets is set, the same procedure is applied to all of the consecutive solenoid/corrector pairs in the segment, as illustrated in Figure 5.71. For example, the central orbit of the beam in segment 1 of the driver linac before

and after correction is shown in Figure 5.72. In this case, the maximum distortions of the central orbit before correction were ~ 32 mm (horizontal) and ~ 21 mm (vertical) and below 5 mm in both planes after correction.

The error analysis for segment 1 indicates that a maximum misalignment of 2 mm for both the solenoidal magnets and the cavities is tolerable. To obtain a statistical sampling of possible error distributions, simulations were performed for multiple random seeds. The beam envelopes along segment 1 for fifty random seeds are shown in Figure 5.73. The central beam orbit correction procedure was applied to correct the beam position for each of the random seeds. The margin between the beam envelope and the aperture indicates that the misalignment tolerances are appropriate and that segment 1 of the driver linac will have an adequate transverse acceptance.

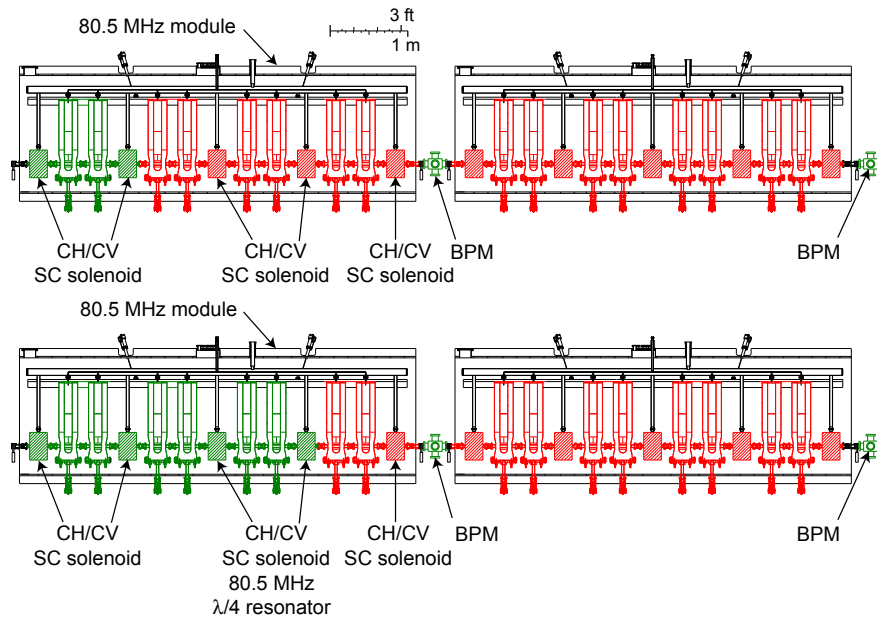


Figure 5.71: Schematic example of the central orbit correction procedure in segment 1 of the driver linac. Elements in green are turned on and elements in red are turned off. The horizontal and vertical correction coils are labeled CH and CV, respectively. Top: In the first iteration, only the first two solenoidal magnets and correction coils are on. Settings for these correctors are found to minimize the beam displacement in the two downstream Beam Position Monitors (BPMs). Bottom: In the second iteration, the procedure is repeated for the next two solenoidal magnets and correction coils. The procedure is continued for all the downstream elements.

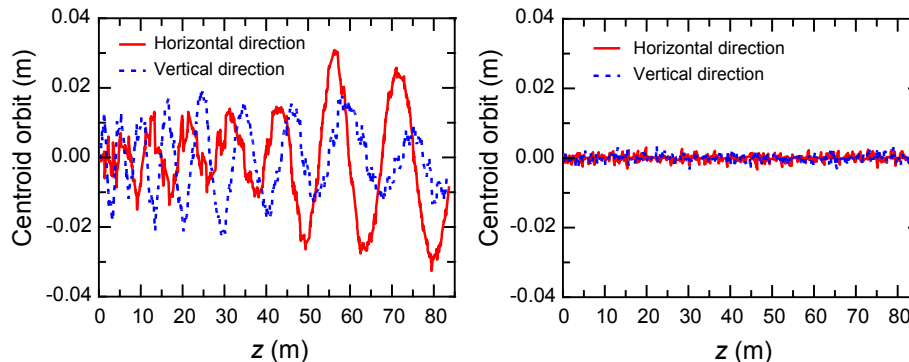


Figure 5.72: Central orbit distortion in segment 1 for a single set of random errors, before (left) and after (right) applying the correction procedure.

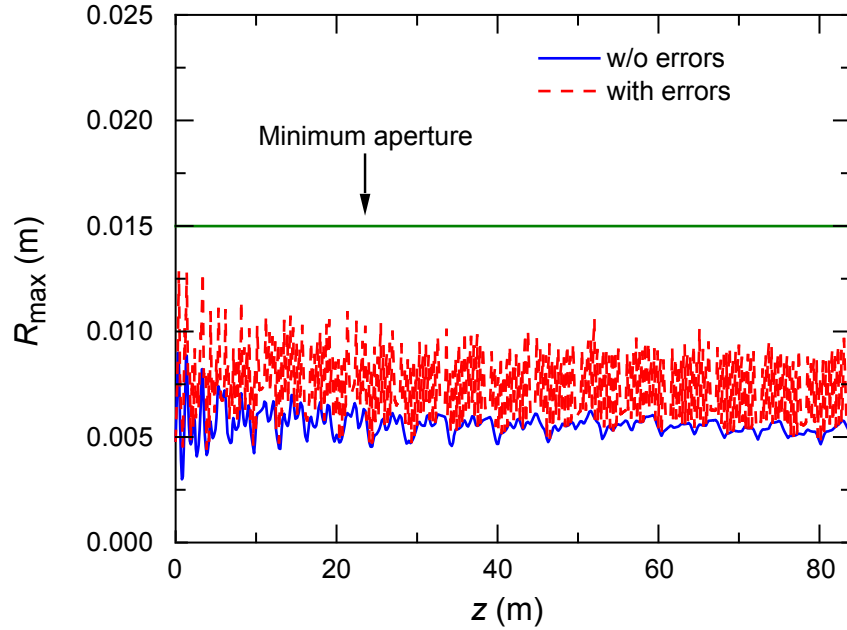


Figure 5.73: The full beam envelope without alignment errors (solid blue line) and with fifty sets of random alignment errors and central orbit corrections (dashed red lines) along segment 1.

Similar misalignment analyses were performed for segments 2 and 3 of the driver linac. Since all three segments use similar solenoidal focusing elements, the same central orbit correction procedure was applied to all segments. The results indicate that the misalignment tolerances for segment 1 will be adequate for segments 2 and 3. Misalignment tolerances for all cavities and solenoidal magnets are listed in Table 5.25.

Table 5.25: Misalignment tolerances for all solenoids and accelerating cavities of the driver linac.

| Element | Misalignment tolerances | |
|----------|-------------------------|--------------------|
| | $\sigma_{x,y}$ (mm) | Maximum value (mm) |
| Cavity | 1.0 | ± 2.0 |
| Solenoid | 1.0 | ± 2.0 |

The results of the error analysis for segments 2 and 3 are shown in Figure 5.74 for beam envelopes without alignment errors and with misalignment plus central orbit corrections. The margin between the beam envelope and the apertures indicates that both segments will have adequate transverse acceptances and that the misalignment tolerances are appropriate in both cases.

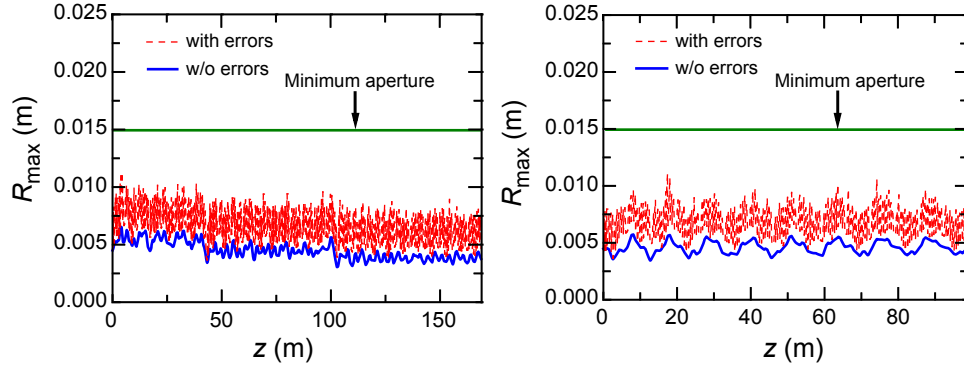


Figure 5.74: Beam envelope without alignment errors (solid blue line) and with alignment errors and corrections (dashed red lines) along segment 2 (left) and segment 3 (right) of the driver linac.

5.1.9.3 End-to-end beam simulations with and without errors

The most challenging beam for the driver linac is the uranium beam with its multiple charge states. Therefore, results for end-to-end beam dynamics will be presented for this beam. Due to the acceleration of multiple charge states and the effects of the stripping foils, both the transverse emittance and the longitudinal emittance increase as the beam propagates through the driver linac, even when no errors are included in the simulations. The normalized 99.5% transverse and longitudinal emittances of the uranium beam at injection into the driver linac are about 0.8π mm mrad and 1.1π keV/u ns, respectively.

To limit the emittance growth in the linac, particular attention was paid to keep the longitudinal acceptance as large as possible so that the beam would only experience the linear field region. As a result, the normalized 99.5% transverse and longitudinal emittances at the exit of the driver linac, will be approximately 1.5π mm mrad and 17.1π keV/u ns, respectively. The corresponding rms emittances are about ten times smaller. Table 5.26 shows the evolution of transverse and longitudinal emittances for the uranium beam in the linac without alignment and rf errors.

To estimate the performance of the linac under more realistic conditions, simulations were performed with physical misalignments, dynamic rf amplitude and phase errors, and variations in the stripping foil thickness. The maximum transverse displacements were assumed to be ± 2 mm for the solenoidal magnets and ± 2 mm for the superconducting cavities. The correction of the beam centroid after misalignment was performed using beam position monitors between cryomodules and dipole windings in the solenoidal magnets as discussed above. The rf phase and amplitude errors for the accelerating cavities were set to $\pm 0.5^\circ$ and $\pm 0.5\%$ throughout the linac. These alignment and rf error tolerances are reasonable and have been achieved at other facilities. Stripper foil thickness variations at the level of $\pm 5\%$ were also included. To achieve thickness variations at this level may be difficult, and further studies to determine the maximum acceptable thickness variation will be done. Table 5.27 shows the evolution of the transverse and longitudinal emittances for the uranium beam with alignment errors, rf errors, and foil thickness variations.

Table 5.26: Emittances of the multi-charge-state uranium beam along the driver linac without errors.

| | | Emittances with no errors | | | | | |
|----------|---------------------|---------------------------|-------|-------------------------|-------|--------------------------|-------|
| | | Horizontal | | Vertical | | Longitudinal | |
| | | $(\pi \text{ mm mrad})$ | | $(\pi \text{ mm mrad})$ | | $(\pi \text{ keV/u ns})$ | |
| | | rms | 99.5% | rms | 99.5% | rms | 99.5% |
| Input to | Front end | 0.08 | 0.72 | 0.08 | 0.74 | — | — |
| | Linac segment 1 | 0.09 | 0.76 | 0.07 | 0.81 | 0.08 | 1.1 |
| | Stripping section 1 | 0.08 | 0.79 | 0.08 | 0.71 | 0.09 | 1.3 |
| | Linac segment 2 | 0.09 | 0.95 | 0.1 | 0.98 | 0.18 | 2.1 |
| | Stripping section 2 | 0.09 | 0.92 | 0.11 | 1.14 | 0.55 | 5.6 |
| | Linac segment 3 | 0.11 | 1.23 | 0.12 | 1.45 | 1.04 | 10.2 |
| | Beam switchyard | 0.12 | 1.51 | 0.11 | 1.29 | 1.66 | 17.1 |

Table 5.27: Emittances of the multi-charge-state uranium beam along the driver linac with alignment errors, rf errors, and foil thickness variations.

| | | Emittances with errors | | | | | |
|----------|---------------------|-------------------------|-------|-------------------------|-------|--------------------------|-------|
| | | Horizontal | | Vertical | | Longitudinal | |
| | | $(\pi \text{ mm mrad})$ | | $(\pi \text{ mm mrad})$ | | $(\pi \text{ keV/u ns})$ | |
| | | rms | 99.5% | rms | 99.5% | rms | 99.5% |
| Input to | Front end | 0.08 | 0.72 | 0.08 | 0.74 | — | — |
| | Linac segment 1 | 0.09 | 0.76 | 0.07 | 0.81 | 0.08 | 1.12 |
| | Stripping section 1 | 0.08 | 0.79 | 0.08 | 0.81 | 0.18 | 2.89 |
| | Linac segment 2 | 0.09 | 0.95 | 0.10 | 1.00 | 0.46 | 3.75 |
| | Stripping section 2 | 0.09 | 1.00 | 0.11 | 1.18 | 1.58 | 10.80 |
| | Linac segment 3 | 0.12 | 1.34 | 0.12 | 1.47 | 2.28 | 17.60 |
| | Beam switchyard | 0.13 | 1.58 | 0.12 | 1.39 | 3.31 | 34.43 |

Table 5.28 lists the resultant emittance growth factors in the linac, and Figure 5.75 and Figure 5.76 show the evolution of the uranium beam emittances along the linac. The increase in the horizontal emittance at the charge-stripping sections apparent in Figure 5.75 is an artifact of the horizontal separation between different charge states due to the dispersion needed for charge state selection.

The end-to-end beam simulations indicate that the driver linac will have adequate transverse and longitudinal acceptances, even for acceleration of the multiple charge states of the uranium beam. The longitudinal acceptance of segment 1 of the driver linac is $8 \pi \text{ keV/u ns}$, whereas the beam emittance from the front end is $1.1 \pi \text{ keV/u ns}$, giving an acceptance-to-emittance ratio of ~ 7.3 . The longitudinal acceptance and emittance values and ratios for segments 2 and 3 with and without errors are listed in Table 5.29. As can be seen, the acceptance to emittance ratios are even larger for the downstream segments.

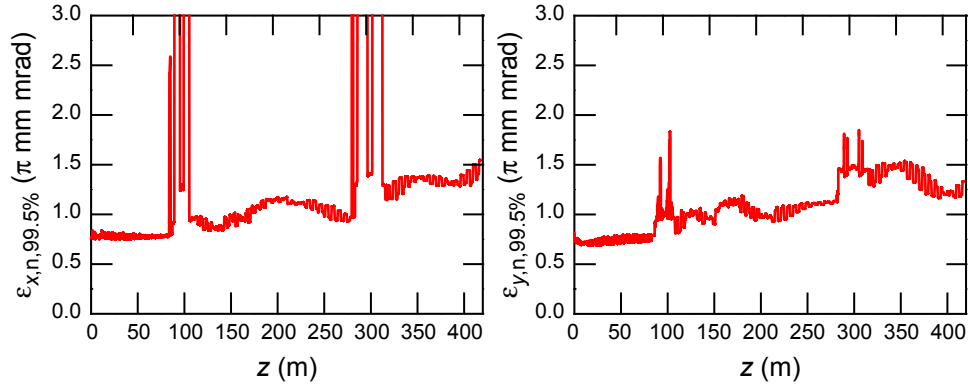


Figure 5.75: Horizontal (left) and vertical (right) emittances along the driver linac for uranium beam with rf errors. Alignment errors and central orbit correction were not included in the simulations, but there was a 12% emittance increase in both planes for a similar lattice [Wu04].

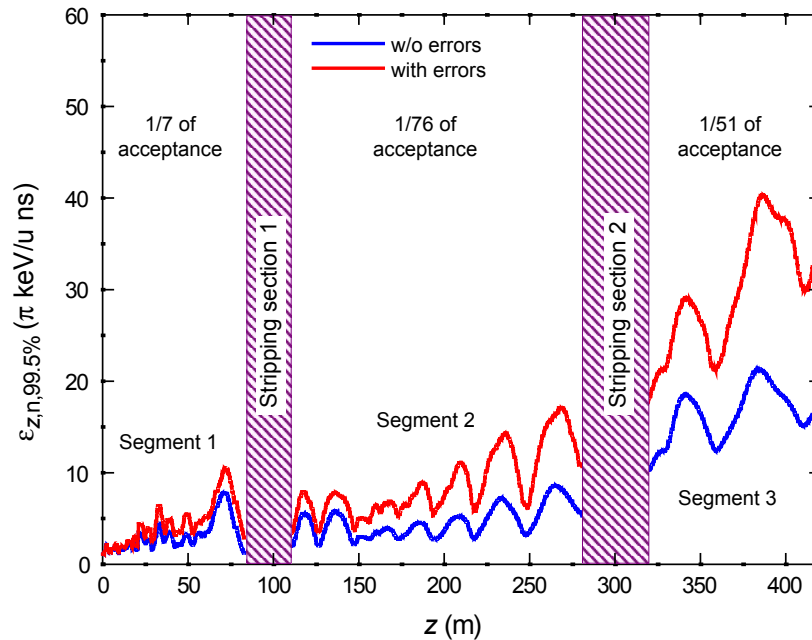


Figure 5.76: Longitudinal emittance along the driver linac for uranium beam with (red) and without (blue) rf errors. Alignment errors and central orbit correction were not included in the simulations, but their impact on the longitudinal emittance was found negligible for a similar lattice [Wu04]. The ratio of longitudinal emittance to acceptance is given for each of the three linac segments for the case without errors.

Table 5-28: Growth of the 99.5% emittances for the multi-charge-state uranium beam in the driver linac.

| | Transverse emittance (π mm mrad) | | Longitudinal emittance (π keV/u ns) | | Transverse emittance growth factor | Longitudinal emittance growth factor |
|----------------|----------------------------------|--------|-------------------------------------|--------|------------------------------------|--------------------------------------|
| | Starting | Ending | Starting | Ending | | |
| Without errors | 0.8 | 1.4 | 1.1 | 17.1 | 1.75 | 15.5 |
| With errors | 0.8 | 1.5 | 1.1 | 34.4 | 1.88 | 31.3 |

Table 5.29: The longitudinal acceptance and 99.5% emittance of the uranium beam at the entrance to each segment of the driver linac.

| | Longitudinal acceptance (π keV/u ns) | Longitudinal beam emittances (π keV/u ns) | | Acceptance to emittance ratio | |
|-----------|---|--|-------------|-------------------------------|-------------|
| | | Without errors | With errors | Without errors | With errors |
| Segment 1 | 8 | 1.1 | 1.1 | 7.3 | 7.3 |
| Segment 2 | 160 | 2.1 | 3.75 | 76.2 | 42.7 |
| Segment 3 | 520 | 10.2 | 17.6 | 51.0 | 29.5 |

Figure 5.77 shows the evolution of the beam envelope through the linac with and without errors, along with the value of the minimum aperture. In all three segments, the minimum aperture is the superconducting cavity diameter of 30 mm. The transverse aperture-to-beam envelope ratios for all three segments of the driver linac are listed in Table 5.30.

The simulation results presented above show that the driver linac will provide good overall performance even for the challenging case of the uranium beam with multiple charge states. The error tolerances were explored in the simulations and were found to be reasonable and have been achieved at other facilities. The emittance growth when all these errors are included was found to be tolerable and remains well within the linac acceptance. The beam envelopes fit adequately within the transverse aperture and no uncontrolled beam loss was observed.

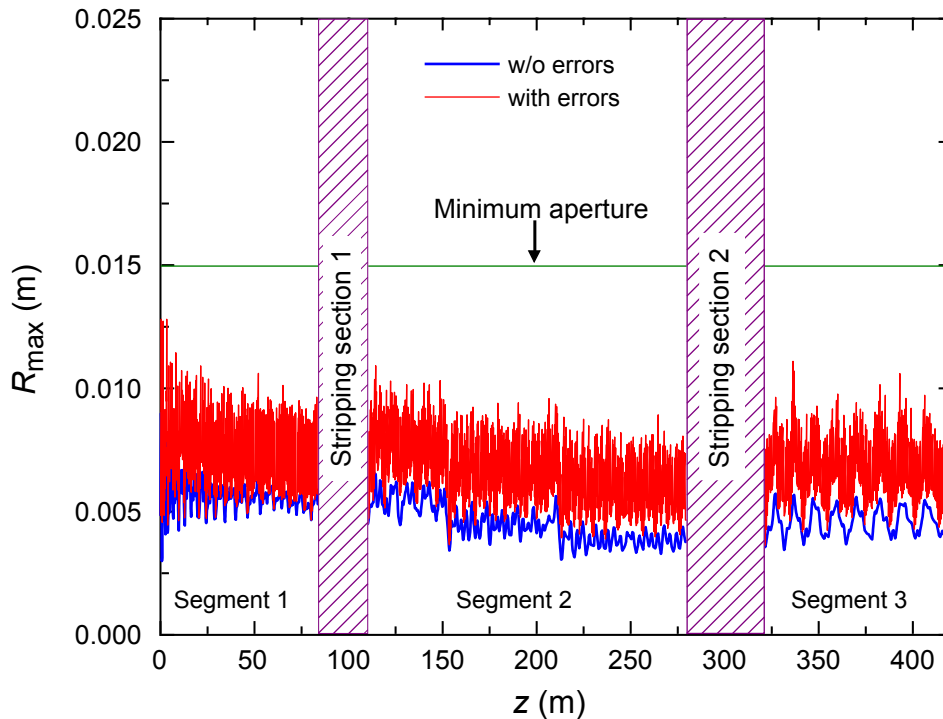


Figure 5.77: Beam envelopes for a multi-charge-state uranium beam without (blue) and with (red) errors along the driver linac. The minimum linac aperture is also indicated.

Table 5.30: Beam envelopes for a multi-charge-state uranium beam in the driver linac.

| | Maximum beam envelope (mm) | | Aperture to beam envelope ratio | |
|-----------|----------------------------|-------------|---------------------------------|-------------|
| | Without errors | With errors | Without errors | With errors |
| Segment 1 | 9.0 | 12.8 | 1.7 | 1.2 |
| Segment 2 | 6.6 | 11.0 | 2.3 | 1.4 |
| Segment 3 | 5.7 | 11.1 | 2.6 | 1.4 |

5.1.10 Beam diagnostics

A high power accelerator requires careful integration of the beam diagnostics system into the accelerating lattice to achieve and maintain the desired performance. The uncontrolled beam loss tolerance for the driver linac is ≤ 1 W/m, similar to the value for the SNS, in order to allow “hands-on” maintenance [Hol04]. As a consequence, the accelerator design must be robust, having acceptances many times larger than the rms emittances. In addition, the beam diagnostics must provide adequate and efficient beam parameter measurements for beam tuning (see [Pel05a,Blo05] for examples). Beam diagnostics are also important to detect and remediate suboptimal accelerator performance [Ale06,Plu06].

Effective operation of the driver linac has several challenges, including controlling and monitoring hundreds of kW of beam power, charge-state selection at the two stripping sections, and longitudinal matching across two frequency transitions [Wu05]. Because these challenges are substantial, we have incorporated beam diagnostics into the lattice design. A basic list of diagnostic elements and their locations was established, and distances between components of the accelerating lattice were chosen not only to satisfy the beam dynamics and engineering considerations mentioned above but also to accommodate the diagnostic elements.

As an example, the schematic layout of the proposed beam diagnostic elements along segment 1 of the driver linac is shown in Figure 5.78. Beam loss monitors will be positioned after every accelerating cryomodule to detect beam loss while the beam is tuned [Pop06]. Beam current monitors will be located at both ends of the segment to continuously monitor the overall beam transmission. Emittance scanners at both ends of the segment will be used to ensure proper beam matching at the entrance of the segment and to assess beam brightness through the segment during low power tuning. To control the beam centroid and envelope, beam position and profile monitors will be placed after each cryomodule.

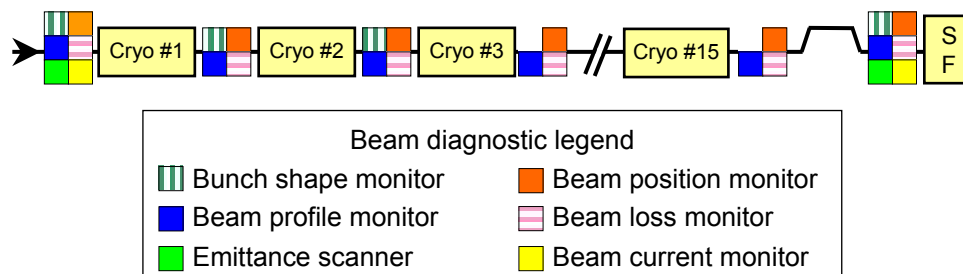


Figure 5.78: Beam diagnostic elements and positions along segment 1 of the driver linac (SF denotes stripping foil).

Three bunch shape monitors [Fes04] will be located early in the segment to provide bunch length measurements at three separate locations. The three-beam-widths emittance measurement technique [Cra97] can be applied with these monitors to determine the beam’s longitudinal Twiss parameters. Using a similar approach, good longitudinal matching of the beam can be achieved at the entrance of the segment; recent operational experience at the SNS indicates that this is an effective method for longitudinal matching [Ale06,Ass06].

Additional beam profile and bunch shape monitors will be used at the end of the segment to monitor the transverse and longitudinal beam size at the stripping foil. Knowing the beam size at this location is critical to minimizing the emittance growth in the stripper.

An approach similar to that described above for segment 1 was applied to determine the diagnostic elements for the other parts of the accelerator complex. For example, the diagnostics for stripping section 1 are shown in Figure 5.79.

The identification of the necessary diagnostic elements was performed during the design stage of the accelerating lattice so that the proposed layout of the accelerator incorporates necessary diagnostic elements. Nevertheless, detailed beam dynamics studies using adequate models for the diagnostic elements (e.g., realistic accuracies) in various scenarios (e.g., basic tuning of the machine or rematching in case of failing components) are needed to develop the final plan.

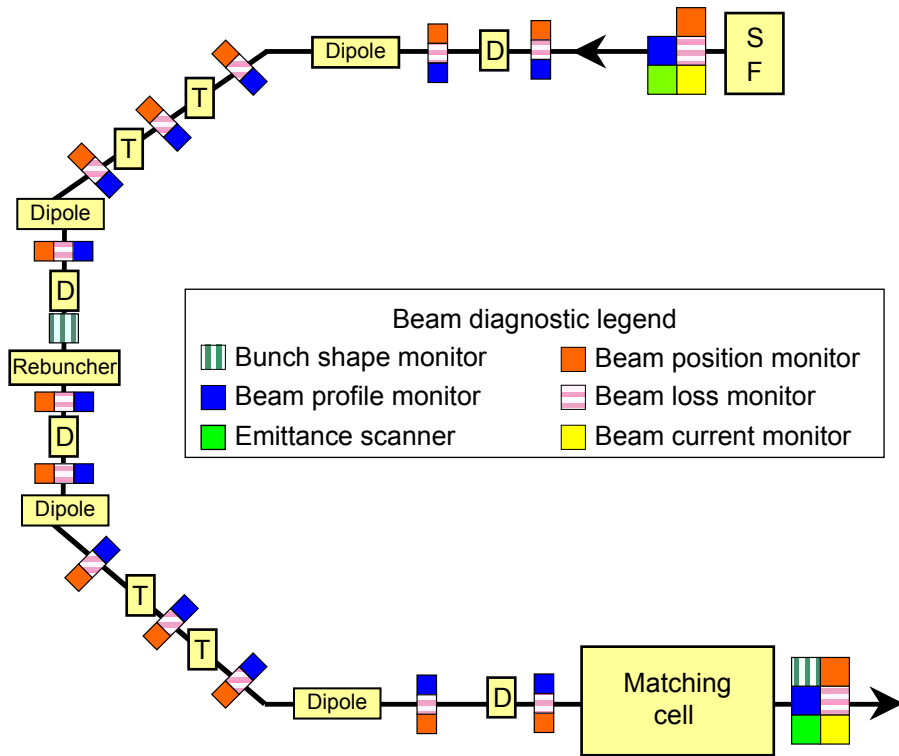


Figure 5.79: Beam diagnostic elements and positions along stripping section 1 of the driver linac (SF = stripping foil, T = quadrupole triplet, D = quadrupole doublet).

5.2 Reaccelerator linac

The reaccelerator linac will be used to accelerate rare isotope beams produced at high energies that, prior to reacceleration, must be thermalized and rapidly collected. The reaccelerator will have to deliver beams with variable energies, 0.5–12 MeV/u, with good beam quality and brightness, and with minimum beam losses to preserve the available beam intensities. The production, ionization, and utilization of the reaccelerated beams is discussed in Section 5.5.4.

The schematic layout of the reaccelerator is shown in Figure 5.80. The rare isotope beam from the in-flight fragmentation and separator system will be brought to rest in a cyclotron stopper and extracted with an RFQ ion guide (see Section 5.5.2).

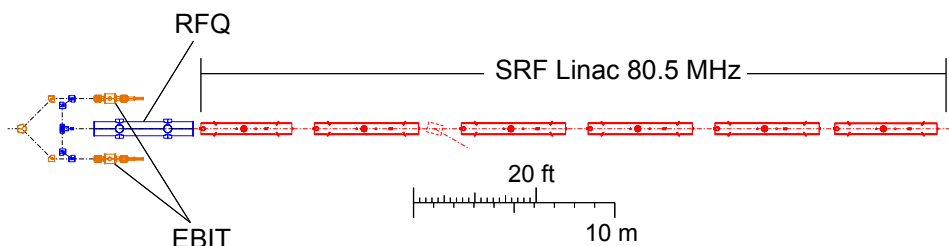


Figure 5.80: Layout of the reaccelerator.

The beam will be transported to an EBIT (see Section 5.5.4.3) charge breeder and then transferred into a radio frequency quadrupole (RFQ) for bunching and acceleration to 0.293 MeV/u. The beam will then be further accelerated in a superconducting linac to a final energy between 0.5 and 12 MeV/u. The final energy will be selected by adjusting the amplitude and phase of the accelerating voltages in the superconducting cavities. There will be a low-energy extraction point for beams with energies less than 3 MeV/u for nuclear astrophysical studies, and a full-energy extraction point at the end of the linac.

The reaccelerator is designed to accept beams from the EBIT with a charge to mass ratio, Q/A , of approximately 1/4. Beams with similar Q/A values have been studied during the light-ion simulations of the driver linac (e.g., oxygen). Since the EBIT will provide smaller longitudinal and transverse emittances than an ECR ion source, the RFQ simulations for the driver linac (see Section 5.1.1.4) will be applicable for the reaccelerator.

After the EBIT removes the majority of the electrons from a rare isotope ($^{240}\text{U}^{64+}$, for example), the ions will be extracted and accelerated to 12 keV/u by an electrostatic potential. The beam will be injected into an 80.5 MHz RFQ for bunching and acceleration to ~ 0.3 MeV/u.

The bunched rare isotope beam from the RFQ will be injected into the superconducting linac. This section of the reaccelerator provides the bulk of the acceleration using the same 80.5 MHz $\lambda/4$ cavity cryomodules as the driver linac. Such a redundancy in the design minimizes the technical risks for the driver and the reaccelerator linacs.

Figure 5.81 shows the transit time and energy gain as a function of β for uranium in the reaccelerator. Table 5.31 shows the number of cavities, superconducting

solenoidal magnets, and cryomodules required to accelerate a rare uranium isotope beam to 12 MeV/u. The magnets are NbTi solenoids with a 40 mm aperture. The number and type of focusing elements, and the number of cavities per cryomodule are based on the same beam dynamics considerations as for the driver linac (see Section 5.1.7).

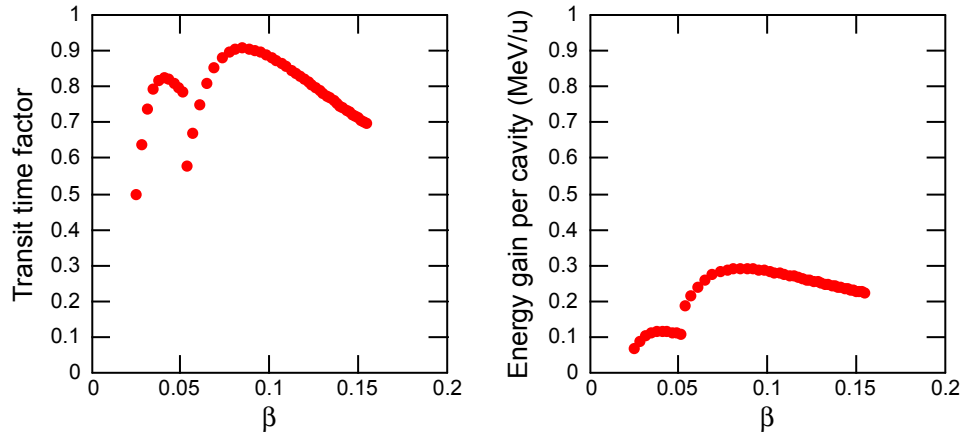


Figure 5.81: Transit time factor and energy gain for $Q/A = 0.25$ in the reaccelerator.

Table 5.31: Cavity and cryomodule count for acceleration of a rare isotope $Q/A = 0.25$ beam to 12 MeV/u in the reaccelerator.

| Type | $\lambda/4$ | $\lambda/4$ |
|---|-------------|-------------|
| β_{opt} | 0.041 | 0.085 |
| Number of cavities | 10 | 40 |
| Magnet length (cm) | 10 | 20 |
| Number of magnets | 6 | 25 |
| Number of accelerating cryomodules | 1 | 5 |
| Accelerating cryomodule slot length (m) | 4.97 | 5.80 |

5.3 RF systems and cryogenics

5.3.1 Low-level rf

A preliminary Low Level Radio Frequency (LLRF) system that can satisfy the requirements of $\pm 0.5\%$ in amplitude and $\pm 0.5^\circ$ in phase has already been built and tested at MSU. The system also provides active microphonic suppression to increase operating efficiency and improve stability. The system uses a digital LLRF controller developed at LBNL for the SNS [Doo03] to regulate the rf amplitude and phase. The LLRF controller works in tandem with a digital microphonics control system developed at MSU, which uses the rf error signal to drive a piezoelectric tuner [Gri04,Kan04]. The LLRF software was modified by LBNL to operate in either cw or pulsed mode. Performance tests of this system in cw mode have successfully demonstrated an architecture for effective rf amplitude and phase control.

Modern digital rf systems under development [Doo03,Doo02,Hov02] can easily satisfy the requirements of the driver linac. The systems are flexible and have the

advantage that their performance and capabilities can be expanded and upgraded over time without changing hardware. For example, operation in the Generator Driven Mode (GDM) or the Self Excited Loop mode (SEL) is a software choice that can be implemented remotely. Figure 5.82 illustrates the basic topology of such a system.

The designers of the LLRF equipment plan to work with collaborators at other laboratories, such as LBNL, JLAB, and ORNL, that are working on similar projects. It is likely that the main work in this area will evolve from hardware development to development of advanced mathematical techniques for monitoring and control to the implementation of the algorithms in software. The establishment of shared online libraries and documentation should be a priority in these efforts. Specific established techniques to regulate the rf amplitude and phase are being implemented in the current hardware and have been described elsewhere [Wan98].

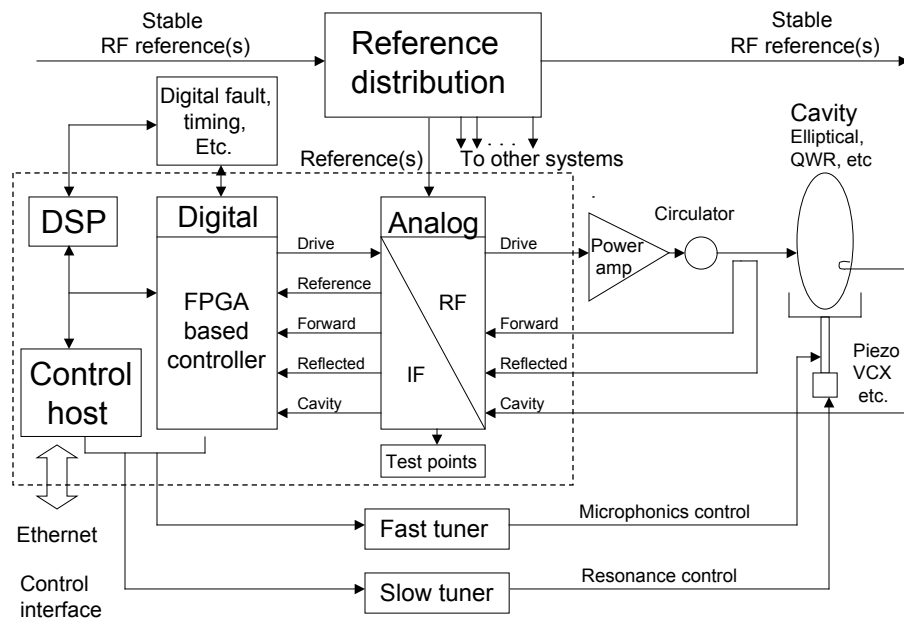


Figure 5.82: Basic topology for the proposed LLRF control system.

Although the LLRF development for this project will be ongoing, the specific design and hardware choices for mass production should be made approximately two years prior to manufacturing. Additionally, once the final digital boards are scheduled for mass production, overproduction by a factor of 1.5 to 2 times the need should be planned to ensure availability of spare components during the lifetime of the project.

Aside from the specific hardware and software choices mentioned, other design choices must be made for signal routing and clock frequencies. In cw systems, problems remain with phase drift in the interconnecting cables and noise pick-up. The choice of the main clock frequency(ies) can mitigate these issues, but this generally conflicts with other modulation and operational concerns. For example, choosing a low clock frequency that is not harmonically related to the rf frequencies of any of the cavities reduces noise and phase drift issues at the expense of ease of measurement and high RF/IF mixing ratios. However, since other labs (notably JLAB and SNS) are currently dealing with these issues, the proposed project will again benefit from experience gained elsewhere.

5.3.2 High-level rf

The proposed driver linac and reaccelerator will consist of five different types of accelerating cavities. Five different power levels and three different frequencies are required to drive the cavities. Table 5.32 gives the required number of rf amplifiers and their specifications. All cavities can be powered with solid-state amplifiers due to the low power requirements (≤ 4 kW). Solid-state amplifiers are preferred over tube amplifiers because of their easier availability.

Table 5.32: Solid-state rf amplifiers and their power requirements for the driver and reaccelerator linacs.

| Cavity | $\lambda/4$ | $\lambda/4$ | $\lambda/2$ | $\lambda/2$ | $\lambda/2$ |
|----------------------------|-------------|-------------|-------------|-------------|-------------|
| β_{opt} | 0.041 | 0.085 | 0.16 | 0.285 | 0.425 |
| Frequency (MHz) | 80.5 | 80.5 | 161 | 322 | 322 |
| Quantity | 30 | 146 | 58 | 92 | 205 |
| $P_{\text{generator}}$ (W) | 300 | 1000 | 1500 | 2000 | 4000 |

5.3.3 Cryogenics

The estimated total cryogenic plant capacity for the driver linac, reaccelerator linac, and experimental areas is shown in Table 5.33. The total calculated cryogenic load was increased by 50% for distribution losses and an additional safety margin. For reference, a one Watt thermal load will boil 1.4 l/hr of liquid helium. To reduce the oxygen deficiency hazard in the tunnel housing the accelerator, the thermal intercept will use 50 K helium return gas, rather than liquid nitrogen.

Table 5.33: Cryogenic plant loads (total/static) for the entire facility.

| | # of modules | 2 K load (kW) | 4.5 K load (kW) | 50 K load (kW) |
|-------------------------|--------------|------------------|------------------|----------------|
| Driver linac 80.5 MHz | 16 | — | 1.92/0.82 | 2.4 |
| Driver linac 161 MHz | 8 | — | 0.85/0.35 | 1.2 |
| Driver linac 322 MHz | 39 | 3.42/1.77 | — | 5.9 |
| Reaccelerator | 6 | — | 0.74/0.32 | 0.9 |
| Superconducting magnets | — | — | 4.50/4.50 | 6.8 |
| TOTAL | 69 | 3.42/1.77 | 8.01/5.99 | 17.2 |

Figure 5.83 shows a cryogenic flow diagram for the cryoplant. The mechanical efficiency of the cryoplant can be inferred from experience at CEBAF (18% at 2 oK and 30 % at 4.5 °K) [Sch03a].

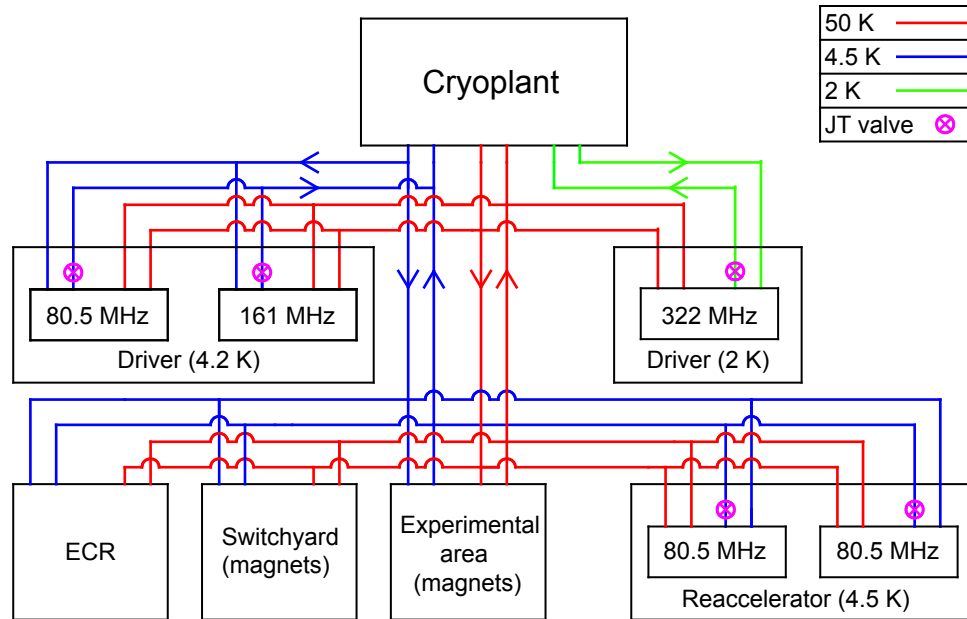


Figure 5.83: Schematic flow diagram of the cryogenics.

5.4 Rare isotope beam production

Rare isotopes will be produced by projectile fragmentation and fission, followed by separation in flight. In-flight separation is accomplished by the use of a two-part zero degree magnetic spectrometer [Mor04]. The separated ions will be available for use in the fast beam experimental area or can be stopped in a gas system and reaccelerated for low-energy experiments. The initial facility will not include an Isotope Separation On Line (ISOL) production capability, but the shielding and infrastructure is included so that this capability can be easily added. In-flight separation has been chosen as the initial production method because it provides a broader scientific reach (see Figure 1.8 in Section 1.3).

The proposed layout is flexible and allows for future upgrades in addition to ISOL, with minimal facility down time. These options will be discussed in detail in Section 6. An upgrade towards higher energy driver beams and increased beam power would improve the yield of rare isotope beams and hence the scientific reach of the facility. Additional target stations could be implemented to provide multi-user capability and increase the productivity of the facility, including greater flexibility with respect to rare isotope beam development. The upgrade options will be driven by the demands of the scientific program as it develops.

Figure 5.84 provides a schematic overview of the rare isotope beam production area. Central to the facility is a well-shielded target building accommodating all rare isotope beam production components that produce high radiation fields or that will become highly activated and contaminated. The target building (Section 5.4.1) will be equipped with shielding designed for rare isotope beam production with up to 400 kW of primary beam power. The target area is designed to accommodate rare isotope beam production by either in-flight separation or the ISOL method. However, the baseline facility will only have in-flight separation implemented, as discussed in detail in Section 5.4.2.

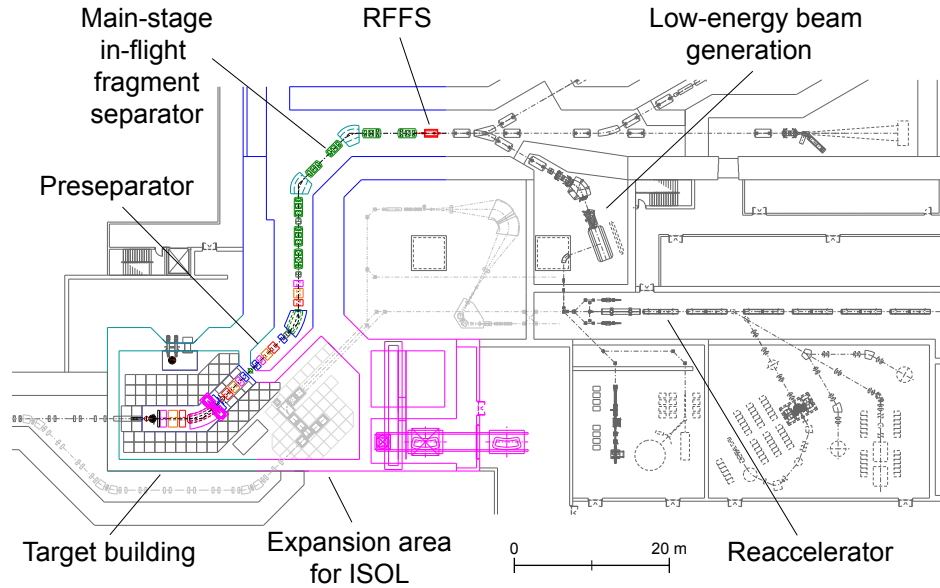


Figure 5.84: Schematic layout of the initial rare isotope production area.

For in-flight production, the first part of the preseparator is inside the target building. This includes the production target, a beam dump, and various magnetic focusing and bending elements. The following stages of separation will purify the rare isotope beams before they are transported to the fast beam experimental areas (Section 5.6.2) or will be converted into low-energy beams for either stopped-beam experiments or for experiments with reaccelerated beams (Section 5.6.1).

For low-energy beam production (Section 5.5) fast ions will be stopped in a novel cyclotron stopper currently under development at NSCL. Reacceleration of these beams to energies between 0.5 and 12 MeV/nucleon (Section 5.5.4) will be achieved with an efficient and compact accelerator scheme based on a charge breeder system coupled to a linear accelerator.

5.4.1 Target building

The development of a concept for the target building has benefited from the extensive expertise at MSU in rare isotope beam production and facility operation. The development has also benefited from detailed target-area RIA R&D work [DOE41313,DOE41322] (this work will be denoted in the following sections by the acronyms RIAFRAG for the in-flight separation facilities and RIAISOL for the ISOL production capabilities). The RIA R&D was carried out under MSU leadership with collaborators from Oak Ridge National Laboratory, Lawrence Livermore National Laboratory, Lawrence Berkeley National Laboratory, Los Alamos National Laboratory, and Argonne National Laboratory. A common target building for fragmentation and ISOL beam production was found to have advantages in terms of cost, schedule, operation, and facility safety. The concept of a common target building allows all target area service rooms and conventional facilities to be located in close proximity. Air handling and High Efficiency Particulate Air (HEPA) filtering systems can be shared as can water-cooling systems, radiation detection equipment, and personnel access systems. This concept of one common target building has been adopted for the present baseline design and hence easily provides ISOL capability as a future option.

The in-flight separation target, preseparator, and associated beam dumps will be located at the ground level of the driver accelerator inside a monolithic target building as shown in Figure 5.85. The components will be surrounded with iron, concrete, and soil to provide the necessary shielding. The shielding was designed to be adequate for primary beam powers up to 400 kW at beam energies of up to 270 MeV/nucleon for the lighter ions and 500 MeV protons. A common hot-cell for the in-flight production and the future ISOL systems will be located above the target shielding. This location allows for cost-efficient sharing of expensive remote-handling equipment for target changes and system maintenance. A component handling and waste removal area with truck access adjacent to the hot cell will provide the main removal path for radioactive material and for the exchange of smaller components inside the target area. A target service gallery above the hot cell will be equipped with a 40-ton overhead crane. Removable shielding sections in the ceiling of the hot cell allow larger components to be exchanged. The crane will be able to lift such components into a target service gallery located above the hot-cell. The crane will have access to the component handling and waste removal area.

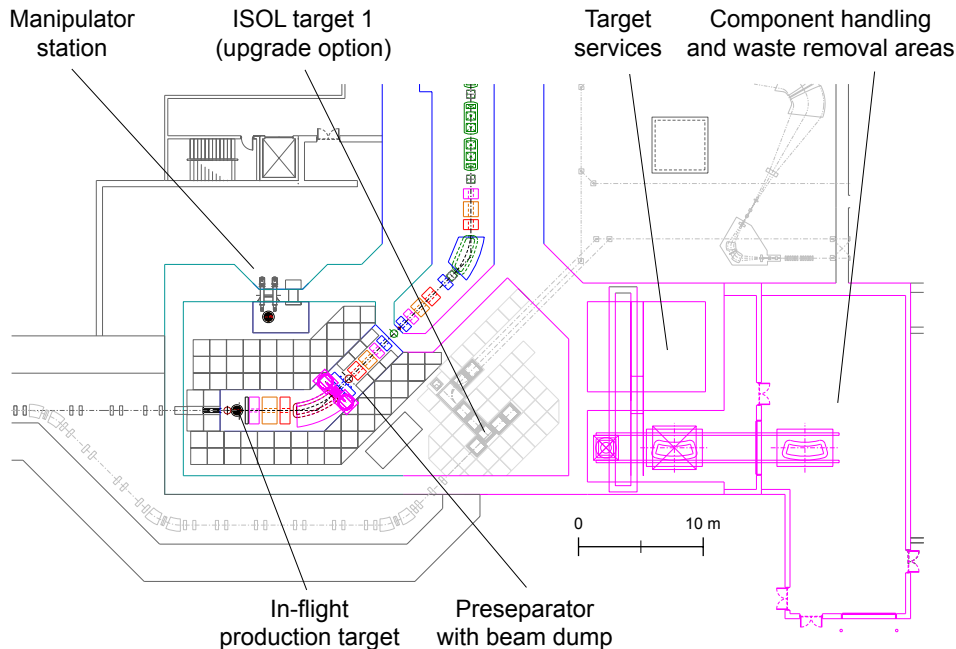


Figure 5.85: Schematic view of the production area. The production area of the baseline facility will be equipped with an in-flight production target and a preseparator. Space is provided for easy implantation of an ISOL target station adjacent to the preseparator.

5.4.1.1 Radiation transport simulations and shielding calculations

It is important to understand and to accurately model secondary radiation and activation of components in the target area. Yields and angular distributions of secondary radiation are required input for shielding, target, magnet, and beam dump design. They are also required for the overall layout since the choice of basic construction materials as well as component functionality depends on the lifetimes of materials exposed to radiation fields. A solid knowledge of the radiation field is mandatory for determining material activation and radiation damage in components, which in turn determines the maintenance intervals and procedures for their

handling. The RIAFRAG and RIAISOL R&D work had progressed towards full characterization of radiation fields from generic ISOL and fragmentation targets and beam dumps [Bol05a,Ron05,Bli05,Bae06,Bol06a,Rem06,Rey06]. The results of this work have been used to determine the shielding requirements for the ISF, to estimate component lifetimes, and to evaluate remote handling requirements.

The magnitude and spatial distribution of the prompt neutron radiation dose rates outside of the bulk shielding were estimated by Monte Carlo radiation transport calculations carried out for p, d, and ^3He light-ion beams using the MCNPX code [Pel05b] and for p, d, ^3He , ^{18}O , ^{22}Ne , ^{48}Ca , ^{136}Xe , and ^{238}U beams using the PHITS code [Iwa01]. Bulk shields of concrete and of cast iron were considered. Results obtained by using both codes for p, d, and ^3He beams were compared and were found to agree reasonably well. Simulations using the PHITS code of dose rates outside of shielding for a carbon beam have been compared to experimental data and also found to agree well. From calculations, it was determined that, for a given power, containment of the radiation from light-mass beams, such as ^{18}O , defines the shielding designs in forward directions. Matrices of neutron dose rates were constructed for different thicknesses of concrete and cast iron in a simple geometric model of spherical shells of shield material surrounding a copper beam dump. The shield was also sectioned to obtain information on the angular distribution of the radiation. As an example, Figure 5.86 shows the calculated neutron dose outside of the concrete shield (ordinary concrete of density 2.34 g/cm^3) as a function of shield thickness at different angles, for a 400 kW ^{18}O primary beam at 266 MeV/nucleon.

The neutron dose rates were parameterized as a function of distance from the source, amount, and type of intervening shielding material and angle with respect to the beam. Using the parameterized doses, matrices of the kind shown in Table 5.34 could then be easily constructed.

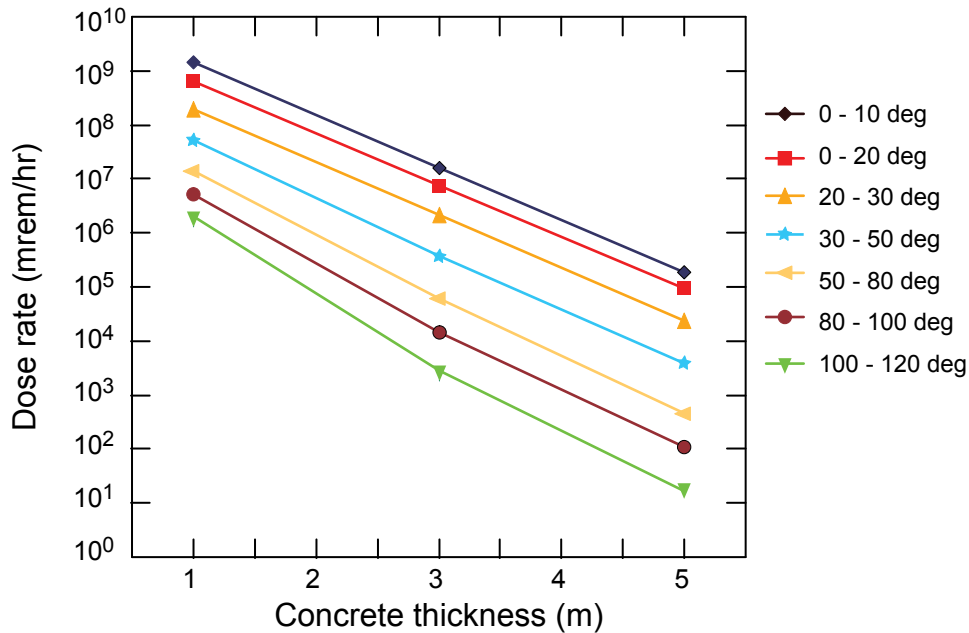


Figure 5.86: The neutron dose rates outside of concrete shielding (density 2.34 g/cm^3) as a function of shield thickness and angle with respect to the beam direction are shown for a 400 kW ^{18}O at 266 MeV/nucleon. Similar calculations were performed for iron shielding.

Table 5.34: Example of a matrix for dose rates (mrem/hr) outside of the shielding at 0°–10° with respect to the beam for a 400 kW 266 MeV/nucleon ¹⁸O primary beam, which is the worst case for production of radiation. The beam is stopped in a copper beam dump.

| Cast iron thickness (m) | Concrete thickness (m) | | | | | |
|-------------------------|------------------------|----------------------|----------------------|----------------------|----------------------|----------------------|
| | 0 | 1 | 2 | 3 | 4 | 5 |
| 0 | | 1.5×10 ⁹ | 1.3×10 ⁸ | 1.3×10 ⁷ | 1.5×10 ⁶ | 1.8×10 ⁵ |
| 1 | 1.6×10 ⁸ | 1.4×10 ⁷ | 1.4×10 ⁶ | 1.6×10 ⁵ | 2.0×10 ⁴ | 2.5×10 ³ |
| 2 | 6.1×10 ⁵ | 5.2×10 ⁴ | 5.3×10 ³ | 6.0×10 ² | 7.2×10 ¹ | 9.2×10 ⁰ |
| 3 | 2.6×10 ³ | 2.3×10 ² | 2.3×10 ¹ | 2.6×10 ⁰ | 3.1×10 ⁻¹ | 4.0×10 ⁻² |
| 4 | 1.3×10 ¹ | 1.1×10 ⁰ | 1.1×10 ⁻¹ | 1.3×10 ⁻² | 1.5×10 ⁻³ | 1.9×10 ⁻⁴ |
| 5 | 6.5×10 ⁻² | 5.6×10 ⁻³ | 5.7×10 ⁻⁴ | 6.5×10 ⁻⁵ | 7.8×10 ⁻⁶ | 9.9×10 ⁻⁷ |

Values in the matrix presented in Table 5.34 above 0.25 mrem per hour are highlighted in red; lower values are in green. The matrix shows, that for a 400 kW ¹⁸O primary beam at 266 MeV/nucleon stopped in a copper beam dump, three meters of cast iron and slightly more than four meters of concrete are necessary to reduce the annual dose to a worker located just outside the shield at an angle between 0 and 10 degrees with respect to the beam axis, to less than 500 mrem (0.25 mrem/hr for 2000 hours per year, as allowed by the MSU ALARA concept).

The minimum bulk shielding requirements for the target building were determined using similar matrices, taking both fragmentation beam production (heavy ions) and future ISOL production (p, d, ³He) with beam powers up to 400 kW into account. In addition to the development of this tool for the determination of bulk shielding, very detailed simulations have been performed for the radiation fields produced using realistic geometries for the in-flight production and ISOL stations. Specific examples will be discussed in Sections 5.4.2.7 and 6.2.2.2.

5.4.1.2 Remote handling

The results of radiation transport calculations and inventory analysis for facility operation show that cooling periods after an extended period of beam on target will be prohibitively long to allow “hands-on” target changes. This is supported by the experience at other high-power target facilities such as ISAC. To maximize facility operation, it is expected that target changes will be required at the rate of one per month. In this high radiation environment, it will be mandatory to perform such routine operations fully remotely.

The remote-handling concept is similar to that used in the SNS target building. Within the RIAFRAG and RIAISOL R&D projects, concepts have been developed for remote handling and maintenance of target and beam dump components. The remote-handling system proposed for this facility is largely based on results of these R&D studies.

A 20-ton crane will be sufficient to move the shielding blocks, target, and other components within the hot cell. The crane will have redundant motor drives for the winches and the horizontal movements and all electric supplies and controls will be located outside the hot cell. In addition to the 20-ton crane, a remote-controlled

overhead manipulator will be installed inside the hot cell. This manipulator will be used to disconnect services from the target plug and to maintain other components installed in the hot-cell. In addition to the overhead manipulator, a service station will be installed along the outside wall of the hot cell. This station will be used for the exchange and maintenance of target systems and other highly activated or contaminated components. It will be equipped with lead glass windows and two-arm manipulators.

5.4.1.3 Storage and waste removal

A common target area for both rare isotope production mechanisms will provide the advantage of a single waste removal path. This reduces risks and simplifies radioprotection and area control. A hatch on one end of the target area will be used for the removal of all spent-target items for final storage. The hatch will be connected to a bay area that can be accessed, using proper procedures, with a truck. This area can also be accessed by a 40-ton crane above the target hot cell, which can be used for removal of large components from the hot cell by removing shielding in the ceiling of the target area hot cell. Inside the target area, hot cell temporary storage space is planned for storing highly active components (for example ISOL targets) to let them cool before final removal from the target building but also for the storage of components that will be reused (wedges and targets for the fragmentation beam production).

5.4.2 In-flight isotope production

The remainder of this section is arranged to introduce the fragment separation technique and then describe the specific implementation of the concepts for the system. The various production methods and the projected rare isotope beam rates are given in Section 5.4.2.2. A detailed discussion of the specifications chosen for the separator is given in Section 5.4.2.3. A key feature of working with high-intensity rare isotope beams is the capability to deliver sufficiently pure beams to the experimental setups and to minimize unwanted ionization in a gas stopper. The level of purity needed requires the use of two stages of separation (Section 5.4.2.4) and the addition of an RFFS for proton-rich beams (Section 5.4.2.5). Details of other main components of the in-flight separation technique, including the production target, the fragment separator itself, beam dump, diagnostics, separator optics, and magnets are described in the Sections 5.4.2.6 – 5.4.2.11.

The in-flight rare isotope production technique has been used at many laboratories around the world and is the basis of the current rare-isotope beam programs at the NSCL (the A1900 [Sto05c]), GANIL (LISE-3 [Ann92]), RIKEN (RIPS [Kub92]), and GSI (FRS [Gei92]). In-flight fragment separation will continue to be a major technique and form the basis for new facilities under construction at RIKEN, (the BigRIPS separator [Kub03]), and at GSI (the SuperFRS [Gei03]). A review of fragment separator concepts can be found in reference [Mor04].

The new separator concept proposed here is an extension of the pioneering work on fragment separators at the NSCL. The A1200, the first fragment separator designed and built at the NSCL in the late 1980s, used existing superconducting beamline magnets. The use of these magnets limited the acceptance to three percent in momentum with a solid angle of one msr. The A1200 was the first separator that could deliver beams to all experimental areas and was used in nearly 80% of

the experimental program during its operational lifetime. In the late 1990s the next generation A1900 separator was designed and built at the NSCL. This device was optimized to have a collection efficiency of approximately 50% for fragments from the MSU Coupled Cyclotron Facility and again delivered those fragments to all experimental devices. The A1900 was commissioned in 2001 and is operated on a daily basis since most of the nuclear physics program uses secondary beams from the separator.

The acceptance of the A1900 is nearly identical to the desired specifications of the new separators listed below. Moreover, the A1900 magnets are sufficiently robust to allow them to be reused for the main separator that follows the preseparator. The radiation environment outside of the preseparator area will be similar to current conditions in the A1900, and the radiation hardness of the A1900 magnets will be adequate. The estimated lifetime of the magnets in this environment is greater than 20 years.

5.4.2.1 Overview of the ISF in-flight separators

The overall layout of the in-flight production area is illustrated in Figure 5.87. The fragment separation system consists of a production target area, a preseparator, and a high resolution (or main separator). Figure 5.88 illustrates the overall concept and individual components of the preseparator and the main separator. The function of the preseparator is to provide a well-defined location where the

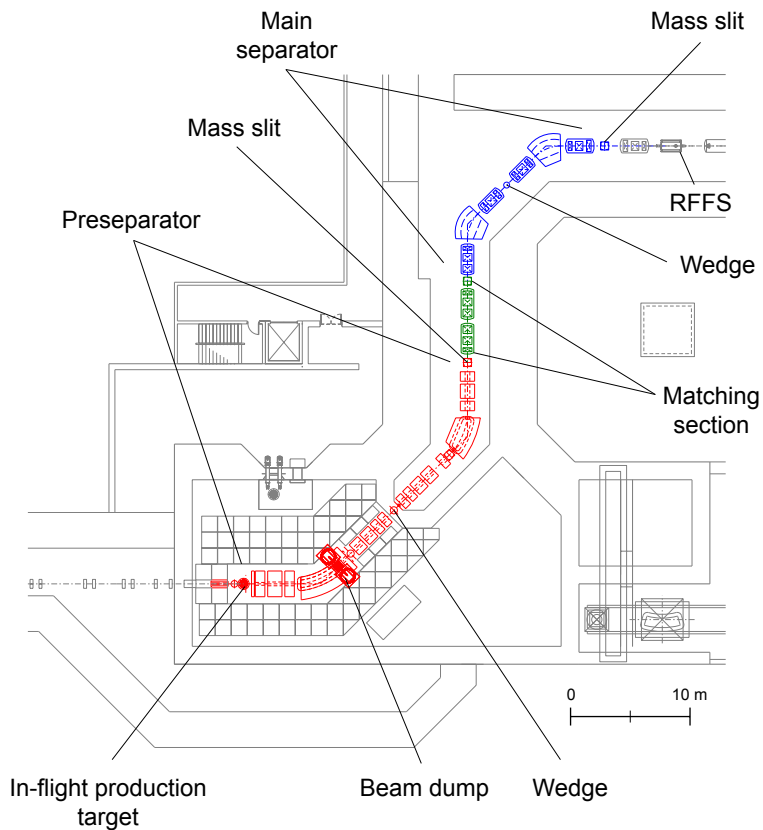


Figure 5.87: Schematic diagram of the fragment separator area. The preseparator components are indicated in red and those for the main separator in blue. The beam from the driver linac enters from the left. The Radio Frequency Fragment Separator (RFFS) and beam distribution system are to the right of the figure. Various key components are labeled in the figure.

primary beam and most of unwanted fragments can be collected. The object of the optical system is at the production target, shown at the left side of the figure. An image is formed after the first dipole and serves as a well-defined location for the primary beam dump. Additional quadrupoles are used to re-image the fragments. The degrading material (wedge) is located at the midpoint of the preseparator. The preseparator area up to the wedge location will reside in the hot cell designed for components in a high-radiation environment. The second part of the preseparator is a mirror image of the first part and provides the second stage of fragment separation. Clean-up apertures will be used to remove any scattered particles at the end of the preseparator prior to the second stage of separation. The main fragment separator will reuse A1900 magnets and consist of two 45° bends and four large-bore, quadrupole triplets. The two stages of separation in the preseparator and main separator are necessary to remove unwanted fragments produced by nuclear interactions in the wedge of the preseparator. Also, if the energy of the desired fragments is sufficiently different in the two stages, additional improvements in the separation efficiency can be gained.

Following the fragment separators, the rare isotope beams will be transported to various existing experimental devices. These devices will include a cyclotron-stopper system with a momentum compensation beamline that will provide thermal velocity secondary ions, as discussed in Section 5.5.

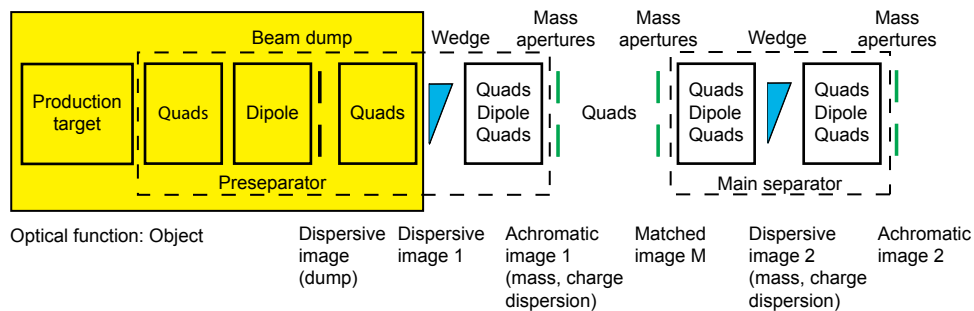


Figure 5.88: Block diagram showing the various parts of the fragment separation system. The yellow area is the high radiation area serviced by remote handling equipment. The primary beam strikes the production target on the left of the figure and fragments are separated in two stages of separation. The function of the various parts is given in the text. Following the final mass aperture, fragments enter the beam distribution system.

5.4.2.2 Production mechanisms and rates

The production of rare isotopes in flight can use a variety of nuclear reaction mechanisms. The two most commonly used are projectile fragmentation and projectile fission. The prediction of the fragment rates based on these mechanisms depend on the kinematic properties (angular and momentum distributions) of the rare isotope products, and their production cross sections. The kinematic properties of the nuclear reactions are well-known and have been incorporated into simulation codes, such as LISE++ [Tar04]. However, the production cross sections are less well-known. Fragmentation and fission models, EPAX 2.1 [SUM00] and LISE++, respectively, reproduce measured cross sections of isotopes near stability within a factor of three for many cases, a level that is sufficient to effectively plan experimental work. However, for both mechanisms, the production of the most neutron or proton-rich nuclei is not well understood. The difficulty is that a number of weak mechanisms may contribute to the very small cross sections. The optimum

production method for the production of the rarest isotopes and the corresponding cross sections are a topic of current research and development at the NSCL and other leading facilities worldwide.

Given the primary beam intensity, the production cross sections, a model of the fragment kinematics, and the separator specifications, the expected yield of any fragment can be calculated. The primary beams and energies as described in the accelerator sections above were used and a primary beam power of 400 kW was assumed for all ions. The separators were assumed to have an angular acceptance of 80 mr by 80 mr and a relative momentum acceptance of 10%. Losses due to nuclear reactions in the wedges as well as losses due to charge changing in the wedges and any detectors were included in the calculations. A beryllium target was used for the calculation of fragmentation rates and a lithium target was used for the rates calculated for uranium fission. There is approximately a 30% gain with a lithium target for both mechanisms due to the higher atom density of lithium, but lithium targets are more complicated to operate. The beryllium and lithium target thicknesses were chosen to provide optimum production of each ion, with the constraint that the beam rigidity remains below 8.0 Tm.

The estimated rates of ions available at the exit of the fragment separator were calculated with LISE++. The estimates include losses due to nuclear reactions in the wedge and losses due to the ions changing their charge state in the two wedges used in a two-stage system. A summary of the prospective rates is shown in Figure 5.89. These fragments will be available for the fast beams experimental program or for experiments where the rare isotopes are stopped for example in a solid detector. The subsequent rates from the gas-stopping system for the low energy experimental program will be reduced by the stopping and extraction efficiencies.

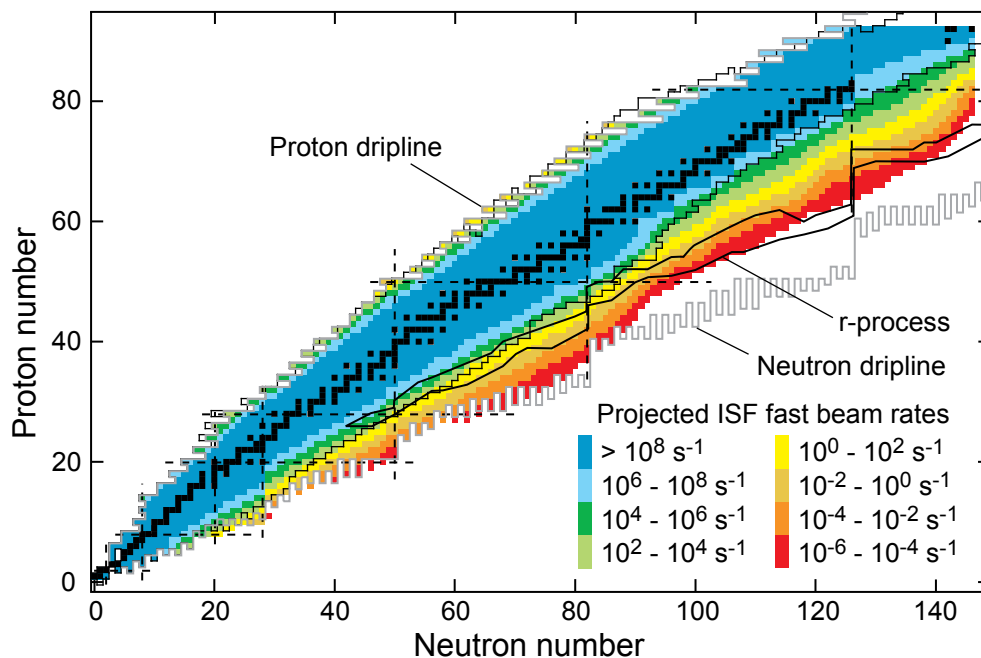


Figure 5.89: Estimated in-flight rates of separated ions following the fragment separation process. The rates are based on calculations with LISE++ using EPAX 2.1 cross sections for fragmentation and the LISE++ abrasion-fission model for fission fragments. For reference, the region of nuclei relevant to the astrophysical r-process is shown by the outlines on the right side of the contours.

5.4.2.3 Fragment separator specifications

The LISE++ code was used to explore the overall parameter space for the separator specifications. A detailed study of fragmentation and fission rates as a function of separator acceptance showed that an angular acceptance of ± 40 mr and a momentum acceptance of at least 10% were required to achieve a collection efficiency greater than 60% for projectile fragments and greater than 30% for fission fragments. We found that a higher momentum acceptance would provide fractionally higher gains in secondary rates, increasing by nearly 50% the rate of fission fragments for an 18% momentum acceptance. To illustrate the dependence, the calculated variation of the rate with momentum acceptance is illustrated in Figure 5.90 for representative fission and fragmentation products produced by 200 MeV/nucleon primary beams. Relative units are used to remove the uncertainty in the production cross section and allows the curves to be plotted together. The three cases shown are fragmentation of ^{48}Ca on beryllium to produce ^{42}Si by fragmentation, fragmentation of ^{112}Sn to produce ^{100}Sn , and fission of 200 MeV/nucleon ^{238}U on a lithium target to produce ^{132}Sn . The figure illustrated that the minimum separator acceptance should be at least 10% in momentum to achieve the desired level of efficiency. A larger momentum acceptance would increase the rates for fission fragments but would add substantially to the cost and increase the image size due to aberrations. A decision was made that an optimum of rate and cost was reached taking a 10% acceptance; however, further research and development will explore options to increase this value.

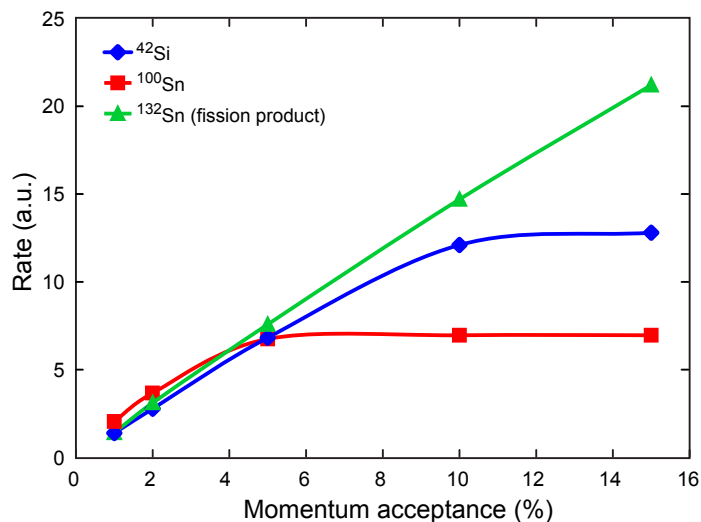


Figure 5.90: The production rate of three representative beams, ^{42}Si ions from ^{48}Ca fragmentation, ^{100}Sn ions from ^{112}Sn fragmentation, and ^{132}Sn ions from ^{238}U fission are shown as a function of the momentum acceptance of the fragment separator. The calculations were performed with LISE++ for primary beams at 200 MeV/nucleon. The optimum target thickness has been used for each calculation.

The LISE++ code was also used to determine the required angular acceptances for the fragment separator system, assuming a momentum acceptance of 10%. Figure 5.91 shows the effect of varying the angular acceptance (horizontal and vertical acceptances were assumed to be the same) on the yield of the same three sample cases displayed in Figure 5.90. The collection of the broadly distributed fission fragments is clearly a difficult task. One can see that the angular acceptance should

be greater than ± 40 mr to saturate the yield of fission fragments, but the finite sizes of realistic magnet apertures and concomitant higher-order aberrations in large magnets limit the achievable acceptance to approximately ± 40 mr.

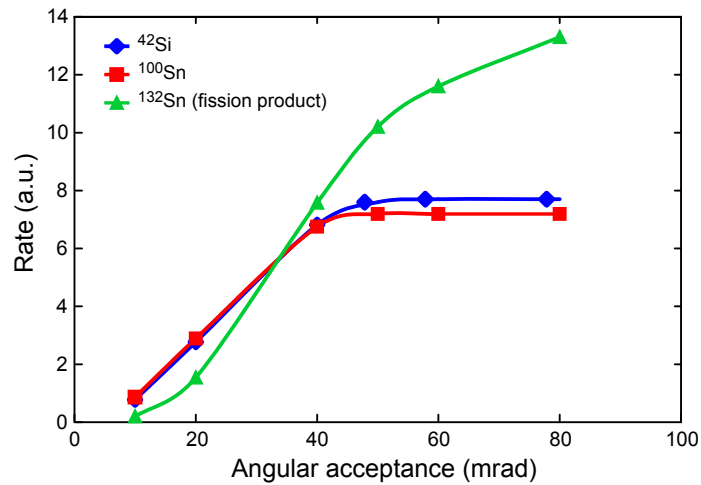


Figure 5.91: The production rate as a function of angular acceptance for fragments from fission and projectile fragmentation for three representative cases. The requirements on the separator from the kinematics of projectile fragmentation are less severe than those from fission, and an angular acceptance of ± 40 mr will allow the collection of nearly 100% of the projectile fragmentation products.

The optimum magnetic rigidity for the separator was determined by considering the fragment rigidity corresponding to the maximum production yield from primary beams at the maximum energy of the ISF linac. In all cases the fragment rigidity was found to be below 8.0 Tm. The range of rigidities is illustrated in Figure 5.92, where the optimum fragment rigidity for each secondary fragment is shown as a function of atomic number. Hence, 8.0 Tm was adopted as the secondary beam maximum rigidity.

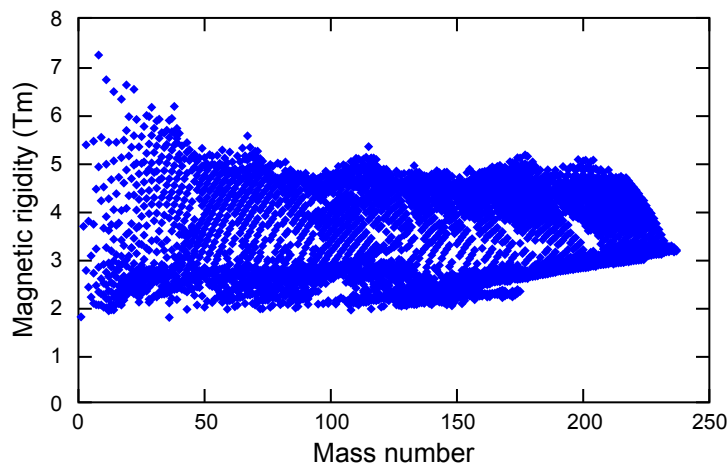


Figure 5.92: The optimum rigidity for fragments produced by maximum energy ISF primary beams is shown as a function of their atomic number. The adopted magnetic rigidity for the separators is 8.0 Tm.

Energy loss straggling and the intrinsic momentum-resolving power of the various stages of separation determine the mass and charge resolving power of any fragment separator. To first order, the effective resolving power in mass number, A , is given by the expression

$$R = \frac{(D/M)(\delta|x)}{\sqrt{[(D/M)\delta_{ws}]^2 + \Delta x_0^2}} \frac{1}{(\delta|\delta)} \quad (5-11)$$

where (D/M) is the ratio of the dispersion to the magnification of the first and second halves of the separator; $(\delta|x)$ is the momentum change as a function of position, x , caused by the wedge; $(\delta|\delta)$ is the increase in the momentum spread caused by the wedge; Δx_0 is the initial beam spot size; and δ_{ws} is the combined effect of straggling and non-uniformity of the wedge. This expression can be used to determine the momentum resolving power (given by D/M) of the segments of the separator needed to cleanly separate the fragments of interest. The ratio D/M is determined primarily by the size of the dipole and quadrupole magnets. While larger magnets result in increased resolving power, they also result in increased cost. From equation 5-11, one can determine that the optimum momentum-resolving power of the various segments is approximately 1 part in 1500 so that the product of (D/M) and the straggling from the wedge ($\delta_{ws} \sim 0.1\%$ in momentum) in the denominator is similar to the contribution from the expected primary beam spot size of 1 mm. A higher resolving power than 1500 would add to the cost but would not be useful in practice since the mass-resolving power would then be dominated by straggling in the wedge. A lower momentum resolving power would provide lower mass resolving power and hence worse secondary beam purity. A momentum resolving power of 1500 will require dipoles bending 45° (with bend radii 4.2 m in the preseparator and 3.1 m in the main separator) and a horizontal beam envelope extent of approximately ± 10 cm in the dipole gaps.

5.4.2.4 Two-stage versus one-stage separation

A serious concern for experimental work with secondary beams is the ratio of the isotope of interest to the total number of fragments (the purity). Low beam purity can lead to unwanted background and increased dead time in electronics. Collection of unwanted fast ions in the gas cell will lead to extra ionization in the gas, resulting in performance losses. In one-stage separation, a large number of fragments reach the wedge location. In the separation process, the wedge is often relatively thick and serves as a secondary production target. Unwanted fragments produced at the secondary beam momentum are transmitted to the end of the separator and lower the purity of the beam. The size of this background can be many orders of magnitude larger than the desired fragment; see for example the recent work of Geissel et al. [Gei06].

The key to improve the beam purity is to have two stages of separation as proposed here. Two stages of separation will significantly reduce the number of contaminant fragments in the secondary beam, a particular advantage for the gas stopping system [Gei03]. The first, preseparator, stage removes the primary beam and most of the unwanted fragments (so that they do not strike the second wedge and induce reactions). The main separator is used to further purify the beam and remove the fragments produced in the wedge.

5.4.2.5 Radio frequency fragment separator

The maximum energy of the primary beams at the ISF is less than 300 MeV/nucleon. A disadvantage of the production of rare isotopes at this energy, compared to production at a higher energy, is that the beams are not as pure. This is particularly true for proton-rich fragments due to the nature of the projectile fragmentation process. A technique to solve this problem is to use an additional degree of separation using a Radio Frequency Fragment Separator (RFFS) that selects particles according to their relative time of flight. It takes advantage of the fact that a velocity difference between ion species translates into a phase difference relative to the frequency of the stable beam accelerator (driver) after some drift length. An electric rf field can then be used to achieve phase dependent deflection leading effectively to velocity filtering. With this device, beam purity for extremely neutron-deficient beams can be improved by factors of a million or more, enabling a wide range of new experiments. The RFFS will be located in the area directly following the main separator, as shown in Figure 5.87.

The contaminants in the neutron-deficient beams are lower in Z, have lower momenta, and originate from the low-energy tails of the fragment momentum distributions. In order to come through the separator, the contaminants must have a lower velocity and, hence, can be separated by their arrival time. Figure 5.93 illustrates the performance of the RFFS for a ^{100}Sn beam produced from ^{124}Xe at 235 MeV/nucleon. The production rate and purity was calculated with LISE++, and the values of the assumed parameters for the separation process are given in the figure. The purity of ^{100}Sn compared to all fragments can be seen to grow through

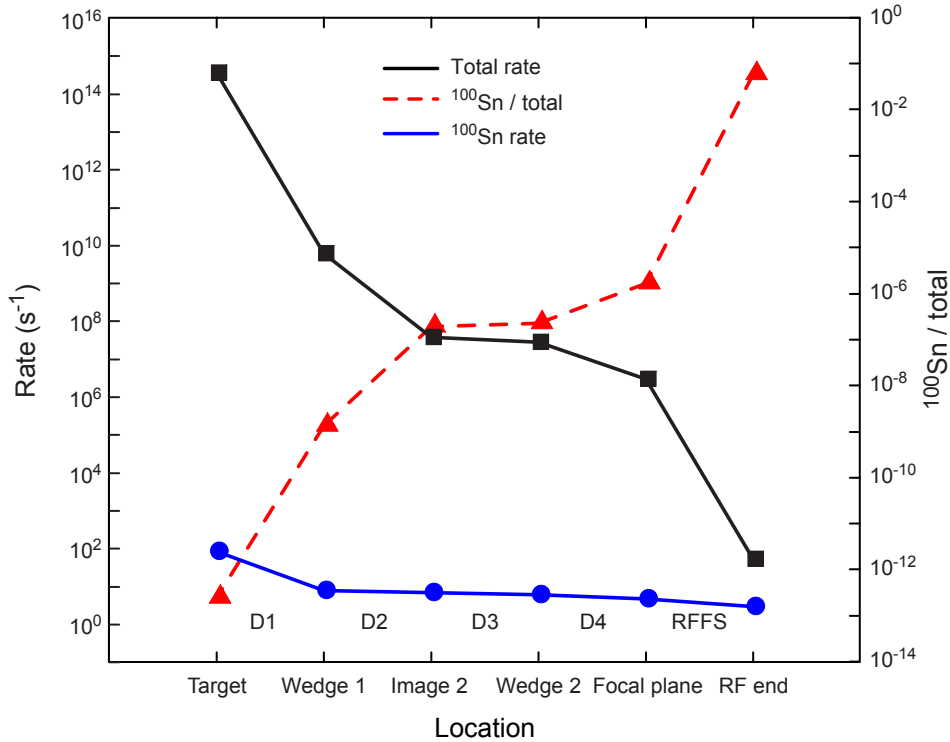


Figure 5.93: The improvement in beam purity for the fragmentation of 235 MeV/nucleon ^{124}Xe to produce ^{100}Sn calculated with LISE++ as a function of position in the separation system. The simulations assumed a beam power of 400 kW, a 800 mg/cm² target and two wedges of thickness 450 and 300 mg/cm², respectively. The momentum acceptance of the separator was $\pm 3\%$ and the operating frequency of the RFFS was 20 MHz.

the various states of the separation process. Notice that at the focal plane of the separator, following two stages of separation, the fraction of ^{100}Sn is still only one part in 10^7 ; however, with an additional RFFS, a purity of about 1 part in 10 can be achieved. The addition of the RFFS increases the purity of ^{100}Sn by more than six orders of magnitude and provides a level of separation in which decay studies become possible.

A similar separation scheme is required for almost all weakly produced proton-rich secondary beams. The rf-separation approach has been pioneered by RIKEN where a similar device is already in use [Yam04].

5.4.2.6 Production targets

Targets for the production of in-flight separated beams must be able to sustain very high power densities imposed by the requirement from the ion optics. In our case the production beam spot must have a diameter of approximately 1 mm. The small beam spot is required to reduce the effects of geometric aberrations in the fragment separator that will limit the collection efficiency in the gas-stopping system. Given this small beam spot and that up to approximately 30% of the primary beam power will be lost in the production target, the power densities in the target will be extremely high, up to 500 kW/cm^3 (assuming a 400 kW uranium primary beam).

For projectile fragmentation and fission, the ideal target should have a low atomic number (Z) and hence more atoms/ cm^2 than a higher Z target. However, it is possible that for certain special cases, e.g., for Coulomb breakup of the primary beam, a higher Z target would be preferable. Prototype work is underway at ANL [Nol03] on a windowless liquid lithium target suitable for the highest power uranium beams. However, the flowing liquid lithium target envisioned for use with the uranium beam will not be appropriate for lighter beams due to the very low density of liquid lithium ($\sim 0.5 \text{ g/cm}^3$). There is also the potential problem of migration of the lithium from the region of the open liquid target. Therefore, for the initial operation of the Isotope Science Facility (ISF) we plan to use a rotating beryllium or carbon target. Similar designs have been prepared for the 100 kW uranium beams at GSI [Gei03] and RIKEN [Yos04b]. These rotating wheel designs are based on a high power rotating carbon target that has been successfully operated for several years at PSI [Hei02]. Calculations show that a 70 cm diameter wheel rotating at several hundred rpm will have a temperature rise of a few hundred degrees centigrade, well below the melting point of beryllium. The anticipated problems with a rotating production target include radiation damage to the motor, bearings, and the wheel material itself. Radiation field calculations done with the PHITS code indicate that the fields are sufficiently low that all mechanical components should have lifetimes of greater than one year.

One remaining area of uncertainty is the damage to the beryllium disk. The standard limit taken for acceptable radiation damage is five displacements per atom (dpa). For the case of fast heavy ions the actual displacement caused per ion is not known; and it is also not known if beryllium can tolerate a higher dpa. This is an area that requires further research and development, and a plan is underway to make the necessary measurements at the NSCL. In any case, the wheel design appears workable and the radiation damage limit will determine how often the wheel must be replaced. A fallback option is to use more radiation tolerant graphite target wheels as utilized in the PSI system [Hei02] with some loss in yield.

Target thickness changes will be accomplished by using a stepped wheel as is planned for the RIKEN facility [Yos04b]. The target will be remotely changed with the remote-manipulator system described in Section 5.4.1.2, hence large thickness changes are expected to take less than eight hours.

In any case, a target design sufficiently robust and long-lived when utilized with the highest beam powers will require additional R&D to achieve a viable system.

5.4.2.7 Fragment separators

In summary, the design criteria for the separator system from the considerations in the previous section are to achieve an 8.0 Tm bending power with a minimum relative momentum acceptance of 10% and an angular acceptance of ± 40 mr. A number of ion-optical designs were explored with the code GICOSY [Wei05a] up to the third order before settling on the technical design described below. The angular and momentum acceptances of a number of possible systems as well as the final design were checked with the Monte Carlo raytracing program MOCADI [Iwa97]. In the following subsections, we will describe the details of the various separator components that will be used to make up the block diagram Figure 5.88.

Preseparator

A preseparator will allow the removal of the primary beam and most unwanted fragments from the ions of interest. The removal reduces the radiation field outside the production area and improves the operational safety of the system. Ideally, the preseparator would also allow the collection of unused isotopes for other applications. The preseparator ion-optics will have a focus after the first dipole so that the primary beam dump can be placed at this location. This placement is essential since the primary beam will be within the separator acceptance for the optimum collection of a number of secondary fragments. Placing the beam dump near the location of the focus will allow the primary beam to be removed cleanly while limiting the extent of the phase space lost from the collection of the desired fragments. This area would also serve as a potential location for isotope recovery for applied research with long-lived isotopes. A shielding wall will be used to separate the first part of the separator from the rest of the system. The whole preseparator will be achromatic and will operate as a standard momentum-loss fragment separator.

Key components of the preseparator and the proposed ion-optical operation include the following criteria:

- A focus after the first dipole to allow the primary beam to be intercepted early in the system. This limits the extent of the high radiation area. A window could be added directly after the following multipole magnet to allow segregation of the vacuum systems.
- The first dipole will be a “C” magnet without a return yoke inside the bend to allow access to beam dumps.
- Water-cooled copper or aluminum beam dumps. Calculations show that rigid beam dumps should be able to dissipate 100 kW of beam power under the proposed operating conditions. Space will be left for the replacement of the fixed beam dumps with new designs that can accommodate beam powers up to 400 kW. Further R&D must be conducted to verify if

the initial concepts developed for a rotating dump will be adequate at the higher power level.

- The beam dump will be movable so that the edges can serve as momentum slits to reduce the number of unwanted fragments transported further into the system. This will reduce radiation damage and activation of later components.

Figure 5.94 shows a schematic layout of the preseparator. The local shielding has been designed to be sufficient for operation with primary beam intensities of 400 kW. Remote handling silos are provided for beam diagnostics before the target, the target itself, and the beam dump.

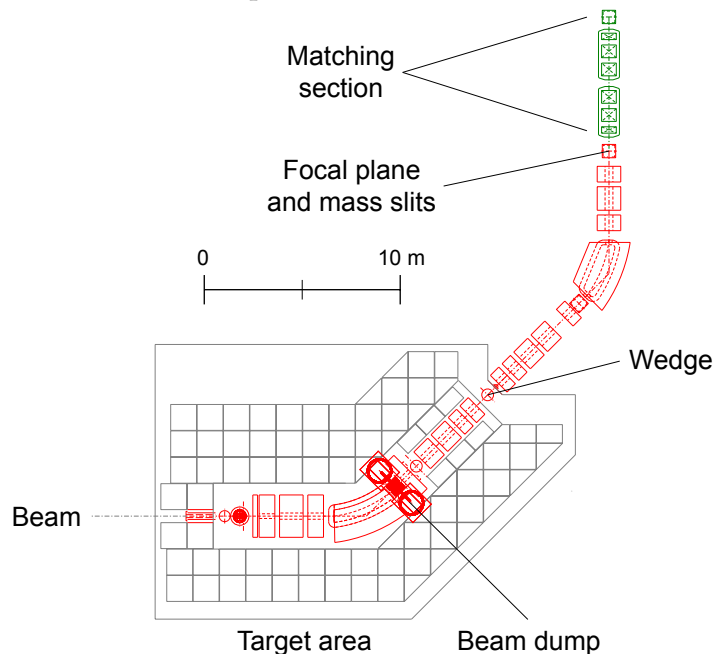


Figure 5.94: The schematic layout of the preseparator with an acceptance of ± 40 mr and a relative momentum acceptance of 10% is shown. The first focus occurs directly after the first dipole, where the primary beam and unwanted fragments can be collected. The high radiation area, which is serviced by the remote-handling equipment, is indicated by the outline and the hatched area.

The ion optics of the final preseparator design were calculated up to fourth order and corrected up to third order by the inclusion of multipole coils in the quadrupole magnets of the separator. Simulations carried out with the MOCADI ray tracing code indicated that approximately 60% of the ions that enter the separator acceptance (assuming uniform illumination) are transmitted. The optical layout as calculated in GICOSY, with all third order aberrations corrected, is shown in Figure 5.95. The image produced by the preseparator should not be larger than two mm, since this image will form the object for the final two stages of separation. An aperture at the image position of the preseparator will be used to form the object for the remainder of the system. Based on experience with the A1900 at the NSCL, a transmission of 90% should be possible with even more careful optimization of the higher order correction elements. In order to perform this optimization, the program MOTER [But91] is currently being adapted for use with the LISE++ simulation package. Completion of this task is expected soon and will allow a full optimization of the separators including realistic wedge designs before construction.

The required parameters for the magnets are shown in Table 5.35. The field values are given for the maximum rigidity secondary beam of 8.0 Tm.

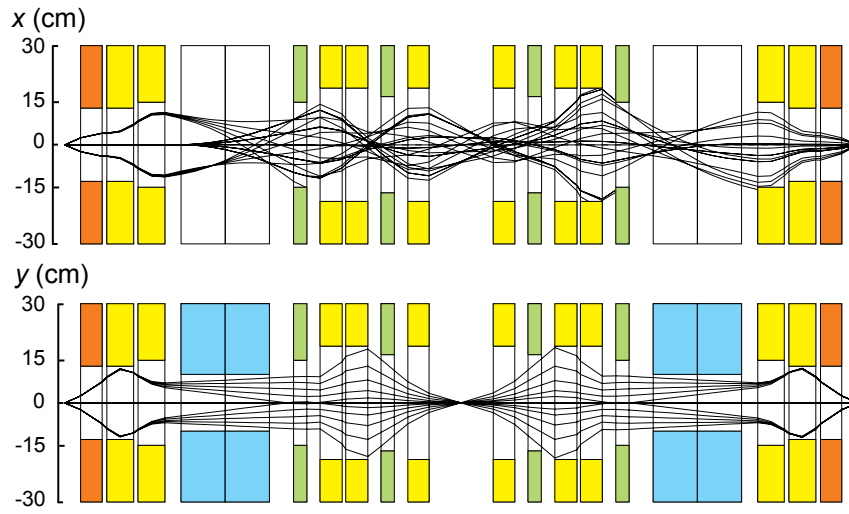


Figure 5.95: The results from the third order calculation of the ion optics for the preseparator using the GICOSY code. The calculation was performed with ± 40 mr angular acceptances and $\pm 5\%$ momentum acceptance. The dipole magnets are indicated in blue, quadrupole magnets with sextupole and octupole correction components in yellow, sextupole magnets with octupole correction components in green, and simple quadrupole magnets in orange (located at the front and back of the system).

Table 5.35: Magnet parameters for the preseparator. The field values are given for the maximum rigidity secondary beam of 8.0 Tm.

| Magnet | Pole radius (m) | Field at pole tip (T) | Sextupole field (T) | Octupole field (T) | Length (m) |
|-------------|-----------------|-----------------------|---------------------|--------------------|------------|
| Quad 1 | 0.13 | 1.55 | — | — | 1.0 |
| Quad 2 | 0.13 | -1.49 | — | -0.01 | 1.0 |
| Quad 3 | 0.15 | 1.029 | — | — | 0.8 |
| Dipole 1 | 0.10 | 1.9 | — | — | 45 degrees |
| Multipole 1 | 0.15 | — | -0.5 | 0.69 | 0.5 |
| Quad 4 | 0.15 | 1.61 | 0.23 | 0.01 | 0.82 |
| Quad 5 | 0.15 | -1.564 | -0.22 | -0.20 | 0.82 |
| Multipole 2 | 0.15 | — | 0.47 | 0.75 | 0.5 |
| Quad 6 | 0.15 | 1.474 | — | — | 0.8 |
| Quad 7 | 0.15 | 1.474 | — | — | 0.8 |
| Multipole 3 | 0.15 | — | 0.47 | 0.75 | 0.5 |
| Quad 8 | 0.15 | -1.564 | -0.22 | -0.20 | 0.82 |
| Quad 9 | 0.15 | 1.61 | 0.23 | 0.01 | 0.82 |
| Multipole 4 | 0.15 | — | -0.5 | 0.69 | 0.5 |
| Dipole 2 | 0.10 | 1.9 | — | — | 45 degrees |
| Quad 10 | 0.15 | 1.029 | — | — | 0.8 |
| Quad 11 | 0.13 | -1.49 | — | -0.01 | 1.0 |
| Quad 12 | 0.13 | 1.55 | — | — | 1.0 |

Preseparator neutronics calculations

Understanding the radiation fields in the preseparator area is critical for the ion optical design as well as for the choice of optical components and shielding. In particular from scoping simulations for shielding [Bae06] and radiation heating [Zel05a], it was observed that for heavy-ion beams with the same beam power, the neutron fluxes were highest for energetic, highest-intensity, lighter-mass beams. Thus, we concentrate here on the calculations performed for the severe challenge presented by a primary ^{48}Ca beam.

Specifically, the interaction between a primary ^{48}Ca beam, having 268 MeV/nucleon energy and 400 kW beam power, and a beryllium production target was simulated using the Monte-Carlo radiation transport code PHITS [Iwa02]. The optimized target thickness (3730 mg/cm^2 , for the production of ^{44}S), the primary beam magnetic rigidity ($B\rho$) after passing through the target, and the optimal fragment $B\rho$ were determined with LISE++ and then put into the PHITS simulation. As discussed in the previous section, both unreacted primary beam and secondary fragments pass through the front end of the preseparator, which consists of three quadrupole magnets and a dipole magnet.

The plane view of the preseparator area as used in the simulations is shown in Figure 5.96. After the dipole, both the primary beam and many unwanted secondary beams will stop in a beam dump located just after the dipole, while the desired fragment (^{44}S in this case) will be transported through the remainder of the preseparator. The preseparator will include a radiation-tolerant multipole magnet, located just behind the beam dump, and superconducting quadrupole magnets after the dipole magnet.

The goal of these initial simulations was to determine the magnitude of the radiation fields in the preseparator area. The PHITS code includes calculation of the ion

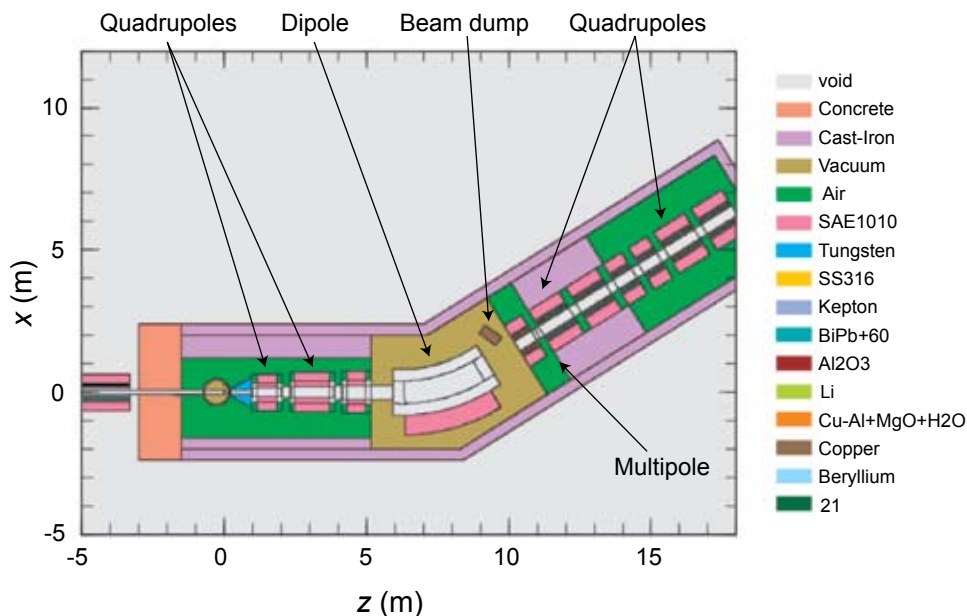


Figure 5.96: Preseparator geometry used in the PHITS simulation is shown with the target module and magnets labeled. The preseparator was surrounded by a steel enclosure in the simulation. The required amount of bulk shielding was determined according to the parameterizations described in Section 5.4.1.1.

trajectories through the preseparator; these were used to check the location of the primary beam dump. The levels of hadron flux and heating were also obtained from these calculations. It was of particular interest to estimate the maximum heating of the magnet coils and pumps and to check that the expected lifetimes are greater than one year.

The sources of heating of the magnet coils and other structures are primarily neutrons that produce secondary charged particles and electrons produced by photon and neutron interactions. Primary and secondary charged particle fragments such as protons and α -particles also make a small contribution. Therefore, it is important to understand the distribution of reaction products inside the preseparator that produce this secondary penetrating radiation. Figure 5.97 shows a representative example of the neutron flux distribution in the preseparator area from the PHITS simulation.

The maximum heating caused by the radiation fields and particle loss for key elements, including the water circulation pump for the beam dump and the coils of the magnetic elements, was calculated and is listed in Table 5.36.

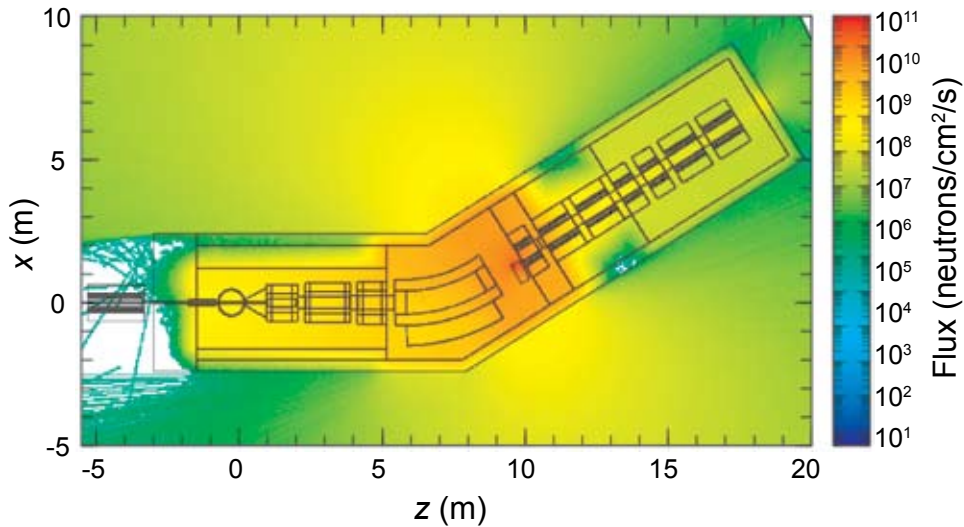


Figure 5.97: The neutron flux distribution in the preseparator area from the PHITS simulation, normalized to 400 kW power.

Table 5.36: Maximum heating of the beam dump water circulation pump and coils of the magnet elements. The pump is inside the target module, the 1st through 3rd quadrupole magnets are before the dipole, and the 4th through 9th quadrupole magnets are after the multipole magnet, which is itself located just downstream of the dipole and beam dump (see Figure 5.96).

| Preseparator system | Maximum heating (mW/cm ³) |
|---|---------------------------------------|
| Pump | 0.01 |
| 1 st , 2 nd , 3 rd Quadrupoles | 0.01–0.02 |
| Dipole | 0.08 |
| Multipole | 8.0 |
| 4 th Quadrupole | 1.2 |
| 5 th Quadrupole | 0.2 |
| 6 th – 9 th Quadrupoles | 0.01–0.05 |

As part of the completed RIAFRAG and RIAISOL R&D work, more detailed calculations of doses and activation levels were performed using the PHITS code with the output processed by the MCNP radiation transport code and by the DCHAIN-SP2001 activation code [KAI01]. The level of air activation around the first quadrupole magnets after thirty days of beam-on and one day of beam-off was found to be on the order of one-thousand times the acceptable derived air concentrations for personnel access. Steel and copper components experiencing this level of flux will become activated to levels on the order of 10^5 Bq/g, with surface dose rates of ~ 10 R/hr. Metals, organic materials, and electronic components in this area will experience doses ranging from ~ 0.5 kGy to ~ 100 kGy during a year of facility operation. One consequence of these levels of air activation and doses is that remote handling for maintenance and repair is essential.

From Table 5.36, explicit tallies for heating indicate ~ 300 kGy per year of operation. For the magnet steel, a heating level of 0.01 mW/cm³ represents 0.1 Gy/s, given a density of 10 g/cm³ or about 1 MGy/yr, taking reasonable operating assumptions. From what is known about the radiation tolerance of superconductors, lifetimes of several years can be expected for the magnets.

Remote handling of preseparator components

The preliminary design of the remote handling equipment was based on work performed in collaboration with ORNL. The production area, through the end of the preseparator, will be enclosed in a hot cell with remote manipulator arms used to make and remove connections. The overhead 20-ton crane described in Section 5.4.1.2 will be used to lift the various plug modules. The modules will be placed in storage areas and replacement modules inserted. In this way, it is anticipated that target and beam dump changes can be completed in less than eight hours.

Remote manipulators will be used to change the wedges and detector systems outside of the target production area. The components to be changed will be loaded into a carousel system that can be accessed by the remote manipulation system. An alternative system could be based on an industrial robot, such as the system used at GSI; however, the flexibility and human interaction with a remote manipulator system is advantageous.

Separator matching section

The optimum charge and mass resolving power for a two-stage fragment separator system depends on the energy-loss processes in the wedge. In order to ensure that the optimum rare-isotope separation can be obtained for all conditions, it is necessary to have a matching section between the two segments of the separator (see Figure 5.94). This section nominally serves as a unit matrix transformation of the beam properties either with or without inversion of the image. The mass dispersion of a two-stage fragment separator (for constant Z) is given by

$$(x|m) = (x|x)_{22} \left[(\delta|x)_2 (x|\delta)_2 + (\delta|x)_1 (x|\delta)_1 (x|x)_{12} (x|x)_{21} (x|x)_m (\delta|\delta)_2 \right] \quad (5-12)$$

where $(x|\delta)_i$ and $(x|x)_{ij}$ are the dispersions and magnifications of the i^{th} segments of the two separators, respectively. The subscript 12 refers to the first segment (object to wedge) of the main separator, while the subscript 22 refers to the second segment of the second separator (wedge to achromatic image). The term $(\delta|x)_1$ is the additional momentum deviation induced by the wedge. From this equation, we can see that the mass dispersion can be adjusted as needed by adjusting $(x|x)_m$.

A drawback of having a matching section is that it will induce higher-order aberrations. These aberrations can be minimized by using six quadrupole magnets in a symmetric configuration. The induced geometric aberrations will be small for this system, and the remaining major aberration is second order chromatic. Correcting the system as a whole up to the next wedge location can minimize this chromatic aberration.

Main separator based on the A1900

The requirements for the main separator can be met by reusing the first half of the existing A1900 (see Figure 5.84). The required magnet parameters shown in Table 5.37 are consistent with the parameters for standard operation of the existing A1900 magnets. Reuse will provide a significant cost savings but will require that the rigidity in this section be limited to 6.4 Tm. This is not expected to be a problem since, as shown in Figure 5.92, most beams start out below this value at their optimum production point, and the remaining beams will normally be slowed to rigidities below this value by the wedge in the preseparator.

The ion optics for the main separator are nearly identical to those used in the existing A1900. The use of only half of the current system allows the relative momentum acceptance to be 10% with an angular acceptance of ± 50 mr (somewhat larger than the ± 40 mr required) in the horizontal and vertical planes. A wedge will be placed at the intermediate image of this segment, with a mass aperture at the following achromatic image position. The final stage of separation can be used for additional secondary beam cleanup or can be used as a location to place detectors to tag the momentum and angle of each ion. Hence, provision will be made to allow detectors at the intermediate image, as is done at the A1900.

Table 5.37: Magnet parameters for the second stage of the separator. Magnets with higher order components are indicated. The field values are given for the maximum rigidity secondary beam of 6.4 Tm. Quadrupoles 3–10 include sextupole and octupole correction components.

| Magnet | Pole radius (m) | Field at pole radius (T) | Length (m) |
|----------|-----------------|--------------------------|------------|
| Quad 1 | 0.133 | 1.55 | 0.748 |
| Quad 2 | 0.133 | -1.95 | 0.748 |
| Quad 3 | 0.15 | 1.55 | 0.43 |
| Dipole 1 | 0.07 | 1.90 | 45 degree |
| Quad 4 | 0.11 | 1.95 | 0.43 |
| Quad 5 | 0.11 | -2.20 | 0.803 |
| Quad 6 | 0.11 | 1.81 | 0.43 |
| Quad 7 | 0.11 | 1.81 | 0.43 |
| Quad 8 | 0.11 | -2.20 | 0.803 |
| Quad 9 | 0.11 | 1.95 | 0.43 |
| Dipole 2 | 0.07 | 1.90 | 45 degree |
| Quad 10 | 0.13 | 1.55 | 0.43 |
| Quad 11 | 0.13 | -1.95 | 0.748 |
| Quad 12 | 0.13 | 1.55 | 0.748 |

Full system ion optics

The conceptual layout and function is shown in Figure 5.88. The first order optics for the full system is illustrated in Figure 5.98. Higher order ion-optical calculations, up to fourth order have been performed for the individual sections, and a full system evaluation and optimization is underway.

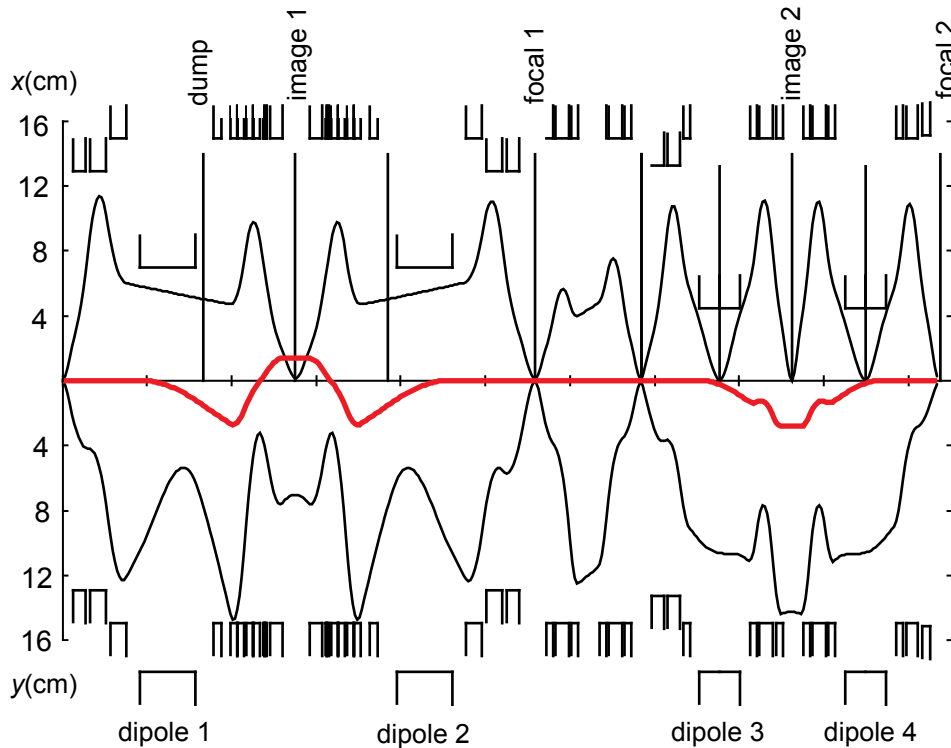


Figure 5.98: First order beam envelopes calculated with the TRANSPORT code for the entire fragment separation system. The red line shows the momentum dispersion in (cm/%). The two stages of separation allow two wedges to be used to remove unwanted secondary fragments produced in the first wedge by the main separation. The main separator can also be used for particle tagging. The wedges will be located at image 1 and image 2.

Wedge design

An important part of the fragment separator operation is the wedge-shaped degrading material used to purify the beams. The required wedges must have a uniformity of better than 0.1% in thickness and hence will require precision flat surfaces. The fragment separators in current operation use curved degraders or flat materials with machined angles to produce achromatic wedges. While these solutions are adequate at present, a conceptual design for a wedge system based on a layer of liquid water between two adjustable ultra-flat plates has been initiated. Such a device will allow the angle of the wedge to be adjusted as needed for the separation of selected isotopes.

Beam dump

The high radiation area near the production target and beam dump is a key issue in the baseline design and is the focus of the RIAFRAG R&D project [DOE41313]. Collection of the hundreds of kilowatts of primary beam in a projectile fragment

separator is a difficult task. To complicate matters further, the desired fragments are often close to the primary beam in rigidity. To accommodate all the requirements, the design concept is to have a momentum focus directly after the first dipole and locate the dump at that focus.

This solution is shown schematically in Figure 5.94, with the dump located directly behind the first dipole. The optical solution shown in Figure 5.95 allows more space for the dump and shielding compared to standard separator systems. This configuration limits the area of high radiation and limits the required number of radiation resistant magnets. Further investigation of this design and of operational issues such as monitoring the location of the primary beam on the beam dump are necessary. For example, a failure mode such as a sudden loss of the target would cause the radius of curvature of the beam to change. The primary beam could miss the dump and continue farther along the separator, perhaps out of the high radiation shielding. Such a dramatic failure mode would be more easily detected and potential radiation exposure minimized in this design.

The difference in magnetic rigidity, $B\rho$, of the desired fragment from that of the primary beam varies considerably and makes the design of the beam dump difficult. Figure 5.99 shows the various rare isotope beams that can be produced with a high-energy fragment separator with a color scale that indicates the magnetic rigidity ratio $F_{B\rho} = B\rho_{\text{fragment}}/B\rho_{\text{beam}}$. The large variation of the location of the primary beam relative to the selected fragment of interest following the first dipole is illustrated in Figure 5.100. The figure shows the trajectories of primary beams as a function of $F_{B\rho}$, with the preseparator dipole set so that the fragment passes through the center of the fragment-selecting aperture, using the $F_{B\rho}$ color code given in Figure 5.99.

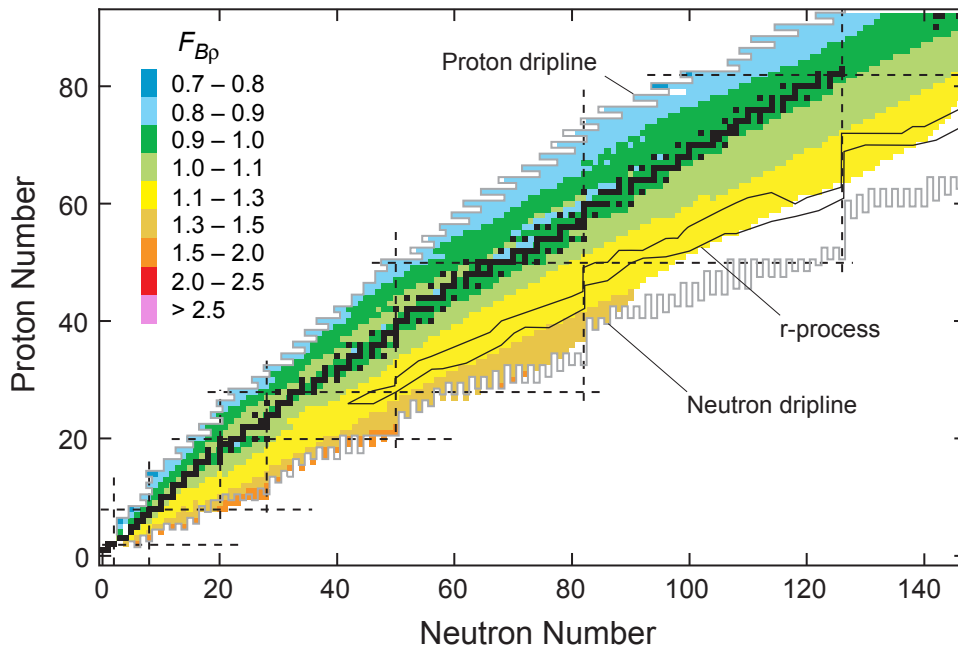


Figure 5.99: The ratio $F_{B\rho} = B\rho_{\text{fragment}}/B\rho_{\text{beam}}$ of the magnetic rigidity of a given fragment to that of the primary beam. The location of the primary beam at the position of the beam dump for the different values of $F_{B\rho}$ is shown in Figure 5.100 with the same color code.

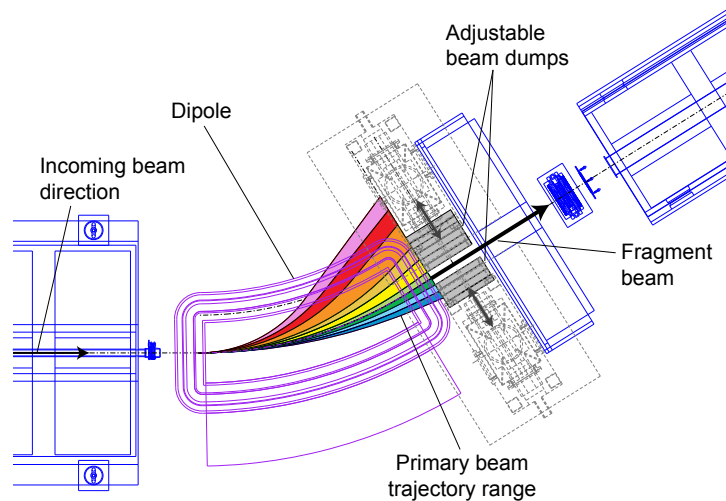


Figure 5.100: Separation of primary beams from the selected fragment beam as a function of F_{Bp} using the color code given in Figure 5.99. The preseparator dipole magnetic field is set so that the selected secondary fragment passes through the center of the selection collimator (shown here wide open). The width of the selection collimator can be varied. Primary beams with $|F_{Bp} - 1| \geq 0.01$ can be intercepted by the collimator.

The variety of beam trajectories is a significant difficulty for the beam dump design. In addition, in the most extreme cases with neutron-rich secondary beams (and corresponding significantly lower primary beam rigidity), some of the defocused primary beam will strike the dipole pole-face. Hence, it will be necessary to place water-cooled liners on the pole faces. There will also have to be fixed catchers to collect unwanted fragments.

Two possible beam dump configurations are being considered. The maximum beam power per unit area that can be tolerated is estimated to be 10 kW/cm^2 . For primary beams near the fragment rigidity, spot sizes at the dump are expected to be approximately 1 cm horizontal by 3 cm vertical. In the case of a uranium primary beam, power will be spread horizontally because the beam will consist of several charge states. A fixed water-cooled copper beam dump with a V-shaped profile to distribute the beam along the entrance surface should be able to achieve the desired power limit for a beam power of $\leq 100 \text{ kW}$. A similar dump design is planned for the 100 kW beams at the BigRIPS separator at RIKEN [Kub03] and at the SuperFRS separator at GSI [Gei03]. Such a stationary profiled dump may also work for 400 kW beams, but the radiation damage of the copper may not be sustainable. Hence we are also considering the design of a rotating dump where ions stop in water contained in an aluminum drum. Such a dump design is expected to have a greater than one year lifetime but is clearly more complicated to operate.

A key research and development task is to determine if a fixed dump will be viable through radiation damage studies with penetrating uranium ions. This can be done at the NSCL and will be pursued in the future.

A concept for the rotating beam dump that will likely work for beams up to 400 kW is shown in Figure 5.101 [Ste06]. Operation of the dumps involves rotating the barrels in order to spread the beam power over the perimeter of the barrel. Water is used to cool the metal of the dumps and absorb the beam power that penetrates the barrel wall. Cooling water enters and exits the barrels along the rotating hollow

shafts that are connected to the water supply. An electric motor is used to drive the rotation of the shaft and barrel. The dumps consist of two assemblies with each assembly having a barrel shape and a shaft that penetrates a vacuum wall structure, a rotating vacuum pass-through at the vacuum wall, a water union coupling, an electric motor and drive belt, and an expansion joint with a motor to allow horizontal motion of each dump.

In order to cover the full range of fragment and beam combinations, the dump consists of two rotating barrel shapes that are placed on each side of the beam centerline. The dumps can be moved perpendicular to the beam path to intercept the primary beam as needed. The dumps are located in a vacuum space surrounding the dipole magnet. Horizontal motion is needed to allow the space between the dumps to be adjusted for cases where the rigidity of the fragment is within 1% of that of the beam.

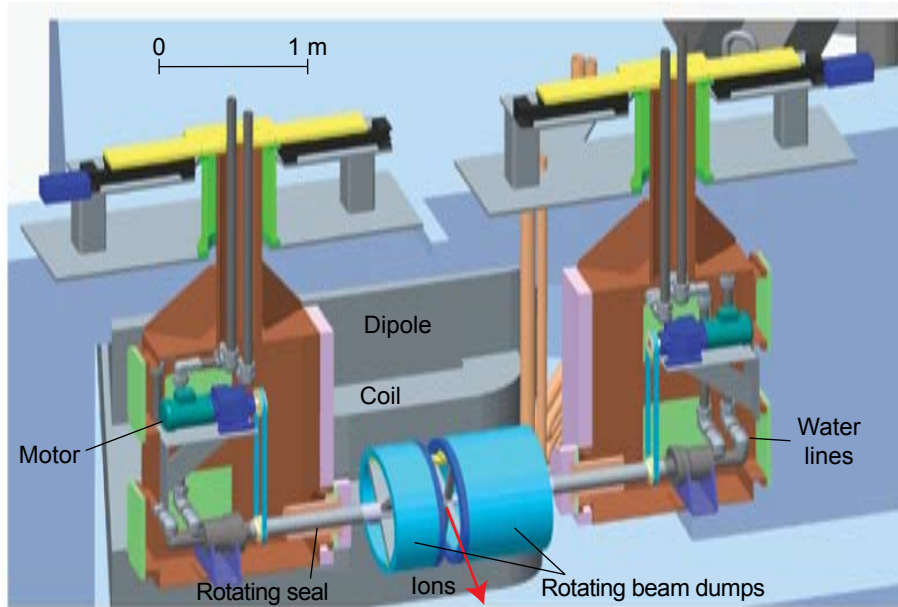


Figure 5.101: Schematic arrangement of the barrel shaped beam dumps located downstream of the first dipole magnet. The view is from the down stream side of the dumps (view from above is given in Figure 5.100).

5.4.2.9 Beam and fragment diagnostics

The required beam diagnostics fall into three main categories, which include primary beam setup and monitoring on the production target, preseparator diagnostics and tuning for initial fragment identification, and main separator diagnostics and on-line beam tracking.

The primary beam diagnostic measurements will be performed with a wire scanning system during the initial beam tuning. Thermal imaging of the beam spot on the target will be used to monitor the beam position and stability. A non-intercepting beam probe will be used to monitor the beam intensity. These components will be supported on a shielding plug located just prior to the production target so that the components can be exchanged with the remote handling system.

The preseparator diagnostic measurements will be similar to those in the A1900 separator, with position and time measured at the wedge position and particle ID

(position, energy loss, and total energy) at the first focal plane. The detectors at the location of the wedge will be remotely removed when production runs are underway. The focal plane of the preseparator will have the capability of γ -ray tagging of isomers to confirm the particle identification.

The diagnostics for the main separator can be reused from the A1900, including the current position and timing detectors from the middle of the A1900 and the particle ID detectors (including γ -ray tagging) from the focal plane.

5.4.2.10 Isotope harvesting possibilities

There will be a large number of isotopes produced that could be harvested and used for a number of applications. Isotope harvesting could be implemented in the separators to allow recovery of these isotopes without significant disruption to the nuclear science program. The locations where unused isotopes could be harvested are the preseparator beam dump with active (water line) or passive catchers, irradiation capabilities in front of or behind beam dumps, or at the mass selection apertures in both stages of the fragment separator. Hundreds of isotopes might be available, depending on the science program and the harvesting techniques.

Radioisotope harvesting would require a radiochemical laboratory for processing the isotopes. Such facilities would also benefit basic research by making available a supply of new radioisotopes for studies in various areas of chemistry, biology, and perhaps industrial research. The preseparator hot cell will have remote manipulation capabilities where some of the processing facility needs can be met. Further, more advanced chemical facilities could be developed in collaboration with the MSU Radiology Department and their PET center, with considerable radiochemical experience on campus. As a result, research quantities of isotopes could be made available for experimental programs.

5.4.2.11 Magnet design

Radiation resistant preseparator magnets

The initial operation of the facility will likely be at beam power levels below 400 kW. This allows, for the first years of operation, the use of cost effective radiation tolerant magnets that might be unacceptable at the 400 kW level. For example, magnets that would only survive for a year at 400 kW will last four years at 100 kW – an acceptable limit. This means that the most demanding radiation resistant magnets need not be implemented initially, and further research and development can be carried out in parallel to initial operation. The first set of magnets will be radiation tolerant, where the useful lifetime is determined by the lifetime of the insulation. This magnet choice introduces an uncertainty in the lifetime estimate because composite materials used in the insulation have variations in their properties and their failure modes are unpredictable. This is a subject of current research and development.

The parameters of the quadrupole and dipole magnets are given in Table 5.35. The quadrupole magnets will be arranged into triplets, with one triplet per cryostat. Although the magnet parameters for the third and fourth triplets are the same as those for the first and second, the latter triplets only need to be radiation “tolerant” and not radiation “hard.”

In order to limit the load on the helium refrigeration system, the heating of any material that is held at 4 K by prompt neutron radiation must be minimized. The first triplet in the RIKEN fragment separator uses an iron-free design [Kus04] that greatly reduces the mass of material at 4 K. The problem with this approach is that the magnetic fields at the coil position are high (7 T), and since the force on the wires goes as the square of the field, the radiation-induced degradation of the insulation will be increased relative to iron-dominated magnets. A solution is based on the design suggested by BNL for high temperature superconducting (HTS) coils [Gup04]. Iron is used at room temperature and the coils are enclosed in cryostats within the iron similar to the dipole coil packages in the A1900. The increased amount of iron is offset by the increased lifetime of the coils because of their operation in lower magnetic fields. A radiation tolerant cyanate ester, such as CTD-422, can be used for total doses of up to 50 MGy. A test dipole using coils insulated with this ester was successfully tested recently at the NSCL [Zel05a]. The development of this type of magnet is the subject of further research and development.

A lifetime dose of 50 MGy should allow a radiation tolerant first quadrupole to survive for about 4–5 years. The requirement to use coils that would last for the life of the project at a power level of 400 kW requires radiation tolerances of greater than 200 MGy. This is beyond the useful lifetime of any organic insulation. Additionally, any future increase in beam power would further reduce the projected lifetime of the magnets. The ultimate limit is the tolerance of the superconductor of about 500 MGy. High power operation means that the insulation must be as tolerant or more so than the superconductor, limiting the choice to inorganic materials. Development of metal oxide insulated Cable-In-Conduit-Conductor (CICC) [Zel05b] is underway at the NSCL. Another option is to build more expensive CICC-coils for replacement of the original coils when they fail. The iron yoke would not need to be replaced.

Main separator magnets

The high acceptance of the separator requires large aperture quadrupoles. A sufficient number of dipoles and quadrupoles are available by reuse of the A1900 magnets. The parameters of the magnets are given in Table 5.37. Since the high-radiation environment is limited to the preseparator, the expected lifetime of the re-used A1900 magnets is greater than 20 years.

5.5 Low-energy beam generation via gas stopping of fragment beams

The stopping of the in-flight separated rare isotope beams in gas to provide low energy beams is an integral part of the ISF concept. The conversion of relativistic fragments into low-energy beams is important because it makes it possible to produce rare isotopes via projectile fragmentation and to use them for experiments at low energies (stopped beams) or for reacceleration. Given that a number of refractory-element beams are not available via the ISOL technique and that fast beams have an advantage in the production of the rarest and most short-lived isotopes, the ISF will allow a wealth of new experiments with stopped and reaccelerated ion beams. The basic principle of gas stopping is simple; after appropriate slowing down of the fast fragments in solid degraders, the ions are finally stopped in a chamber with helium gas. As the ions remain singly- or doubly-charged, they

can be guided out of the gas cell using static or rf electric fields and gas flow, and then they can be converted into a low-emittance, low-energy ion beam by means of rf ion guiding techniques.

In order to maximize the benefit of the gas stopping approach, the following requirements must be fulfilled:

- Short extraction times. In order to minimize decay losses, the extraction time should be comparable to or shorter than the shortest half-life of the ions to be studied. Extraction times of 10 ms or less would be ideal.
- Handling of high beam intensities. The facility should provide secondary beam intensities of up to 10^9 s⁻¹, many orders of magnitude higher than those available at present fragmentation facilities.
- Applicability to all fragment beams. In order to be universal, the gas stopper needs to be able to handle beams with a large range of atomic numbers and neutron-to-proton ratios.

Gas stopping devices for fast fragments have been built and extensively studied [Wei05b,Wad03,Tak05] at present-generation (low-power) fragmentation facilities. Although these devices have been used successfully for experimental programs, they fall short of fulfilling the requirements indicated above. The ISF will use a new powerful gas-stopping concept, the cyclotron stopper [Bol05b,Kat98]. This device is based on a gas-filled cyclotron magnet combined with radio-frequency ion guiding techniques in the extraction region. The new technique will provide extraction times down to several milliseconds, beam-handling capability of $>10^8$ s⁻¹, and can be applied to a large range of isotopes without introducing significant losses of efficiency.

5.5.1 Limitations of classical gas stopper concepts

Several groups from around the world are currently working on projects to stop ion beams in gas filled chambers from both projectile fragmentation processes [Wei05b,Wad03,Tak05] and low-energy reactions [Sik03,Sav03]. All of the groups use elongated gas-filled chambers, and the fast ions are stopped after energy bunching and degrading. The gas-stopping cells are equipped with electrodes to transport the stopped ions to a small orifice by means of static and/or rf electric fields. The ions are swept out of the gas cell through this orifice by the gas flow and are then guided with rf techniques through a series of differential pumping stages before they are accelerated to the desired beam energy. The efficient collection of fragmentation beams, with large momentum distributions from the production reaction, requires ion-optical compression [Wei00] of the secondary beam momentum distribution in order to keep the gas cell size reasonable and to minimize ion extraction times.

Three facilities are currently available worldwide for the testing of gas stopping of high-energy fragmentation beams. At RIKEN, substantial R&D work has been performed [Wad03,Tak05] on stopping very light ion beams at energies of about 80 MeV/nucleon, and the first successful experiments with ⁸Be have recently been reported. A slightly smaller gas catcher built by a collaboration headed by the ANL group [Tri04] was tested with low-energy beams from ATLAS and with radioactive sources before it was shipped to GSI in 2004 for testing with relativistic projectile

fragments. Up to date only one experiment at low beam rates has been performed (as of summer 2006), that successfully demonstrated the stopping and extraction of neutron deficient chromium isotopes produced by the GSI fragment separator at energies of about 280 MeV/nucleon.

At the NSCL, the secondary beam energies are typically 90–100 MeV/nucleon, only about a factor of 1.5 lower than the secondary beam energies to be expected at the ISF. The NSCL gas stopping system has seen the largest number of experimental tests and the widest range of extracted beams (more than three years of operation and 15 experimental runs). Significant expertise and a solid understanding of the performance and limitations of linear gas stoppers have been gained from these tests. Systematic studies of range compression, stopping, and extraction of energetic fragments have been completed and compared to detailed simulations, and the results have been published [Wei04a-c]. The NSCL device was the first projectile fragment gas stopper used for nuclear physics experiments. An experimental program using thermalized beams has very successfully started with high-precision Penning-trap mass measurements on a number of short-lived isotopes [Bol06b].

Published results from systematic studies not only obtained at fragmentation facilities but also from gas stoppers for low-energy beams and reaction recoils show an overall decrease in the efficiency with increasing beam rate and the resulting ionization density in the stopping gas. The reduction in efficiency comes from the ionization of the helium gas during the stopping process of the incoming ions. The electrons are removed very quickly by the applied electric fields, leaving the remaining positive charge of the helium ions in the stopping volume. This positive space charge pushes the desired ions towards the walls of the gas cell and counteracts the voltage applied to drift the ions toward the extraction region of the gas cell. A recent review [Huy02] suggested that the critical parameter for these devices is the ionization-rate density, i.e., the number of ion-pairs created per unit gas volume and time.

Figure 5.102 presents a summary of the reported extraction efficiencies as a function of the ionization rate density for very different systems and different beam energy regimes that nonetheless shows a concordance of the data [Mor06]. In the case of gas cells built by ANL, efficiency values have been published but information on the ionization rate density was incomplete. Best estimates for parameters have been made leading to ionization rate density values in the range indicated by the grey area in Figure 5.102. A clear trend of decreasing efficiency with increasing ion-density is observed. If a large gas cell with more than 10 liters of stopping volume and maximum beam rates of 10^9 s^{-1} were used, the ionization rate density would be of the order of 10^{11} ion-electron pairs (IP) per second and per cubic centimeter. In such a case, the previous work summarized in the figure predicts large extraction losses. Particle-in-cell and mean-field simulations of ion-motion in such linear gas cells performed at the NSCL support these findings [Sch06d] as does a classical analysis performed by the RIKEN group [Tak05].

Another significant shortcoming of the linear gas cells is their relatively long ion extraction time. The average extraction time is determined by the gas pressure, the average distance that the thermalized ion has to travel, and the maximum electric field that can be applied without creating discharges in the helium gas. For stopping high-energy fragment beams (100 MeV/nucleon), the gas cell “thickness”

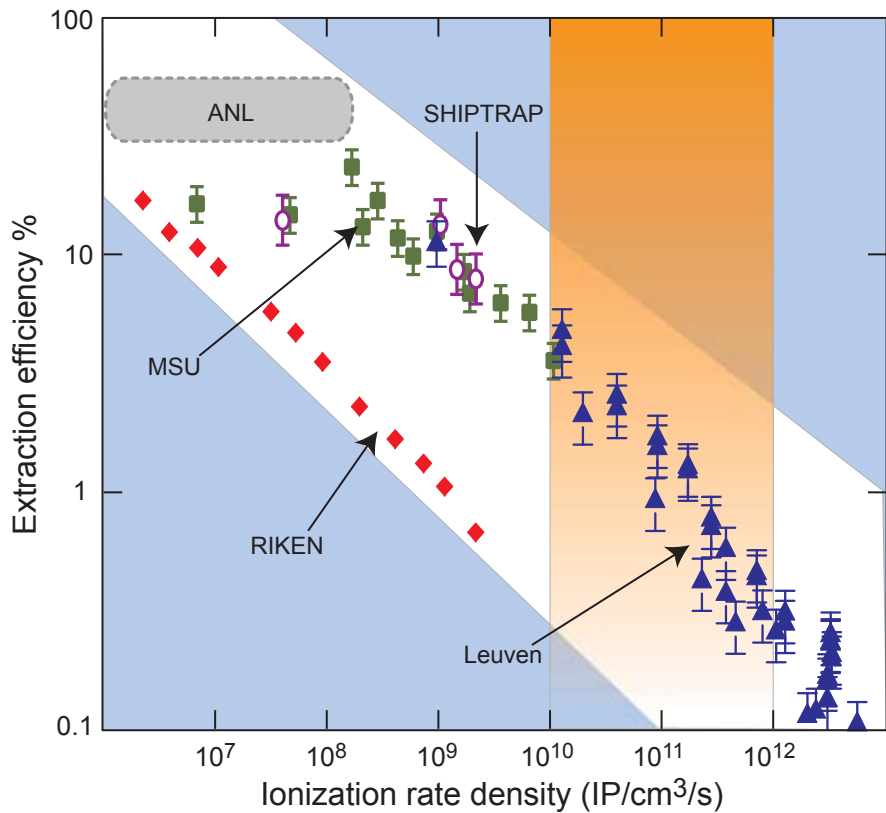


Figure 5.102: Observation of beam rate-dependent efficiencies as a function of the ionization rate density in low and high-energy linear gas stopping systems at MSU, RIKEN, GSI/SHIPTRAP, LISOL/Leuven, and ANL. The vertical band indicates the range of ionization rate densities to be expected at next-generation facilities like the ISF.

needs to be approximately $pL = 0.5$ bar m of helium gas due to range straggling in the solid degraders. The typical electric field strength that can be applied for guiding the ions towards the exit of the gas cell is on the order of $E = 10$ V/cm. Using a typical reduced ion mobility of $K = 20$ cm²/(Vs) for an atomic ion at room temperature in helium results in an extraction time, t , for an ion starting at the entrance window of the gas cell of $t = pL / (EKp/p_0) = 250$ bar ms, where p_0 is the normal pressure. Assuming a constant electric drift field and uniform stopping in the gas cell at a pressure of 1 bar, this leads to an average extraction time of 125 ms. This time is independent of the length of the gas cell if the pressure is adjusted to keep the target thickness pL constant. Such long extraction times would impose a serious limitation on the shortest half-lives that can be extracted from a linear gas cell and used in subsequent experiments.

The third shortcoming of linear cells is the fact that it is very difficult to stop light ions in gas with a high efficiency due to the large longitudinal range straggling of light ions, which easily exceeds the length of the gas cell. For example, the RIKEN gas cell (two meters long and operated at a pressure of 100 mbar) can stop only 11% of the incoming ⁸Li ions [Tak05]. Employing much larger gas cells for a more efficient stopping of such light ions is impractical and the use of higher pressures is limited. Radio frequency guiding devices such as rf carpets, rf walls, or rf funnels are only effective at low pressures because the effective force generated by the rf fields which prevents the ions from touching the electrodes decreases quadratically

with gas pressure. In summary, the stopping of beams of light ions is only possible in linear gas cells if significant efficiency losses can be tolerated.

5.5.2 The cyclotron stopper

A new device for the thermalization of fast ion beams based on the slowing down of ions in a buffer gas in a focusing magnetic field is under development at the NSCL. The device being developed can be used at the ISF. The focusing properties of a cyclotron-type magnet confine the ions in the radial and axial dimensions during the deceleration process, and the ionization is distributed along a much longer path at lower pressure compared to “conventional” linear gas cells. Figure 5.103 shows a schematic overview of such a cyclotron ion beam stopper. It consists of a cyclotron magnet and a gas-filled vacuum chamber with charge collection electrodes (for the helium ions) close to the pole faces.

The fast rare isotope beam is injected tangentially into the system and passes through a solid degrader with a thickness adjusted such that the degraded beam follows an inward spiraling motion around the center of the system. The final transport of the ions to the extraction orifice on the central axis uses an rf carpet [Kat98]. Once on the axis, an rf quadrupole ion guide will transport the ions through a differential pumping system in the yoke of the magnet. Such a cyclotron stopper scheme is not completely new, since gas-filled cyclotrons have been successfully used to stop antiprotons, pions, and muons [Sim88,Sim93]; Katayama et al. have proposed a related scheme [Kat98] to stop light ions.

The full benefit of the cyclotron stopper concept, in particular the ability to stop high intensity beams, was shown in initial computer simulations carried out at the NSCL [Bol05b]. Figure 5.104 illustrates the important features of this system for a 100 MeV/nucleon beam of ^{78}Br ions degraded to 610 MeV inside a 2 T magnet system (for details of the calculations see [Bol05b]). The device is operated at a helium gas pressure of 10 mbar and the ions stop after traveling about 60 m. The most

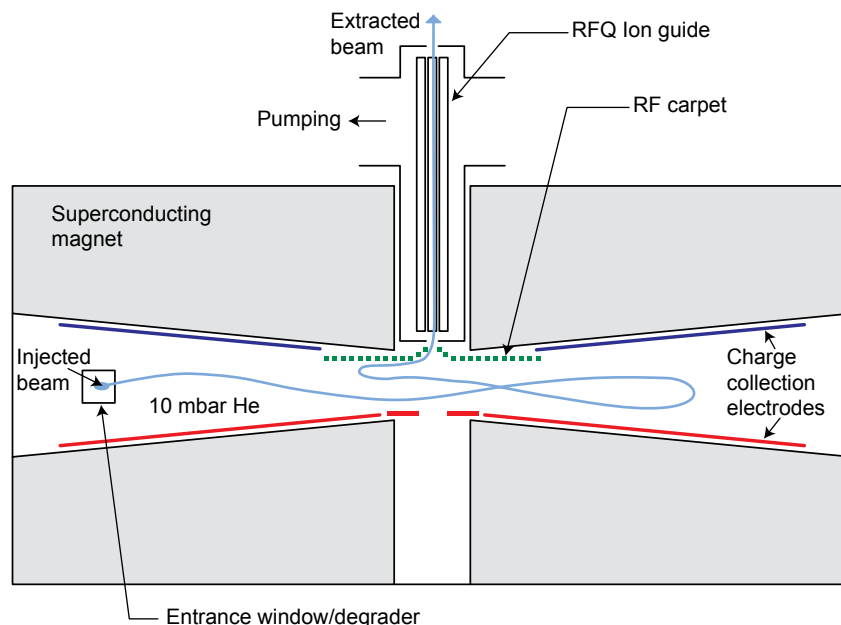


Figure 5.103: Schematic diagram of the cyclotron stopper concept for stopping fast ion beams in gas for extraction as low-energy ion beams.

remarkable feature of this system is the spatial separation of stopped-ion distribution near the center and the high ionization density in a ring further from the center. This separation is the key to minimizing losses of the thermalized ions due to the space charge effects described above. It turns out that even with 10^8 incoming ions per second, the space charge due to helium ions can be essentially removed with a weak axial electric field between charge collection electrodes near the pole faces, as indicated in Figure 5.103. Notice that the incident ions are still very energetic (MeV) when they traverse the region of maximum ionization density and will not be affected by the space charge very much. Therefore, the rate limit of this system is expected to be far above $10^8/s$ incident particles. Once stopped, the ions will be guided to an extraction orifice on the central axis. This guiding can be done with electrostatic fields combined with an rf carpet [Kat98], a planar arrangement of concentric rf electrodes providing a repelling force (see Section 5.5.2.2). For example, a guiding field of 10 V/cm towards the center of the carpet and a helium pressure of 10 mbar will bring the ions from a radius of 50 cm to the extraction orifice in less than 5 ms.

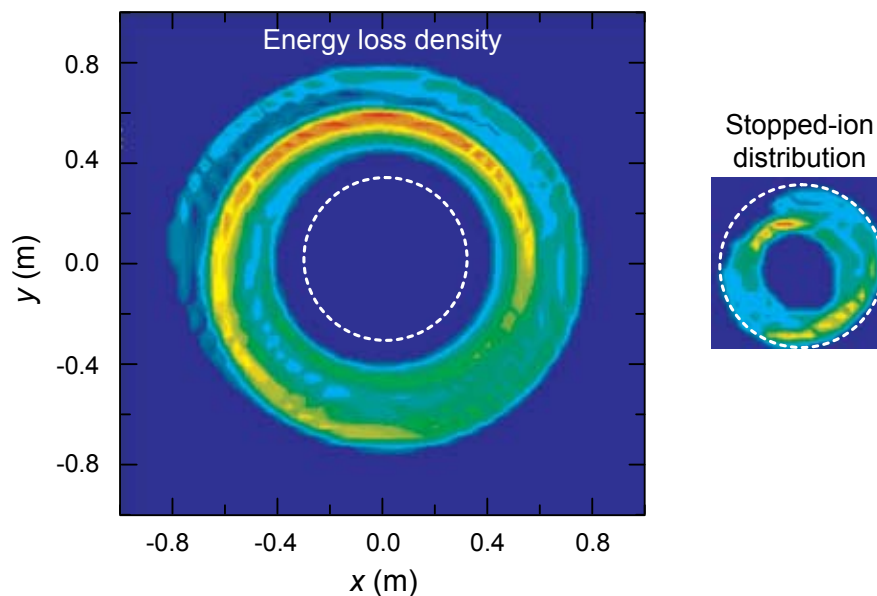


Figure 5.104: Left: Energy loss density distribution in the plane of the cyclotron stopper caused by the stopping of ^{78}Br ions. Right: Final distribution of stopped ions in the same plane on the same scale (N.B., the dashed circle has the same radius in both figures).

The initial simulations [Bol05b] have been followed by a series of much more detailed studies going hand-in-hand with the conceptual design of the full system. From the results obtained to date, the expected properties of the cyclotron stopper can be summarized as:

- a fast extraction time of <10 ms for practically all beams produced at the ISF, matching the advantages of the in-flight separation technique
- a secondary beam rate limit higher than $10^8/s$, compatible with the highest beam intensities available at second-generation facilities such as the ISF
- the capability to stop secondary beams of light to heavy elements with a mass-to-charge ratio A/Z of $1.75 < A/Z < 3$ with very high efficiencies again matching the advantages of the in-flight separation technique

5.5.2.1 Magnet and mechanical design

The present design for the magnet has been obtained through an iterative approach involving magnet coil and mechanical design, detailed magnetic field simulation, and ion-trajectory simulation in the calculated magnetic field. The design process is not completed but is approaching the phase of fine-tuning system performance and features. The present cyclotron stopper design concept, shown in Figure 5.105, uses a vertically oriented iron-dominated superconducting magnet with maximum field strength of 2.1 Tesla. Figure 5.106 shows the two-dimensional variation of the magnetic field in the midplane of the magnet. The vertical magnet arrangement was chosen because it will allow the extraction of low-energy beams in the horizontal plane, which simplifies low-energy ion transport out of the stray field.

The magnet will be constructed such that half of the yoke can be moved to allow access to the internal components. Penetrations in the yoke needed for beam injection and extraction as well as chamber support and instrumentation will be arranged in a symmetric pattern. The inner vacuum chamber will form the volume in which the ions are slowed down and stopped. In the present design, the stopping chamber has a radius of approximately 120 cm and an inner height of approximately 10 cm. The injection radius has been increased to about 105 cm compared to the first simulations to maximize the acceptance for neutron-rich beams. The chamber will be equipped with a set of ionization collection plates and a central rf carpet for the extraction of the stopped secondary ions. A beam degrader, adjustable in position and thickness, will be inserted radially along with charged-particle detectors for determination of the beam position and energy after degradation. The entire internal chamber will be cryogenically cooled to provide ultra-high vacuum conditions and ensure high purity of the stopping gas inside the chamber. In order to minimize heat transfer, super insulation and a guard vacuum will surround the stopping chamber.

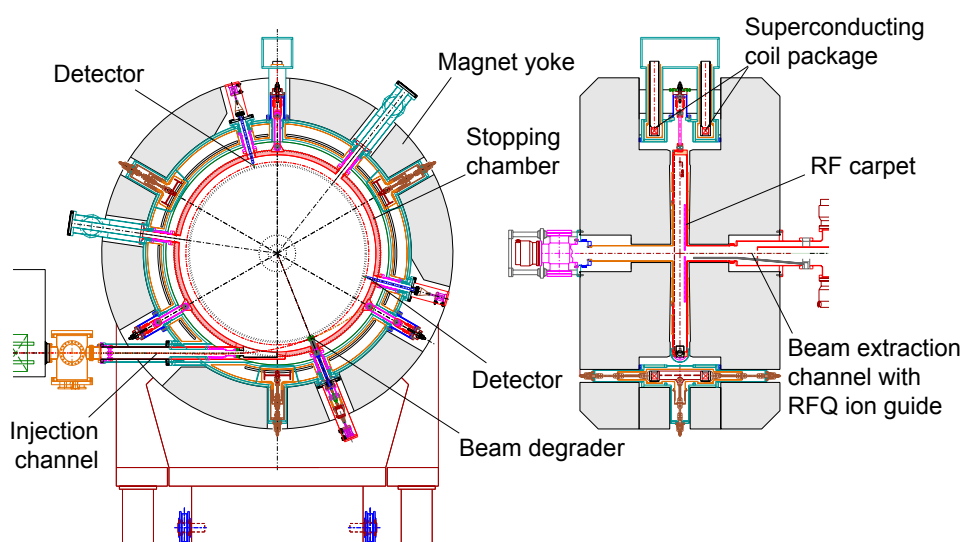


Figure 5.105: Mechanical design of the cyclotron stopper. The fast ion beam will be injected into a gas-filled vacuum chamber located between the pole faces of a superconducting, iron-dominated, cyclotron-type magnet. An adjustable degrader will be used to achieve the beam rigidity required to confine and slow down the beam. Once stopped, the ions will be guided out of the system via an rf carpet and an RFQ ion guide system.

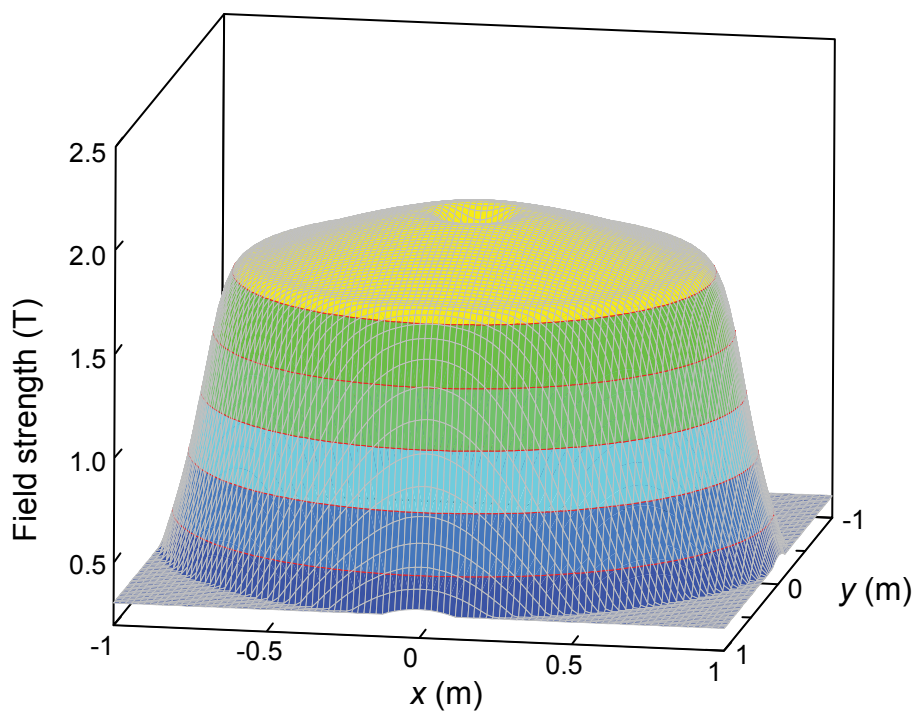


Figure 5.106: The calculated magnetic field created on the midplane of a superconducting 2-Tesla magnet system. This is one field option considered for the cyclotron stopper. The central depression is due to the axial extraction bore of the system.

Once the secondary ions reach the center of the guiding rf-carpet, they leave the stopping chamber through an orifice on the central axis. Since the gas pressure in the cyclotron stopper is low compared to existing gas cells, larger orifice diameters can be used than those in a linear gas stopper. The larger orifice eases the ion extraction and also minimizes space charge effects in the transition region. Using concepts already demonstrated with the NSCL gas stopper and the Low-Energy Beam and Ion Trap (LEBIT) facility [Rin06], very effective differential pumping can be realized by a combination of two large-aperture rf ion guides separated by a micro-RFQ. Cooling the ion guide to cryogenic temperatures is also being considered. A cryogenic ion-guide would allow beams with very low emittances to be extracted from the gas stopper, similar to those currently extracted from the LEBIT beam cooler [Sch03b]. A final pumping stage is used to reach a vacuum of $<10^{-6}$ mbar in a chamber following the ion guide system. Here, an electrostatic acceleration system will be used to increase the ion energy to approximately 30 keV for further transport.

The last major component of the low-energy beam production system is a mass separation stage. A mass separator is needed to suppress undesired stable molecular ion beams resulting from the charge-exchange of the residual gas with the helium ions created during the slowing down process in the stopping chamber. Such molecular impurities are expected to be very low from the cryogenic stopping chamber compared to the linear stoppers currently operated at room temperature. Nevertheless, as an additional measure to obtain very pure low-energy beams, a mass separation stage will be useful. With the excellent beam quality from the cyclotron stopper, resolving powers of a few hundred can be easily achieved in a compact magnetic system.

5.5.2.2 Beam dynamics studies

Beam transport and momentum compression

To maximize the acceptance of the system, it is necessary to reduce the momentum spread of the rare isotope beam provided by the fragment separator ($\Delta p/p \approx 5\%$) before passing through the final degrader in the cyclotron stopper. A mono-energetic beam will have the maximum separation between the region of large ionization and ion stopping. Simulations of the high energy beam optics and present results with the existing NSCL gas cell indicate that a reduction of the momentum spread by an order of magnitude to $\Delta p/p \approx 0.5\%$ is possible and sufficient for this purpose.

Momentum compression can be achieved by implementing an ion-optical scheme [Wei00,Wei04b] in the secondary beam transport line before the cyclotron stopper with momentum dispersion and a degrader shaped to match the dispersion. By choosing an appropriate thickness and wedge angle, a reduction in momentum spread is achieved at the cost of a larger beam emittance, thus the compression must occur immediately before the cyclotron stopper.

A conceptual layout for the momentum compensation stage is shown in Figure 5.107.

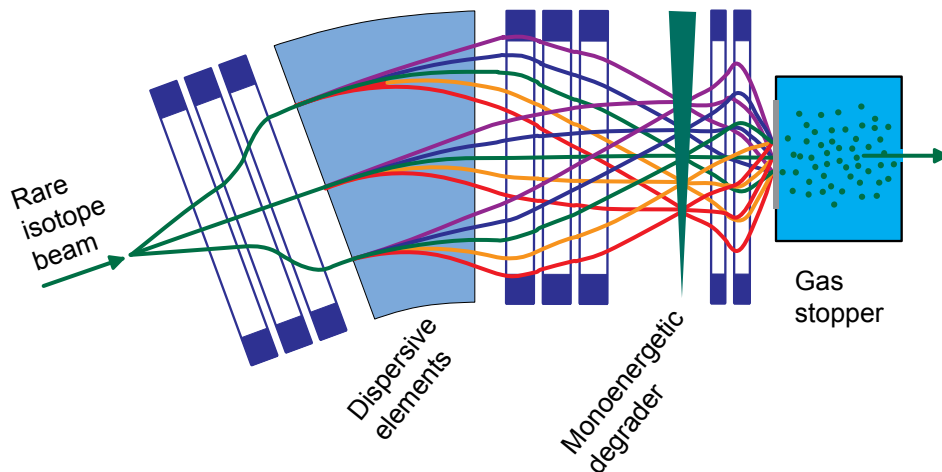


Figure 5.107: Schematic drawing of the momentum compensation stage placed just before the cyclotron stopper in order to minimize range straggling.

A key specification for the momentum compression stage is the momentum resolving power. Due to aberrations in the separator, we anticipate that the first order spot size of 1 mm will be doubled to 2 mm. Hence, to achieve a momentum resolving power of 1000, a dispersion-to-magnification ratio D/M of 2000 will be required in the momentum compressor. We have designed a momentum compensation stage with these specifications, and Figure 5.108 shows the results for the range straggling as a function of momentum resolving power for this system. The desired resolving power can be achieved by the use of two triplet magnets and one 45° bend dipole (equivalent to an A1900 dipole).

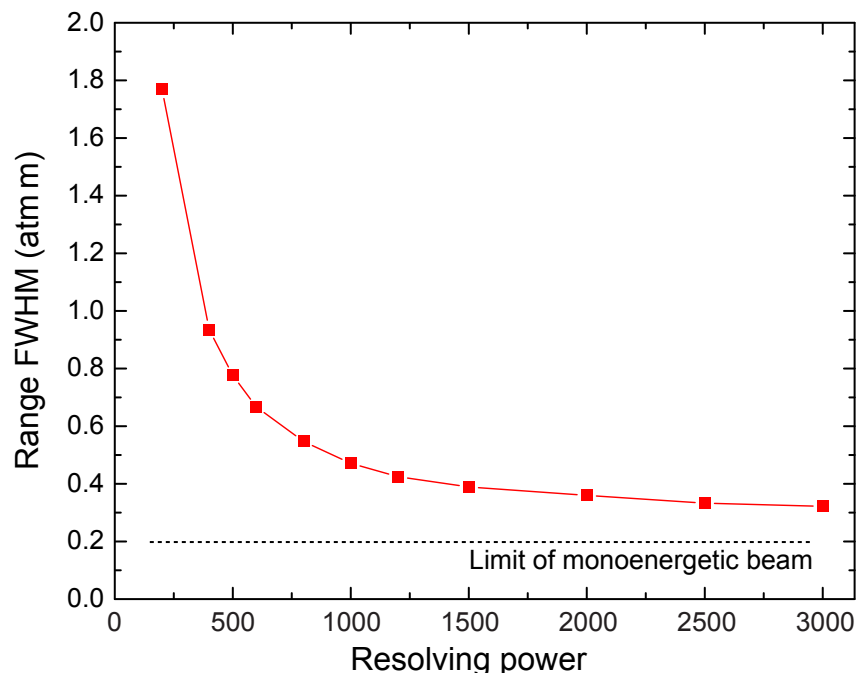


Figure 5.108: Illustration of the reduction of range straggling as a function of the resolving power of the momentum compression stage. The range width of a ^{72}Br beam at 150 MeV/nucleon with a 10% momentum acceptance and a 2 mm objects spot size is shown. The figure indicates that this stage should have a momentum resolving power of better than 1000. The limit is due to energy loss straggling in the degrading material.

Ion injection

After the momentum compression stage, a triplet will have to be used to match the beam to the acceptance of the cyclotron stopper. The fragments will then have to be transported through the fringe field of the cyclotron magnet before they reach the degrader position. There they should hit the degrader at an angle very close to the tangent of the first orbit. Thus, the momentum dispersion and beam deflection in the injection channel have to be considered carefully. The initial studies show that for a momentum spread of approximately $\Delta p/p = 0.5\%$, the dispersion in the injection channel is small and the increase of beam size on the degrader does not exceed a few millimeters.

It will be important that one can handle beams with a mass-to-charge ratio of $1.75 < A/Z < 3$, which covers essentially the full range from the most proton-rich to most neutron-rich isotopes. While the full suite of simulations has not been completed, it appears that a large range of A/Z beams can be injected into the cyclotron stopper by carefully choosing the target, all of the energy degraders, and the monochromatic wedge. The cyclotron stopper operates with an approximately constant magnetic rigidity after the final degrader. The initial estimates indicate that it will also be possible to operate the momentum compressor and the entrance channel at nearly fixed rigidities. Small variations in the rigidity of the secondary beam can be compensated by either actively correcting the beam path with steering magnets in the injection channel or by allowing the degrader to be moved not only radially but also azimuthally with respect to the center of the magnet system. Both solutions are technically feasible and are being evaluated.

Ion stopping

A large number of simulations have been performed to investigate the stopping of fast fragment ions in helium gas inside a focusing magnetic field. The studies have been performed both with ideal and realistic fields. They included beams with A/Z ratios in the range from 1.75 to 3 and for elements ranging from lithium to indium. The choice of elements was mostly determined by the availability of appropriate data for charge-exchange cross sections. The goal of the simulations was twofold, to develop a solid understanding of the properties of a cyclotron stopper and to optimize the operational parameters and to identify any critical regions of the parameter space.

Two independent Monte Carlo programs were written and used to study ion stopping in a cyclotron stopper. The results from the programs were cross checked and found to provide essentially identical results. One program was optimized for large-scale parameter exploration after the ions pass through the degrader, while the other program includes the injection path of the ions through the yoke and into the strong field at the degrader. The effect of the degrader itself on the secondary beam is taken from SRIM [Zie04] and LISE++ [Tar04], which provide information on beam dispersion and momentum spread. The stopping process in both programs follows the calculated ion motion, taking the Lorentz force and the energy-dependent stopping power into account as well as the charge-exchange and small-angle multiple scattering. Multiple-electron loss or capture is neglected since these cross sections are more than an order of magnitude smaller than those for one-electron processes. The stopping power inside the gas is obtained from SRIM stopping tables for the desired ion species in helium and parameterized in the energy range from 1 GeV down to 100 eV.

The charge state of the ion during the stopping process is considered in some detail in both programs. The cross sections for electron capture and loss, and the average charge, depend strongly on the ion velocity and the atomic number of the ion. Experimental cross sections are only known for a very limited number of elements and energies. In order to determine the charge-exchange cross sections and the evolution of the average charge state (see [Bol05b] for more details), the formulae and charge-exchange data summarized in a review article by Betz [Bet72] and data from [Woi92] were used. For a ^{79}Br ion with an injection energy of about 600 MeV and a helium pressure of $p_{\text{He}} = 10$ mbar, the mean free path λ is about 6 mm and becomes more than two orders of magnitude smaller when the ions come to rest. This indicates the fact that the ions very closely follow the trajectory given by the equilibrium charge state. Small-angle multiple scattering is also taken into account during the slowing down process of the ions following the procedures discussed in [Sig74]. The correctness of this procedure and its implementation in the programs were checked by comparing angular straggling results from SRIM simulations with those obtained without a magnetic field.

Figure 5.109 shows some representative results for the stopping of a variety of secondary beams. The calculated losses are typically less than a few percent in each case. The only exceptions are very light, neutron-rich, high-rigidity beams. As an extreme example, if the maximum injection rigidity of the system is about 1.6 Tm, a ^{11}Li beam ($A/Z = 3.67$) has to be slowed to an energy of a few tens of MeV to match the system. This is only possible if the degrader is so thick that some of the ions stop inside the degrader and the exiting beam has a relatively

large momentum and angular spread. Nevertheless, even in such an extreme case, preliminary simulation results indicate stopping efficiencies of about 10%. This, together with the fast extraction times, makes the cyclotron stopper the only concept that allows such very exotic and short-lived nuclei to be stopped and extracted with good efficiency.

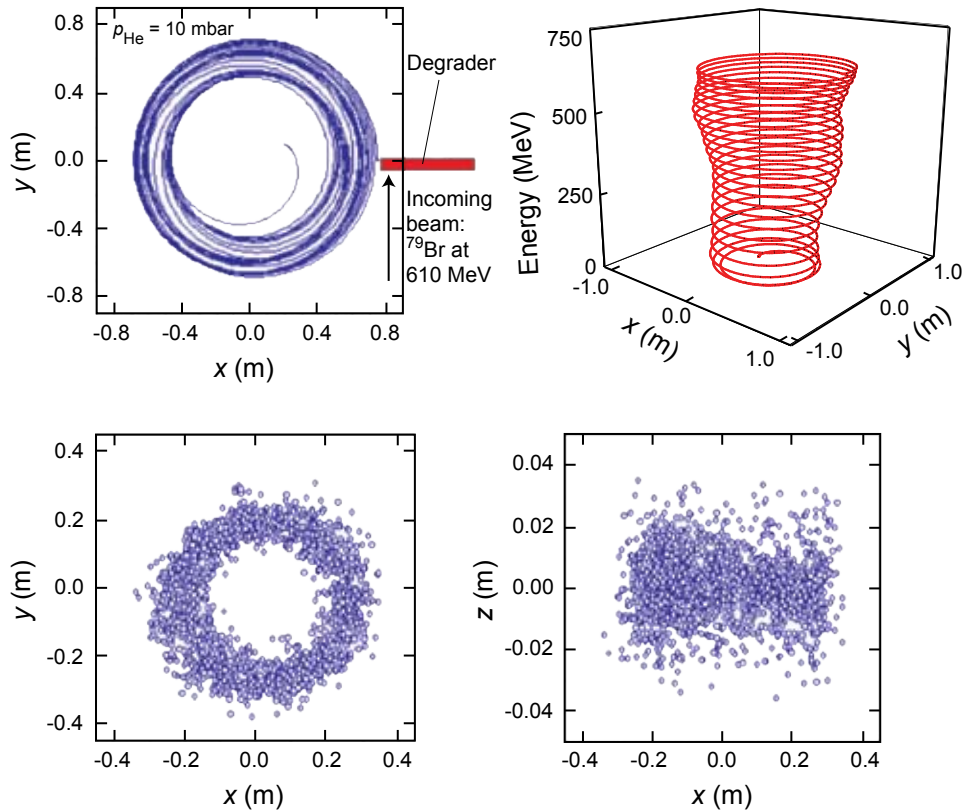


Figure 5.109: Schematic display of the stopping of fast ions in the cyclotron stopper. The top panels show the ion trajectories, while the lower panels show the positions of the stopped ions.

As discussed above, the density distribution of single ionization processes (IP) inside the gas volume can place an important limitation on the extraction efficiency. Given the example shown in Figure 5.104, the average ionization rate density inside the ionization donut is approximately $100 \text{ IP/cm}^3/\text{s}$ per incident rare isotope ion, while the ionization rate density per incident ion drops to $<1 \text{ IP/cm}^3/\text{s}$ in the critical central stopping region. These numbers have to be compared to $1,000\text{--}10,000 \text{ IP/cm}^3/\text{s}$ in linear gas cells for fast beams, which also do not have the advantage of a spatial separation of maximum ionization and stopping. Furthermore, an rf carpet operated at low gas pressure provides an efficient way to very effectively remove He^+ ions (the transport properties of the rf carpet are mass dependent) while transporting the heavier secondary ions to the extraction orifice (see below). In principle, this selection process could also further mitigate space charge problems in linear gas cells (see, for example, discussion in [Tak05]). However, due to the large gas pressure in linear gas cells ($>100 \text{ mbar He}$), the effective repelling potential is two to three orders of magnitude smaller than that achievable in the cyclotron stopper, which also limits the effectiveness of a selective helium ion removal without losing the desired ions in high pressure gas cells.

Ion extraction with an rf carpet system

Once the ions are nearly stopped (thermalized) in the central region of the stopping chamber, they need to be extracted as fast as possible through the central orifice. Since the transverse focusing due to the motion of the ions in the inhomogeneous magnetic field only operates at high velocities, the extraction scheme has to provide both transverse confinement and radial transport of the ions. The cyclotron stopper will use a combination of static and radio-frequency electric fields, as illustrated in Figure 5.110, to collect the thermalized secondary ions. An rf carpet will be used to provide a repelling wall for the ions and at the same time an electric field pointing towards the carpet's center.

The operating principle of an rf carpet [Kat98] relies on the fact that the inhomogeneous, oscillating electric field in which the ions move creates an effective potential that repels the ions. Typical parameters for the operation of such devices are: 10-100 mbar pressure, frequencies in the MHz range, maximum rf amplitudes of a few hundred volts, and neighboring electrode stripes with a pitch of about 1 mm. The low helium pressure in the cyclotron stopper provides an ideal environment for the operation of rf carpets. The modest buffer-gas damping of the particle motion at low pressure, as compared to the over-damping in high-pressure linear gas cells, allows rf carpets to be used with a relatively large pitch and low voltages while still providing a strong repelling force.

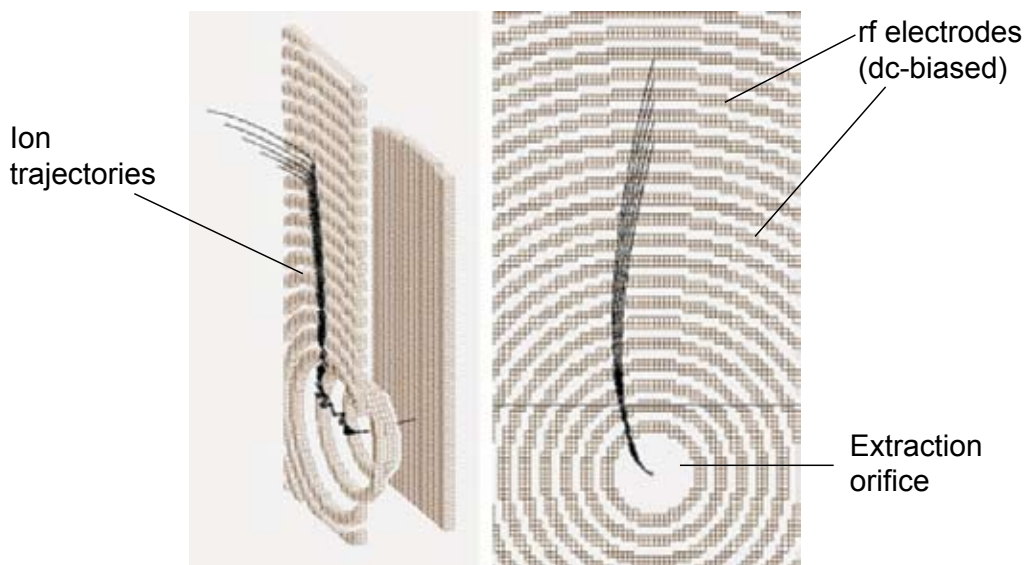


Figure 5.110: Schematic drawing of the rf carpet device used to bring the ions to the extraction region of the cyclotron stopper.

On the opposite side of the chamber from the carpet, an electrode system (pusher) will be used to provide a static potential gradient similar to that on the rf carpet, which will be biased with respect to the carpet to a voltage sufficient to drift the stopped ions towards the rf carpet.

As already mentioned, efficient rf ion guides will be used to transport the ions extracted through the carpet orifice out of the magnet system and into a high-vacuum environment where they can be accelerated for further transport.

5.5.3 Development of the low-energy beam generation system

The low-energy beam generation scheme with momentum compression, cyclotron stopper, and low energy beam transport will be realized and fully tested at the NSCL. This equipment will serve the ongoing low-energy physics program at the LEBIT facility, at a planned laser spectroscopy beamline, and as the proof-of-principle of an efficient reaccelerator scheme involving charge breeding (see Section 5.5.4). The NSCL system will be fully transferred and used at the ISF.

5.5.4 Reacceleration of low-energy beams

Reacceleration of low-energy rare isotope beams available from the cyclotron stopper (see Section 5.5.2) or later, if implemented, from the ISOL station (see Section 6), is an important aspect of the ISF concept. Beams with energies up to 12 MeV/nucleon will be available to carry out an experimental program ranging from low-energy Coulomb excitation experiments and transfer reaction studies to the precise study of astrophysical reactions. The connection of a reacceleration scheme to the gas stopper is of particular importance, since it will provide high quality beams of nuclei not available in this energy regime at any other facility.

In order to maximize the scientific reach of the ISF, the reacceleration scheme must have the following properties:

- high efficiency (>20%) for ions of all elements available at the facility
- high beam rate capacity that matches the maximum secondary beam rates
- high beam purity to minimize background and to avoid ambiguities in the experimental results
- variable time structure of the reaccelerated beam from microsecond pulses to continuous beams to meet a wide range of experimental requirements

The reacceleration scheme that was chosen for the ISF was optimized with respect to these properties. It is based on the acceleration of highly charged (n^+) ions. The scheme, denoted as n^+ reacceleration, offers advantages over schemes based on the acceleration of singly-charged (1^+) ions. This will be discussed in the following pages.

Figure 5.111 illustrates the n^+ reacceleration concept, and Figure 5.112 and Figure 5.113 illustrate the layout of the proposed reaccelerator. The beam from the gas stopper will first pass through a fast electrostatic switchyard that will alternate sending the ion beam into one of two Electron Beam Ion Trap (EBIT) charge breeders (see Section 5.5.4.3). The EBITs will be located on individual high voltage (HV) platforms. The platform voltages can be raised to a potential of a few tens of keV during breeding and before extraction to match the velocity of the newly created, highly charged ions to the requirements of the following RFQ-accelerator. The n^+ ions will pass through an achromatic Q/A separator to select the desired charge state and to suppress unwanted background ions before entering the accelerator. The compact linac (see Sections 5.2 and 5.5.4.4) consists of an RFQ followed by SRF structures. The two EBITs will be operated in a “push-pull” mode to achieve the maximum efficiency in both continuous beam and pulsed beam operation.

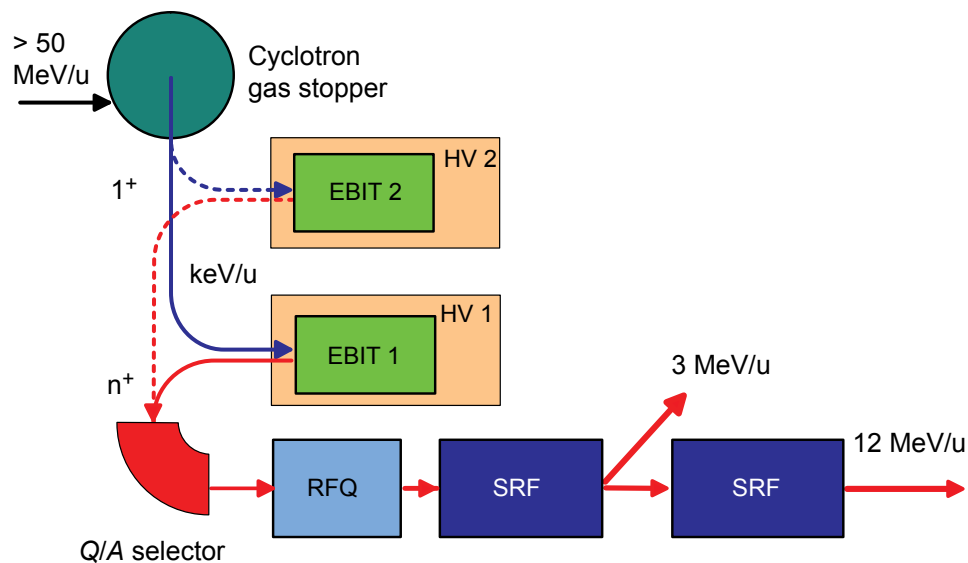


Figure 5.111: Conceptual block diagram of the reaccelerator system.

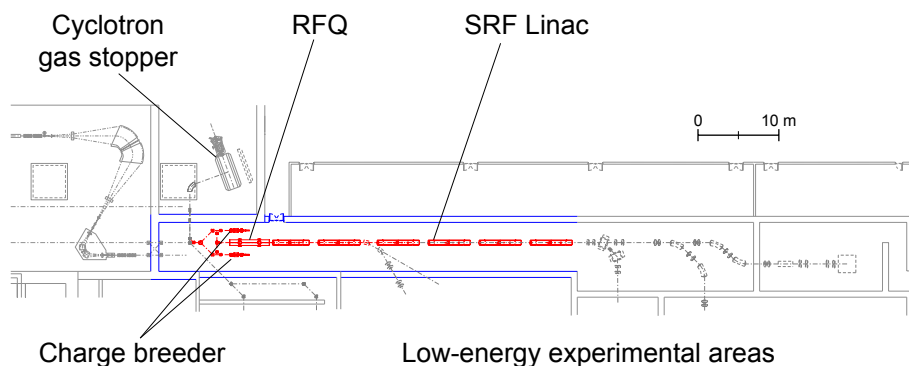


Figure 5.112: Schematic diagram of the reaccelerator system for thermalized secondary beams from the cyclotron stopper consisting of a charge-breeder, an RFQ, and a superconducting linac. The reaccelerated beams will be distributed to the low-energy beam experimental areas located at the bottom of the figure.

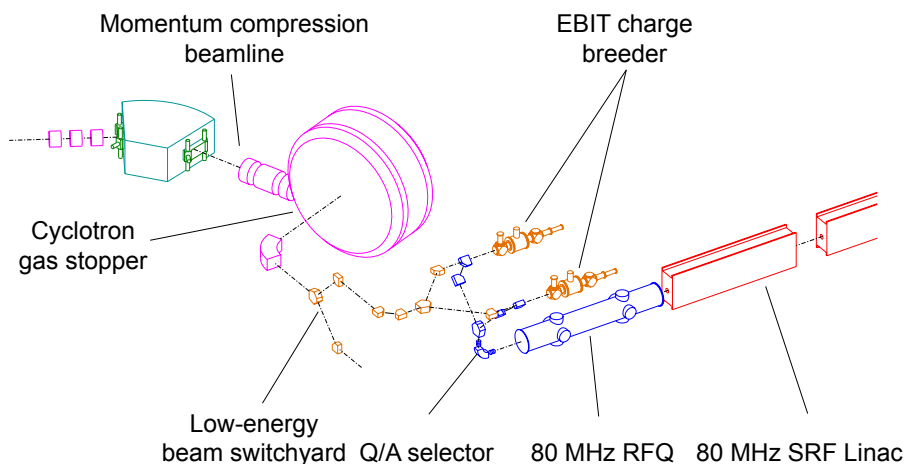


Figure 5.113: An isometric view of the low-energy beam generation facility connected to the reaccelerator. Low-energy beams from the gas stopper will be sent alternately to one or the other Electron Beam Ion Trap (EBIT) charge breeders. The highly-charged ions then pass through a Q/A selector before entering the linear accelerator.

The NSCL is in the process of designing and building such a reaccelerator as a proof of principle. A system consisting of one EBIT, the Q/A selector, the RFQ, and the cryomodules containing superconducting $\lambda/4$ cavities will be built and tested in the near future. All components can be reutilized in the final system for the ISF illustrated in Figure 5.111.

5.5.4.1 1^+ versus n^+ reacceleration schemes

Reacceleration starting with singly charged ions and subsequent stripping between acceleration stages is the classical approach to bring stable or rare isotope beams up to energies of a few MeV/nucleon, realized for example, at ISAC. The techniques involved in such a 1^+ scheme are all well established. However, such systems are complex and costly and have significant losses in efficiency for heavier beams. Figure 5.114 shows an example of a 1^+ scheme that was studied at the NSCL as part of the evaluation of different reacceleration options.

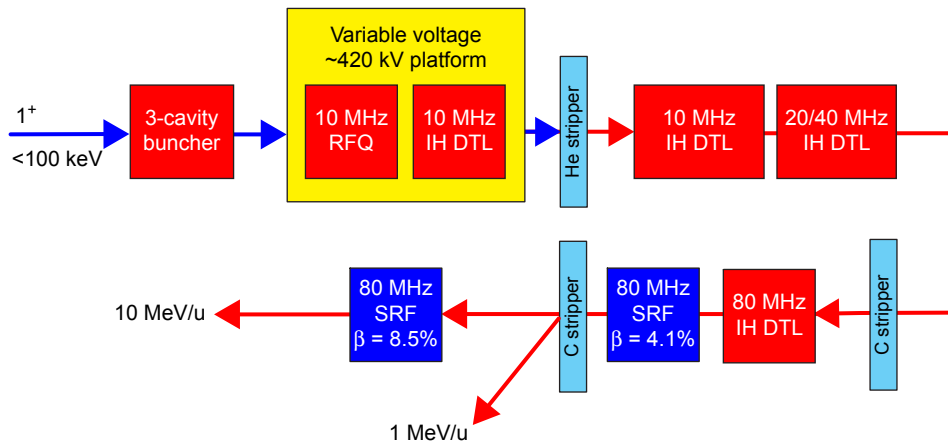


Figure 5.114: Schematic block diagram of a 1^+ reaccelerator that reaches 10 MeV/nucleon.

Different rf frequencies are needed together with the operation of a large (low frequency) RFQ on a high-voltage platform, complicated inter-digital drift tubes (IH DTL), and a large number of $\lambda/4$ cryostats. The system requires three charge-state strippers, each of which introduces efficiency losses. Transmission efficiencies for such a system were calculated. They range from about 50% for light elements ($Z < 10$) (single charge states) to 10–15% for the sum of 4–5 charge states in the case of heavier elements ($Z > 50$).

The implementation of charge-state boosting as the first step in a reaccelerator is recognized as the best way to obtain a very compact and cost-efficient reacceleration scheme. This was first demonstrated with REX-ISOLDE [Kes03] at CERN. A compact linac composed of a room-temperature RFQ and SRF structures can be used, and all resonators can be operated at the same frequency. If a high efficiency can be obtained for breeding ions into a single charge state, then the performance of the n^+ reacceleration scheme will surpass that of the 1^+ scheme. The best choice for a charge breeder for rare isotope beams is an Electron Beam Ion Trap (EBIT), as will be discussed in the following subsection.

5.5.4.2 Options for charge breeding

In order to make the n^+ postacceleration scheme a viable and better option compared to the classical 1^+ scheme, the charge breeding technique must meet the following requirements:

- high breeding efficiencies and small charge-state distributions to minimize rare isotope beam losses (ideally all the ions will be bred into a single charge state)
- short breeding times not exceeding a few tens of milliseconds to minimize decay losses of short-lived isotopes
- a high beam intensity capability that matches the rare isotope beam rates available at the ISF
- a low background current of stable atomic or molecular beams to deliver pure rare isotope beams (also available for low beam intensities of the most exotic isotopes)

There are two different approaches for boosting the charge state of an atomic ion. The most common approach relies on passing the ions through Electron Cyclotron Resonance Ion Sources (ECRIS). There is a lot of experience with ECRIS systems due to their use as sources of high intensity, moderately charged ions for stable-beam accelerators. They are also considered as charge breeders (for a recent review see [Lam06]). A number of studies have been made of the charge-state boosting performance of ECRIS systems for 1^+ ions at, for example, LPSC [Lam02], TRIUMF [Ame06], ISOLDE [Del06], and KEK [Jeo04]. The PHOENIX source [Lam02] is one example of a dedicated charge breeder system. Performance tests with stable beams [Lam02] showed a breeding efficiency of about 4% for $\text{Sn}^{1+} \rightarrow \text{Sn}^{22+}$. Typical breeding times for such charge states are > 100 ms. An undesired feature of ECR sources are the large currents ($> \text{mA}$) of stable ions that come along with the beam of interest. Despite all the experience with ECR devices and their long-standing operation, up to date, no rare isotope beam experiment has been performed with reaccelerated beams involving an ECR ion source as a charge breeder.

Alternative systems for boosting the charge states of atomic ions are the Electron Beam Ion Traps (EBIT) [Lev89] and the Electron Beam Ion Sources (EBIS) [Don85]. The ions are radially trapped in these devices by the space charge of an intense electron beam and are ionized to very high charge states by electron impact. The ions are confined longitudinally in an additional electrostatic potential usually generated with a set of cylindrical electrodes. The general principle of an EBIT is shown in Figure 5.115. The main differences between an EBIS and an EBIT are the length of the trapping region and the electron current density. The EBIT systems typically use a much shorter trapping region and a much higher electron beam density than the EBIS devices. A common feature of the devices is their operation at ultra-high vacuum, which results in a very small background current. A very small source diameter also leads to a low emittance of the extracted highly charged ion beam.

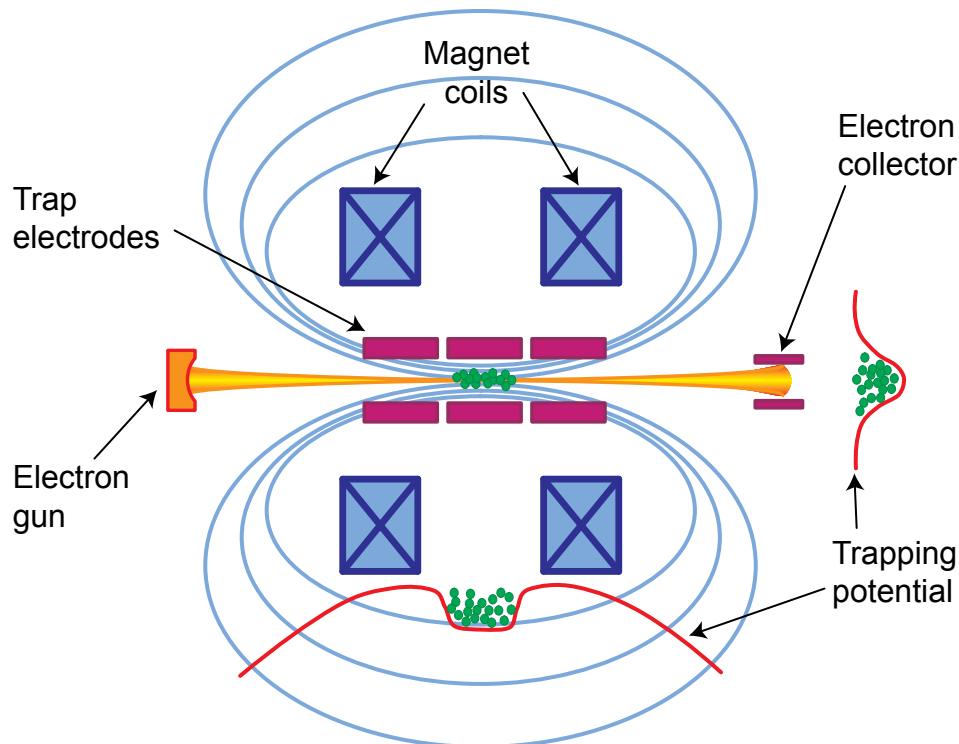


Figure 5.115: Overview of the operation principles of an Electron Beam Ion Source (EBIS) or Trap (EBIT). An intense electron beam is injected into and compressed by a solenoidal magnetic field. The resulting high electron beam current density provides the electric field for the radial confinement for positive ions as well as the electrons needed to rapidly strip electrons from the ions. Axial confinement is achieved by creating an electrostatic potential well with cylindrical electrodes.

EBIT devices are in wide use for spectroscopic studies of trapped, highly-charged stable ions and they have been shown to be very efficient sources of highly-charged stable ions.

The only operating charge-state booster for rare isotope beams using the EBIS/EBIT principle is REX-EBIS [Wen06], a part of the REX-ISOLDE postaccelerator project [Kes03] at ISOLDE/CERN. REX-ISOLDE came into operation in 2001, and several experiments with reaccelerated rare isotope beams have already been performed. REX-EBIS is operating at one-half of its nominal electron current density, but breeding times for Na^{1+} to Na^{8+} (peak charge) of ~ 18 ms and for Cs^{1+} to Cs^{32+} of ~ 150 ms have been found. Average charge breeding efficiencies of 10%, and in isolated cases $>20\%$, have been observed [Wen06]. Another EBIS charge breeder device, BRIC, [Bra00b,Var02] is currently under development in Legnaro, Italy, for the SPES project. A dedicated EBIS for charge breeding studies, MAXEBIS [Kes06], has been brought into operation recently at GSI in Darmstadt. A group at Brookhaven National Lab has successfully developed a high performance EBIS, the RHIC Test EBIS [Pik06], for stable beams. An electron beam of 10 A at 20 keV in this new device provides an electron density larger than 400 A/cm^2 , which provides a charge capacity that exceeds 3×10^{11} . The maximum beam rate that could be obtained with a 100 Hz repetition rate in such a device would be in the range of 10^{12} ions/s.

Marrs and Slaughter evaluated the potential gains associated with using a high-intensity EBIT (5A, 10^5 A/cm^2 for 30 keV electrons) as a charge-booster for RIA

[Mar99d]. They found that such a device would have charge-breeding properties for rare isotopes superior to any other device at present. For example, neon-like Sn^{40+} (a Sn nucleus with ten electrons) could be produced in about 3 ms. Very narrow charge-state distributions can be obtained by tuning the electron beam energy. For closed-shell configurations it was experimentally found that a breeding efficiency of up to 90% can be achieved [Mar88]. Very recently an EBIT charge breeder has been built by a collaboration between TRIUMF and the Max Planck Institute for Nuclear Physics in Heidelberg. This charge breeder [Sik05b] will be used for TITAN [Dil06], an ion trap project intended to measure highly charged-ions of rare isotopes produced at ISAC. This is the first high-intensity EBIT system optimized for charge breeding of externally injected ions. The device has been built and successfully passed the first offline tests and is now being brought into operation at TRIUMF. The expected performance of the TITAN charge breeder is close to that required for an efficient reacceleration scheme at the ISF. The EBIT charge breeder planned for the ISF, to be discussed in more detail below, will be very similar to the TITAN EBIT in most aspects.

5.5.4.3 EBIT charge breeder

The charge breeder for the ISF will be based on a modified design of the TITAN EBIT shown in Figure 5.116. Modifications are considered (Table 5.38) to optimize the performance of the system with respect to the reacceleration of rare isotope beams. The increased field strength of 9 Tesla will provide faster breeding and larger ion storage capacity, which will also benefit from a larger trap length. The use of a 4-coil magnet system will provide a large degree of freedom in shaping the magnetic field in the capture region and in the final trapping region. The compensation coil at the electron gun will be designed such that it can compensate the field at this location to practically zero strength and can be ramped very

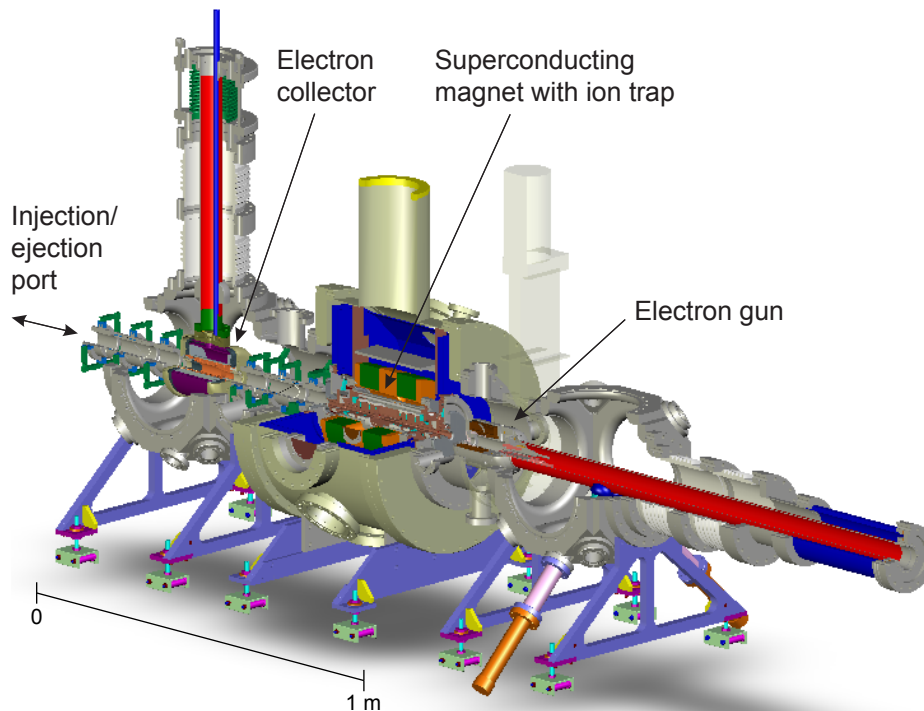


Figure 5.116: Mechanical design of the TITAN EBIT.

quickly (1 ms). Both measures will help achieving large breeding efficiencies and fast breeding times. The parameters for the ISF EBIT are preliminary at this stage and may change as a result of ongoing detailed simulations and tests of the TITAN EBIT. As an example of such simulation work performed at the NSCL, Figure 5.117 shows the injection of an ion beam into the TITAN EBIT.

Table 5.38: Design parameters of the TITAN EBIT and the ISF EBIT.

| | TITAN | ISF |
|--|------------------|------------------------------|
| Electron beam energy (keV) | < 60 | < 60 |
| Electron beam current (A) | < 5 | < 5 |
| Central current density (A/cm ²) | <10 ⁵ | <10 ⁵ |
| Magnet design (# coils) | 2 | 4, optional low-field region |
| Magnetic field (T) | 6 | 9 |
| Trap length (m) | 0.3 m | 0.5 m |

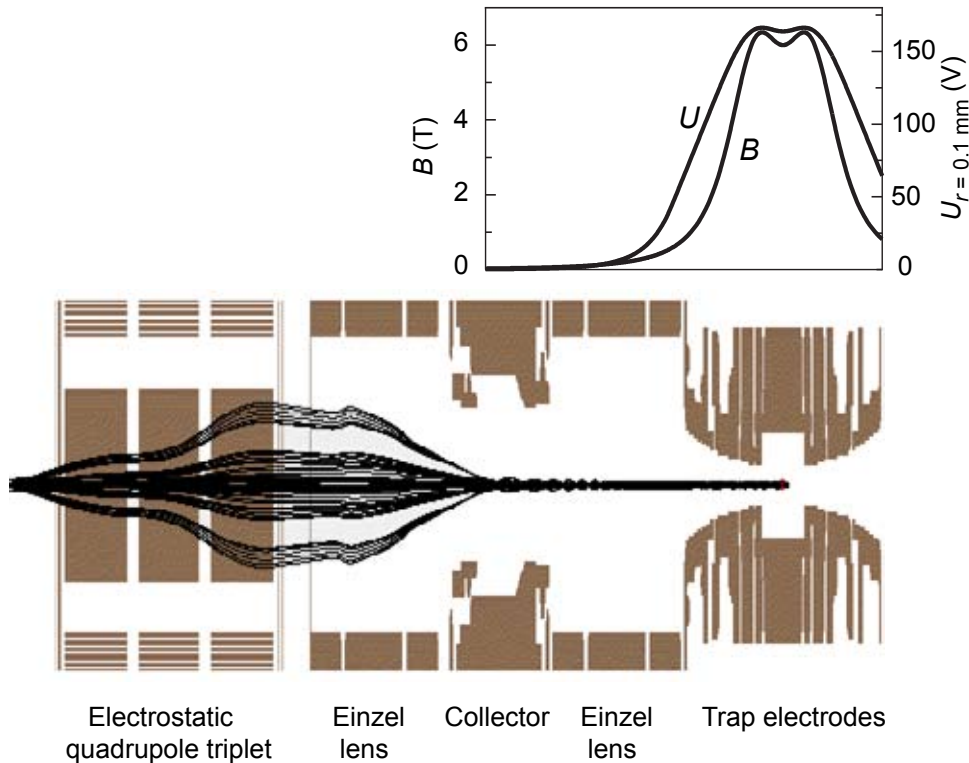


Figure 5.117: Results of the simulated injection of ions into a system similar to the TITAN EBIT. An electron beam current of 0.2 A is used. The injected ion beam has an energy of 11 keV and a beam emittance of 20π mm mrad. The upper panel shows the magnetic field and the electric potential seen by an ion at a radius $r = 100 \mu\text{m}$ from the central axis.

Breeding efficiency

The breeding efficiency of the EBIT will be determined by the acceptance of the incoming singly charged ion beam, the efficiency of breeding into a particular state in a given breeding time, and the extraction efficiency. Wenander [Wen01] derived

an analytical expression for the acceptance of an EBIT for ions that are trapped in a non-compensated electron beam. A number of critical machine parameters enter this expression, including the electron beam radius, the magnetic field in the trap, and the energy with which the ions are injected into the trap. The electron beam radius [Her58] depends on the magnetic field strengths at the cathode (launching field) and inside the ion trap, the size of the cathode, and the electron current and energy. Table 5.39 lists the calculated electron beam radii and the transverse acceptance for a range of operating parameters expected for the ISF EBIT. The mass of the ion injected into the EBIT has little effect on the acceptance, so ions with mass number $A = 50$ were assumed.

Table 5.39: The electron beam diameter, current density, and acceptance for a combination of operating parameters of the EBIT proposed for the ISF. Modes A-C correspond to different operational scenarios considered.

| | | | |
|---|-------------|-------------|--------------|
| Mass of ion M (u) | 50 | | |
| Ion energy E_i (keV) | 20 | | |
| Cathode temperature T_c (K) | 1750 | | |
| Electron energy E_e (keV) | 8 | | |
| Cathode radius r_c (mm) | 5 | | |
| Electron current I_e (A) | 4 | | |
| | Mode | | |
| | A | B | C |
| Launching field B_c (G) | 20 | 200 | 800 |
| Breeding field B (T) | 9 | 2 | 9 |
| e-beam radius r_H (μm) | 77 | 174 | 472 |
| Current density dI/dA (A/cm ²) | 21425 | 4227 | 572 |
| Acceptance ε (π mm mrad) | 14.6 | 32.4 | 101.0 |

The achievable electron density depends on the ratio of the magnetic field at the electron gun and at the trap location. Both can be varied and result in different current densities and acceptances. Mode A in Table 5.39 leads to a very high current density, desirable for fast breeding, but the acceptance does not provide a safety margin for the efficient injection and capture of the well-cooled beam (10–20 π mm mrad at 20 keV) emerging from the cyclotron stopper's RFQ cooler. It is therefore prudent to study ways to increase the beam acceptance of the EBIT. Two options are considered at present.

The first option makes use of the planned four-coil design, the beam is first injected into a low magnetic-field region. A 2 T field (Mode B) doubles the acceptance. Once adiabatically transferred into a 9 T trapping region (Mode A), the ions are quickly charge-bred to the desired charge state. In the second option the electron beam diameter is dynamically changed. For capture, a non-zero magnetic field at the cathode is chosen (Mode C), resulting in a large-diameter electron beam and a large acceptance. Once the ions have shed a few electrons, this launching field is ramped to close to zero (Mode A) for maximal electron beam compression and a fast completion of the breeding process.

The design of the ISF EBIT will allow both scenarios and combinations of them to be tested and employed.

Breeding times and charge-state distributions

The goal of the charge breeder for the reaccelerator is to breed all secondary ions of a given isotope into a single charge state or, if this is not possible, into a very narrow charge-state distribution within a breeding time of less than 10 ms. Compared to ECR ion sources, EBITs have a large advantage in that the breeding process can be manipulated in detail by varying the electron beam density and the electron beam energy. Since the electron beam is essentially mono-energetic, it is possible to use the atomic structure of the ion to enhance the efficiency for single charge states. This is illustrated in Figure 5.118, which shows the evolution of the charge-distribution for titanium ions ($Z = 22$) as a function of breeding time as calculated with the Lotz formula [Lot67]. The electron beam energies have been chosen such that the breeding process stops after reaching a Ne-like (ten electron, $q = 12^+$) or He-like (two electron, $q = 20^+$) electronic configuration. The breeding time depends linearly on the electron beam density. For an electron density of 10^4 A/cm^2 , breeding times of less than 1 ms and 10 ms, respectively, are required to reach these closed-shell configurations and to bring the ions into a single charge state.

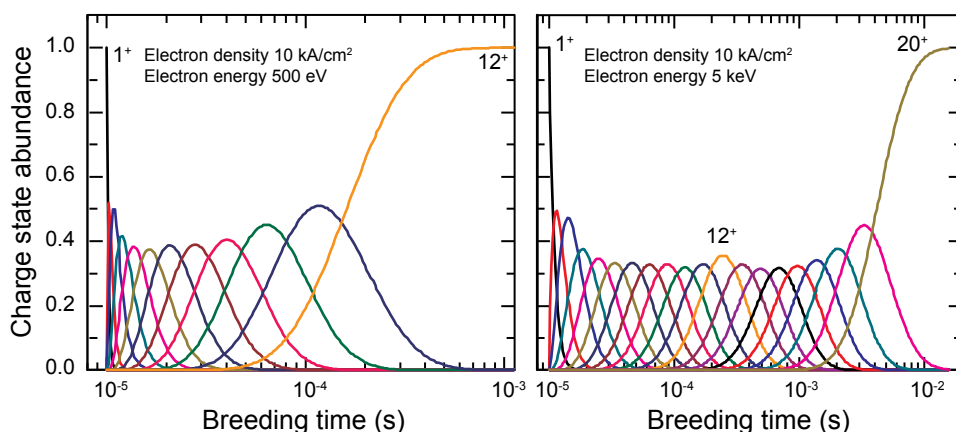


Figure 5.118: Charge-state distributions as a function of breeding time for titanium ions in an EBIT. The electron beam energy was adjusted to maximize the production of neon-like Ti^{12+} (left) and of helium-like Ti^{20+} (right).

For heavier systems ($Z > 50$) nickel-like (28 electrons) configurations are more suitable. An electron beam density of 10^5 A/cm^2 can breed lead ions into such a closed-shell configuration (Pb^{54+}) within 10 ms. However, it should be noted that such high electron densities are rarely required because the β -decay half-lives for the majority of heavy nuclei available with rates suitable for experiments with reaccelerated beams are in most cases well above 100 ms, allowing for correspondingly long breeding times.

While breeding into closed shell configurations is straightforward and provides single charge-state efficiencies near unity, other charge states can be populated with high efficiencies, if desired. One technique is to breed the ions into a narrow distribution of charge states centered slightly above the desired charge state. At that point the ions that have higher than the desired charge state can then be forced to recombine successively down to the wanted charge state by tuning the electron

beam energy through successively lower dielectronic resonances. Such recombination schemes have been tested and the recombination times are in the microsecond domains after the electron beam energy has been adjusted. Another possible technique [Kes04] is to drive the ions with an rf field resonantly out of the electron beam once the charge breeding process has arrived at the desired charge state.

Beam rate capability

The maximum beam intensity that can be processed by an EBIT charge breeder is determined by the trap capacity and the breeding time, which in turn determines the repetition rate with which the breeder can be filled and the highly charged ions can be extracted. The trap capacity can be estimated from formulas used to determine the breeding rate (of gas). The production rate R_i of highly charged ions is [Cur05] proportional to $I_e^2 \cdot l \cdot B$, where I_e is the electron beam current, l the trap length, and B the magnetic field strength. An example taken from [Cur05] for Kr^{33+} with very modest operating parameters ($I_e = 0.1$ A, $l = 1$ cm, $B = 3$ T, $r_c = 1$ mm, $E_e = 10$ kV), the breeding rate is as high as $R_i \sim 2 \cdot 10^7$ /s. The ISF EBIT will have a factor ~ 40 higher electron current, a factor of 30 larger trap length, and a factor of 3 higher magnetic field, giving a gain factor of more than 10^5 . Provided this simple scaling is valid, the throughput rate should be well above 10^{11} /s.

Beam properties and quality

The beam properties of the extracted ions will depend on the operational parameters of the EBIT and the extraction mode. The energy spread grows with the space charge potential of the electrons and the radial spread of the ions. In addition, the energy spread depends on the ejection scenario and is smallest for quasicontinuous extraction. In the case of pulsed extraction, energy spreads on the order of 1 keV can be expected, requiring an achromatic beam transport system to the RFQ linac. In the case of pulsed extraction, an ion pulse length as short as several microseconds can be easily achieved. The transverse beam emittance will be determined by the trapping potential provided by the electron beam, the ion cloud size, ion charge state and mass, magnetic field, and the acceleration voltage. Typically, for the operating parameters listed in Table 5.38, beams extracted with a 20 kV acceleration voltage will have beam emittance values below 20π mm mrad, which is well within the acceptance of the RFQ.

5.5.4.4 The linear accelerator

The reaccelerator (Figure 5.119) is designed to accept beams from the EBIT with a charge to mass ratio, Q/A , of approximately $1/4$. The beam extracted from the EBIT will be transferred into a RFQ for bunching and acceleration to 0.293 MeV/nucleon. The beam will then be further accelerated in a superconducting linac to a final energy between 0.5 and 12 MeV/nucleon. Details of the design have already been discussed in Section 5.2. There will be a low-energy extraction point for beams with energies less than 3 MeV/nucleon for nuclear astrophysical studies, and a full-energy extraction point at the end of the linac. Important features are the compactness of the accelerator and its simplicity due to the use of only one rf frequency.

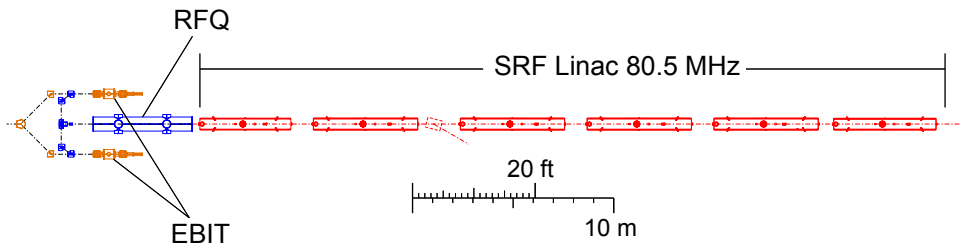


Figure 5.119: Layout of the reaccelerator.

5.5.4.5 Operational schemes and performance of the reaccelerator

The proposed concept of two charge breeders makes the system very flexible and can deliver beams with a variable duty-cycle without making unnecessary compromises in the overall efficiency. Having a large duty factor will be important in experiments that require low peak beam rates because of rate limitations in the detectors. Other experiments will benefit from short ion pulses (i.e., low duty factor) to improve the signal-to-background ratios.

Figure 5.120 illustrates two different operational scenarios, one for providing a quasi-continuous beam (very long beam pulses > 10 ms) and another for the delivery of very short ion pulses, in addition; operation with one or two EBITs is shown.

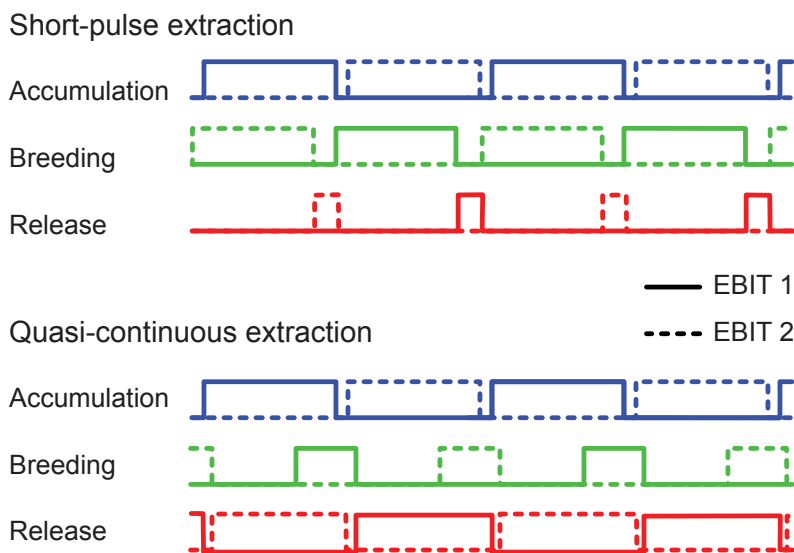


Figure 5.120: Operational scenarios for charge breeding. The solid lines correspond to the operation of one EBIT. The dashed line illustrates push-pull operation with a second EBIT.

The scenario with two EBITs provides its largest benefit for the generation of quasi-continuous beams. If the half-life of the isotope permits using an accumulation time significantly larger than the breeding time, then the total efficiency will be essentially determined by the charge-breeding efficiency. This will be the case for practically all isotopes of interest, since breeding times of less than 10 milliseconds are expected for the ISF EBIT. In the pulsed extraction scenario, the two-EBIT system would nearly double the efficiency for similar accumulation and breeding times; an example would be the acceleration of an isotope with a half-life of a few tens of milliseconds.

The high-intensity EBIT concept should allow ions to be bred into the charge state required for reacceleration with at least 70% efficiency. Assumed injection, extraction, and other losses of less than 20% and an efficiency of 90% for the linear accelerator leads to an estimated total efficiency of about 50% for the ISF reaccelerator. This efficiency should be practically element independent and be significantly higher than that for a 1^+ reacceleration scheme (see 5.5.4.1).

5.5.4.6 Expected reaccelerated beam rates

Figure 5.121 shows estimated beam rates for reaccelerated beams at the ISF. The rates are based on calculated ISF rates (see Figure 5.89), adjusted for losses in the gas stopping and reacceleration processes. An efficiency of 50% was assumed for gas stopping, 60% for charge breeding, and 90% each for the acceleration in the linac and for the beam transport. In addition, decay losses were taken into account based on a total of 20 milliseconds for the stopping and breeding processes. The color code has a lower limit of 100/s, considered to be a typical minimum rate for reaccelerated beam experiments.

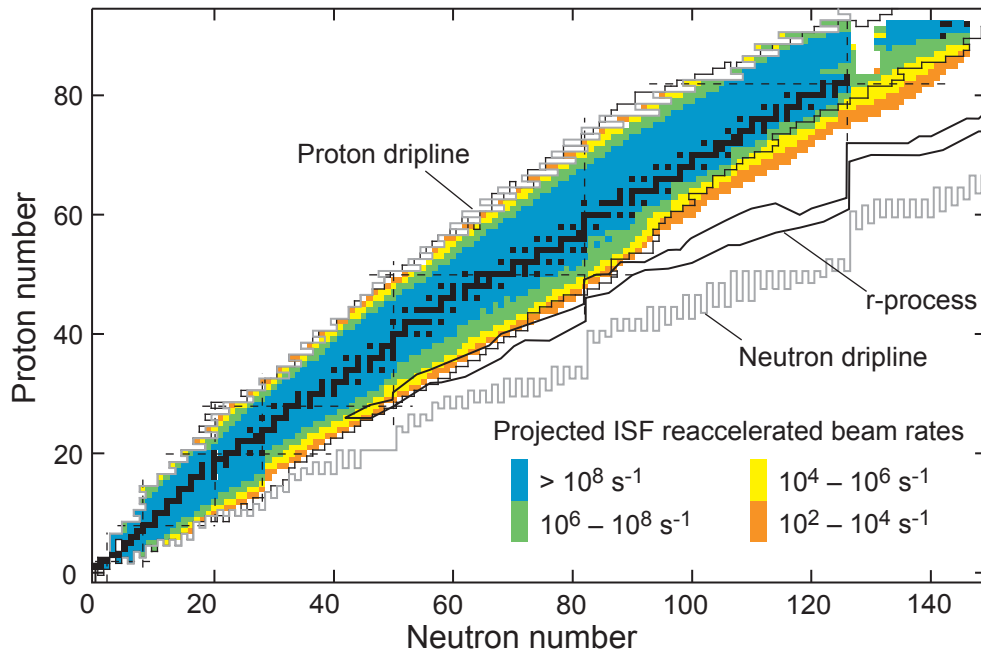


Figure 5.121: Expected beam rates for reaccelerated beams at the ISF.

5.6 Experimental areas

5.6.1 Low-energy beam experimental areas

The beams from the cyclotron stopper will serve three areas dedicated for low-energy experiments. The stopped beam area will accommodate experiments that can be completed using rare isotope beams having energies of a few keV or less. The reaccelerated beam area will include an experimental area for nuclear astrophysics experiments with beams having a maximum energy of 3 MeV/nucleon and an area for low-energy nuclear structure and reactions experiments where the reaccelerated beams will have a maximum energy of 12 MeV/nucleon.

The three low-energy experimental areas will share a common highbay area as illustrated in Figure 5.122. This will permit manipulation of experimental apparatus in any of these three areas using an overhead crane. The stopped beam area will be located close to the cyclotron stopper. The astrophysics and low-energy nuclear science areas will be placed along the acceleration cavities to minimize distances for beam delivery.

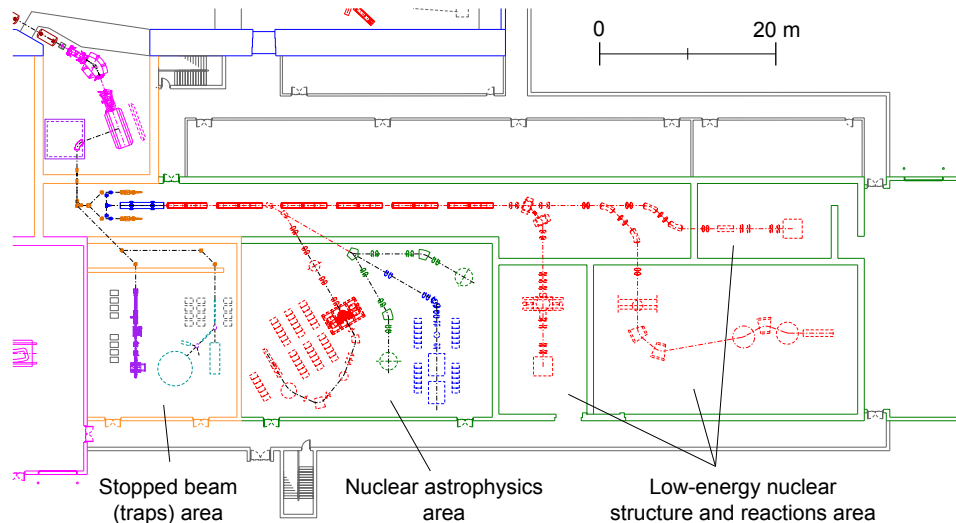


Figure 5.122: Schematic layout of low-energy experimental area, which includes a stopped beam (traps) area and a reaccelerated beam area. The reaccelerated beam area is divided for use in nuclear astrophysics ($E \leq 3$ MeV/nucleon) and low-energy nuclear structure and reactions ($E \leq 12$ MeV/nucleon).

5.6.1.1 Stopped beam area

The stopped beam area will serve experiments in ion trapping, laser spectroscopy, and nuclear decay studies. The rare isotope beams delivered to the stopped beam area will range in energy from a few eV to a maximum of 60 keV.

Layout

The schematic layout of the stopped beam experimental area is shown in Figure 5.123. Three experimental stations are envisioned: one dedicated to Penning-trap mass spectrometry, one for laser spectroscopy and polarization, and a general-purpose beamline that can accommodate equipment for nuclear decay studies. The area is at grade level, and the footprint is on the order of 365 m².

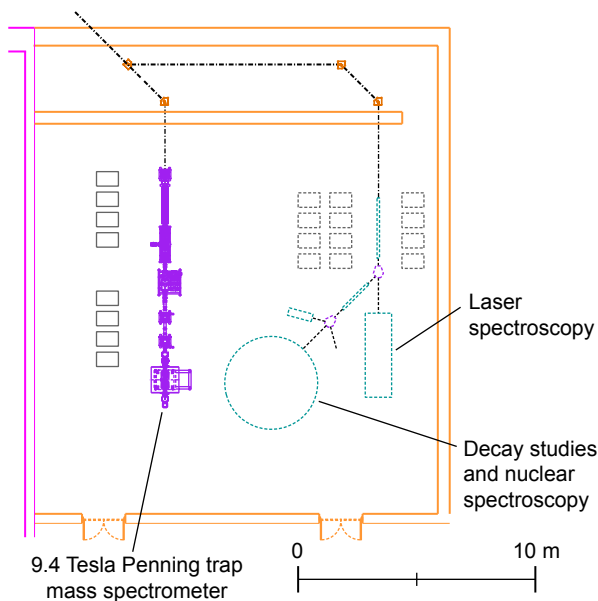


Figure 5.123: Schematic layout of stopped beam (traps) experimental area.

Beam transport hardware

The beam transport line will be made of successive electrostatic quadrupole elements to permit the tuning of any mass to the stopped beam end stations without retuning the beamline optics, provided the beam energy remains constant. The layout of the electrostatic elements will consist of repeated beam focusing, drift, and steering modules. Beam characterization diagnostics, including two-dimensional wire scanners and suppressed Faraday cups, will be placed in the beamline as determined from the optics parameters. The NSCL has experience in fabricating and installing a low energy beam transport system, as demonstrated by the successful Low-Energy Beam and Ion Transport (LEBIT) area that makes use of all such elements in delivering beams to the 9.4 T Penning-trap mass spectrometer.

Off-line ion sources will be needed for testing and calibrating the mass spectrometer and laser spectroscopy systems, and for developing and improving beam transport optics. A plasma-type ion source will offer the most flexibility regarding ion species; however, provision will be made to accommodate other source types.

Beam cooler and buncher systems based on gas-filled radio-frequency quadrupole ion guides and traps will be used for beam preparation. They will improve the beam emittance and can deliver short ion pulses. The latter is important for the efficient capture of ions in traps and for enhancing the signal to noise ratio in the experiments.

Utilities/services

The diversity in experimental equipment planned for the stopped beam area will require a wide and varying range of utilities and services in this area. The beam buncher/coolers and germanium detectors used in γ -ray spectroscopy experiments will require liquid nitrogen. The Penning-trap solenoid magnet requires liquid helium. Dry nitrogen, roughing pump exhaust lines, city water, and low conductivity water will be required at each of the experimental end stations.

The electrical power requirements will depend on the nature of each of the three experiments. Isolated clean power will be required to power detectors, nuclear electronics, and data acquisition systems. A capacity of 60 kW is sufficient for most applications.

The precision experiments utilizing ion trapping and laser spectroscopy will have strict requirements on vibration stability, shielding from radiation and magnetic field sources, and air handling. The optical complexity of the laser spectroscopy experiments demand that the lasers are placed in a controlled environment.

User access

The experimental end stations in the stopped beam area should be categorized as “unlimited access.” This includes the apparatus receiving the rare isotope beam. Such access conditions are employed at all current stopped beam facilities as well as the LEBIT experimental area at the NSCL. In rare instances when the secondary beam currents exceed 10^6 s^{-1} , local monitoring of beam interaction points may be required and local shielding employed to maintain exposure levels as low as reasonably achievable.

5.6.1.2 Reaccelerated beam areas

The reaccelerated beam areas will serve experiments in nuclear astrophysics and low-energy nuclear structure and reactions. The areas are defined by the maximum energy provided from the reaccelerator. The rare isotope beams delivered to the astrophysics area will have maximum energy of 3 MeV/nucleon, while those delivered to the low-energy nuclear structure and reactions area will have the full energy available from the reaccelerator, 12 MeV/nucleon.

The reaccelerated beam area will require devices to analyze the products from interaction of the incoming rare isotope beam with a fixed target. Since a final decision on the specific type of separator to be implemented has not yet been made, the footprint reserved for separation devices for both reaccelerated beam areas is based on currently implemented devices at other low-energy facilities in North America. The γ -ray energy-tracking array GRETINA [Lee04] (and later GRETA) will be deployed at times in the reaccelerated beam areas, both as a standalone device and in concert with recoil or magnetic separators. The mobile nature of GRETINA and GRETA will require that each potential site location have the requisite utilities (power, liquid nitrogen, air handling for electronics) to support this important device.

Layout

A potential layout of the reaccelerated beam experimental areas is shown schematically in Figure 5.124.

The nuclear astrophysics area, which will accommodate rare isotope beams accelerated to a maximum energy of 3 MeV/nucleon, has provision for three experimental end stations. One of these experimental end stations will be occupied by a recoil separator capable of separating low-energy reaction products from the primary beam with unit mass separation. A device similar to the DRAGON [Eng05] recoil separator at TRIUMF/ISAC is shown as a placeholder in Figure 5.124. The object position of the recoil separator will have sufficient space to mount a gas target system,

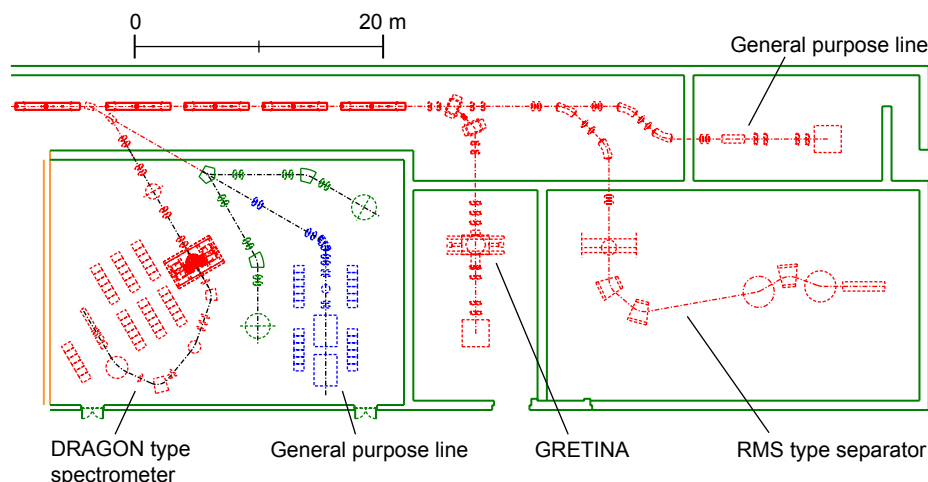


Figure 5.124: Schematic layout of the reaccelerated beam experimental areas.

vital to the nuclear astrophysics experimental program. Space will also be available upstream of the separator object position to mount nonpermanent equipment for measurements requiring only a small area of floor space. Other potential experiments proposed for this area include elastic and inelastic scattering experiments.

Two experimental end stations are planned for the full beam energy of 12 MeV/nucleon from the reaccelerator. One end station will host a mass separator device for fusion-evaporation experiments. A device similar to the Oak Ridge Recoil Mass Separator is given as an example in Figure 5.124. Space has been reserved at both the target position and focal plane of the separator to accommodate GREY or GREY. A second beamline that can accommodate GREY or GREY when operated in stand-alone mode is also planned. There will be sufficient room at the end station of this second beamline to install a solenoid magnet (for example, the proposed HELIOS device [Wuo04]) for applications in (d,p) transfer studies).

The footprint of the reaccelerated beam area has a dimension of 1760 m², shared between the nuclear astrophysics area (610 m²) and the low-energy nuclear structure and reactions area (1150 m²). For comparison, the astrophysics areas at ORNL and TRIUMF have footprints of 180 m² and 360 m², respectively, while the floor area dedicated to low-energy nuclear structure and reactions experiments at ORNL is 585 m². The ISAC-II facility at TRIUMF has assigned 680 m² of floor space to experiments in low-energy nuclear structure and reactions. The layout of the reaccelerated experimental areas will permit the extension of the highbay area, should additional experimental floor space be required in the future.

Beam transport hardware

The beam transport hardware in the reaccelerated beam area will be composed of magnetic dipole and quadrupole elements, with associated high vacuum (better than 10⁻⁷ torr) beamlines. The beam transport diagnostics in this region are not trivial due to the potential low intensities of some rare isotope beam species. Microchannel plates and gas counters will most likely substitute for Faraday cups and wire scanners. This will require more sophisticated nuclear electronics as well as more experienced beam transport physicists to reliably deliver beams to the reaccelerated beam experimental areas.

Utilities/services

The recoil separator for nuclear astrophysics and the mass separator for fusion-evaporation studies will have significant power and low conductivity water needs. Dry nitrogen, roughing pump exhaust lines, city water, and low conductivity water will also be required at nearly all the experimental end stations.

Gas targets will be employed at the target of the recoil separator for nuclear astrophysics experiments, and the infrastructure needs for such a system must be met. This includes electrical power and other utilities for a differential pumping system composed of large roots blowers and high throughput turbomolecular pumps.

GRETINA will require liquid nitrogen (120 l/day, GRETA will require 500 l/day), as well as air handling and electrical power (40 kW, GRETA will require 150 kW) for the accompanying nuclear electronics. As noted earlier, since GRETINA is a moveable device, such services will be required at all potential GRETINA locations.

A 50-ton crane runs the full length of the low-energy experimental areas and will service the stopped and reaccelerated beam areas.

User access

Access to the reaccelerated beam areas will be based on integrated dose rates, similar to procedures followed at operating low-energy heavy-ion facilities at ANL and ORNL.

5.6.2 Fast beam experimental area

Rare isotope beams from the in-flight separator will be available in three dedicated experimental vaults: a multipurpose vault sized to accommodate large detectors under discussion [such as GRETA or a Time Projection Chamber (TPC)]; a spectrograph vault housing a large-acceptance, high-resolution superconducting magnetic spectrograph with auxiliary detector surrounding its target position; and a neutron-time-of-flight area with a superconducting sweeper magnet. The layout of the fast beam experimental areas will be located in a highbay as illustrated in Figure 5.125. It will permit extension of the highbay area with minimal impact on the experimental program when scientific needs require additional experimental floor space in the future.

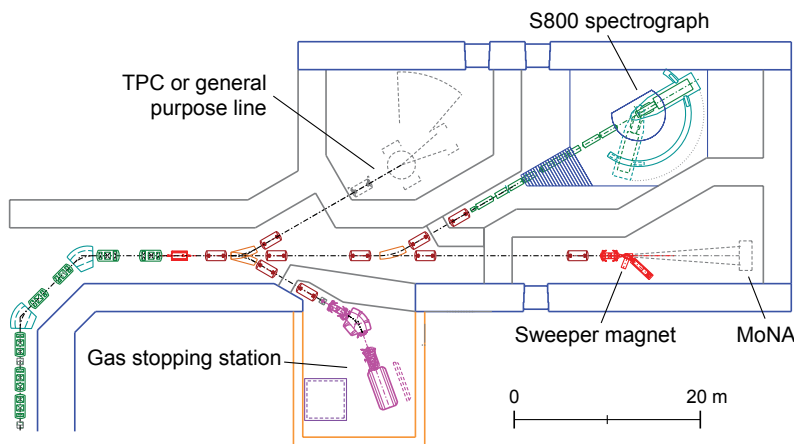


Figure 5.125: Schematic layout of fast and stopped (solids) beam experimental area, which includes a general purpose vault, a spectrograph vault, and a neutron time-of-flight vault.

Layout of the multipurpose area

The multipurpose area is about 220 m² in size and can be reconfigured for different detector setups. It is large enough to accommodate a beta-decay detector for stopped beam experiments, the envisioned GRETA detector, a TPC, or other detectors of similar size. Cryogenic connection will be available to cool superconducting magnets or cryogenic detectors.

Layout of the spectrograph vault

The spectrograph vault houses the existing S800 superconducting spectrograph, the analysis beamline, and, possibly, auxiliary detectors at the spectrograph target position. The spectrograph is installed vertically on a carriage that can rotate from 0° to 60°. It covers a solid angle of 20 msr and a momentum acceptance of 5%. The maximum rigidity of the S800 is 4 Tm and 4.9 Tm for the analysis line. The analysis line has two modes of operation: a focus mode and dispersion matching mode. Auxiliary detectors can be located at the spectrograph's target location. GRETINA or GRETA can be employed for in-beam γ -ray detection, or a scattering chamber can be installed to house charged-particle detectors in vacuum.

Layout of the neutron time-of-flight area

The neutron time-of-flight area accommodates the NSCL Sweeper magnet to sweep the rare isotope beams away from zero degree in order to perform neutron-fragment coincidence measurements. The existing Modular Neutron detector Array (MoNA) can be used for this purpose. Neutron flight paths up to 14 m can be accommodated and the neutron detectors can cover angles up to 30° with respect to the incoming beam direction.

Beam transport hardware

The fast beam transport hardware to the experimental area will be composed of magnetic dipole, quadrupole, and sextupole elements with designs taken from the current NSCL S800 analysis beamline. Associated high vacuum components can be reused from the current NSCL (better than 10⁻⁶ torr) beamlines. Beam diagnostics will be based on the current NSCL system of phosphor screens with sensitive CCD cameras. Beam intensities of 1000 s⁻¹ can be viewed in this way. Transport of lower beam intensity will require tracking detectors.

Utilities/services

The highbay is serviced by a 50-ton overhead bridge crane, allowing manipulation of experimental equipment in each vault. Each vault will be serviced with cryogenics (liquid nitrogen and liquid helium), dry nitrogen, compressed air and low-conductivity water, as well as city water and drains, electric utility power and clean electric power (60 kW), network connections and telephone, and control system network connections. The beam transport systems to each vault in the fast beam experimental area will be able to transmit beams with rigidities of up to 6.3 Tm.

User access

User access to fast experimental areas will be limited to times when no beam is present in the experimental area. An interlock system for each vault will be used to sweep and secure an area with the shielding door closed prior to a beam being allowed to enter, similar to systems in use at the NSCL and GANIL.

5.7 Conventional facilities

The physical structures, access roads, and parking areas will occupy a land space of approximately 50 acres as shown in Figure 5.126.

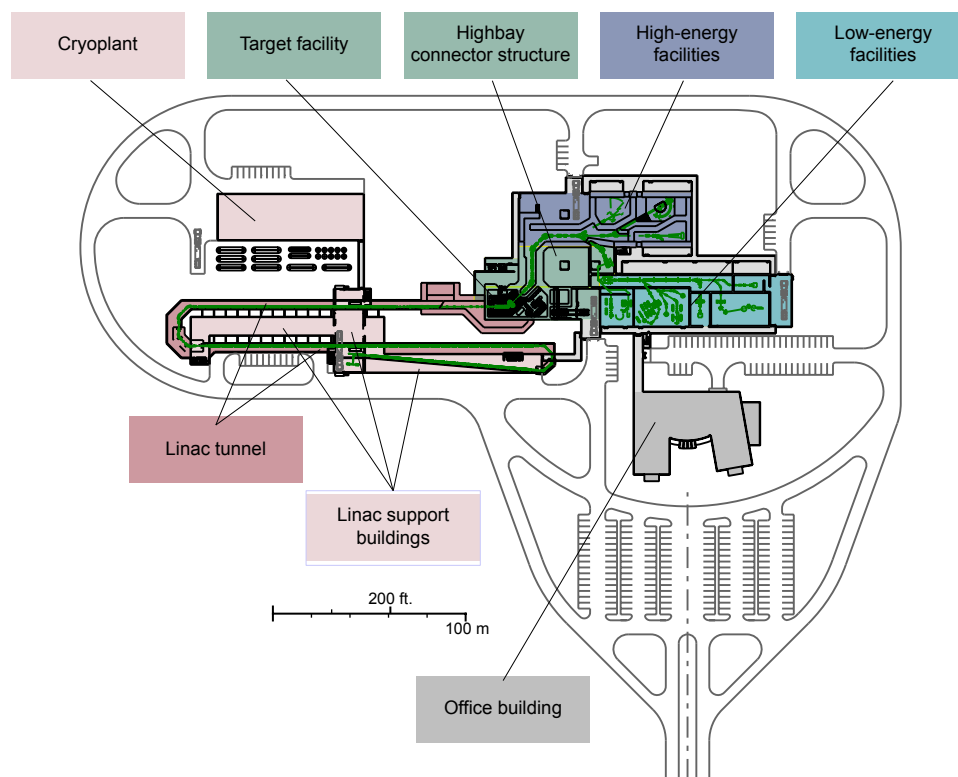


Figure 5.126: Facility layout.

The complex will be composed of eight major interconnected structures, the underground linac tunnel, the above ground linac support buildings, the cryoplant, the target facility, the highbay connector structure, the high-energy facility, the low energy facility, and the office building.

The access roads will provide truck service to the four crane bays, various loading docks, and the cryoplant and car access to parking spaces for staff and visitors. All structures will have fire protection provided by a wet pipe sprinkler system and complete fire alarm system, including visual and audible alarms, pull stations at exits, and heat/smoke detectors as required by code. All temperature controls will be direct digital type, capable of being monitored at a central location or remote site. The facility electrical power requirement is expected to be 25–30 MW, which will be supplied by a new on-site high voltage utility bulk power substation. The substation will feed 15 kV switchgear located in the cryogenic building, which will supply the distribution system for the facility. The cost estimate includes extending the required utilities to the site from the appropriate campus and municipal systems.

Linac tunnel

Figure 5.127 shows a 3-D aerial view of the complex with the underground linac tunnel highlighted. The structure will have a footprint of 3,000 m² and will be constructed via an open cut excavation (cut and fill). The foundation slab will be

supported on drilled piers at 6 m centers that will extend down to bedrock (approximately 25 m below grade). The tunnel slab, walls, and ceiling will be 0.5 m reinforced concrete except at the stripping areas, where the thickness will be 2 m to provide the necessary shielding. The parallel tunnel sections will be connected by a reinforced concrete slab to minimize differential settlement. The tunnel floor will be 6.75 m below grade and the structure will be waterproofed and equipped with a perimeter drain tile and sump pump system. Access to the at-grade structures will be via four stairwells and two freight elevators. Large pieces of equipment will be lowered into the tunnel through access hatches in the at-grade crane bay. The tunnel will include provisions for upgrading the linac at a future date with minimal disruption to facility operation.

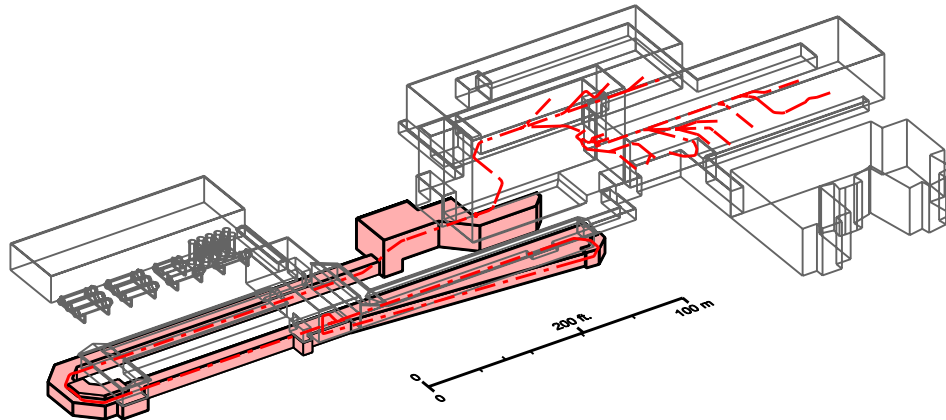


Figure 5.127: Linac tunnel.

Linac support buildings

Figure 5.128 shows the at-grade linac support structures, consisting of a 770 m² highbay equipped with a 30-ton overhead crane and 2,000 m² of single story structures, providing space for the linac/magnet power supplies and controls. The heating and air conditioning for the tunnel and at-grade structures will be provided by a series of indoor air handling units that will have steam heating coils, chilled water cooling coils, and steam humidifiers. Variable volume terminal units will be provided in the air supply distribution system to achieve temperature control.

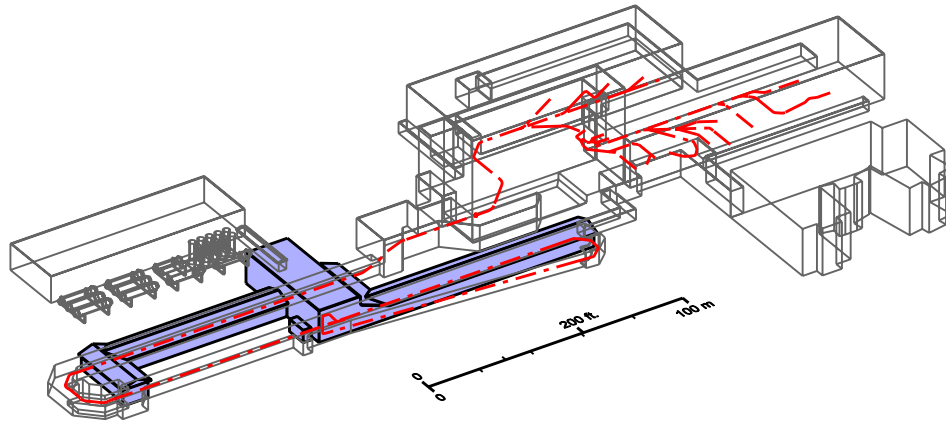


Figure 5.128: Linac support structures.

Cryoplant

Figure 5.129 shows the 1,900 m² cryoplant that is modeled on the existing NSCL cryogenic building. The building will be a structural steel frame with masonry-insulated walls. It will be divided longitudinally into two halves with one half being a high-ceiling single-story structure for refrigeration cycle equipment and controls. The other half will be a two-story design with compressors on the main floor and electrical switchgear plus process cooling equipment on the second floor.

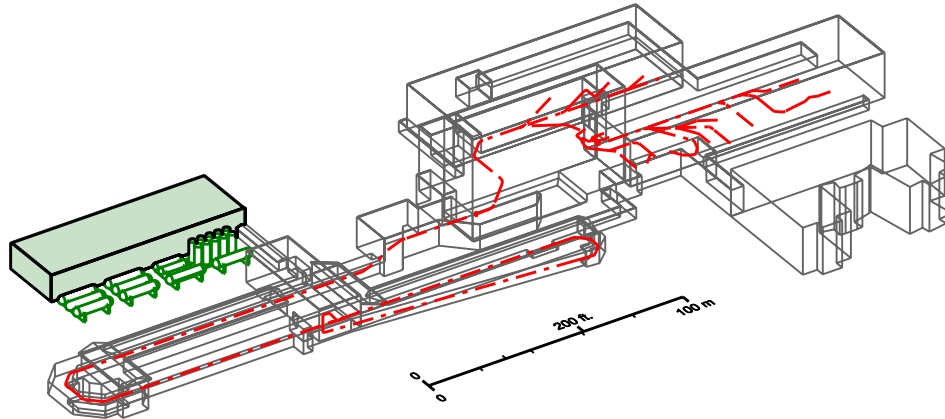


Figure 5.129: Cryoplant.

Target building

Figure 5.130 shows the target building, which will be a three-floor structure. The lower floor will be the target room with a 3 m thick floor supported on drilled piers extending to bed rock and will be designed for a floor loading of 33,000 kg/m² to support the beamline components and bulk radiation shielding. The walls will be at least 1.5 m thick and up to 3 m high in the high radiation areas. The second floor will be a limited access remote handling gallery with 1.5 m concrete walls and ceiling. This level will be equipped with rail systems for a remote control crane and manipulator arm equipment. The third floor will be a 100-ton crane bay with structural steel frame and masonry walls. The crane rail system will extend past the lower two floors to a truck bay that spans all three floors on the opposite end of the building from the linac beam entrance. The building will include all required structural features required for future installation of an ISOL target system and beamlines.

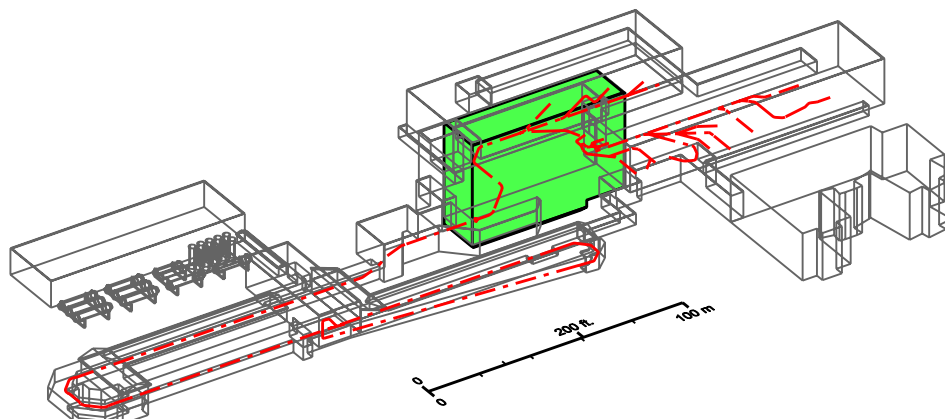


Figure 5.130: Target building.

Highbay connector structure

Figure 5.131 shows the four-floor structure that connects the target building to the high- and low-energy facility buildings. The first floor will be occupied by in-flight fragment separator components from the production target and will provide space for future installation of the ISOL system's high-resolution separator and low-energy beam distribution. The target hot cell maintenance area will also be located on this floor. The second and third floors will be used for target support systems adjacent to the target areas and will provide space for the control and data systems over the low-energy areas. The fourth level will provide access to the upper crane bay in the target building. Total space for the structure will be 3,300 m².

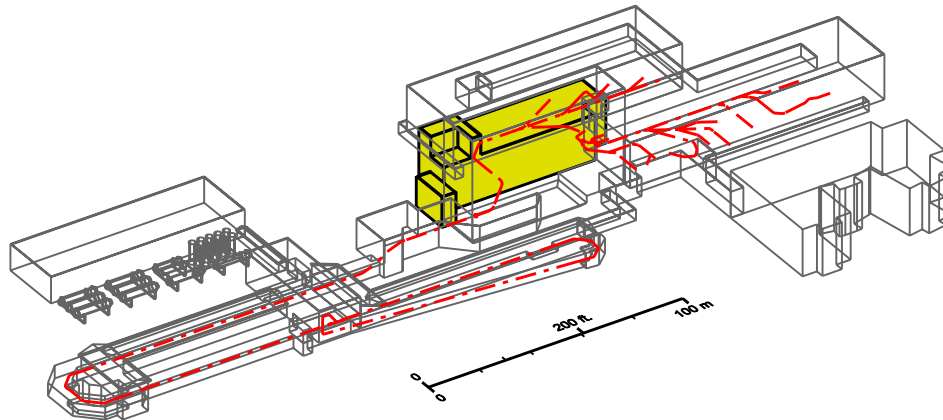


Figure 5.131: Connector structure.

High-energy facility

Figure 5.132 shows the 2,500 m² highbay structure that will house the high-energy facility apparatus. The steel frame structure will be equipped with a 12 m hook height overhead crane with 50-ton capacity. The exterior vault walls will be 3 m thick reinforced concrete. Reinforced concrete roof beams and modular concrete walls will provide interior radiation shielding. The vault shielding doors will utilize a vertical motion hydraulic ram-activated concrete block design. The S800 spectrograph will be housed in a 7 m deep pit similar to the NSCL's S800 pit.

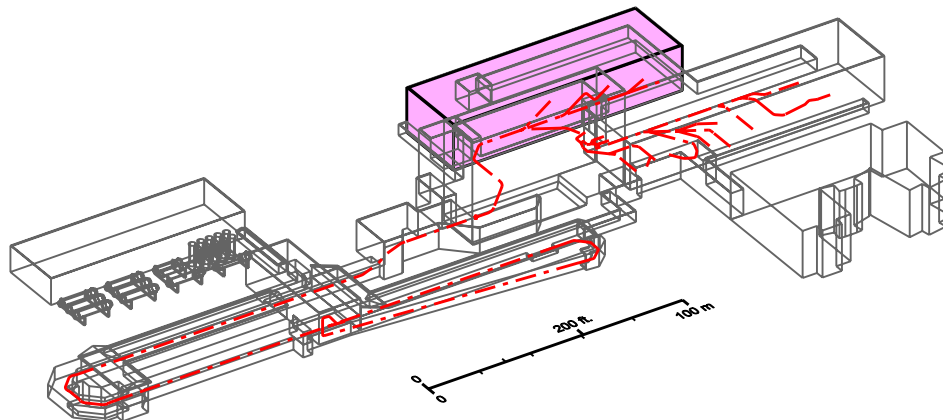


Figure 5.132: High-energy facility.

Low-energy facility

Figure 5.133 shows the 2,700 m² highbay structure that will house the low-energy facility. The steel structure will be equipped with a 10 m hook height 30-ton overhead crane. Local radiation shielding will be modular and provided as needed.

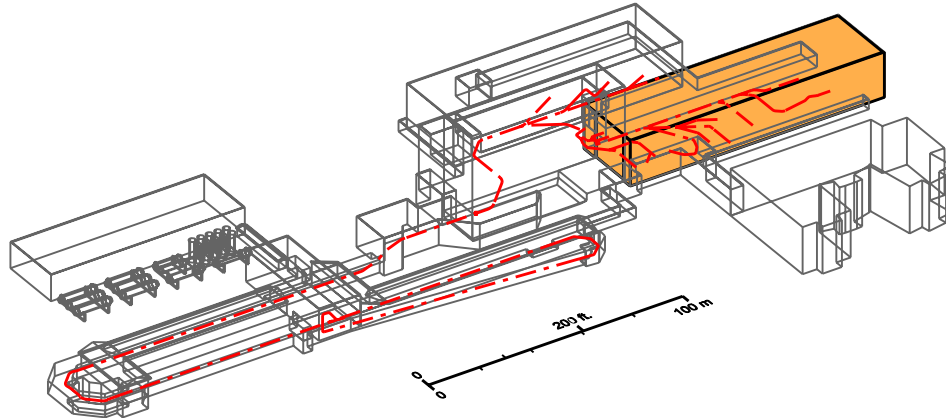


Figure 5.133: Low-energy facility.

Office building

The office building will provide about 8,000 m² of office and light laboratory space as shown in Figure 5.134. This together with the office and light lab space at the NSCL will meet the initial requirements for these functions. The office building footprint allows for building additions to meet future demands.

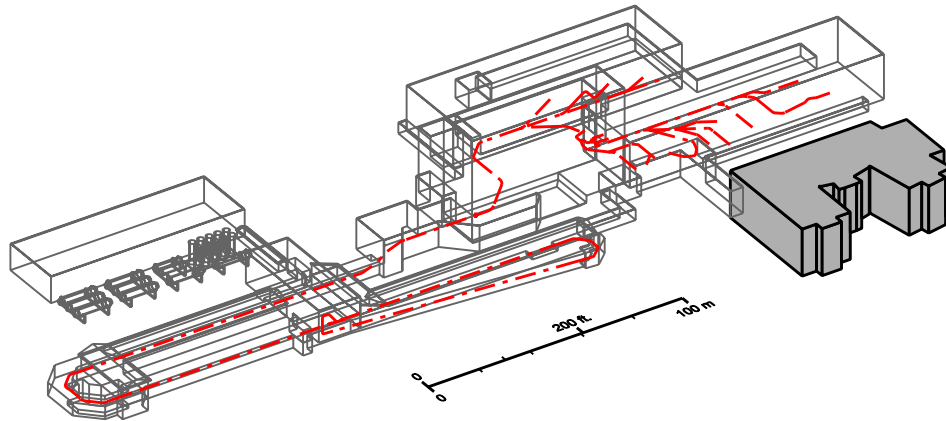


Figure 5.134: Office building.



6. Future upgrade options

The layout of the ISF has been optimized to easily allow the implementation of various modular upgrade options that can increase the scientific reach and productivity of the facility. ISF upgrades can be performed in a flexible way, responding to evolving nuclear science needs. They can also be implemented with minimum facility shutdowns, guaranteeing a continuation of the ongoing research program. Other alternative upgrade paths can be easily developed and accommodated at the ISF.

For reference, the baseline ISF described in Section 5 includes:

- a driver linac with a room temperature front end and a superconducting linac capable of producing 400 kW primary beams of stable isotopes with energies ranging from 200 MeV/nucleon for uranium to 525 MeV for protons
- a beam switchyard that delivers primary beams from the driver linac to an in-flight production target in a heavily shielded target hall
- an in-flight production target system followed by a two-stage fragment separator
- conventional construction for an ISOL target system in the target hall
- a secondary beam switchyard to deliver secondary beams from the fragment separator to the in-flight experimental areas and a gas stopper
- a gas stopping system for the generation of low-energy beams
- a reaccelerator based on an Electron Beam Ion Trap (EBIT) charge breeder, a room temperature RFQ, and a superconducting linac
- experimental areas for fast beams, low-energy beams from the cyclotron stopper, and reaccelerated beams

Figure 6.1 shows the ISF baseline facility together with the upgrade options that have been investigated and that will be discussed in this section. The upgrade options (not all independent of each other) are illustrated and outlined below:

- **An energy upgrade of the driver linac from 200 MeV/nucleon to 400 MeV/nucleon for uranium beams and from 525 MeV to 1 GeV for protons**

This would broaden the scientific reach of the facility by increasing both the ISOL and in-flight rates by factors of 4 to 20. The higher energy will also make the in-flight separation more selective, reducing contamination. Figure 6.1 illustrates how the energy upgrade can be implemented as discussed in Section 6.1 in a very compact way and with practically no changes to the initial accelerator system. The higher energy beams could be available to the target areas of the base facility as well as proposed second target areas, as described in Sections 6.1.9.

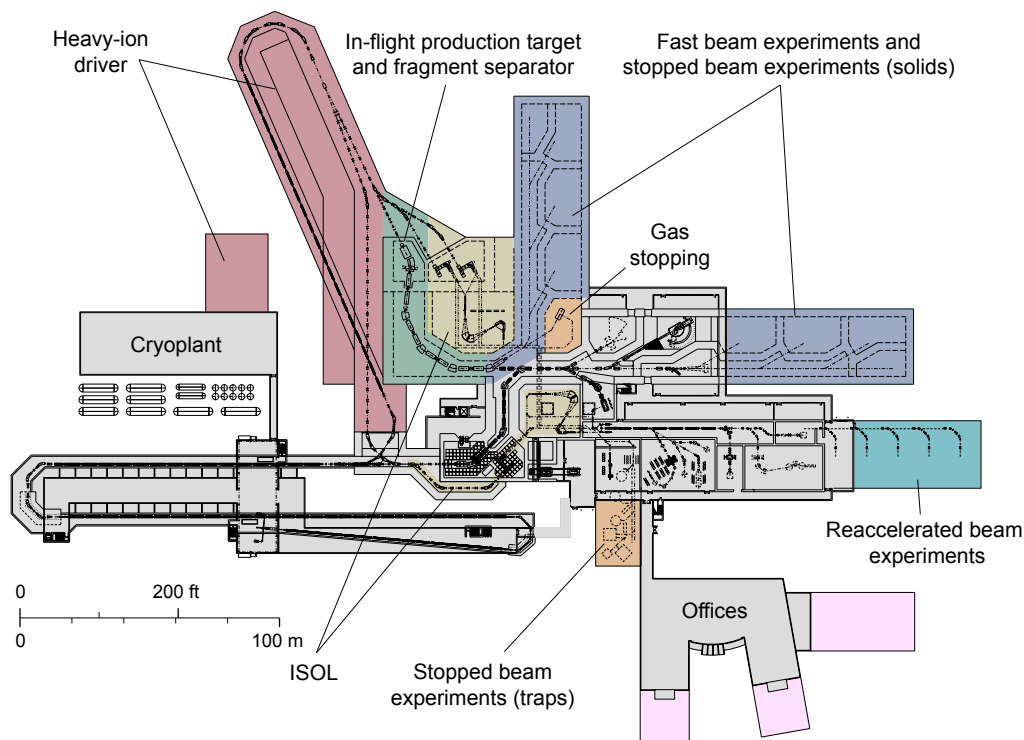


Figure 6.1: Layout of the ISF together with possible upgrade options. The base facility is shown in gray with the upgrade options shown in color.

- **The implementation of ISOL beam production using the conventional infrastructure constructed as an element of the initial ISF**

This would broaden the scientific reach of the facility by providing the intense beams possible from an ISOL source. The ISOL method's main advantage is very high beam intensities for isotopes of certain elements that have relatively long half-lives. Implementing ISOL beam production at the ISF would surpass capabilities of existing facilities. The construction of the base facility will be prepared to house an ISOL target station, the concomitant beam separation, and transport systems. Section 6.1.10 describes the realization of the primary beam transport to the ISOL target station. Section 6.2 discusses the aspects of high-power ISOL beam production and its implementation at the ISF.

- **A second target production area and associated in-flight and ISOL beam production systems**

This would implement multi-user capability and allow two simultaneous and independent users. For example, it would be possible to perform a fast-beam experiment simultaneously with a reaccelerated beam experiment fed from the gas-stopping station. As the layout in Figure 6.1 illustrates, the realization of the energy upgrade of the driver linac opens the door to the installation of a second target area, discussed in more detail in Section 6.3. The target area depicted would have one in-flight beam and two ISOL beam production systems.

- **A new additional experimental area for fast beam experiments and possible expansion of the reaccelerated beam and stopped beam experimental areas**

The areas for experiments with stopped and reaccelerated beams can be easily expanded without significant impact on operations. Multi-user capability can be implemented by providing beams to the stopped beam area simultaneously to the delivery of reaccelerated beams. In the case of an expansion of a fast beam experimental area, the realization of a new experimental area is the best option. The old and the new fast beam experimental areas can be served with beams from both in-flight beam production systems with maximum flexibility in operation and multi-user capability. Details of these upgrades are discussed in Section 6.4.

Section 6.1 describes the accelerator upgrade to higher energies together with the various beam transport systems to the target stations in the baseline ISF and the optional additional target station. This will be followed by a discussion of the implementation of ISOL beam production (Section 6.2), a second target station (Section 6.3), the upgrade of the experimental areas (Section 6.4), and the necessary civil construction details (Section 6.5). These options are shown in Figure 6.2.

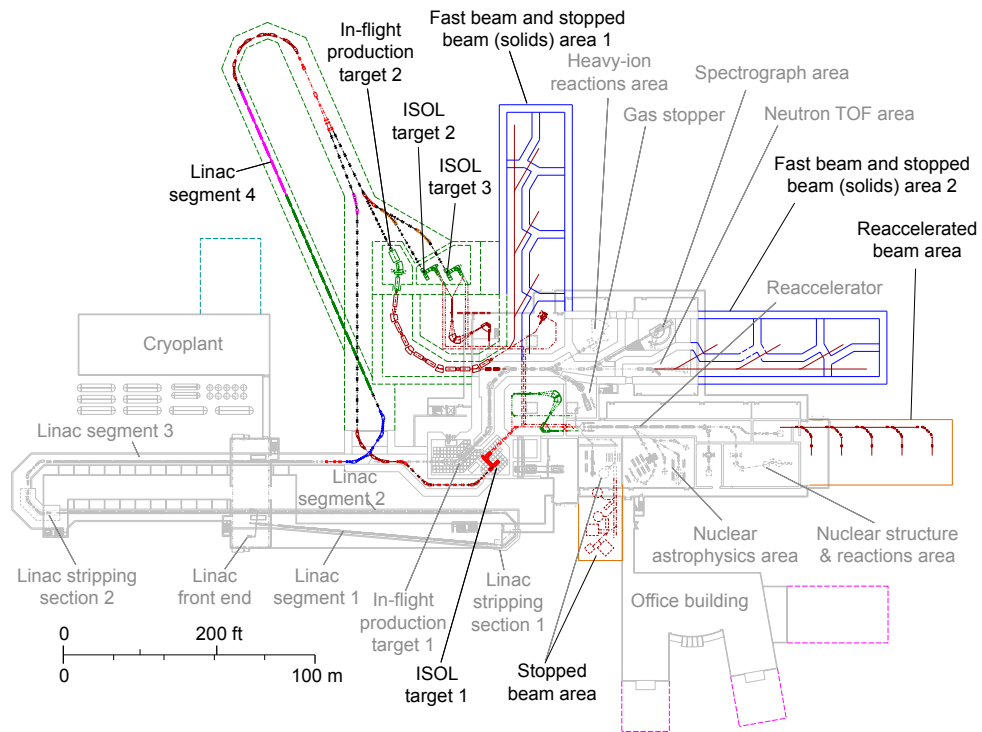


Figure 6.2: Schematic layout ISF showing the possible upgrade paths. The baseline ISF complex is shown in gray.

6.1 Driver linac upgrade

The driver linac upgrade increases the primary beam energy and distributes it to the target areas, as shown schematically in Figure 6.3. The upgrade uses a 200 MeV/u beamline to bring the beam from the baseline driver linac to the linac segment 4, which accelerates a uranium beam to 400 MeV/u and protons to 1 GeV. The beams are then transported via the 400 MeV/u beamline to the 400 MeV/u beam switchyard that will deliver and distribute the primary beams to both the baseline target area and possibly to a second target area. The following sections describe the beam transport and acceleration systems necessary to accomplish this upgrade.

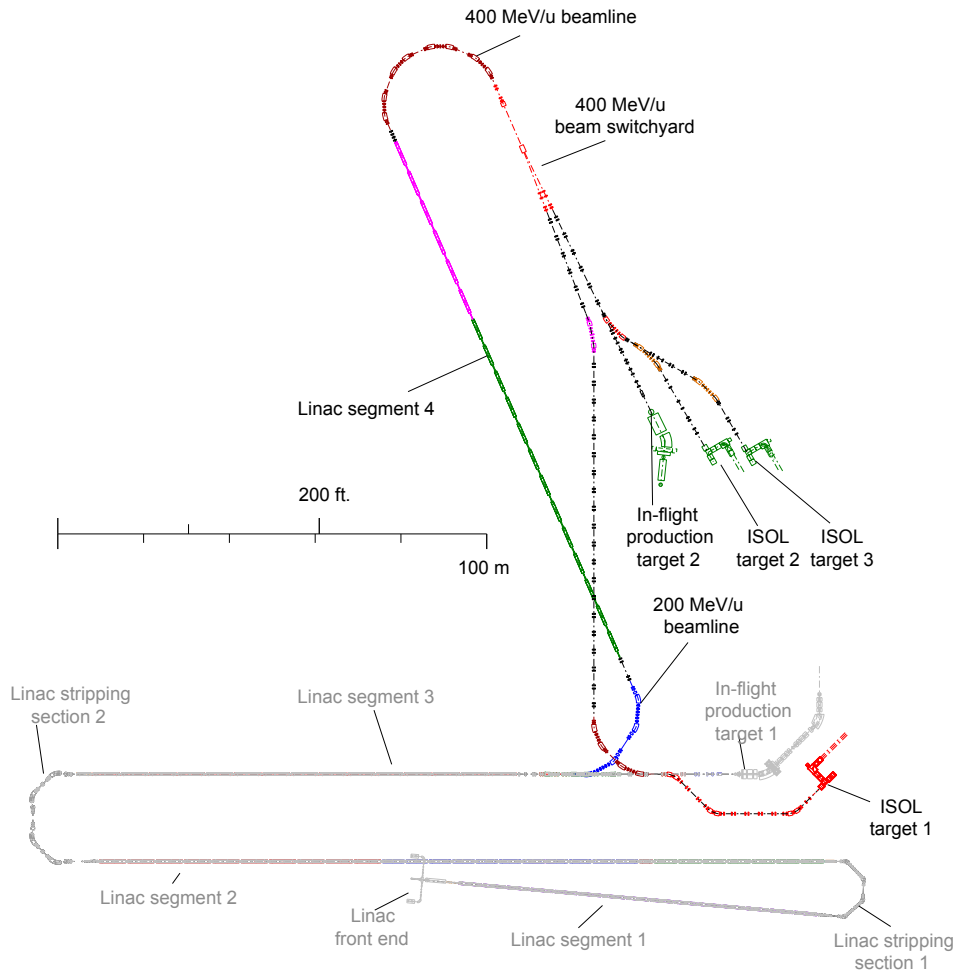


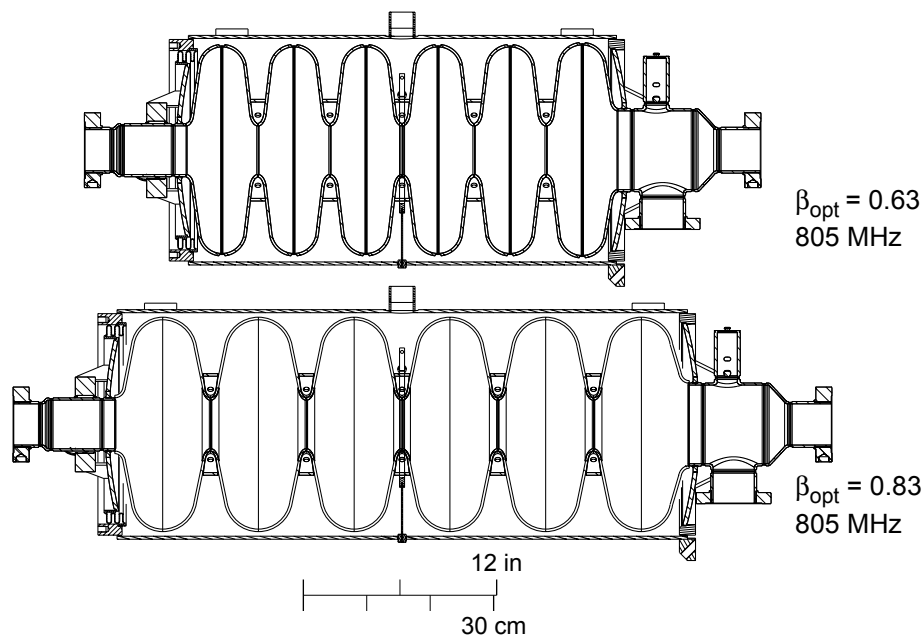
Figure 6.3: Schematic layout of driver linac upgrade, including the connecting beamlines and 400 MeV/u switchyard, with the baseline accelerator shown in gray.

6.1.1 SRF cavity design

Linac segment 4 will use the $\beta_{\text{geo}} = 0.61$ ($\beta_{\text{opt}} = 0.63$) and $\beta_{\text{geo}} = 0.81$ ($\beta_{\text{opt}} = 0.83$) 805 MHz superconducting elliptical accelerating structures developed for the SNS at ORNL [Kne02] to accelerate the uranium beam to 400 MeV/u and protons to 1 GeV. One important advantage of elliptical cavities is their large aperture (77 mm), which minimizes beam loss, relaxes alignment criteria, and eliminates the need for additional higher-order-mode couplers. The high energy SRF cavity design parameters are given in Table 6.1 and scale drawings of the cavities are shown in Figure 6.4.

Table 6.1: Elliptical cavity parameters.

| Type | 6-cell $\beta_{\text{opt}} = 0.63$ | 6-cell $\beta_{\text{opt}} = 0.83$ |
|-------------------------------|---------------------------------------|---------------------------------------|
| f (MHz) | 805 | 805 |
| E_p (MV/m) | 32.5 | 32.5 |
| V_a (MV) | 8.17 | 13.46 |
| L (m) | 0.682 | 0.906 |
| E_{acc} (MV/m) | 12.0 | 14.9 |
| E_p / E_{acc} | 2.7 | 2.2 |
| B_p (mT) | 68.6 | 70.2 |
| Aperture (m) | 0.077 | 0.077 |
| Max. transverse dimension (m) | 0.33 | 0.33 |
| Mass (kg) | 88 | 104 |
| T (K) | 2 | 2 |

**Figure 6.4:** Mechanical drawing of the high energy elliptical cavities.

The simple shape of the elliptical cavities allows effective utilization of chemical processing and high pressure rinsing in a clean room environment. As a consequence, elliptical cavities have reliably demonstrated maximum peak fields above 50 MV/m and 100 mT at 2 K. The design values for the elliptical cavities are $E_p = 32.5$ MV/m and $B_p \leq 70$ mT. This is less than the design values for the SNS cavities ($E_p = 35$ MV/m and $B_p = 76$ mT). Typically, the elliptical cavities can operate at a higher E_p than the $\lambda/4$ and $\lambda/2$ cavities because they were optimized for lower B_p .

The elliptical cavities were designed to generate a maximum accelerating voltage (V_a) at an optimum velocity (β_{opt}). The voltage gain is effective over a limited range

of velocities in these multigap structures. Figure 6.5 shows the transit time factor and energy gain per cavity as a function of β for a uranium beam. For acceleration of uranium up to 400 MeV/u (corresponding to $\beta = 0.72$), there is no advantage in switching to the last elliptical cavity type ($\beta_{\text{opt}} = 0.83$), but the addition will provide a significantly higher energy for protons due to the effectiveness of this cavity at higher velocity. Since the $\beta_{\text{opt}} = 0.83$ elliptical cavity has already been developed, there is no technical risk and a minimal increase in cost for a significantly higher proton energy. Using the cavity parameters listed in Table 6.1, the number of cavities, superconducting quadrupoles, and cryomodules needed to accelerate uranium to 400 MeV/u and protons to 1 GeV are given in Table 6.2.

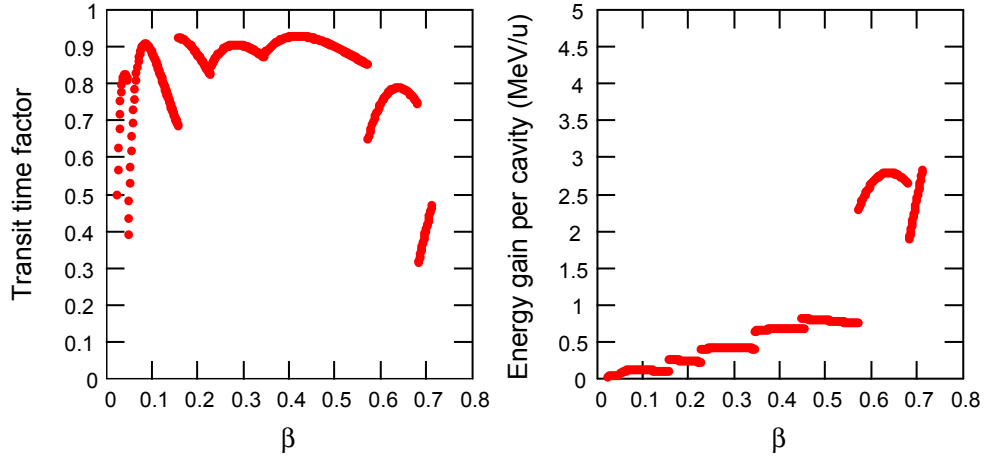


Figure 6.5: Transit time factor (left) and energy gain per cavity (right) as a function of the particle velocity for the uranium beam in the driver linac. The two traces at the larger β correspond to segment 4 of the linac (for 89^+ charge state).

Table 6.2: Cavity and cryomodule count for the driver linac upgrade using the design gradients of Table 6.1.

| Type | $\lambda/2$ $\beta_{\text{opt}} = 0.425$ | 6-cell $\beta_{\text{opt}} = 0.63$ | 6-cell $\beta_{\text{opt}} = 0.83$ |
|------------------------------------|---|---------------------------------------|---------------------------------------|
| Number of cavities | 5 | 53 | 24 |
| Number of quadrupole magnets | — | 28 | 14 |
| Number of accelerating cryomodules | — | 13 | 6 |
| Number of matching cryomodules | 1 | 1 | — |
| Total number of cryomodules | 1 | 14 | 6 |
| Accelerating cryomodule length (m) | — | 6.62 | 7.51 |
| Matching cryomodule length (m) | 2.718 | 1.485 | — |

6.1.2 SRF cryogenic requirements

The operating temperature and cryogenic load of the superconducting cavities were calculated to determine the additional cryoplant capacity and cost. The analysis is the same as for the baseline linac (See Section 5). The power dissipation is inversely proportional to $(R/Q)G$, whose values are given in Table 6.3. The 6-cell elliptical cavities have larger values of $(R/Q)G$ than the $\lambda/2$ cavities, but they also produce larger accelerating voltages and hence a larger cryogenic load per cavity.

Table 6.3: Electromagnetic and cryogenic parameters.

| Type | $\lambda/2$ $\beta_{\text{opt}} = 0.425$ | 6-cell $\beta_{\text{opt}} = 0.63$ | 6-cell $\beta_{\text{opt}} = 0.83$ |
|-------------------------------------|---|---------------------------------------|---------------------------------------|
| f (MHz) | 322 | 805 | 805 |
| T (K) | 2 | 2 | 2 |
| R/Q (Ω) | 199 | 279 | 483 |
| G (Ω) | 86 | 179 | 260 |
| GR/Q ($k\Omega^2$) | 18.1 | 49.9 | 126.0 |
| E_p (MV/m) | 30 | 32.5 | 32.5 |
| V_a (MV) | 2.51 | 8.17 | 13.46 |
| U (J) | 14.93 | 47.2 | 74.2 |
| $R_{\text{BCS,min}}$ (n Ω) | 0.7 | 4.2 | 4.2 |
| $R_{\text{res,min}}$ (n Ω) | 5 | 5 | 5 |
| Q_{max} | 1.5×10^{10} | 2.0×10^{10} | 2.8×10^{10} |
| $Q_{\text{design}} = Q_o$ | 7×10^9 | 1.0×10^{10} | 1.4×10^{10} |
| P_{design} (W/cav) = P_o | 4.3 | 23.9 | 26.8 |

The variation of the BCS component of the surface resistance is shown as a function of temperature in Figure 6.6 for reactor grade (RRR~25) and high purity (RRR~250) niobium at 322 and 805 MHz. A lower BCS resistance can occur on the rf surface of high RRR niobium due to contamination (surface impurities) that, for example, arise from processing or bake-out. The elliptical cavities in linac segment 4 will be operated at 2 K to give minimum BCS surface resistances of less than 5 n Ω for all cavity types.

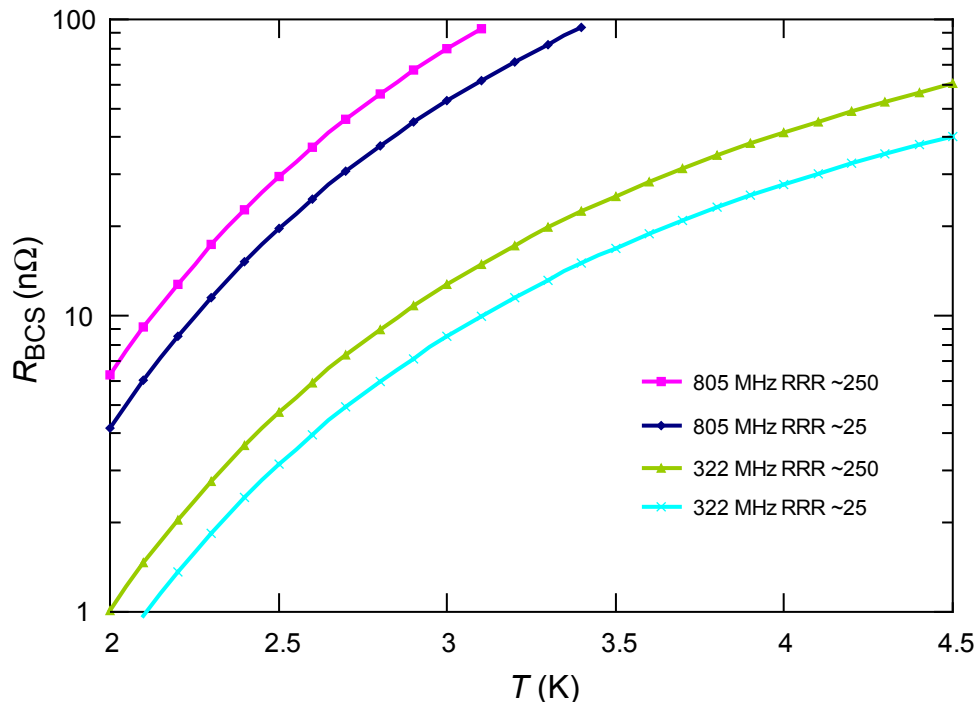


Figure 6.6: The variation of R_{BCS} values with temperature for niobium with various values of RRR. The operating temperature for the elliptical and $\lambda/2$ cavities will be 2 K.

The final parameter left to be determined is the residual resistance. Well-processed elliptical cavities can yield residual resistances of 2–10 nΩ [Pad98]. As a design goal, we assume a residual resistance of 5 nΩ for all cavity types, which, along with the BCS term, gives a minimum possible surface resistance. From this value a maximum possible Q , Q_{\max} , is given in Table 6.3. For all cavities, a safety factor of two is used to obtain a Q_{design} that is half of Q_{\max} . The operating elliptical cavities of SNS exceed these requirements [Hen06]. To compare power levels at different cryogenic temperatures requires taking into account Carnot efficiency and mechanical efficiencies of 18% at 2 K and 30% at 4.5 K [Sch03a].

The estimates of the resulting cryogenic loads are shown in Table 6.4. These loads were calculated from the number of cavities per cryomodule with their design dynamic loads plus a 25 W static load per cryomodule for thermal radiation and intercepts. The cavities present a dynamic load when the beam is being accelerated, so the cryogenic plant has excess capacity during the cool-down phase of operations. The thermal shield of each cryomodule will use 50 K helium return gas, with a load of less than 100 W load per cryomodule.

Table 6.4: Estimated cryogenic load per cryomodule with the total/static loads shown separately.

| Operating temperature | 2 K load |
|--------------------------------------|----------|
| 322 MHz $\beta_{\text{opt}} = 0.425$ | 38/25 W |
| 805 MHz $\beta_{\text{opt}} = 0.63$ | 121/25 W |
| 805 MHz $\beta_{\text{opt}} = 0.83$ | 133/25 W |

6.1.3 SRF beam loading, rf, and microphonics requirements

Superconducting cavities require very little rf power to generate large accelerating gradients, and therefore have very high cavity quality factors, Q_o . For example, Q_o will be greater than 10^8 for the low β cavities and greater than 10^{10} for high β cavities. However, additional rf power will be required for beam acceleration and control of microphonics. Under ideal conditions, the beam loading is large enough so that the system bandwidth is much larger than any detuning. In this case, the rf generator power (P_g) is equal to the beam power (P_{beam}). To account for microphonics and other sources of detuning, P_g is chosen to be twice as large as P_{beam} .

Using the uranium beam current for the ISF baseline described in Section 5, the beam loading values for the linac upgrade are shown in Table 6.5. Because the $\beta_{\text{opt}} = 0.83$ cavity does not accelerate uranium at the peak of its transit time curve, the maximum beam loading is nearly the same as that for the maximum value in the $\beta_{\text{opt}} = 0.63$ cavities. The allowable detuning, assuming a generator power that is twice the beam power, is also shown in Table 6.5. Most of the cavities will be able to handle significantly higher detuning than that shown in Table 6.6 since the beam loading will be smaller than the maximum beam loading. The measured microphonics levels indicate that the values in Table 6.5 are adequate with passive and active dumping.

Table 6.5: Beam loading requirements for the 400 MeV/u uranium beam in the ISF driver linac upgrade.

| Type | $\lambda/2$ $\beta_{\text{opt}} = 0.425$ | 6-cell $\beta_{\text{opt}} = 0.63$ | 6-cell $\beta_{\text{opt}} = 0.83$ |
|---|---|---------------------------------------|---------------------------------------|
| V_a (MV) | 2.51 | 8.17 | 13.46 |
| I_{beam} (pμA) | 8.3 | 8.3 | 8.3 |
| $\langle Q \rangle$ | 89 | 89 | 89 |
| P_{beam} (W) | 1610 | 5220 | 5140 |
| Q_{beam} | 1.9×10^7 | 4.6×10^7 | 7.1×10^7 |
| P_g (W) | 3210 | 10,440 | 10,280 |
| Q_L | 6.2×10^6 | 1.5×10^7 | 2.4×10^7 |
| Control bandwidth Δ_{allowed} (Hz) | 47 | 49 | 32 |

Table 6.6: Number of cryomodules needed for the driver linac upgrade.

| | Matching cryomodules (# modules) | Accelerating cryomodules (# modules) |
|--|----------------------------------|--------------------------------------|
| $\lambda/2 \beta_{\text{opt}} = 0.425$ | 1 | — |
| 6-cell $\beta_{\text{opt}} = 0.63$ | 1 | 13 |
| 6-cell $\beta_{\text{opt}} = 0.83$ | — | 6 |
| Total | 2 | 19 |

6.1.4 Cryomodule development

Linac segment 4 will use elliptical cavities for acceleration along with cryomodules for beam matching that use both elliptical and half-wave cavities. All modules will be based on a cold titanium alignment rail to support the cavities and focusing elements [Gri03b]. The beamline vacuum will be isolated from the insulating vacuum. The rail will be suspended from a plate that will be the top of a rectangular box. A low carbon steel box will be assembled around the cold mass and welded shut. Table 6.6 shows the number of cryomodules needed for segment 4.

Cross-sectional views of the driver linac upgrade cryomodules are shown in Figure 6.7 through Figure 6.10. The accelerating lattice will use room temperature quadrupole doublets in the same configuration as the SNS.

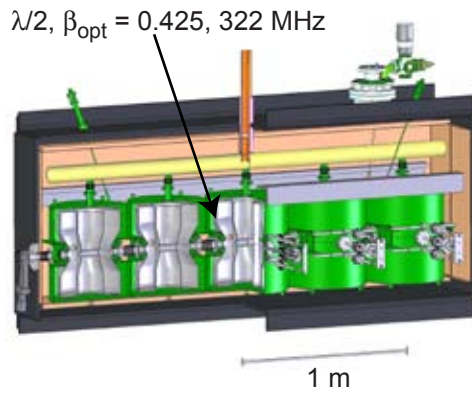


Figure 6.7: Cross section of the matching cryomodule with five $\lambda/2$ cavities ($\beta_{opt} = 0.425$) at 322 MHz. The left side of the figure shows a sectional view of the cavities.

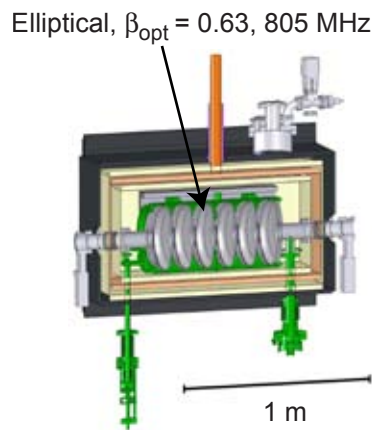


Figure 6.8: Cross section of the matching cryomodule with one elliptical cavity ($\beta_{opt} = 0.63$) at 805 MHz.

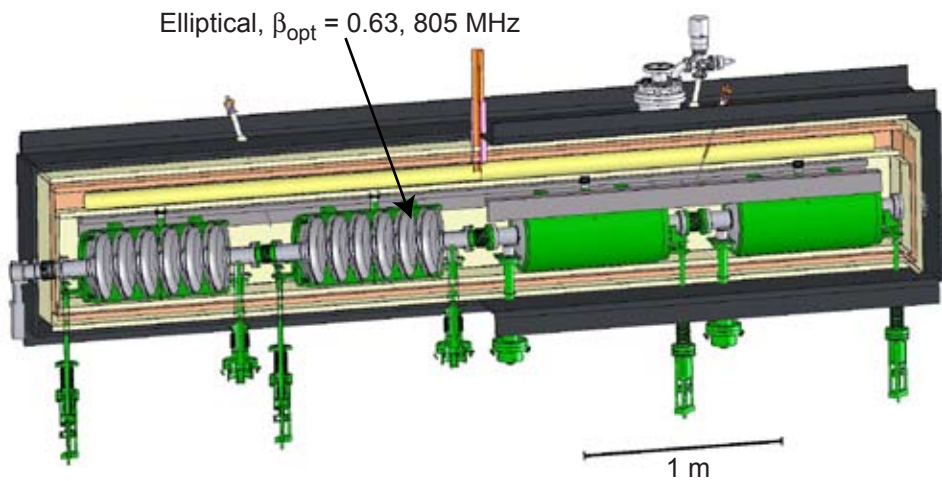


Figure 6.9: Cross section of an accelerating cryomodule with four elliptical ($\beta_{opt} = 0.63$) cavities at 805 MHz. The left side of the figure shows a sectional view of the cavities.

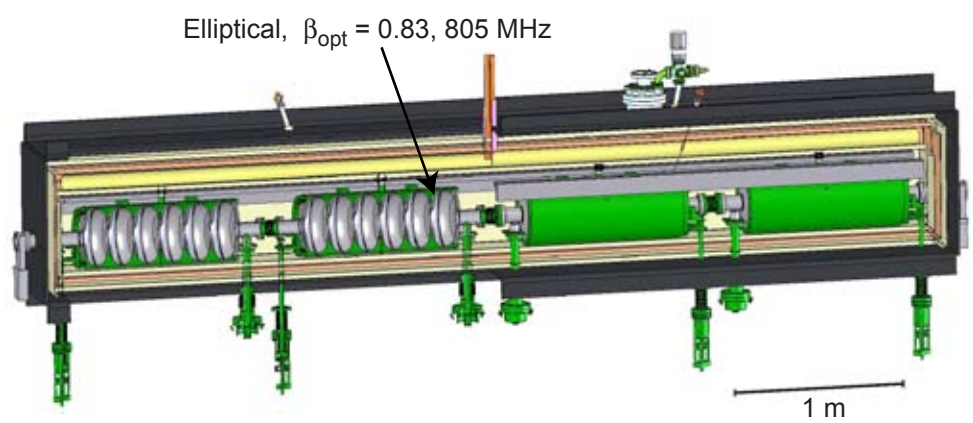


Figure 6.10: Cross section of an accelerating cryomodule with four elliptical cavities ($\beta_{opt} = 0.83$) at 805 MHz. The left side of the figure shows a sectional view of the cavities.

6.1.5 RF systems and cryogenics

The same low level rf system will be used in the baseline driver linac (see Section 5) and the linac upgrade. The cavities operated at 322 MHz will be powered by solid-state rf amplifiers due to the low power requirements and their availability. The cavities operated at 805 MHz will be powered by tetrode vacuum tubes, which are the best solution currently available for power levels up to 10 kW. The rf requirements for the driver linac upgrade are shown in Table 6.7.

Table 6.7: RF amplifier requirements for the driver linac upgrade.

| Cavity | $\lambda/2$ $\beta_{opt} = 0.425$ | 6-cell $\beta_{opt} = 0.63$ | 6-cell $\beta_{opt} = 0.83$ |
|---------------------|--------------------------------------|--------------------------------|--------------------------------|
| Frequency (MHz) | 322 | 805 | 805 |
| Quantity | 5 | 53 | 24 |
| $P_{generator}$ (W) | 4000 | 12,000 | 12,000 |
| Amplifier type | Solid-state | Tetrode vacuum tube | |

The rf power source of an accelerator can be a significant cost. A lower cost solution of using tetrode vacuum tubes as opposed to costly inductive output tubes or klystrons has been tested by the NSCL for the 805 MHz cavities. In this prototype, an effort was made to use off-the-shelf components as much as possible. The only custom component in the final system consists of a circuit used to interface the control hardware. The backbone of the amplifier is a THALES TH 382 vacuum tetrode and a TH 18482 rf tuning cavity. This tube was selected because of its proven track record in the broadcasting industry. The prototype at NSCL uses an air-cooled design for ease of mobility. The proposed system would use the TH 582 water-cooled tube as well as its matching TH 18582 cavity to reduce cost and size. Water is already needed to cool the circulator and load at the output of the amplifier.

The additional cryoplant capacity that will be required for the driver linac upgrade is shown in Table 6.8. Cryogenic loads have been increased by 50% to include distribution losses and an additional safety margin. For reference, a one watt thermal load will boil 1.4 l/h of liquid helium. The thermal intercept will use 50 K helium gas, so no liquid nitrogen will be used in the tunnels, which will reduce oxygen deficiency hazards. The flow diagram for the cryoplant with the additional load due to segment 4 is shown in Figure 6.11. The assumed mechanical efficiency of the cryoplant was inferred from experience at CEBAF [Sch03a].

Table 6.8: Additional cryoplant load (total/static) for the driver linac upgrade.

| | # modules | 2 K Load (kW) | 4.5 K load (kW) | 50 K load (kW) |
|-------------------------|-----------|------------------|-----------------|----------------|
| Cryomodules | 21 | 3.69/0.79 | — | 3.1 |
| Superconducting magnets | — | — | 3 | 3.6 |
| Total | 21 | 3.69/0.79 | 3 | 6.7 |

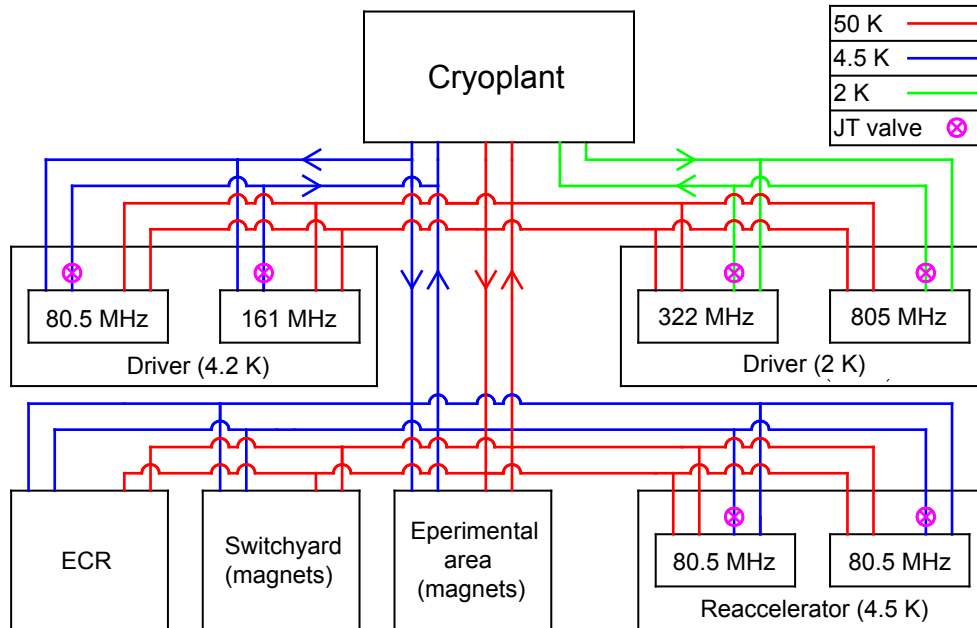


Figure 6.11: Cryogenic flow diagram.

6.1.6 The 200 MeV/u beamline

The 200 MeV/u beamline of the driver linac upgrade will transport the beam from the existing beam switchyard of the baseline facility to linac segment 4 for further acceleration. Similar to the optical design of the baseline driver linac stripping sections, the 200 MeV/u beamline will have three distinct sections. A straight section consisting of four quadrupoles will first provide transverse focusing and phase space matching capability. The second section will be a horizontal second order achromat to bend the incoming multiple charge state beams by 113.5° while minimizing growth of the transverse and longitudinal emittances. A third section will be used to match the beams transversely and longitudinally into linac segment 4. Figure 6.12 shows the layout of the 200 MeV/u beamline.

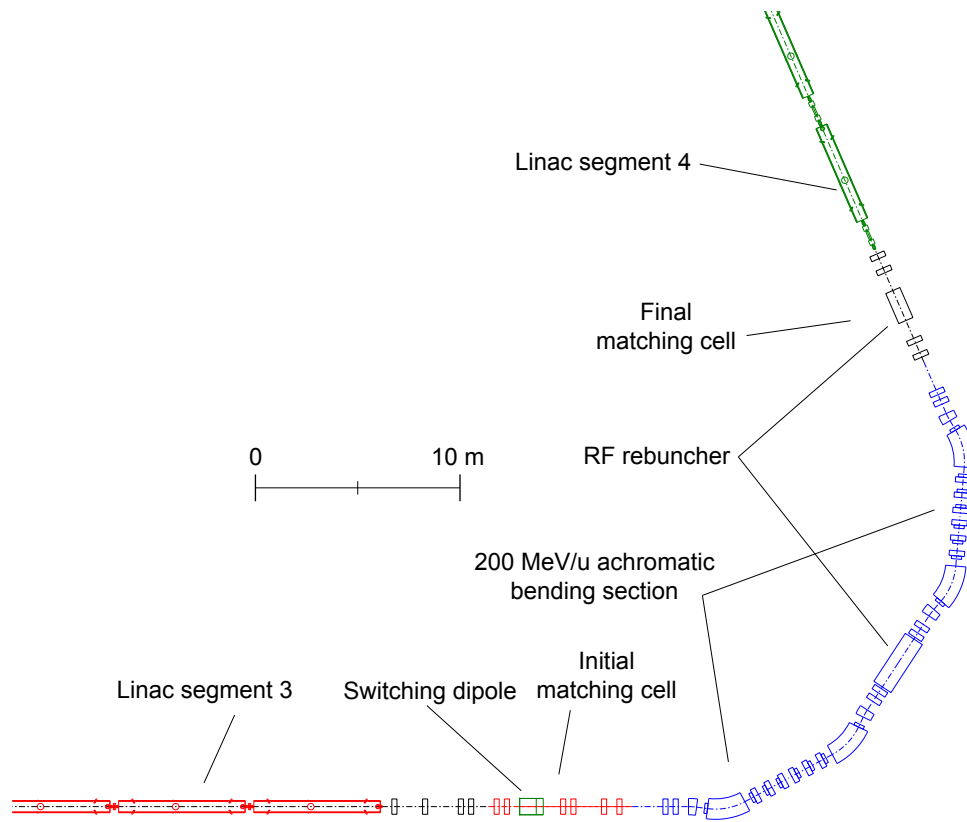


Figure 6.12: Schematic layout of the 200 MeV/u beamline of the driver linac upgrade. The switching dipole is a vertical bending magnet that is part of the baseline system.

The first dipole of the vertical achromat in the baseline beam switchyard will act as a switching magnet. This magnet will either bend the beam up to the baseline target area or send the beam into the 200 MeV/u beamline on the same level. In this later case, four quadrupole magnets will be used to provide the initial focusing after the switching dipole.

In the 113.5° horizontal achromat of the 200 MeV/u beamline, four reverse -7.5° dipoles will be combined with four $+35.875^\circ$ main dipoles to achieve an isochronous condition for all charge states and avoid significant longitudinal emittance growth. Five $\lambda/2$ cavities ($\beta_{\text{opt}} = 0.425$) at 322 MHz will be used as rebunchers in the middle of the bending achromat (see Figure 6.12).

The last section of the 200 MeV/u beamline will be a matching cell using four quadrupole magnets and a single cryomodule with one elliptical cavity ($\beta_{\text{opt}} = 0.63$) at 805 MHz to achieve the required beam conditions at the entrance of the linac segment 4. The transverse and longitudinal betatron functions in the 200 MeV/u beamline are shown in Figure 6.13. The input and output parameters for a uranium beam are listed in Table 6.9.

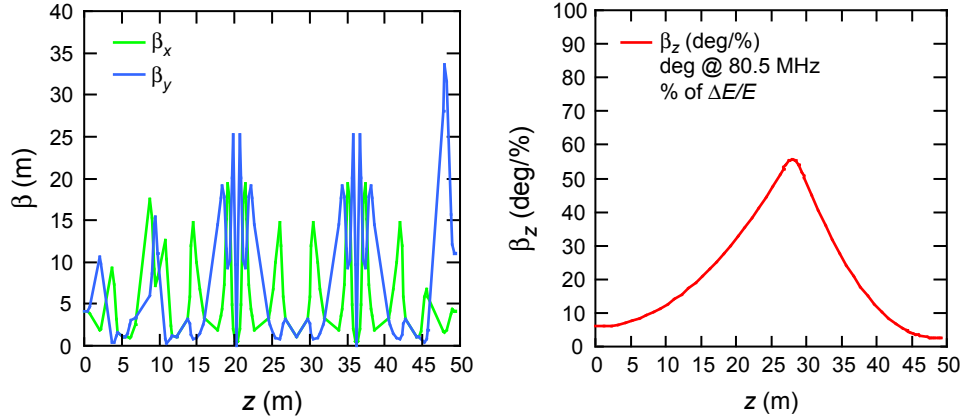


Figure 6.13: Transverse (left) and longitudinal (right) betatron functions of the 200 MeV/u beamline.

Table 6.9: Parameters for the uranium beam (Twiss parameters are for 89⁺) in the 200 MeV/u beamline.

| | Input | Output |
|-------------------|-------|--------|
| Energy (MeV/u) | 200 | 200 |
| β_z (deg/%) | 5.98 | 2.73 |
| α_z | -0.03 | 0.21 |
| β_x (m) | 4.07 | 4.15 |
| α_x | -0.02 | 0.44 |
| β_y (m) | 4.07 | 10.97 |
| α_y | -0.02 | 2.08 |
| Q | 88–90 | 88–90 |
| A | 238 | 238 |

6.1.7 Linac segment 4

Segment 4 of the driver linac will be used to accelerate the three charge states of the uranium beam (88⁺ to 90⁺) from 200 MeV/u to 400 MeV/u, using thirteen $\beta_{\text{opt}} = 0.63$ and six $\beta_{\text{opt}} = 0.83$ accelerating cryomodules (Section 6.1.4). Quadrupole doublets will be placed between the cryomodules to provide transverse focusing. Segment 4 will be ~130 meters long, and the minimum transverse aperture will be the 50 mm aperture diameter of the quadrupole magnets.

The overall longitudinal acceptance of linac segment 4 together with the uranium beam is shown in Figure 6.14. The 99.5% beam longitudinal emittance (without alignment or rf errors) at the entrance of linac segment 4 is approximately 17π keV/u ns (see Section 5.1). The longitudinal acceptance for the segment is ~262 π keV/u ns, giving a comfortable acceptance to emittance ratio of ~15. The longitudinal and transverse phase advances along linac segment 4 are also illustrated in Figure 6.14. As in the other linac segments of the ISF baseline, no parametric resonance was expected nor observed in the simulations.

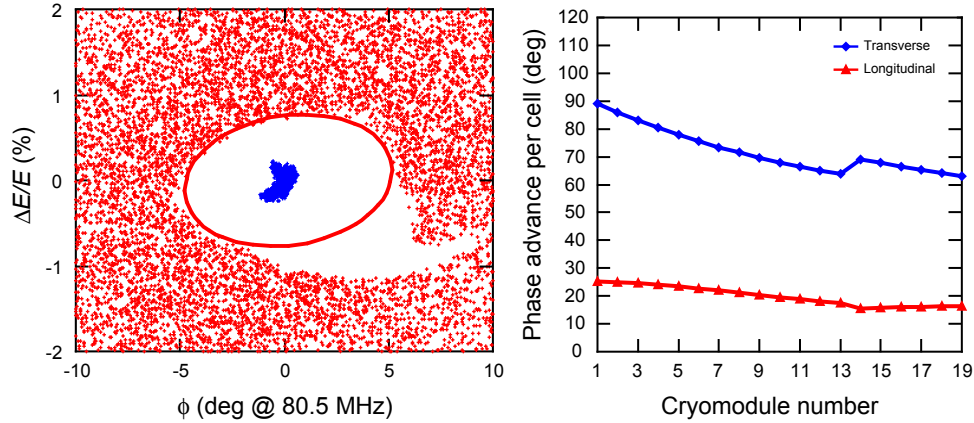


Figure 6.14: Left: Longitudinal acceptance (area with red ellipse) of linac segment 4 together with the input uranium beam (blue). The full phase space displayed was populated with particles; those particles that were lost are displayed as red dots. The acceptance to emittance ratio is ~ 15 . Right: Phase advances (charge state 89^+) along linac segment 4.

The transverse and longitudinal betatron functions for the uranium beam in segment 4 are illustrated in Figure 6.15 and the beam parameters entering and exiting the segment are summarized in Table 6.10. Beam dynamics simulations were performed in linac segment 4 for the most challenging case, the multiple-charge-state uranium beam. Due to the acceleration of multiple charge states, the transverse and longitudinal emittances increase as the beam propagates through the segment, even when errors are not included in the simulations. The initial normalized 99.5% transverse and longitudinal emittances of the uranium beam at injection are about 1.5π mm mrad and 17.1π keV/u ns, respectively (see Section 5.1). Beam simulations show that the emittances at the exit of the segment will be 1.6π mm mrad and 23.2π keV/u ns, respectively. The corresponding rms emittances are about ten times smaller. The emittance growths in the segment are acceptable and the maximum beam envelope along the segment will be ~ 10 mm, leading to a transverse aperture to beam envelope ratio of ~ 2.5 . Thus, beam dynamics studies indicate that linac segment 4 has adequate transverse and longitudinal acceptances, even for acceleration of the multiple charge states of the uranium beam.

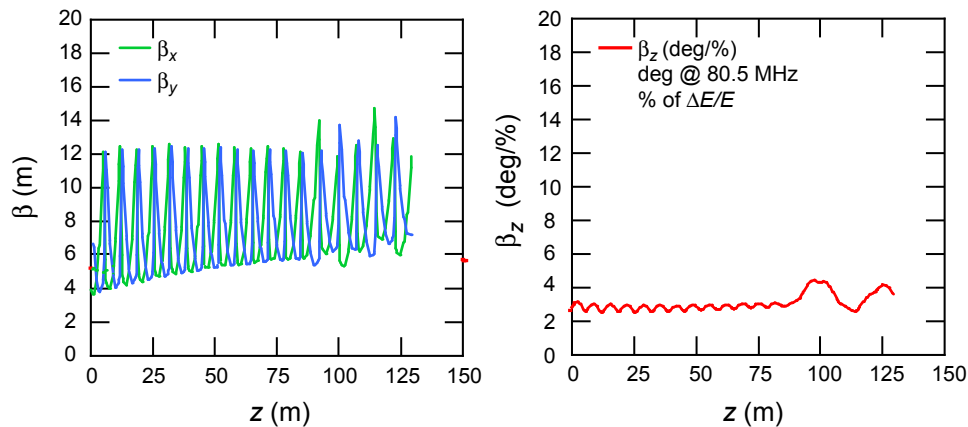


Figure 6.15: Transverse and longitudinal betatron functions in linac segment 4 for the uranium beam (89^+).

Table 6.10: Uranium beam parameters (Twiss parameters for 89⁺) in linac segment 4.

| | Input | Output |
|-------------------|-------|--------|
| Energy (MeV/u) | 200 | 400 |
| β_z (deg/%) | 2.73 | 3.60 |
| α_z | 0.21 | -0.27 |
| β_x (m) | 4.15 | 11.84 |
| α_x | 0.44 | -1.24 |
| β_y (m) | 10.97 | 7.23 |
| α_y | 2.08 | -0.12 |
| Q | 88–90 | 88–90 |
| A | 238 | 238 |

6.1.8 The 400 MeV/u beamline

The 400 MeV/u beamline of the driver linac upgrade will be a 180° bending section to transport the beam from linac segment 4 to the 400 MeV/u beam switchyard. The 400 MeV/u beamline will have two sections as shown in Figure 6.16. The first section is a straight section consisting of four quadrupole magnets to provide the initial transverse focusing and phase space matching capability. The second section is a second order achromat to simultaneously bend the beam 180° toward

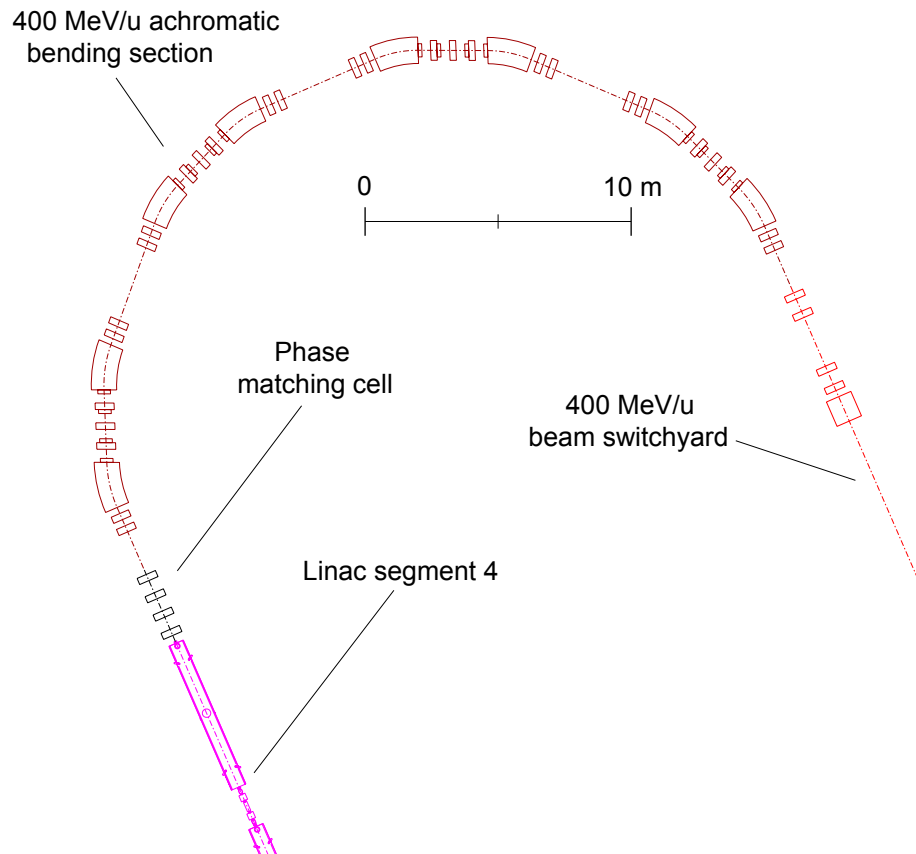


Figure 6.16: The layout of the 400 MeV/u beamline of the driver linac upgrade.

the 400 MeV/u beam switchyard and bring the beam up from the linac tunnel to ground level. A total of eight 22.5° dipole magnets will be used to obtain the total bending angle of 180°. Correction sextupole magnets will be used to limit the second order chromatic aberrations and minimize beam transverse emittance growth. The transverse betatron functions and beam envelopes of the 400 MeV/u beamline are shown in Figure 6.17 and the input and output parameters for the uranium beam are listed in Table 6.11.

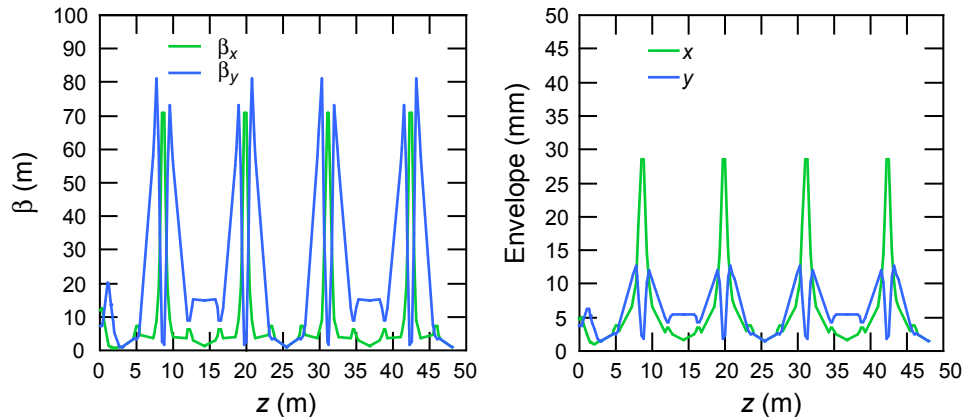


Figure 6.17: Betatron functions (left) and beam envelopes (right) for the uranium beam in the 400 MeV/u beamline.

Table 6.11: Parameters of the uranium (89^+) beam in the 400 MeV/u beamline.

| | Input | Output |
|-------------------|-------|--------|
| Energy (MeV/u) | 400 | 400 |
| β_z (deg/%) | 3.60 | 97.0 |
| α_z | -0.27 | 5.28 |
| β_x (m) | 11.84 | 1.00 |
| α_x | -1.24 | 0.00 |
| β_y (m) | 7.23 | 1.00 |
| α_y | -0.12 | 0.00 |
| Q | 88–90 | 88–90 |
| A | 238 | 238 |

6.1.9 The 400 MeV/u beam switchyard

The 400 MeV/u beam switchyard of the driver linac upgrade will deliver and distribute the multiple charge states of the primary beams with final energies ≥ 400 MeV/u to both the baseline target area and possibly to a second target area (see Section 6.3). Beam dynamics simulations for the multiple charge states uranium beam were performed to confirm design performance. The basic parameters used in the simulations are listed in Table 6.12.

Table 6.12: Uranium beam parameters used for beam simulations in the 400 MeV/u beam switchyard.

| Parameter | Value |
|--|------------------------------------|
| Energy (MeV/u) | 400 |
| Charge states | 88 ⁺ to 90 ⁺ |
| Magnetic rigidity (Tm) | 8.5 |
| Beam frequency (MHz) | 80.5 |
| 99.5% transverse emittance (π mm mrad) | 1.6 |
| 99.5% longitudinal emittance (π keV/u ns) | 23.2 |

The 400 MeV/u beam switchyard will service both target areas. The required beam conditions for ISOL and for in-flight production are significantly different. For the ISOL target, light ion beams are desired with a beam size on target of about 10 to 50 mm in diameter. The in-flight production target will use heavy-ion beams with a beam size on target approximately 1 mm in diameter. In addition, the 400 MeV/u beam switchyard should be able to simultaneously feed at least two target stations.

Figure 6.18 shows the layout of the 400 MeV/u beam switchyard. As illustrated, the beam can be transported to either the baseline target area or to the second target area (see Section 6.3) using a beam distribution system. The beam will then be transported to any downstream target using various beam transport lines.

6.1.9.1 Beam distribution system

In the 400 MeV/u beam switchyard, a beam distribution system will be able either to feed any single target using a switching dipole or to feed two targets simultaneously using an rf kicker and septum magnet. Quadrupole magnets will be used before and after the beam distribution system to provide adequate transverse focusing and achieve required matching conditions.

The quadrupole magnets located in front of the rf kicker will provide transverse focusing to produce reasonable transverse beam envelopes in the system and a small horizontal beam spot at the entrance of the septum magnet to avoid beam loss on the septum. As shown in Figure 6.19, the rf kicker and switching dipole have the same kick angle of ± 1.5 mrad and will be used to split or switch the incoming beam into the two downstream beamlines. A 10 m long drift after the beam split will generate enough separation to accommodate a 10 mm septum in the septum magnet. Tables 6.13 and 6.14 list the hardware parameters for the rf kicker and septum magnet.

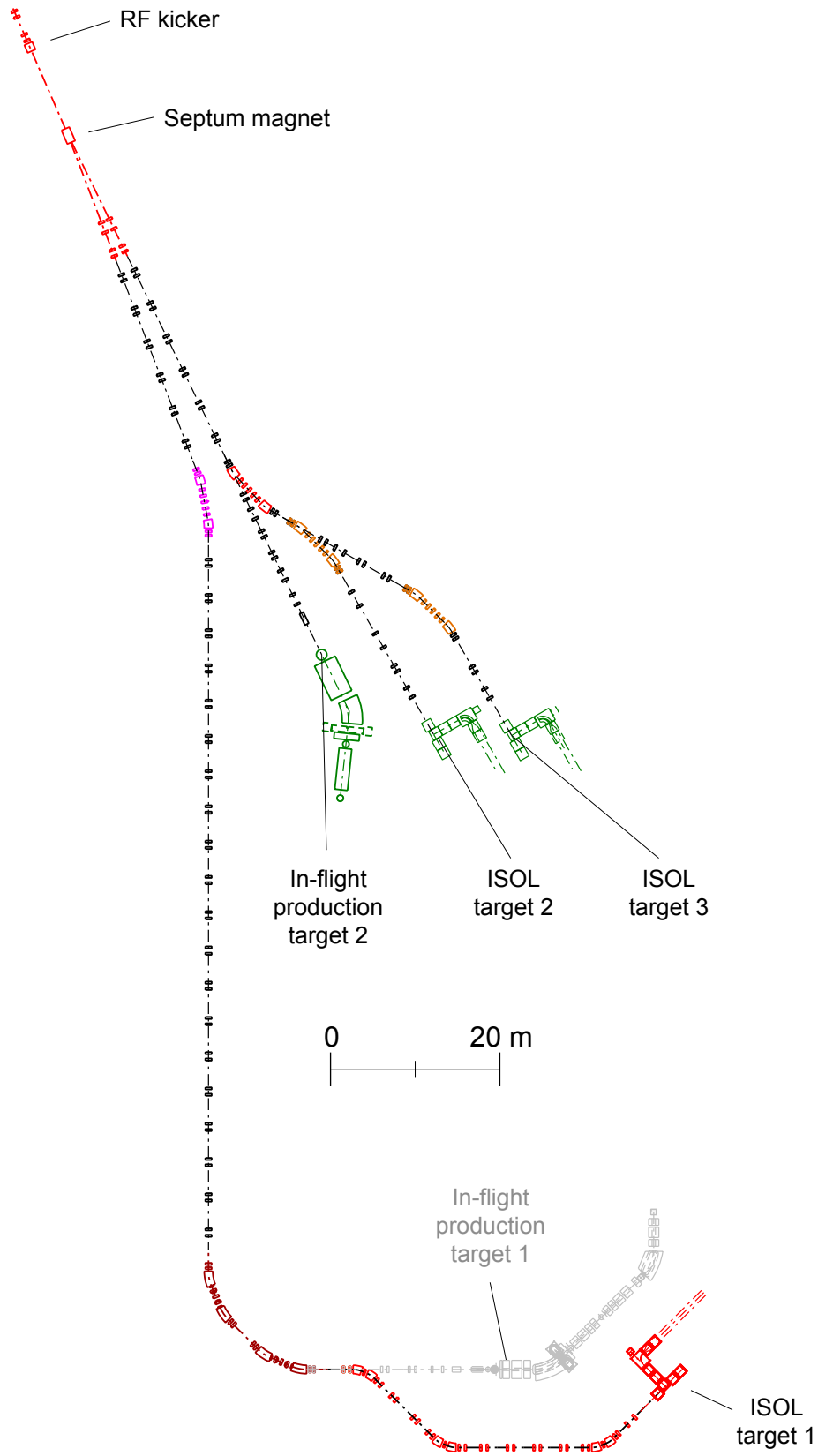


Figure 6.18: Schematic layout of the 400 MeV/u beam switchyard and target areas.

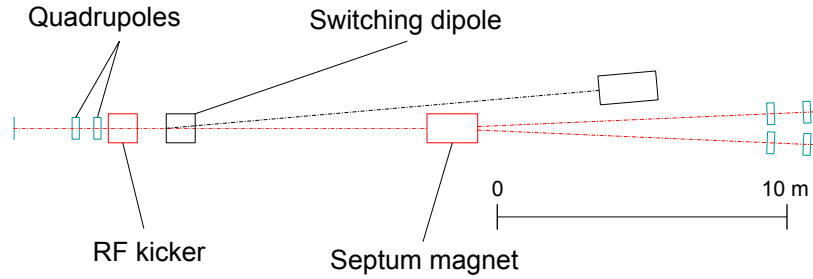


Figure 6.19: Layout of the beam distribution system. Two beams will be simultaneously provided to downstream targets using an rf kicker. In addition, all of the beam can be fed to a single target by using the switching dipole in lieu of the rf kicker.

Table 6.13: RF kicker parameters.

| Parameter | Value |
|----------------------|--------|
| Beam frequency (MHz) | 80.5 |
| RF harmonic number | 1.5 |
| RF frequency (MHz) | 120.75 |
| Peak rf voltage (kV) | 240 |
| Full gap (cm) | 5.0 |
| Effective length (m) | 0.88 |

Table 6.14: Septum magnet parameters.

| Parameter | Value |
|----------------------|-----------|
| Bending angle (°) | ± 2.5 |
| Effective length (m) | 1.75 |
| Full gap (cm) | 5.0 |
| Pole tip field (T) | 0.22 |

6.1.9.2 Beamline to baseline target area

A new beamline will be used to deliver the higher energy beams back to the baseline target area. The initial focusing section of the transfer line will consist of four quadrupole magnets to achieve symmetric beam conditions. The beam will then be transported using two consecutive segments made of three and ten π phase advance cells, respectively, with a 21° achromatic bending section between them. Finally, a 90° achromatic bending section will transport the beam to the baseline beam switchyard. The beam betatron functions and the beam envelopes along the beamline are given in Figure 6.20.

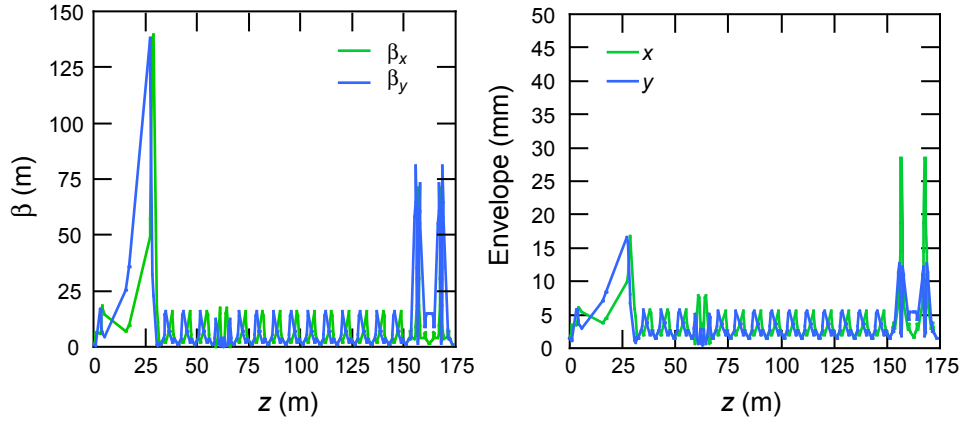


Figure 6.20: Betatron functions (left) and beam envelopes (right) along the beamline to the baseline target area.

6.1.9.3 Beamlines to second target area

A beamline will deliver the beam to the in-flight production target and the two ISOL targets of the second target area. An initial focusing section consisting of four quadrupole magnets will be used to achieve symmetric beam conditions. Then, a 3π phase advance section and three 32° achromatic bending sections will distribute the beam to the in-flight production target and to the two ISOL targets.

The final beamline section to the in-flight production target consists of a matching cell, a π phase advance cell, and a final focusing system of four quadrupoles plus a solenoid magnet to achieve the required beam spot size on target of ~ 1 mm. Corresponding beam betatron functions are given in Figure 6.21.

The final beamline sections to the two ISOL targets consist of a matching cell, a π phase advance cell, and a final focusing system of four quadrupoles to achieve the required beam spot size on a target of ~ 10 mm. The corresponding beam betatron functions are given in Figures 6.22 and 6.23.

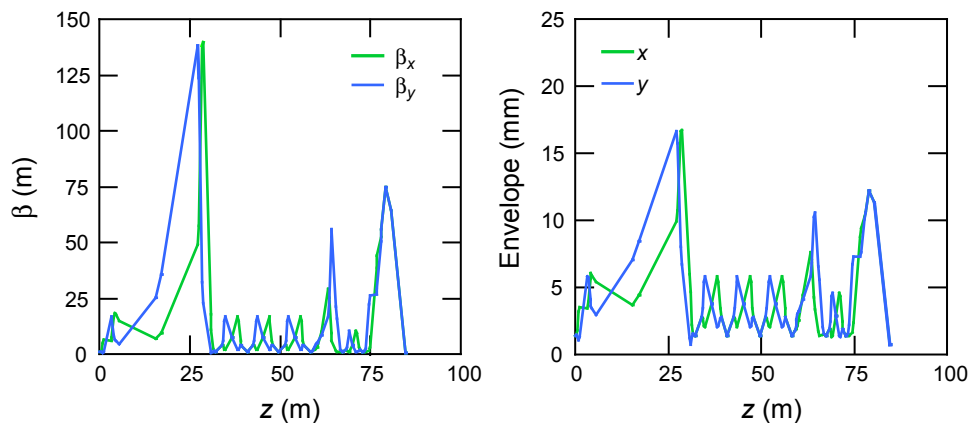


Figure 6.21: Betatron functions (left) and beam envelopes (right) along the beamline to the in-flight production target 2, located in the second target area (see Section 6.3).

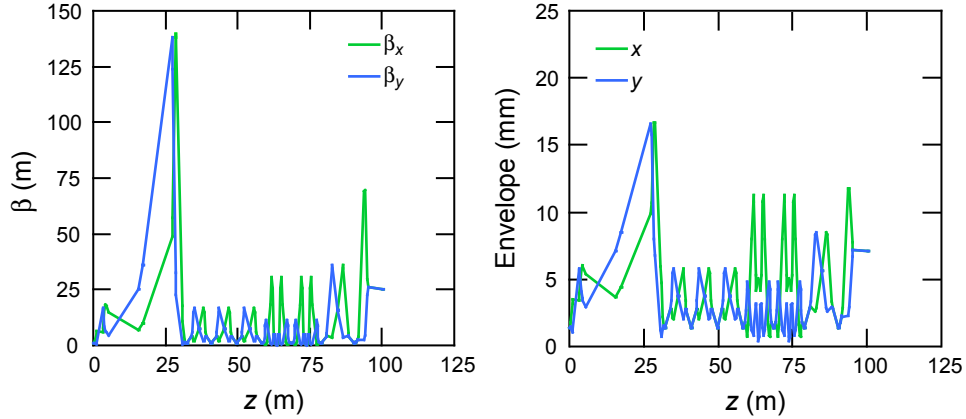


Figure 6.22: Betatron functions (left) and beam envelopes (right) along the beamline to the ISOL target 2 located in the second target area (see Section 6.3).

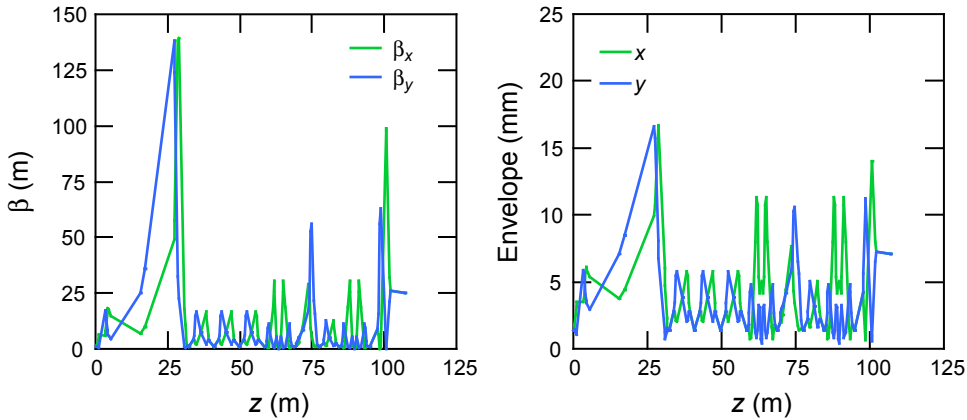


Figure 6.23: Betatron functions (left) and beam envelopes (right) along the beamline to the ISOL target 3, located in the second target area (see Section 6.3).

6.1.10 Beamline to ISOL target 1

As a possible upgrade, a beam transport segment can be added from the beam switchyard of the baseline driver linac (see Section 5) to the ISOL target area housed in the initial target hall (see Figure 6.24 and Section 6.2).

As discussed above, the beam conditions required for an ISOL target are significantly different than those for an in-flight production target. A large beam spot of 10 to 50 mm in diameter is required for single-charge state light ion beams. Only first order achromatic conditions are necessary in the transport line to the ISOL target to minimize the dependence of the size of the beam with its the energy spread.

Figure 6.24 shows a schematic layout of the beamline to ISOL target 1 in the baseline target area. After the vertical bending achromat of the baseline beam switchyard, the single-charge state light ion beams will be transported onto the ISOL target via a bending section using six dipole magnets. The beam transport between the bending magnets is accomplished by π -phase advance cells. A parallel beam with the required beam spot size is achieved on the ISOL target with a final focusing section using four quadrupole magnets.

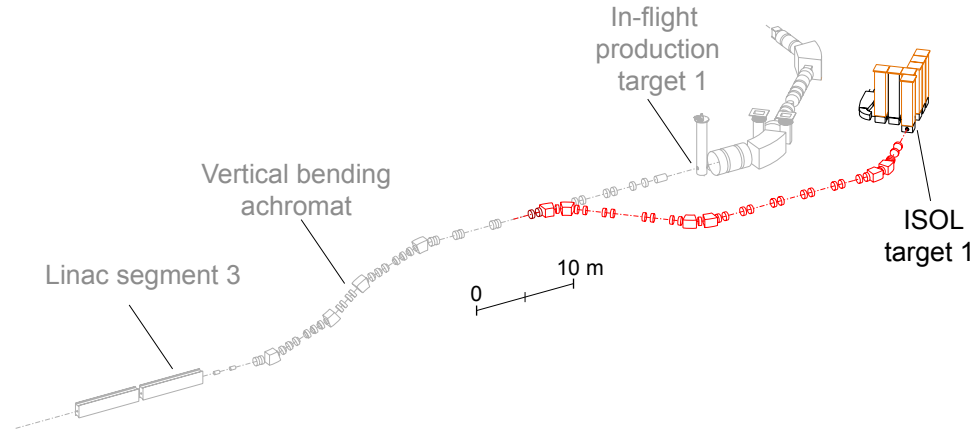


Figure 6.24: Schematic layout of the beamline to the ISOL target in the baseline target area. The grayed portion shows elements of the baseline switchyard. The colored elements show the upgrade with the ISOL target system and associated beam transport line.

A separation of five meters between the last focusing element and the ISOL target will be needed to provide the appropriate radiation shielding for the ISOL target. The beam transverse betatron functions and the corresponding beam envelopes along the beamline to the ISOL target in the baseline target area are shown Figure 6.25.

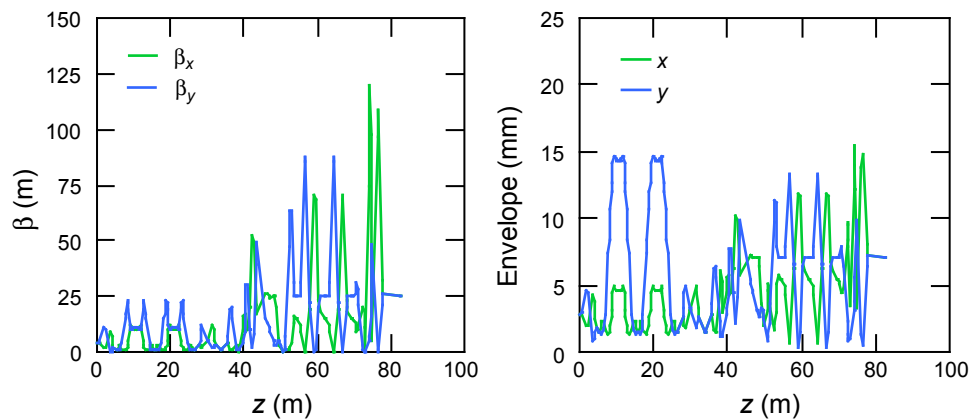


Figure 6.25: Betatron functions (left) and beam envelopes (right) along the beamline to the ISOL target in the baseline target area. The tracking starts at the end of linac segment 3 and includes the vertical bending achromat.

6.2 ISOL beam production

The implementation of rare isotope beam production by the ISOL technique is included in the baseline ISF civil construction but will only be implemented through an upgrade. The driver linac upgrade (Section 6.1) will allow the installation of a second target station for rare isotope beam production with the in-flight and ISOL methods.

Important criteria for the development of the ISOL system at the ISF are the beam production with p , d , and ${}^3\text{He}$ beams at beam powers up to 400 kW, a high degree of flexibility with respect to implementing new target and ion source concepts, and full remote handling for target changes to ensure minimum downtimes and ALARA radiation doses.

The ISOL beam production concepts have been developed by comparing approaches taken at existing ISOL facilities with other high-power target facilities, and by considering simultaneous employment of different rare isotope production schemes at the ISF. It should be noted that the development of the ISOL concept has benefited from the MSU-led multi-institutional RIA R&D project [DOE41322].

Figure 6.26 provides an overview of the components required for an ISOL upgrade of the baseline version of the ISF. An ISOL target station will be installed in a prepared pit in the target building hot cell. Preseparated beams could be either sent directly to the stopped beam area, to the reaccelerator, or be further purified with a high-resolution separator.

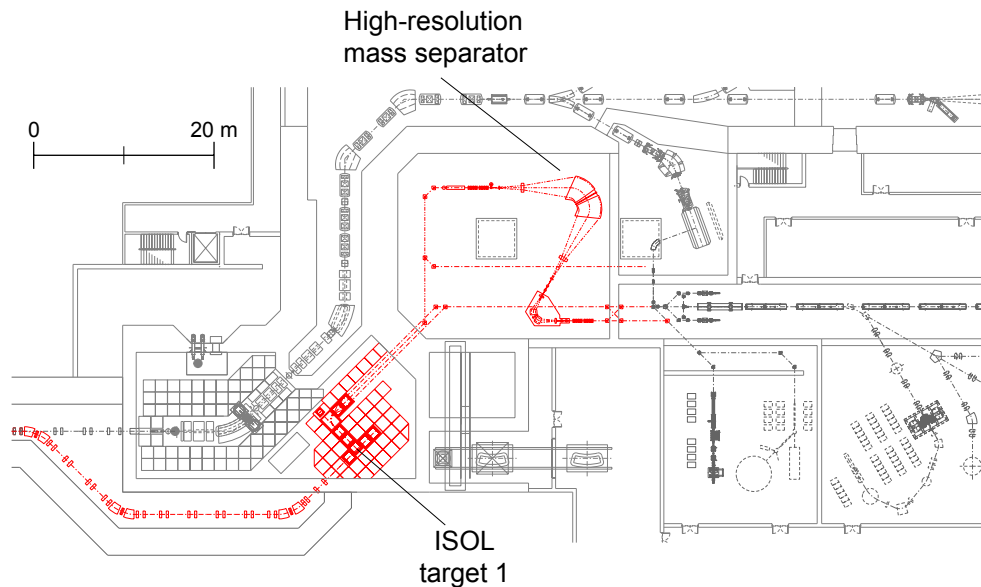


Figure 6.26: Schematic layout of the components of the upgrade of the baseline ISF to ISOL capability.

6.2.1 Rare isotope beam production with the ISOL method

ISOL beam production relies on light energetic ions impinging on thick high-temperature production targets where rare isotopes are produced by fission or spallation reactions. The rare isotopes diffuse out of the target material and effuse to an ion source where the atoms are ionized. The ions are accelerated to energies of 60–100 keV and mass separated.

6.2.1.1 Target ion-source systems for rare isotope beam production

Several different classes of ISOL target systems will be needed to produce the broadest range of secondary beams. The two basic classes of ISOL targets are illustrated schematically in Figure 6.27. The first category consists of high power versions of classical ISOL targets in which the primary beam impinges directly onto the target material that is placed in a thin-walled target container. These one-step targets can contain many different types of target material and are each optimized for the production of a certain isotope. One-step targets will be used for isotope production via spallation reactions and can be used for production via fission reactions. The second category consists of two-step targets for the production of high-intensity beams from fission reactions. As illustrated in Figure 6.27, the primary

light ion beam hits a neutron production target in close proximity to a secondary target that contains fissionable actinide target material. In both cases the isotope production targets will be connected to an ion source via a transfer line (either heated or cooled as necessary for chemical selection). Different ionizers such as surface ionizers, hot-plasma ion sources, ECRs, and laser ion sources are available to produce the singly-charged ISOL beams. The choice of ion source will depend on the isotope to be produced.

The availability of different light ion beams will allow optimization of the rare isotope beam production. While protons are considered to be the beam of choice in the case of rare isotope production via spallation reactions, deuterons and ^3He may offer advantages in the case of fission reactions using two-step targets with neutron converters.

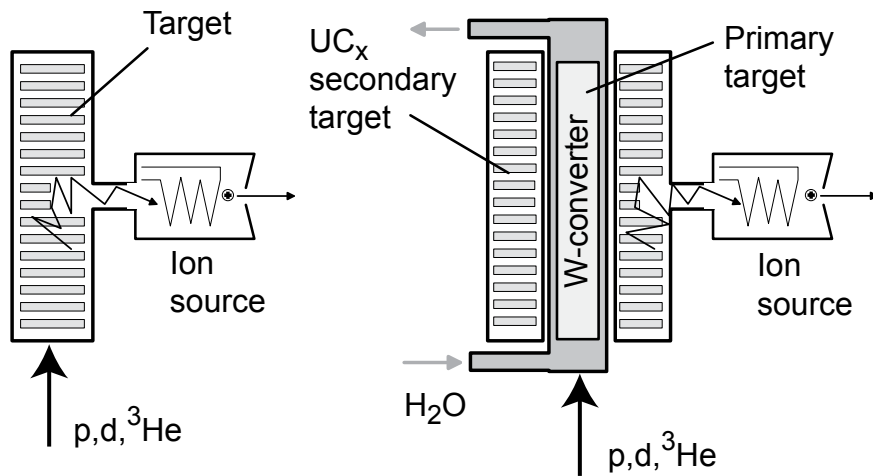


Figure 6.27: Target ion source configurations for rare isotope beam production. The target containers are connected to the ion source with a transfer line. Two systems are illustrated: one-step targets (left) and two-step fission targets with a water-cooled tungsten target as the neutron converter (right).

Several versions of one-step ISOL targets using metal foils to produce beams of a number of elements have been developed at ISAC for beam powers up to a few tens of kW. A prototype target using metal foils has been developed for the 100 kW ISIS facility but was not run [Wal91]. It is generally accepted that a beam power of 100 kW is sustainable with metal foil targets that can tolerate high temperatures and be cooled by radiation. In the case of other target materials, such as metal oxides, the situation is generally less favorable and a substantial R&D effort will be required to find the optimum target materials and geometries for each element.

A very promising recent concept for the production of rare isotopes via fission is the two-step target (see Figure 6.27, right). The advantage of this target type is that the target for neutron production and the target for isotope production are physically separate and can be optimized independently. Several options for the neutron production target are available. In the originally proposed concept [Nol02], deuterons impinge on a porous tungsten target cooled by flowing liquid lithium. This material acts as a neutron converter for the primary beam that is surrounded by a secondary target made of a blanket of fissionable material to produce the rare isotopes to be extracted from the system. Part of the RIAISOL R&D effort was aimed

at the study of such target systems [Bol06a] with proton, deuteron, and ^3He beams. It was found that a water-cooled tungsten target should work well and would not require circulating molten lithium. Neutronics calculations, radiation damage analysis, and thermal studies showed that there are no fundamental obstacles to operating such a converter for beam powers up to 400 kW. The main advantages of the water-based system over more standard targets are largely reduced safety issues with similar support services and waste handling.

The type of ion source connected to the target will depend largely on the element to be ionized and the desired beam purity. In fact, the ion source determines the beam purity. It is clear after a half-century of work at CERN/ISOLDE that no ion source exists with all of the properties needed for ISOL beam production. The ion source that comes closest to a universal ion source is a laser ionization source (Figure 6.28). This source uses stepwise resonant photo-absorption to be highly selective while maintaining high ionization efficiency for many elements. Laser ionization has been successfully used for rare-isotope production of approximately twenty elements. Laser ionization sources are rather new and have significant potential for further development.

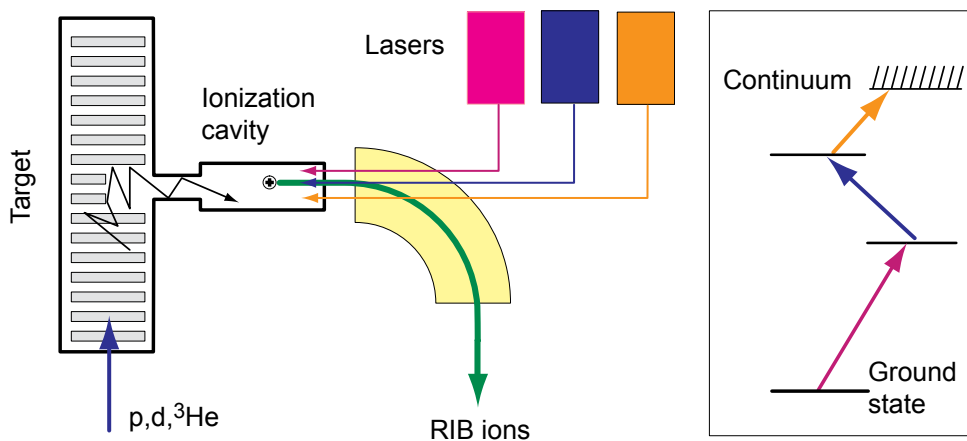


Figure 6.28: The principle of laser ion sources for rare isotope beam production (left) and a three-step resonant ionization scheme (right). Intense laser beams of the appropriate wavelengths sent into a heated cavity connected to the production target are absorbed in sequence to resonantly ionize the desired rare isotope atoms.

The surface ionization source is the workhorse for ionization of alkali elements, Earth alkali, and some rare earth elements. Hot-temperature plasma ion sources are used for ionization of gaseous elements or rare isotopes delivered from the targets as gaseous molecules. The development of sources for the most efficient ionization of noble gases is currently based on constructing radiation-hard ECR ion sources.

6.2.1.2 High-power beam dumps for light ion beams

The beam dump for any 400 kW beam, and an ISOL beam in particular, presents major challenges. Typically, less than one-quarter of the beam power is dissipated in the ISOL production target and the rest must be dissipated in the beam dump. For maintenance, the length of the dump should be less than about one meter. While beam dumps for protons at a MW power level exist, the particular difficulty

at the ISF is the necessity to stop both proton and ^3He beams, which have significantly different stopping ranges in a given material. A water-cooled copper beam dump with a length of less than one meter would be able to stop a proton beam but could not be used with a ^3He beam because the power density would be too high. Also within the RIAISOL R&D work, collaborators from LLNL have investigated the feasibility of a dump using copper and aluminum plates of increasing thickness with water flowing in between the plates. The one-meter long beam dump has mostly aluminum plates in the front and mostly copper plates in the back. Simulations show that both proton and ^3He beams can be stopped in such a system, so that only one dump design would be necessary.

6.2.1.3 Estimated beam rates from ISOL beam production

ISOL beam production with beam powers beyond a few tens of kilowatts has not yet been demonstrated. At present, it is not yet clear which target materials are the best for high-power targets and which geometries should be used. In order to cope with the high power deposition, the target systems can be expected to be larger, resulting in longer effusion times out of the target into the ion source. Primary and secondary radiation inside the target may affect the release of the produced rare isotopes. Therefore, any estimate of ISOL beam rates for beam powers exceeding those of present facilities can be expected to have large uncertainties.

To obtain a coarse estimate of the maximum rates from ISOL beam production at the ISF, we proceeded as follows. EPAX [Sum00] was used for calculating intrinsic production yields for 1 GeV protons on targets of 46.2 g/cm^2 ^{93}Nb , 120 g/cm^2 ^{139}La , 122 g/cm^2 ^{181}Ta , and 9.7 g/cm^2 ^{238}U as UC_x . Fission of ^{238}U was included using cross sections from LISE++ [Tar04] and results from PHITS [Iwa01] for a generic UC_x target. In all cases, the largest production yield was selected on a nucleus-by-nucleus basis and compared to the corresponding maximum yield obtained at ISOLDE [Iso06]. The ratio of these data was considered to represent the specific extraction efficiency for this isotope. These values were then fit to a functional form [Luk06] on an element-by-element basis. Experimental half-lives were used where available; theoretical predictions for half-lives were used for the remainder. This procedure was found to reproduce the experimental data very well, so the calculated nucleus-specific extraction efficiencies were used for the prediction of the expected ISOL beam rates at the ISF.

Production rates in the target were calculated using EPAX for a 400-kW beam of 525-MeV protons or 375-MeV/nucleon ^3He ions bombarding the targets listed above. Fission of ^{238}U was included using cross sections from LISE. The results of calculations with PHITS for a two-step target based on a tungsten-converter and a $^{238}\text{UC}_2$ secondary target were also included. The highest rate was selected and multiplied by the specific extraction efficiency for each nucleus to obtain the ISOL beam rate estimates shown in Figure 6.29.

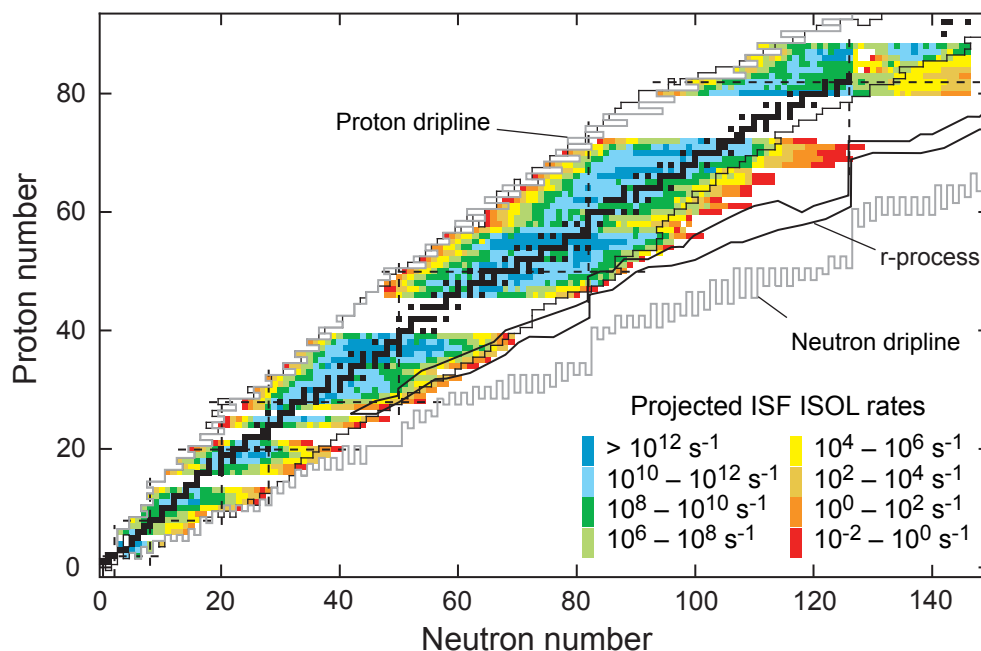


Figure 6.29: Estimated maximum beam rates at the ISF from the ISOL production method, with 400 kW primary beams of 525-MeV protons or 375-MeV/nucleon ^3He ions. For reference, the regions of nuclei relevant to the astrophysical r-process are shown by the outlines on the right side of the contours.

6.2.2 ISOL target station

6.2.2.1 ISOL target concept

The target stations concept chosen for the ISF was adapted from that used at the ISAC facility at TRIUMF. The concept of the target station is shown in Figure 6.30. The individual components are mounted at the bottom of long iron-shielded modules suspended in an evacuated tank. The tank contains several such modules equipped with various components, for example, the target itself, diagnostics for primary and secondary beams, and the beam dump for p, d, and ^3He beams. The service connections and vacuum seals will be located on top of the modules about 3 m away from the primary beam axis to limit radiation damage to critical components. Massive iron shields outside the target and beam dump vacuum tanks, surrounded by concrete, will be used to attenuate the radiation field from the target during proton bombardment. Radiation transport calculations have shown that it will be necessary to cool the iron shielding closest to the beam dump and the targets. Further investigations indicate that forced-air cooling will be sufficient to remove the heat from the absorbed radiation.

There are a couple of design constraints for the plugs and their components. The high radiation field close to the target forbids the use of elastomers. High conductance paths are required to allow for high pumping rates. To obtain good vacuum conditions in the ion sources and secondary beamlines without using elastomer vacuum seals, the two-stage or differential vacuum arrangement used at ISAC will be employed. A primary vacuum ($<10^{-6}$ torr) will be maintained inside the target module and in the exit modules that contain the optics components for beam transport to the preseparator. The remainder of the target assembly vacuum outside

these modules will be in a secondary vacuum ($<10^{-5}$ torr). Although the containment modules will not be fully leak-tight, the conductance to the surrounding secondary vacuum will be low. Inflatable seals will be used to join the vacuum enclosures of the target module and neighboring modules. This concept allows the target, optics, and beam dump plugs to be removed for servicing without having to connect or disconnect intervening short beam pipes.

The required services for the target will be guided through the shielding plug in dog-legged channels designed to minimize the external neutron flux. One vacuum channel per plug will be used to provide the primary pumping of the enclosed target or optics module. The secondary vacuum in the outer vacuum enclosure will be provided by pumping channels through the outer shielding directly to the bottom of this chamber. The only constraints on the design of these rough-pumping channels will be the vacuum conductance requirements and low neutron leakage.

A first-stage or low-resolution mass separation (see Figure 6.30) will be made for the beam extracted from the ISOL target ion source system in order to minimize the amount of radioactivity leaving the ISOL production area and to simultaneously deliver beams of different masses from one target. A preseparator with a resolving power of $m/\Delta m \sim 1000$ will provide this separation. Because of the radiation fields, a radiation-hardened magnet will be used for the preseparator. The separator will be followed by a beam switchyard (not shown in the figure) allowing up to three masses to be simultaneously extracted from the focal plane. The neighboring beamlines could be used for harvesting isotopes that are needed for stockpile-stewardship-related research as well as for other applications. The beams from each ISOL station will be either directed to the high-resolution mass separator or directly connected to a beamline system for delivery to the reaccelerator and the stopped beam experimental area.

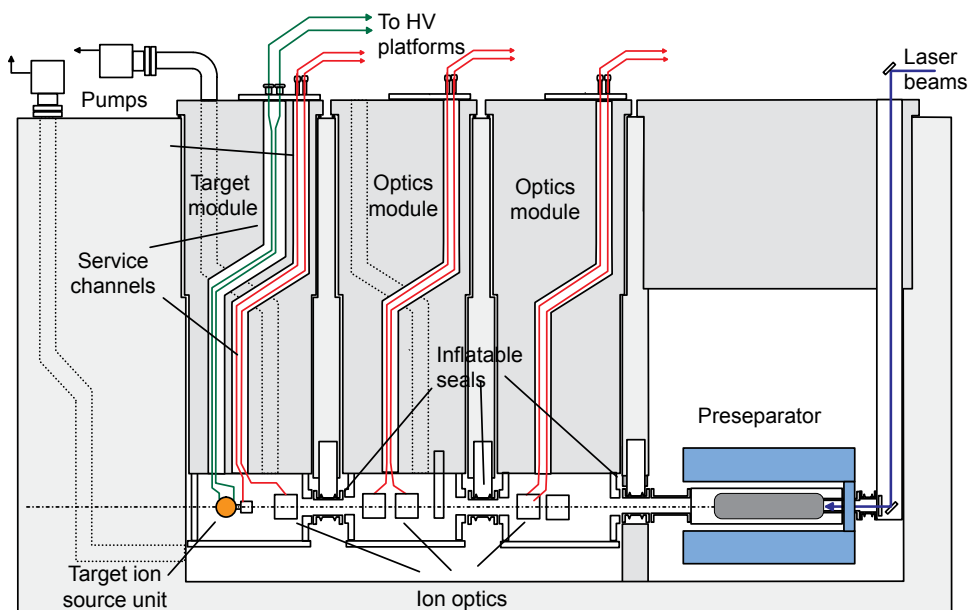


Figure 6.30: Concept of an ISOL target station (side view) using a vertical plug concept and a horizontal beam preseparation system. Also shown is the last part of the laser line for the laser ion source. The primary beam is going into the figure at the target position.

6.2.2.2 Component lifetimes and shielding

Within the RIAISOL R&D work, simulations were performed to study the effects of radiation fields emerging from ISOL targets and the beam dump with respect to the heating of surrounding components and material damage.

With respect to materials in close vicinity to the targets and beam dump, it was found that there are no radiation damage issues if the choice of materials is limited to ceramics and metals. The radiation field in the preseparator region will be low enough that a conventional magnet using polyimide insulated coil material can be expected to last for the lifetime of the facility. The radiation fields at the top of the large plugs will be low enough to allow elastomer seals, which simplifies vacuum seals and allows the use of standard vacuum components. In addition to the beam production targets, other components directly exposed to the primary beam, such as the beam window isolating the ISOL station vacuum from the accelerator vacuum and the beam window of the beam dump, will have to be replaced at certain intervals. The assumptions of a maximum beam power of 400 kW and an effective beam on target time of about 2000 h/yr result in expected lifetimes that will be longer than a year for these components.

Shielding calculations have been performed for the ISOL stations, using both simple and realistic models. An example of realistic calculations is the analysis of radiation levels in the soil below the shielding of an ISOL target station. Operating a high-power ISOL station has the potential of activating the soil, rock, and water in the vicinity of the beam enclosure. The activation depends on the source of radiation, enclosure geometry, and the surrounding geological environment that is site specific.

Two limits were used for the maximum allowable ground water activation [DOE5400]. If the activated water has the potential to reach the water table, then the DOE limits for drinking water were applied. Surface water limits were used if the activated water was discharged on the Earth's surface. A comprehensive study of this matter was carried out by the NuMI project [Gro04a,Gro04b], and we have adapted the conclusions drawn. One factor is the reduction from decay and dispersion of the radioactive nuclei in transit to the aquifer, which depends on the distance to the beam enclosure and geological formations between the enclosure and the aquifer. The reduction was estimated to be $\sim 10^{-10}$ for the Fermilab Main Injector, and it is assumed that a similar situation exists at the MSU site. The most conservative scenario is then to assume that the activated water will be pumped out from beneath of the ISOL target station and dumped onto the surface.

The density of inelastic collisions of products radiated from the target and dump can be converted to a radioactive nucleus concentration using a number of site-specific factors. This density below the ISOL target station was studied with the MARS15 model [Mok95,Mok04]. A view of the model developed with the geometry editor MORITZ [Van04] is shown in Figure 6.31. The model includes the target, vacuum tank with appropriate shielding, radiation shielding blocks, tank enclosure (pit), and radiation shielding around the pit. For the purpose of illustration, the roof of the pit and some of the shielding are not shown. Below the target pit is shielding composed of one meter of iron, three meters of concrete, followed by one meter of soil. Calculations of the density of inelastic collisions in the soil were performed with the kinetic energy threshold of particles of 50 MeV. These calculations were performed with a 400 kW proton beam at 1 GeV.

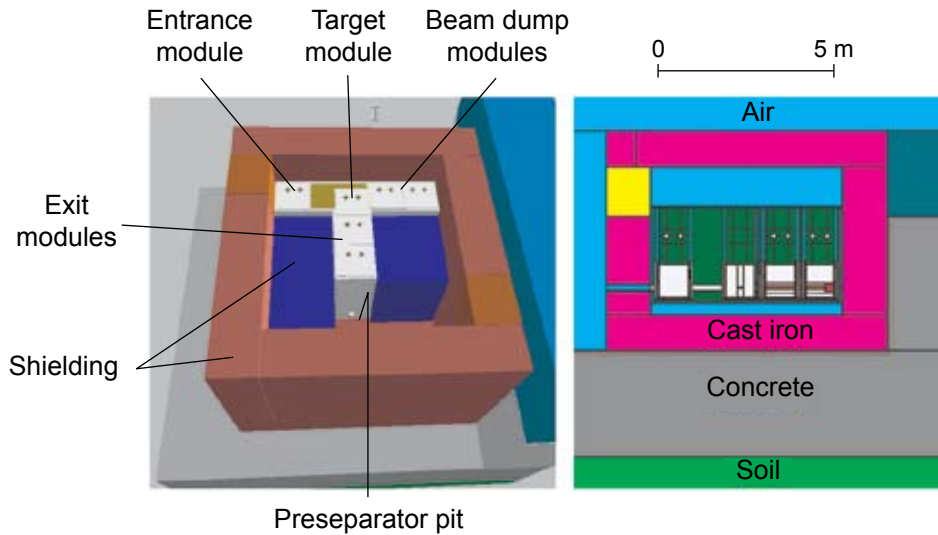


Figure 6.31: (left): 3-D view of the model of the ISOL target station. The top shielding layer is removed. (right): Elevation view of the model as used in MARS [Mok95,Mok04].

Figure 6.32 shows the density of inelastic collisions in the top 10 cm of soil below the bottom of the concrete shielding of the ISOL station and in a thin vertical slice ± 20 cm around the beam axis. The distribution reaches levels up to about $10^3/\text{cm}^3/\text{s}$ in soil close to the concrete, corresponding to a maximum level of $3 \cdot 10^{10}/\text{cm}^3/\text{year}$. If the limit on sump water activation is about $6 \cdot 10^{10}/\text{cm}^3/\text{year}$ (the number used for the beamline of the Fermilab experiment MIPP (E907) [Kos03]), then the proposed shielding below the ISOL target station will be sufficient, in particular because the average beam power levels on the target will be lower than the assumed value of 400 kW.

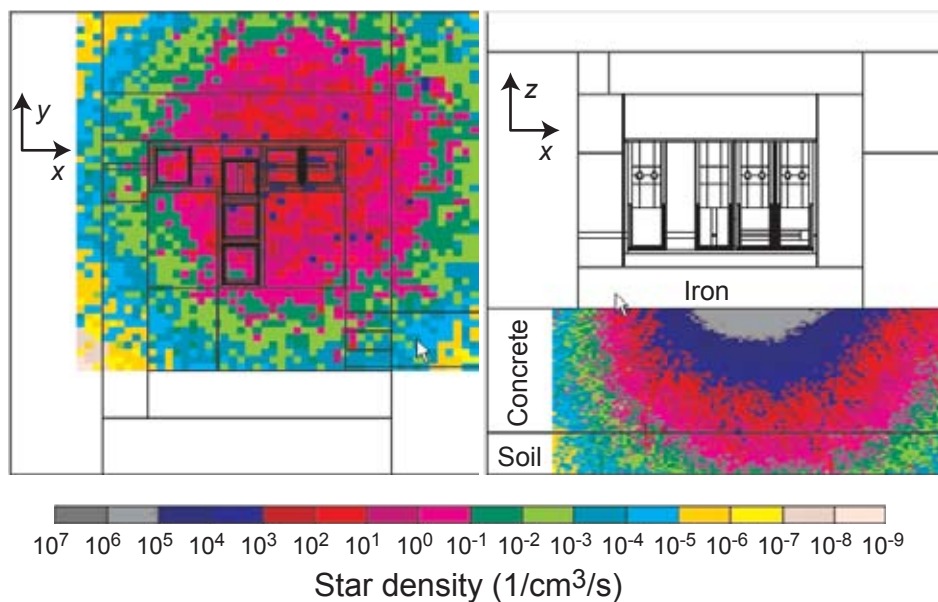


Figure 6.32: (left): The density distribution of inelastic collisions in the top 10 cm of soil underneath the concrete shielding, see text. The distribution is overlapped with a horizontal view of the studied system. (right): The same density distribution in a vertical slice 40 cm wide and centered on the beam axis.

6.2.3 High-resolution mass separation

In all ISOL scenarios foreseen for the ISF, beams from the ISOL station can be either sent directly to the reaccelerator or to the stopped beam area. However, experience at other ISOL facilities shows that further beam purification will be essential for many experiments. The ion sources can only provide a limited selectivity, and a high-resolution separator, capable of resolving isobars, is often required. The majority of rare isotope beams will require a high resolving power of $m/\Delta m \sim 20,000$ to fully purify the beam. In addition to establishing the required separation between masses, the performance of a high-resolution mass separator is also judged on the overall suppression of neighboring masses.

The large high-resolution separator designed for RIA by Portillo et al. [Por01] is thought to be a reasonable first approximation of the final optimized design of the isobar separator for the ISF. For medium mass beams ($A = 100$) with a beam emittance of about $20 \pi \text{ mm mrad}$ at 100 keV and an energy spread of $\pm 10 \text{ eV}$, this separator could realize a resolving power of $\sim 20,000$, with cross contamination on the order of 5%. This beam emittance is very low and cannot be expected from all ion sources. Therefore, the calculated performance values must be considered to be upper limits.

A promising way to satisfy the stringent beam emittance characteristics necessary for isobar separation is to employ beam cooling between the ISOL preseparator and the high-resolution separator. Gas-filled RFQ ion guides are now used routinely to prepare high-quality low-intensity beams for individual experiments, and substantial experience exists at the NSCL in building such devices [Sch03b]. For reduced transverse beam emittance and reduced beam energy spread, a more compact mass separator and higher resolving powers can be realized. Isobar separation could become a realistic goal. Beam cooling has also a very positive general impact on the entire beam transport system and its operation. An ion beam loses all memory of its previous properties in a beam cooler, a feature that allows the downstream beam tuning to be completely decoupled from upstream beam transport. The installation of beam coolers after the ISOL preseparators will result in beams with properties that are independent of the target/ion source system.

The technical challenge for beam cooling at a high power facility is that orders of magnitude higher beam intensities have to be processed compared to the low intensities at present facilities. An R&D project is underway at MSU to theoretically and experimentally investigate high intensity beam cooling. Beam simulations for intensities up to $1 \mu\text{A}$ have been performed. The simulation results indicate that such intensities can be handled provided sufficiently large rf amplitudes (15 kV at 5 MHz) can be applied to the RFQ. A phase space plot of a beam inside the cooler is shown in Figure 6.33. If such a beam were extracted and accelerated to 60 keV, it would have a beam emittance of $\epsilon_{95\%} \approx 3 \pi \text{ mm mrad}$. The construction of a test setup for studying high intensity beam cooling is in progress at the NSCL.

6.3 Second target area

The driver linac upgrade discussed in Section 6.1 creates the option of installing a second target area, which would greatly enhance the productivity of the ISF. Figure 6.34 shows a possible layout of the second beam production area. The target building for in-flight and ISOL beam production are shown. The concept for

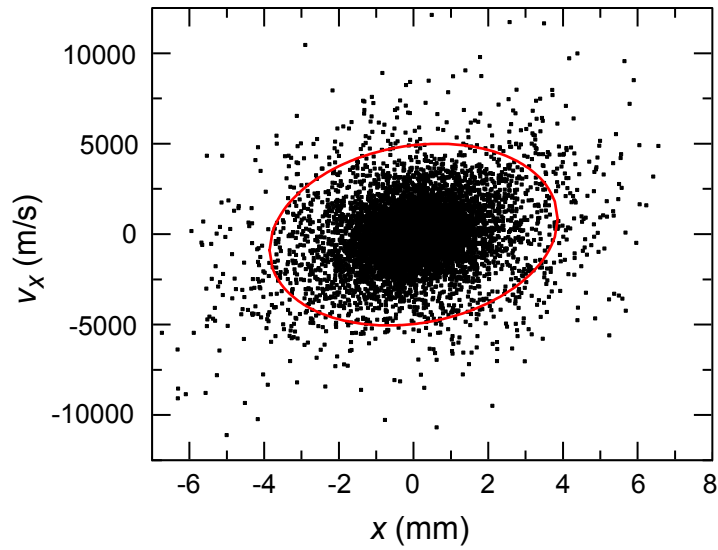


Figure 6.33: Calculated phase space plot of a 1- μA $^{133}\text{Cs}^+$ ion beam cooled inside a low-energy beam cooler based on a gas-filled RFQ ion guide.

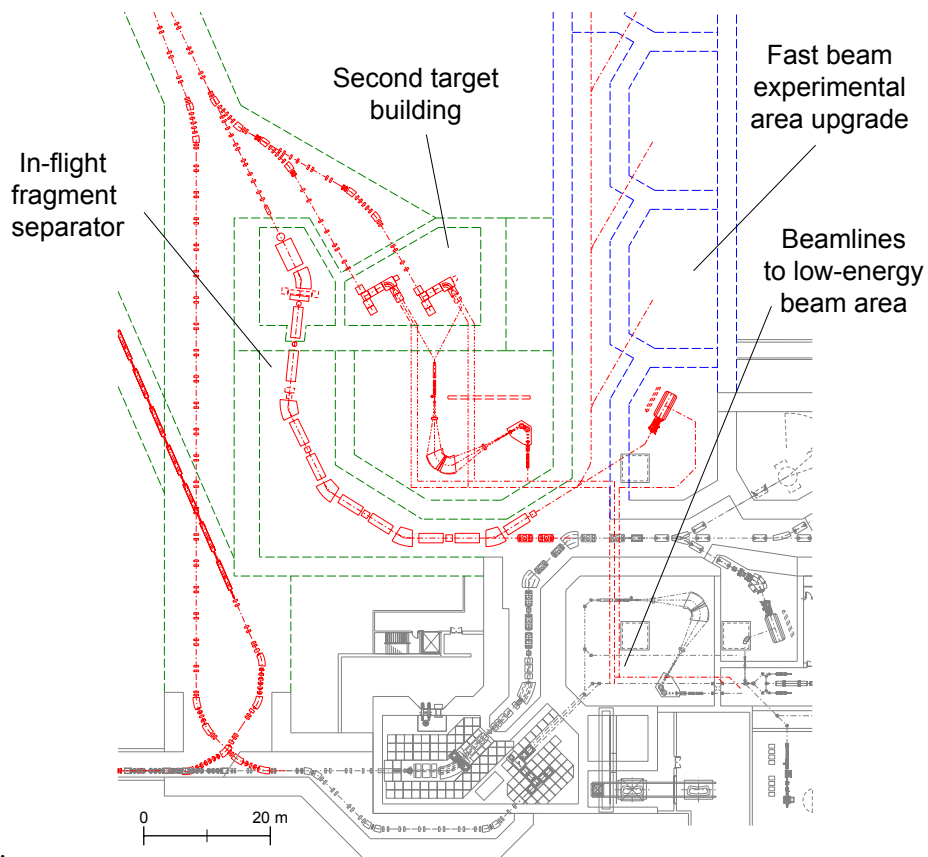


Figure 6.34: Possible layout for a second rare isotope beam production area at the ISF.

the target building is very similar to that used in the base facility (see Section 5). The new target building will be larger in size if, as shown, two ISOL stations are installed. The fast-beam production target and the preseparator are also located inside the hot cell. After leaving the hot cell, the projectile fragments are further separated in a new main separator. The beams can then be distributed to the existing fast beam experimental area and, if built, to a new fast beam experimental area. A second cyclotron stopper will be installed for the next generation of low-energy experiments. As in the case of the ISOL upgrade for the base facility (Section 6.2) a high-resolution mass separator will be necessary for beam purification. The low energy beams from the ISOL stations and the cyclotron stopper will be transported to the stopped beam experimental area and the reaccelerator.

6.3.1 ISOL beam production

The ISOL stations are envisioned to be identical to the one discussed as an optional upgrade for the base facility (Section 6.2). The availability of up to three ISOL stations will provide a substantial increase in productivity of these systems, for example, the downtime for target cooling and exchange will be reduced. A target development program, a key component of ISOL beam production, can be maintained with minimized impact on the beam production for the experimental program.

6.3.2 In-flight beam production

Multi-user capability for fast beams and reaccelerated beams from the gas stopping station could be implemented with the addition of a second fragment separator as shown in Figure 6.34. To match the upgraded driver linac, the new in-flight fragment separator should be optimized for 400 kW operation at 400 MeV/nucleon. This implies the separator should have to have a maximum rigidity of 10 Tm as compared to 8 Tm in the initial system, but the other parameters, such as momentum and angular acceptances could remain the same. As in the initial implementation, the system should consist of a preseparator followed by a main separator.

The preseparator design is nearly identical to the design discussed in Section 5. However, the reversed bend of the second dipole requires that there be no image at the midpoint and hence the wedge be located at the second image just in front of the second dipole. The second stage separator optics is, again, identical with the exception that the bend angles reduced to 32 degrees to allow for operation at 10 Tm and maintain a central field in the dipoles below 2 T. The production target and beam dump designs will be identical to those used in the initial implementation.

6.4 Experimental areas

The beams from the cyclotron stopper will serve two areas dedicated for low-energy experiments. The stopped beam area will accommodate experiments that can be completed using rare isotope beams having energies of a few keV or less. The reaccelerated beam area will include an area for nuclear astrophysics experiments with beams having a maximum energy of 3 MeV/nucleon and an area for low-energy nuclear structure and reactions experiments where the reaccelerated beams will have a maximum energy of 12 MeV/nucleon.

The low-energy experimental areas will share a common highbay area as illustrated in Figure 6.35.

The sections below provide details regarding the upgrade pathways for the two low-energy experimental areas.

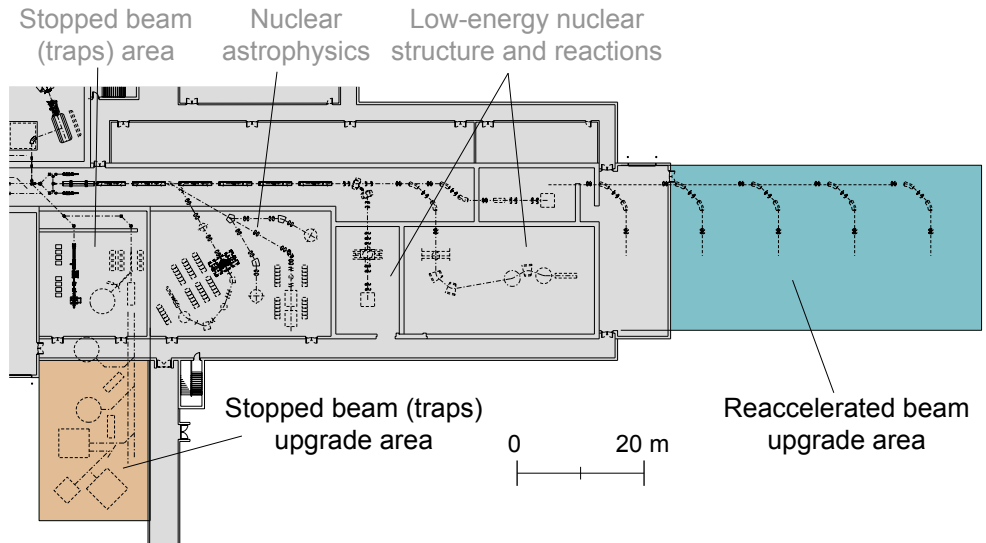


Figure 6.35: Schematic layout of low-energy beam experimental area, which includes a stopped beam (traps) area and a reaccelerated beam area. Expansion pathways for each area are highlighted.

The stopped beam area is at grade level, and the planned footprint at the ISF is 365 m². Expansion of this area can be accommodated by a building extension down from the stopped beam area (traps) depicted in Figure 6.35. There are no other existing building elements that will restrict the dimensions of a building extension in this direction. Other stopped beam facilities have elected in the past to avoid civil construction costs and expand in the vertical direction. However, the vertical expansion option restricts access to major components on grade level.

Construction of a building addition will not interrupt ongoing activities in the stopped beam area. The stopped beamlines will be brought to the building extension using electrostatic steering magnets to cross the existing hallway structure shown at the bottom of Figure 6.35. The building extension will have utility and access requirements as discussed for the ISF in Section 5.

The reaccelerated beam area has a planned footprint of dimension 1760 m², shared between the nuclear astrophysics area (610 m²) and the low-energy nuclear structure and reactions area (1150 m²). Expansion of this area will be accomplished by extension of the highbay area to the right of the reaccelerated beam area depicted in Figure 6.35. The division of the additional floor space between astrophysics experiments and low-energy nuclear structure and reactions experiments will be driven by scientific need.

Experimental operations in the reaccelerated beam area will not be interrupted during the civil construction period. Some user down time would be experienced if significant relocating of experimental equipment were required. For example, expansion of the nuclear astrophysics area (where beam energies less than 3 MeV/nucleon are used) will require the displacement of some equipment associated with the low-energy nuclear structure and reactions program. However, the utilities and access requirements are similar for the areas, and infrastructure

changes in the reassigned areas will not be significant. The highbay addition will include extension of the service crane to cover all experimental areas.

The possible expansion of the fast beam experimental area is shown in Figure 6.36. This area could be fed with beams from the initial ISF fragment separator or from the new separator upgrade, if it has been implemented. The implementation of a new area will allow the program in the original experimental area to continue with minimal interruption. With the addition of the second experimental area and second fragment separator, two simultaneous and independent experiments could be performed. This would provide the facility with a high degree of flexibility.

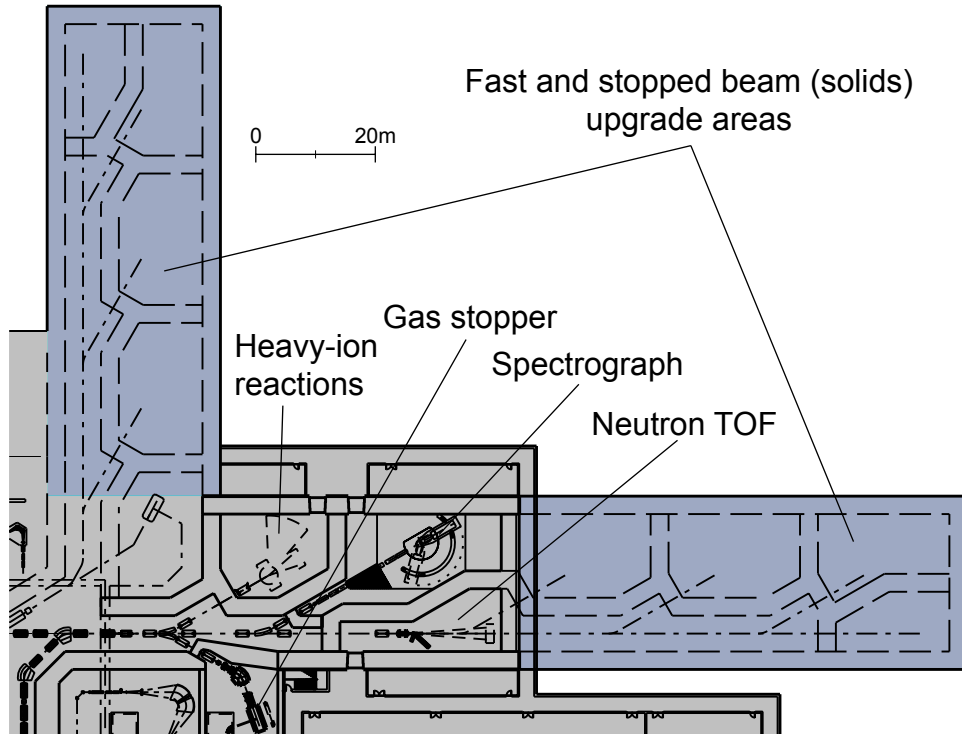


Figure 6.36: Schematic layout of fast and stopped (solids) beam experimental area showing two possible expansion paths.

Details of the expansion's size and the experimental equipment will be driven by the needs of the user community. There are minimal space constraints, so the areas can be optimized for various needs. The beam distribution system will be designed to efficiently transport beams at 8.0 Tm rigidity, based on experience from the current system at the NSCL.

6.5 Conventional facilities

The conceptual layout of the facility with all of the upgrades in addition to the baseline facility and the ISOL target area is shown in Figure 6.37. The entire facility will be composed of nine new major structures – the underground linac tunnel, the above ground linac support building, the cryoplant, the target facility, the connector structure, the fast beam experimental area, the reaccelerated beam experimental area, the stopped beam experimental area, and the office building. All structures will have fire protection provided by a wet pipe sprinkler system and a complete fire alarm system, including visual and audible alarms, pull stations

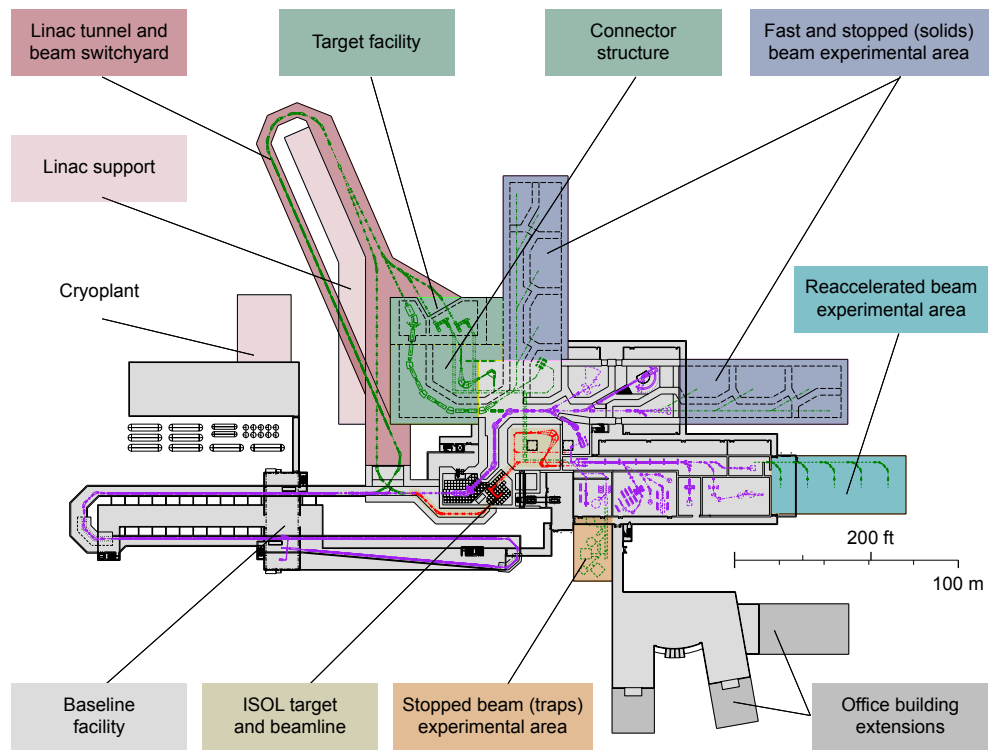


Figure 6.37: Facility layout.

at exits, and heat/smoke detectors as required by code. All temperature controls will be the direct digital type capable of being monitored at a central location or remote site.

The linac tunnel and beam switchyard structure will have an area of 3,100 m² and will be constructed via an open cut excavation (cut & fill). The foundation slab will be supported on drilled piers at six meter centers that will extend down to bedrock (approximately 25 m below grade). The tunnel slab, walls, and ceiling will be 0.5 m reinforced concrete except at the stripping areas, where the thickness will be two meters to provide the necessary shielding. Parallel sections will be connected by a reinforced concrete slab to minimize differential settlement. The tunnel floor will be 6.75 m below grade and the structure will be waterproofed and equipped with a perimeter drain tile and sump pump system.

The at-grade linac support building will be a 1,600 m² single story structure providing space for the linac/magnet power supplies and controls. The heating and air conditioning for the tunnel and at-grade structures will be provided by a series of indoor air handling units, which will have steam heating coils, chilled water cooling coils, and steam humidifiers. Variable volume terminal units will be provided in the air supply distribution system to achieve temperature control.

The cryoplant upgrade will be an 800 m² structure modeled on the existing NSCL cryogenic building. The building will have a structural steel frame and masonry insulated walls. It will be divided into two halves longitudinally, with one half being a single-story structure for refrigeration cycle equipment and controls. The other half will be a two-story design with compressors on the main floor and electrical switchgear plus process cooling equipment on the second floor.

The new target building will be a three-floor structure with a base area of 1,100 m². The lower floor will be the target room with provisions for one in-flight target with preseparator and two ISOL targets. The structure will have a three meter thick floor support on drilled piers that will extend to bed rock and be designed for a floor loading of 33,000 kg/m² to support the beamline components and bulk radiation shielding. The walls will be nominal 1.5 m thick and go up to three meters in the high radiation areas. The second floor will be a limited access remote handling gallery with 1.5 m thick concrete walls and ceiling. This level will be equipped with rail systems for a remote control crane and manipulator arm equipment. The third floor will be a 100-ton crane bay with structural steel frame and masonry walls.

The connector building will be a four-floor structure, with a 1,500 m² footprint, that connects the target building to the baseline structures and beamlines. The first floor will be occupied by in-flight fragment separator components from the production target and ISOL system high-resolution separator and low energy beam distribution. The second and third floors will be used for target support systems. The fourth level will provide access to the upper crane bay in the target building.

The stopped beam experimental area upgrade will be a one-story structural steel frame/masonry wall structure providing 500 m² of experimental equipment floor space.

The reaccelerated beam experimental area upgrade will be a 1,600 m² highbay steel frame/masonry wall structure. The structure will be an extension of the baseline 30-ton crane highbay. Local radiation shielding will be modular and provided as needed.

The fast beam experimental upgrade options will be 2,400 m² highbay structures that will house the experimental apparatus. The steel frame/masonry wall structure will be equipped with a 12-m hook height overhead crane with a 50-ton capacity. The lower exterior vault walls will be three meter thick reinforced concrete and the interior radiation shielding will be provided by reinforced concrete roof beams and modular concrete walls. The vault shielding doors will be a vertical motion hydraulic ram activated concrete block design.

The office building upgrade will provide an additional 200–300 offices.

7. NSCL site option

The utilization of the present site of the NSCL provides a less costly alternative to the baseline facility described in Section 5. An upgrade of the current NSCL by addition of a heavy-ion booster linac could provide stable beams of heavy ions at energies ≥ 200 MeV/nucleon, with a beam power greater than 65 kW. Figure 7.1 shows the layout considered for the NSCL site-upgrade option. This option makes use of the existing NSCL infrastructure and experimental equipment and, as the figure shows, large parts of the existing facility, in particular the experimental areas. Other parts, especially the mechanical shop and south assembly building, must be demolished and rebuilt elsewhere.

One possible version of the upgrade will reutilize the K1200 cyclotron as an injector to a superconducting driver linac operated at a base frequency of 80.5 MHz. Two stripping stations and multiple-charge-state acceleration will be used for the heavier ions. The 9 MeV/nucleon injector will include an ECR source, a bunching system, and the existing K1200 superconducting cyclotron with axial injection. The superconducting driver linac will largely use cavities already designed, prototyped, tested and shown to satisfy all the design criteria. Rare isotope beams will be produced in a high-power target via in-flight production and separation. The existing A1900 fragment separator will have to be reconfigured. Experimental areas and experimental equipment will be reused, along with a new gas stopper and a reacceleration system.

Also shown in Figure 7.1 is an alternative, but more expensive, option of using a superconducting linac instead of the K1200 cyclotron as the injector to the driver linac (see Section 7.1.2). In this alternative, it would be possible to produce stable beams of heavy ions at energies ≥ 200 MeV/nucleon with beam powers of 400 kW.

A comparison between the NSCL-based facility discussed below and the baseline facility described in Section 5 is given in the Epitome. Use of the linac injector would provide rare isotope beam rates identical to those of the south campus option, while the less expensive cyclotron injector would have a reduced intensity of a factor of four to six. A serious disadvantage of the local NSCL upgrade option would be the significant interruption to the science program. Based upon a preliminary evaluation, it is anticipated that the Nuclear Science program will be interrupted for about 18 months while modifications are done that will affect present accelerator and research areas and while existing equipment such as the A1900 fragment separator is reconfigured for the new layout.

7.1 Driver linac

Utilization of the existing superconducting cyclotrons at the NSCL as part of the driver accelerator system was one of the alternatives that were evaluated. The concept of injection from a cyclotron into a linac has been considered in the past [Lax92]. End-to-end beam simulations of the cyclotron-injection system demonstrate that beams extracted from the cyclotron with a longitudinal emittance of $\leq 30 \pi$ keV/u ns and a normalized transverse emittance of $\leq 0.25 \pi$ mm mrad can be successfully injected into a superconducting linac with a base frequency of 80.5 MHz. However, to achieve these emittances requires that 10% of the beam out of the K1200 cyclotron be collimated and stopped. At the same time, the maximum

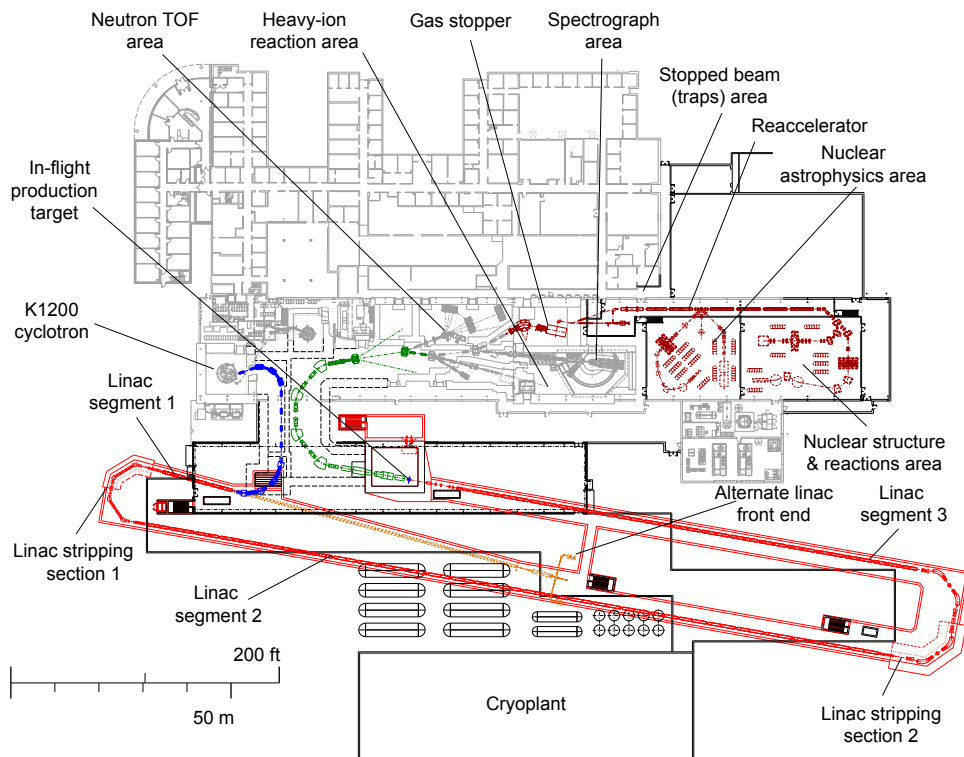


Figure 7.1: Schematic layout of the upgrade on the existing NSCL site. Grayed regions are existing infrastructure and experimental equipment. The blue line shows a possible injection path for 9 MeV/nucleon K1200 cyclotron beams into a subterranean superconducting linac. Also shown in orange is an alternative linac injection system using a front end and additional superconducting accelerating structures. A single rare isotope beam production target is proposed, followed by a reconfigured A1900 fragment separator. A low-energy research program will be supported by a gas stopping and reacceleration system with an associated experimental area.

extracted power out of the K1200 cyclotron is constrained by the fact that beam losses in the cyclotron extraction channel must be limited to <1 kW. Assuming 80% extraction efficiency, the extracted cyclotron beam power is limited to 4 kW. Another limitation of using a cyclotron as a linac injector is that light ions ($Q/A > 0.13$) cannot be accelerated. Given these limitations, the more expensive alternative of using a superconducting linac as the injector to the driver linac was also investigated and is described in Section 7.1.2.

Utilization of a cyclotron injector reduces facility cost when compared to a linac injector. There is, however, a performance penalty of about a factor of four to six. A summary of the beam energy and power for selected stable ions for the cyclotron and linac injector options is given in Table 7.1.

Table 7.1: Final beam energy and beam power for selected stable ion beams for driver linac using either a cyclotron or a linac injector.

| Isotope | | ^1H | ^{40}Ar | ^{86}Kr | ^{136}Xe | ^{238}U |
|---------------------------|-----------------|--------------|------------------|------------------|-------------------|------------------|
| Cyclotron injector | Energy (MeV/u) | - | 250 | 230 | 220 | 200 |
| | Beam power (kW) | - | 100 | 75 | 75 | 65 |
| Linac injector | Energy (MeV/u) | 525 | 265 | 230 | 220 | 200 |
| | Beam power (kW) | 400 | 400 | 400 | 400 | 400 |

7.1.1 Driver linac with cyclotron injector

Cyclotrons use multiple passes through rf acceleration structures and thus offer a less costly option than linacs to accelerate ions to intermediate energies. At the present time the highest power accelerator with a cw beam power in excess of 1 MW is the Paul Scherrer Institute’s (PSI) cyclotron complex. The outstanding performance of the PSI accelerator is due in large part to utilization of a single ion species (protons), large rf systems, and significant physical space for beam extraction. However, the primary beam for the production of rare isotope beams must cover a large range of stable isotopes with different energies, making it difficult to obtain a high performance extraction system under all conditions. In addition, a superconducting linac can simultaneously accelerate multiple charge states [Dei95] while a cyclotron can accelerate only one charge state at a time. Therefore, for a given level of ion source performance, a linac provides greater beam power.

There are two operating variable frequency superconducting cyclotrons, the K1200 and the K500, at the NSCL that are capable of accelerating all ions from hydrogen to uranium to variable output energies. Overall the K1200 was found to provide a better performance match for linac injection and that possibility is shown in Figure 7.2.

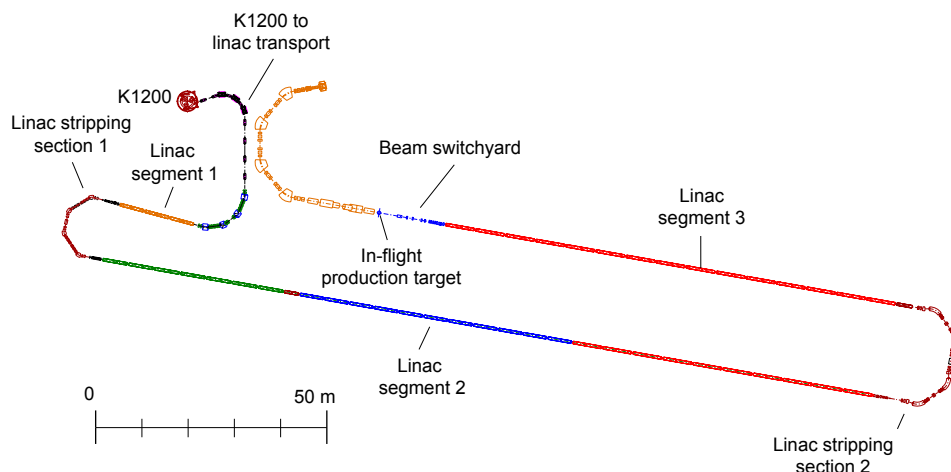


Figure 7.2: Schematic layout of the accelerator complex using the K1200 superconducting cyclotron as an injector for the driver linac.

7.1.1.1 K1200 Cyclotron Injector

K1200 cyclotron harmonic selection

The cyclotron rf frequency must be a subharmonic of the operating frequency of the linac. In this way, all of the beam bunches from the cyclotron will be accepted by the linac and no loss of intensity will occur as long as the phase space of the cyclotron beam is smaller than the acceptance of the linac.

The energy of the ions extracted from the cyclotron is determined by the orbital frequency ω_o . This frequency is determined by the rf frequency ω_r and the harmonic number h ($h = \omega_r / \omega_o$). Since the cyclotron rf frequency must be a subharmonic of the linac rf frequency, there are only a limited number of possible values of the cyclotron frequency for integer harmonic values. The frequency of the linac is 80.5 MHz and since the NSCL cyclotrons operate between 9 and 27 MHz, the highest possible frequency in this range is 20.125 MHz. The highest cyclotron

frequency is desirable to maximize the longitudinal acceptance to emittance ratio in the driver linac.

An analysis was made for both the K500 and the K1200 cyclotrons to determine if either could be used as an injector to the linac. The appropriate operational region required for the K500 was found to be quite narrow and required operation at high magnetic fields for which axial injection would be problematic. The K1200 was found to have a more favorable operating regime. Figure 7.3 shows the operating region for the K1200 cyclotron in the Q/A vs. B plane for a fixed rf frequency of 20.125 MHz, the fourth subharmonic of the base linac frequency. The curves define the possible combinations for different values of the cyclotron harmonic.

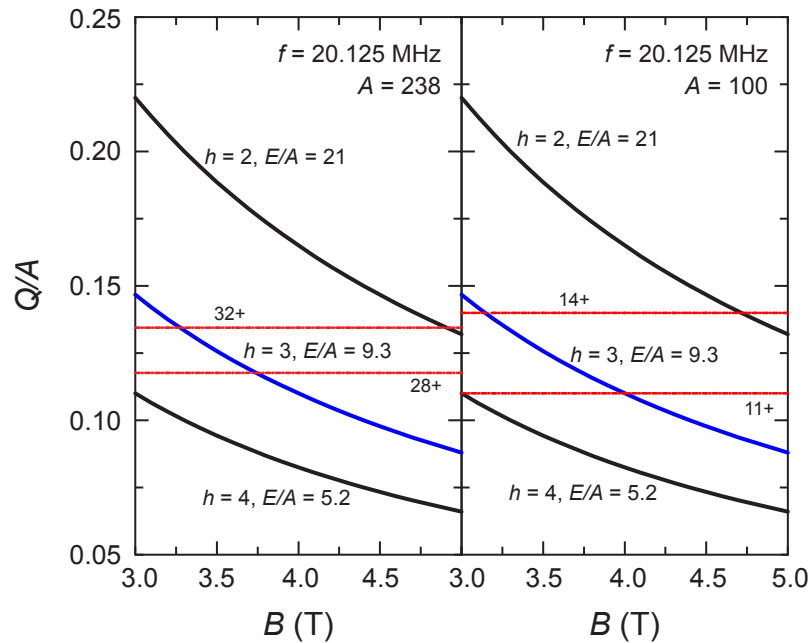


Figure 7.3: Operating region of the K1200 at a cyclotron rf frequency of 20.125 MHz. The solid curves give the relation between the charge-to-mass ratio Q/A of the accelerated ion and magnetic field B for different values of the harmonic h . The two horizontal red straight lines define a band of acceptable charge states (^{238}U with charge states from 28^+ to 32^+ on the left, and an ion with $A = 100$ with charge states from 11^+ to 14^+ on the right).

The left panel of Figure 7.3 indicates the band of charge-to-mass ratio, Q/A , near the production peak from an ECR ion source for ^{238}U with charge states from 28^+ to 32^+ that intersects both the $h = 2$ and $h = 3$ lines. The intersection with the $h = 2$ curve is limited to a high field region near 5 T and is not desirable because the large fringe field of the cyclotron makes axial injection more difficult; the intersection with the $h = 3$ curve occurs at a more favorable magnet field of approximately 3.5 T. In addition, second harmonic ($h = 2$) operation has an extraction energy of 21 MeV/u compared to 9.3 MeV/u for third harmonic. Assuming an extraction efficiency similar to that of present operations (85%) and maintaining a similar maximum beam power loss (1 kW) on the deflector, the number of ions extracted at 21 MeV/u would be proportionately lower than at 9.3 MeV/u due to the higher energy of the ions striking the deflector. The right panel of Figure 7.3 shows a similar calculation for an ion with $A = 100$. In this case, the band shows charge states 11^+ to 14^+ and again the $h = 3$ harmonic provides the preferred operating values.

Due to the transition from the cyclotron operating frequency of 20.125 MHz to the linac frequency of 80.5 MHz, the phase width of the beam effectively increases by a factor of four, which increases the likelihood of beam loss in the linac. Therefore, the possibility of modifying the present cyclotron rf system to obtain the second subharmonic of the linac frequency i.e., 40.25 MHz, was evaluated and the results are shown in Figure 7.4. In this case, the preferred cyclotron harmonic would be the fifth ($h = 5$) providing an output energy of 13 MeV/u. Again, a 1 kW beam loss at 13 MeV/u will limit the extracted beam to a lower value compared to extraction at an energy of 9.3 MeV/u for the 20.125 MHz $h = 3$ operation.

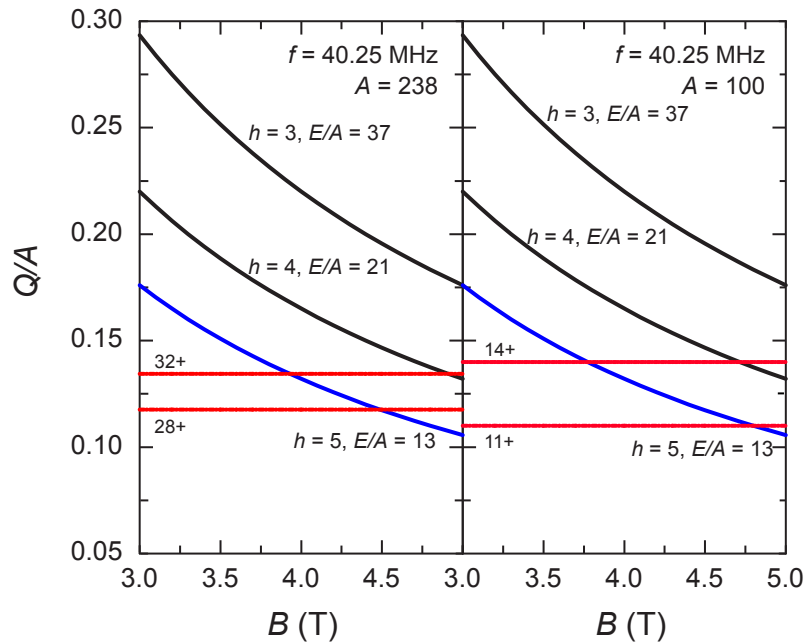


Figure 7.4: Operating region of the K1200 for a cyclotron rf frequency of 40.25 MHz. The solid curves give the relation between the charge-to-mass ratio Q/A of the accelerated ion and magnetic field B for different values of the cyclotron harmonic h . The two horizontal dashed straight lines define a band of possible charge states (^{238}U with charge states from 28^+ to 32^+ on the left, and an ion with $A = 100$ with charge states from 11^+ to 14^+ on the right).

The K1200 operational parameters were set at 20.125 MHz, $h = 3$ to estimate the characteristics of the beam at extraction. Note that by choosing to operate at 20.125 MHz the charge-to-mass ratio for accelerating light ions will be limited to values < 0.13 , but this will not significantly affect operational effectiveness given that the rare isotope beam production mechanism will utilize in-flight production that generally requires heavier primary beams.

K1200 extraction calculations

The performance of the extraction system of the K1200 was evaluated for operation at 20.125 MHz ($h = 3$). The extraction energy was taken to be approximately 9.3 MeV/u for all ions. The acceleration of uranium was used as a test case.

A Dee voltage of 30 kV was used to accelerate the $^{238}\text{U}^{29+}$ beam. The average energy gain per turn was 0.022 MeV/u, requiring about 450 turns to obtain 9.3 MeV/u. The present K1200 operation uses approximately 800 turns to accelerate ions to approximately 140 MeV/u. The lower energy gain due to a lower Dee voltage is

partially compensated by the increased efficiency (factor two) of the acceleration in third harmonic ($h = 3$) compared to acceleration in the first harmonic at present.

Simulations of the acceleration were performed to determine the characteristics of the beam at extraction by using several different starting times (each one degree within $\pm 15^\circ$) and with phase space of the eigen ellipses populated around the central rays. The ions were tracked up to the entrance of the deflector and then through the extraction channel. A small first harmonic bump of three Gauss was added to the normal first harmonic used to cancel the intrinsic imperfections and center the beam. This small additional first harmonic induces a precession of the beam when crossing the $\nu_r = 1$ resonance that separates the extracted turn from the previous turns. The position of the deflector septum was selected to optimize the energy and radial spread of the beam. Because a central region design is not complete, the central rays were started in the simulation at a radius of two inches so that most of the acceleration effect was included.

Figure 7.5 shows, in a simplified way, how the beam is selected for extraction. The left panel shows the radii of the central rays at the entrance of the electrostatic deflector for several turns as a function of starting phase. The shape of the curves in R - ϕ space is given by the $\cos(\phi)$ -like behavior of the energy as shown on the right panel of the figure. The energy increases for each consecutive turn and the radius also increases. During the first extraction turn (40.15 inches), some ions cross the radius of the septum and, due to the electric field of the electrostatic deflector, start to separate from the internal beam. Those ions will not make another turn and are removed from the circulating beam. The ions that did not reach this radius will continue circulating until they go beyond the deflector radius and are deflected out.

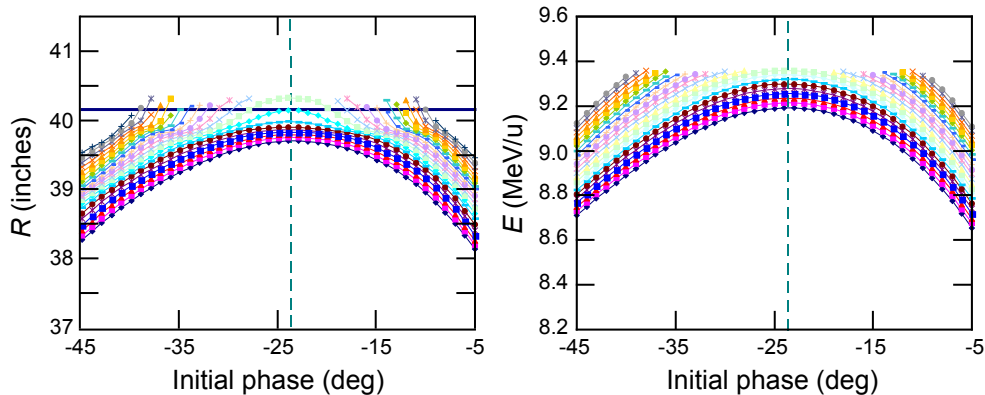


Figure 7.5: Left: radius vs. initial phase for the central rays of the accelerated beam (Dee voltage of 30 kV). Several turns are plotted showing the radius gain per turn. Imperfections in the magnetic field induce the precession observed on the edge of the field. Right: central ray energies are shown for the corresponding turns. In the extraction calculations, a $\pm 15^\circ$ width around the central phase was used.

The large frequency change between the cyclotron (20.125 MHz) and the linac (80.5 MHz) can cause difficulties. The size of the longitudinal phase space (in rf degrees) will be multiplied by a factor of four when changing frequencies. To evaluate the expected performance of the cyclotron beam that is injected into the linac, the transverse and longitudinal phase space of the beam extracted from the cyclotron were determined. The longitudinal phase space at the entrance of the deflector is shown on the left panel of Figure 7.6, and the transverse r - p_r phase space at the entrance of the electrostatic deflector is shown in the right panel.

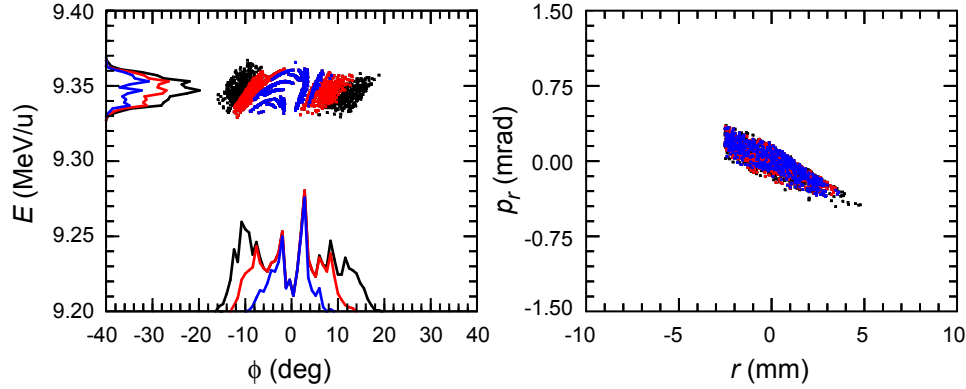


Figure 7.6: Energy E vs. phase ϕ (left) and p_r vs. r (right) at the entrance of the electrostatic septum. The color codes the range of initial phases in each group; blue is $\pm 5^\circ$, red $\pm 10^\circ$, and black $\pm 15^\circ$.

The beam phase space at the end of the extraction channel is shown in Figure 7.7. The beam losses in the extraction channel were approximately 19%. The phase space was found to be (90% of the beam) $28 \pi \text{ keV/u ns}$ in the longitudinal plane and $0.24 \pi \text{ mm mrad}$ (normalized) in the transverse plane.

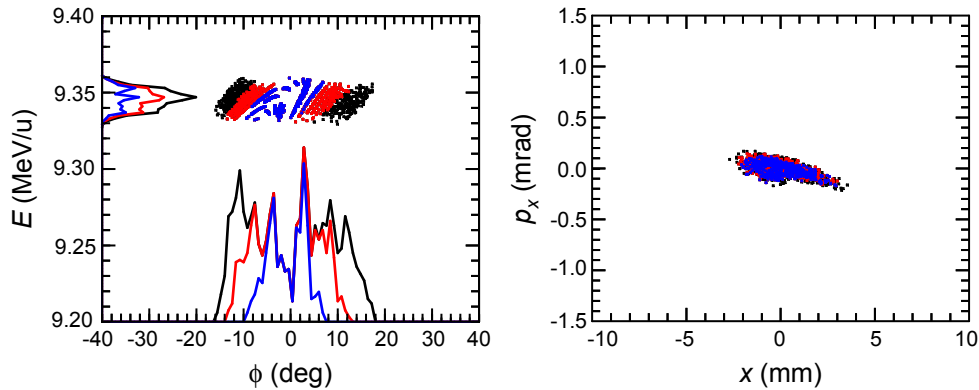


Figure 7.7: Energy vs. phase (left) and p_x vs. x (right) at the exit of the extraction channel. The color codes the range of initial phases in each group; blue is $\pm 5^\circ$, red $\pm 10^\circ$, and black $\pm 15^\circ$.

7.1.1.2 K1200 to linac beamline

The beamline between the K1200 and the linac will transport the beam as well as match the transverse and longitudinal phase spaces of the ion beam emerging from the K1200 cyclotron to those required at the entrance of the driver linac segment 1. The layout of the K1200 to linac beamline is illustrated in Figure 7.8.

The beamline between the K1200 and the linac will consist of four functional sections. The first section is the initial phase matching section consisting of two quadrupole doublets and a cryomodule with a single 80.5 MHz $\lambda/4$ cavity to provide initial transverse and longitudinal focusing for ion beams from the K1200 cyclotron. The second section has three dipole magnets and two quadrupole doublets forming a horizontal achromatic bending section. The third section is a 2π phase advance cell consisting of four quadrupole doublets to transport the beam and obtain reasonable beam envelopes in the system. A cryomodule with two 80.5 MHz $\lambda/4$ cavities is used for longitudinal focusing in the section.

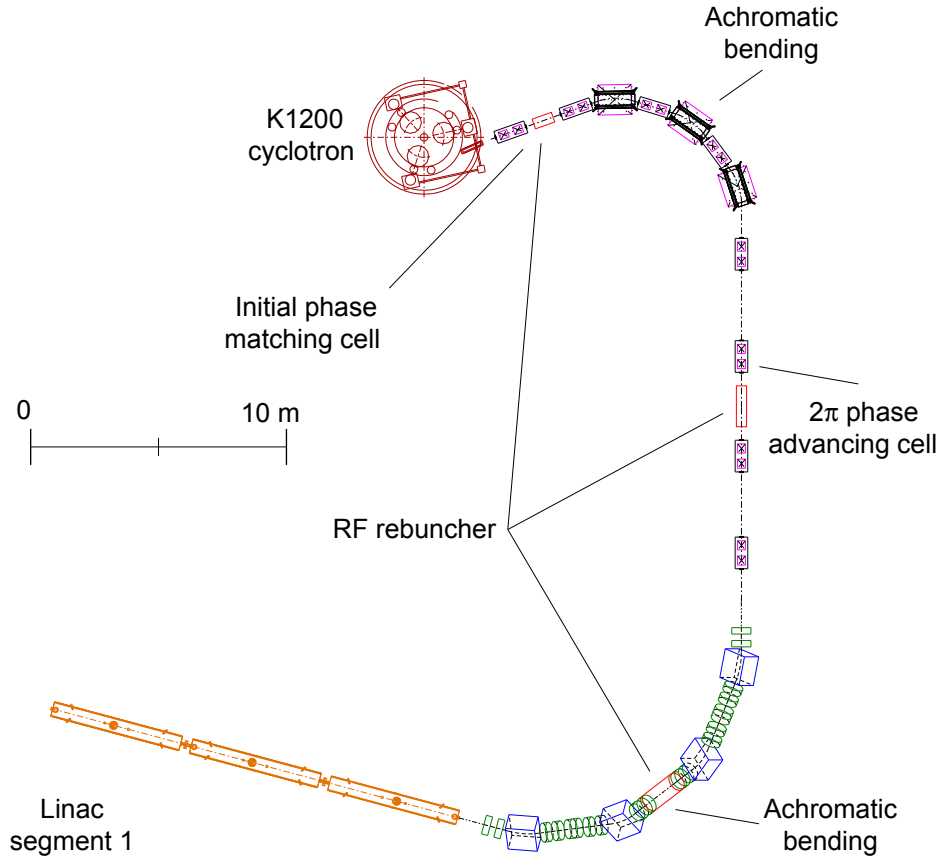


Figure 7.8: Schematic layout of K1200 to linac beamline.

Since the cyclotron is at ground level and the linac accelerating segments are subterranean, the fourth section of the K1200 to linac beamline will use two achromatic bending sections in two separate bending planes to inject beams into linac segment 1 while changing elevation. A cryomodule with two 80.5 MHz $\lambda/4$ cavities will be used in this last section to provide final longitudinal focusing and matching into segment 1 of the driver linac. The transverse and longitudinal lattice functions of the beamline are shown in Figure 7.9 and the input and output beam parameters for the uranium beam are listed in Table 7.2.

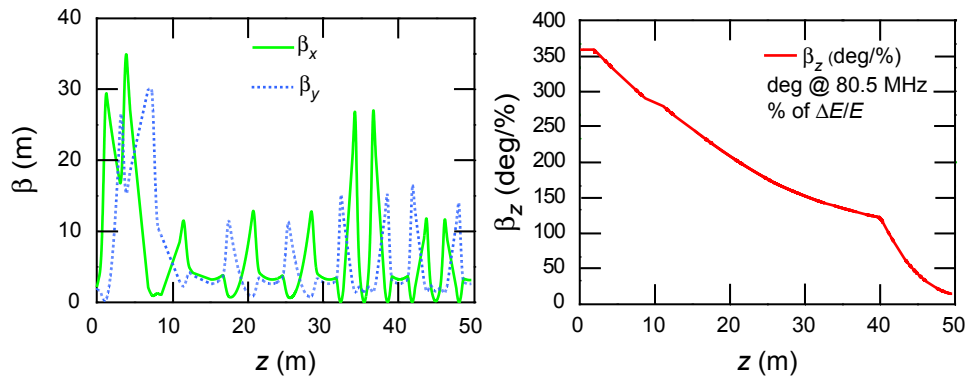


Figure 7.9: Transverse (left) and longitudinal (right) β functions for uranium beam (29^+) in the K1200 to linac beamline.

Table 7.2: Uranium beam parameters (29⁺) in the K1200 to linac beamline.

| | Input | Output |
|-------------------|-------|--------|
| Energy (MeV/u) | 9.30 | 9.30 |
| β_z (deg/%) | 360 | 13.20 |
| α_z | 0.0 | 0.01 |
| β_x (m) | 2.14 | 2.35 |
| α_x | 1.95 | -0.12 |
| β_y (m) | 1.88 | 2.35 |
| α_y | -0.41 | -0.12 |
| Q | 29 | 29 |
| A | 238 | 238 |

7.1.1.3 Linac accelerating segments

Linac segment 1 of the driver linac using a cyclotron as an injector is a shorter version of the linac segment 1 used in the driver linac for the baseline facility discussed in Section 5. The remainder of the driver linac, including linac segments 2 and 3 and the stripping sections 1 and 2 are identical to those of the driver linac baseline facility (see Section 5).

The three cryomodules that will be used to bring the beam energy from 9.3 MeV/u to ~12 MeV/u contain each eight $\lambda/4$ cavities ($\beta_{opt} = 0.085$) at 80.5 MHz. Figure 7.10 shows the longitudinal acceptance of linac segment 1 together with the transverse and longitudinal phase advance along this segment for the uranium beam.

Because the energy of the beam from the cyclotron is relatively high, the transverse and longitudinal phase advances along segment 1 are small as shown in Figure 7.10. The transverse and longitudinal β functions for the uranium beam in linac segment 1 are illustrated in Figure 7.11 and the beam parameters entering and exiting the segment are summarized in Table 7.3.

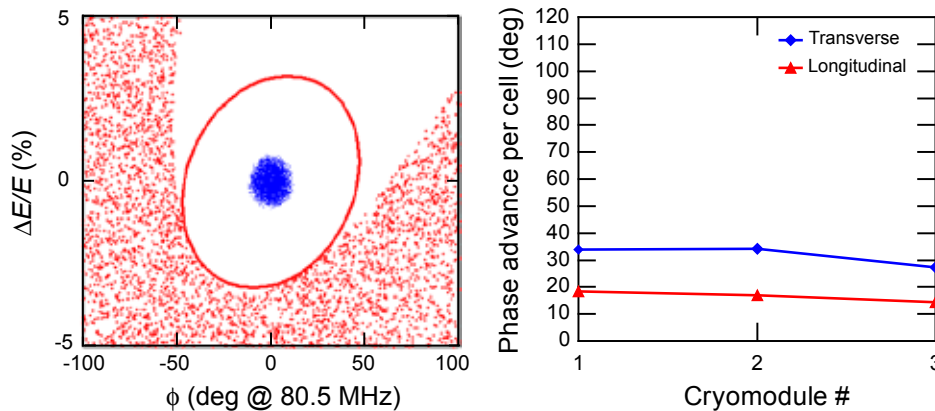


Figure 7.10: Left: Longitudinal acceptance of linac segment 1. The acceptance to emittance ratio is ~15 for uranium beam. The scales for the two axes were chosen to show details near the beam distribution. Nonetheless, the typical “golf club” shape for the acceptance is observable when the plot area is increased. The acceptance is not centered on the beam because the segment is short with less than a period of longitudinal oscillation. Right: Phase advance along linac segment 1 for uranium beam.

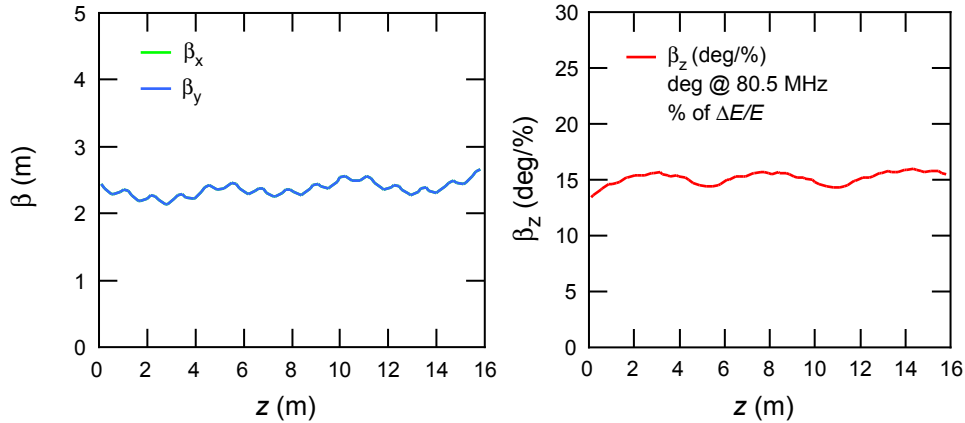


Figure 7.11: Transverse (left) and longitudinal (right) β functions in linac segment 1 for a uranium beam ($^{29+}$). Note the green horizontal β function (β_x) is underneath the blue vertical β function (β_y).

Table 7.3: Uranium beam parameters ($^{29+}$) in linac segment 1.

| | Input | Output |
|-------------------|-------|--------|
| Energy (MeV/u) | 9.30 | 11.40 |
| β_z (deg/%) | 13.20 | 15.31 |
| α_z | 0.01 | -0.05 |
| β_x (m) | 2.35 | 2.60 |
| α_x | -0.12 | 0.04 |
| β_y (m) | 2.35 | 2.60 |
| α_y | -0.12 | 0.04 |
| Q | 29 | 29 |
| A | 238 | 238 |

7.1.1.4 Beam switchyard

A single in-flight production target for the driver linac will be at the same level as the main linac tunnel. No elevation change is required at this point, simplifying the design of the beam switchyard. The design goal is a beam size on the in-flight production target of ~ 1 mm in diameter to limit the otherwise large geometric aberrations in the fragment separator downstream as in the baseline facility. Figure 7.12 shows the layout of the beam switchyard for the driver linac.

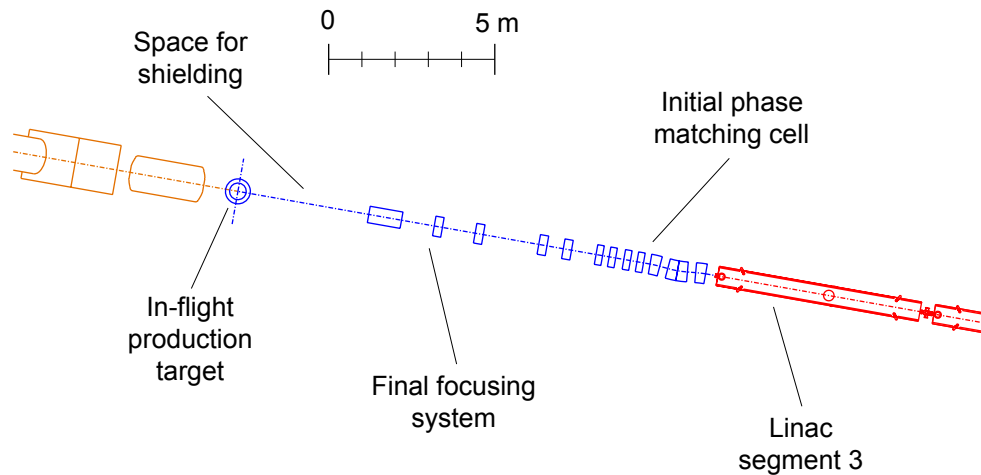


Figure 7.12: The schematic layout of the beam switchyard for the driver linac at the existing NSCL site.

The beam switchyard will consist of two sections. The first section will be the initial phase matching cell to provide transverse focusing and to achieve a symmetric beam spot. To shield the superconducting cavities of linac segment 3 from the particle fragmentation target and prevent possible contamination by target effluents, a dog-leg ($-\alpha, 2\alpha, -\alpha$) achromatic magnetic chicane is used to shift the beam axis by approximately 5 cm. Four quadrupole magnets will then be used to provide the required transverse focusing. The second section is the final focusing system with four quadrupole magnets and one solenoidal magnet to achieve the final beam spot on the in-flight production target. To provide proper radiation shielding, a separation of ~ 4 m between the last focusing element and the target was required, as shown in Figure 7.12. The transverse and longitudinal β functions for the uranium beam along the beam switchyard are shown in Figure 7.13.

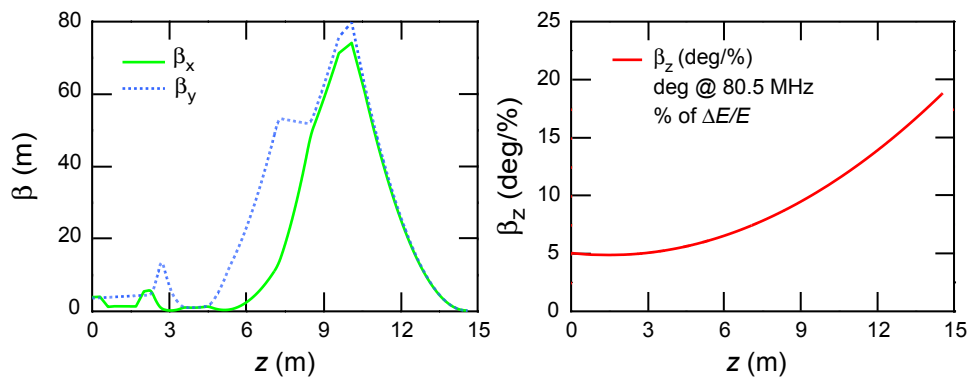


Figure 7.13: Transverse (left) and longitudinal (right) β functions for the uranium beam (89^+) along the beam switchyard.

The performance of the beam switchyard was evaluated by particle tracking using the beam phase space from linac segment 3 with the IMPACT code. The results showed that the delivery of multiple charge states of the beam onto the target will yield a transverse Gaussian distribution with a σ of ~ 0.25 mm. This distribution will be adequate for proper operation of the downstream in-flight fragment separator.

7.1.1.5 End-to-end beam simulation of the driver linac with cyclotron injector

Some of the results of the end-to-end simulation of the system are shown in Figure 7.14 to Figure 7.16 for the cyclotron driver linac delivering a uranium beam. Error tolerances used in the simulations are identical to those used in the driver linac baseline facility discussed in Section 5.

Figure 7.14 and Figure 7.15 show the evolution of the transverse and longitudinal uranium beam emittances along the driver linac using the beam parameters from the cyclotron injector. Figure 7.16 shows the maximum beam envelopes with and without errors. In all three linac segments, the 15 mm radial apertures of the superconducting cavities determine the minimum transverse aperture.

The simulation results show that even for the most challenging case of a uranium beam comprised of multiple charge states, the cyclotron injector option satisfies the design requirements with tolerable emittance growths. The ratio of the longitudinal emittance to acceptance is adequate in all three linac segments and the maximum transverse envelope fits adequately within the transverse aperture with no uncontrolled beam loss observed.

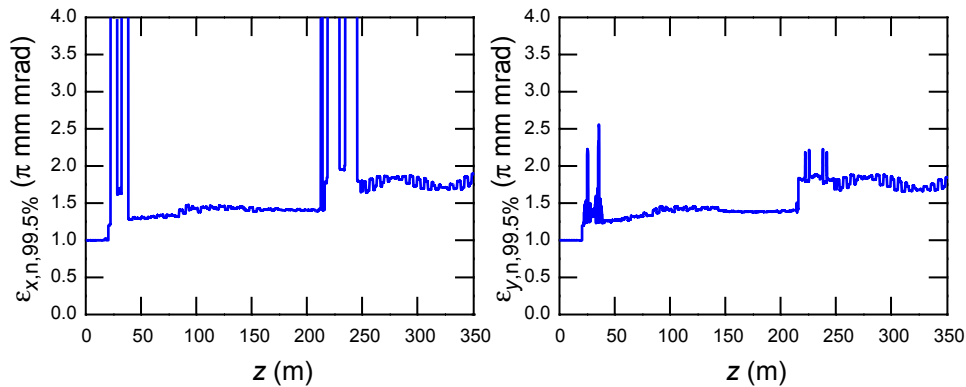


Figure 7.14: Horizontal (left) and vertical (right) emittances along the driver linac for uranium beam with rf errors. Alignment errors and central orbit correction were not included in these simulations, but there was a 12% emittance increase in both planes for a similar lattice [Wu04].

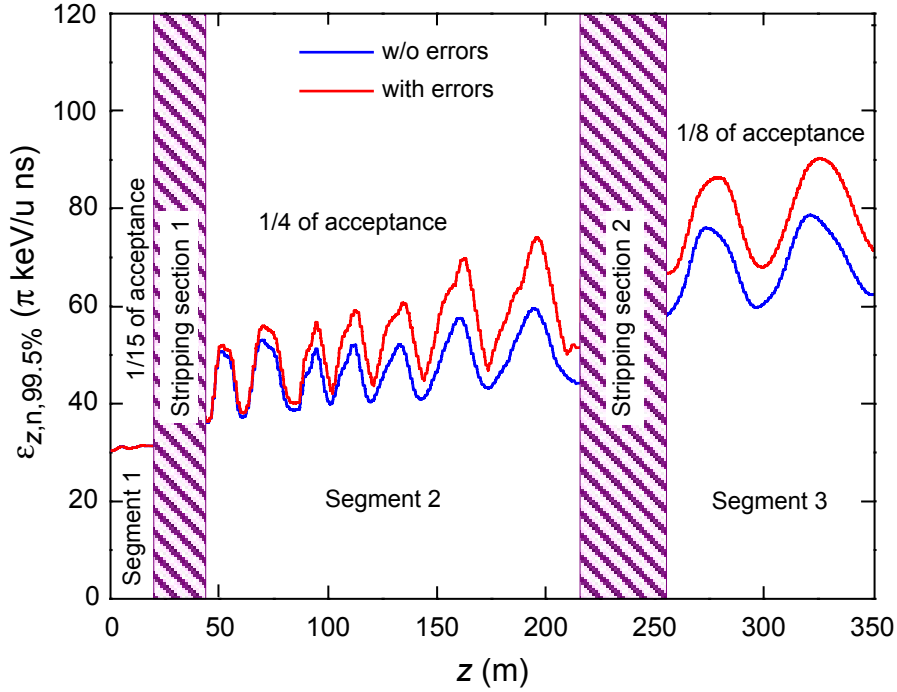


Figure 7.15: Longitudinal emittance along the driver linac for uranium beam with (red) and without (blue) rf errors. Alignment errors and central orbit correction were not included in these simulations, but their impact on the longitudinal emittance was found negligible for a similar lattice [Wu04]. The ratio of longitudinal emittance to acceptance is given for each of the three linac segments in the case without errors.

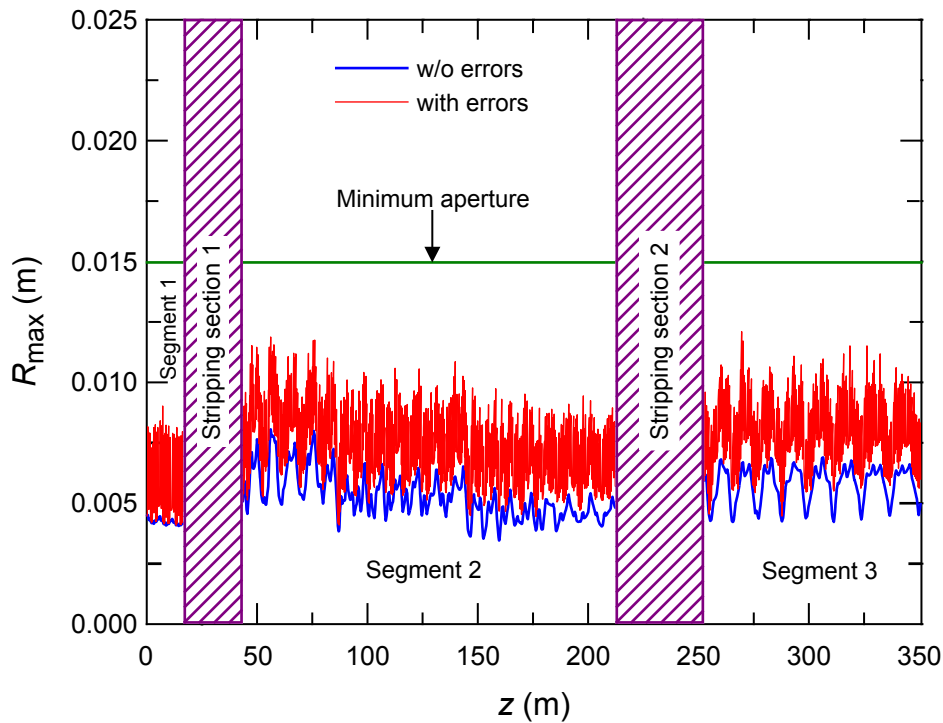


Figure 7.16: Maximum beam envelopes (outmost particles) along the driver linac for uranium beam with (red) and without (blue) errors. The minimum linac aperture of 15mm is also indicated.

7.1.2 Driver linac with linac injector

As an alternative to utilization of the K1200 cyclotron as an injector, it is possible to implement the same driver linac on the NSCL site as that delineated in Section 5. This design was shown to satisfy all the design criteria. The linac injector and main linac on the NSCL site is illustrated in Figure 7.17. This option is more expensive than the cyclotron injector option but leads to higher beam power on the production target as shown in Table 7.1.

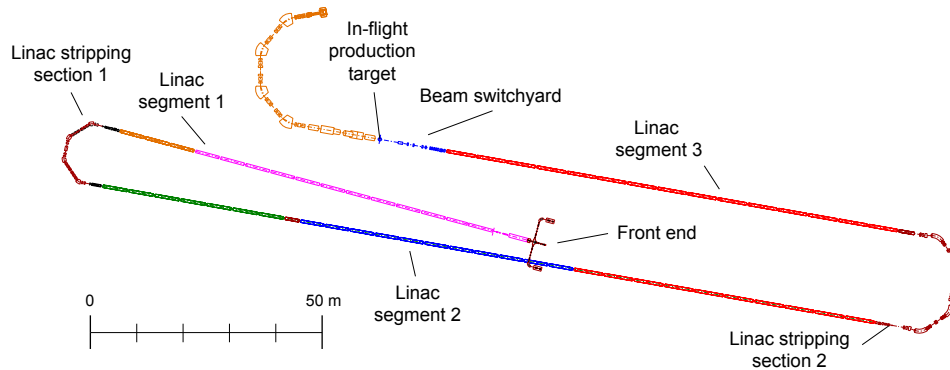


Figure 7.17: Schematic layout of the driver linac option on the existing NSCL site.

7.2 Rare isotope beam production

The beam production area is similar in most aspects to the target area for the baseline facility described in Section 5. Figure 7.18 illustrates the components related to beam production, the experimental areas and the reaccelerated beam area. The main difference to the baseline facility is that no ISOL option is possible due to the space constraints of the current NSCL site.

The target hot cell will contain the production target and the preseparator, which bends the beam in the vertical direction (see Section 7.2.2.1). The main separator consists of two stages and will be reconfigured from the existing A1900 fragment separator. An RFFS will be added following the modified A1900, prior to the beam distribution system. The existing NSCL beamlines will be used to transport the rare isotope beams to the high-energy experimental target areas and the cyclotron stopper. A new experimental area will be constructed for the low-energy experimental equipment.

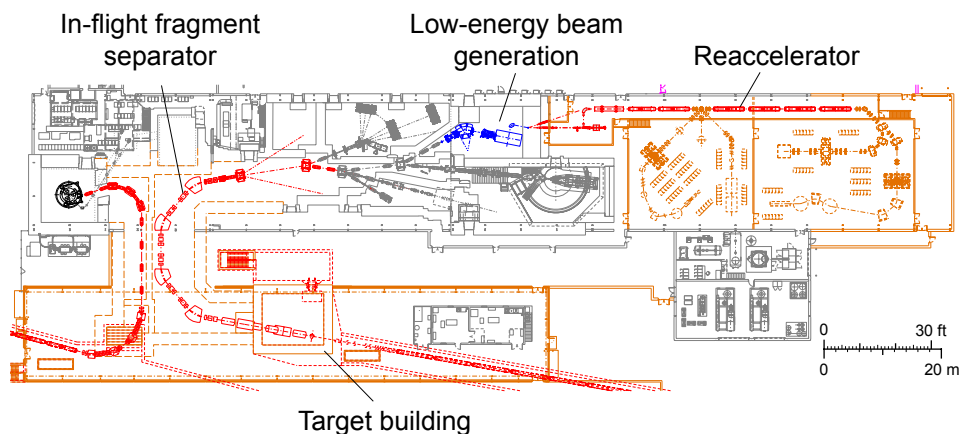


Figure 7.18: Beam production and distribution components at the upgraded NSCL-based facility.

7.2.1 Production target

Since no place for an ISOL station is needed, the hot cell is more compact than that in the baseline facility layout. Shielding requirements were established using the same approach as for the baseline facility described in Section 5. As in the case of the baseline facility, the high beam power available at the NSCL-based site makes remote handling of targets and system maintenance mandatory. A 20-ton bridge crane inside the hot-cell will be used to move components. A second crane will transport an overhead manipulator, which will be used for all remote operations, such as target changes, standard maintenance, and repairs. In addition, a service position equipped with a through-the-wall manipulator will be installed on one of the walls.

Neutronics calculations were carried out for the NSCL-based facility site as those described for the baseline facility in Section 5. The preseparator is vertical in the NSCL-based facility; hence, special attention was paid to bulk shielding behind the beam dump to minimize the level of secondary radiation, including skyshine.

7.2.2 Fragment separator

Figure 7.19 illustrates the overall concept and individual components of the separator. The function of the preseparator will be the same as in the baseline facility, but in addition it will be used to bring the fragments from the lower elevation of the linac to the experimental area on grade. The preseparator area will reside in the high-radiation environment. Cleanup apertures will be used to remove stray particles. The two-stage main fragment separator that follows the preseparator will reuse the A1900 magnets to create two identical stages with two 45° bends and four large-bore quadrupole triplets. The two stages of fragment separation will be necessary to remove unwanted tertiary fragments produced in the wedge (an integral part of the separation process).

Production yields will be identical to those presented for the baseline facility (see Section 5), assuming that the primary beam parameters are identical. The separator specifications are nearly identical, with the only difference being that the preseparator is limited to a maximum magnetic rigidity of 6.3 Tm due to space constraints. With 6.3 Tm as the maximum separator rigidity, a limited set of beams with extreme A/Q values, such as ^{11}Li , ^{19}B , and ^{22}C would have rigidity above these values. This will reduce the production rate of these fragments below the optimum by less than 50%.

The design goals are to achieve a minimum momentum acceptance of 10% and an angular acceptance of ± 40 mrad. The basic optical designs were calculated with the code GICOSY [Wei05a] up to the fourth order. The angular and momentum acceptances were checked with the Monte Carlo program MOCADI [Iwa97]. The following subsections describe the various separator components illustrated in the block diagram in Figure 7.20.

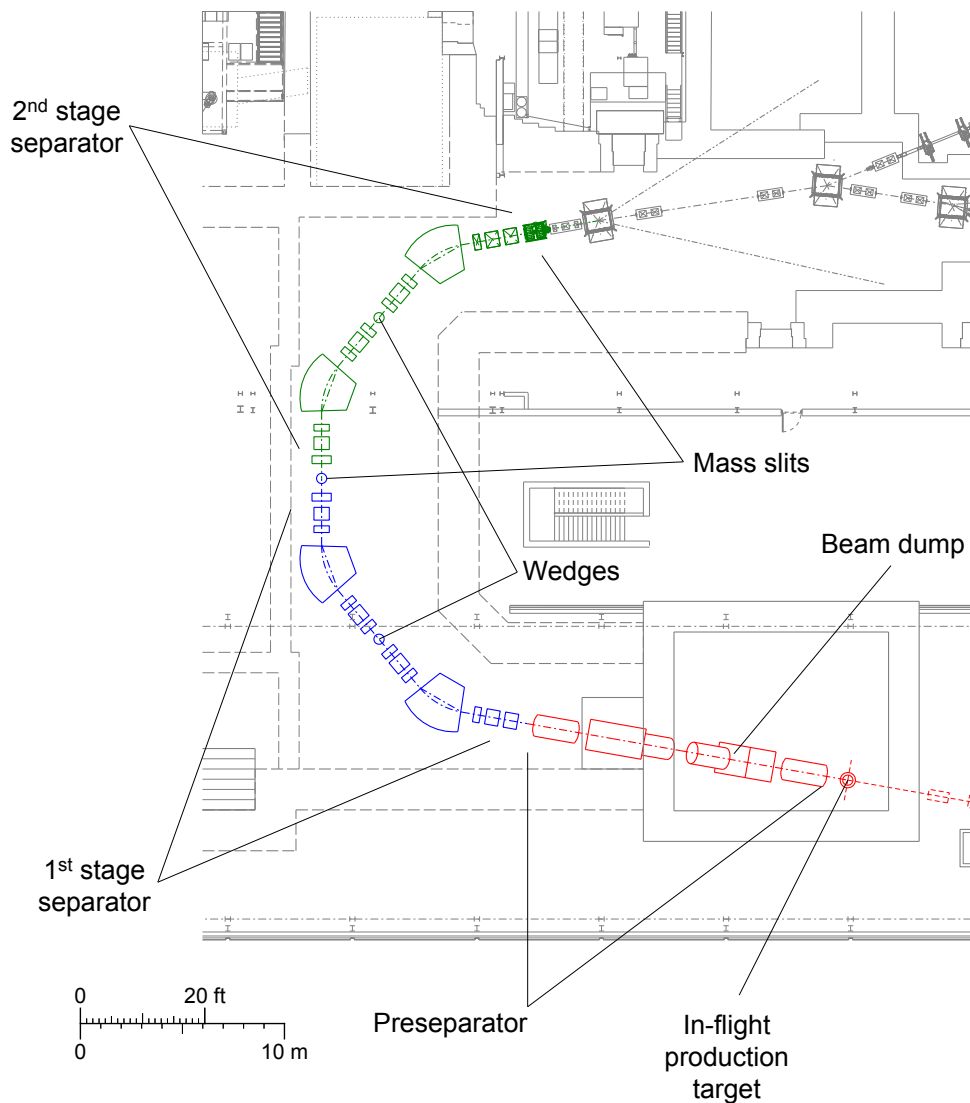


Figure 7.19: Schematic layout of the in-flight beam production system at the NSCL-based facility. The preseparator is vertical and brings the beam from the lower, linac level to the ground-level experimental facility. The main separator is based on a reconfigured A1900 separator.

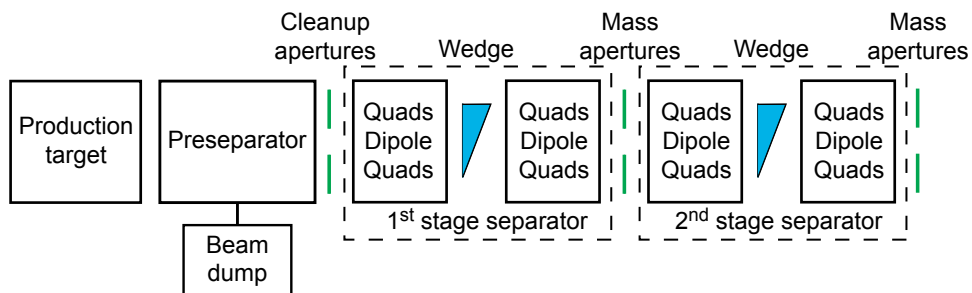


Figure 7.20: Block diagram showing the various parts of the fragment separation system. The primary beam strikes the production target represented on the left and fragments are separated in three stages of separation. The function of the various parts is described in the text. Following the final aperture, the fragments enter the NSCL beam distribution system.

7.2.2.1 Preseparator

As in the case of the baseline facility, a preseparator will be used to remove the primary beam and most of the unwanted fragments from the ions of interest. This removal will reduce the radiation field outside the production area and will improve the operational safety of the system. In addition, the number of contaminants passed to the gas stopping system must be minimized. The reduction of unwanted ions will lead directly to higher extraction efficiencies. Ideally, the preseparator would also allow the collection of unused isotopes for other applications. The preseparator optics will have a focus after the first dipole, and the beam dump will be placed at this location. This area will also serve as the potential location for isotope recovery. A shielding wall will be used to separate the first part of the separator from the rest of the system. The whole system will be achromatic and will be operated as a standard momentum-loss fragment separator.

The key components of the preseparator and the approach chosen are the same as for the preseparator of the baseline design (see Section 5):

- A focus after the first dipole to allow the primary beam to be intercepted early in the system. This limits the extent of high radiation area. A window could be added directly after the dump to allow segregation of the vacuum systems.
- The first dipole will be a “C” magnet with the topside open to allow access for beam dumps.
- Water-cooled copper or aluminum beam dumps. Fixed dumps should be able to dissipate 100kW of beam power under these conditions. Space will be left for future developments that will be able to accommodate beam power levels up to 400 kW. Further R&D will be conducted to verify if a rotating dump in a different scenario will be adequate.
- The edges of the beam dump will be moveable and can serve as a momentum aperture to reduce the number of unwanted fragments transported further in the system. This will reduce radiation damage and activation of subsequent components.

Figure 7.21 shows a schematic layout of the preseparator. The shielding was designed to be sufficient to operate the facility with primary beam intensities up to 400 kW. Remote handling silos are provided for beam diagnostics before the target, at the target itself, at the beam dump, and at the separation window after the dump.

The ion optics of the preseparator have been calculated to the fourth order and corrected to the third order by the inclusion of multipole coils in the quadrupole magnets of the preseparator. Simulations carried out with MOCADI indicated that approximately 50% of the ions that enter the phase space (assuming uniform illumination) will be transmitted. The image produced by the preseparator was assumed to be less than 2 mm, since this will form the object for the final two stages of separation. An aperture at the image position of the preseparator will be used to form the object for the remainder of the system. The required parameters for the magnets are shown in Table 7.4.

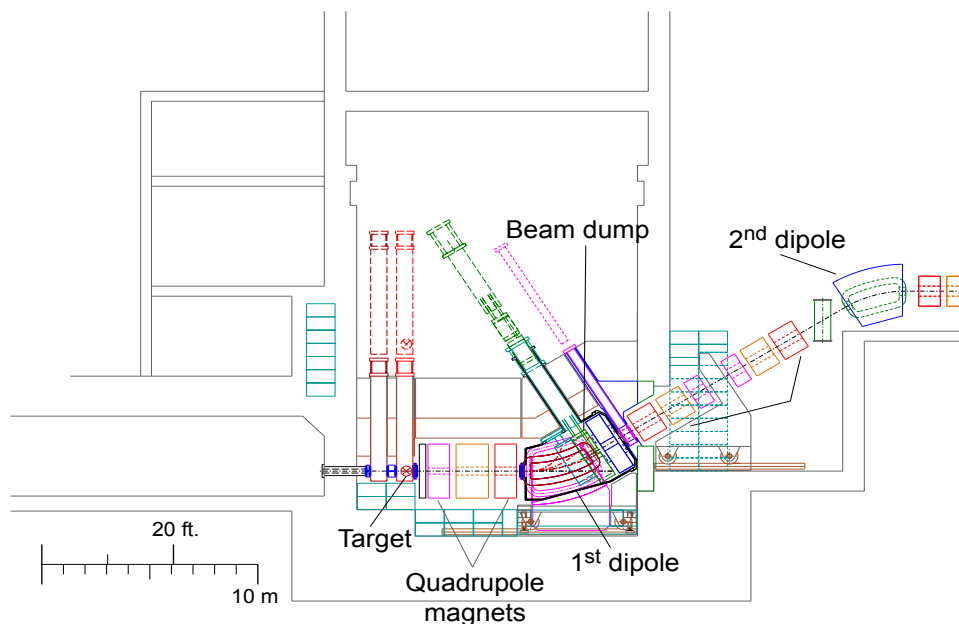


Figure 7.21: Schematic layout of the NSCL-based facility preseparator with an acceptance of ± 40 mrad and a momentum acceptance of 10%. The first focus will occur directly after the first dipole, where the beam and unwanted fragments can be collected. One of the advantages of this design is that it also brings the fragments up to ground level and reduces overall civil construction costs.

Table 7.4: Magnet parameters for the proposed preseparator at the NSCL-based facility. Quadrupole magnets that will require higher-order multipoles are indicated in the table.

| Magnet | Pole radius (m) | Field at pole tip radius (T) | Sextupole | Octupole | Length (m) |
|----------|-----------------|------------------------------|-----------|----------|------------|
| Quad 1 | 0.13 | 1.55 | | | 0.748 |
| Quad 2 | 0.13 | -2.07 | | | 0.748 |
| Quad 3 | 0.13 | 2.22 | | yes | 0.43 |
| Dipole 1 | 0.07 | 1.9 | | | 45 degree |
| Quad 4 | 0.11 | 2.39 | yes | yes | 0.43 |
| Quad 5 | 0.11 | -1.20 | yes | yes | 0.803 |
| Quad 6 | 0.11 | 0.508 | | yes | 0.43 |
| Quad 7 | 0.11 | 0.508 | | yes | 0.43 |
| Quad 8 | 0.11 | -1.2 | yes | yes | 0.803 |
| Quad 9 | 0.11 | 2.39 | yes | yes | 0.43 |
| Dipole 2 | 0.07 | 1.9 | | | 45 degree |
| Quad 10 | 0.13 | 2.22 | | yes | 0.43 |
| Quad 11 | 0.13 | -2.07 | | | 0.748 |
| Quad 12 | 0.13 | 1.55 | | | 0.748 |

There are three main differences between the preseparator design of the baseline facility and that of the NSCL-based facility:

- The NSCL-based facility separator is vertical in order to bring the fragments up to ground level; the baseline facility separator is horizontal.
- The maximum rigidity of the preseparator is 6.3 Tm for the NSCL-based option. The maximum rigidity of the preseparator for the baseline facility is 8.0 Tm.
- The NSCL-based facility preseparator will not include a wedge because it was not possible to correct image aberrations at the wedge position due to the limited space available. The two wedges for two-stage separation will be located in the subsequent separator in the NSCL-based option.

The impact of the differences between the fragment separator designs for the baseline facility and the NSCL-based facility should be small. The largest concern is the lower magnetic rigidity will limit the production of the most exotic neutron-rich nuclei.

7.2.2.2 Main separator based on the A1900

Given the similar specifications for the high-resolution separator at the NSCL-based facility and the existing A1900, it will be possible to reconfigure the A1900 magnets to meet the new specifications. The magnet parameters are nearly identical to those used currently in the A1900. The main difference is the change of the bend direction for the middle two dipoles, which results in a two-stage separator. The modular layout of the components will allow the operation of the high acceptance separator in several ion-optical modes. The largest purification will be obtained by operation with two stages of separation (two wedges), as indicated in Figure 7.20. Two stages of separation will significantly reduce the number of contaminant fragments in the secondary beam, a particular advantage for the gas stopping system [Gei06].

Wedges will be placed at the intermediate images of the two segments of the main separator. The aperture following the first segment provides mass selection and is located at the object location of the second segment. The final stage of separation can be used for additional secondary beam cleanup or can be used as a location for detectors to tag the momentum and angle of each ion. Space is provided following the end of the main stage separator to add a RFFS. This will be needed for clean separation of proton-rich beams.

7.2.3 Low-energy beam generation and reacceleration

The NSCL-based option will also include an identical cyclotron gas stopping system as planned for the baseline facility. In fact, the generation of low-energy beams of rare isotopes produced by in-flight separation is already a key component of the research program at the NSCL, and the system envisioned for both facility will be implemented at the NSCL in the next few years. The cyclotron stopper [Bol05b] currently under development will replace the linear gas stopping cell [Wei05b] currently in use for the LEBIT project [Rin06]. The cyclotron stopper will overcome deficits of linear gas cell systems with respect to reduced efficiencies with increasing beam rates and long extraction times. The cyclotron stopper will provide high-quality low-energy beams for low-energy beam experiments and for reacceleration.

A reacceleration system is also under development as a proof of principle. The NSCL-based options could use this system in its planned location, which is shown in right side of Figure 7.18. The concept is based on acceleration of highly charged ions, charge bred in an Electron Beam Ion Trap (EBIT). The reaccelerator included a room temperature RFQ and SRF cavities will allow acceleration of beams to 2-3 MeV/nucleon initially. The plan is that after the successful demonstration of this n^+ reacceleration concept, an accelerator upgrade to 12 MeV/nucleon will be performed. This system would be available to be used as the reaccelerator for the NSCL-based option.

7.3 Experimental areas

All experimental areas at the NSCL site option share a common highbay area as shown in Figure 7.18. The sharing will permit manipulation of experimental apparatus in any of these areas using one 40-ton overhead crane. The fast beams area follows directly the fragment separator and the stopped beam area will be located close to the cyclotron stopper. The astrophysics and low-energy nuclear science areas will be placed along the reacceleration cavities to minimize distances for beam delivery.

The schematic layout of the stopped beam experimental area is shown in Figure 7.22. The rare isotope beams delivered to this area will range in energy from a few eV to a maximum of 60 keV. Three experimental stations are envisioned: one dedicated to Penning-trap mass spectrometry, and two general-purpose beamlines that can accommodate equipment for a variety of experiments, including laser spectroscopy, polarization, and nuclear decay studies.

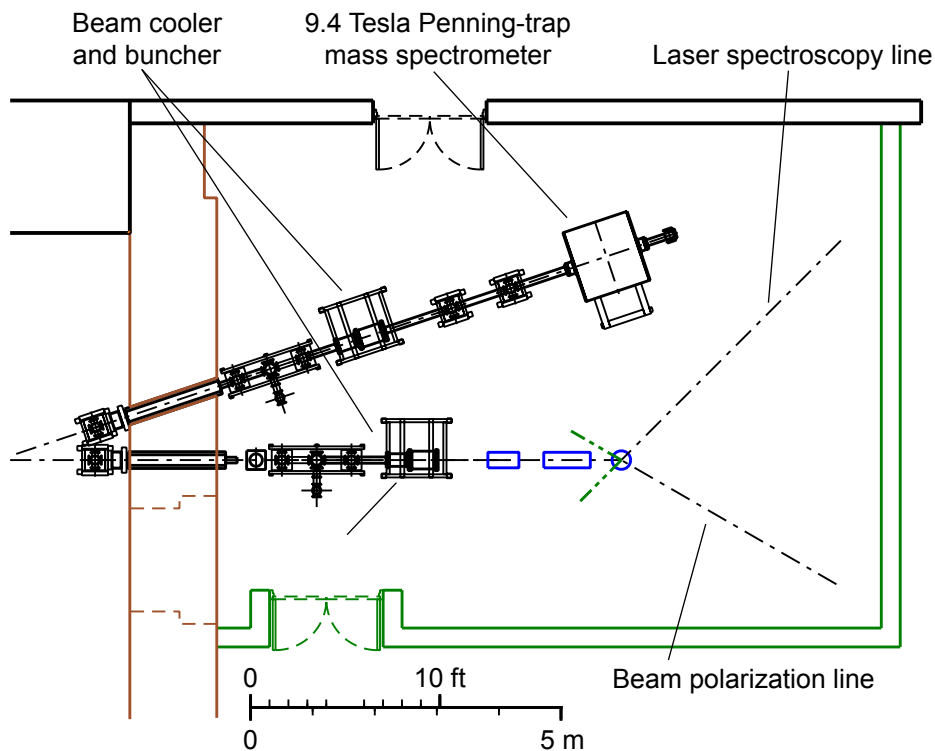


Figure 7.22: Schematic layout of the stopped beam experimental area located below the reaccelerator balcony.

The area is at grade level below the reaccelerator balcony and approximately 100 m² in size. This area is smaller than the area planned for the baseline facility (365 m²). All other aspects, beam transport, services, utilities and user access will be the same as in the baseline facility (see Section 5.6.1.1),

The reaccelerated beam areas will serve experiments in nuclear astrophysics and low-energy nuclear structure and reaction as shown in Figure 7.23. The existing highbay will be enlarged by 600 m² to accommodate these experimental setups. The two areas are defined by the maximum energy provided from the reaccelerator. The secondary beams delivered to the astrophysics area will have maximum energy of 3 MeV/nucleon, while those delivered to the low-energy nuclear structure and reactions area will have the full energy available from the reaccelerator - 12 MeV/nucleon.

Since the accelerating structures will be located on the second floor, the reaccelerated beam will be brought to the experimental beamline level using two 90° magnetic steering elements. The second steering element that serves the nuclear astrophysics area will be designed to pivot about 360° in the horizontal plane to make connections with the three planned beamlines in that area. Such a design will permit future expansion of the nuclear astrophysics area to the north of the accelerating elements, if dictated by programmatic needs.

The size of the nuclear astrophysics (490 m²) is only slightly smaller than the planned area at the baseline facility (610 m²) and is still able to accommodate a recoil separator similar to DRAGON. In addition, there will be space for two additional general purpose end stations.

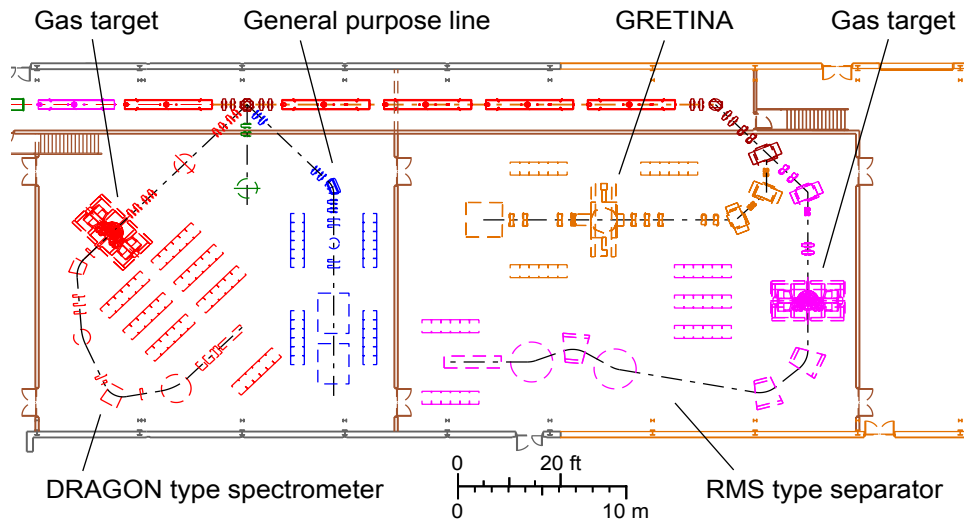


Figure 7.23: Schematic layout of the reaccelerated beam (traps) experimental areas at the NSCL-based facility.

The low-energy nuclear structure and reactions area (610 m²) will also be smaller compared to the baseline facility (1150 m²) with two end stations. One end station will host a mass separator device similar to the ORNL mass separator. The γ -ray tracking array GRETINA can be located at the second end station for stand alone experiments or it can be placed at the target or focal plane of the separator. When GRETINA is not in stand alone operation, other equipment (e.g., a solenoid spectrometer) can be accommodated.

Other details of the reaccelerator areas are the same as for the baseline facility as described in Section 5.6.1.2. Note that the proposed layout of the reaccelerated experimental areas will permit the extension of the highbay area should additional experimental floor space be required in the future (see Figure 7.25).

The fast beam experiments can be performed at the existing NSCL experimental areas shown in Figure 7.24. All current and newly developed experimental equipment will be available for experimentation.

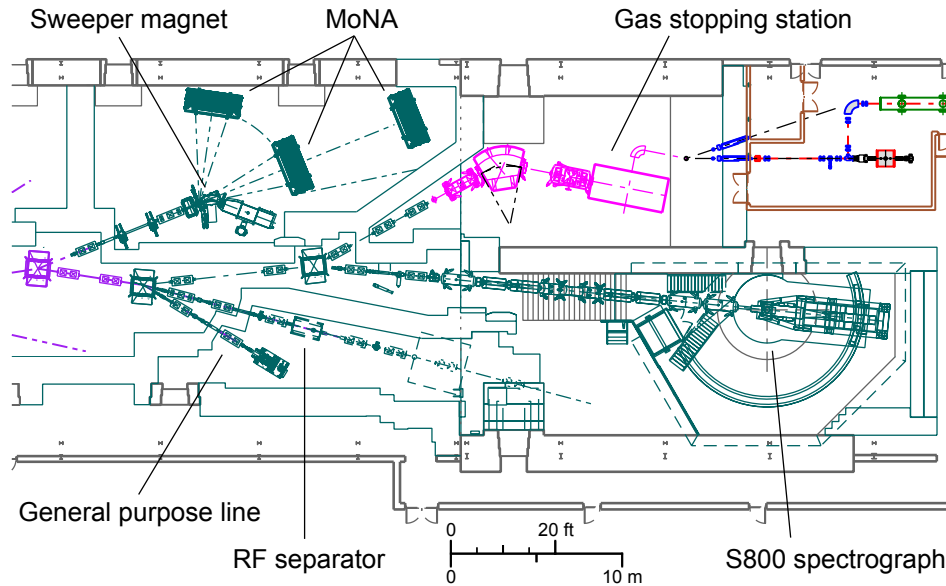


Figure 7.24: Fast beam experimental area at the NSCL-based facility.

7.4 Conventional facilities

The physical structures, access roads, and parking areas will occupy a land space of approximately 11 acres at the present NSCL location on the MSU campus, as shown in Figure 7.25.

The construction will be composed of eight major interconnected structures - the underground linac tunnel, the above ground linac support building, the cryoplant, the target facility, the new south highbay, the highbay connector structure, the existing highbay extension and the shop/assembly/office addition. Access roads will provide truck service to the two crane bays, to the loading dock, and to the cryoplant. Limited parking spaces for staff and visitors will be available. Additional staff and visitor parking will be available at nearby MSU parking facilities. All structures will have fire protection provided by a wet pipe sprinkler system and a complete fire alarm system, including visual and audible alarms, pull stations at exits, and heat/smoke detectors as required by code. All temperature controls will be a direct digital type capable of being monitored at a central location or remote site. The facility electrical power requirement is expected to be 25-30 MW, which will be supplied by a new high voltage utility bulk power substation located within one mile of the NSCL site. Two medium voltage feeders, sized for a maximum power of 30 MW each, will run from the substation to 15 kV primary switchgear located in the new cryoplant. From there, electrical power will be distributed to the new facilities. The present NSCL electrical system will continue to supply the existing facility equipment. The cost estimate includes extending the required utilities from the campus systems to the new structures.

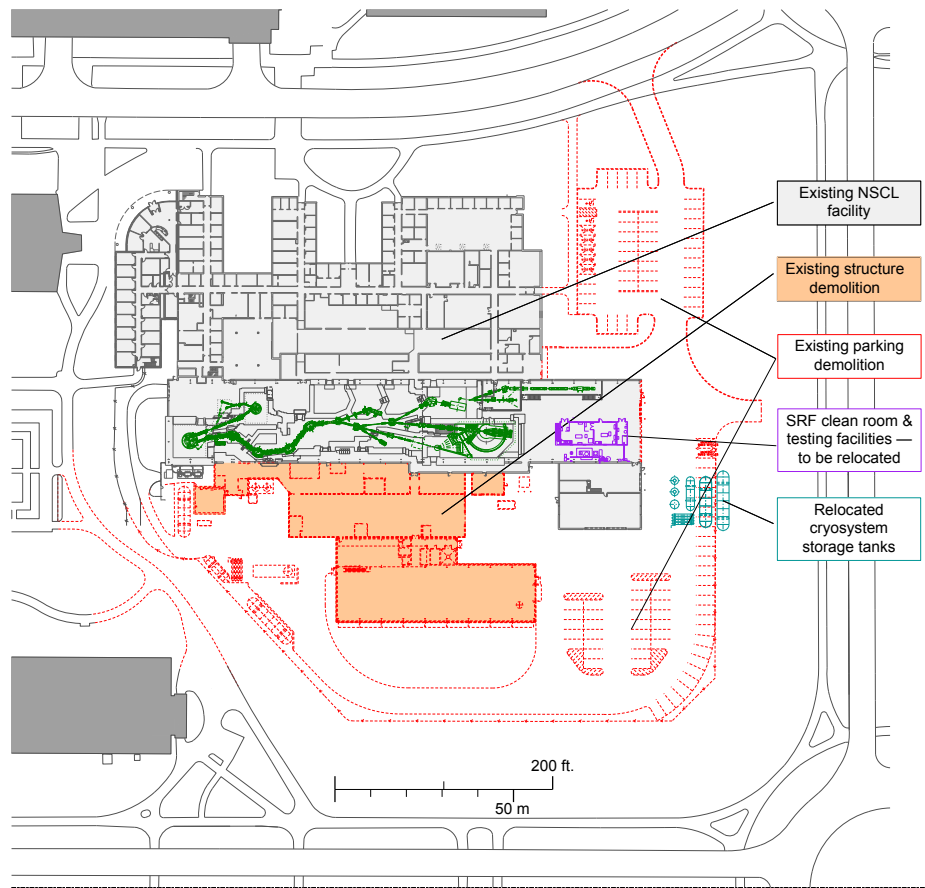


Figure 7.25: NSCL site facility layout.

Figure 7.26 shows the demolition of existing shop buildings and south highbay that will be required to make space for the new facility structures. Also, the existing loading dock and parking areas will be removed. Existing cryogenic system storage tanks will be relocated to a consolidated space east of the existing cryoplant.

The Linac tunnel will have a footprint of 2,700 m² and will be constructed employing an open cut excavation (cut & fill). The foundation slab will be supported on drilled piers at six meter centers that will extend down to bedrock (approximately 25 m below grade). The tunnel slab, walls, and ceiling will be 0.5 m reinforced concrete except at the stripping areas where the thickness will be two meters to provide necessary shielding. The parallel tunnel sections will be connected by a reinforced concrete slab to minimize differential settlement. The tunnel floor will be 6.75 m below grade and the structure will be waterproofed and equipped with a perimeter drain tile and sump pump system. Access to the at-grade structures will be via three stairwells and a freight elevator. Large pieces of equipment will be lowered into the tunnel through access hatches in the at-grade new south highbay.

The 2,300 m² linac support building will be a single story structure providing space for the linac/magnet power supplies and controls. The heating and air conditioning for the tunnel and at-grade structures will be provided by a series of indoor air handling units which will have steam heating coils, chilled water cooling coils, and steam humidifiers. Variable volume terminal units will be provided in the air supply distribution system to achieve temperature control.

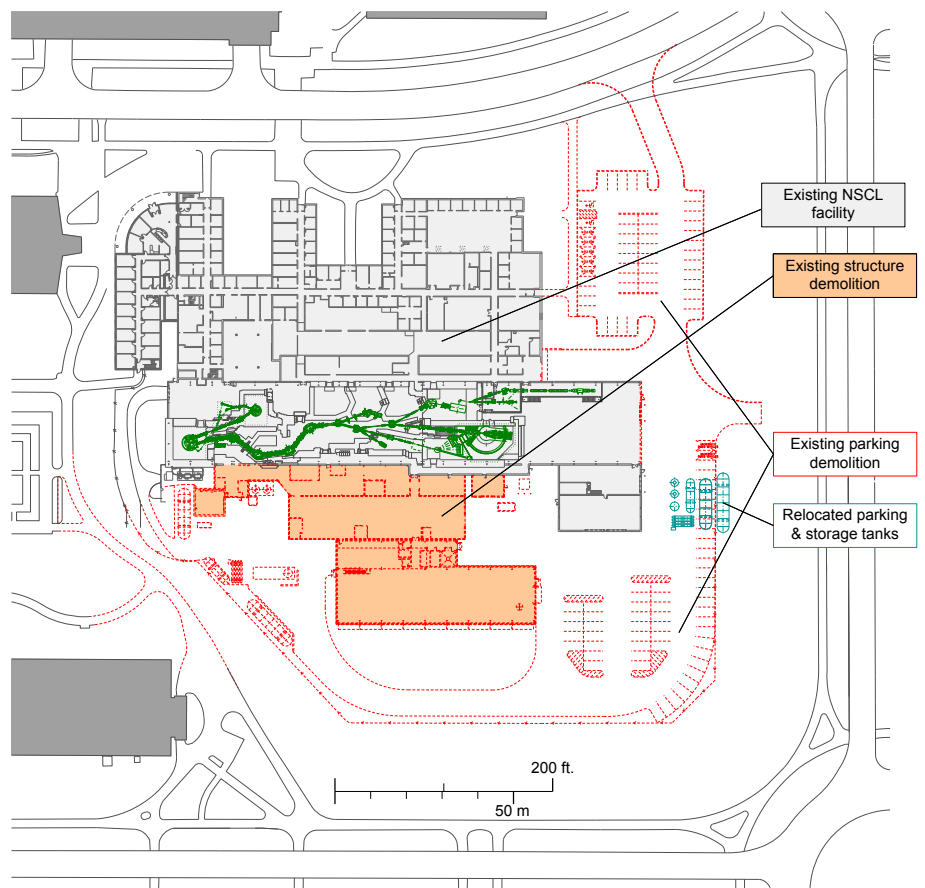
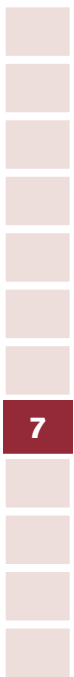


Figure 7.26: Plan for the demolition of existing buildings and the relocation of storage tanks.

The 1,900 m² cryoplant will be modeled on the existing NSCL cryogenic building. The building will be a structural steel frame with masonry insulated walls. It will be divided into two halves longitudinally, with one half being a single-story structure for refrigeration cycle equipment and controls, and the other half being a two-story design with compressors on the main floor and electrical switchgear plus process cooling equipment on the second floor.

The target facility will be a two-story structure located at the end of the linac tunnel and extending up into the new south highbay. The lower floor will be the target room with a three meter thick floor supported on drilled piers that will extend to bed rock and designed for a floor loading of 33,000 kg/m² to support the beamline components and bulk radiation shielding. Walls will be nominal 1.5 m thick with 3 m in the high radiation areas. The second floor will be a limited access remote handling gallery with 1.5 m concrete walls and ceiling. This level will be equipped with rail systems for the remote control crane and manipulator arm equipment. Hatches in the roof of the remote handling gallery will allow the new south highbay crane system to deliver and remove equipment from the target complex. The north side of the complex will also include access to remote manipulation systems for equipment repair and maintenance.

The new south highbay will be a 1,500 m² structure similar in construction to the removed south highbay. All possible equipment, including the 30-ton bridge crane will be salvaged and reused in the new structure. The building will serve as an



equipment assembly, testing, and repair facility for target and linac systems. The existing SRF clean room functions will be relocated here from the existing facility main crane bay to make room for the reaccelerated beam experimental facilities. In addition, it will house beam transport systems from the existing cyclotron to the linac and fragment separator components from the target facility back to the existing NSCL experimental areas.

The highbay connector structure will serve to connect the new south highbay to the existing NSCL main crane bay. The west end of the structure will house beam transport to and from the new linac/target systems. The center section adjacent to the new target facility will house two floors of target systems support equipment. The east end first floor will be workbench and office space for the technical support functions, and the second floor will be devoted to mechanical and electrical building equipment.

The 600 m² extension of the main facility crane bay will serve to house new low energy experimental equipment.

The shop/assembly/office addition will consist of three floors. The 1,200 m² area at grade level will house new shop/assembly space, replacing the areas that had to be removed on the south side of the complex, and a new facility loading dock and receiving area. The top two floors will house 2,400 m² of new office space.



8. Project cost estimate

Cost estimates were generated for the current plan of the ISF on a new site on the south campus of MSU as described in Section 5, possible future upgrade opportunities (Section 6), and an alternative cost reducing option on the present NSCL site (Section 7). All cost estimates are presented in 2006 dollars.

A standard cost estimating approach similar to that used for the Advanced Laser Interferometer Gravitational-Wave Observatory (LIGO) and the particle physics detector ATLAS at CERN was used to provide a uniform methodology for determining costs.

The cost is generally referred to as the Total Estimated Cost (TEC) and the Total Project Cost (TPC). The TPC is equal to the TEC plus the cost of Research and Development (R&D) and the costs for commissioning operations (pre-operations costs). The cost estimates are presented in the form of a hierarchical system-based Work Breakdown Structure (WBS).

Labor costs were applied at the average MSU loaded rates for two categories of labor consisting of engineer/scientist and technician/trades. Pre-operations costs were determined by the integral of expected personnel required to commission devices or for the operation of commissioned devices necessary for other commissioning activities, including the cost of the supporting supplies and services.

The information necessary to reliably estimate the cost of this facility has steadily improved over the past six years. R&D programs have been instituted to build and test prototypical system elements. For example, superconducting cavities in a cryomodule configuration including the necessary power sources and electronics have been fabricated and tested, thereby establishing the cost and performance parameters.

8.1 Cost estimating plan

The cost estimating plan defines the guidelines and methodology that were used to prepare the cost estimate. The cost estimate was developed from a bottoms-up estimate performed at the lowest reasonable level based on the conceptual design. These estimates are in 2006 dollars. The WBS was used to sum estimates to intermediate and upper levels.

The primary objective was to develop a comprehensive cost. This includes the costs for engineering, design, analysis, procurement, fabrication, assembly, installation, and commissioning for the entire facility.

Technical experts who are experienced in the required field of specialization have prepared the cost estimates. Vendor quotations, engineering calculations, drawings, and other pertinent information used to support the cost estimate were collected and organized into Basis of Estimate (BOE) documents.

Large, complex, and challenging projects entail uncertainty, including technical, cost, and schedule risks. Contingencies to cover anticipated costs resulting from these uncertainties were developed using a standardized risk analyses as discussed in Section 8.2.3. The risk was directly applied as a contingency at the line item level. The risks evaluated do not include unquantifiable future conditions, such as escalations in material or energy costs.

8.1.1 Work breakdown structure

The WBS is a product-oriented hierarchy that identifies the elements of the project and their parent/child relationships. The WBS hierarchy logically delineates all subsystems and divides these subsystems into successively lower levels. Cost estimators, in cooperation with management, developed the subsystem WBS hierarchies. The cost can broadly be separated into four pieces:

- Conventional construction (WBS 1.1). An architectural firm estimated the conventional construction costs and schedule. Minor modifications to the conventional construction during optimization exercises were accounted for by using square foot costs derived from the architectural estimates.
- Technical equipment (WBS 1.2 through 1.8). The technical equipment costs were derived using the methodology described in the next subsection.
- Management (WBS 1.9). The management cost was estimated by assuming it is a percentage of the overall accrued labor.
- Pre-operations and R&D. The pre-operations costs cover the scope of efforts beyond design, fabrication, installation, and initial component testing necessary to support full system commissioning activities. The R&D costs cover those activities necessary to develop technical solutions that satisfy performance requirements.

8.1.2 Confidence indicator and basis of estimate

Procurement and labor costs were specified at the lowest levels of the WBS hierarchy. The cost estimators provided confidence information in the form of a Confidence Indicator (CI) tag and supporting information in the form of a BOE document for each WBS level line item. The CI tag qualitatively characterizes the uncertainty associated with the estimate. The CI tags established for the project in decreasing order of confidence include the following information:

- Existing equipment: Components to be reused in the new facility that currently exist and are in good working operation with significant remaining service years.
- Architectural estimate: An estimate and schedule have been supplied by a reputable architectural firm.
- Historical data: Components that have been designed and built before, with well-known performance and associated costs.
- Catalog prices: Components that are off-the-shelf and routinely available either from vendors or within the organization, with well-known reasonably static costs.
- Vendor quotations: Component that must be custom designed and built for which a vendor quotation has been received.
- Engineering estimates: An estimate by an expert in the field for which a specific design has not yet been established.

The BOEs contain supporting information substantiating the estimates including vendor quotations, engineering calculations, graphs, figures, etc. Standardized BOEs were used to determine the cost of system elements that appeared repeatedly (e.g., power supplies, ac connections, controls, etc.) throughout the cost estimate.

8.1.3 Contingency, risk analyses, and risk assessment methodology

Contingency is based on a standardized risk analysis as described below. Each cost estimator was responsible for providing risk factors for their WBS elements.

A risk analysis was used to calculate contingency. The method was based on the estimator’s evaluation of the technical, cost, and schedule risk for every activity. Risk factors are determined from a standard table of parameters. Standard ranges for these parameters (see Table 8.1) are 1 to 15 for technical and cost risk and 2 to 8 for schedule risk.

Technical, cost, and schedule risk analyses were performed at the lowest WBS level that ranged from level 4 (e.g., for cryoplant) to level 8 (e.g., for cryomodule). Risk factors were assigned as described in Table 8.1. A risk factor was obtained from the table for each of the three categories of risk consisting of technical, cost, and schedule. A risk factor of 1 denotes minimal risk while a risk factor of 15 denotes the highest risk. Each of the risk factors obtained are further multiplied by a risk percentage, which are supplied in Table 8.2. The resulting three numbers are added together to establish the total risk for the activity. The risk was then applied directly as contingency. The minimum contingency percentage using this approach was 5% and the maximum was 98%.

Table 8.1: Risk factors used to develop contingencies. Adapted from [LIGO00].

| Risk Factor | Technical | Cost | Schedule |
|-------------|---|---|--|
| 1 | Existing component or off-the-shelf hardware | Off-the-shelf or catalog item | Not used |
| 2 | Minor modifications to an existing design | Vendor quote from established drawings | No schedule impact on any other item |
| 3 | Extensive modification to an existing design | Vendor quote with some design sketches | Not used |
| 4 | New design within established product line | In-house estimate for item within current production line | Delays completion of noncritical path subsystem item |
| 6 | New design different from established product line with existing technology | In-house estimate for item with minimal company experience but related to existing capabilities | Not used |
| 8 | New design, requires some R&D development but does not advance the state-of-the-art | In-house estimate for item with minimal company experience and in-house capability | Delays completion of critical path subsystem item |
| 10 | New design development of new technology which advances the state-of-the-art | Top down estimate from analogous programs | Not used |
| 15 | New design way beyond the current state-of-the-art | Engineering judgment | Not used |

Table 8.2: Risk percentage used to develop contingencies. Adapted from [LIGO00].

| | Condition | Risk percentage |
|-----------|---------------------------------------|-----------------|
| Technical | Design or manufacturing concerns only | 2% |
| | Design and manufacturing concerns | 4% |
| Cost | Material cost or labor rate concern | 1% |
| | Material and labor rate concern | 2% |
| Schedule | | 1% |

There may be special cases where the parameter limitations defined above are not appropriate. Some high-risk elements may deserve contingencies greater than 98%. In those cases, the estimator worked with project management to establish the appropriate risk and required supporting documentation.

8.1.4 Labor pricing

Labor hours and material and subcontract costs were based on information provided by the cost estimator. The estimator provided labor estimates in hours that were then priced according to MSU average rates. The hourly rates were loaded rates with the exception of management overhead which was accrued separately at index WBS 1.9. The labor categories available for estimating were engineer/scientist (\$60.00/hr in 2006 dollars) and technician/trades (\$45.00/hr in 2006 dollars).

Labor rates are fully loaded and have been adjusted to include paid leave such as sick leave, vacations, holidays, etc. One full-time equivalent (FTE) accrues a total of 2080 normally paid hours per year. However, paid leave hours reduce the productive year for estimating purposes to approximately 1800 hours. Hourly labor rates have been adjusted so that 1800 hours will accrue one full year of salary. Thus one FTE converts to 1800 hours of available effort per year.

8.1.5 Escalation

The project estimate is based on 2006 dollars. Escalation will be computed using standard escalation rates appropriate for the project schedule.

8.2 ISF (south campus option) costs

The cost estimates for the ISF assumed continued utilization of the NSCL site for office space and large scale fabrication and assembly functions. It includes a cost allowance to move and install existing NSCL equipment including nuclear science experimental equipment, beamline magnets, fragment separator, and gas-stopping system. To move or fabricate any additional experimental equipment it will be necessary to obtain funding. Figure 8.1 and Figure 8.2 show the layout of the ISF and possible funding profile for the construction, respectively.

The cost elements for the TEC are listed in Table 8.3. The TPC is a sum of the TEC and \$25M pre-operations costs. It is assumed that at groundbreaking all major R&D has been completed so that no significant additional R&D cost will be needed. A summary of the TEC and TPC costs are listed in Table 8.4.

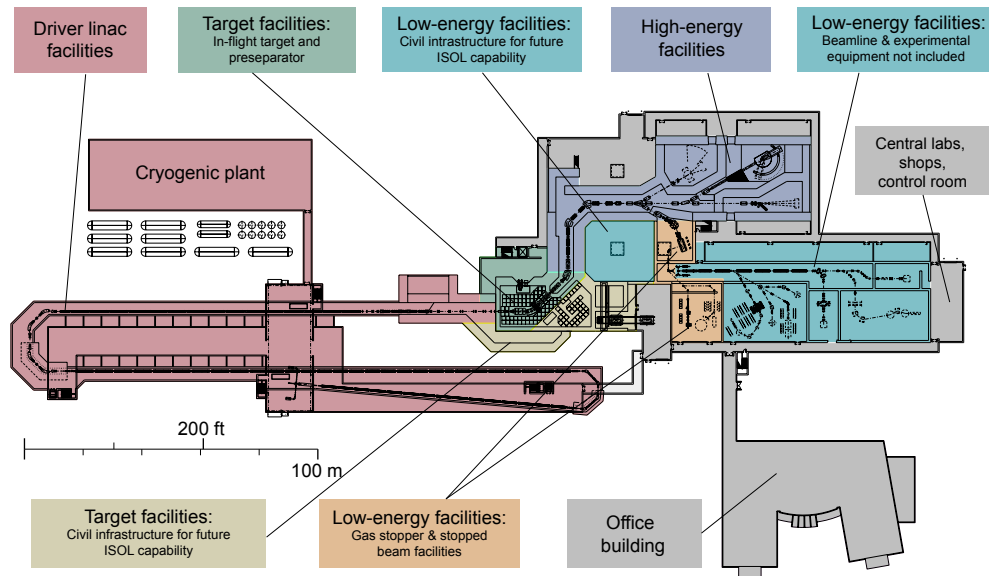


Figure 8.1: Layout of the ISF (south campus option).

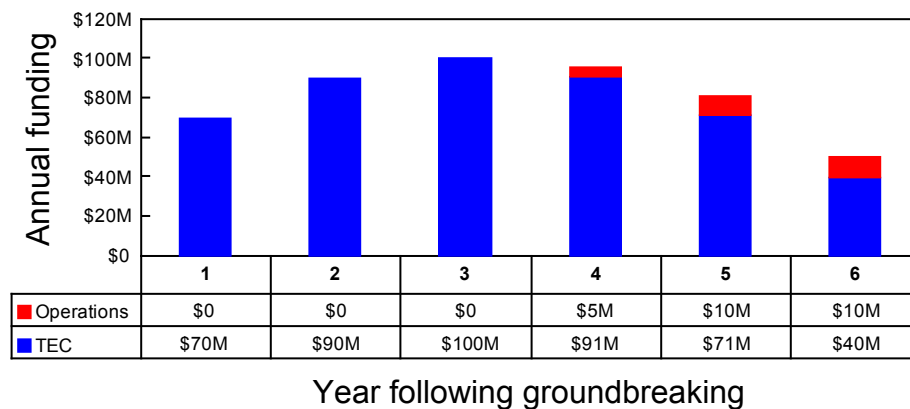


Figure 8.2: Possible funding profile for ISF construction in 2006 dollars.

Table 8.3: Details of the TEC cost elements for the ISF (south campus options) in 2006 dollars. Elements are shown to WBS level 4. The WBS structure was kept the same for the south campus option and the NSCL site option and, as a consequence, some WBS elements do not have costs, as indicated by dashes.

| WBS | Description | Total (M\$) | Risk |
|---------|-------------------------|-------------|------|
| 1 | TEC | 462.0 | 21% |
| 1.1 | Conventional facilities | 144.0 | 15% |
| 1.1.1 | Site work | 25.7 | |
| 1.1.2 | Driver linac facilities | 24.7 | |
| 1.1.2.1 | Tunnel | 16.0 | |
| 1.1.2.2 | Klystron building | 8.7 | |
| 1.1.3 | Target facilities | 25.8 | |
| 1.1.4 | High-energy facilities | 14.3 | |
| 1.1.5 | Low-energy facilities | 10.3 | |

| WBS | Description | Total (M\$) | Risk |
|------------|---------------------------------|--------------|------------|
| 1.1.6 | Central labs/shops/control room | 10.5 | |
| 1.1.7 | Cryogenic plant | 7.7 | |
| 1.1.8 | Office building | 25.0 | |
| 1.1.9 | Facility changes | - | |
| 1.2 | Cryogenics (20 kW max) | 34.7 | 32% |
| 1.2.1 | Cryogenic plant | 30.7 | 32% |
| 1.2.2 | Distribution | 4.0 | 32% |
| 1.3 | 200 MeV/nucleon driver | 149.2 | 24% |
| 1.3.1 | Linac front end | 12.2 | |
| 1.3.1.1 | Room temperature magnets | 5.8 | 15% |
| 1.3.1.2 | Superconducting magnets | 0.3 | 15% |
| 1.3.1.3 | Low-beta cryomodules | - | |
| 1.3.1.4 | High-beta cryomodules | - | |
| 1.3.1.5 | RF systems & platforms | 6.1 | 26% |
| 1.3.2 | Driver linac segment 1 | 26.8 | |
| 1.3.2.1 | Room temperature magnets | - | |
| 1.3.2.2 | Superconducting magnets | - | |
| 1.3.2.3 | Low-beta cryomodules | 26.8 | 25% |
| 1.3.2.4 | High-beta cryomodules | - | |
| 1.3.3 | Stripping station 1 | 6.3 | |
| 1.3.3.1 | Room temperature magnets | 2.5 | 15% |
| 1.3.3.2 | Superconducting magnets | 1.0 | 16% |
| 1.3.3.3 | Low-beta cryomodules | 1.2 | 25% |
| 1.3.3.4 | High-beta cryomodules | - | |
| 1.3.3.5 | Stripper mechanism | 1.6 | 74% |
| 1.3.4 | Driver linac segment 2 | 47.2 | |
| 1.3.4.1 | Room temperature magnets | - | |
| 1.3.4.2 | Superconducting magnets | - | |
| 1.3.4.3 | Low-beta cryomodules | 47.2 | 25% |
| 1.3.4.4 | High-beta cryomodules | - | |
| 1.3.5 | Stripping section 2 | 10.2 | |
| 1.3.5.1 | Room temperature magnets | 4.5 | 15% |
| 1.3.5.2 | Superconducting magnets | 1.3 | 16% |
| 1.3.5.3 | Low-beta cryomodules | 2.8 | 25% |
| 1.3.5.4 | High-beta cryomodules | - | |
| 1.3.5.5 | Stripper mechanism | 1.6 | 74% |
| 1.3.6 | Driver linac segment 3 | 26.9 | |
| 1.3.6.1 | Room temperature magnets | - | |
| 1.3.6.2 | Superconducting magnets | - | |

| WBS | Description | Total (M\$) | Risk |
|------------|--|-------------|------------|
| 1.3.6.3 | Low-beta cryomodules | 26.9 | 25% |
| 1.3.6.4 | High-beta cryomodules | - | |
| 1.3.7 | Driver linac beam switch yard | 7.0 | |
| 1.3.7.1 | Room temperature magnets | 4.6 | 16% |
| 1.3.7.2 | Superconducting magnets | 2.3 | 16% |
| 1.3.7.3 | Low-beta cryomodules | - | |
| 1.3.7.4 | High-beta cryomodules | - | |
| 1.3.8 | Driver linac beam diagnostics | 12.6 | 25% |
| 1.4 | Target | 40.2 | 33% |
| 1.4.1 | ISOL targets | - | |
| 1.4.2 | High-energy targets | 24.2 | 26% |
| 1.4.3 | Shared target services | 16.0 | 45% |
| 1.5 | High-energy systems | 10.7 | 24% |
| 1.5.1 | Fragment separator | - | |
| 1.5.2 | Beam selection and transport | 10.7 | 24% |
| 1.6 | Low-energy systems | 17.2 | 35% |
| 1.6.1 | Fragment separator | - | |
| 1.6.2 | Gas cell system | 0.6 | 30% |
| 1.6.3 | Low-energy transport system | 0.9 | 26% |
| 1.6.4 | Booster linac | 15.8 | 35% |
| 1.7 | Scientific instruments | 10.0 | 35% |
| 1.7.1 | Low-energy systems | - | |
| 1.7.2 | High-energy systems | - | |
| 1.7.3 | Shared detectors | - | |
| 1.7.4 | Relocate NSCL equipment | 10.0 | 35% |
| 1.8 | Central systems & integration | 24.0 | 19% |
| 1.8.1 | Central control systems | 2.6 | 20% |
| 1.8.2 | Central computer systems | 1.3 | 20% |
| 1.8.3 | Central rf systems | 0.7 | 20% |
| 1.8.4 | Alignment systems | 2.2 | 6% |
| 1.8.5 | Safety systems | 5.6 | 20% |
| 1.8.6 | Central LCW systems | 9.6 | 20% |
| 1.8.7 | Shielding and miscellaneous. | 1.9 | 30% |
| 1.9 | Management | 31.9 | 0% |
| 1.9.1 | Procurement G&A | 8.6 | |
| 1.9.2 | Project management (5% of labor) | 5.1 | |
| 1.9.3 | Line management (20% of labor) | 16.3 | |
| 1.9.4 | Executive management (2% of labor) | 2.0 | |

Table 8.4: Summary cost for the ISF in 2006 dollars.

| | M\$ |
|----------------------|-----|
| Total estimated cost | 462 |
| Total project cost | 487 |

8.3 Costs of future upgrade options

The ISF was designed to allow for various science driven upgrades, including increased driver energy, additional fragmentation and/or ISOL target stations, multi-user capability, and additional expansions of the various experimental areas. Figure 8.3 shows the layout of the ISF upgrade options. The cost estimates for these upgrades are listed in Table 8.5. These estimates do not include costs associated with moving or fabricating any additional experimental equipment.

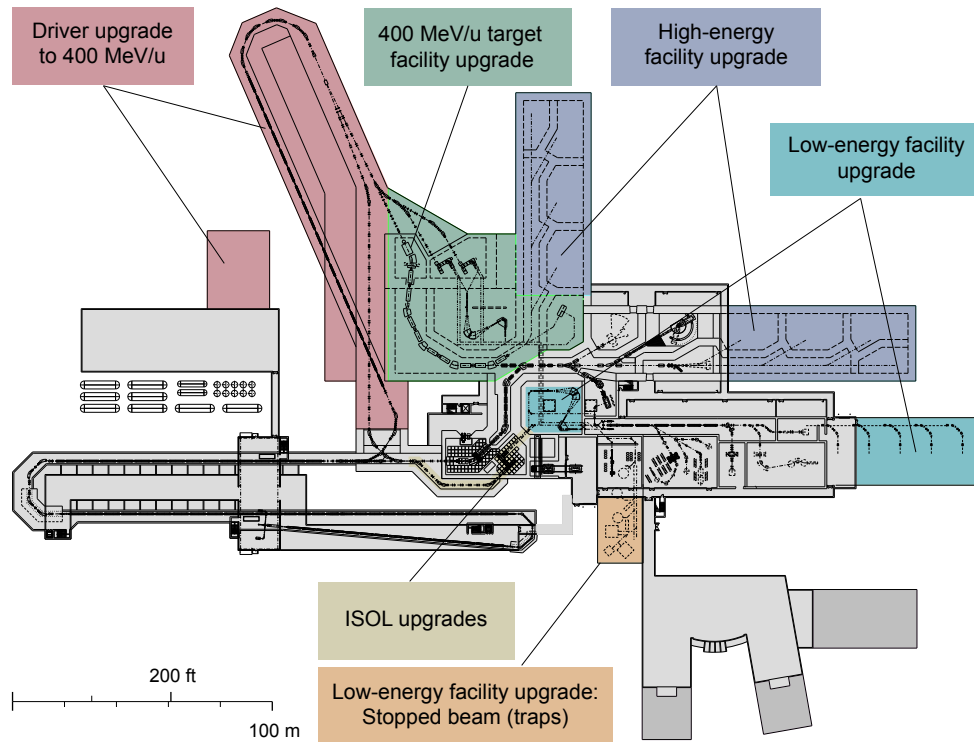


Figure 8.3: Layout of the ISF upgrade options.

Table 8.5: TEC costs of possible ISF upgrade options in 2006 dollars. Costs are shown at approximately WBS level 2. Costs were developed down to levels 4 to 8.

| Description | Total (M\$) | Risk |
|--|--------------|------------|
| Driver upgrade to 400 MeV/nucleon | 144.4 | 26% |
| Conventional construction | 32.4 | 24% |
| Cryogenic plant & distribution upgrade | 26.0 | 33% |
| Linac | 85.9 | 24% |
| ISOL upgrades | 17.8 | 37% |
| ISOL target | 9.1 | 45% |
| Gas cell and transport systems | 8.7 | 30% |
| Targets | 18.2 | 45% |
| Shared target services | 16.0 | 45% |
| Fragment separator & beam transport | 49.2 | 28% |
| Gas cell and transport systems | 11.1 | 30% |
| High-energy facility upgrade | 27.0 | 24% |
| Low-energy facility upgrade | 7.4 | 24% |

8.4 NSCL site option costs

The alternative of building the ISF on the current NSCL site assumed only existing NSCL experimental equipment. New experimental equipment would require additional funding. Figure 8.4 shows the layout of the ISF at the NSCL site. It includes the options to utilize the K1200 as part of the driver accelerator system or to use a fully superconducting linac. The possible funding profile for the second option is shown in Figure 8.5. The cost elements for the TEC listed in Table 8.6 include the full linac driver accelerator.

The difference between the full driver linac and the cyclotron injector affects WBS 1.3.1 and 1.3.2. In WBS 1.3.1 the linac front-end cost (\$12.2M) is substituted by the cost for the cyclotron merging system (\$12.8M) and the cost for the driver linac segment 1 (WBS 1.3.2) is reduced from \$26.8M to \$5.5M. The details of the WBS 1.3.1 and 1.3.2 for the cyclotron injector are listed in Table 8.7. This reduces the cost for the 200 MeV/nucleon driver from \$143.1M to \$122.5M. The overall TEC and TPC for both options are listed in Table 8.8.

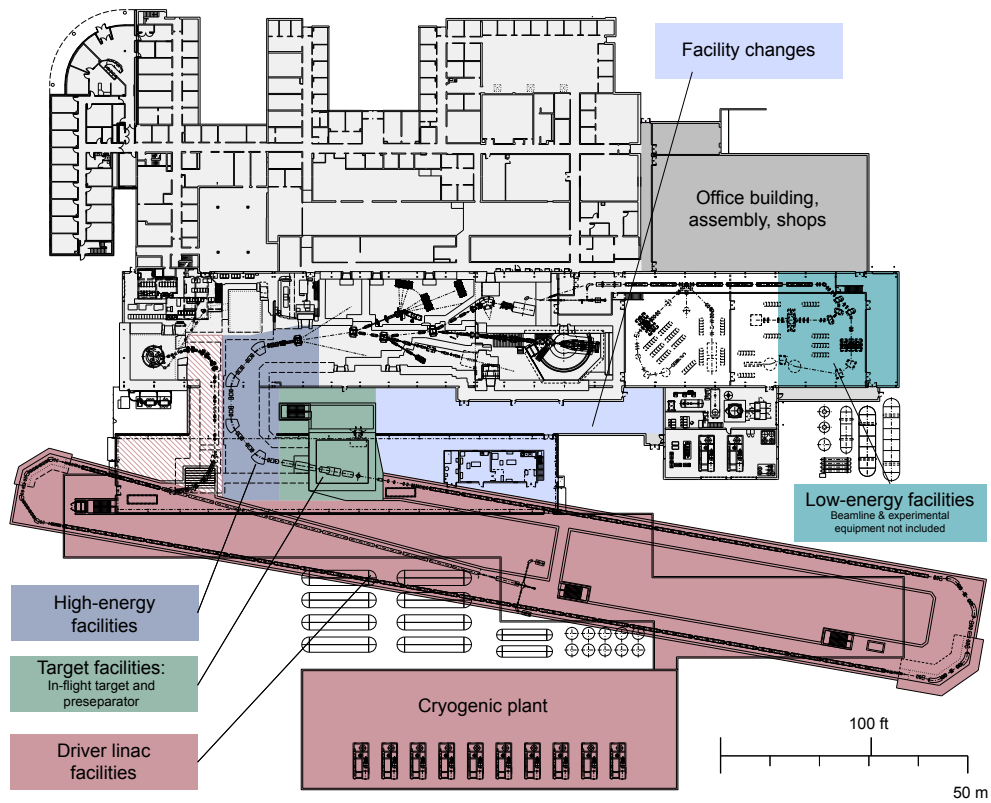


Figure 8.4: Layout of the NSCL site option.

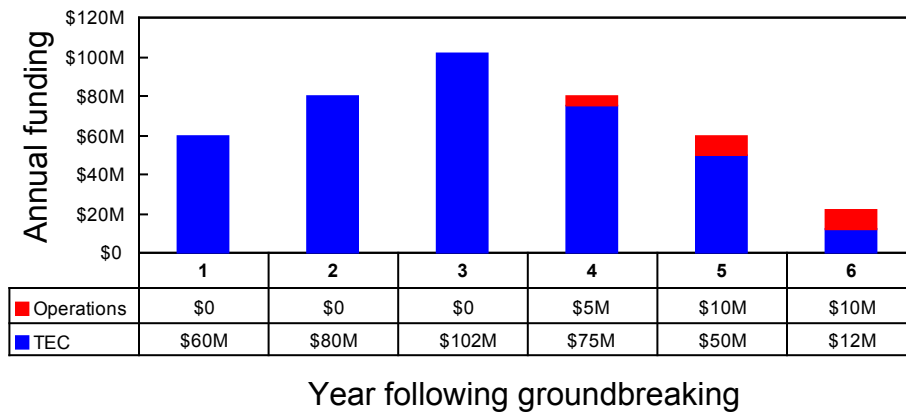


Figure 8.5: Possible funding profile for the ISF at the NSCL site and a full linac driver accelerator in 2006 dollars.

Table 8.6: Details of the TEC cost elements for the ISF using the NSCL site and a full linac driver accelerator in 2006 dollars. Elements are shown to WBS level 4. The WBS structure was kept the same for the south campus options and the NSCL site option and, as a consequence, some WBS elements do not have costs, as indicated by dashes.

| WBS | Description | Total (M\$) | Risk |
|------------|---------------------------------|--------------|------------|
| 1 | TEC | 379.7 | 21% |
| 1.1 | Conventional facilities | 88.8 | 15% |
| 1.1.1 | Site work | 32.7 | |
| 1.1.2 | Driver linac facilities | 22.6 | |
| 1.1.2.1 | Tunnel | 15.2 | |
| 1.1.2.2 | Klystron building | 7.4 | |
| 1.1.3 | Target facilities | 4.1 | |
| 1.1.4 | High-energy facilities | - | |
| 1.1.5 | Low-energy facilities | 2.4 | |
| 1.1.6 | Central labs/shops/control room | 4.3 | |
| 1.1.7 | Cryogenic plant | 7.8 | |
| 1.1.8 | Office building | 6.8 | |
| 1.1.9 | Facility changes | 8.1 | |
| 1.2 | Cryogenic (20 kW max) | 34.7 | 32% |
| 1.2.1 | Cryogenic plant | 30.7 | 32% |
| 1.2.2 | Distribution | 4.0 | 32% |
| 1.3 | 200 MeV/nucleon driver | 146.3 | 24% |
| 1.3.1 | Linac front end | 12.2 | |
| 1.3.1.1 | Room temperature magnets | 5.8 | 15% |
| 1.3.1.2 | Superconducting magnets | 0.3 | 15% |
| 1.3.1.3 | Low-beta cryomodules | - | |
| 1.3.1.4 | High-beta cryomodules | - | |
| 1.3.1.5 | RF systems & platforms | 6.1 | 26% |
| 1.3.2 | Driver linac segment 1 | 26.8 | |
| 1.3.2.1 | Room temperature magnets | - | |
| 1.3.2.2 | Superconducting magnets | - | |
| 1.3.2.3 | Low-beta cryomodules | 26.8 | 25% |
| 1.3.2.4 | High-beta cryomodules | - | |
| 1.3.3 | Stripping station 1 | 6.3 | |
| 1.3.3.1 | Room temperature magnets | 2.5 | 15% |
| 1.3.3.2 | Superconducting magnets | 1.0 | 16% |
| 1.3.3.3 | Low-beta cryomodules | 1.2 | 25% |
| 1.3.3.4 | High-beta cryomodules | - | |
| 1.3.3.5 | Stripper mechanism | 1.6 | 74% |
| 1.3.4 | Driver linac segment 2 | 47.2 | |
| 1.3.4.1 | Room temperature magnets | - | |

| WBS | Description | Total (M\$) | Risk |
|------------|--|-------------|------------|
| 1.3.4.2 | Superconducting magnets | - | |
| 1.3.4.3 | Low-beta cryomodules | 47.2 | 25% |
| 1.3.4.4 | High-beta cryomodules | - | |
| 1.3.5 | Stripping station 2 | 10.2 | |
| 1.3.5.1 | Room temperature magnets | 4.5 | 15% |
| 1.3.5.2 | Superconducting magnets | 1.3 | 16% |
| 1.3.5.3 | Low-beta cryomodules | 2.8 | 25% |
| 1.3.5.4 | High-beta cryomodules | - | |
| 1.3.5.5 | Stripper mechanism | 1.6 | 74% |
| 1.3.6 | Driver linac segment 3 | 26.9 | |
| 1.3.6.1 | Room temperature magnets | - | |
| 1.3.6.2 | Superconducting magnets | - | |
| 1.3.6.3 | Low-beta cryomodules | 26.9 | 25% |
| 1.3.6.4 | High-beta cryomodules | - | |
| 1.3.7 | Driver linac beam switch yard | 4.0 | |
| 1.3.7.1 | Room temperature magnets | 0.6 | 16% |
| 1.3.7.2 | Superconducting magnets | 3.4 | 16% |
| 1.3.7.3 | Low-beta cryomodules | - | |
| 1.3.7.4 | High-beta cryomodules | - | |
| 1.3.8 | Driver linac beam diagnostics | 12.6 | 25% |
| 1.4 | Target | 37.0 | 33% |
| 1.4.1 | ISOL targets | - | |
| 1.4.2 | High-energy targets | 22.9 | 26% |
| 1.4.3 | Shared target services | 14.1 | 45% |
| 1.5 | High-energy systems | - | |
| 1.6 | Low-energy systems | 15.8 | 35% |
| 1.6.1 | Fragment separator | - | |
| 1.6.2 | Gas cell system | - | |
| 1.6.3 | Low-energy transport system | - | |
| 1.6.4 | Booster linac | 15.8 | 35% |
| 1.7 | Scientific instruments | 2.7 | 35% |
| 1.7.1 | Low-energy systems | - | |
| 1.7.2 | High-energy systems | - | |
| 1.7.3 | Shared detectors | - | |
| 1.7.4 | Relocate NSCL equipment | 2.7 | 35% |
| 1.8 | Central systems & integration | 24.0 | 19% |
| 1.8.1 | Central control systems | 2.6 | 20% |
| 1.8.2 | Central computer systems | 1.3 | 20% |
| 1.8.3 | Central rf systems | 0.7 | 20% |
| 1.8.4 | Alignment systems | 2.2 | 6% |

| WBS | Description | Total (M\$) | Risk |
|------------|------------------------------------|-------------|-----------|
| 1.8.5 | Safety systems | 5.6 | 20% |
| 1.8.6 | Central LCW systems | 9.6 | 20% |
| 1.8.7 | Shielding and miscellaneous | 1.9 | 30% |
| 1.9 | Management | 30.4 | 0% |
| 1.9.1 | Procurement G&A | 8.6 | |
| 1.9.2 | Project management (5% of labor) | 4.8 | |
| 1.9.3 | Line management (20% of labor) | 15.2 | |
| 1.9.4 | Executive management (2% of labor) | 1.8 | |

Table 8.7: Details of the cost elements of WBS 1.3.1 and 1.3.2 for the cyclotron injector in 2006 M\$. Elements are shown to WBS level 4. The WBS structure was kept the same for the south campus options and the NSCL site option and, as a consequence, some WBS elements do not have costs, indicated by dashes.

| WBS | Description | Total (M\$) | Risk |
|---------|--------------------------|-------------|------|
| 1.3.1 | Cyclotron merging system | 12.8 | |
| 1.3.1.1 | Room temperature magnets | - | |
| 1.3.1.2 | Superconducting magnets | 8.2 | 16% |
| 1.3.1.3 | Low-beta cryomodules | 1.6 | 25% |
| 1.3.1.4 | High-beta cryomodules | - | |
| 1.3.1.5 | Refurbish cyclotron | 3.0 | |
| 1.3.2 | Driver linac segment 1 | 5.5 | |
| 1.3.2.1 | Room temperature magnets | - | |
| 1.3.2.2 | Superconducting magnets | - | |
| 1.3.2.3 | Low-beta cryomodules | 5.5 | 25% |
| 1.3.2.4 | High-beta cryomodules | - | |

Table 8.8: Summary costs for the ISF using the NSCL site using a full linac driver and a cyclotron as an injector in 2006 dollars.

| NSCL Site | Full linac driver (M\$) | Cyclotron injector (M\$) |
|----------------------|-------------------------|--------------------------|
| Total estimated cost | 380 | 357 |
| Total project cost | 405 | 382 |

8.5 Cost summary

The cost estimates in this section are based on about six years of cost evaluations for similar facilities. At this point, significant cost changes would only be expected from changes in scope, or unforeseeable market developments outpacing inflation, similar to recent rises in the cost of steel, oil, and natural gas.

Table 8.9 shows the results of an assessment of the confidence indicators as described in Section 8.2.2 for the overall project. Table 8.10 summarizes the cost differences

between the south campus and the NSCL site option (with the full driver linac) of the ISF. The overall project contingency is about 21% based on the standardized methodology described.

Table 8.9: Distribution of confidence indicators of the TEC in decreasing order of confidence.

| Confidence indicator | % of TEC |
|------------------------|------------|
| Existing equipment | 1 |
| Architectural estimate | 24 |
| Historical data | 25 |
| Catalog prices | 5 |
| Vendor quotations | 15 |
| Engineering estimates | 30 |
| Total | 100 |

Table 8.10: ISF costs for the south campus site, the NSCL site (with full driver linac), and the difference Δ (south campus – NSCL) in 2006 dollars.

| WBS | South campus site (M\$) | NSCL site (M\$) | Δ (M\$) |
|-------------------------------|-------------------------|-----------------|----------------|
| Conventional facilities | \$144.0 | \$88.8 | \$55.2 |
| Cryogenic (20 kW max) | \$34.7 | \$34.7 | \$0.0 |
| Driver | \$149.2 | \$146.3 | \$2.9 |
| Target | \$40.2 | \$37.0 | \$3.2 |
| High-energy systems | \$10.7 | \$0.0 | \$10.7 |
| Low-energy systems | \$17.2 | \$15.8 | \$1.5 |
| Scientific instruments | \$10.0 | \$2.7 | \$7.3 |
| Central systems & integration | \$24.0 | \$24.0 | \$0.0 |
| Management | \$31.9 | \$30.4 | \$1.5 |
| TEC | \$462.0 | \$379.7 | \$82.3 |
| Pre-operations | \$25.0 | \$25.0 | \$0.0 |
| TPC | \$487.0 | \$404.7 | \$82.3 |

Epitome

This document has presented a compelling scientific case for the construction of a new Isotope Science Facility (ISF) at Michigan State University that will replace the NSCL's current Coupled Cyclotron Facility (CCF). The ISF will make it possible to produce broad swaths of unknown nuclei that offer the potential for a wide range of new discoveries. Detailed technical assessments have been made of how one can produce the most intense primary heavy-ion beams and deliver them to production targets, and of how the secondary beams of rare isotopes can be rapidly yet cleanly separated and used for nuclear science research.

A new concept for rapid and efficient thermalization of the fast-ion beams has been presented that will allow precision experiments in traps as well as efficient reacceleration. With this reacceleration capability, additional important and complementary studies will be possible that are not feasible with the powerful fast beam techniques currently employed at the NSCL and leading laboratories around the world. The ISF will allow experimentation over the entire gamut of energies from rest to 200 MeV/nucleon and with the highest intensities possible – a capability that does not exist and is not currently planned anywhere else in the world.

Detailed simulations, successful prototypes, forefront experimental techniques, and cutting-edge equipment extant and under development at MSU and in the U.S. rare isotope science community all indicate that the ISF will have a high likelihood of success. Construction of the ISF on the MSU campus will build on the existing experience and strength of NSCL faculty and staff and reuse existing NSCL equipment to provide significant cost savings and a rapid start to the experimental program.

For due diligence, two options have been explored in significant technical detail, and their costs have been carefully outlined and evaluated. One option is construction on a large new site on the southern part of the MSU campus. The other option is construction on the current NSCL site. In the short term, either site can accommodate the most important science of the proposed baseline facility, but a new site will be able to accommodate a large variety of upgrades as science advances. Construction on a new site offers the additional advantage of negligible interference with the ongoing nuclear science program, allowing continued optimal access to the CCF to more than 700 registered NSCL users and a seamless transition from CCF-based to ISF-based research and education activities with about six months interruption. Construction of the ISF on the present NSCL site will require a much longer shutdown of the research program – about 18 months. Ongoing excavation and construction activities on the NSCL site will unavoidably interfere with the concurrent user program in ways that cannot yet be fully foreseen.

The table below compares the two site options. NSCL faculty and staff believe that the significant advantages of the south campus site outweigh its initially higher cost and that the nation will be better served in the long-run with this option. In the presence of extremely tight budget constraints, however, the NSCL site offers a viable option to carry out a world-class rare isotope science program.

| ISF feature | South campus site | Existing NSCL site |
|--|---|---|
| Driver energy for ^{238}U | $E/A \sim 200 \text{ MeV}$ | $E/A \sim 200 \text{ MeV}$ |
| Driver beam power (after R&D on stripper) | Up to 400 kW | Up to 400 kW (65 kW for K1200 injection) |
| Reaccelerator energy for all elements | $E/A = 12 \text{ MeV}$ | $E/A = 12 \text{ MeV}$ |
| Expected shutdown of experimental program | $\sim 6 \text{ months}$ | $\sim 18 \text{ months}$ |
| Interference of construction with ongoing CCF operations | None | Significant |
| ISOL target upgrade option | Yes | No |
| Driver energy upgrade option | Yes | No |
| Expansion of experimental areas | Limited only by funds | Limited by site constraints and requires sacrifice of assembly area |
| Reaccelerator energy upgrade option | Limited only by funds | Limited by site constraints |
| Multi-user upgrade option | Yes | No |
| In-flight experimental area | 1,600 m ² | 940 m ² |
| Stopped beam experimental area | 365 m ² | 100 m ² |
| Reaccelerated beam experimental area | 1,760 m ² 610 m ² for $E/A \leq 3 \text{ MeV}$ 1,150 m ² for $E/A \sim 3 - 12 \text{ MeV}$ | 1,100 m ² 490 m ² for $E/A \leq 3 \text{ MeV}$ 610 m ² for $E/A \sim 3 - 12 \text{ MeV}$ |
| Final costs (TEC / TPC) | 462 / 487 M\$ | 380 / 405 M\$ (357 / 382 M\$ for K1200 injection) |

References

- [Ade99] E.G. Adelberger *et al.*, Phys. Rev. Lett. 83, 1299 (1999)
- [Adr05] P. Adrich *et al.*, Phys. Rev. Lett. 95, 132501 (2005)
- [Afa99] A.V. Afanasjev *et al.*, Phys. Rep. 322, 1 (1999)
- [Afa03] A.V. Afanasjev *et al.*, Phys. Rev. C 67, 024309 (2003)
- [Afa05] A.V. Afanasjev and S. Frauendorf, Phys. Rev. C 72, 031301 (2005)
- [Ahm05] I. Ahmad *et al.*, Phys. Rev. C 72, 054308 (2005)
- [Ale04] A. Alexakis *et al.*, Ap. J. 602, 931 (2004)
- [Ale06] A. Aleksandrov *et al.*, Proc. of EPAC, Edinburgh, UK, p. 342 (2006)
- [Amb06] C. D'ambrosio *et al.*, Nucl. Instr. and Meth. A 556, 187 (2006)
- [Ame06] F. Ames *et al.*, Rev. Sci. Instr. 77, 03B103 (2006)
- [Amo06] K. Amos *et al.*, Phys. Rev. Lett. 96, 032503 (2006)
- [And93] V.A. Andreev and G. Parisi, PAC, Washington, DC, p. 3124 (1993)
- [And94] V.A. Andreev and G. Parisi, Proc. of EPAC, London, UK, p. 1300 (1994)
- [And00] A.N. Andreyev *et al.*, Nature 405, 430 (2000)
- [And04] V. Andreev *et al.*, NSCL Internal Report, MSU (2004)
- [Ann92] R. Anne and A.C. Mueller, Nucl. Instr. and Meth. B 70, 276 (1992)
- [Ari77] A. Arima *et al.*, Phys. Lett. B 66, 205 (1977)
- [Arn03] M. Arnould and S. Goriely, Phys. Rep. 384, 1 (2003)
- [Asa90] K. Asahi *et al.*, Phys. Lett. B 251, 488 (1990)
- [Ass06] S. Assadi, Proc. of EPAC, Edinburgh, UK, p. 3161 (2006)
- [Aud03] G. Audi *et al.*, Nucl. Phys. A 729, 337 (2003)
- [Aue84] N. Auerbach and A. Klein, Phys. Rev. C 30, 1032 (1984)
- [Aue89] N. Auerbach *et al.*, Phys. Lett. B 219, 184 (1989)
- [Aum99a] T. Aumann *et al.*, Phys. Rev. C 59, 1252 (1999)
- [Aum99b] T. Aumann *et al.*, Nucl. Phys. 649, 297c (1999)
- [Aus70] N. Austern, John Wiley & Sons, New York (1970)
- [Bac00] Th. Bachelts and R. Schaefer, Chem. Rev. Lett. 324, 365 (2000)
- [Bae06] I. Baek *et al.*, Amer. Nucl. Soc.'s 14th Biennial Topical Meeting of the Rad. Protection and Shielding Div., Carlsbad, New Mexico (2006)
- [Bal77] R.M. Baltrusaitis and F.P. Calaprice, Phys. Rev. Lett. 38, 464 (1977)
- [Bar79] E. Baron, GANIL Report 79R/146/TF14 (1979)
- [Bar99] D.W. Bardayan *et al.*, Phys. Rev. Lett. 83, 45 (1999)
- [Bar01] V. Baran *et al.*, Phys. Rev. Lett. 87, 182501 (2001)
- [Bar02] D.W. Bardayan *et al.*, Phys. Rev. Lett. 89, 262501 (2002)
- [Bar04] S. Baroni *et al.*, J. Phys. G 30, 1353 (2004)
- [Bar05] V. Baran *et al.*, Phys. Rep. 410, 335 (2005)
- [Bat05] P. Batham *et al.*, Phys. Rev. C 71, 064608 (2005)
- [Bau96] G. Baur and H. Rebel, Annu. Rev. Nucl. Sci. 46, 321 (1996)
- [Bau03] T. Baumann *et al.*, Phys. Rev. C 67, 061303R (2003)
- [Bay68] B.F. Bayman and N.M. Hintz, Phys. Rev. 172, 1113 (1968)
- [Baz03] D. Bazin *et al.*, Phys. Rev. Lett. 91, 012501 (2003)
- [Bee06] T.C. Beers, private communication

-
- [Bel00] S. Belomestnykh *et al.*, Proc. of the 9th Workshop on RF Superconductivity, Santa Fe, NM (1999), Report LA-13782-C, p. 24 (2000)
- [Bel03] S. Belomestnykh, Proc. of the 11th Workshop on RF Superconductivity, Travemünde, Germany (2003)
- [Ben80] N. Benczer-Koller *et al.*, Annu. Rev. Nucl. Sci. 30, 53 (1980)
- [Ben99] M. Bender *et al.*, Phys. Rev. C 60, 034304 (1999)
- [Ben01] M. Bender *et al.*, Phys. Lett. B 515, 42 (2001)
- [Ben02] J. Benlliure *et al.*, Eur. Phys. J. A 13, 93 (2002)
- [Ben03] M. Bender *et al.*, Rev. Mod. Phys. 75, 121 (2003)
- [Ben06] M. Bender *et al.*, Phys. Rev. C 73, 034322 (2006)
- [Ber88] G.F. Bertsch and S. Das Gupta, Phys. Rep. 160, 189 (1988)
- [Ber99] G.F. Bertsch and K. Yabana, Nucl. Phys. A 649, 423c (1999)
- [Ber05] G.F. Bertsch *et al.*, Phys. Rev. C 71, 054311 (2005)
- [Bet72] H.-D. Betz, Rev. Mod. Phys. 44, 465 (1972)
- [Bis98] G. Bisoffi *et al.*, Proc. of the 8th Int. Conf. on Heavy Ion Accel. Tech., p. 173, Argonne, IL (1998)
- [Bis00] G. Bisoffi *et al.*, Proc. of EPAC, Vienna, Austria, p. 324 (2000)
- [Bis03] S. Bishop *et al.*, Phys. Rev. Lett. 90, 162501 (2003)
- [Biz02] P.G. Bizzeti and A. M. Bizzeti-Sona, Phys. Rev. C 66, 031301 (2002)
- [Bje67] J.H. Bjerregaard *et al.*, Nucl. Phys. A 103, 33 (1967)
- [Bla80] J.P. Blaizot, Phys. Rep. 64, 171 (1980)
- [Bla00] B. Blank *et al.*, Phys. Rev. Lett. 84, 1116 (2000)
- [Bla01] D. Blaschke *et al.*, eds., Physics of neutron star interiors (Springer, 2001)
- [Bla05] B. Blank *et al.*, Phys. Rev. Lett. 94, 232501 (2005)
- [Bli05] V. Blideanu *et al.*, Proc. of PAC, Knoxville, TN, p. 3561 (2005)
- [Blo89] H. Blosser *et al.*, IEEE Trans. on Magnetics 25, 1746 (1989)
- [Blo93] H. Blosser *et al.*, NSCL Internal Report, MSUCL-874 (1993)
- [Blo05] W. Blokland *et al.*, Proc. of PAC, Knoxville, TN, p. 1395 (2005)
- [Boh75] A. Bohr and B. Mottelson, Nuclear Structure, Benjamin, New York, 1975
- [Boh84] D. Bohle *et al.*, Phys. Lett. B 137, 27 (1984)
- [Bol05a] J.L. Boles *et al.*, Proc. of PAC, Knoxville, TN, p. 3227 (2005)
- [Bol05b] G. Bollen *et al.*, Nucl. Instr. and Meth. A 550, 27 (2005)
- [Bol06a] G. Bollen *et al.*, Nucl. Instr. and Meth. A 562, 915 (2006)
- [Bol06b] G. Bollen *et al.*, Phys. Rev. Lett. 96, 152501 (2006)
- [Bon90] P. Bonche *et al.*, Nucl. Phys. A 519, 509 (1990)
- [Bot05] A.S. Botvina and I.N. Mishustin, Phys. Rev. C 72, 048801 (2005)
- [Bou97] M.A. Bouchiat and C. Bouchiat, Rep. Prog. Phys. 60, 1351 (1997)
- [BPA03] Board on Physics and Astronomy, Connecting Quarks with the Cosmos: Eleven Science Questions for the New Century, The National Academies Press (2003)
- [Bra93] M. Brack, Rev. Mod. Phys. 65, 677 (1993)
- [Bra00] F. Brachwitz *et al.*, Ap. J. 536, 934 (2000)
- [Bra01] G. Brautti *et al.*, AIP Conf. Proc. 572, 74 (2001)
- [Bro73] R.A. Broglia *et al.*, Adv. Nucl. Phys. 6, 287 (1973)

-
- [Bro81] T.A. Brody *et al.*, Rev. Mod. Phys. 53, 385 (1981)
- [Bro82] K.L. Brown, SLAC Report No. 75, Rev. 4 (1982)
- [Bro90] R. Brockmann and R. Machleidt, Phys. Rev. C 42, 1965 (1990)
- [Bro91] B.A. Brown, Phys. Rev. C 43, R1513 (1991)
- [Bro94] B.A. Brown and K. Rykaczewski, Phys. Rev. C 50, R2270 (1994)
- [Bro98] B.A. Brown, Phys. Rev. C 58, 220 (1998)
- [Bro00a] B.A. Brown, Phys. Rev. Lett. 85, 5296 (2000)
- [Bro00b] P. Brown *et al.*, Proc. of the 9th Workshop on RF Superconductivity, Santa Fe, NM (1999), Report LA-13782-C, p. 1 (2000)
- [Bro01] B.A. Brown, Prog. Part. Nucl. Phys. 47, 517 (2001)
- [Bro02a] B.A. Brown *et al.*, Phys. Rev. C 65, 045802 (2002)
- [Bro02b] B.A. Brown *et al.*, Phys. Rev. C 65, 061601 (2002)
- [Bro04] E.F. Brown, Ap. J. Lett. 614, L57 (2004)
- [Bue84] M. Buenerd, J. Phys. (Paris), Colloq. C-4, 115 (1984)
- [Bur95] A. Burrows *et al.*, Ap. J. 450, 830 (1995)
- [Bur06] A. Burrows *et al.*, Ap. J. 640, 878 (2006)
- [But91] H.S. Butler *et al.*, Proc. of PAC, San Francisco, CA, p. 281 (1991)
- [But96] P.A. Butler and W. Nazarewicz, Rev. Mod. Phys. 68, 349 (1996)
- [Cac06] E.M. Cackett *et al.*, arXiv:astro-ph/0605490 (2006)
- [Cak05] R.B. Cakirli *et al.*, Phys. Rev. Lett. 94, 092501 (2005)
- [Cal74] F.P. Calprice *et al.*, Phys. Rev. D 9, 519 (1974)
- [Cal77] F.P. Calprice *et al.*, Phys. Rev. C 15, 381 (1977)
- [Cam01] A.G.W. Cameron, Ap. J. 562, 456 (2001)
- [Cam02] P. Campbell *et al.*, Phys. Rev. Lett. 89, 082501 (2002)
- [Cas73] R.F. Casten *et al.*, Phys. Lett. B 43, 473 (1973)
- [Cas01] R.F. Casten and N.V. Zamfir, Phys. Rev. Lett. 87, 052503 (2001)
- [Cas06] E. Casajeros *et al.*, Phys. Rev. C 73, 014319 (2006)
- [Cay01] R. Cayrel *et al.*, arXiv:astro-ph/0104448 (2001)
- [Cha92] A.E. Champagne and M. Wiescher, Annu. Rev. Nucl. Sci. 42, 39 (1992)
- [Cha96] M. Chartier *et al.*, Phys. Rev. Lett. 77, 2400 (1996)
- [Cha97] R.R. Chasman and I. Ahmad, Phys. Lett. B 392, 255 (1997)
- [Cha01] R.R. Chasman, Phys. Rev. C 64, 024311 (2001)
- [Cha03] M. Champion *et al.*, Proc. of PAC, Portland, OR, p. 3377 (2003)
- [Che95] B. Chen *et al.*, Phys. Lett. B 355, 37 (1995)
- [Che01] L. Chen *et al.*, Phys. Lett. B 505, 21 (2001)
- [Che04] L.W. Chen *et al.*, Phys. Rev. C 69, 054606 (2004)
- [Che05] L.W. Chen *et al.*, Phys. Rev. Lett. 94, 032701 (2005)
- [Che06] A. Chester *et al.*, Nucl. Instr. and Meth. A 562, 230 (2006)
- [Cho73] M.S. Chowdhury and H.M. Sen Gupta, Nucl. Phys. A 205, 454 (1973)
- [Chr64] J.H. Christenson *et al.*, Phys. Rev. Lett. 13, 138 (1964)
- [Ciz05] J.A. Cizewski *et al.*, Nucl. Instr. and Meth. B 241, 200 (2005)
- [Cla01] R.M. Clark *et al.*, Phys. Rev. Lett. 87, 202502 (2001)
- [Cla03a] B.C. Clark *et al.*, Phys. Rev. C 67, 054605 (2003)

-
- [Cla03b] R.M. Clark *et al.*, Phys. Rev. C 68, 037301 (2003)
- [Cle04] R.R.C. Clement *et al.*, Phys. Rev. Lett. 92, 172502 (2004)
- [Coc97] J.F.C. Cocks *et al.*, Phys. Rev. Lett. 78, 2920 (1997)
- [Col96] B.J. Cole, Phys. Rev. C 54, 1240 (1996)
- [Col02] Collinear Laser Spectroscopy Group, University Mainz,
is389-proj-collaps.web.cern.ch/is389%2Dproj%2Dcollaps/
[Col04] G. Colò *et al.*, Phys. Rev. C 70, 024307 (2004)
- [Col06] A.L. Cole *et al.*, Phys. Rev. C 74, 034333 (2006)
- [Com94] E.R. Commins *et al.*, Phys. Rev. A 50, 2960 (1994)
- [Coo06] R.L. Cooper and R. Narayan, arXiv:astro-ph/0608068 (2006)
- [Cor02] L. Corradi *et al.*, Nucl. Phys. A 701, 109 (2002)
- [Cot02] J. Cottam *et al.*, Nature 420, 51 (2002)
- [Cow91] J.J. Cowan *et al.*, Phys. Rep. 208, 267 (1991)
- [Cow06] J.J. Cowan, private communication
- [Cra94] K. Crandall, Proc. of LINAC, Tsukuba, Japan, p.227 (1994)
- [Cra97] K.R. Crandall and D.P. Rusthoi, LANL Report,
LA-UR-97-886 (1997)
- [Cra05] K.R. Crandall *et al.*, LANL Report, LA-UR-96-1836, revised (2005)
- [Cum06] A. Cumming *et al.*, Ap. J. 646, 429 (2006)
- [Cur05] F. Currell and G. Fussmann, IEEE Trans. Plasma Sci. 33, 1763 (2005)
- [Cwi96] S. Cwiok *et al.*, Nucl. Phys. A 611, 211 (1996)
- [Cwi05] S. Cwiok *et al.*, Nature 433, 705 (2005)
- [Dah82] M. Dahlinger *et al.*, Nucl. Phys. A 376, 94 (1982)
- [Dan84a] P. Danielewicz, Ann. Phys. 152, 239 (1984)
- [Dan84b] P. Danielewicz, Ann. Phys. 152, 305 (1984)
- [Dan02] P. Danielewicz *et al.*, Science 298, 1592 (2002)
- [Dan03] P. Danielewicz, Nucl. Phys. A 727, 233 (2003)
- [Dav98] C.N. Davids *et al.*, Phys. Rev. Lett. 80, 1849 (1998)
- [Dav01] B. Davids *et al.*, Phys. Rev. Lett. 86, 2750 (2001)
- [Dav04] C.N. Davids *et al.*, Phys. Rev. C 69, 011302 (2004)
- [Dav06] A.D. Davies *et al.*, Phys. Rev. Lett. 96, 112503 (2006)
- [Dec91] P. Decroock *et al.*, Phys. Rev. Lett. 67, 808 (1991)
- [Dei95] H. Deitinghoff, Proc. of PAC, Dallas, TX, p. 1158 (1995)
- [Del93] Th. Delbar, Phys. Rev. C 47, R14 (1993)
- [Del06] P. Delahaye *et al.*, Rev. Sci. Instr. 77, 03, B 105 (2006)
- [Des04] Ph. Dessagne *et al.*, Eur. Phys. J. A 20, 405 (2004)
- [Dew05] A. Dewald *et al.*, J. Phys. G. 31, S1427 (2005)
- [Dic04] W.H. Dickhoff and C. Barbieri, Prog. Part. Nucl. Phys. 52,
377 (2004)
- [Die03] A.E.L. Dieperink *et al.*, Phys. Rev. C 68, 064307 (2003)
- [Dil03] I. Dillmann *et al.*, Phys. Rev. Lett. 91, 162503 (2003)
- [Dil06] J. Dilling *et al.*, Int. J. Mass. Spec. 251, 198 (2006)
- [Dim00] V.I. Dimitrov *et al.*, Phys. Rev. Lett. 84, 5732 (2000)
- [Din04] M. Dine and A. Kusenko, Rev. Mod. Phys. 76, 1 (2004)
- [Din05] D.C. Dinca *et al.*, Phys. Rev. C 71, 041302R (2005)

-
- [Dob94] J. Dobaczewski *et al.*, Phys. Rev. Lett. 72, 981 (1994)
- [Dob96] J. Dobaczewski *et al.*, Phys. Rev. C 53, 2809 (1996)
- [Dob03] J. Dobaczewski *et al.*, Phys. Rev. C 67, 034308 (2003)
- [DOE41313] DOE grant: DE-FG02-04ER41313: Development of a Concept for High Power Beam Dumps and Catchers, and the Preseparator Area Layout for Fragment Separators for the Rare Isotope Accelerator Project, MSU-ANL-LLNL-LBNL-ORNL Collaboration
- [DOE41322] DOE grant: DE-FG02-04ER41322: Development of a Concept for the ISOL Stations for the Rare Isotope Accelerator Project, MSU-ANL-LLNL-LBNL-ORNL Collaboration
- [DOE5400] Radiation Protection of the Public and the Environment, DOE Order 5400.5 and 40 CFR 141
- [Dol03] M. Doleans and S.-H. Kim, Proc. of PAC, Portland, OR, p. 1599 (2003)
- [Dol05] M. Doleans *et al.*, Proc. of PAC, Knoxville, TN, p. 1826 (2005)
- [Don85] E.D. Donets, Nucl. Instr. and Meth. B 9, 522 (1985)
- [Don89] D. Donets, The physics and technology of ion sources, edited by I.G. Brown, p. 245, Wiley, New York (1989)
- [Doo02] L. Doolittle *et al.*, Proc. of LINAC, Gyeongju, South Korea, p. 371 (2002)
- [Doo03] L. Doolittle *et al.*, Proc. of PAC, Portland, OR, p. 1464 (2003)
- [Dos05] C. Dossat *et al.*, Phys. Rev. C 72, 054315 (2005)
- [Dud88] J. Dudek *et al.*, Phys. Lett. B 211, 252 (1988)
- [Dud02] J. Dudek *et al.*, Phys. Rev. Lett. 88, 252502 (2002)
- [Dud04] J. Dudek *et al.*, Eur. Phys. J. A 20, 15 (2004)
- [Dud06] J. Dudek *et al.*, Phys. Rev. Lett. 97, 072501 (2006)
- [Dup00] R. Duperrier *et al.*, Proc. of LINAC, Monterey, CA, p.839 (2000)
- [Dup03] R. Duperrier and D. Gorelov, Proc. of PAC, Portland, OR, p. 2805 (2003)
- [Dup05] R. Duperrier, NSCL Internal Report, MSU (2005)
- [Eji05] H. Ejiri, J. Phys. Soc. Jpn 74, 2101 (2005)
- [Ell02] S.R. Elliott and P. Vogel, Annu. Rev. Nucl. Sci. 52, 115 (2002)
- [Eng05] S. Engel *et al.*, Nucl. Instr. and Meth. A 553, 491 (2005)
- [Eri63] T. Ericson, Ann. Phys. 23, 390 (1963)
- [Exl01] GSI, Conceptual Design Report: An International Accelerator Facility for Beams of Ions and Antiprotons (2001)
- [Eva04] A.O. Evans *et al.*, Phys. Rev. Lett. 92, 252502 (2004)
- [Fac98] A. Facco *et al.*, Proc. of EPAC, Stockholm, Sweden, p. 1846 (1998)
- [Fac99] A. Facco and V. Zviagintsev, Proc. of the 9th Workshop on RF Superconductivity, Santa Fe, NM (1999), Report LA-13782-C (2000)
- [Fac04] A. Facco *et al.*, Proc. of EPAC, Lucerne, Switzerland, p. 2086 (2004)
- [Fae02] T. Faestermann *et al.*, Eur. Phys. J. A 15, 185 (2002)
- [Fes04] A. Feschenko *et al.*, Proc. of LINAC, Lübeck, Germany, p. 408 (2004)
- [Fis03] S.M. Fischer *et al.*, Phys. Rev. C 67, 064318 (2003)
- [Fis06] J.L. Fisker *et al.*, arXiv:astro-ph/0410561 (2006)
- [Fla95a] V.V. Flambaum and V.G. Zelevinsky, Phys. Lett. B 350, 8 (1995)

-
- [Fla95b] V.V. Flambaum and G.F. Gribakin, *Prog. Part. Nucl. Phys.* 35, 423 (1995)
- [For04] B. Fornal *et al.*, *Phys. Rev. C* 70, 064304 (2004)
- [Fos74] D.B. Fossan and W.K. Warburton, *Nuclear Spectroscopy and Reactions, Part C*, ed. J. Cerny, Academic Press, New York and London, 307 (1974)
- [Fra83] M.A. Franey and W.G. Love, *Phys. Rev. C* 31, 488 (1983)
- [Fra01] S. Frauendorf, *Rev. Mod. Phys.* 73, 463 (2001)
- [Fra03] C. Fransen *et al.*, *Phys. Rev. C* 67, 024307 (2003)
- [Fra05] S. Fracasso and G. Colo, *Phys. Rev. C* 72, 064310 (2005)
- [Fre99] C. Freiburghaus *et al.*, *Ap. J.* 516, 381 (1999)
- [Fre04] S.J. Freeman *et al.*, *Phys. Rev. C* 69, 064301 (2004)
- [Fri95] F. Frisk *et al.*, *Phys. Rev. C* 52, 2468 (1995)
- [Fri05a] J. Fridmann *et al.*, *Nature* 435, 922 (2005)
- [Fri05b] S. Fritsch *et al.*, *Nucl. Phys. A* 750, 259 (2005)
- [Fri06] J. Fridmann *et al.*, *Phys. Rev. C* 74, 034313 (2006)
- [Fro05] C. Frohlich *et al.*, *arXiv:astro-ph/0410208* (2005)
- [Fry04] C.L. Fryer and M.S. Warren, *Ap. J.* 601, 391 (2004)
- [Fuc01] C. Fuchs, *et al.*, *Phys. Rev. Lett.* 86, 1974 (2001)
- [Fuj05] Y. Fujita *et al.*, *Phys. Rev. Lett.* 95, 212501 (2005)
- [Fuk04] N. Fukuda *et al.*, *Phys. Rev. C* 70, 054606 (2004)
- [Gad03] A. Gade *et al.*, *Phys. Rev. C* 68, 014302 (2003)
- [Gad04a] A. Gade *et al.*, *Phys. Rev. C* 69, 034311 (2004)
- [Gad04b] A. Gade *et al.*, *Phys. Rev. Lett.* 93, 042501 (2004)
- [Gad05] A. Gade *et al.*, *Phys. Rev. Lett.* 95, 022502 (2005)
- [Gad06] A. Gade *et al.*, *Phys. Rev. C* 74, 021302 (2006)
- [Gal04] D.K. Galloway *et al.*, *Ap. J.* 601, 466 (2004)
- [Gal06a] D.K. Galloway, private communication
- [Gal06b] D.K. Galloway *et al.*, *Ap. J.* 639, 1033 (2006)
- [Gam04] V.N. Gamezo *et al.*, *Phys. Rev. Lett.* 92, 211102 (2004)
- [Gar06] U. Garg, *Nucl. Phys. A*, to be published
- [Gas05] L.R. Gasques *et al.*, *Phys. Rev. C* 72, 025806 (2005)
- [Gau06] L. Gaudefroy *et al.*, *Eur. Phys. J. A* 27, 309 (2006), *Phys. Rev. Lett.* 97, 092501 (2006)
- [Gee06] D.F. Geesaman *et al.*, *Annu. Rev. Nucl. Sci.* 56, in press
- [Geh98] R.D. Gehrz *et al.*, *Publ. Astr. Soc. Pac.* 110, 3 (1998)
- [Gei92] H. Geissel *et al.*, *Nucl. Instr. and Meth. B* 70, 286 (1992)
- [Gei03] H. Geissel *et al.*, *Nucl. Instr. and Meth. B* 204, 71 (2003)
- [Gei06] H. Geissel *et al.*, *Nucl. Instr. and Meth. B* 247, 368 (2006)
- [Gel96] R.R. Geller, *Electron cyclotron resonance ion sources and ECR plasmas*, Institute of Physics Publishing, Bristol/Philadelphia (1996)
- [Geo06] G. Georgiev, private communication
- [Ghe04] R. Ghetti *et al.*, *Phys. Rev. C* 70, 034601 (2004)
- [Gio02] J. Giovinazzo *et al.*, *Phys. Rev. Lett.* 89, 102501 (2002)
- [Gla98] T. Glasmacher, *Annu. Rev. Nucl. Sci.* 48, 1 (1998)

-
- [Gle04] N.K. Glendenning, *Direct Nuclear Reactions*, World Scientific (2004)
- [Goe02] A. Görgen *et al.*, *Phys. Rev. C* 65, 027302 (2002)
- [Gol60] V.I. Goldansky, *Nucl. Phys.* 19, 482 (1960)
- [Gom06] E. Gomez *et al.*, *Rep. Prog. Phys.* 69, 79 (2006)
- [Goo79] A.L. Goodman, *Adv. Nucl. Phys.* 11, 263 (1979)
- [Gor96] D. Gorelov and P. Ostroumov, *Proc. of EPAC, Barcelona, Spain* (1996)
- [Gor98] S. Goriely, *Phys. Lett. B* 436, 10 (1998)
- [Gor05] A. Gorelov *et al.*, *Phys. Rev. Lett.* 94, 142501 (2005)
- [Gor06] S. Goriely *et al.*, *Nucl. Phys. A* 773, 279 (2006)
- [Gra92] H.-D. Gräf, *Proc. of the 5th Workshop on RF Superconductivity, Hamburg, Germany* (1991), DESY M-92-01, p. 317 (1992)
- [Gra02] H. Grawe *et al.*, *Nucl. Phys. A* 704, 211c (2002)
- [Gre85] L. Grenacs, *Annu. Rev. Nucl. Sci.* 35, 455 (1985)
- [Gre00] G. Gregoire *et al.*, *Rev. Sci. Instr.* 71, 1097 (2000)
- [Gri03a] T.L. Grimm *et al.*, *Proc. of PAC, Portland, OR*, p. 1353 (2003)
- [Gri03b] T.L. Grimm *et al.*, *Proc. of PAC, Portland OR*, p. 1350 (2003)
- [Gri04] T.L. Grimm *et al.*, *Proc. of LINAC, Lübeck, Germany*, p. 763 (2004)
- [Gro03] D.E. Groh *et al.*, *Phys. Rev. Lett.* 90, 202502 (2003)
- [Gro04a] N. Grossman and R. Rameika, *NuMI-NOTE-BEAM-0970*, July 2004
- [Gro04b] N. Grossman, *NuMI-NOTE-BEAM-1020*, August 2004
- [Grz98] R. Grzywacz *et al.*, *Phys. Rev. Lett.* 81, 766 (1998)
- [Guh98] T. Guhr *et al.*, *Phys. Rep.* 299, 189 (1998)
- [Gup05] R. Gupta *et al.*, *IEEE Trans. Applied Superconductivity* 15, 1148 (2005)
- [Hag04] M. Hagemann *et al.*, *Phys. Lett. B* 579, 251 (2004)
- [Hal84] A.L. Hallin *et al.*, *Phys. Rev. Lett.* 52, 337 (1984)
- [Ham98] I. Hamamoto *et al.*, *Phys. Rev. C* 57, R1064 (1998)
- [Ham00] I. Hamamoto and H. Sagawa, *Phys. Rev. C* 62, 024319 (2000)
- [Han95] P.G. Hansen *et al.*, *Annu. Rev. Nucl. Sci.* 45, 591 (1995)
- [Han99a] M. Hannawald *et al.*, *Phys. Rev. Lett.* 82, 1391 (1999)
- [Han99b] P.G. Hansen, *Nucl. Phys. A* 649, 355c (1999)
- [Han01] P.G. Hansen and B.M. Sherrill, *Nucl. Phys. A* 693, 133 (2001)
- [Han03a] P.G. Hansen and J.A. Tostevin, *Annu. Rev. Nucl. Sci.* 53, 219 (2003)
- [Han03b] P. Haensel and J.L. Zdunik, *Astron. Astrophys.* 404, L33 (2003)
- [Har99] P.G. Harris *et al.*, *Phys. Rev. Lett.* 82, 904 (1999)
- [Har01] M.N. Harakeh and A. van der Woude, *Oxford Studies in Nuclear Physics* 24, Clarendon Press, Oxford, 2001
- [Har03] W. Hartung *et al.*, *Proc. of the 11th Workshop on RF Superconductivity, Travemünde, Germany* (2003)
- [Har05a] J.C. Hardy and I.S. Towner, *Phys. Rev. C* 71, 055501 (2005)
- [Har05b] J.C. Hardy and I.S. Towner, *Phys. Rev. Lett.* 94, 092502 (2005)
- [Hax01] W.C. Haxton and C E. Wieman, *Annu. Rev. Nucl. Sci.* 51, 261 (2001)
- [Hee94] P.-H. Heenen *et al.*, *Phys. Rev. C* 50, 802 (1994)

-
- [Hee02] P.-H. Heenen and W. Nazarewicz, *Europhysics News* 33, 1 (2002)
- [Heg01] A. Heger *et al.*, *Ap. J.* 560, 307 (2001)
- [Hei02] G. Heidenreich, *AIP Conf. Proc.* 642, 122 (2002)
- [Hel03] M. Hellstrom *et al.*, *Proc. of the 3rd Int. Conf. on Fission and Properties of Neutron-Rich Nuclei*, J.H. Hamilton, A.V. Ramayya, and H.K. Carter, eds., p. 22 (World Scientific, River Edge, 2003)
- [Hen06] S. Henderson, *Proc. of LINAC*, Knoxville, TN, to be published (2006)
- [Her58] G. Herrmann, *J. Appl. Phys.* 29, 127 (1958)
- [Her97] H. Herndl and B.A. Brown, *Nucl. Phys. A* 627, 35 (1997)
- [Her04] R.-D. Herzberg, *J. Phys. G* 30, R123 (2004)
- [Her06] R.-D. Herzberg *et al.*, *Nature* 442, 896 (2006)
- [Hes06] F.P. Hessberger *et al.*, *Eur. Phys. J. A* 29, 165 (2006)
- [Hit06] G.W. Hitt *et al.*, *Nucl. Instr. and Meth. A* 566, 264 (2006)
- [Hix03] W.R. Hix *et al.*, *Phys. Rev. Lett.* 91, 201102 (2003)
- [Hof06] C. Hoffman, to be published
- [Hoh64] P. Hohenberg and W. Kohn, *Phys. Rev.* 136, B864 (1964)
- [Hol72] B.R. Holstein, *Phys. Rev. C* 5, 1529 (1972)
- [Hol04] N. Holtkamp, *Proc. of LINAC*, Lübeck, Germany, p. 837 (2004)
- [Hon02] M. Honma *et al.*, *Phys. Rev. C* 65, 061301 (2002)
- [Hon04] M. Honma *et al.*, *Phys. Rev. C* 69, 034335 (2004)
- [Hor99] M. Horoi *et al.*, *Phys. Rev. Lett.* 82, 2064 (1999)
- [Hor01] C.J. Horowitz *et al.*, *Phys. Rev. C* 63, 025501(2001)
- [Hor05] M. Horoi and K.A. Jackson, *AIP Conf. Proc.* 777, 112 (2005)
- [Hos05] P.T. Hosmer *et al.*, *Phys. Rev. Lett.* 94, 112501 (2005)
- [Hov02] C. Hovater *et al.*, *Proc. of LINAC*, Gyeongju, South Korea, p. 698 (2002)
- [Hub78] G. Huber *et al.*, *Phys. Rev. C* 18, 2342 (1978)
- [Hub03] R. Huber *et al.*, *Phys. Rev. Lett.* 90, 202301 (2003)
- [Huh98] M. Huhta *et al.*, *Phys. Rev. C* 57, R2790 (1998)
- [Hus92] M.S. Hussein *et al.*, *Phys. Rev. C* 46, 377 (1992)
- [Huy02] M. Huyse *et al.*, *Nucl. Instr. and Meth. B* 187, 535 (2002)
- [Iac00] F. Iachello, *Phys. Rev. Lett.* 85, 3580 (2000)
- [Iac03] F. Iachello, *Phys. Rev. Lett.* 91, 132502 (2003)
- [Iac06] F. Iachello and A. Arima, *The Interacting Boson Model*, Cambridge Monographs on Mathematical Physics (2006)
- [Ili99] C. Iliadis *et al.*, *Ap. J.* 524, 434 (1999)
- [Ili02] C. Iliadis *et al.*, *Ap. J. Suppl.* 142, 105 (2002)
- [Ima04] N. Imai *et al.*, *Phys. Rev. Lett.* 92, 062501 (2004)
- [Int04] J.J.M. in 't Zand *et al.*, *arXiv:astro-ph/0407087* (2004)
- [Isa92] P. Van Isacker *et al.*, *Phys. Rev. C* 45, R13 (1992)
- [Isa95] P. Van Isacker *et al.*, *Phys. Rev. Lett.* 74, 4607 (1995)
- [Iso06] ISOLDE yield information, isolde.web.cern.ch/ISOLDE/
- [Ito06] M. Ito *et al.*, *Phys. Lett. B* 637, 53 (2006)
- [Iwa97] N. Iwasa *et al.*, *Nucl. Instr. and Meth. B* 126, 284 (1997)

-
- [Iwa99] K. Iwamoto *et al.*, Ap. J. Suppl. 125, 439 (1999)
- [Iwa01] H. Iwase *et al.*, Nucl. Instr. and Meth. B 183, 374 (2001)
- [Iwa02] H. Iwase *et al.*, J. Nucl. Sci. Tech. 39, 1142 (2002)
- [Izu96] H. Izumi *et al.*, Phys. Lett. B 366, 51 (1996)
- [Jac88] K.P. Jackson *et al.*, Phys. Lett. B 201, 25 (1988)
- [Jan91] R.V.F. Janssens and T.L. Khoo, Annu. Rev. Nucl. Sci. 41, 321 (1991)
- [Jan02] R.V.F. Janssens *et al.*, Phys. Lett. B 546, 55 (2002)
- [Jen04] A.S. Jensen *et al.*, Rev. Mod. Phys. 76, 215 (2004)
- [Jeo04] S.C. Jeong *et al.*, Rev. Sci. Instr. 75, 1631 (2004)
- [Jew99] J.K. Jewell *et al.*, Phys. Lett. B 454, 181 (1999)
- [Joh63] C.H. Johnson *et al.*, Phys. Rev. 132, 1149 (1963)
- [Jon04] K.L. Jones *et al.*, Phys. Rev. C 70, 067602 (2004)
- [Jon05] P.B. Jones, arXiv:astro-ph/0502182 (2005)
- [Jos05] J. Jose *et al.*, Nucl. Phys. A 752, 540c (2005)
- [Jun03] K. Jungmann *et al.*, Phys. Scrip. T 104, 178 (2003)
- [Kad62] L.P. Kadanoff and G. Baym, Quantum Statistical Mechanics, W. A. Benjamin, New York (1962)
- [Kae99] F. Kaeppler, Prog. Part. Nucl. Phys. 43, 419 (1999)
- [Kai01] T. Kai *et al.*, DCHAIN-SP2001: High Energy Particle Induced Radioactivity Calculation Code, JAERI-Data/Code 2001-016 (2001)
- [Kan04] T. Kandil, Proc. of LINAC, Lübeck, Germany, p. 447 (2004)
- [Kar02] S. Karataglidis *et al.*, Phys. Rev. C 65, 044306 (2002)
- [Kar03] M. Karny *et al.*, Phys. Rev. Lett. 90, 012502 (2003)
- [Kar05] M. Karny *et al.*, Eur. Phys. J. A 25, s01, 135 (2005)
- [Kar06] M. Karny *et al.*, Eur. Phys. J. A 27, 129 (2006)
- [Kat98] I. Katayama *et al.*, Hyperfine Int. 115, 165 (1998)
- [Kau00] T. Kautzsch *et al.*, Eur. Phys. J. A 9, 201 (2000)
- [Kei00] M. Keim *et al.*, Eur. Phys. J. A 8, 31 (2000)
- [Kel97] J.H. Kelley *et al.*, Phys. Rev. C 56, R1206 (1997)
- [Kel06] A. Kelic and K.-H. Schmidt, Phys. Lett. B 634, 362 (2006)
- [Kes03] O. Kester *et al.*, Nucl. Instr. and Meth. B 204, 20 (2003)
- [Kes04] O. Kester *et al.*, J. Phys.: Conf. Ser. 2, 107 (2004)
- [Kes06] O. Kester *et al.*, Rev. Sci. Instr. 77, 03B102 (2006)
- [Kif06] K. Kifonidis *et al.*, Astron. Astrophys. 453, 661 (2006)
- [Kil57] W.D. Kilpatrick, Rev. Sci. Instr. 28, 824 (1957); S. Koscielniak, LANL report AT-1 (1982)
- [Kil87] G. Kilgus *et al.*, Z. Phys. A 326, 41 (1987)
- [Klu03] H.-J. Kluge and W. Nörtershäuser, Spectrochimica Acta Part B: Atomic Spectroscopy 58, 1031 (2003)
- [Kne02] P. Kneisel *et al.*, Proc. of EPAC, Paris, France, p. 2247 (2002)
- [Kne03] I. Knezevic and D.K. Ferry, Physica E 19, 71 (2003)
- [Koi04] T. Koike *et al.*, Phys. Rev. Lett. 93, 172502 (2004)
- [Kos94] S. Koscielniak, Proc. of LINAC, Tsukuba, Japan, p. 526 (1994); S. Koscielniak *et al.*, Proc. of LINAC, Geneva, Switzerland, p. 402 (1996)

-
- [Kos03] M.A. Kostin, <http://ppd.fnal.gov/experiments/e907/Beam/sas.pdf>
- [Koz06a] R.L. Kozub *et al.*, Phys. Rev. C 73, 044307 (2006)
- [Koz06b] V.Y. Kozlov *et al.*, Int. J. Mass. Spec. 251, 159 (2006)
- [Kra93] K.-L. Kratz *et al.*, Ap. J. 403, 216 (1993)
- [Kra99] A. Krasznahorkay *et al.*, Phys. Rev. Lett. 82, 3216 (1999)
- [Kra00] K.-L. Kratz *et al.*, Hyperfine Int. 129, 185 (2000)
- [Kra01] G.J. Kramer *et al.*, Nucl. Phys. A 679, 267 (2001)
- [Kra04] K.-L. Kratz *et al.*, New Astr. Rev. 48, 105 (2004)
- [Kra06] K.-L. Kratz and B. Pfeiffer, private communication
- [Kru00] R. Krücken, J. Res. Natl. Inst. Stand. Technol. 105, 53 (2000)
- [Kru02] R. Krücken *et al.*, Phys. Rev. Lett. 88, 232501 (2002)
- [Kry93] R.A. Kryger *et al.*, Phys. Rev. C 47, R2439 (1993)
- [Kub92] T. Kubo *et al.*, Nucl. Instr. and Meth. B 70, 309 (1992)
- [Kub03] T. Kubo, Nucl. Instr. and Meth. B 204, 97 (2003)
- [Kus04] K. Kusaka *et al.*, RIKEN Accel. Prog. Rep. 37, 297 (2004)
- [Laf00] D.R. LaFosse *et al.*, Phys. Rev. C 62, 014305 (2000)
- [Lal99] G.A. Lalazissis *et al.*, Phys. Rev. C 60, 014310 (1999)
- [Lam02] T. Lamy *et al.*, Rev. Sci. Instr. 73, 717 (2002)
- [Lam06] T. Lamy *et al.*, Rev. Sci. Instr. 77, 03B101 (2006)
- [Lan86] M. Langevin *et al.*, Nucl. Phys. A 455, 149 (1986)
- [Lan97] G.J. Lane *et al.*, Phys. Rev. C 55, R2127 (1997)
- [Lan03] K. Langanke *et al.*, Rev. Mod. Phys. 75, 819 (2003)
- [Lat77] J.M. Lattimer *et al.*, Ap. J. 213, 225 (1977)
- [Lat01] J.M. Lattimer and M. Prakash, Ap. J. 550, 426 (2001)
- [Lat04] J.M. Lattimer and M. Prakash, Science 304, 536 (2004)
- [Lax92] R.E. Laxdal and W. Joho, Proc. of EPAC, Berlin, Germany, p. 590 (1992)
- [Lea81] C.R. Leavens and E.W. Fenton, Phys. Rev. B 24, 5086 (1981)
- [Lee04] I.Y. Lee *et al.*, Nucl. Phys. A 746, 255c (2004)
- [Lee06a] J. Lee *et al.*, Phys. Rev. C 73, 044608 (2006)
- [Lee06b] I.Y. Lee and P. Fallon, private communication
- [Lei99] M. Leino *et al.*, Eur. Phys. J. A 6, 63 (1999)
- [Lei01a] A. Leistenschneider *et al.*, Phys. Rev. Lett. 86, 5442 (2001)
- [Lei01b] B. Leibundgut, Annu. Rev. Astron. Astrophys. 39, 67 (2001)
- [Lei01c] M.A. Leitner *et al.*, Proc. of PAC, Chicago, IL, p. 67 (2001)
- [Lei03a] D. Leitner *et al.*, Proc. of PAC, Portland, OR, p. 86 (2003)
- [Lei03b] D. Leitner *et al.*, RIA R&D Workshop, Bethesda, MD (2003)
- [Lei04] M. Leino and F.P. Hessberger, Annu. Rev. Nucl. Sci. 54, 175 (2004)
- [Lei05] D. Leitner *et al.*, Nucl. Instr. and Meth. B 235, 486 (2005)
- [Lev85] S. Levit and P. Bonche, Nucl. Phys. A 437, 426 (1985)
- [Lev89] M.A. Levine *et al.*, Nucl. Instr. and Meth. B 43, 431 (1989)
- [Lew95] M. Lewitowicz *et al.*, Nucl. Phys. A 588, 197c (1995)
- [Li00] B.A. Li, Phys. Rev. Lett. 85, 4221 (2000)
- [Li02] B.A. Li, Phys. Rev. Lett. 88, 192701 (2002)
- [Li04a] B.A. Li, Phys. Rev. C 69, 034614 (2004)

-
- [Li04b] B.A. Li, Nucl. Phys. A 734, 593c (2004)
- [Li05] B.A. Li *et al.*, Phys. Rev. C 71, 054603 (2005)
- [Li06] B.A. Li and A.W. Steiner, Phys. Lett. B (2006) in press
- [Lia06] J.F. Liang *et al.*, Phys. Rev. Lett. 96, 029903 (2006)
- [Lid04a] S.N. Liddick *et al.*, Phys. Rev. Lett. 92, 072502 (2004)
- [Lid04b] S.N. Liddick *et al.*, Phys. Rev. C 70, 064303 (2004)
- [Lie05] M. Liebendorfer *et al.*, Ap. J. 620, 840 (2005)
- [LIGO00] Cost estimating plan LIGO II, LIGO-M990310-04-M (2000)
- [Lip82] E. Lipparini and S. Stringari, Phys. Lett. B 112, 421 (1982)
- [Lis00] L.J. Lising *et al.*, Phys. Rev. C 62, 055501 (2000)
- [Lis04] A.F. Lisetskiy *et al.*, Phys. Rev. C 70, 044314 (2004)
- [Lon98] C. Longour *et al.*, Phys. Rev. Lett. 81, 3337 (1998)
- [Lot67] W. Lotz, Z. Phys. 206, 205 (1967)
- [Lov81] W.G. Love and M.A. Franey, Phys. Rev. C 24, 1073 (1981)
- [Luk02] A.M. Lukyanov *et al.*, J. Phys. G 28, L41 (2002)
- [Luk06] S. Lukic *et al.*, Nucl. Instr. and Meth. A 565, 784 (2006)
- [Lun05] D. Lunney, private communication
- [Ma06] H. Ma *et al.*, Phys. Rev. ST AB 9, 032001 (2006)
- [Mac00] A.O. Macchiavelli *et al.*, Phys. Rev. C 61, 041303 (2000)
- [MAF00] The MAFIA collaboration, MAFIA User Manual (Version 4.106), CST Inc. (2000)
- [Man06] F. Mannucci *et al.*, MNRAS 370, 773 (2006)
- [Mar88] R.E. Marrs *et al.*, Phys. Rev. Lett. 60, 1715 (1988)
- [Mar99a] G. Martinez-Pinedo *et al.*, Nucl. Phys. A 651, 379 (1999)
- [Mar99b] F. Maréchal *et al.*, Phys. Rev. C 60, 034615 (1999)
- [Mar99c] F. Maréchal *et al.*, Phys. Rev. C 60, 064623 (1999)
- [Mar99d] R.E. Marrs and D.R. Slaughter, AIP Conf. Proc. 475, 322 (1999)
- [Mar00] K. Markenroth *et al.*, Phys. Rev. C 62, 034308 (2000)
- [Mar06] W.J. Marciano and A. Sirlin, Phys. Rev. Lett. 96, 032002 (2006)
- [Mat96] K. Matsuta *et al.*, Hyperfine Int. 97/98, 519 (1996)
- [Mat04] I. Matea *et al.*, Phys. Rev. Lett. 93, 142503 (2004)
- [Mav03] A. Mavanur *et al.*, Proc. of PAC, Portland, OR, p. 1407 (2003)
- [McC05] E.A. McCutchan *et al.*, J. Phys. G 31, S1485 (2005)
- [Mel67] H. Meldner, Ark. Fys. 36, 593 (1967)
- [Mer06] T.J. Mertzimekis *et al.*, Phys. Rev. C 73, 024318 (2006)
- [Mez98] A. Mezzacappa *et al.*, Ap. J. 495, 911 (1998)
- [Mic04] N. Michel *et al.*, Phys. Rev. C 70, 064313 (2004)
- [Mic06] S. Michimasa *et al.*, Phys. Lett. B 638, 146 (2006)
- [Min92] T. Minamisono *et al.*, Phys. Rev. Lett. 69, 2058 (1992)
- [Min02] K. Minamisono *et al.*, Phys. Rev. C 65, 015501 (2002)
- [Min06] K. Minamisono *et al.*, Phys. Rev. Lett. 96, 102501 (2006)
- [Mok95] N.V. Mokhov, Fermilab-FN-628 (1995)
- [Mok04] N.V. Mokhov *et al.*, Fermilab-Conf-04/053 (2004)
- [Mol92] P. Möller and J.R. Nix, Nucl. Phys. A 549, 84 (1992); J. Phys. G 20, 1681 (1994)

-
- [Mol95] P. Moller *et al.*, At. Data Nucl. Data Tables 59, 185 (1995)
- [Mon06a] C. Monrozeau, Nucl. Phys. A to be published
- [Mon06b] F. Montes *et al.*, Phys. Rev. C 73, 5801 (2006)
- [Mor57] M. Morita and R. Saito Morita, Phys. Rev. 107, 1316 (1957)
- [Mor04] D.J. Morrissey and B.M. Sherrill, The Euroschool Lectures on Physics of Exotic Beams, Vol. I, Eds. Al-Khalili and Roeckl, p. 113 (Springer, 2004)
- [Mor06] D.J. Morrissey *et al.*, Proc. of RNB7, Cortina d'Ampezzo, Italy, to be published
- [Mot95] T. Motobayashi *et al.*, Phys. Lett. B 346, 9 (1995)
- [Mot04] T. Motobayashi, Nucl. Phys. A 734, 623 (2004)
- [Muk05a] I. Mukha *et al.*, Phys. Rev. Lett. 95, 022501 (2005)
- [Muk05b] A.M. Mukhamedzhanov and F.M. Nunes, Phys. Rev. C 72, 017602 (2005)
- [Muk06] A.M. Mukhamedzhanov *et al.*, Eur. Phys. J. A 27, 205 (2006)
- [Mye69] W.D. Myers and W.J. Swiatecki, Ann. Phys. 55, 395 (1969)
- [Mye98] W.D. Myers and W.J. Swiatecki, Phys. Rev. C 57, 3020 (1998)
- [Nac04] E. Nacher *et al.*, Phys. Rev. Lett. 92, 232501 (2004)
- [Nas06] H. Nassar *et al.*, Phys. Rev. Lett. 96, 041102 (2006)
- [Nav00] A. Navin *et al.*, Phys. Rev. Lett. 85, 266 (2000)
- [Nay02] T.K. Nayak *et al.*, Phys. Rev. C 45, 132 (1992)
- [Naz84] W. Nazarewicz *et al.*, Nucl. Phys. A 429, 269 (1984)
- [Neg06] A. Negret *et al.*, Phys. Rev. Lett. 97, 062502 (2006)
- [Ney05] G. Neyens *et al.*, Phys. Rev. Lett. 94, 022501 (2005)
- [Nie02] A. Nieminen *et al.*, Phys. Rev. Lett. 88, 094801 (2002)
- [Nil68] S.-G. Nilsson *et al.*, Nucl. Phys. A 115, 545 (1968)
- [Nil69] S.-G. Nilsson *et al.*, Nucl. Phys. A 131, 1 (1969)
- [Nol88] P.J. Nolan and P.J. Twin, Annu. Rev. Nucl. Sci. 38, 533 (1988)
- [Nol94] P.J. Nolan *et al.*, Annu. Rev. Nucl. Sci. 44, 561 (1994)
- [Nol02] J.A. Nolen *et al.*, Nucl. Phys. A 701, 312 (2002)
- [Nol03] J.A. Nolen *et al.*, Nucl. Instr. and Meth. B 204, 293 (2003)
- [Not02] M. Notani *et al.*, Phys. Lett. B 542, 49 (2002)
- [NRC99] National Research Council, Nuclear Physics: The Core of Matter, the Fuel of Stars, National Academies Press (1999)
- [NSAC02] DOE/NSF Nuclear Science Advisory Committee, DOE/NSF Nuclear Science Advisory Committee, Opportunities in Nuclear Science: A Long-Range Plan for the Next Decade, April 2002
- [NSB06] Memorandum to members of the National Science Board, Arden Bement, NSB-2006-71, July 10, 2006
- [Obe06] A. Obertelli *et al.*, Phys. Lett. B 633, 33 (2006)
- [Ong06] H.J. Ong *et al.*, Phys. Rev. C 73, 024610 (2006)
- [Orm96] W.E. Ormand, Phys. Rev. C 53, 214 (1996)
- [Ost92] F. Osterfeld, Rev. Mod. Phys. 64, 491 (1992)
- [Ost00] P.N. Ostroumov *et al.*, Proc. of LINAC, Monterey, CA, p. 202 (2000)
- [Ost02a] P.N. Ostroumov, Phys. Rev. ST AB 5, 030101 (2002)

-
- [Ost02b] P.N. Ostroumov, Proc. of LINAC, Gyeongju, South Korea, p. 64 (2002)
- [Ost04] P.N. Ostroumov, Proc. of LINAC, Lübeck, Germany, p. 584 (2004)
- [Ots78] T. Otsuka *et al.*, Nucl. Phys. A 309, 1 (1978)
- [Ots01] T. Otsuka *et al.*, Phys. Rev. Lett. 87, 082502 (2001)
- [Ots05] T. Otsuka *et al.*, Phys. Rev. Lett. 95, 232502 (2005)
- [Ots06] T. Otsuka *et al.*, Phys. Rev. Lett. 97, 162501 (2006)
- [Oza00] A. Ozawa *et al.*, Phys. Rev. Lett. 84, 5493 (2000)
- [Oza01] A. Ozawa *et al.*, Nucl. Phys. A 691, 599 (2001)
- [Oze06] F. Ozel, Nature 441, 1115 (2006)
- [Paa05] N. Paar *et al.*, Phys. Lett. B 606, 288 (2005)
- [Pad98] H. Padamsee *et al.*, RF Superconductivity for Accelerators, John Wiley & Sons, New York (1998)
- [Pag05] D. Page and A. Cumming, Ap. J. Lett. 635, L157 (2005)
- [Pai06] S.D. Pain *et al.*, Phys. Rev. Lett. 96, 032502 (2006)
- [Par00] R. Pardo and G. Zinkann, Proc. of the 9th Workshop on RF Superconductivity, Santa Fe, NM (1999), Report LA-13782-C, p. 10 (2000)
- [Par03] S. Park *et al.*, Ap. J. 598, L95 (2003)
- [Pat89] Z. Patyk *et al.*, Nucl. Phys. A 491, 267 (1989)
- [Pat91] Z. Patyk *et al.*, Nucl. Phys. A 533, 132 (1991)
- [Pea92] J.M. Pearson *et al.*, IOP Conf. Proceedings 132, 857 (1992)
- [Pec04] A. Pecchia and A. Di Carlo, Rep. Prog. Phys. 67, 1497 (2004)
- [Pek71] L.K. Peker *et al.*, Phys. Lett. B 36, 547 (1971)
- [Pel05a] T. Pelaia and P. Chu, Proc. of PAC, Knoxville, TN, p. 1425 (2005)
- [Pel05b] D.B. Pelowitz (Ed.), LANL Report, LA-CP-05-0369 (2005)
- [Per99] S. Perlmutter *et al.*, Ap. J. 517, 565 (1999)
- [Pet03] W.A. Peters *et al.*, Phys. Rev. C 68, 034607 (2003)
- [Pfe01] B. Pfeiffer *et al.*, Nucl. Phys. A 688, 575 (2001)
- [Pfu02] M. Pfu02ner *et al.*, Eur. Phys. J. A 14, 279 (2002)
- [Pha95] K. Pham *et al.*, Phys. Rev. C 51, 526 (1995)
- [Pha06] L. Phair, private communication
- [Phi86] W.R. Phillips *et al.*, Phys. Rev. Lett. 57, 3257 (1986)
- [Pie03] D. Pierroutsakou *et al.*, Eur. Phys. J. A 16, 423 (2003)
- [Pik06] A. Pikin *et al.*, Rev. Sci. Instr. 77, 03A910 (2006)
- [Pla88] R. Planeta *et al.*, Phys. Rev. C 38, 195 (1988)
- [Ple04] T. Plewa *et al.*, Ap. J. Lett. 612, L37 (2004)
- [Plu06] M. Plum *et al.*, Proc. of EPAC, Edinburgh, UK, p. 351 (2006)
- [Pod02] H. Podlech *et al.*, Proc. of EPAC, Paris, France, p. 945 (2002)
- [Pod06] P. Podsiadlowski *et al.*, arXiv:astro-ph/0608324 (2006)
- [Pop06] I. Popova *et al.*, Proc. of EPAC, Edinburgh, UK, p. 977 (2006)
- [Por96] A.M. Porcellato *et al.*, Proc. of the 7th Workshop on RF Superconductivity, Gif sur Yvette, France (1995), Report CEA/Saclay 96 080/1, p. 43 (1996)
- [Por01] M. Portillo, Proc. of PAC, Chicago, IL, p. 3015 (2001)
- [Pov01] A. Poves *et al.*, Nucl. Phys. A 694, 157 (2001)

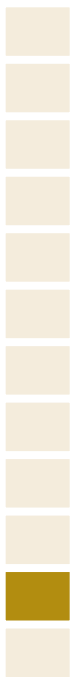
-
- [Pru05] J. Pruet *et al.*, *Ap. J.* 623, 325 (2005)
- [Pud96] B.S. Pudlinger *et al.*, *Phys. Rev. Lett.* 76, 2416 (1996)
- [Qia97] Y.-Z. Qian *et al.*, *Phys. Rev. C* 55, 1532 (1997)
- [Qia98] Y.-Z. Qian *et al.*, *Ap. J.* 494, 285 (1998)
- [Qia03] Y.-Z. Qian, *Prog. Part. Nucl. Phys.* 50, 153 (2003)
- [Qia04] J. Qiang *et al.*, *J. Comput. Phys.* 198, 278 (2004)
- [Qin00] L. Qingfeng *et al.*, *Phys. Rev. C* 62, 014606 (2000)
- [Qin05] L. Qingfeng *et al.*, *J. Phys. G* 31, 1359 (2005)
- [Raa04] R. Raabe *et al.*, *Nature* 431, 823 (2004)
- [Rad02] D.C. Radford *et al.*, *Phys. Rev. Lett.* 88, 222501 (2002)
- [Rai06] G. Rainovski *et al.*, *Phys. Rev. Lett.* 96, 122501 (2006)
- [Rak02] S. Rakers *et al.*, *Nucl. Instr. and Meth. A* 481, 253 (2002)
- [Ram06] M.J. Ramsey-Musolf, arXiv:nucl-th/0608035 (2006)
- [Rap06] W. Rapp *et al.*, arXiv:astro-ph/0608341 (2006)
- [Reh98] K.E. Rehm *et al.*, *Phys. Rev. Lett.* 80, 676 (1998)
- [Rei99] P. Reiter *et al.*, *Phys. Rev. Lett.* 82, 509 (1999)
- [Rei00] P. Reiter *et al.*, *Phys. Rev. Lett.* 84, 3542 (2000)
- [Rei02] S.M. Reimann and M. Manninen, *Rev. Mod. Phys.* 74, 1283 (2002)
- [Rem06] I. Remec *et al.*, *Nucl. Instr. and Meth. A* 562, 896 (2006)
- [Rey06] S. Reyes *et al.*, *Nucl. Instr. and Meth. A* 562, 610 (2006)
- [RIA06] The Science of the Rare Isotope Accelerator (RIA), A Brochure from the RIA Users Community, www.orau.org/ria/pdf/RIAFINAL.pdf
- [Rie98] A.G. Riess, *Astronomical Journal* 116, 1009 (1998)
- [Rii00] K. Riisager *et al.*, *Europhys. Lett.* 49, 547 (2000)
- [Ril99] L.A. Riley *et al.*, *Phys. Rev. Lett.* 82, 4196 (1999)
- [Ril05] L.A. Riley *et al.*, *Phys. Rev. C* 72, 024311 (2005)
- [Rin06] R. Ringle *et al.*, *Int. J. Mass. Spec.* 251, 300 (2006)
- [Riz05] J. Rizzo *et al.*, *Phys. Rev. C* 72, 064609 (2005)
- [Rob05] A.P. Robinson *et al.*, *Phys. Rev. Lett.* 95, 032502 (2005)
- [Rod99] C. Rode and R. Ganni, *Handbook of Accelerator Physics and Engineering*, p. 322, Alexander Wu Chao & Maury Tigner, Editors, World Scientific, Singapore (1999)
- [Rod05] D. Rodriguez *et al.*, *Eur. Phys. J. A* 25, s01, 705 (2005)
- [Rom01] M.V. Romalis *et al.*, *Phys. Rev. Lett.* 86, 2505 (2001)
- [Ron05] R. Ronningen *et al.*, *Proc. of PAC*, Knoxville, TN, p. 3594 (2005)
- [Rop06] F.K. Roepke *et al.*, arXiv:astro-ph/0506107 (2006)
- [Rot91] I. Rotter, *Rep. Prog. Phys.* 54, 635 (1991)
- [Rot06] V. Rotival *et al.*, to be published
- [Rui06] C. Ruiz *et al.*, *Phys. Rev. Lett.* 96, 252501 (2006)
- [Rut97] K. Rutz *et al.*, *Phys. Rev. C* 56, 238 (1997)
- [Sag98] H. Sagawa *et al.*, *J. Phys. G* 24, 1445 (1998)
- [Sag01] H. Sagawa and K. Asahi, *Phys. Rev. C* 63, 064310 (2001)
- [Sag02] H. Sagawa, *Phys. Rev. C* 65, 064314 (2002)
- [Sag05] H. Sagawa, *Workshop on Nuclear Incompressibility and EOS*, Notre Dame University, 2005

-
- [Sak99] H. Sakurai *et al.*, Phys. Lett. B 448, 180 (1999)
[Sak00] A. Sakharuk and V. Zelevinsky, Phys. Rev. C 61, 014609 (2000)
[Sak06] H. Sakai, private communication
[Sam06] F. Sammruca, private communication
[San65] P.G. Sandars, Phys. Lett. 14, 194 (1965)
[San06] R. Sanchez *et al.*, Phys. Rev. Lett. 96, 033002 (2006)
[Sat99] K. Sato *et al.*, Nucl. Phys. A 654, 735c (1999)
[Sat01] W. Satula and R. Wyss, Phys. Rev. Lett. 87, 052504 (2001)
[Sat06] W. Satula *et al.*, Phys. Rev. C 74, 011301R (2006)
[Sav03] G. Savard *et al.*, Nucl. Instr. and Meth. B 204, 582 (2003)
[Sav05] G. Savard *et al.*, Phys. Rev. Lett. 95, 102501 (2005)
[Sch94] W.-D. Schmidt-Ott *et al.*, Z. Phys. A 350, 215 (1994)
[Sch98] H. Schatz *et al.*, Phys. Rep. 294, 167 (1998)
[Sch01] H. Schatz *et al.*, Phys. Rev. Lett. 86, 3471 (2001)
[Sch02] H. Schatz *et al.*, Ap. J. 579, 626 (2002)
[Sch03a] W.J. Schneider *et al.*, Proc. of PAC, Portland, OR, p. 2863 (2003)
[Sch03b] S. Schwarz *et al.*, Nucl. Instr. and Meth. B 204, 474 (2003)
[Sch04a] J.P. Schiffer *et al.*, Phys. Rev. Lett. 92, 162501 (2004)
[Sch04b] N. Schunck *et al.*, Phys. Rev. C 69, 061305R (2004)
[Sch06a] H. Schatz and K.E. Rehm, arXiv:astro-ph/0607624 (2006)
[Sch06b] H. Schatz, arXiv:astro-ph/0607625 (2006)
[Sch06c] F. Schümann, Phys. Rev. C 73, 015806 (2006)
[Sch06d] S. Schwarz *et al.*, to be published
[Sci04] N.D. Scielzo *et al.*, Phys. Rev. Lett. 93, 102501-1 (2004)
[Ser85] R. Servranckx *et al.*, SLAC Report 285, UC-28 (1985)
[Sev06] N. Severijns *et al.*, Rev. Mod. Phys. 78, 991 (2006)
[Sha90] I.S. Shapiro, Nucl. Phys. A 518, 73 (1990)
[Sha00] I.S. Shapiro *et al.*, Phys. At. Nuclei 63, 1533 (2000)
[She99] B.M. Sherrill *et al.*, Nucl. Instr. and Meth. A 432, 299 (1999)
[She02] J. Shergur *et al.*, Phys. Rev. C 65, 034313 (2002)
[She05] J.A. Sheikh *et al.*, Phys. Rev. C 72, 041301 (2005)
[Shi96] H. Shiomi, Nucl. Phys. A 603, 281 (1996)
[Shi03] L. Shi and P. Danielewicz, Phys. Rev. C 68, 064604 (2003)
[Sig74] P. Sigmund and K.B. Winterbon, Nucl. Instr. and Meth. 119, 541 (1974)
[Sig05] A.J. Signoracci, Research Experience for Undergraduate Report, MSU/NSCL 2005, B.A. Brown, private communication
[Sik03] G. Sikler *et al.*, Nucl. Instr. and Meth. B 204, 482 (2003)
[Sik05a] G. Sikler *et al.*, Nucl. Phys. A 763, 45 (2005)
[Sik05b] G. Sikler *et al.*, Eur. Phys. J. A 25, s01, 63 (2005)
[Sim88] L.M. Simons, Phys. Scrip. T 22, 90 (1988)
[Sim93] L.M. Simons, Hyperfine Int. 81, 253 (1993)
[Sim99] H. Simon *et al.*, Phys. Rev. Lett. 83, 496 (1999)
[Sin02] B. Singh *et al.*, Nuclear Data Sheets 97, 241 (2002)
[Smi98] J.F. Smith *et al.*, Phys. Rev. C 57, R1037 (1998)

-
- [Smo97] R. Smolanczuk, Phys. Rev. C 56, 812 (1997)
- [Sne03] C. Sneden *et al.*, Ap. J. 591, 936 (2003)
- [Son06] K. Sonnabend *et al.*, Eur. Phys. J. 27, 149 (2006)
- [Sok89] V.V. Sokolov and V.G. Zelevinsky, Nucl. Phys. A 504, 562 (1989)
- [Sok90] V.V. Sokolov and V.G. Zelevinsky, Fizika (Zagreb) 22, 303 (1990)
- [Sok92] V.V. Sokolov and V.G. Zelevinsky, Ann. Phys. 216, 323 (1992)
- [Sol04] T. Soldner *et al.*, Phys. Lett. B 581, 49 (2004)
- [Son00] A.A. Sonzogni *et al.*, Phys. Rev. Lett. 84, 1651 (2000)
- [Sor93] O. Sorlin *et al.*, Phys. Rev. C 47, 2941 (1993)
- [Sor03] O. Sorlin *et al.*, Eur. Phys. J. A 16, 55 (2003)
- [Spe97] V. Spevak *et al.*, Phys. Rev. C 56, 1357 (1997)
- [Sta72] S. Starrfield *et al.*, Ap. J. 176, 169 (1972)
- [Sta94] J. Staples, Proc. of LINAC, Tsukuba, Japan, p. 755 (1994);
Particle Accelerators 47, 191 (1994)
- [Sta99] S. Starrfield, Phys. Rep. 311, 371 (1999)
- [Sta01] K. Starosta *et al.*, Phys. Rev. Lett. 86, 971 (2001)
- [Ste05a] A.W. Steiner *et al.*, Phys. Rep. 411, 325 (2005)
- [Ste05b] J.W. Stetson *et al.*, Proc. of PAC, Knoxville, TN, p. 2281 (2005)
- [Ste06] W. Stein *et al.*, LLNL Report UCRL-TR-221121 (2006)
- [Sto03] M.V. Stoitsov *et al.*, Phys. Rev. C 68, 054312 (2003)
- [Sto05a] A. Stolz *et al.*, Phys. Lett. B 627, 32 (2005)
- [Sto05b] N.J. Stone *et al.*, Phys. Rev. Lett. 94, 192501 (2005)
- [Sto05c] A. Stolz *et al.*, Nucl. Instr. and Meth. B 241, 858 (2005)
- [Str03] T.E. Strohmayer and L. Bildsten, arXiv:astro-ph/0301544 (2003)
- [Str04] T.E. Strohmayer, arXiv:astro-ph/0401465 (2004)
- [Sug69] K. Sugimoto, Phys. Rev. 182, 1051 (1969)
- [Sum00] K. Sümmerer and B. Blank, Phys. Rev. C 61, 034607 (2000)
- [Sum06] C. Sumithrarachchi *et al.*, Phys. Rev. C 74, 024322 (2006)
- [Sur05] R. Surman and G.C. McLaughlin, Nucl. Phys. A 758, 189 (2005)
- [Suz90] Y. Suzuki *et al.*, Prog. Theor. Phys. 83, 180 (1990)
- [Suz95] T. Suzuki *et al.*, Phys. Rev. Lett. 75, 3241 (1995)
- [Tac90] T. Tachibana *et al.*, Prog. Theor. Phys. 84, 641 (1990)
- [Tak91] N. Takigawa and H. Sagawa, Phys. Lett. B 265, 23 (1991)
- [Tak94] K. Takahashi *et al.*, Astron. Astrophys. 286, 857 (1994)
- [Tak98] S. Takeuchi and M. Matsuda, Proc. of the 8th Workshop on RF
Superconductivity, Abano Terme, Italy (1997), Report LNL-INFN
133/98, p. 237 (1998)
- [Tak05] A. Takamine *et al.*, Rev. Sci. Instr. 76, 103503 (2005)
- [Tan95] I. Tanihata, Prog. Part. Nucl. Phys. 35, 505 (1995)
- [Tan06] S.K. Tandel *et al.*, Phys. Rev. Lett. 97, 082502 (2006)
- [Tar04] O.B. Tarasov and D. Bazin, Nucl. Phys. A 746, 411c (2004)
- [Ter02] J. Terasaki *et al.*, Phys. Rev. C 66, 054313 (2002)
- [Ter04] J.R. Terry *et al.*, Phys. Rev. C 69, 054306 (2004)
- [Ter06] J.R. Terry *et al.*, Phys. Lett. B 640, 86 (2006)
- [The98] L.-S. The *et al.*, Ap. J. 504, 500 (1998)

-
- [Thi75] C. Thibault *et al.*, Phys. Rev. C 12, 644 (1975)
[Thi04] F.-K. Thielemann *et al.*, New Astr. Rev. 48, 605 (2004)
[Tho99] M. Thoennessen *et al.*, Phys. Rev. C 59, 111 (1999)
[Tho04] M. Thoennessen, Rep. Prog. Phys. 67, 1187 (2004)
[Tho05] J.S. Thomas *et al.*, Phys. Rev. C 71, 021302R (2005)
[Tig94] R.J. Tighe *et al.*, Phys. Rev. C 49, R2871 (1994)
[Tim03] F.X. Timmes *et al.*, Ap. J. Lett. 590, L83 (2003)
[Tin90] G.M. Tino *et al.*, Phys. Rev. Lett. 64, 2999 (1990)
[Toh87] M. Tohyama, Phys. Rev. C 36, 187 (1987)
[Tom06] B.E. Tomlin, Ph.D. Thesis, Michigan State University (2006)
[Tos04] J.A. Tostevin *et al.*, Phys. Rev. C 70, 064602 (2004)
[Tos06] J.A. Tostevin and B.A. Brown, Phys. Rev. C, submitted for publication (2006)
[Tow04] D.M. Townsley and L. Bildsten, Ap. J. 600, 390 (2004)
[Tra04] C. Travaglio *et al.*, Ap. J. 601, 864 (2004)
[Tri04] W. Trimble *et al.*, Nucl. Phys. A 746, 415c (2004)
[Tru02] J.W. Truran *et al.*, Publ. Astr. Soc. Pac. 114, 1293 (2002)
[Try02] E. Tryggestad *et al.*, Phys. Lett. B 541, 52 (2002)
[Tsa01] M.B. Tsang *et al.*, Phys. Rev. Lett. 86, 5023 (2001)
[Tsa04] M.B. Tsang *et al.*, Phys. Rev. Lett. 92, 062701 (2004)
[Twi49] R.Q. Twiss and N.H. Frank, Rev. Sci. Instr. 20, 1 (1949)
[Twi86] P.J. Twin *et al.*, Phys. Rev. Lett. 57, 811 (1986)
[Uen04] H. Ueno *et al.*, Nucl. Phys. A 738, 211 (2004)
[Uen05] H. Ueno *et al.*, Phys. Lett. B 615, 186 (2005)
[Ume03] A. Umeya and K. Muto, Nucl. Phys. A 722, 558 (2003)
[Uts04] Y. Utsuno, Phys. Rev. C 70, 011303 (2004)
[Vam04] C. Vaman *et al.*, Phys. Rev. Lett. 92, 032501 (2004)
[Van02] E.V.D. van Loef *et al.*, Nucl. Instr. and Meth. A 486, 254 (2002)
[Van04] K.A. Van Riper, White Rock Science (2004)
[Var98] R.L. Varner *et al.*, AIP Conf. Proc. 455, 245 (1998)
[Var02] V. Variale *et al.*, PRAMANA J. Phys. 59, 765 (2002)
[Vit98] A. Vitturi, J. Phys. G 24, 1439 (1998)
[Vol01] A. Volya *et al.*, Phys. Lett. B 509, 37 (2001)
[Vol03a] A. Volya and V. Zelevinsky, Phys. Rev. C 67, 54322 (2003)
[Vol03b] A. Volya and V. Zelevinsky, Phys. Lett. B 574, 27 (2003)
[Vol05] A. Volya and V. Zelevinsky, Phys. Rev. Lett. 94, 052501 (2005)
[Vol06] A. Volya and V. Zelevinsky, Phys. Rev. C, accepted for publication (2006)
[Vor83] O.K. Vorov and V.G. Zelevinsky, Sov. J. Nucl. Phys. 37, 830 (1983);
Yad. Fiz. 37, 1392 (1983)
[Vor85] O.K. Vorov and V.G. Zelevinsky, Nucl. Phys. A 439, 207 (1985)
[Vre01] D. Vretenar *et al.*, Nucl. Phys. A 692, 496 (2001)
[Vre03] D. Vretenar *et al.*, Phys. Rev. Lett. 91, 262502 (2003)
[Wad94] R. Wadsworth *et al.*, Phys. Rev. C 50, 483 (1994)
[Wad03] M. Wade *et al.*, Nucl. Instr. and Meth. B 204, 570 (2003)

-
- [Wal81] R.K. Wallace and S.E. Woosley, *Ap. J. Suppl.* 45, 389 (1981)
- [Wal91] T.G. Walker, *Nucl. Instr. and Meth. B* 56, 521 (1991)
- [Wal05] R. Walder *et al.*, *Ap. J.* 626, 317 (2005)
- [Wan98] T. Wangler, *Principles of RF Linear Accelerators*, John Wiley & Sons, Inc. (1998)
- [War90] E.K. Warburton *et al.*, *Phys. Rev. C* 41, 1147 (1990)
- [War96] D. Ward *et al.*, *Nucl. Phys. A* 600, 88 (1996)
- [War03] D. Warner, *Nature* 425, 570 (2003)
- [War04] D. Warner, *Nature* 430, 517 (2004)
- [Wat06] A.L. Watts and T.E. Strohmayer, *arXiv:astro-ph/0512630* (2006)
- [Wei58] S. Weinberg, *Phys. Rev.* 112, 1375 (1958)
- [Wei00] H. Weick *et al.*, *Nucl. Instr. and Meth. B* 164-165, 168 (2000)
- [Wei04a] L. Weissman *et al.*, *Nucl. Instr. and Meth. A* 522, 212 (2004)
- [Wei04b] L. Weissman *et al.*, *Nucl. Instr. and Meth. A* 531, 416 (2004)
- [Wei04c] L. Weissman *et al.*, *Nucl. Phys. A* 746, 655c (2004)
- [Wei05a] H. Weick, GICOSY, private communication
- [Wei05b] L. Weissman *et al.*, *Nucl. Instr. and Meth. A* 540, 245 (2005)
- [Wei06] N.N. Weinberg *et al.*, *Ap. J.* 639, 1018 (2006)
- [Wen01] F. Wenander, PhD Thesis, Chalmers University of Technology, Gothenburg, Sweden 2001
- [Wen06] F. Wenander *et al.*, *Rev. Sci. Instr.* 77, 03B105 (2006)
- [Wie98] M. Wiescher *et al.*, *Phil. Trans. Roy. Soc. Lond.* 356, 2105 (1998)
- [Wie99a] I. Wiedenhöver *et al.*, *Phys. Rev. Lett.* 83, 2143 (1999)
- [Wie99b] M. Wiescher *et al.*, *J. Phys. G* 25, R133 (1999)
- [Wij04] R. Wijnands, *arXiv:astro-ph/0405089* (2004)
- [Wil00] D.H. Wilkinson, *Eur. Phys. J. A* 7, 307 (2000)
- [Woi98] O. Voitke *et al.*, *Phys. Rev. A* 57, 2692 (1998)
- [Wol87] H. Wollnik, *Optics of charged particles*, Academic Press, Inc., San Diego (1987)
- [Woo90] S.E. Woosley *et al.*, *Ap. J.* 356, 272 (1990)
- [Woo92] S.E. Woosley and R.D. Hoffman, *Ap. J.* 395, 202 (1992)
- [Woo97] C.S. Wood *et al.*, *Science* 275, 1759 (1997)
- [Woo04] S.E. Woosley *et al.*, *Ap. J. Suppl.* 151, 75 (2004)
- [Woo05] S. Woosley and T. Janka, *Nature Physics* 1, 147 (2005)
- [Wu04] X. Wu *et al.*, *Proc. of LINAC*, Lübeck, Germany, p. 594 (2004)
- [Wu05] X. Wu *et al.*, *Proc. of PAC*, Knoxville, TN, p. 1868 (2005)
- [Wuo04] A.H. Wuosmaa *et al.*, *Proposal to D.O.E., Nuclear Physics* (2004)
- [Wuo05a] A.H. Wuosmaa *et al.*, *Phys. Rev. Lett.* 94, 082502 (2005)
- [Wuo05b] A.H. Wuosmaa *et al.*, *Phys. Rev. C* 72, 061301R (2005)
- [Yak01] D.G. Yakovlev *et al.*, *Astron. Astrophys.* 379, L5 (2001)
- [Yak04] D.G. Yakovlev and C.J. Pethick, *Annu. Rev. Astron. Astrophys.* 42, 169 (2004)
- [Yak06] D. Yakovlev *et al.*, *MNRAS* 371, 1322 (2006)
- [Yam04] K. Yamada *et al.*, *Nucl. Phys. A* 746, 156c (2004)
- [Yan03] Y. Yanagisawa *et al.*, *Phys. Lett. B* 566, 84 (2003)

-
- 
- [Yao06] W.M. Yao *et al.*, J. Phys. G 33, 1 (2006)
[Yon06] K. Yoneda *et al.*, Phys. Rev. C 74, 021303 (2006)
[Yos04a] S. Yoshida and H. Sagawa, Phys. Rev. C 69, 024318 (2004)
[Yos04b] A. Yoshida *et al.*, Nucl. Instr. and Meth. A 521, 65 (2004)
[Yos06] S. Yoshida and H. Sagawa, Phys. Rev. C 73, 044320 (2006)
[You93] B.M. Young *et al.*, Phys. Rev. Lett. 71, 4124 (1993)
[You95] A.R. Young *et al.*, Phys. Rev. C 52, R464 (1995)
[You96] D.H. Youngblood *et al.*, Phys. Rev. Lett. 76, 1429 (1996)
[You97] D.H. Youngblood *et al.*, Phys. Rev. C 55, 2811 (1997)
[You99] D.H. Youngblood *et al.*, Phys. Rev. Lett. 82, 691 (1999)
[You05] L.M. Young *et al.*, LANL Report, LA-UR-96-1835, revised (2005)
[Yur04a] K.L. Yurkewicz *et al.*, Phys. Rev. C 70, 054319 (2004)
[Yur04b] K.L. Yurkewicz *et al.*, Phys. Rev. C 70, 034301 (2004)
[Zam02] N.V. Zamfir *et al.*, Phys. Rev. C 65, 044325 (2002)
[Zav05] P. Zavodszky *et al.*, Nucl. Instr. and Meth. B 241, 959 (2005)
[Zbe06] K. Zberecki *et al.*, arXiv:nucl-th/0604047 (2006)
[Zeg03] R.G.T. Zegers *et al.*, Phys. Rev. Lett. 90, 202501 (2003)
[Zeg05] R.G.T. Zegers *et al.*, Nucl. Phys. A 758, 6c (2005)
[Zeg06] R.G.T. Zegers *et al.*, Phys. Rev. C 74, 024309 (2006)
[Zel96a] V. Zelevinsky *et al.*, Phys. Rep. 276, 85 (1996)
[Zel96b] V. Zelevinsky, Annu. Rev. Nucl. Sci. 46, 237 (1996)
[Zel02] A.F. Zeller *et al.*, IEEE Trans. Applied Superconductivity 12, 329 (2002)
[Zel03] A.F. Zeller and J.C. DeKamp, Proc. of PAC, Portland, OR, p. 161 (2003)
[Zel04] V. Zelevinsky (ed.), Workshop on Nuclei and Mesoscopic Physics, East Lansing, 2004, AIP Conf. Proc. 777 (2005)
[Zel05a] A.F. Zeller *et al.*, IEEE Trans. Applied Superconductivity 15, 1181 (2005)
[Zel05b] A.F. Zeller, Topical Meeting on Insulation and Impregnation Techniques for Magnets, CERN (2005)
[Zel06a] V. Zelevinsky and A. Volya, AIP Conf. Proc. 819, 493 (2006)
[Zel06b] V. Zelevinsky and A. Volya, Proc. of the 11th Varenna Conference on Nuclear Reaction Mechanisms, Varenna, 2006, to be published
[Zha02] D.L. Zhang and Y.X. Liu, Phys. Rev. C 65, 057301 (2002)
[Zha04] Q. Zhao *et al.*, Proc. of ECRIS, Berkeley, CA (2004)
[Zhu05] S. Zhu *et al.*, Phys. Lett. B 618, 51 (2005)
[Zie04] J.F. Ziegler, Nucl. Instr. and Meth. B 219, 1027 (2004)
[Zuo02] W. Zuo *et al.*, Eur. Phys. J. A 14, 469 (2002)



Abbreviations

- A1200:** Fragment separator at the NSCL until 1999. The number 1200 refers to the maximum bending power of the device. The A stands for analysis.
- A1900:** Current NSCL fragment separator. The A stands for analysis.
- ALARA:** As low as reasonably achievable
- ALPI:** Superconducting booster linac at the Laboratori Nazionali di Legnaro, Italy
- ANC:** Asymptotic Normalization Coefficient
- ANL:** Argonne National Laboratory, Argonne, Illinois
- ARTEMIS:** Advanced Room Temperature Ion Source at the NSCL
- ATLAS:** Argonne Tandem-Linac Accelerator System
- ATOMKI:** Institute of Nuclear Research of the Hungarian Academy of Sciences, Debrecen, Hungary
- AURA:** Association of Universities for Research in Astronomy
- BCS:** Bardeen-Cooper-Schrieffer
- BeppoSAX:** Italian-Dutch X-ray Satellite
- BigRIPS:** Big RIKEN Projectile Fragment Separator
- BNL:** Brookhaven National Laboratory, Upton, New York
- BOE:** Basis of Estimate
- BPM:** Beam Position Monitor
- BRIC:** Breeding Ion Charge Experiment at INFN Bari, Italy
- BUU:** Boltzmann-Ühling-Uhlenbeck
- CCF:** Coupled Cyclotron Facility at the NSCL
- CEBAF:** Continuous Electron Beam Accelerator Facility at JLAB
- CERN:** European Organization for Nuclear Research
- CESR:** Cornell Electron Storage Ring at the Laboratory for Elementary-Particle Physics, Cornell University, Ithaca, New York
- CEU:** Conference Experience for Undergraduates
- Chandra:** Satellite X-ray Observatory
- CI:** Confidence Indicator
- CICC:** Cable in Conduit Conductor
- CKM:** Cabibbo-Kobayashi-Maskawa
- CP:** Product of Charge and Parity
- CPT:** Product of Charge, Parity, and Time
- CVC:** Conserved Vector Current
- cw:** continuous wave
- CXC:** Chandra X-ray Center
- dc:** direct current
- DOE:** Department of Energy
- DRAGON:** Detector of Recoils and Gammas of Nuclear Reactions at TRIUMF
- DWBA:** Distorted Wave Born Approximation
- EBIS:** Electron Beam Ion Source
- EBIT:** Electron Beam Ion Trap

EC: Electron Capture
ECR: Electron Cyclotron Resonance
ECRIS: Electron Cyclotron Resonance Ion Source
EDF: Energy Density Functional
EDM: Electric Dipole Moment
EOS: Equation of State
ESA: European Space Agency
EXOSAT: European Space Agency's X-ray Observatory
Fermilab: Fermi National Accelerator Laboratory, Batavia, Illinois
FNAL: Fermi National Accelerator Laboratory, Batavia, Illinois
FRDM: Finite Range Droplet Model
FRS: Fragment Separator at GSI
GANIL: Grand Accélérateur National d' Ions Lourds, Caen, France
GDM: Generator Driven Mode
GDR: Giant Dipole Resonance
GMR: Giant Monopole Resonance
GRETA: Gamma-Ray Energy Tracking Array
GRETINA: First stage of GRETA
GSI: Gesellschaft für Schwerionenforschung, Darmstadt, Germany
GT: Gamow-Teller
GXPf1: A shell model interaction
HAPPEX: Hall A Proton Parity Experiment at JLAB
HBF: Hartree-Fock-Bogoliubov
HELIOS: Helical Orbit Spectrometer proposed by Western Michigan University, Kalamazoo, Michigan
HEPA: High Efficiency Particulate Air
HERES: Hamburg/ESO r-process Enhanced Star Survey
Hfb9: A Skyrme Interaction
HRIBF: Holifield Radioactive Ion Beam Facility at ORNL
HTS: High Temperature Superconductor
IBM: Interacting Boson Model
IF: Intermediate Frequency
IH DTL: Interdigital H-type Drift Tube Linac
INFN: Istituto Nazionale di Fisica Nucleare, Italy
IP: Ionization Processes
ISAC: Isotope Separator and Accelerator at TRIUMF
ISF: Isotope Science Facility proposed at the NSCL
ISIS: Pulsed Neutron & Muon Source, Rutherford Appleton Laboratory, Chilton, UK
ISOL: Isotope Separation On-Line
ISOLDE: Isotope Separator On-Line at CERN, Geneva, Switzerland
IVSGMR: Isovector Spin Giant Monopole Resonance
JAERI: Japan Atomic Energy Research Institute, Kashiwa, Japan
JINA: Joint Institute for Nuclear Astrophysics

JLAB: Jefferson Laboratory or Thomas Jefferson National Accelerator Facility (TJNAF), Newport News, Virginia

K50, K100, K500, K1200: Cyclotron accelerators built at the NSCL

KB3G: A shell model interaction

KEK: National Laboratory for High Energy Physics, Tsukuba, Japan

KEK-B: An asymmetric electron positron collider for B physics at KEK

KVI: Kernfysisch Versneller Instituut, Groningen, The Netherlands

LBNL: Lawrence Berkeley National Laboratory, Berkeley, California

LCW: Low Conductivity Water

LEP: Large Electron and Positron Collider at CERN

LEBIT: Low Energy Beam and Ion Trap Facility at the NSCL

LEBT: Low Energy Beam Transport

linac: linear accelerator

LISE: Ligne d'Ions Super Epluchés at GANIL

LISE-3: LISE and Wien filter combination at GANIL

LISOL: Leuven Isotope Separator On-Line at Louvain-la-Neuve

LLNL: Lawrence Livermore National Laboratory, Livermore, California

LLRF: Low Level Radio Frequency

LNS: Laboratori Nazionali del Sud, Catania, Italy

LPC: Laboratoire de Physique Corpusculaire, Caen, France

LPSC: Laboratoire de Physique Subatomique et de Cosmologie, Grenoble, France

MAXEBIS: EBIS test setup at GSI

MAYA: Active gas target detector at GANIL

MEBT: Medium Energy Beam Transport

MHB: Mult-Harmonic Buncher

MIPP: Main Injector Particle Production at FNAL

MISTRAL: Mass Measurements at Isolde Using a Transmission Radiofrequency Spectrometer On-Line at ISOLDE/CERN

MoNA: Modular Neutron Array at the NSCL

MRI: Major Research Instrumentation Program funded by the NSF

MSU: Michigan State University, East Lansing, Michigan

MUSIC: Multiple Sampling Ion Chamber

NASA: National Aeronautics and Space Administration

NMR: Nuclear Magnetic Resonance

NQR: Nuclear Quadrupole Resonance

NSAC: Nuclear Science Advisory Committee

NSCL: National Superconducting Cyclotron Laboratory, East Lansing, Michigan

NSE: Nuclear Statistical Equilibrium

NSF: National Science Foundation

NuMI: Neutrinos at the Main Injector at FNAL

ORNL: Oak Ridge National Laboratory, Oak Ridge, Tennessee

QRPA: Quasiparticle Random Phase Approximation

PAC: Program Advisory Committee

PAN: Physics of the Atomic Nucleus, JINA outreach program at the NSCL
PET: Positron Emission Tomography
PHOENIX: Charge breeding ECRIS developed at the Institut des Sciences Nucléaires, Grenoble, France
PPARC: Particle Physics and Astronomy Research Council
PSI: Paul Scherrer Institut, Villigen, Switzerland
R&D: Research and Development
RDM: Recoil Distance Method
REU: Research Experience for Undergraduates
REX-ISOLDE: Radioactive beam Experiment (reaccelerator) at ISOLDE/CERN
rf: radio frequency
RFFS: Radio Frequency Fragment Separator
RFQ: Radio Frequency Quadrupole
RHIC: Relativistic Heavy Ion Collider at BNL
RIA: Rare Isotope Accelerator
RIAFRAG: DOE RIA Fragmentation proposal DE-FG02-04ER41313
RIAISOL: DOE RIA ISOL proposal DE-FG02-04ER41322
RIB: Radioactive Ion Beam
RIBF: Radioactive Ion Beam Factory at RIKEN
RIKEN: The Institute of Physical and Chemical Research, Wako, Japan
RIPS: Riken Projectile Fragment Separator
RLD: Rotating Liquid Drop
rms: root-mean-square
RPA: Random Phase Approximation
RRR: Residual Resistivity Ratio
RXTE: Rossi X-ray Timing Explorer
S800: S800 Spectrograph at the NSCL. The number 800 refers to the maximum bending power of the device. The S stands for spectrograph.
SAO: Smithsonian Astrophysical Observatory
SC: Superconducting
SCC: Second Class Current
SciDAC: Scientific Discovery through Advanced Computing
S-DALINAC: Superconducting Darmstadt LInear Accelerator, Darmstadt, Germany
SDPF-M: Shell model interaction
SDSS: Sloan Digital Sky Survey
SeGA: Segmented Germanium Array at the NSCL
SEGUE: Sloan Extension for Galactic Understanding and Exploration
SEL: Self Excited Loop
SHARAQ: Spectroscopy of Hadron Systems by Radioactive Quantum Beams planned for the RIBF/RIKEN
SHIPTRAP: Separator of Heavy Ion Reaction Products TRAP at GSI
Sly4, Skp, Skx: Skyrme interactions
SNS: Spallation Neutron Source at ORNL

SPES: Study and Production of Exotic Species at INFN Legnaro, Italy
SRF: Superconducting Radio Frequency
STAR: Solenoidal Tracker at RHIC
STScI: Space Telescope Science Institute
SuperFRS: Super Fragment Separator at GSI
SuSI: Superconducting Source for Ions at the NSCL
SUSY: Supersymmetry
TAS: Total Absorption Spectroscopy
TDPAD: Time Dependent Perturbed Angular Distribution
TITAN: TRIUMF's Ion Trap Facility for Atomic and Nuclear Science
TOF: Time of Flight
TEC: Total Estimated Cost
TPC: Total Project Cost
TPC: Time Projection Chamber
TRIUMF: TRI-University Meson Facility, Vancouver, Canada
TRI μ P: Trapped Radioactive Atoms, μ -Laboratories for Fundamental Physics at KVI
UNEDF: Universal Nuclear Energy Density Functional
USD: Shell model interaction
VCX: Voltage Controlled Reactance
VENUS: Versatile ECR ion source for Nuclear Science at LBNL
VLT: The Very Large Telescope Project, European Southern Observatory, Garching, Germany
WBS: Work Breakdown Structure
WITCH: Weak Interaction Trap for Charged Particles at ISOLDE/CERN
XMM-Newton: X-ray Multi-Mirror Newton, orbiting X-ray observatory